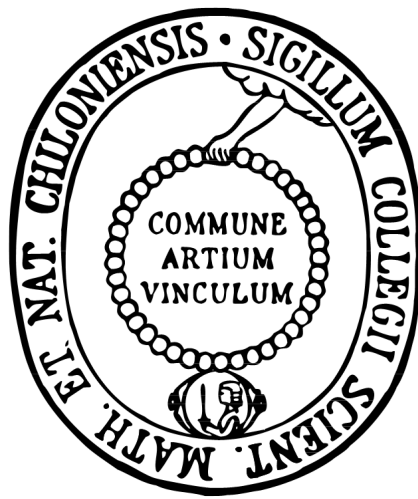# The Uniform Electron Gas at Warm Dense Matter Conditions

A Permutation Blocking Path Integral Monte Carlo Perspective

Tobias Dornheim

Institut für Theoretische Physik und Astrophysik

Christian-Albrechts-Universität zu Kiel

This dissertation is submitted for the degree of

Doctor Rerum Naturalium

January 2018

1st supervisor: Prof. Dr. Michael Bonitz

2nd supervisor:

The repetitive epic is the most elegant form of Cardassian literature ...

Elim Garak
(Star Trek: Deep Space Nine)

Abstract

This thesis is devoted to the *ab initio* path integral Monte Carlo (PIMC) simulation of electrons at finite temperature. The antisymmetry of fermions with respect to exchange is the origin of the notorious *fermion sign problem* (FSP). In particular, the FSP leads to an exponential increase in computation time both with system size and inverse temperature and prohibits standard PIMC simulations when fermionic exchange effects become important.

The first major goal of this thesis is the development and implementation of a new approach—the *permutation blocking* PIMC (PB-PIMC) method—that is substantially less affected by the FSP at medium to strong degeneracy. The basic idea is given by the combination of antisymmetric imaginary-time propagators (determinants) with a fourth-order factorization of the density matrix and a novel Monte Carlo sampling algorithm.

As a first test bed, electrons in a $2D$ harmonic trap are considered, since the PB-PIMC results can be compared to exact reference data both from standard PIMC (strong coupling) and configuration PIMC (CPIMC, weak nonideality). It is demonstrated that PB-PIMC significantly extends standard PIMC towards stronger degeneracy and allows for the computation of highly accurate data for conditions where no other *ab initio* quantum Monte Carlo (QMC) simulations are feasible.

The second major goal of this thesis is the description of the uniform electron gas (UEG) at warm dense matter (WDM) conditions, i.e., at extreme density and temperature. For this purpose, PB-PIMC is extended to the simulation of periodic systems and, again, proofs to be a substantial improvement with respect to standard PIMC. It is shown that the combination of PB-PIMC with the complementary CPIMC approach—which does not have a sign problem for the ideal system, but breaks down with increasing coupling strength—makes it possible to carry out *ab initio* QMC simulations of the warm dense UEG over the entire density range.

To extrapolate the QMC data for the finite model system to the thermodynamic limit, a new finite-size correction, which is based on a combination of QMC data with the long-range behavior from linear response theory, is presented and shown to be accurate within the full scope of WDM. This allows to obtain extensive results for the interaction energy of the UEG for a broad range of densities, temperature, and spin polarizations, with an unprecedented accuracy of the order of 0.3%. Subsequently, these data are used as input for the construction

of a complete parametrization of the exchange–correlation (XC) free energy, f_{xc}, over the entire WDM regime.

This XC-functional constitutes the capstone of the present thesis and provides a complete thermodynamic description of the UEG. In addition to its expected utility as input for thermal density functional theory, astrophysical models, and beyond, it allows to assess the accuracy of previous approximations. In particular, comparisons to, e.g., linear response theory, the finite-temperature Green function method, and PIMC calculations in the fixed-node approximation are presented in detail.

Finally, the possibility to compute *ab initio* results for the static density response function of the UEG by extending PB-PIMC to the simulation of the harmonically perturbed system is outlined, motivated and demonstrated. The thesis is concluded with a brief outlook to the reconstruction of the dynamic structure factor of the UEG from PIMC results for an imaginary-time correlation function.

Kurzfassung

Die folgende Arbeit ist der *ab initio* Pfadintegral Monte-Carlo (PIMC) Simulation von Elektronen bei endlicher Temperatur gewidmet. Die Antisymmetrie von Fermionen bezüglich Vertauschens ist die Ursache des berüchtigten *fermionischen Vorzeichenproblems* (FVP). Insbesondere führt das FVP zu einem exponentiellen Anstieg in der Rechenzeit sowohl mit der Systemgröße, als auch mit der inversen Temperatur, und verhindert Standard-PIMC Simulationen sobald fermionische Austauscheffekte wichtig werden.

Das erste Hauptziel dieser Arbeit ist die Entwicklung und Implementierung eines neuen Zugangs—der *permutation blocking* PIMC (PB-PIMC) Methode—welche bei mittlerer bis starker Entartung deutlich weniger vom FVP beeinträchtigt ist. Die Grundidee besteht in der Kombination von anti-symmetrischen imaginär-zeitigen Propagatoren (Determinanten) mit einer Faktorisierung der Dichtematrix in vierter Ordnung, und einem neuartigen Monte-Carlo Sampling-Algorithmus.

Als erstes Testumfeld werden Elektronen in einer zwei-dimensionalen harmonischen Falle betrachtet, da die PB-PIMC Ergebnisse hier mit exakten Referenzdaten von Standard-PIMC (starke Kopplung) und Configuration PIMC (CPIMC, schwache Nicht-Idealität) verglichen werden können. Es wird gezeigt, dass PB-PIMC den Standard-PIMC Zugang hin zu deutlich größerer Entartung erweitert, und die Berechnung hochakkurater Daten für Parameterbereiche erlaubt, welche für kein anderes Quanten-Monte-Carlo (QMC) Verfahren zugänglich sind.

Das zweite Hauptziel dieser Arbeit ist die Beschreibung des homogenen Elektronengases (HEG) unter Bedingungen der warmen dichten Materie (WDM), das heißt, bei extremen Dichten und Temperaturen. Zu diesem Zweck wird PB-PIMC für die Simulation periodischer Systeme erweitert, und es wird erneut eine substantielle Verbesserung im Vergleich zu Standard-PIMC gefunden. Es wird gezeigt, dass die Kombination von PB-PIMC mit dem komplementären CPIMC Zugang—welcher kein Vorzeichenproblem für das ideale System aufweist, aber mit zunehmender Kopplungsstärke versagt—die Durchführung von *ab initio* QMC-Simulationen des warmen dichten HEGs über den gesamten Dichtebereich ermöglicht.

Um die QMC-Daten für endliche Modellsysteme zum thermodynamischen Limes zu extrapolieren, wird eine neue *Finite-Size*-Korrektur präsentiert, welche auf einer Kombination

der QMC-Daten mit dem langreichweitigen Verhalten der *Linear-Response*-Theorie basiert, und über den gesamten WDM-Parameterbereich akkurat ist. Dies ermöglicht die Berechnung umfangreicher Ergebnisse für die Wechselwirkungs-Energie des HEGs über einen weiten Bereich von Dichten, Temperaturen, und Spin-Polarisierungen, mit einer zuvor unerreichten Genauigkeit in der Größenordnung von 0.3%. Anschließend werden diese Daten als Input für die Konstruktion einer vollständigen Parametrisierung der freien Austausch-Korrelations Energie, f_{xc}, verwendet, welche den gesamten WDM-Bereich abdeckt.

Dieses Austausch-Korrelations-Funktional stellt das krönende Ergebnis der vorliegenden Arbeit dar und bietet eine vollständige thermodynamische Beschreibung des HEGs. Zusätzlich zu dem erwarteten Nutzen als Input für beispielsweise die thermische Dichtefunktionaltheorie und astrophysikalische Modelle, ermöglicht dies die Beurteilung der Genauigkeit früherer Näherungen. Insbesondere werden detaillierte Vergleiche zu, unter anderem, der *Linear-Response*-Theorie, der thermischen Green-Funktions Methode, und PIMC-Rechnungen unter der Näherung fixierter Knotenflächen präsentiert.

Schließlich wird die Möglichkeit zur Berechnung von *ab initio* Ergebnissen für die statische Antwortfunktion des HEGs unter Erweiterung des PB-PIMC Zugangs zur Simulation des harmonisch gestörten Systems skizziert, motiviert, und demonstriert. Die Arbeit wird mit einem knappen Ausblick über die Rekonstruktion des dynamischen Strukturfaktors des HEGs ausgehend von PIMC Ergebnissen für eine imaginärzeitige Korrelationsfunktion abgeschlossen.

Table of contents

Chapter 1

Introduction

The raison d'être of modern computational physics is the numerical solution of the well-known, but highly complex equations that describe the universe around us. This is necessary since, in Paul Dirac's words [1], "*the fundamental laws necessary for the mathematical treatment of a large part of physics and the whole of chemistry are thus completely known, and the difficulty lies only in the fact that application of these laws leads to equations that are too complex to be solved.*"

No less than Richard Feynman picked up this challenge and outlined two completely different strategies forward: (i) the construction of a quantum-simulator [2], or general quantum computer [3, 4], that uses the intrinsically quantum mechanical nature of our world to compute properties of specific materials (thereby providing a solution to, e.g., the Schrödinger equation without having to do the math), and (ii) the mapping of a complicated quantum system onto an ensemble of classical ring-polymers via the path integral formalism [5, 6].

Despite the paradigm changing nature of the first idea and its many theoretical advantages[1], the field of quantum computation still remains in its infancy [10] and various practical challenges prevent the large-scale application to realistic many-body problems, see, e.g., Ref. [11]. Hence, the present work is devoted to Feynman's second idea, i.e., the formulation of thermodynamic expectation values as high-dimensional integrals in the imaginary-time path integral formalism [12]. Since the high dimensionality quickly renders standard quadrature methods impractical, one usually makes use of stochastic integration methods, which, remarkably, are almost completely unaffected by this problem [13, 14]. Here, *stochastic* implies the use of random numbers, hence the umbrella term *Monte Carlo* methods [15].

In particular, the utilization of the Metropolis Monte Carlo algorithm [16–18] within the imaginary-time path integral formulation is the basic idea of the highly successful

---

[1]Of particular relevance in the context of the present work is the absence both of the fermion sign problem [7, 8], and the dynamical sign problem in time-dependent quantum Monte Carlo simulations [9].

path integral Monte Carlo (PIMC) method [19–21]. Since its first applications to the simulation of ^{4}He in the 1960s [22, 23], PIMC has been of fundamental importance for the investigation of many exciting physical effects such as superfluidity [24–28], Bose–Einstein condensation [29, 30] and collective excitations [31–34]. Moreover, recent advances in Monte Carlo sampling techniques [35, 36] now allow for quasi-exact[2] simulations of up to $N \sim 10^4$ bosons (such as ^{4}He) or boltzmannons (distinguishable particles, e.g., Refs. [37, 38]).

Unfortunately, for the even more important case of fermions (such as electrons, in which I am interested in this work), the situation turns out to be entirely different. The antisymmetry of the fermionic density matrix with respect to pair exchange requires a complete summation over all $N!$ possible permutations (with N being the number of fermions from the same particle species, e.g., spin-up electrons), where each term has either a negative or positive sign, depending on the parity of a particular permutation [5]. This can result in an almost complete cancellation of different contributions, which, ultimately, might lead to a vanishing signal-to-noise ratio. This is the origin of the notorious *fermion sign problem* (FSP) [39, 40], which causes an exponential increase in the computation time both with system size N and also with inverse temperature $\beta = 1/k_\mathrm{B}T$ (with T and k_B denoting temperature, and Boltzmann constant, respectively). Further, I mention that the FSP in Metropolis Monte Carlo simulations has been shown to even be *NP*-hard for certain types of Hamiltonians [40].

In practice, the FSP prevents standard PIMC simulations of fermions at strong degeneracy, i.e., towards low temperature and weak coupling [41–43]. More specifically, this eliminates the possibility of PIMC simulations of electrons at warm dense matter (WDM, see Sec. 1.2) conditions, and overcoming this obstacle constitutes a central goal of the present work.

1.1   Path Integral Monte Carlo Simulation of Fermions

Being inspired by the success of the fixed-node approximation [44, 45] in ground-state quantum Monte Carlo (QMC) simulations [46, 47], Ceperley introduced an extension of this idea to finite temperature [48, 49], often denoted as restricted PIMC (RPIMC). The basic idea is to use the nodes of the fermionic density matrix to recast the partition function into a sum that only contains positive terms. While being formally exact[3], the required complete knowledge of the nodal structure is equivalent to a solution of the full many-body problem, thereby rendering the RPIMC calculation obsolete. Therefore, in practice, one uses approximate *trial nodes*—typically those of the ideal density matrix. In a nutshell, RPIMC

---

[2]Here, *quasi-exact* means that the exact result is recovered in the limit of infinitely many Monte Carlo steps, or, equivalently, that the statistical uncertainty can be made arbitrarily small.

[3]Note that the formally exact nature of RPIMC was disputed by Filinov [50, 51].

allows for fermionic QMC simulations without a sign problem at arbitrary degeneracy[4], but this comes at the cost of an uncontrolled approximation[5] such that the quasi-exact *ab initio* character of standard PIMC is lost. Nevertheless, RPIMC has been applied to the simulation of many realistic warm dense matter applications, e.g., Refs. [53–58], which makes a critical assessment of the nodal error highly desirable[6].

A different strategy to at least mitigate the FSP is given by the introduction of anti-symmetric imaginary-time propagators, i.e., determinants [41, 60–62]. This allows one to combine permutations of different signs into a single term (often denoted as *blocking*), so that a substantial part of the cancellation is carried out before the Monte Carlo evaluation. The thus achieved reduction of the FSP has successfully been exploited within the fermionic PIMC simulations of numerous systems by Filinov and co-workers, see, e.g., Refs. [63–71].

Unfortunately, as I will demonstrate in this work, there is a major problem with this approach. With increasing quantum degeneracy, i.e., towards low temperature and weak coupling, one either looses the benefits from the determinants or the quasi-exact nature of the PIMC methods. This is particularly disadvantageous, as the FSP is most severe precisely in this regime. This problem is solved by the new *permutation blocking* PIMC (PB-PIMC) approach [72], the development, implementation, and benchmarking of which constitutes the first central achievement of my thesis (see Sec. 3.1).

A detailed overview over different thermodynamic QMC methods for the simulation of fermions, including the configuration PIMC (CPIMC) approach that has been developed in our group [73–76] and has played an important role for the development of PB-PIMC [72, 77], can be found in Chpt. 2.

1.2 The Uniform Electron Gas at Warm Dense Matter Conditions

Over the last decade, there has been remarkable progress in the investigation of so-called warm dense matter [78, 79], which is of high relevance for, e.g., astrophysical objects such as brown and white dwarfs [80–84], giant planets [85–88], and meteor impacts [83]. Moreover, WDM plays an important role in inertial confinement fusion research [89–91], see Chpt. 2 for an extensive overview. From an experimental point of view, WDM conditions are now

---

[4]Note that, in practice, the *reference point freezing* problem [52] might prevent RPIMC simulations at low temperature and high density, see Chpt. 2 for more details.

[5]In the ground state, the nodes are variational with respect to the energy E, which can be exploited for optimization. At finite temperature, the same is true only for the free energy F, a quantity that is not easily accessible within a PIMC simulation and requires an additional coupling constant integration [52], see Sec.6.2.

[6]This was first achieved in 2015 by Schoof *et al.* [59] using the recent Configuration PIMC method.

routinely investigated at large research centers such as the national ignition facility (NIF) [92], the Linac Coherent Light Source (LCLS) [93–95], or the European X-FEL (i.e., free electron laser) near Hamburg [96, 97]. This extreme state (i.e., high temperature and density) is typically characterized by two parameters being of the order of unity: the Brückner parameter (also known as Wigner–Seitz radius) $r_s = (4\pi n/3)^{-1/3}$ and the degeneracy temperature[7] $\theta = k_B T/E_F$, with E_F denoting the Fermi energy. A thorough theoretical description of WDM is highly nontrivial [79] as it must incorporate the intricate interplay of (i) fermionic exchange, (ii) long-range Coulomb coupling, and (iii) thermal excitation effects. Since *ab initio* quantum Monte Carlo simulations of realistic warm dense matter applications are severely limited by the fermion sign problem, the combination of a density functional theory (DFT) treatment of the electrons with a classical molecular dynamics (MD) simulation for the heavier (and, thus, often classically treated) ions constitutes the working horse in this field [99–103]. More specifically, for each MD-step of the ions, a thermal DFT calculation [104–106] of the electronic sub-system, which is subject to the attractive Coulomb potential of the ions, is carried out.

The basic idea of density functional theory is to map the nonideal many-body system of interest onto an effective single-particle problem, which leads to a great reduction in computational cost. At finite temperature, the total free energy is expressed as a functional of the electronic density n as [107]

$$F[n] = K_0[n] - T S_0[n] + F_H[n] + F_{xc}[n] \quad , \tag{1.1}$$

where K_0 and S_0 correspond to the ideal (i.e., non-interacting) kinetic energy and entropy, F_H to the mean field Coulomb contribution, and F_{xc} to the exchange–correlation free energy. The task at hand for the DFT simulation[8] is then to find the particular electronic density that minimizes $F[n]$. While the first three terms on the rhs. of Eq. (1.1) are known, the exact knowledge of $F_{xc}[n]$ would presuppose the solution of the full many-body problem so that nothing was gained. Therefore, the quality of the DFT results crucially depends on the accuracy of the employed approximation for F_{xc}, which must be supplied as input in advance.

In the ground state, a major step towards the arguably unrivaled success of DFT simulations [108–110] is the so-called *local density approximation* (LDA), where the exchange–correlation energy of the inhomogeneous system of interest is locally approximated by the

---

[7]Note that θ is related to the usual degeneracy parameter, $\chi = n\lambda_\beta^3$, with $\lambda_\beta = \sqrt{2\pi\beta}$ being the thermal wavelength (in atomic units), by $\theta = 4\pi/(3\pi^2)^{2/3}\chi^{-2/3}$, see, e.g., Ref. [98].

[8]Note that for $T = 0$, the minimization is carried out with respect to the total energy $E[n]$ and the entropic contribution vanishes.

value for a uniform electron gas[9] (UEG) of the same density, $E_{xc}^{UEG}[n]$. Therefore, the LDA requires accurate knowledge of the exchange–correlation energy of the UEG over the entire relevant density range. This was achieved in the beginning of the 1980s, when Ceperley and Alder [111] employed ground-state QMC calculations to obtain the energy, which was subsequently used as input for parametrizations, most notably by Vosko *et al.* [112] and Perdew and Zunger [113]. In addition, these parametrizations form the basis of the more sophisticated generalized gradient approximations, with the Perdew–Burke–Ernzerhof (PBE) functional [114] being one of the most highly cited works in physics[10].

Naturally, at warm dense matter conditions the use of ground-state exchange–correlation functionals is often not appropriate [115–117]. To carry over the success of ground-state DFT—starting with LDA—to finite temperature [118], we require a parametrization of the exchange–correlation free energy of the UEG with respect to both density and temperature[11], which, in turn, depends on accurate simulation data for the warm dense electron gas. While there have long existed many results based on various uncontrolled approximations [107, 119–128] (see Ref. [129] for a recent overview), their respective accuracy has remained unclear.

In the present work, we[12] apply the new PB-PIMC method—in combination with CPIMC, which is used at strong degeneracy and weak coupling—to the simulation of the warm dense UEG (Chpt. 4) and derive a highly accurate extrapolation to the thermodynamic limit (finite-size correction, see Sec. 5.1). The final construction of a complete parametrization[13] of $f_{xc}(r_s, \theta, \xi)$ with respect to density (r_s), temperature (θ), and spin-polarization (ξ) that covers the entire WDM regime and is based on our extensive new *ab initio* data constitutes the capstone of this thesis (Sec. 6.2). This allows us to assess the accuracy of previous approximations, and we find systematic errors of $\Delta f_{xc} \sim 1 - 10\%$ in all parametrizations.

Although the importance of DFT for modern many-body theory can hardly be overstated, it should be noted that the accurate description of the UEG is of high importance for many other applications. In the ground state, it has facilitated key insights such as Fermi-liquid theory [130, 131], the quasi-particle picture of collective excitations [132, 133], and the Bardeen–Cooper–Schrieffer (BCS) theory of superconductivity [134]. Moreover, the UEG is often employed as a simple model for conducting electrons in alkali metals [131, 135]

---

[9]The uniform electron gas is given by an infinite system of Coulomb interacting electrons in a positive neutralizing background, see Chpt. 2 for a detailed introduction.

[10]In December 2017, scholar.google.com lists over 79.000 citations for PBE [114], and over 13.900 citations for the ground-state QMC study by Ceperley and Alder [111].

[11]A third variable is the spin-polarization $\xi = |N^\uparrow - N^\downarrow|/(N^\uparrow + N^\downarrow)$, which is necessary for DFT calculations in the local spin-density approximation [107].

[12]As a rule of thumb, the usage of *I* refers strictly to my own work, whereas *we* indicates the collaboration with my co-workers.

[13]Note that lower case letters denote energies per particle, i.e., $f_{xc} = F_{xc}/N$.

(especially Na [136]) and qualitatively reproduces phenomena such as Wigner crystallization [137–139] and a spin-polarization transition [140].

Similarly, at warm dense matter conditions the thermodynamic description of the UEG (i.e., the parametrization of f_{xc}) is of high importance as input for, e.g., quantum hydrodynamics [141, 142] and astrophysical models [143–145], or for the further development of Fermi-liquid theory [146].

In addition, the UEG is frequently employed as a test bed for the development of many-body simulation methods, e.g., Refs. [147–156]. Thus, the extensive new QMC data for various quantities and the parametrization of $f_{xc}(r_s, \theta, \xi)$ that are presented within this work will also be valuable as a benchmark for the future development of methods. Moreover, these new results put us in the unique position to gauge the accuracy of various previous approximations such as RPIMC [157], dielectric methods (linear response theory) [158, 126, 128], and finite-temperature Green functions [155, 159, 160, 59], which is presented in detail in Chpt. 2.

1.3 Outline: How to read this Thesis

The present work is a cumulative thesis and contains all my publications that are of relevance to it (see Sec. 1.3.1 for a complete list). To increase the readability and provide a golden thread, I decided against a chronological order and, instead, grouped together different papers that are devoted to a similar topic. Chapter 2 contains an extensive review article of the UEG at WDM conditions, Ref. [161], and can be read from cover to cover to get a complete overview of our work and key results, including the state of the art when we entered the field, the development of new QMC methods, the construction of the parametrization of f_{xc}, the extensive comparison to various different approximations, and more. All subsequent sections can be viewed as an appendix to Chpt. 2, and contain the various publications in which we investigated in more technical detail the separate aspects of our work, such as the development of PB-PIMC and its first application to the UEG. Each of these sections is accompanied by a brief introduction that outlines the specific tasks that are addressed in the corresponding papers, and puts them into the broader context of this thesis.

- **Chapter 2: The Uniform Electron Gas at Warm Dense Matter Conditions**
  An extensive review [161] of the uniform electron gas at warm dense matter conditions. Provides a concise overview of WDM applications and the corresponding system parameters and a comprehensive discussion of previous works in the field. All our key results are presented in detail and compared to other theories and approximations.

- **Chapter 3: Method Development**
  Motivation for and situation during the development of the PB-PIMC approach, and its first application to electrons in a $2D$ harmonic confinement, Ref. [72]. Implementation of a new *center-two particle correlation function* and proof of concept regarding future investigations in this direction, Ref. [38]. First application of PB-PIMC to the warm dense UEG, comparison to CPIMC and RPIMC, and demonstration of the complementary nature to the former, Ref. [77].

- **Chapter 4: Combination of PB-PIMC and CPIMC**
  Combination of PB-PIMC (at stronger coupling) and CPIMC (at higher degeneracy) to achieve an accurate description of the warm dense UEG over the entire density range, both for the spin-polarized (Ref. [162]) and unpolarized (Ref. [163]) case.

- **Chapter 5: Finite-Size Corrections, Static Structure Factors and Pair Correlation Functions**
  Discussion of the extrapolation of QMC data for a finite number of electrons to the thermodynamic limit[14] and derivation of a new, improved finite-size correction, Ref. [164]. Presentation of extensive results for the static structure factor, Ref. [165], and discussion of the pair-correlation functions, including a comparison to dielectric approximations (Sec. 5.2.1). Road map towards the construction of a full parametrization of $f_{xc}(r_s, \theta, \xi)$, Ref. [42].

- **Chapter 6: Parametrization of the Exchange–Correlation Free Energy**
  Overview of existing parametrizations of f_{xc}, including a detailed discussion of their respective construction and range of applicability, Ref. [129]. Presentation of our new, highly accurate parametrization of $f_{xc}(r_s, \theta, \xi)$ based on our *ab initio* QMC data, Ref. [166]. Comparison against previous results and presentation of consistency-checks.

- **Chapter 7: The Inhomogeneous Electron Gas**
  Discussion of the extension of our QMC methods to the simulation of the harmonically perturbed electron gas to compute the static density response function and local-field correction. Proofs of principle are given regarding both PB-PIMC, Ref. [167], and CPIMC, Ref. [168].

- **Chapter 8: Other Works**
  Collection of further publications that are of relevance to this thesis, in particular the

---

[14]I.e., to the limit of an infinite amount of electrons, at a constant density.

construction of ion–ion potentials on the basis of the static density response of the UEG, Ref. [169], and a brief review of various aspects of the recent research initiative *SFB-TR24* including a juxtaposition of the UEG with the classical one-component plasma, Ref. [98].

- **Chapter 9: Summary and Outlook**
  Summary and discussion of the present results regarding both the development of the PB-PIMC method and the accurate description of the warm dense UEG. Concise overview of possible future applications of PB-PIMC and discussion of the utility of the UEG results both as input for, e.g., DFT or quantum hydrodynamics, as benchmark for method development, and beyond. Finally, the feasibility to obtain the dynamic structure factor of the UEG on the basis of *ab initio* PIMC simulations is demonstrated and motivated (Sec. 9.2.3).

1.3.1   List of related Publications

The following list contains all publications that are included in this work. To increase the transparency, for each paper I explicitly state my contribution to it. Moreover, as a result of the close collaboration with S. Groth (SG), there are six publications with equal contributions from SG and the me (TD). In the following, these articles are indicated by the green font of the author names.

1. **T. Dornheim**, S. Groth, A. Filinov and M. Bonitz, Permutation blocking path integral Monte Carlo: a highly efficient approach to the simulation of strongly degenerate non-ideal fermions, *New J. Phys.* **17**, 073017 (2015)

   - TD contributed 85% to this work by developing and implementing the permutation blocking PIMC algorithm, and carrying out all simulations. In addition, TD wrote the entire manuscript, and created all figures. The paper is included on p. 134.

2. **T. Dornheim**, T. Schoof, S. Groth, A. Filinov, and M. Bonitz, Permutation blocking path integral Monte Carlo approach to the uniform electron gas at finite temperature, *J. Chem. Phys.* **143**, 204101 (2015)

   - TD contributed 80% by extending the PB-PIMC algorithm to the simulation of the electron gas and carrying out all calculations. Further, TD wrote the entire manuscript and created all figures except Fig. 1. The paper is included on p. 165.

3. **T. Dornheim**, H. Thomsen, P. Ludwig, A. Filinov, and M. Bonitz, Analyzing Quantum Correlations Made Simple, *Contrib. Plasma Phys.* **56**, 371 (2016)

   - TD contributed 50% to this work by implementing a new correlation function into the PB-PIMC algorithm, and carrying out all calculations. In addition, TD wrote substantial parts of the text. The paper is included on p. 154.

4. S. Groth, T. Schoof, **T. Dornheim**, and M. Bonitz, *Ab Initio* quantum Monte Carlo simulations of the uniform electron gas without fixed nodes, *Phys. Rev. B* **93**, 085102 (2016)

   - TD contributed 20% to this work by carrying out all PB-PIMC calculations. Moreover, TD wrote the PB-PIMC specific section of the text and worked on the rest of the manuscript. The paper is included on p. 174.

5. **T. Dornheim**, S. Groth, T. Schoof, C. Hann, and M. Bonitz, *Ab initio* quantum Monte Carlo simulations of the uniform electron gas without fixed nodes: The unpolarized case, *Phys. Rev. B* **93**, 205134 (2016)

   - TD contributed 45% by further developing the PB-PIMC method to allow for simulations of the unpolarized electron gas and carrying out all PB-PIMC simulations. In addition, TD wrote half of the manuscript, in particular the PB-PIMC specific parts. The paper is included on p. 187.

6. **T. Dornheim**, S. Groth, T. Sjostrom, F.D. Malone, W.M.C. Foulkes, and M. Bonitz, *Ab Initio* Quantum Monte Carlo Simulation of the Warm Dense Electron Gas in the Thermodynamic Limit, *Phys. Rev. Lett.* **117**, 156403 (2016)

   - TD contributed 45% by carrying out all PB-PIMC simulations, writing substantial parts of the manuscript and creating all figures. The central idea for the finite-size correction was worked out in equal parts by TD and SG. The paper is included on p. 205.

7. S. Groth, **T. Dornheim**, and M. Bonitz, Free energy of the uniform electron gas: Testing analytical models against first-principles results, *Contrib. Plasma Phys.* **57**, 137 (2017)

   - TD contributed 45% by writing substantial parts of the text. The paper is included on p. 243.

8. **<u>T. Dornheim</u>**, S. Groth, F.D. Malone, T. Schoof, T. Sjostrom, W.M.C. Foulkes, and M. Bonitz, *Ab initio* quantum Monte Carlo simulation of the warm dense electron gas, *Phys. Plasmas* **24**, 056303 (2017)

   - TD contributed 45% by writing substantial parts of the manuscript and by creating three of the figures. The paper is included on p. 231.

9. S. Groth, **<u>T. Dornheim</u>**, T. Sjostrom, F.D. Malone, W.M.C. Foulkes, and M. Bonitz, *Ab initio* Exchange–Correlation Free Energy of the Uniform Electron Gas at Warm Dense Matter Conditions, *Phys. Rev. Lett.* **119**, 135001 (2017)

   - TD contributed 45% by carrying out all PB-PIMC calculations and writing substantial parts of the text. The central ideas needed for the parametrization of the exchange–correlation free energy were worked out in equal parts by TD and SG. The paper is included on p. 255.

10. **<u>T. Dornheim</u>**, S. Groth, J. Vorberger, and M. Bonitz, Permutation-blocking path-integral Monte Carlo approach to the static density response of the warm dense electron gas, *Phys. Rev. E* **96**, 023203 (2017)

    - TD contributed 80% to this work by extending the PB-PIMC algorithm to the harmonically perturbed electron gas, implementing the related observables, and carrying out all simulations. Further, the entire text and all figures have been produced by TD. The paper is included on p. 271.

11. S. Groth, **<u>T. Dornheim</u>**, and M. Bonitz, Configuration path integral Monte Carlo approach to the static density response of the warm dense electron gas, *J. Chem. Phys.* **147**, 164108 (2017)

    - TD contributed 15% to this work by providing PB-PIMC benchmark results and partly working on the theory regarding the finite-size correction. The paper is included on p. 286.

12. **<u>T. Dornheim</u>**, S. Groth, and M. Bonitz, Ab initio results for the static structure factor of the warm dense electron gas, *Contrib. Plasma Phys.* **57**, 468 (2017)

    - TD contributed 80% to this work by performing the spline interpolations, writing the bulk of the manuscript and creating all figures. The paper is included on p. 216.

13. Zh.A. Moldabekov, S. Groth, **T. Dornheim**, M. Bonitz, and T.S. Ramazanov, Ion potential in non-ideal dense quantum plasmas, *Contrib. Plasma Phys.* **57**, 532 (2017)

    - TD contributed 10% to this work by working on the text, in particular the linear response theory section. The paper is not included as a full text version in this work.

14. T. Ott, H. Thomsen, J. Abraham, **T. Dornheim**, and M. Bonitz, Recent progress in the theory and simulation of strongly correlated plasmas: phase transitions, transport, quantum, and magnetic field effect, accepted for publication in *Eur. Phys. J. D*

    - TD contributed 10% to this work by writing the PB-PIMC specific parts of the text and providing references. The paper is not included as a full text version in this work.

15. **T. Dornheim**, S. Groth, and M. Bonitz, The Uniform Electron Gas at Warm Dense Matter Conditions, *arXiv:1801.05783*, submitted as an invited article to Phys. Rep. (2018)

    - This review was written in equal parts by SG (45%) and me (45%). It constitutes the centerpiece of both our PhD theses and is included on p. 14 (Chpt. 2). To provide maximum transparency, a detailed breakdown of our respective contributions to the different chapters is listed in the following:

        - **1. Introduction:** SG and TD contributed equally.
        - **2. Important quantities and definitions:** SG and TD contributed equally.
        - **3. Dielectric Approximations and Linear Response Theory:** written by SG.
        - **4. Other Approximate Approaches:** written by SG (20%, half of Sec. 4.1) and TD (80%, Sec. 4.2 and half of Sec. 4.1)
        - **5. Quantum Monte Carlo Methods:** SG wrote the CPIMC section (25%), and TD the rest (75%).
        - **6. Finite-Size Correction of QMC Data:** written by TD .
        - **7. Benchmarks of other methods:** written by TD.
        - **8. Parametrizations of the XC Free Energy:** written by SG .
        - **9. Inhomogeneous Electron Gas: QMC study of the density response:** SG wrote Sec. 9.3.2 (33%), and TD the rest (67%).
        - **10. Summary and Outlook:** SG and TD contributed equally.

Chapter 2

The Uniform Electron Gas at Warm Dense Matter Conditions

Our recently published highly accurate parametrization of the exchange–correlation free energy over the entire warm dense matter regime [166] allows for the computation of all other thermodynamic quantities of the uniform electron gas. The following review, Ref. [161], aims to bring the ongoing investigation of the static properties of the UEG to a conclusion.

In addition to a broad motivation and a concise overview of the state of the art in the field, we provide an extensive discussion of the most important theoretical methods, including all approaches that are of relevance to the present work. In particular, we discuss in detail the dielectric formalism (linear response theory, p. 10 et seq. in Ref. [161]) and different approximation schemes for the static local field correction such as the Singwi–Tosi–Land–Sjölander (STLS) approach that is of high importance both for the finite-size correction of QMC data (see Sec. 5.1) and for the construction of the parametrization of the exchange–correlation free energy f_{xc} (see Sec. 6.2). Moreover, we provide an extensive yet accessible discussion of fermionic QMC simulations at finite temperature (p. 18 et seq. in Ref. [161]). In particular, the ubiquitous path integral Monte Carlo method is introduced (p. 19 et seq.) and the fermion sign problem is discussed. To avoid the FSP, we employ two complementary methods, namely the PB-PIMC approach (p. 26 et seq. in Ref. [161]) that was developed in the present thesis and the CPIMC method by Schoof and co-workers (p. 31 et seq.).

Further, we address the extrapolation of QMC data to the thermodynamic limit (p. 45 et seq. in Ref. [161]) and provide extensive comparisons of our new *ab initio* data for various quantities to other approximations (p. 52 et seq. in Ref. [161]).

Of particular importance is the discussion of the exchange–correlation free energy (p. 59 et seq. in Ref. [161]), where we present the construction of our new parametrization and gauge the accuracy of previous approximate results. Finally, we outline the possibility to use

QMC simulations of the inhomogeneous electron gas to obtain accurate results for the static density response of the UEG (p. 74 et seq. in Ref. [161]).

In a nutshell, Ref. [161] contains all our key results regarding the warm dense UEG and can be read from cover to cover to get a comprehensive overview of the present thesis.

The Uniform Electron Gas at Warm Dense Matter Conditions

Tobias Dornheim†, Simon Groth†, Michael Bonitz

† *These authors contributed equally to this work.*
Institut für Theoretische Physik und Astrophysik, Christian-Albrechts-Universität zu Kiel, Leibnizstr. 15, 24098 Kiel, Germany

Abstract

Motivated by the current high interest in the field of warm dense matter research, in this article we review the uniform electron gas (UEG) at finite temperature and over a broad density range relevant for warm dense matter applications. We provide an exhaustive overview of different simulation techniques, focusing on recent developments in the dielectric formalism (linear response theory) and quantum Monte Carlo (QMC) methods. Our primary focus is on two novel QMC methods that have recently allowed us to achieve breakthroughs in the thermodynamics of the warm dense electron gas: Permutation blocking path integral MC (PB-PIMC) and configuration path integral MC (CPIMC). In fact, a combination of PB-PIMC and CPIMC has allowed for a highly accurate description of the warm dense UEG over a broad density-temperature range. We are able to effectively avoid the notorious fermion sign problem, without invoking uncontrolled approximations such as the fixed node approximation. Furthermore, a new finite-size correction scheme is presented that makes it possible to treat the UEG in the thermodynamic limit without loss of accuracy. In addition, we in detail discuss the construction of a parametrization of the exchange-correlation free energy, on the basis of these data – the central thermodynamic quantity that provides a complete description of the UEG and is of crucial importance as input for the simulation of real warm dense matter applications, e.g., via thermal density functional theory.

A second major aspect of this review is the use of our *ab inito* simulation results to test previous theories, including restricted PIMC, finite-temperature Green functions, the classical mapping by Perrot and Dharma-wardana, and various dielectric methods such as the random phase approximation, or the Singwi-Tosi-Land-Sjölander (both in the static and quantum versions), Vashishta-Singwi and the recent Tanaka scheme for the local field correction. Thus, for the first time, thorough benchmarks of the accuracy of important approximation schemes regarding various quantities such as different energies, in particular the exchange-correlation free energy, and the static structure factor, are possible. In the final part of this paper, we outline a way how to rigorously extend our QMC studies to the inhomogeneous electron gas. We present first *ab initio* data for the static density response and for the static local field correction.

Keywords: `elsarticle.cls`, LATEX, Elsevier, template
2010 MSC: 00-01, 99-00

Contents

1. Introduction

1.1. The uniform electron gas at zero temperature

The uniform electron gas (UEG), often referred to as "jellium", is one of the most important model systems in physics and quantum chemistry, and consists of Coulomb interacting electrons in a positive neutralizing background [1]. Therefore, it constitutes the quantum mechanical analogue of the classical one-component plasma (OCP) [2] and qualitatively reproduces many physical phenomena [3] such as Wigner crystallization, spin-polarization transitions, and screening. Often, it is used as a simple model system for conducting electrons in alkali metals [1, 4]. The investigation of the UEG at zero temperature has lead to several key insights, like the BCS theory of superconductivity [5], Fermi liquid theory [6, 1], and the quasi-particle picture of collective excitations [7, 8]. Further, as a continuous correlated electronic quantum system, it has served as a workbench for the development of countless computational many-body methods, most prominently dielectric approximations, e.g., Refs. [8, 9, 10, 11, 12, 13, 14] and quantum Monte Carlo (QMC) methods [15, 16, 17, 18, 19, 20, 21, 22]. Even though the UEG itself does not represent a real physical system, its accurate description has been of paramount importance for the unrivaled success of density functional theory (DFT) [23, 24], the working horse of modern many-body simulations of realistic materials in solid state physics, quantum chemistry, and beyond [25, 26, 27]. Within the DFT framework, the complicated interacting many-electron system is mapped onto an effective one-particle (non-interacting) system via the introduction of an effective potential containing all exchange and correlation effects. While exact knowledge of the latter would require a complete solution of the many-body problem so that nothing was gained, it can often be accurately approximated by the exchange-correlation energy of the UEG, using a parametrization in dependence of density [28, 29, 30].

The first accurate data of the ferromagnetic and paramagnetic UEG were obtained in 1980 by Ceperley and Alder [16], who carried out ground state QMC simulations (see Ref. [17] for a review) covering a wide range of densities. Subsequently, these data were used as input for parametrizations, most notably by Vosko *et al.* [28] and Perdew and Zunger [29]. Since then, these seminal works have been used thousands of times for DFT calculations in the local (spin-)density approximation (L(S)DA) and as the basis for more sophisticated gradient approximations, e.g., Refs. [31, 32]. Note that, in the mean time, there have been carried out more sophisticated QMC simulations [33, 34, 35, 36, 37, 38], with Spink *et al.* [38] providing the most accurate energies available.

In addition to the exchange-correlation energy, there exist many parametrizations of other quantities on the basis of QMC simulations such as pair distribution functions and static structure factors [39, 40, 41, 42] and the momentum distribution [34, 35, 43, 44, 45, 46, 47, 48, 49, 50, 51, 52, 53, 54]. Finally, we mention the QMC investigation of the inhomogeneous electron gas [55, 56, 57, 58, 59], which gives important insights into the density response formalism, see Sec. 9 for more details.

1.2. Warm dense matter

Over the last decades, there has emerged a growing interest in the properties of matter under extreme conditions, i.e., at high temperature and densities exceeding those in solids by several orders of magnitude. This exotic state
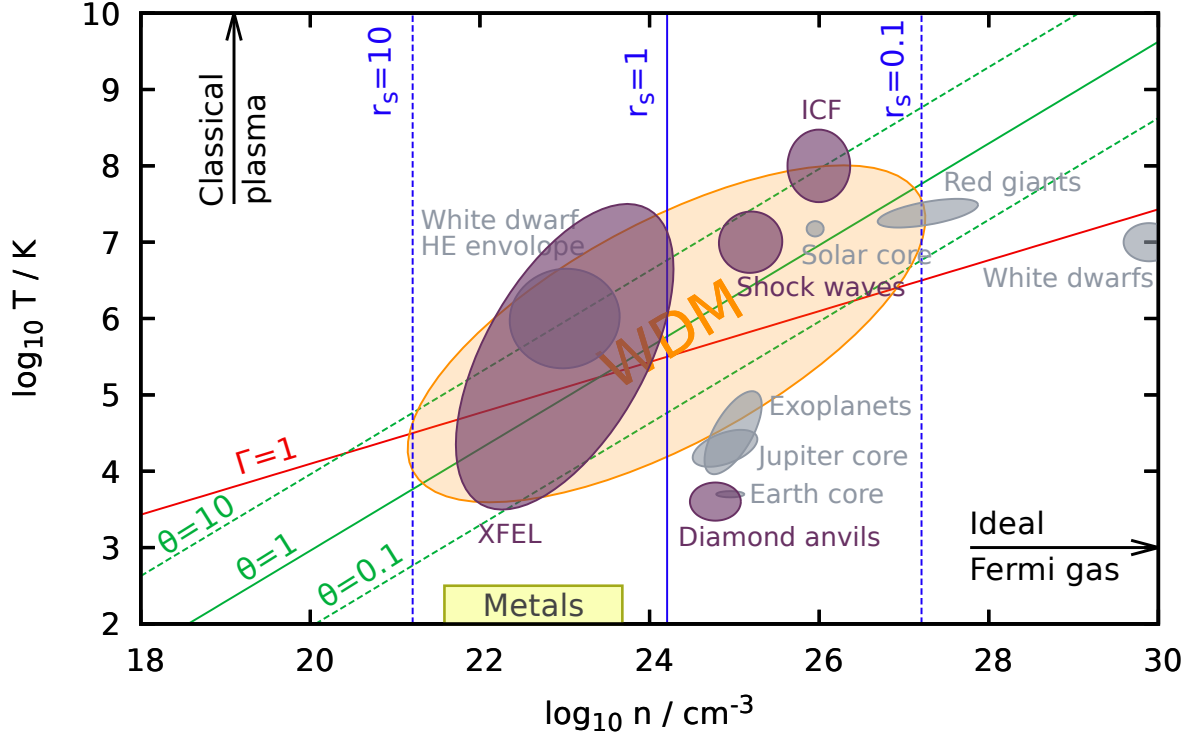
Figure 1: Temperature-density plane around the warm dense matter (WDM, orange) regime – Shown are lines of constant density parameter r_s (blue) and reduced temperature θ (green). Purple and grey bubbles schematically sketch experimental and astrophysical applications, respectively. The various parameter ranges have been taken from Refs. [60, 61].

is usually referred to as *warm dense matter* (WDM) and is characterized by two parameters being of the order of unity: (i) the density parameter (Wigner-Seitz radius) r_s, and (ii) the reduced temperature θ

$$r_s\, a_{\mathrm{B}} = \left(\frac{3}{4\pi n}\right)^{1/3} \quad , \quad \theta = \frac{k_{\mathrm{B}}T}{E_{\mathrm{F}}} \quad , \tag{1}$$

with E_{F} being the Fermi energy defined in Eq. (5). Here r_s plays the role of a quantum coupling parameter: at high density ($r_s \to 0$), the electrons behave as an ideal Fermi gas and towards low density, the Coulomb repulsion predominates, eventually leading to a Wigner crystal [62, 63, 64, 37]. Further, θ can be understood as the quantum degeneracy parameter, where $\theta \gg 1$ indicates a classical system (typically characterized by the classical coupling parameter $\Gamma = 1/(r_s a_{\mathrm{B}} k_{\mathrm{B}} T)$, cf. the red line in Fig. 1); for an overview on Coulomb correlation effects in classical systems, see ref. [65]. On the other hand, the case $\theta \lesssim 1$ characterizes a strongly degenerate quantum system. Thus, in the WDM regime, Coulomb coupling correlations, thermal excitations, and fermionic exchange effects are equally important at the same time. Naturally, this makes an accurate theoretical description of such systems most challenging [66].

In nature, WDM occurs in astrophysical objects such as giant planet interiors [67, 68, 69, 70, 71, 72, 73, 74, 75, 76, 77], brown and white dwarfs [78, 79, 80, 81, 82] and neutron star crusts [83], see Refs. [60, 84] for a recent review. Further areas of interest contain the physics of meteor impacts [81] and nuclear stewardship [85]. Another highly important aspect of warm dense matter research is the concept of inertial confinement fusion [86, 87, 88, 89, 90, 91], which could become a potentially nearly infinite source of clean energy in the future.

WDM conditions are now routinely realized at large research facilities such as the national ignition facility (NIF) at Lawrence Livermore National Lab, California [92, 93], the Z-machine at the Sandia National Labs in New Mexico [94, 95, 96, 97, 98], the Linac Coherent Light Source (LCLS) in Stanford, California [99, 100, 101], FLASH and the European X-FEL (free electron laser) in Hamburg, Germany [102, 103] and other laser and free electron laser laboratories. Moreover, we mention shock-compression experiments, e.g. [104, 105, 95]. Of particular importance is X-ray Thomson scattering (XRTS), e.g. Refs. [106, 107, 108, 109, 110, 102, 111], which provides a widespread diagnostics for warm dense matter experiments, see Ref. [112] for a review. More specifically, it allows for the direct measurement of the dynamic structure factor, which can subsequently be used to obtain, for example, the temperature [112]. Finally, we stress that WDM experiments allow for the investigation of many other quantities, such as the dielectric function [113, 114], electrical and thermal conductivities [115, 116, 117, 118], the

electron-ion temperature equilibration [119] and even the formation of transient nonequilibrium states [120, 117]. As a schematic overview, in Fig. 1 various important applications are depicted in the density-temperature plane around the warm dense matter regime. For a recent text book overview we refer to [121].

Despite the remarkable experimental progress, a thorough theoretical description of warm dense matter is still lacking (even in the case of thermodynamic equilibrium), and it is well-known that simple analytic models do not sufficiently reproduce experimental measurements [122, 123]. Naturally, an exact quantum mechanical treatment that incorporates all correlation and excitation effects is not feasible. Unfortunately, quantum Monte Carlo methods which often allow for accurate results in the ground state are not straightforwardly extended to the simulation of fermionic matter at finite temperature. More specifically, exact fermionic path integral Monte Carlo (PIMC) simulations (see Sec. 5.2) are severely hampered by the so-called fermion sign problem; nevertheless, there has been made some progress in direct fermionic QMC simulations by Filinov and co-workers [124, 125, 126, 127, 128, 129, 130, 131, 132]. To avoid the fermion sign problem, usually the fixed node approximation is utilized [133, 134, 135] (also "Restricted PIMC", RPIMC, see Sec. 5.3) breaks down at low temperature and high density. Therefore, RPIMC is not available over substantial parts of the warm dense regime, and the accuracy is, in general, unknown.

The probably most widespread simulation technique for warm dense matter is the combination of molecular dynamics (for the heavy ions) with a thermal density functional theory description of the electrons [136, 137, 138], usually denoted as DFT-MD [139, 140, 141, 142, 143]. Naturally, the decoupling of the ionic and electronic systems according to the Born-Oppenheimer approximation might not be appropriate in all situations. In addition, similar to the ground state, the accuracy of the DFT calculation itself strongly relies on the specific choice of the exchange-correlation functional [144, 145]. An additional obstacle for thermal DFT calculations is the explicit dependence of the exchange-correlation functional on temperature [146, 147], a topic which has only recently attracted serious attention, but might be crucial to achieve real predictive capability [66, 148]. Even worse, at moderate to high temperature, the usual thermal Kohn-Sham (KS) treatment of DFT becomes unfeasible, due to the increasing number of orbitals necessary to reach convergence. For this reason, Militzer and co-workers have proposed to combine RPIMC at high temperature with DFT elsewhere, and successfully applied this idea to the simulations of many different materials at warm dense matter conditions [149, 150, 151, 152, 153, 154]. A possible extension of KS-DFT towards stronger excitations is given by the so-called orbital free (OF) DFT [155, 156, 157, 158, 159, 160], where the total electronic density is not represented by Kohn-Sham orbitals. While being computationally cheap and, in principle, still exact, in practice orbital free DFT relies on an approximation for the ideal part of the (free) energy [161], whereas the latter is treated exactly within KS-DFT. Since the ideal part usually constitutes the largest contribution, it is widely agreed that OF-DFT does not provide sufficient accuracy, and, therefore, cannot give a suitable description of warm dense matter [160]. A recent, more promising, strategy to extend KS-DFT towards higher temperature has been introduced by Zhang and co-workers, see Refs. [162, 160, 163] for details.

On the other hand, even at relatively low temperature, when the electrons are in the ground state, a DFT description for the electronic component is often not sufficient [144, 145]. For this reason, Ceperley, Pierleoni and co-workers proposed to combine a classical Monte Carlo (instead of MD) for the heavy ions, with highly accurate ground-state QMC calculations for the electrons. This so-called coupled electron-ion QMC (CEIMC) method [164, 165, 166, 167] has subsequently been applied, e.g., to the (controversially discussed, see also the recent experiments in Ref. [168]) liquid-liquid phase transition in hydrogen [169, 170]. Note that, within the CEIMC approach, quantum effects of the ions can easily be included, e.g., Refs. [170]. In a similar spirit, Sorella and co-workers [171, 172, 173, 174, 175, 176] introduced a combination of electronic ground state QMC calculations with classical MD for the ions, although, to our knowledge, no consensus with CEIMC (and, for that matter, with DFT-MD) simulations has been reached so far regarding liquid hydrogen.

In addition, there has been remarkable recent progress in the development of real time-dependent DFT calculations [177, 178, 179, 180], which would also give direct access to the dynamic properties of the electrons, although this topic remains in its infancy due to the high computational cost of accurate exchange correlation functionals.

Finally, we mention the possiblity of so-called quantum-classical mappings employed by Dharma-wardana *et al.* [181, 182, 183, 184], where the complicated quantum mechanical system of interest is mapped onto a classical model system with an effective "quantum temperature", see Sec. 4.2 for more details.

1.3. The warm dense electron gas

Of particular interest for the theoretical description of WDM are the properties of the warm dense uniform electron gas. As mentioned above, an accurate parametrization of the exchange-correlation free energy with respect to temperature θ, density r_s, and spin-polarization ξ is of paramount importance for thermal DFT simulation both in the local (spin) density approximation or as a basis for more sophisticated gradient approximations [185, 32]. Further, direct applications of such a functional include astrophysical models [186, 187, 188, 189, 190, 191], quantum

hydrodynamics [192, 193, 194], and the benchmark for approximations, such as finite-temperature Green function methods [195, 196], for a recent study see Ref. [197].

However, even the description of this simple model system, without an explicit treatment of the ionic component, has turned out to be surprisingly difficult. Throughout the eighties of the last century, Ebeling and co-workers [198, 199, 200, 201, 202] proposed various interpolations between different known limits (i.e., high temperature, weak coupling, and the ground state). A more sophisticated approach is given by the dielectric formalism, which, at finite temperature, has been extensively developed and applied to the UEG by Ichimaru, Tanaka, and co-workers, see Refs. [203, 204, 205, 206, 207, 208]. For a more comprehensive discussion of recent improvements in this field, see Sec. 3. In addition, we mention the classical-mapping based scheme by Perrot and Dharma-wardana [209, 210], the application of which is discussed in Sec. 4.2.1. Unfortunately, all aforementioned results contain uncontrolled approximations and systematic errors of varying degrees, so that their respective accuracy has remained unclear.

While, in principle, thermodynamic QMC methods allow for a potentially exact description, their application to the warm dense UEG has long been prevented by the so-called fermion sign problem, see Sec. 5. For this reason, the first QMC results for this system were obtained by Brown *et al.* [211] in 2013 by employing the fixed node approximation (i.e., RPIMC). While this strategy allows for QMC simulations without a sign problem, this comes at the cost of the exact ab-initio character and it has been shown that results for different thermodynamic quantities are not consistent [212]. Nevertheless, these data have subsequently been used as the basis for various parametrization [213, 212, 214].

This overall unsatisfactory situation has sparked remarkable recent progress in the field of fermionic QMC simulations of the UEG at finite temperature. The first new development in this direction has been the configuration path integral Monte Carlo method (CPIMC, see Sec. 5.5), which, in contrast to standard PIMC, is formulated in second quantization with respect to plane waves, and has been developed by Schoof, Groth and co-workers [215, 216, 217]. In principle, CPIMC can be viewed as performing a Monte Carlo simulation on the exact, infinite perturbation expansion around the ideal system. Therefore, it excels at high density and strong degeneracy, but breaks down around $r_s \sim 1$ and, thus, exhibits a complementary nature with respect to standard PIMC in coordinate space. Surprisingly, the comparison of exact CPIMC data [218] for $N = 33$ spin-polarized electrons with the RPIMC data by Brown *et al.* [211] revealed systematic deviations exceeding 10% towards low temperature and high density, thereby highlighting the need for further improved simulations. Therefore, Dornheim and co-workers [219, 220] introduced the so-called permutation blocking PIMC (PB-PIMC, see Sec. 5.4) paradigm, which significantly extends standard PIMC both towards lower temperature and higher density. In combination, CPIMC and PB-PIMC allow for an accurate description of the UEG over the entire density range down to half the Fermi temperature [217, 221]. Soon thereafter, these results were fully confirmed by a third independent method. This density matrix QMC (DMQMC, see Sec. 5.6) [222, 223, 224] is akin to CPIMC by being formulated in Fock space. Hence, there has emerged a consensus regarding the description of the electron gas with a finite number of particles [225]. The next logical step is the extrapolation to the thermodynamic limit, i.e., to the infinite system at a constant density, see Sec. 6. As it turned out, the extrapolation scheme utilized by Brown *et al.* [211] is not appropriate over substantial parts of the warm dense regime. Therefore, Dornheim, Groth and co-workers [221, 226] have developed an improved formalism that allows to approach the thermodynamic limit without the loss of accuracy over the entire density-temperature plane.

Finally, these first *ab initio* results have very recently been used by the same authors to construct a highly accurate parametrization of the exchange-correlation free energy of the UEG covering the entire WDM regime [227], see Sec. 8. Thereby, a complete thermodynamic description of the uniform electron gas at warm dense matter conditions has been achieved.

1.4. Outline of this article

- In Sec. 2, we start by providing some important definitions and physical quantities that are of high relevance for the warm dense UEG. Further, we discuss the jellium Hamiltonian for a finite number of electrons in a box with periodic boundary conditions, and the corresponding Ewald summation.

- In Sec. 3, we give an exhaustive introduction to the dielectric formalism within the density-density linear response theory and its application to the uniform electron gas, both in the ground state and at finite temperature. Particular emphasis is put on the STLS approach, which is extensively used throughout this work. Most importantly, it is a crucial ingredient for the accurate extrapolation of QMC data to the thermodynamic limit, see Sec. 6. In addition, we summarize all relevant equations that are required for the implementation and numerical evaluation of various dielectric approximations.

- In Sec. 4, we briefly discuss other approximate methods that have been applied to the warm dense UEG. This includes the finite-temperature Green function approach, as well as two different classical mapping formalisms.

- In Sec. 5, we provide an all-encompassing discussion of the application of quantum Monte Carlo methods to the uniform electron gas at warm dense matter conditions. We start with a brief problem statement regarding the calculation of thermodynamic expectation values in statistical physics. The solution is given by the famous Metropolis algorithm, which constitutes the backbone of most finite-temperature quantum Monte Carlo methods (Sec. 5.1). Undoubtedly, the most successful among these is the path integral Monte Carlo method (Sec. 5.2), which, unfortunately, breaks down for electrons in the warm dense matter regime due to the notorious fermion sign problem (Sec. 5.2.3). Two possible workarounds are given by our novel permutation blocking PIMC (Sec. 5.4) and configuration PIMC (Sec. 5.5) methods, which we both introduce in detail. Further mentioned are the approximate restricted PIMC method (Sec. 5.3) and the recent independent density matrix QMC approach (Sec. 5.6). The section is concluded with a thorough comparison between results for different quantities by all of these methods for a finite number of electrons (Sec. 5.7).

- In Sec. 6, we discuss the extrapolation of QMC data that has been obtained for a finite number of electrons to the thermodynamic limit. A brief introduction and problem statement (Sec. 6.1) is followed by an exhaustive discussion of the theory of finite-size effects (Sec. 6.2). Due to the demonstrated failure of pre-existing extrapolation schemes, in Sec. 6.3 we present our improved finite-size correction and subsequently illustrate its utility over the entire warm dense matter regime (Sec. 6.4).

- In Sec. 7, we use our new data for the thermodynamic limit to gauge the accuracy of the most important existing approaches, both for the interaction energy and the static structure factor.

- In Sec. 8, we give a concise introduction (Sec. 8.1) of the state of the art of parametrizations of the exchange-correlation energy of the warm dense uniform electron gas, and of their respective construction (Sec. 8.2). Particular emphasis is put on the parametrization of the spin-dependence, Sec. 8.3. Finally, we provide exhaustive comparisons (Sec. 8.4) of f_{xc} itself, and of derived quantities, which allows us to gauge the accuracy of the most widely used functionals.

- In Sec. 9, we extend our QMC simulations to the inhomogenous electron gas. This allows us to obtain highly accurate results for the static density response function and the corresponding local field correction (Sec. 9.1). As a demonstration, we give two practical examples at strong coupling using PB-PIMC (Sec. 9.3.1) and at intermediate coupling using CPIMC (Sec. 9.3.2). Further, we employ our parametrization of f_{xc} to compute the long-range asymptotic behavior of the local field correction via the compressibility sum-rule and find excellent agreement to our QMC results.

- In Sec. 10, we provide a summary and give an outlook about future tasks and open questions regarding the warm dense electron gas.

2. Important quantities and definitions

2.1. Basic parameters of the warm dense UEG

In the following, we introduce the most important parameters and quantities regarding the warm dense electron gas. Observe, that Hartree atomic units are assumed throughout this work, unless explicitly stated otherwise. Of high importance is the above mentioned density parameter (often denoted as Wigner-Seitz radius, or Brueckner parameter)

$$r_s = \left(\frac{3}{4\pi n}\right)^{1/3} \quad , \tag{2}$$

which is independent of temperature and spin-polarization and solely depends on the combined density of both spin-up and -down electrons, $n = n^\uparrow + n^\downarrow$. The spin-polarization parameter ξ is defined as

$$\xi = \frac{n^\uparrow - n^\downarrow}{n} \in [0, 1] \quad , \tag{3}$$

where it is implicitly assumed that $n^\uparrow \geq n^\downarrow$. Thus, $\xi = 0$ corresponds to the unpolarized (paramagnetic) case, whereas $\xi = 1$ is being referred to as the spin-polarized (ferromagnetic) case. For completeness, we mention that r_s and ξ are sufficient to fully determine the thermodynamics of the UEG in the ground state. At warm dense matter

conditions, we also require information about the temperature, usually characterized by the quantum degeneracy parameter

$$\theta = \frac{k_\mathrm{B} T}{E_\mathrm{F}} \quad , \tag{4}$$

with

$$E_\mathrm{F} = \frac{(k_\mathrm{F}^\uparrow)^2}{2} \tag{5}$$

denoting the Fermi energy. Observe that we always define E_F with respect to the Fermi wave vector of the spin-up electrons,

$$k_\mathrm{F}^\uparrow = (6\pi^2 n^\uparrow)^{1/3} \quad . \tag{6}$$

Hence, for an ideal electron gas at zero temperature E_F defines the maximum energy of the occupied one-particle orbitals. Note that in the relevant literature, there exists another possible definition of E_F, where the Fermi wave vector is computed with respect to the total electron density, i.e., using $k_\mathrm{F} = (3\pi^2 n)^{1/3}$ in Eq. (4).

The warm dense matter regime, to which the present work is devoted, is roughly characterized by $0.1 \leq r_s \leq 10$ and $0 \leq \theta \leq 10$.

2.2. The Jellium Hamiltonian: Coordinate representation

The description of an infinite system based on a quantum Monte Carlo simulation of a finite number of electrons N in a finite simulation box with volume $V = L^3$ is usually realized by making use of periodic boundary conditions. In addition to the Coulomb interaction of the electrons in the simulation cell, one also includes the interaction with all electrons in the infinitely many images (the same applies to the positive homogeneous background). Unfortunately, such an infinite sum with diverging positive and negative terms is only conditionally convergent, i.e., the result depends on the ordering of the terms and is not well defined [228]. In practice, one usually employs the Ewald summation technique (see Ref. [229] for a recent accessible discussion), which corresponds to the solution of Poisson's equation in periodic boundary conditions [230, 231]. The full Hamiltonian is then given by

$$\hat{H} = -\frac{1}{2} \sum_{i=1}^{N} \nabla_i^2 + \sum_{i=1}^{N} \sum_{k>i}^{N} W_\mathrm{E}(\mathbf{r}_i, \mathbf{r}_k) + \frac{N}{2} \xi_\mathrm{M} \quad , \tag{7}$$

with the periodic Ewald pair potential being defined as [231]

$$W_\mathrm{E}(\mathbf{r}, \mathbf{s}) = \frac{1}{V\pi} \sum_{\mathbf{G} \neq 0} \left(G^{-2} e^{-\frac{\pi^2 G^2}{\kappa^2} + 2\pi i \mathbf{G} \cdot (\mathbf{r} - \mathbf{s})} \right) - \frac{\pi}{\kappa^2 V} + \sum_{\mathbf{R}} \frac{\mathrm{erfc}(\kappa |\mathbf{r} - \mathbf{s} + \mathbf{R}|)}{|\mathbf{r} - \mathbf{s} + \mathbf{R}|} \quad , \tag{8}$$

where $\mathbf{G} = \mathbf{n}L$ and $\mathbf{R} = \mathbf{m}L^{-1}$ denote reciprocal and real lattice vectors, respectively ($\mathbf{n}, \mathbf{m} \in \mathbb{Z}^3$). Furthermore, ξ_M is the so-called Madelung constant, which takes into account the interaction of a charge with its own background and array of images,

$$\xi_\mathrm{M} = \lim_{\mathbf{r} \to \mathbf{s}} \left(W_\mathrm{E}(\mathbf{r}, \mathbf{s}) - \frac{1}{|\mathbf{r} - \mathbf{s}|} \right) \tag{9}$$

$$= \frac{1}{V\pi} \sum_{\mathbf{G} \neq 0} G^{-2} e^{-\frac{\pi^2 G^2}{\kappa^2}} - \frac{\pi}{\kappa^2 V} + \sum_{\mathbf{R} \neq 0} \frac{\mathrm{erfc}(\kappa R)}{R} - 2\kappa \pi^{-\frac{1}{2}} \quad . \tag{10}$$

Observe that both Eqs. (8) and (9) are independent of the specific choice for the Ewald parameter κ, which can be exploited for optimization. Further, we note that in Eq. (7) there appear no additional terms describing the uniform positive background as the average value of $W_\mathrm{E}(\mathbf{r}, \mathbf{s})$ within the simulation box vanishes [231].

Let us conclude this section with some practical remarks. Obviously, a direct evaluation of the infinite sums in reciprocal and real space in Eq. (8) is not possible. Fortunately, the optimal choice of the free parameter κ leads to a rapid convergence of both sums. Furthermore, there exist numerous schemes to accelerate the computation of the Ewald potential that are advisable in different situations, such as multipole expansions [232] or using a basis of Hermite interpolants [233], see, e.g., Refs. [230, 234] for an overview. Finally, we mention the possibility for *pre-averaged* pair potentials, e.g., Refs. [235, 236, 237, 238], which can potentially get rid of "artificial crystal effects" due to the infinite periodic array of images, and are computationally cheap. Recently, this idea has been applied to quantum Monte Carlo simulations of an electron gas by Filinov and co-workers [130].

2.3. The Jellium Hamiltonian: Second quantization

Second quantization is an efficient way to incorporate the symmetry or anti-symmetry of quantum particles in a many-particle description. Due to the indistinguishability of quantum particles the relevant observables are the occupation numbers of individual single-particle orbitals $|i\rangle$ which are solutions of the one-particle problem. Here we will concentrate on the UEG where the natural choice of orbitals are plane waves spin states. For a general introduction to the theory of second quantization we refer the reader to standard text books, e.g. [195, 239].

In case of the UEG, the quantization is naturally performed with respect to plane wave spin orbitals, $|i\rangle \to |\mathbf{k}_i \sigma_i\rangle$, with the momentum and spin eigenvalues $\mathbf{k}_i$ and σ_i, respectively. In coordinate representation they are written as $\langle \mathbf{r}\sigma \, | \mathbf{k}_i \sigma_i \rangle = \frac{1}{L^{3/2}} e^{i\mathbf{k}_i \cdot \mathbf{r}} \delta_{\sigma,\sigma_i}$ with $\mathbf{k} = \frac{2\pi}{L}\mathbf{m}$, $\mathbf{m} \in \mathbb{Z}^3$ and $\sigma_i \in \{\uparrow,\downarrow\}$ so that the UEG Hamiltonian, Eq. (7), becomes

$$\hat{H} = \frac{1}{2}\sum_i \mathbf{k}_i^2 \hat{a}_i^\dagger \hat{a}_i + \sum_{\substack{i<j,k<l \\ i\neq k, j\neq l}} w_{ijkl}^- \hat{a}_i^\dagger \hat{a}_j^\dagger \hat{a}_l \hat{a}_k + N\frac{\xi_M}{2} \; . \tag{11}$$

Here, the creation (annihilation) operator $\hat{a}_i^\dagger$ ($\hat{a}_i$) creates (annihilates) an electron in the i-th spin orbital, and for electrons (fermions) the operators obey the standard anti-commutation relations. Also, $w_{ijkl}^- = w_{ijkl} - w_{ijlk}$ denotes the antisymmetrized two-electron integral with

$$w_{ijkl} = \frac{4\pi e^2}{L^3 (\mathbf{k}_i - \mathbf{k}_k)^2} \delta_{\mathbf{k}_i + \mathbf{k}_j, \mathbf{k}_k + \mathbf{k}_l} \delta_{\sigma_i,\sigma_k} \delta_{\sigma_j,\sigma_l} \; , \tag{12}$$

and we used the Fourier representation of the Coulomb potential. Further, the $N-$particle states are given by Slater determinants

$$|\{n\}\rangle = |n_1, n_2, \ldots\rangle \; , \tag{13}$$

with the fermionic occupation number $n_i \in \{0,1\}$ of the i-th plane wave spin-orbital. Obviously, the second quantization representation of the UEG Hamiltonian has two practical advantageous compared to its coordinate representation: 1) the Ewald interaction only enters in a trivial way via the Madelung constant, ξ_M, thus not requiring any elaborate evaluation of the interaction part, and 2), the correct Fermi statistics are automatically incorporated via the usual fermionic anti-commutator relations of the creation and annihilation operators.

3. Dielectric Approximations and Linear Response Theory

3.1. Introduction

Before the advent of the first exact but computationally highly demanding quantum Monte Carlo simulations of the UEG in the late 1970s, the approximate approaches based on the dielectric formulation [11, 12, 13, 14, 1] have arguably constituted the most vital tool for gaining crucial insights into correlated quantum many-body systems. In the ground state, a seminal work in this direction have been provided by Bohm and Pines with the formulation of the random phase approximation (RPA) [8, 14, 240], which becomes exact in both the long wavelength and high density limit and thus sufficiently describes long-range phenomena. Later, an alternative derivation of the RPA has been performed by Gell-Mann and Brueckner [241] through a summation of Feynman diagrams leading to the first exact expansion of the correlation energy of the UEG in the high density regime. However, at metallic densities, $r_s \approx 1.5, \ldots, 7$, the RPA dramatically overestimates short-range correlations between the electrons resulting in significantly too low correlation energies and an unphysical negative value of the pair-correlation function at zero distance. To overcome these shortcomings, Singwi, Tosi, Land and Sjölander (STLS) [9] proposed a self-consistent scheme that allows for an approximate but greatly improved treatment of the short-range exchange and correlation effects. Most notably, the STLS scheme predicted the exchange-correlation energies that have later been accurately computed by Ceperley and Alder [15, 16] with an impressive accuracy of $\sim 1\%$ even up to densities $r_s \sim 20$ (see e.g. Ref. [242]). Nevertheless, the obtained pair-correlation functions still become slightly negative at densities $r_s \geq 4$, but, compared to the RPA, the magnitude of this error is strongly reduced. A further issue regarding the STLS scheme is the violation of the exact compressibilty sum rule, Eq. (39). Vashishta and Singwi (VS) could modify the self-consistent scheme by also taking the density derivative of the pair-correlation function into account so that the compressibility sum rule is almost exactly verified [10, 243], though this lead to a reduced quality of the pair-correlation function and exchange-correlation energy.

All of the mentioned schemes beyond RPA rely on a static (frequency-independent) approximation of the so-called local field correction, the central quantity in the dielectric formulation. There have been many attempts to

further increase the overall accuracy of the static dielectric methods (for an overview see e.g. Ref. [13]), and even the extension to a more consistent formulation based on a dynamical local field correction has been achieved [244, 245]. However, regarding the interaction energy, the static STLS scheme turned out to give the most accurate results.

Due to a former lack of experimental motivation, the extension of some of the dielectric approaches to finite temperature and their application to the UEG were carried out much later. The first calculations in the RPA have been carried out by Gupta and Rajagopal [246, 247, 137], which have later been revised and parametrized by Perrot and Dharma-wardana [248]. After that, countless important contributions to this field have been made by Tanaka and Ichimaru [203, 204, 205, 206, 207, 208], who applied many of the static dielectric methods, i.e. with some static ansatz for the LFC, to the quantum and classical UEG at finite temperature. Among these works is the finite temperature STLS scheme [204], which, likewise to the ground state, predicted the exact exchange-correlation energy [227, 242, 249] with a similar impressive accuracy of $\sim 1\%$, cf. Sec. 7. However, a consistent extension of the static finite temperature VS scheme [250] could only be achieved much later [213], since the fulfillment of the compressibility sum rule turned out to be more elaborate here. Furthermore, Schweng and Böhm developed the finite temperature version of the dynamical STLS scheme [251] and successfully used it for a detailed investigation of the static LFC of the UEG, while a generalization to arbitrary spin-polarization of this formalism has been provided only very recently [252].

We mention that, regarding the benefits and merits of the specific variants of the dielectric methods, the qualitative statements for the ground state given above also apply to their finite temperature extensions. Moreover, in addition to its predictive capabilities prior to the advent of the more accurate QMC simulations, in particular the RPA and STLS approach played an important role in the extrapolation of the results obtained from a finite simulation system (finite particle number N and simulation box with volume V) to the thermodynamic limit, i.e. $N, V \xrightarrow{n=\text{const}} \infty$ (see Sec. 6). In addition, very recently, the temperature dependence of the STLS interaction energy has been successfully used to bridge the gap between the ground state and finite temperature QMC data which are available only above half the Fermi temperature (see Sec. 8).

3.2. Density response, dielectric function, local field correction, and structure factor

The dielectric formulation is derived within the framework of the linear density-density response theory, where we are interested in the change of the electron density when a periodic (both in space and time) external potential with wavenumber $\mathbf{q}$, frequency ω, and amplitude $\Phi(\mathbf{q}, \omega)$ is applied to the system, i.e.,

$$\Phi_{\text{ext}}(\mathbf{r}, t) = \frac{1}{V}\Phi(\mathbf{q}, \omega)\, e^{i[\mathbf{q}\mathbf{r} - (\omega - i\eta)t]} + \text{c.c.} \tag{14}$$

The infinitesemal positive constant $\eta = 0^+$ ensures that the perturbation vanishes at $t \to -\infty$ so that we can assume that the system has been in thermal equilibrium in the past and the external field has been switched on adiabatically. Provided that the amplitude is sufficiently small and the unperturbed system is homogeneous, one can show that the resulting change in the electron density is given by [1, 207]

$$\delta n(\mathbf{r}, t) = n(\mathbf{r}, t) - n(\mathbf{r})_0 = \frac{1}{V}\Phi(\mathbf{q}, \omega)\chi(\mathbf{q}, \omega)e^{i(\mathbf{q}\mathbf{r} - \omega t)} + \text{c.c.} \ , \tag{15}$$

where we have introduced the Fourier transform of the density-density response function

$$\chi(\omega, \mathbf{q}) = \lim_{\eta \to 0}\int_{-\infty}^{\infty} \mathrm{d}\tau \ e^{(i\omega - \eta)\tau}\tilde{\chi}(\mathbf{q}, \tau) \ . \tag{16}$$

with its standard definition[1]

$$\tilde{\chi}(\mathbf{q}, \tau) = -i\left\langle [\hat{n}(\mathbf{q}, \tau), \hat{n}(-\mathbf{q}, 0)]\right\rangle_0 \Theta(\tau) \ . \tag{17}$$

Here, $\langle\cdot\rangle_0$ denotes the ensemble average of the unperturbed system, and the time dependence of the Fourier transform of the density operator $\hat{n}(\mathbf{q}) = \sum_i e^{-i\mathbf{q}\hat{\mathbf{r}}_i}$ is determined by the Heisenberg picture with respect to the unperturbed Hamiltonian, i.e., $\hat{n}(\mathbf{q}, t) = e^{i\hat{H}_0 t}\hat{n}(\mathbf{q})e^{-i\hat{H}_0 t}$. From Eq. (15) we immediately see that the amplitude of the induced density fluctuations is simply

$$n(\mathbf{q}, \omega) = \frac{1}{V}\Phi(\mathbf{q}, \omega)\chi(\mathbf{q}, \omega) \ . \tag{18}$$

---

[1]Note that we restrict ourselves to the unpolarized case throughout the present section. Therefore, the response function χ is equal to the total response function of both spin-up and -down electrons.

Hence, all information of the system's response to the external perturbation, Eq. (14), is contained in the density-density response function $\chi(\mathbf{q}, \omega)$. Via the polarization potential approach [207] it can be shown that the exact density response function can always be expressed in terms of the ideal (Lindhard) response function, χ_0, and the so-called local field correction (LFC), G, as

$$\chi(\mathbf{q}, \omega) = \frac{\chi_0(\mathbf{q}, \omega)}{1 - \frac{4\pi}{q^2}[1 - G(\mathbf{q}, \omega)]\chi_0(\mathbf{q}, \omega)} \ , \tag{19}$$

where the RPA response function is recovered when setting $G \equiv 0$, i.e.,

$$\chi_{\mathrm{RPA}}(\mathbf{q}, \omega) = \frac{\chi_0(\mathbf{q}, \omega)}{1 - \frac{4\pi}{q^2}\chi_0(\mathbf{q}, \omega)} \ . \tag{20}$$

Thus, the LFC covers all correlation effects in the response of the system to a weak external potential. The imaginary part of the response function is linked to the dynamic structure factor $S(\mathbf{q}, \omega)$ via the fluctuation dissipation theorem [1]

$$\mathrm{Im}\chi(\mathbf{q}, \omega) = -\frac{\pi}{V}\left(1 - e^{-\beta\omega}\right)S(\mathbf{q}, \omega) \ , \tag{21}$$

which can in turn be utilized to express the static structure factor

$$S(\mathbf{q}) = \frac{1}{N}\int d\omega\, S(\mathbf{q}, \omega) = \frac{1}{N}\langle\hat{n}(\mathbf{q})\hat{n}(-\mathbf{q})\rangle_0 \tag{22}$$

in terms of the response function

$$S(\mathbf{q}) = -\frac{1}{2\pi n}\mathcal{P}\int_{-\infty}^{\infty}d\omega \coth\left(\frac{\omega}{2T}\right)\mathrm{Im}\chi(\mathbf{q}, \omega) \ , \tag{23}$$

where $\mathcal{P}$ denotes the principal value, which is necessary due to the poles of the integrand on the real axis. Thereby we have obtained a direct connection between the dynamic properties of the system, i.e., within the linear response regime, and its thermodynamic properties. Note that the response function obeys the Kramers-Kronig relations

$$\mathrm{Re}\chi(\mathbf{q}, \omega) = \frac{2}{\pi}\mathcal{P}\int_0^{\infty}d\nu\,\frac{\nu\,\mathrm{Im}\chi(\mathbf{q}, \omega)}{\nu^2 - \omega^2} \ , \tag{24}$$

$$\mathrm{Im}\chi(\mathbf{q}, \omega) = -\frac{2\omega}{\pi}\mathcal{P}\int_0^{\infty}d\nu\,\frac{\mathrm{Re}\chi(\mathbf{q}, \omega)}{\nu^2 - \omega^2} \ ,$$

and hence, the real part of the response function can always be computed from its imaginary part and vice versa. The central idea of all dielectric approaches consists in deriving an approximate expression for the LFC so that it is expressed as a functional of the static structure factor, i.e. $G = G[S]$. Then, together with Eqs. (19) and (24), one has a closed set of equations, which, in principal can be solved iteratively starting from the RPA ($G = 0$), where the real and imaginary part of the ideal (Lindhard) response function, χ_0, are readily evaluated numerically [1]. However, from a numerical point of view this approach is highly inconvenient due to the infinitely many poles of the integrands in the Eqs. (23) and (24). A solution to this problem has been provided by Tanaka and Ichimaru [204], who reformulated the aforementioned set of equations for the complex valued density-density response function defined by

$$\tilde{\chi}(\mathbf{q}, z) := \int_{-\infty}^{\infty}\frac{d\nu}{\pi}\frac{\mathrm{Im}\chi(\mathbf{q}, \nu)}{\nu - z} \ , \tag{25}$$

which, under the frequency integral, fulfills $2i\mathrm{Im}\chi(\mathbf{q}, \omega) = \lim_{\eta\to 0^+}\tilde{\chi}(\mathbf{q}, \omega + i\eta) - \tilde{\chi}(\mathbf{q}, \omega - i\eta)$, so that Eq. (23) becomes

$$S(\mathbf{q}) = -\frac{1}{4\pi in}\mathcal{P}\lim_{\eta\to 0}\int_{-\infty}^{\infty}d\omega \coth\left(\frac{\omega}{2T}\right)[\tilde{\chi}(\mathbf{q}, \omega + i\eta) - \tilde{\chi}(\mathbf{q}, \omega - i\eta)] \ . \tag{26}$$

Now the integral can be interpreted as a closed contour integral

$$S(\mathbf{q}) = -\frac{1}{4\pi in}\lim_{\epsilon\to 0^+}\lim_{\eta\to 0^+}\lim_{R\to\infty}\oint_C dz \coth\left(\frac{z}{2T}\right)\mathrm{Im}\tilde{\chi}(\mathbf{q}, z) \ , \tag{27}$$

11
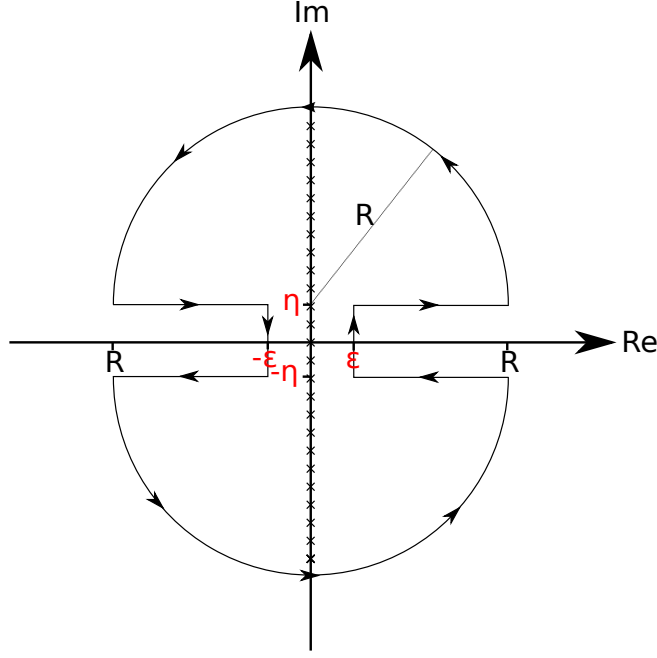
Figure 2: Illustration of the integration contour C in Eq. (27). Crosses indicate the poles of the hyperbolic cotangent.

with the explicit form of the contour being depicted in Fig. 2, where the limit $R \to \infty$ is taken prior to the integration whereas $\epsilon, \eta \to 0^+$ is taken afterwards. Since the integrand is analytic on C, the contour integral can be solved by applying the residue theorem yielding

$$S(\mathbf{q}) = -\frac{T}{n} \sum_{l=-\infty}^{\infty} \tilde{\chi}(\mathbf{q}, z_l) , \qquad (28)$$

with the Matsubara frequencies z_l representing the poles of the cotangent hyperbolic function on the imaginary axis,

$$z_l = 2\pi i l T . \qquad (29)$$

Hence, the frequency integral in Eq. (23) can be replaced by a sum over the Matsubara frequencies, which is much more convenient for numerical evaluation.

Similar to the real frequency dependent response function, cf. Eq. (19), the exact complex valued response function can be rewritten in terms of the complex valued ideal response function and LFC [203, 251],

$$\tilde{\chi}(\mathbf{q}, z) = \frac{\tilde{\chi}_0(\mathbf{q}, z)}{1 - \frac{4\pi}{q^2}[1 - \tilde{G}(\mathbf{q}, z)]\tilde{\chi}_0(\mathbf{q}, z)} . \qquad (30)$$

In the thermodynamic limit[2], the finite temperature complex valued ideal response function is given by

$$\tilde{\chi}_0(\mathbf{q}, z) = -2 \int \frac{d\mathbf{k}}{(2\pi)^3} \frac{f(\mathbf{k} + \mathbf{q}) - f(\mathbf{k})}{z - \epsilon_{\mathbf{k}+\mathbf{q}} + \epsilon_{\mathbf{k}}} , \qquad (31)$$

with $\epsilon_{\mathbf{k}} = k^2/2$ and f being the Fermi distribution

$$f(\mathbf{k}) = \frac{1}{e^{k^2/(2T)-\alpha} + 1} , \qquad (32)$$

---

[2]As usual, replacing $\frac{1}{V}\sum_{\mathbf{q}}$ by $\int \frac{d\mathbf{q}}{(2\pi)^3}$ transforms the expressions for the finite system (with periodic boundary conditions) to the thermodynamic limit.

where the reduced chemical potential $\alpha = \mu/T$ is determined by the normalization condition

$$\int \frac{d\mathbf{k}}{(2\pi)^3} f(\mathbf{k}) = \frac{n}{2} . \tag{33}$$

For numerical evaluation of the ideal response function at the different Matsubara frequencies the following form is most suitable [203, 204]:

$$\tilde{\chi}_0(\mathbf{q}, z_l) = -\frac{2}{q} \int_0^\infty \frac{dk}{(2\pi)^2} \frac{k}{e^{k^2/(T2)-\alpha}+1} \ln\left[\frac{(4\pi lT)^2 + (q^2 + 2qk)^2}{(4\pi lT)^2 + (q^2 - 2qk)^2}\right] . \tag{34}$$

3.3. Approximations for the local field correction

In the static dielectric approaches one approximates the dynamic LFC by its static value, i.e., replacing $\tilde{G}(\mathbf{q}, z)$ by $\tilde{G}(\mathbf{q}, 0)$ in Eq. (30), which turns out to be highly accurate in many cases. The most successful and widely used approximation for the static LFC is given by the one utilized in the STLS scheme [9]

$$\begin{aligned}
G_{\text{STLS}}(\mathbf{q}, 0) &= -\frac{1}{n} \int \frac{d\mathbf{k}}{(2\pi)^3} \frac{\mathbf{q} \cdot \mathbf{k}}{\mathbf{k}^2} [S(\mathbf{q} - \mathbf{k}) - 1] \\
&= -\frac{1}{n} \int_0^\infty \frac{dk}{(2\pi)^2} k^2 [S(k) - 1] \left[\frac{q^2 - k^2}{4kq} \ln\left(\frac{(q+k)^2}{(q-k)^2}\right) + 1\right] .
\end{aligned} \tag{35}$$

This expression is derived from the classical equation of motion of the one-particle distribution function, $f(\mathbf{r}_1, \mathbf{p}_1, t)$, by making the following product ansatz for the two-particle distribution function[3]:

$$f(\mathbf{r}_1, \mathbf{p}_1, \mathbf{r}_2, \mathbf{p}_2, t) \approx f(\mathbf{r}_1, \mathbf{p}_1, t) f(\mathbf{r}_2, \mathbf{p}_2, t) g_{\text{eq}}(\mathbf{r}_1 - \mathbf{r}_2) , \tag{36}$$

where $g_{\text{eq}}(\mathbf{r})$ denotes the exact equilibrium pair-distribution function. Since the two-particle distribution function couples to the three-particle distribution function and so on, Eq. (36) serves as a closure relation of the hierarchy.

The equations (28), (30), and (35) now form a closed set of equations, which are self-consistently solved as follows:

1. Compute the reduced chemical potential α by solving Eq. (33).
2. Compute and store the values of the ideal response function, $\chi_0(\mathbf{q}, z_l)$, for sufficiently large values of l ensuring that Eq. (28) always converges throughout the iteration.
3. Compute the response function from Eq. (30), initially by setting $G = 0$.
4. Compute the static structure factor $S(\mathbf{q})$ from Eq. (28).
5. Compute the new LFC $G_{\text{STLS}}(\mathbf{q}, 0)$ from Eq. (35).
6. Repeat steps 3 to 5 until convergence is reached.

For completeness we mention that, in particular at low temperature, the sum in Eq. (28) may only converge for extremely large values of l, but this obstacle can be overcome by separating those contributions for which the summation can be performed analytically beforehand, see Ref. [203] for details.

Naturally, from the converged static structure factor we directly obtain the interaction energy (per particle) for the corresponding temperature and density parameter,

$$v(\theta, r_s) = \frac{1}{\pi} \int_0^\infty dk \, [S(k; r_s, \theta) - 1] , \tag{37}$$

which can in turn be used to compute the exchange-correlation free energy via the standard coupling constant integration

$$f_{\text{xc}}(r_s, \theta) = \frac{1}{r_s^2} \int_0^{r_s} d\bar{r}_s \, v(\theta, \bar{r}_s) . \tag{38}$$

As mentioned before, both in the ground state and at finite temperature, the STLS scheme provides highly accurate interaction energies, which is partly the result of a favourable error cancellation in Eq. (37) as the STLS static

---

[3]Note that this ansatz can be further improved by considering an explicitly time-dependent pair distribution function, see Refs. [253, 254].

structure factor tends to be slightly too large for small k-vector and vice versa, see Fig. 31 in Sec. 6. It is important to note that, compared to the RPA, the STLS structure factor and related thermodynamic properties are of substantially higher accuracy. In particular, the negative values of the pair-distribution function at zero distance, $g(0)$, are significantly reduced, although it still becomes slightly negative at lower densities [204]. However, there is a well-known drawback regarding the consistency of the STLS results: the compressibility sum rule (CSR) is violated. The CSR is an exact property of the UEG linking the long-wavelength limit of the static LFC $G(q,0)$ to the second derivative of the exchange-correlation free energy:

$$\lim_{q \to 0} G(q,0) = -\frac{q^2}{4\pi} \frac{\partial^2}{\partial n^2} (n f_{\rm xc}) \ . \tag{39}$$

Substituting $G^{\rm STLS}(q,0)$ and $f_{\rm xc}^{\rm STLS}$ on the left- and right-hand side of Eq. (39) gives different results, which demonstrates that the STLS scheme does not provide a consistent physical description of the UEG. Moreover, the long range limit of the LFC differs significantly from the exact QMC result, which is shown in Fig. 43 in Sec. 9. In the ground state, Vashishta and Singwi [10] proposed to modify the STLS expression, Eq. (35), for the LFC such that

$$G^{\rm VS}(\mathbf{q},0) = \left(1 + an\frac{\partial}{\partial n}\right) G^{\rm STLS}(\mathbf{q},0) \ , \tag{40}$$

where the right choice of the additional free parameter a, in principle, allows for the exact fulfillment of Eq. (39). In fact, they empirically found that setting $a = 2/3$ reasonably satisfies the CSR for all densities in the ground state. Only recently, Sjostrom and Dufty [213] successfully extended this approach to the finite temperature UEG. They even refined the approach by making the free parameter dependent on density and temperature, i.e., $a = a(r_s, \theta)$, and actually included the CSR, Eq. (39), into the self-consistent scheme, which requires to simultaneously perform calculations for different values of r_s. Thereby, the obtained results are physically more consistent in that they do exactly fulfill the CSR. However, the overall quality of the thermodynamic quantities is decreased compared to the STLS scheme; for example, $g(0)$ becomes more negative [213].

Since the accuracy of the STLS scheme decreases when the density parameter becomes too large, $r_s \gtrsim 20$, there have been many attempts to derive more refined expressions for the static LFC that perform better in the strong coupling regime (see e.g. [206, 13]). Among them are the so-called (modified) convolution [(M)CA] and hypernetted chain approximations [(M)HNC] for the LFC. Both are known to be highly accurate for the description of the classical one-component plasma over the entire fluid regime [206]. While the MCA scheme has been used earlier for the construction of a temperature, density, and spin-dependent parametrization of the exchange-correlation free energy of the UEG [205], the HNC scheme has only recently been applied to the UEG at warm dense matter conditions [242] and, compared to the STLS scheme, showed overall improved results for the thermodynamic properties but not for the interaction energy. The LFC in the HNC approximation is derived from the hypernetted chain equation for classical liquids [255, 256], which yields [242]

$$G^{\rm HNC}(\mathbf{q},0) = G^{\rm STLS}(\mathbf{q},0) + \frac{1}{n} \int \frac{d\mathbf{k}}{(2\pi)^3} \frac{\mathbf{q} \cdot \mathbf{k}}{k^2} [S(\mathbf{q} - \mathbf{k}) - 1][G(\mathbf{k},0) - 1][S(\mathbf{k}) - 1] \ , \tag{41}$$

where the CA expression is recovered by setting $G(\mathbf{k},0) \equiv 0$ on the left-hand side of Eq. (41). Further, the corresponding modified versions, MCA and MHNC, are obtained by replacing $S(\mathbf{q} - \mathbf{k})$ by a screening function

$$\bar{S}(q) = \frac{q^2}{q^2 + q_s^2} \ . \tag{42}$$

The screening parameter q_s is determined consistently from the condition

$$\frac{1}{2} \int \frac{d\mathbf{q}}{(2\pi)^3} \frac{4\pi}{q^2} [\bar{S}(q) - 1] = \frac{1}{2} \int \frac{d\mathbf{q}}{(2\pi)^3} \frac{4\pi}{q^2} [S(q) - 1] \ , \tag{43}$$

so that S and $\bar{S}$ must correspond to the same interaction energy. Using the modified versions with the screening function has the practical advantage that, like the STLS contribution to the total LFC, cf. Eq. (35), also the second term in Eq. (41) can be recast into a one-dimensional integral [242], i.e.,

$$G^{\rm MHNC}(\mathbf{q},0) = G^{\rm STLS}(\mathbf{q},0) + \frac{q_s^2}{n} \int_0^\infty \frac{dk}{(2\pi)^2} \left[1 + \frac{k^2 + q^2 + q_s^2}{4qk} \ln\left(\frac{(k-q)^2 + q_s^2}{(k+q)^2 + q_s^2}\right)\right] [G(k) - 1][S(k) - 1] \ , \tag{44}$$

14

which significantly speeds up the convergence process. Unfortunately, this is not possible for the full HNC LFC, Eq. (41), and thus, one actually must carry out the three dimensional integration.

At this point it is important to note that all the above static dielectric schemes are somewhat classical in spirit since the utilized approximate expressions for the static LFC are all derived within purely classical theories. In other words, the discussed methods may be interpreted as being quantum mechanically only on the level of the RPA, while correlation effects are treated classically. In accordance to Eqs. (19) and (34) the exact LFC must also depend on the frequency. First, Hasegawa and Shimizu [244] performed the formal derivation of the dynamic STLS LFC by closing the hierarchy for the equation of motion of the Wigner distribution with the same product ansatz, Eq. (36), that has been used in the static STLS formalism for the classical distribution function. Due to its consistent quantum mechanical derivation, this approach has been termed quantum STLS (qSTLS). In the ground state, the first numerical calculations and detailed investigations have been carried out by Holas and Rahman [245]. Later, the qSTLS scheme has also been applied to the finite temperature UEG, and more recently, it has been generalized to allow for the calculation of spin-resolved quantities [251, 252]. The dynamical LFC in the qSTLS scheme is given by

$$G^{\mathrm{qSTLS}}(\mathbf{q}, z_l) = -\frac{1}{n} \int \frac{\mathrm{d}\mathbf{k}}{(2\pi)^3} \frac{\bar{\chi}_0(\mathbf{q}, \mathbf{k}, z_l)}{\bar{\chi}_0(\mathbf{q}, z_l)} \frac{k^2}{q^2} [S(\mathbf{k} - \mathbf{q}) - 1] \ , \tag{45}$$

with the generalized response function (two arguments) being defined as

$$\chi_0(\mathbf{q}, \mathbf{k}, z_l) = -2 \int \frac{\mathrm{d}\mathbf{p}}{(2\pi)^3} \frac{f(\mathbf{p} + \mathbf{k}/2) - f(\mathbf{p} - \mathbf{k}/2)}{z - \epsilon_{\mathbf{p}+\mathbf{q}/2} + \epsilon_{\mathbf{p}-\mathbf{q}/2}} \tag{46}$$
$$= -\frac{2}{q} \int_0^\infty \frac{\mathrm{d}p}{(2\pi)^2} \, p \, f(p) \ln \left[\frac{(4\pi l T)^2 + (2pq + \mathbf{q}\mathbf{k})}{(4\pi l T)^2 + (2pq - \mathbf{q}\mathbf{k})} \right] \quad .$$

For practical purposes, the qSTLS LFC, Eq. (45), can be reduced to a three-dimensional integral [251]. Overall, compared to the static STLS approach, the qSTLS approach significantly improves the short-range behavior of the pair-correlation function. Most notably, the obtained results for the static LFC are physically more reasonable as they can exhibit important physical features. For example, they can actually have a maximum larger than one, a necessary condition for the occurrence of charge density waves [251]. This is in stark contrast to the static dielectric approaches where the static LFC usually converges monotonically to unity with increasing $k-$vector. Yet, the improvement of the interaction energy due to the qSTLS scheme is rather small.

An exhaustive overview of comparison between the dielectric approximation and recent, highly accurate quantum Monte Carlo data can be found in Sec. 7 for the static structure factor and the interaction energy and, in Sec. 9, for the static density response function and local field correction.

4. Other approximate approaches

4.1. Finite-temperature (Matsubara) Green functions

An alternative derivation of the dielectric function encountered in the previous section can be achieved within the framework of quantum kinetic theory [239]. In this formalism, correlation effects are usually incorporated by approximating the collision integrals, which take the role of the local field correction in the dielectric formulation. For instance, completely neglecting collisions gives the random phase approximation, whereas invoking the relaxation time approximation [257, 258] leads to the well-known Mermin dielectric function.

A closely related strategy is used in Green functions theory where a suitable approximation of the so-called self-energy is used to truncate the Martin-Schwinger hierarchy [259]. In the following, we briefly outline the approximation introduced by Montroll and Ward [260] and also the additional e^4-contribution (see Ref. [218] for a recent application to the warm dense UEG). For simplicity, we restrict ourselves to the spin-polarized case and write the total energy as a perturbation expansion with respect to coupling strength (dropping terms beyond second order) as [195, 196]

$$E = E_0^{\mathrm{id}}(T, \alpha_e) + E^{\mathrm{HF}} + E^{\mathrm{MW}} + E^{e^4} \ . \tag{47}$$

Here E_0 denotes the ideal energy

$$E_0 = \frac{3}{2} \frac{T}{\lambda_{\mathrm{DB}}^3} I_{3/2}(\alpha) \quad , \tag{48}$$

15

with $\lambda_{\mathrm{DB}} = \sqrt{2\pi\hbar^2\beta/m}$ being the thermal wavelength, and E^{HF} corresponds to the well-known Hartree-Fock energy

$$E^{\mathrm{HF}} = \lambda_{\mathrm{DB}}^{-4} \int_{-\infty}^{\alpha} d\alpha' \, I_{-1/2}^2(\alpha') - \frac{3}{2\lambda_{\mathrm{DB}}^4} I_{-1/2}(\alpha) I_{1/2}(\alpha) \quad , \tag{49}$$

where I_k is the Fermi integral of order k, see, e.g., Ref. [195], and $\alpha = \beta\mu$. As usual, the chemical potential μ is defined by the normalization of the Fermi function to the total density, see Eq. (33). To compute the Montroll-Ward (MW) and e^4-contribution, it is convenient to utilize the pressure p, which is connected to the different parts of the total energy by

$$E^{\mathrm{j}} = -p^j + T\frac{\partial}{\partial T}p^j, \qquad j = \mathrm{MW}, \, e^4. \tag{50}$$

The MW-component of the pressure is then given by

$$p^{\mathrm{MW}} = \frac{-1}{4\pi^3} \int_0^\infty dp\, p^2 \, \mathcal{P} \int_0^\infty d\omega \, \coth\left(\frac{\beta\omega}{2}\right)\left[\arctan\frac{\mathrm{Im}\,\varepsilon_{\mathrm{RPA}}(p,\omega)}{\mathrm{Re}\,\varepsilon_{\mathrm{RPA}}(p,\omega)} - \mathrm{Im}\,\varepsilon_{\mathrm{RPA}}(p,\omega)\right] \quad , \tag{51}$$

with $\varepsilon_{\mathrm{RPA}}(p,\omega)$ denoting the dielectric function in the random phase approximation, see Sec. 3. Therefore, neglecting the e^4-term in Eq. (47) gives the total energy in the RPA. To include second order contributions, we compute

$$p^{e^4} = \int \frac{d\mathbf{p}\,d\mathbf{q}_1\,d\mathbf{q}_2}{64\pi^7} \frac{1}{p^2(\mathbf{p}+\mathbf{q}_1+\mathbf{q}_2)^2} \frac{f_{q_1}f_{q_2}\bar{f}_{\mathbf{q}_1+\mathbf{p}}\bar{f}_{\mathbf{q}_2+\mathbf{p}} - f_{\mathbf{q}_1+\mathbf{p}}f_{\mathbf{q}_2+\mathbf{p}}\bar{f}_{q_1}\bar{f}_{q_2}}{q_1^2 + q_2^2 - (\mathbf{p}+\mathbf{q}_1)^2 - (\mathbf{p}+\mathbf{q}_2)^2} \tag{52}$$

with $f_p = [\exp(\beta p^2/2 - \beta\mu) + 1]^{-1}$ being the Fermi function, and $\bar{f}_p = [1 - f_p]$ denotes the Pauli blocking factor. Detailed benchmarks of the energy computed from Eq. (47) will be presented in Sec. 7.

For completeness, we also mention the recent finite-temperature extension of the retarded cumulant Green function approach [197] that is predicted to allow, both, for the computation of thermodynamic properties of the UEG (see Sec. 8.4 for a comparison to QMC data) and, in addition, spectral properties.

4.2. Classical mapping approaches

In addition to the dielectric formalism (Sec. 3) and the quantum Monte Carlo methods introduced in Sec. 5, quantum-classical mappings constitute a third independent class of approaches to a thermodynamic description of the electron gas. In this section, we give a concise overview of two different formulations, namely the works by F. Perrot and M.W.C Dharma-wardana [210, 209] and the more recent and rigorous works by S. Dutta and J.W. Dufty [261, 262, 263].

4.2.1. Classical mapping approach by Perrot and Dharma-wardana

The basic idea of the formalism by Perrot and Dharma-wardana [210, 209] (hereafter denoted as *PDW*) is to define a classical system of charged particles at an effective *quantum temperature* T_q, such that an input value for the ground state exchange-correlation energy E_{xc} obtained from outside the theory is reproduced. While, in principle, data from any theory could be used, PDW chose the then most accurate data based on quantum Monte Carlo calculations by Ortiz and Ballone [34]. The properties of the effective classical system are approximately computed by solving the corresponding hyppernetted chain (HNC) equations [255, 256]. A potentially more accurate albeit computationally considerably more demanding treatment using the classical Monte Carlo or Molecular Dynamics methods, e.g. Ref. [264], was deemed unnecessary as the error due to the HNC approximation was expected to be negligible for the densities of interest. For completeness, we mention that this assumption was somewhat contradicted by the recent works of Liu and Wu [265], who found that a more accurate inclusion of short-range correlations is important to describe the first peak in the pair distribution function at low density. Once the classical system is solved (thereby recovering the input value for E_{xc}), it is straightforward to obtain other observables such as the pair distribution function (or, equivalently, the static structure factor, cf. Sec. 6) or the static density response function $\chi(\mathbf{k})$, cf. Sec. 3. A particular advantage of the classical mapping approach is that the resulting PDF is always positive. This is in stark contrast to the dielectric approximations from Sec. 3, where the PDF tends to become negative at small distances for intermediate to strong coupling. Further, a comparison of the classical mapping with the ground state QMC results revealed quantitative agreement.

To extend this formalism to finite temperature T, for which back in the early 2000s no accurate data for $E_{\mathrm{xc}}(r_s, T)$ existed, PDW introduced a modified classical temperature

$$T_{\mathrm{cf}} = \left(T^2 + T_q^2\right)^{1/2} \quad , \tag{53}$$

which is motivated by the fact that the leading dependence of the energy on T is quadratic. Note that the expression for T_q in Eq. (53) depends only on the density parameter r_s,

$$T_q = \frac{1}{a + b\sqrt{r_s} + cr_s} \quad , \tag{54}$$

where the free parameters a, b, and c were obtained to reproduce the ground state data for E_{xc} as explained above. It is easy to see that Eq. (53) becomes exact for high and low temperature, but constitutes an uncontrolled approximation for intermediate temperatures, most notably in the warm dense matter regime.

In their seminal paper from 2000, PDW [210] provided extensive results for the uniform electron gas at finite temperature, including a parametrization of the exchange-correlation free energy f_{xc} with respect to temperature, density, and spin-polarization. A concise introduction of the latter is presented in Sec. 4.2.1, where it is compared to the recent, highly accurate parametrization by Groth, Dornheim and co-workers [227].

Further, the PDW formalism for the classical-mapping has subsequently been employed in numerous calculations of more realistic (and, thus, more complicated) systems, e.g., Refs. [181, 182, 183], and an excellent review can be found in Ref. [184]. Finally, we mention that the shortcoming of the PDW classical-mapping at intermediate temperature was recently somewhat remedied by Liu and Wu [266], who replaced the simple interpolation for T_{cf} from Eq. (53) by the explicitly temperature-dependent expression

$$T_{\mathrm{cf}} = \frac{1}{a(T) + b(T)\sqrt{r_s} + c(T)r_s} \quad , \tag{55}$$

where the functions $a(T)$, $b(T)$, and $c(T)$ where chosen to reproduce the RPIMC data by Brown *et al.* [211] for E_{xc}, see Ref. [266] for more details. It was found that this gives better data for the pair correlation function, in particular for the description of long-range correlations.

4.2.2. Classical mapping approach by Dutta and Dufty

Recently, Dufty and Dutta [267, 263] presented a more rigorous classical-mapping formalism operating in the grand canonical ensemble (volume V, chemical potential μ, and inverse temperature β are fixed). While the volume V is equal both for the *true* quantum system and the *effective* classical one, a modified inverse temperature β_c, chemical potential μ_c, and pair potential $\phi_c(r)$ are introduced. To determine these two parameters and one function, we enforce the equivalence of pressure p, electron number density n and of the pair distribution function $g(r)$ for the true and effective systems,

$$
\begin{aligned}
p_c(\beta_c, V, \mu_c | \phi_c(r)) &\equiv p(\beta, V, \mu | \phi(r)) \\
n_c(\beta_c, V, \mu_c | \phi_c(r)) &\equiv n(\beta, V, \mu | \phi(r)) \\
g_c(r, \beta_c, V, \mu_c | \phi_c(r)) &\equiv g(r, \beta, V, \mu | \phi(r)) \quad ,
\end{aligned}
\tag{56}
$$

where, for the uniform electron gas, $\phi(r)$ is simply given by the Coulomb potential. Observe that the vertical bars in Eq. (56) indicate that all three quantities are in fact functionals of the classical or quantum pair potentials, in addition to the functional dependence on the three thermodynamic variables. In practice, one has to provide expressions for p, n and $g(r)$ of the quantum system, starting from which the relations in Eq. (56) can be inverted for μ_c, β_c, and $\phi_c(r)$.

Since providing two thermodynamic and one structural property of the system of interest as input for an approximate many-body formalism might admittedly seem like circular reasoning, we must ask ourselves what kind of information has been gained at which point. The answer is as follows: in practice, we provide the quantum input computed from the random phase approximation (see Sec. 3), and subsequently compute the classical parameters β_c, μ_c, and $\phi_c(r)$ by solving Eq. (56) in the classical weak-coupling approximation. The main assumption is that the quantum effects are either local (such as diffraction) or weakly nonideal (such as antisymmetry under particle-exchange). In this case, the bulk of the more pronounced nonideality effects would be captured by subsequently feeding the obtained results for β_c, μ_c, and $\phi_c(r)$ into a more accurate classical many-body method, such as the classical Monte-Carlo method, molecular dynamics, or, like in the PDW approach, the hypernetted chain approximation.

Overall, the application of the Dufty-Dutta formalism to the UEG at warm dense matter conditions [262, 261] has given results of similar accuracy as the PDW formalism, although not nearly as extensive data have been presented. For completeness, we mention that this approach is not limited to the UEG or, in general, to homogeneous systems. For example, first results for charges in a harmonic confinement have been reported in Refs. [262, 268]. The application to a realistic electron-ion plasma remains an important task for the future.

5. Quantum Monte Carlo Methods

In the following section, we will discuss in detail various quantum Monte Carlo methods and discuss the fermion sign problem, which emerges for the simulations of electrons. In particular, we introduce the Metropolis algorithm [269], which constitutes the backbone of all subsequent path inegral Monte Carlo methods except the density matrix QMC paradigm. Not mentioned are the multilevel blocking idea by Mak, Egger and co-workers [270, 271, 272, 273, 274] and the expanded-ensemble approach by Vorontsov-Velyaminov *et al.* [275, 276].

5.1. The Metropolis algorithm

Due to its fundamental importance for the understanding of the quantum Monte Carlo methods introduced below, in this section we give a comprehensive introduction of the widely used Metropolis algorithm [269].

5.1.1. Problem statement

In statistical many-body physics, we often encounter probabilities of the form

$$P(\mathbf{X}) = \frac{W(\mathbf{X})}{Z} \ . \tag{57}$$

For example, the multi-dimensional variable $\mathbf{X}$ might correspond to a configuration of classical particles, or spin-alignments in an Ising model, and $W = \exp(-E(\mathbf{X})\beta)$ to the corresponding "Boltzmann distribution" describing the probability of $\mathbf{X}$ to occur (with $E(\mathbf{X})$ being the energy of said configuration). The aim of a Monte Carlo simulation is then to generate a set of random configurations $\{\mathbf{X_i}\}$ that are distributed according to Eq. (57), which can subsequently be used to compute averages such as the internal energy.

Usually, the problem with such a statistical description of a system is that the normalization of Eq. (57),

$$Z = \int d\mathbf{X} \, W(\mathbf{X}) \ , \tag{58}$$

is not readily known. For the canonical ensemble (volume V, particle number N and inverse temperature β are fixed), to which we will restrict ourselves throughout this work, Z corresponds to the canonical partition function. In this case, the exact knowledge of Z allows to directly compute all observables (e.g., energies, pressure, etc.) via thermodynamic relations, thereby eliminating the need for a Monte Carlo simulation in the first place. The paramount achievement by Metropolis *et al.* [269] was to introduce an algorithm that allows to generate a set of random variables $\{\mathbf{X}_i\}$ with an unknown normalization Z. The significance of this accomplishment can hardly be overstated and the Metropolis algorithm has emerged as one of the most successful algorithms in computational physics and beyond.

5.1.2. The detailed balance condition

The starting point is the imposition of the so-called *detailed balance condition*,

$$T(\mathbf{X} \to \tilde{\mathbf{X}}) = T(\tilde{\mathbf{X}} \to \mathbf{X}) \ , \tag{59}$$

which states that the transition probability T to go from a state $\mathbf{X}$ to another state $\tilde{\mathbf{X}}$ is equal to the same probability the other way around. While Eq. (59) constitutes an unnecessary rigorous restriction, it allows for a simple straightforward solution. Prior to that, we split the transition probability into a product of three separate parts,

$$T(\mathbf{X} \to \tilde{\mathbf{X}}) = P(\mathbf{X}) \, S(\mathbf{X} \to \tilde{\mathbf{X}}) \, A(\mathbf{X} \to \tilde{\mathbf{X}}) \ , \tag{60}$$

specifically the probabilities to occupy the initial state $\mathbf{X}$, $P(\mathbf{X})$, to propose the target state $\tilde{\mathbf{X}}$ starting from $\mathbf{X}$, $S(\mathbf{X} \to \tilde{\mathbf{X}})$, and finally to accept the proposed transition, $A(\mathbf{X} \to \tilde{\mathbf{X}})$. Inserting Eq. (60) into (59) leads to the generalized form of the detailed balance equation,

$$P(\mathbf{X}) \, S(\mathbf{X} \to \tilde{\mathbf{X}}) \, A(\mathbf{X} \to \tilde{\mathbf{X}}) = P(\tilde{\mathbf{X}}) \, S(\tilde{\mathbf{X}} \to \mathbf{X}) \, A(\tilde{\mathbf{X}} \to \mathbf{X}) \ , \tag{61}$$

which is of central importance for the development and design of state of the art quantum Monte Carlo algorithms. The solution of Eq. (61) for the acceptance probability by Metropolis *et al.* [269] is given by

$$
\begin{aligned}
A(\mathbf{X} \to \tilde{\mathbf{X}}) &= \min\left(1, \frac{P(\tilde{\mathbf{X}})}{P(\mathbf{X})} \frac{S(\tilde{\mathbf{X}} \to \mathbf{X})}{S(\mathbf{X} \to \tilde{\mathbf{X}})}\right) \ , \\
&= \min\left(1, \frac{W(\tilde{\mathbf{X}})}{W(\mathbf{X})} \frac{S(\tilde{\mathbf{X}} \to \mathbf{X})}{S(\mathbf{X} \to \tilde{\mathbf{X}})}\right) \ ,
\end{aligned} \tag{62}
$$

which can be easily verified by considering Eq. (60) for the cases $P(\tilde{\mathbf{X}})S(\tilde{\mathbf{X}} \to \mathbf{X}) > P(\mathbf{X})S(\mathbf{X} \to \tilde{\mathbf{X}})$ and vice versa. Observe that the unknown normalization Z cancels in Eq. (62), which means that the acceptance probability can be readily evaluated.

We conclude this section with a sketch of a practical implementation of the Metropolis algorithm:

1. Start with an (in principle arbitrary) initial configuration $\mathbf{X}_0$.
2. Propose a new configuration $\tilde{\mathbf{X}}$ according to some pre-defined sampling probability $S(\mathbf{X}_i \to \tilde{\mathbf{X}})$.
3. Evaluate the corresponding acceptance probability $A(\mathbf{X}_i \to \tilde{\mathbf{X}})$, see Eq. (62), and subsequently draw a uniform random number $y \in [0, 1)$. If we have $y \leq A(\mathbf{X}_i \to \tilde{\mathbf{X}})$, the update is accepted and the configuration is updated to $\mathbf{X}_{i+1} = \tilde{\mathbf{X}}$. Otherwise, we reject the update and the "new" configuration is equal to the old one, $\mathbf{X}_{i+1} = \mathbf{X}_i$.
4. Repeat steps 2 and 3 until we have generated sufficiently many configurations.

Assuming an ergodic set of Monte Carlo updates (random ways to change between different configurations), the outlined algorithm can be used to generate a Markov chain of configurations $\{\mathbf{X}_i\}$ that are distributed according to $P(\mathbf{X})$, as asked in the problem statement. The concept of ergodicity is of central importance for the design of QMC algorithms and updates and means that (i) all possible configurations must be reachable in a finite (though, in principle, arbitrarily large) number of updates and (ii) the probability to go from one configuration $\mathbf{X}$ to another configuration $\tilde{\mathbf{X}}$ must only depend on $\mathbf{X}$ itself (no memory effects). A possible segment of such a Markov chain as generated by the Metropolis algorithm is given by

$$\mathbf{X}_0 = \mathbf{a} \to \mathbf{X}_1 = \mathbf{a} \to \mathbf{X}_2 = \mathbf{b} \to \mathbf{X}_3 = \ldots \quad .$$

Starting at an initial configuration $\mathbf{X}_0$, a new configuration is proposed, but the update is rejected. Therefore the second element of the Markov chain is equal to the first one, $\mathbf{X}_0 = \mathbf{X}_1 = \mathbf{a}$. The second update is accepted, meaning that the third element is changed to the new configuration, $\mathbf{X}_2 = \mathbf{b}$. It is important to understand that, even if a proposed update from $\mathbf{X}$ to $\tilde{\mathbf{X}}$ is rejected, the old configuration must still be counted as a new element in the Markov chain. Appending the Markov chain only after an update has been accepted is plainly wrong.

5.2. Path Integral Monte Carlo

The path integral Monte Carlo approach [277] (see Ref. [278] for a review) is one of the most successful methods in quantum many body physics at finite temperature. The underlying basic idea is to map the complicated quantum system onto a classical system of interacting ring polymers [279]. The high dimensionality of the resulting partition function (each particle is now represented by an entire ring polymer consisting of potentially hundreds of parts) requires a stochastic treatment, i.e., the application of the Metropolis Monte Carlo method [269]. In particular, PIMC allows for quasi-exact simulations of up to $N \sim 10^4$ bosons (and distinguishable, spinless particles, often referred to as boltzmannons, e.g., Ref. [280]) and has played a crucial role for the theoretical understanding of such important phenomena as superfluidity [281, 282, 283, 284], Bose-Einstein condensation [285, 286, 287] or the theory of collective excitations [288, 289]. Unfortunately, as we will see, PIMC simulations of electrons (and fermions, in general) are severely limited by the so-called fermion sign problem [290, 291].

5.2.1. Distinguishable particles

Let us start the discussion of the PIMC method by considering the partition function of N distinguishable particles (so-called boltzmannons), in the canonical ensemble (i.e., volume V and and inverse temperature $\beta = 1/k_\mathrm{B}T$ are fixed)

$$Z = \mathrm{Tr}\,\hat{\rho}\,. \tag{63}$$

Here $\hat{\rho} = e^{-\beta\hat{H}}$ denotes the canonical density operator and the Hamiltonian is given by the sum of a kinetic and potential part,

$$\hat{H} = \hat{K} + \hat{V}\,. \tag{64}$$

In coordinate space, Eq. (63) reads

$$Z = \int \mathrm{d}\mathbf{R}\,\langle\mathbf{R}|\,e^{-\beta\hat{H}}\,|\mathbf{R}\rangle\,, \tag{65}$$

with $\mathbf{R} = \{\mathbf{r}_1, \ldots, \mathbf{r}_N\}$ containing all $3N$ particle coordinates. The problem is that the matrix elements are not known, as $\hat{K}$ and $\hat{V}$ do not commute

$$e^{-\beta(\hat{K}+\hat{V})} = e^{-\beta\hat{V}}e^{-\beta\hat{K}}e^{-\beta^2\hat{C}}\,, \tag{66}$$

where the error term is obtained from the Baker-Campbell-Hausdorff formula as [292]

$$\hat{C} = \frac{1}{2}[\hat{V}, \hat{K}] - \beta \left(\frac{1}{6}[\hat{V}, [\hat{V}, \hat{K}]] - \frac{1}{3}[[\hat{V}, \hat{K}], \hat{K}] \right) + \dots . \tag{67}$$

To overcome this obstacle, we exploit the group property of the exponential function

$$e^{-\beta \hat{H}} = \prod_{\alpha=0}^{P-1} e^{-\epsilon \hat{H}} , \tag{68}$$

where $\epsilon = \beta/P$. By using Eq. (68) and simultaneously inserting $P - 1$ unity operators of the form

$$\hat{1} = \int d\mathbf{R}_\alpha \ |\mathbf{R}_\alpha\rangle \langle \mathbf{R}_\alpha| \ , \tag{69}$$

we obtain

$$Z = \int d\mathbf{X} \ \langle \mathbf{R}_0 | e^{-\epsilon \hat{H}} | \mathbf{R}_1 \rangle \langle \mathbf{R}_1 | \dots | \mathbf{R}_{P-1} \rangle \langle \mathbf{R}_{P-1} | e^{-\epsilon \hat{H}} | \mathbf{R}_0 \rangle \ . \tag{70}$$

Observe that Eq. (70) is still exact and the integration is carried out over P sets of particle coordinates, $d\mathbf{X} = d\mathbf{R}_0 \dots d\mathbf{R}_{P-1}$. Despite the increased dimensionality of the integral, this re-casting proves to be advantageous since each of the matrix elements must now be evaluated at a P times higher temperature, and for sufficiently many factors we can introduce a high temperature approximation, e.g., the primitive factorization

$$e^{-\epsilon \hat{H}} \approx e^{-\epsilon \hat{K}} e^{-\epsilon \hat{V}} , \tag{71}$$

which, according to the Trotter formula [293, 294], becomes exact in the limit of $P \to \infty$

$$e^{-\beta(\hat{K}+\hat{V})} = \lim_{P \to \infty} \left(e^{-\epsilon \hat{K}} e^{-\epsilon \hat{V}} \right)^P . \tag{72}$$

A more vivid interpretation of Eq. (68) is given in terms of imaginary time path integrals. In particular, we note that the density operator is equivalent to a propagation in imaginary time by $\tau = -i\beta$ (henceforth, we shall adopt the more conventional definition $\tau \to \tau/(-i) \in [0, \beta]$). Therefore, Eq. (68) corresponds to the introduction of P imaginary "time slices" of length ϵ and a factorization like Eq. (71) to an imaginary time propagator. Inserting Eq. (71) into (70) finally gives

$$Z = \int d\mathbf{X} \ \prod_{\alpha=0}^{P-1} \left(e^{-\epsilon V(\mathbf{R}_\alpha)} \rho_0(\mathbf{R}_\alpha, \mathbf{R}_{\alpha+1}, \epsilon) \right) , \tag{73}$$

where $V(\mathbf{R}_\alpha)$ denotes all potential energy terms on time slice α,

$$V(\mathbf{R}_\alpha) = \sum_{i=1}^{N} V_{\text{ext}}(\mathbf{r}_{\alpha,i}) + \sum_{k>i}^{N} W(|\mathbf{r}_{\alpha,i} - \mathbf{r}_{\alpha,k}|) , \tag{74}$$

and $W(r)$ is an arbitrary pair interaction, e.g., the Coulomb repulsion, $W_{\text{C}}(r) = 1/r$, and $V_{\text{ext}}(\mathbf{r})$ denotes an external potential. The ideal part of the density matrix is given by

$$\rho_0(\mathbf{R}_\alpha, \mathbf{R}_{\alpha+1}, \epsilon) = \frac{1}{\lambda_\epsilon^{3N}} \prod_{i=1}^{N} \left[\sum_{\mathbf{n}} \exp \left(-\frac{\pi}{\lambda_\epsilon^2} (\mathbf{r}_{\alpha,k} - \mathbf{r}_{\alpha+1,k} + \mathbf{n}L)^2 \right) \right] , \tag{75}$$

with $\lambda_\epsilon = \sqrt{2\pi\epsilon}$ being the thermal wavelength corresponding to the P-fold increased temperature. The sum over $\mathbf{n} = (n_x, n_y, n_z)^T$, $n_i \in \mathbb{Z}$, is due to the periodic boundary conditions. For completeness, we note that, technically, Eq. (75) constitutes an approximation as the correct ideal density matrix in a periodic box is given by an elliptic theta function [278]. However, this difference is of no practical consequence and, for $P \to \infty$, Eq. (75) becomes exact.

Following Chandler and Wolynes [279], Eq. (73) can be visualized as interacting ring polymers via the so-called "classical isomorphism", which is illustrated in Fig 3. The complicated quantum many-body system has been
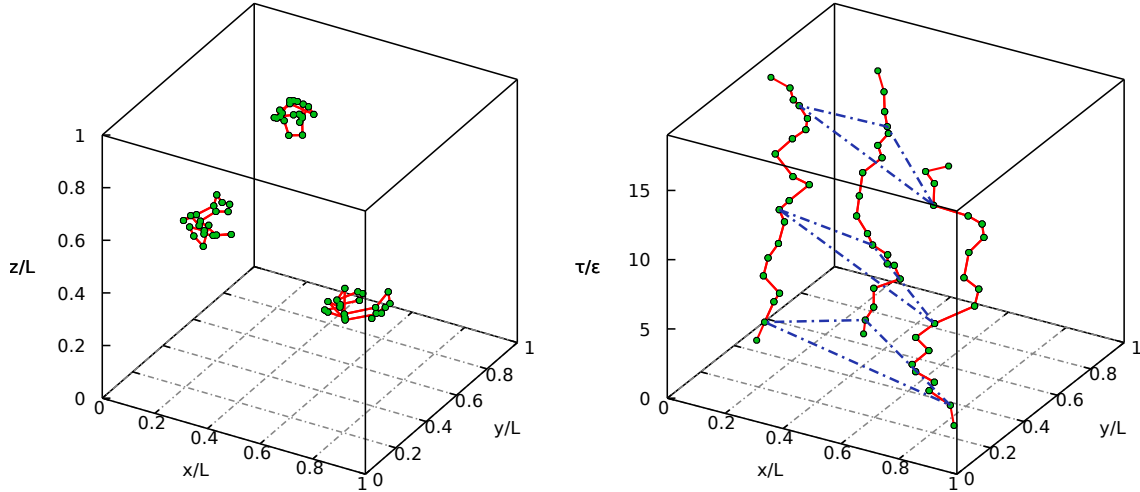
Figure 3: Schematic illustration of path integral Monte Carlo: The left panel shows a random configuration of three particles in a $3D$ simulation box. The right panel shows the same configuration, but the z-axis has been replaced by the imaginary time τ. Beads on adjacent slices are harmonically linked by the free particle density matrix (see Eq. (75), red lines) and beads from different particles on the same time slice are subject to the pair interactions (dashed blue lines).

mapped onto a classical system of interacting ring polymers. Each particle is represented by a closed path of P "beads" (i.e., the polymer), see the left panel. Beads on adjacent time slices are effectively linked by a harmonic interaction, see Eq. (75). This is further illustrated in the right panel of Fig. 3, where the z-axis has been replaced by the imaginary time τ. In addition, we note that beads from different particles on the same time slice interact via the given pair interaction $W(r)$, cf. the dashed blue lines. The extension of the paths of each particle roughly corresponds to the thermal wavelength λ_β. At high temperature, the paths resemble point particles and quantum effects are negligible. With increasing β, however, the ring polymers become more extended and the quantum nature of the system of interest starts to dominate. In practice, Eq. (73) requires a high dimensional integration, which is most effectively achieved using Monte Carlo methods. In particular, we employ the Metropolis algorithm to generate all possible configurations $\mathbf{X}$ according to the corresponding configuration weight W,

$$Z = \int d\mathbf{X} \, W(\mathbf{X}) \, , \tag{76}$$

where $W(\mathbf{X})$ is defined by Eq. (73).

Furthermore, we stress that we are not interested in the partition function itself, but instead in thermodynamic expectation values of an (in principle arbitrary) observable $\hat{A}$,

$$\langle \hat{A} \rangle = \frac{1}{Z} \int d\mathbf{R} \, \langle \mathbf{R} | \hat{A} \hat{\rho} | \mathbf{R} \rangle \, . \tag{77}$$

In practice, we have to derive a Monte Carlo estimator $A(\mathbf{X})$ so that we can estimate $\langle \hat{A} \rangle$ from the set of N_{MC} randomly generated configurations $\{\mathbf{X}\}_{\mathrm{MC}}$

$$\langle \hat{A} \rangle \quad \approx \quad A_{\mathrm{MC}} \qquad \text{and} \tag{78}$$

$$A_{\mathrm{MC}} \quad = \quad \frac{1}{N_{\mathrm{MC}}} \sum_{\mathbf{X}} A(\mathbf{X}) \, . \tag{79}$$

Eq. (78) seems to imply that the path integral Monte Carlo approach does not allow to obtain the exact thermodynamic expectation value of interest, but, instead, constitutes an approximation. More precisely, the MC estimate from a PIMC calculation is afflicted with a statistical uncertainty

$$\Delta A = \sqrt{\frac{\langle \hat{A}^2 \rangle - \langle \hat{A} \rangle^2}{N_{\mathrm{MC}}}} \, . \tag{80}$$

The statistical interpretation of Eq. (80) is that A_{MC} is with a probability of 66% within $\pm\Delta A$ of the exact result. Furthermore, this uncertainty interval decreases with an increasing number of MC samples N_{MC} so that, in principle, an arbitrary accuracy is possible. Therefore, PIMC is often described as "quasi-exact".
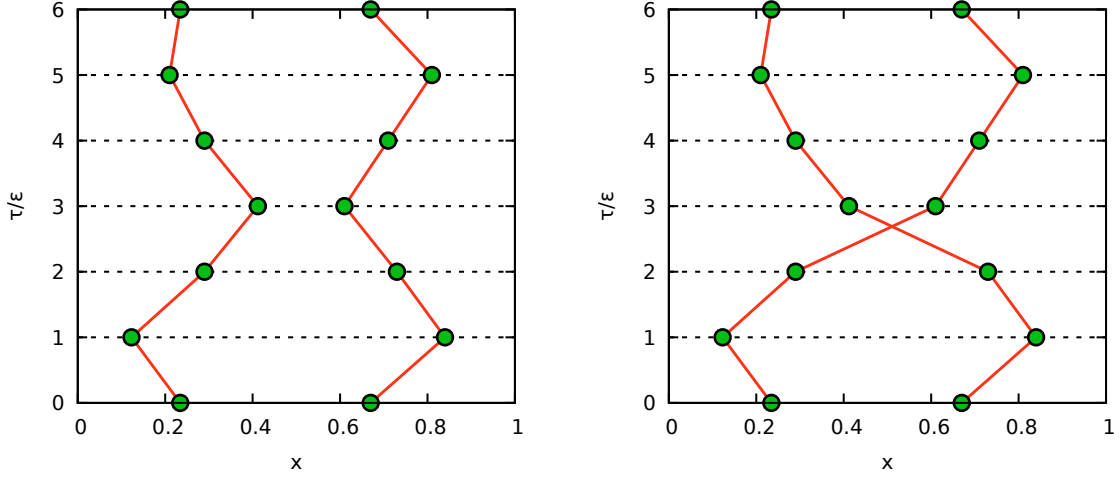
Figure 4: Schematic illustration of path integral Monte Carlo: Shown are two PIMC configurations in the τ-x-plane with no pair exchange (left) and a single pair exchange (right). The corresponding configuration weights $W(\mathbf{X})$ are positive and negative.

5.2.2. PIMC simulations of fermions

Let us now extend our considerations to the PIMC simulation of $N = N^\uparrow + N^\downarrow$ electrons, with $N^\uparrow$ and $N^\downarrow$ denoting the number of spin-up and spin-down electrons, respectively. To take into account the antisymmetric nature due to the indistinguishability of fermions, we must extend the PIMC partition function from Eq. (73) by the sum over all permutations of electrons from the same species ($S_{N^\uparrow}$ and $S_{N^\downarrow}$)

$$
Z = \frac{1}{(N^\uparrow! \, N^\downarrow!)^P} \int \mathrm{d}\mathbf{X} \prod_{\alpha=0}^{P-1} \left(\sum_{\sigma_\alpha^\uparrow \in S_{N^\uparrow}} \sum_{\sigma_\alpha^\downarrow \in S_{N^\downarrow}} \mathrm{sgn}(\sigma_\alpha^\uparrow) \mathrm{sgn}\left(\sigma_\alpha^\downarrow\right) e^{-\epsilon V(\mathbf{R}_\alpha)} \rho_0(\mathbf{R}_\alpha, \hat{\pi}_{\sigma_\alpha^\uparrow} \hat{\pi}_{\sigma_\alpha^\downarrow} \mathbf{R}_{\alpha+1}, \epsilon) \right) . \tag{81}
$$

Here $\hat{\pi}_{\sigma_\alpha^{\uparrow,\downarrow}}$ denotes the exchange operator corresponding to a particular permutation $\sigma^{\uparrow,\downarrow}$ and $\mathrm{sgn}(\sigma^{\uparrow,\downarrow})$ denotes the corresponding signum. Note that, due to the idempotency of the antisymmetry operator, the sum over all permutations can be carried out on each time slice without changing the result. In practice, the sum over all possible configurations $\mathbf{X}$ in the PIMC simulation must now be extended to include paths incorporating more than a single particle. This is illustrated in Fig. 4 where two PIMC configurations with $N = N^\uparrow = 2$ spin-polarized electrons are shown. In the left panel, there are two distinct paths. Hence, there is no pair exchange and the sign $\mathrm{sgn}(W(\mathbf{X}))$ is positive. In contrast, in the right panel, the paths cross and a single path incorporates both particles. Due to this single pair exchange, the sign of the configuration weight is negative.

5.2.3. The fermion sign problem

At this point, we must ask ourselves how to generate the configurations $\mathbf{X}$ when the corresponding weights can be both positive and negative. Obviously, this cannot be done using the Metropolis algorithm in a straightforward way, since probabilities must be strictly positive. To circumvent this issue, we switch to a modified configuration space, where we generate paths according to the absolute value of their weights, and define the modified partition function

$$
Z' \quad = \quad \int \mathrm{d}\mathbf{X} \, W'(\mathbf{X}) = \int \mathrm{d}\mathbf{X} \, |W(\mathbf{X})| . \tag{82}
$$

The correct fermionic observables are then calculated as

$$
\langle \hat{A} \rangle = \frac{\langle \hat{S} \hat{A} \rangle'}{\langle \hat{S} \rangle'} , \tag{83}
$$

where $\langle \ldots \rangle'$ denotes the expectation value corresponding to the modulus weights

$$
\langle \hat{A} \rangle' = \frac{1}{Z'} \int \mathrm{d}\mathbf{X} \, |W(\mathbf{X})| A(\mathbf{X}) , \tag{84}
$$

22

and $\hat{S}$ measures the sign of a configuration,

$$\langle \hat{S} \rangle' = \frac{1}{Z'} \int d\mathbf{X} \, S(\mathbf{X}) |W(\mathbf{X})| = \frac{Z}{Z'} \, , \tag{85}$$

with $S(\mathbf{X}) = W(\mathbf{X})/|W(\mathbf{X})|$. The problem with Eq. (83) is that for a decreasing average sign $S = \langle \hat{S} \rangle'$, both the enumerator and the denominator vanish simultaneously. This, in turn, leads to an exponentially increasing statistical uncertainty [225, 295]

$$\frac{\Delta A}{A} \sim \frac{1}{\sqrt{N_{\mathrm{MC}}} \, \langle S \rangle'} \sim \frac{e^{\beta N(f - f')}}{\sqrt{N_{\mathrm{MC}}}} \, , \tag{86}$$

where f and f' denote the free energies per particle of the original and modified systems, respectively. In particular, Eq. (86) implies that the statistical uncertainty exponentially increases with the particle number N. However, even for a fixed system size the simulations can become infeasible towards low temperature and weak coupling. Note that Troyer and Wiese [291] have shown that the FSP is NP-hard for a certain class of Hamiltonians. Therefore, a general solution to this problem is unlikely. The FSP within fermionic path integral Monte Carlo simulations is illustrated in Fig. 5, where we show two random configurations from a PIMC simulation of the uniform electron gas with $N = 33$ spin-polarized electrons, $P = 100$ imaginary time slices and a density parameter $r_s = 1$ (for completeness, we mention that we use a sampling scheme based on the worm algorithm [296, 297]). In the top panel, we chose $\theta = 4$, i.e., a relatively high temperature. Therefore, the particle paths are only slightly extended and the thermal wavelength is significantly smaller than the average inter-particle distance. This, in turn, means that pair exchange only seldom occurs within the simulation and the average sign is large, rendering such conditions perfectly suitable for PIMC simulations. In the bottom panel, the temperature is decreased to $\theta = 1$. At such conditions, λ_β is comparable to the particle distance and fermionic exchange plays an important role. This is manifest in the many exchange cycles, i.e., the paths that contain more than a single particle. Since each pair exchange leads to a sign change in the weight function, positive and negative weights occur with a nearly equal frequency, resulting an average sign of $S \sim 10^{-3}$, cf. Fig. 6. For this reason, standard PIMC simulations are confined to relatively high temperature or strong coupling where the exchange effects are suppressed by the Coulomb repulsion of the electrons.

This is investigated more quantitatively in Fig. 6. In the left panel, we show the r_s-dependence of the average sign of PIMC simulations of the UEG of $N = 33$ spin-polarized electrons, which corresponds to a closed momentum shell and, therefore, is often used in QMC studies [211, 218, 220, 217, 223]. The number of imaginary time propagators was chosen as $P = 50$ and the green, red, and blue points correspond to $\theta = 4$, $\theta = 1$, and $\theta = 0.5$, respectively. All three curves exhibit the same qualitative behavior, that is, a decreasing sign towards smaller r_s (i.e, towards high density). This can be understood by recalling that the density parameter r_s plays the role of the coupling parameter for the UEG [298]: For strong coupling, the paths of different particles in the PIMC simulation are spatially separated and, hence, exchange cycles are not very probable. With decreasing r_s, the system becomes more ideal and the occurring pair exchanges lead to smaller values of S. Furthermore, we observe that this effect is significantly increased for lower temperatures, see the discussion of Fig. 5 above. For $\theta = 4$, the sign does not drop below $S = 0.3$ and standard PIMC simulations are efficient over the entire density range. For $\theta = 1$, simulations for $r_s = 4$ are barely feasible with reasonable computational effort, whereas for $\theta = 0.5$, even $r_s = 10$, which corresponds to relatively strong coupling, is difficult.

In the right panel, we show the dependence of the average sign on system size for a constant density parameter $r_s = 1$. For all three depicted temperatures, S exhibits an exponential decay with N as predicted by Eq. (86), which becomes significantly more steep for low θ. For $\theta = 4$, simulations of $N \sim 100$ spin-polarized electrons are feasible. Yet, we stress that even at such high temperatures, fermionic exchange leads to an exponential increase of computation time with respect to N. For $\theta = 1$, the situation is considerably worse and the decay of S restricts PIMC simulations to $N < 20$. Finally, for $\theta = 0.5$, even simulations of $N = 10$ electrons are not feasible.

We thus conclude that standard PIMC cannot be used to obtain an accurate description of the UEG at warm dense matter conditions since the FSP renders simulations unfeasible towards high density and low temperature.

5.3. Restricted Path Integral Monte Carlo

A relatively common strategy to avoid the fermion sign problem is the so-called *fixed node approximation*, which is also known as the restricted PIMC (RPIMC) method [133]. On the one hand, RPIMC gets completely rid of the FSP and, therefore, simulations are feasible at low temperature and strong degeneracy. On the other hand, as we shall see, this comes at the cost of an uncontrollable systematic error so that the exact *ab initio* character of the quantum Monte Carlo paradigm is lost.
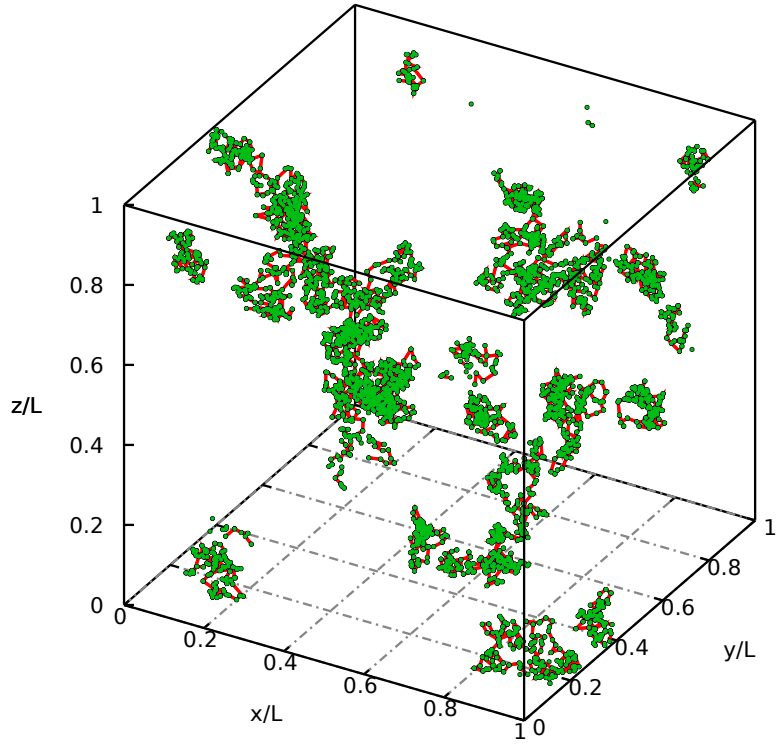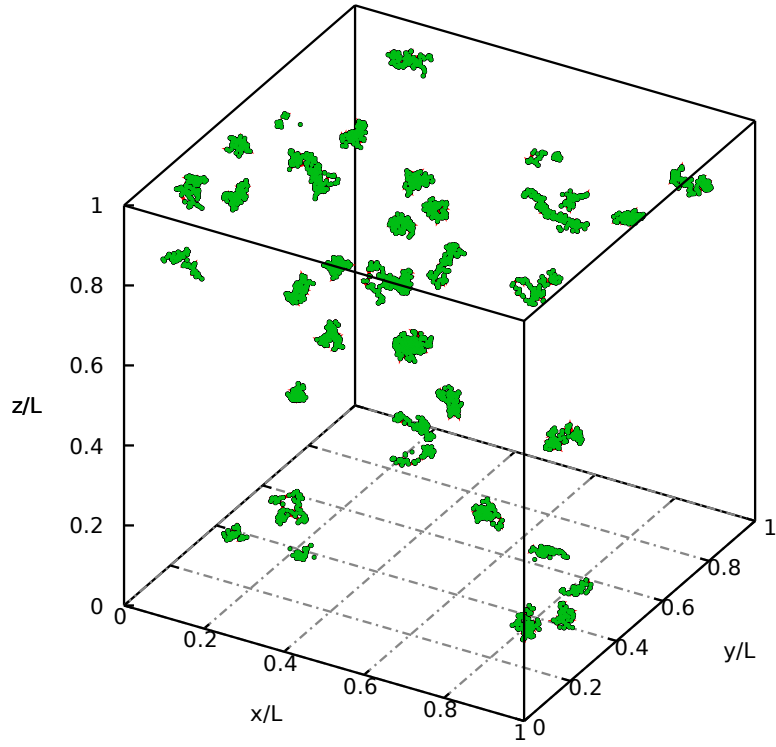
Figure 5: Screenshots from PIMC simulations of the warm dense electron gas with $N = 33$ spin-polarized electrons, $P = 100$, and $r_s = 1$ with $\theta = 4$ (top) and $\theta = 1$ (bottom).
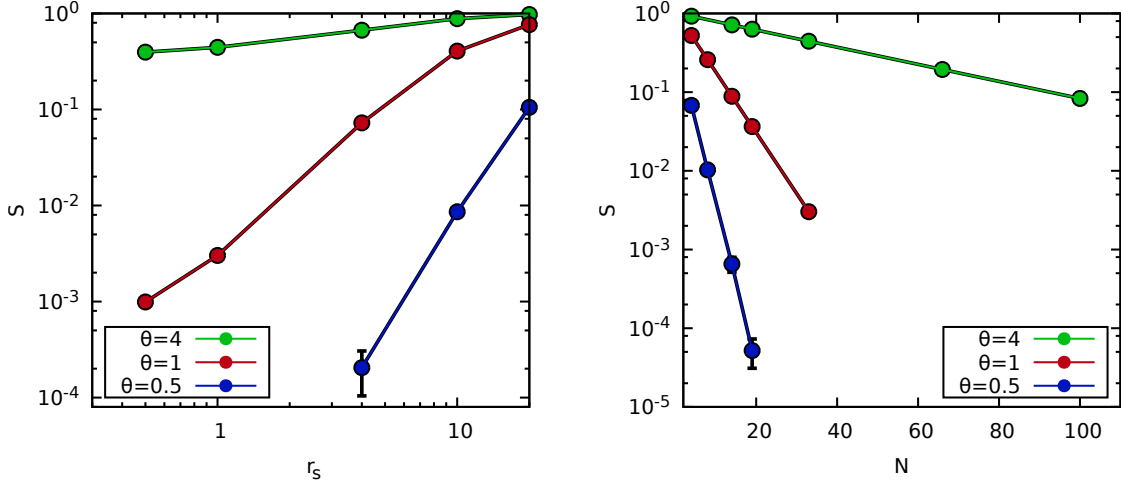
Figure 6: Average sign of PIMC simulations of the spin-polarized UEG: The left panel shows S in dependence of the density parameter r_s for $N = 33$ electrons for $\theta = 4$ (green), $\theta = 1$ (red), and $\theta = 0.5$. The right panel shows the dependence on system size for a fixed density parameter $r_s = 1$. All points have been obtained with $P = 50$ imaginary time propagators.

In statistical mechanics, the fermionic density matrix elements in coordinate space $\rho(\mathbf{R}, \mathbf{R}', \beta)$ are often introduced as the solution to the Bloch equation

$$-\frac{\mathrm{d}}{\mathrm{d}\beta} \, \rho(\mathbf{R}, \mathbf{R}', \beta) = \hat{H}\rho(\mathbf{R}, \mathbf{R}', \beta) \, , \tag{87}$$

with the initial condition

$$\rho(\mathbf{R}, \mathbf{R}', 0) = \hat{A}\delta(\mathbf{R} - \mathbf{R}') \, , \tag{88}$$

where $\hat{A}$ denotes the antisymmetrization operator. For the restricted path integral Monte Carlo approach developed by Ceperley [133, 134], the initial condition from Eq. (88) is replaced with a zero boundary condition. Following Ref. [133], we denote the second argument of the density matrix as the reference slice $\mathbf{R}_0$. Assuming that Eq. (88) holds, we can define a nodal surface

$$\gamma(\mathbf{R}_0, \tau) = \{\mathbf{R} \mid \rho(\mathbf{R}, \mathbf{R}_0, \tau) = 0\} \, , \tag{89}$$

for all imaginary times $0 \leq \tau \leq \beta$. Obviously, Eq. (89) divides the total configuration space into sub-regions of a fixed sign, described by the so-called *reach*

$$\Gamma(\mathbf{R}_0, \tau) = \{\mathbf{R}_\tau \mid \rho(\mathbf{R}, \mathbf{R}_0, \tau) \neq 0\} \, . \tag{90}$$

Equation (90) can be interpreted as the set of all paths $\mathbf{R}_\tau \to \mathbf{R}_0$ avoiding the nodes, which are the only paths contributing to the thermal density matrix. Odd permutations cross the nodal surface an odd number of times and, therefore, do not satisfy Eq. (90). They do not contribute to $\rho(\mathbf{R}, \mathbf{R}_0, \tau)$ as they cancel with the node-crossing paths of even permutation, which is sometimes denoted as the *tiling property* proved in Ref. [133]. This, in turn, means that all contributions to the thermal density matrix of a fixed reference slice $\mathbf{R}_0$ are strictly positive and, thus, perfectly suited for a Metropolis Monte Carlo simulation similar to Sec. 5.2 without the sign problem. The fermionic expectation value of an arbitrary observable can then be computed by averaging over $\mathbf{R}_0$ itself. In principle, this re-casting of the fermionic path integral Monte Carlo scheme in terms of different nodal regions is exact, given complete knowledge of the nodes. However, this information can only be obtained from a solution of the full fermionic many-body problem in the first place and, thus, little seems to be gained. In practice, we introduce an approximate *trial ansatz* for the density matrix, most commonly from the ideal system (i.e., a Slater determinant or, for multiple particle species, a product thereof). Naturally, one would assume that the ideal nodes work best for weak coupling, i.e., at high temperature and density. In particular, RPIMC simulations of the UEG should become exact for $r_s \to 0$.

In practice, within a RPIMC simulation we propose a new path and subsequently enforce the nodal constraint, Eq. (90), by computing the sign of the new configuration weight and by rejecting the move if the sign is negative.

This becomes particularly problematic when the reference slice $\mathbf{R}_0$ is changed (remember that RPIMC simulations require us to average over $\mathbf{R}_0$) since the constraint then has to be checked on all time slices. The problem is that for low temperature (i.e., for long paths, see Sec. 5.2) the nodal surface for large distances in imaginary time τ to the reference slice can significantly change for small changes of the latter. This means that even small updates of $\mathbf{R}_0$ can be rejected most of the time and the reference point *freezes*. This purely practical ergodicity problem potentially introduces a second source of systematic bias to RPIMC simulations. A comprehensive comparison of RPIMC data to other QMC methods can be found in Sec. 5.7.

As a final note, we mention that, in contrast to the ground state, the fixed node approximation as outlined above constitutes an uncontrolled approximation since the total energy is not variational. A possible strategy to overcome this issue is to perform an additional coupling constant integration (see Sec. 8) to compute the free energy f. The next step would then be to introduce a parametrization of the nodes with respect to a set of free parameters, which can be used to minimize f. However, this is substantially more complicated than at $T = 0$ and, to the best of our knowledge, has not yet been pursued in practice. Furthermore, we mention that RPIMC has nevertheless been applied to various realistic systems (such as deuterium, neon, or carbon plasmas) at warm dense matter conditions, e.g., Refs. [135, 149, 150, 151].

5.4. Permutation Blocking Path Integral Monte Carlo

The permutation blocking PIMC (PB-PIMC) approach [219, 220, 217, 221, 299] can be viewed as a further development of the standard PIMC method from Sec. 5.2 and allows to go both towards lower temperature and increased density, i.e., towards the WDM regime where fermionic exchange is crucial. Here 'blocking' refers to the combination of multiple configurations with different signs into a single weight, which means that some part of the cancellation due to the fermion sign problem is carried out analytically. To further explore this point, let us consider an illustrative example. Let us split the partition function into the two parts

$$Z = \int_{\mathbf{X}^-} d\mathbf{X} \, W(\mathbf{X}) + \int_{\mathbf{X}^+} d\mathbf{X} \, W(\mathbf{X}) \, , \tag{91}$$

where $\mathbf{X}^-$ ($\mathbf{X}^+$) denotes those configurations with a negative (positive) weight W. Now suppose that you could pair each negative weight $\mathbf{X}_i^-$ with a positive weight $\mathbf{X}_i^+$ with a larger (or equal) modulus weight and, in this way, obtain a new 'meta-configuration' $\tilde{\mathbf{X}}_i$ with a meta-configuration weight

$$\tilde{W}(\tilde{\mathbf{X}}_i) = W(\mathbf{X}_i^-) + W(\mathbf{X}_i^+) \geq 0 \, . \tag{92}$$

In this way, we have recast the partition function as the integral over terms that are strictly positive,

$$Z = \int d\tilde{\mathbf{X}} \, \tilde{W}(\tilde{\mathbf{X}}), \tag{93}$$

and the fermion sign problem would be solved. Unfortunately, in practice, such a perfect implementation of the blocking idea is not possible. Instead, we combine positive and negative permutations from the fermionic partition function, Eq. (81), within determinants both for the spin-up and down electrons. The benefits due to such intrinsically antisymmetric imaginary time propagators have long been known, see e.g. Refs. [300, 301, 302, 303]. In particular, they have been successfully exploited within the PIMC simulations by Filinov and co-workers [124, 125, 126, 127, 128, 129, 130, 131, 132]. As we will see, the problem with this approach is that with an increasing number of time slices P [which are needed to decrease the commutator errors due to the primitive factorization, cf. Eq. (67)], the effect of the blocking due to the determinant vanishes and the original sign problem is recovered. For this reason, the second key ingredient of the PB-PIMC approach is the introduction of a more sophisticated fourth-order factorization scheme that allows for sufficient accuracy with fewer time slices [304, 305, 306, 307, 308]. The simulation scheme is completed by an efficient update scheme that allows for ergodic sampling in the new configuration space [219].

Let us begin the derivation of the PB-PIMC partition function with an introduction of the fourth-order factorization of the density matrix [305]

$$e^{-\epsilon \hat{H}} \approx e^{-v_1 \epsilon \hat{W}_{a_1}} e^{-t_1 \epsilon \hat{K}} e^{-v_2 \epsilon \hat{W}_{1-2a_1}} e^{-t_1 \epsilon \hat{K}} e^{-v_1 \epsilon \hat{W}_{a_1}} e^{-2t_0 \epsilon \hat{K}} \, , \tag{94}$$

which has been studied extensively by Sakkos *et al.* [307]. First and foremost, we note that there occur three factors involving the kinetic energy operator $\hat{K}$. Therefore, for each imaginary time propagator there are three time slices. This is illustrated in the left panel of Fig. 7, where the path of a single particle is shown in the τ-x-plane with

26
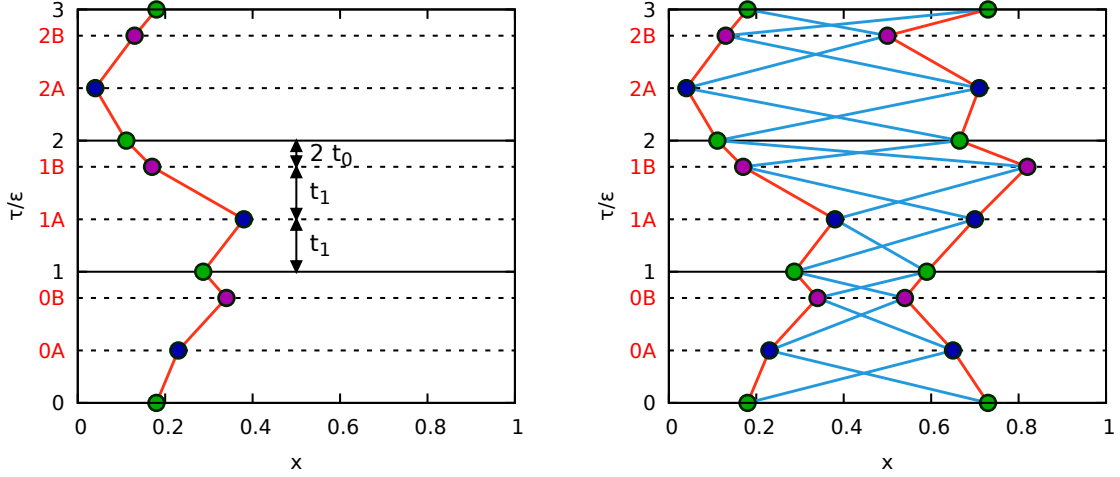
Figure 7: Schematic illustration of the PB-PIMC approach – Left panel: Illustration of the fourth-order factorization from Eq. (94) in the τ-x-plane. Beads of different colors correspond to the main (green), ancilla A (blue), and ancilla B (purple) slices, which occur for each of the $P = 3$ imaginary time propagators. The ratio t_0/t_1 is not fixed and can be used for optimization. Right panel: Combination of $3PN!$ configurations from standard PIMC into a new 'meta-configuration' due to the determinants on all time slices.

$P = 3$ fourth-order factors. For each propagator of length ϵ, there are two equidistant slices of length $t_1\epsilon$, which we denote as the main slice (green beads) and ancilla slice A (blue beads). Furthermore, there is a third slice of length $2t_0\epsilon = \epsilon(1 - 2t_1)$, i.e., ancilla slice B (purple beads). Note that the ratio of t_0/t_1 is not fixed and t_0 can be chosen freely within $0 \leq t_0 \leq (1 - 1/\sqrt{3})$, which can be exploited to further accelerate the convergence with P [307]. In order to fully cancel the first error terms from the factorization error, Eq. (67), the $\hat{W}$-operators in Eq. (94) combine the potential energy $\hat{V}$ with double commutator terms

$$[[\hat{V}, \hat{K}], \hat{V}] = \sum_{i=1}^{N} |\mathbf{F}_i|^2 \ , \tag{95}$$

with $\mathbf{F}_i = -\nabla_i V(\mathbf{R})$ denoting the entire force on particle i. In particular, it holds

$$\hat{W}_{a_1} = \hat{V} + \frac{u_0}{v_1} a_1 \epsilon^2 \sum_{i=1}^{N} |\mathbf{F}_i|^2 \ , \tag{96}$$

$$\hat{W}_{1-2a_1} = \hat{V} + \frac{u_0}{v_2}(1 - 2a_1)\epsilon^2 \sum_{i=1}^{N} |\mathbf{F}_i|^2 \ ,$$

and the coefficients u_0, v_1, and v_2 are fully determined by the choice for t_0 and $0 \leq a_1 \leq 1$,

$$u_0 = \frac{1}{12}\left(1 - \frac{1}{1 - 2t_0} + \frac{1}{6(1 - 2t_0)^3}\right) \ , \tag{97}$$

$$v_1 = \frac{1}{6(1 - 2t_0)^2} \ , \tag{98}$$

$$v_2 = 1 - 2v_1 \ . \tag{99}$$

Eq. (96) implies that, in addition to the potential energy, we have to evaluate all forces (both due to an external potential and pair interactions) on all slices for each propagator, albeit the weight of the individual contributions from the different kind of slices can be adjusted. For example, by choosing $a_1 = 0$, the forces are only relevant on ancilla slice A, whereas for $a_1 = 1/3$ all three slices contribute equally. Again, we stress that this second free parameter (in addition to t_0) can be used for optimization.

Incorporating the fourth-order partition function into the expression for Z from Eq. (81) leads to the final result for the PB-PIMC partition function [221]

$$Z = \frac{1}{(N^\uparrow! N^\downarrow!)^{3P}} \int \mathrm{d}\tilde{\mathbf{X}} \prod_{\alpha=0}^{P-1} \left(e^{-\epsilon\tilde{V}_\alpha} e^{-\epsilon^3 u_0 \tilde{F}_\alpha} D_\alpha^\uparrow D_\alpha^\downarrow\right) \ , \tag{100}$$

where $\tilde{V}_\alpha$ and $\tilde{F}_\alpha$ contain all contributions due to the potential energy and the forces for a specific propagator α,

$$\tilde{V}_\alpha = v_1 V(\mathbf{R}_\alpha) + v_2 V(\mathbf{R}_{\alpha A}) + v_1 V(\mathbf{R}_{\alpha B}) , \tag{101}$$

$$\tilde{F}_\alpha = \sum_{i=1}^{N} (a_1 |\mathbf{F}_{\alpha,i}|^2 + (1 - 2a_1)|\mathbf{F}_{\alpha A,i}|^2 + a_1 |\mathbf{F}_{\alpha B,i}|^2) . \tag{102}$$

Further, we stress that the integration has to be carried out over all possible coordinates on the ancilla slices as well, i.e.,

$$\mathrm{d}\tilde{\mathbf{X}} = \prod_{\alpha=0}^{P-1} \mathrm{d}\mathbf{R}_\alpha \mathrm{d}\mathbf{R}_{\alpha A} \mathrm{d}\mathbf{R}_{\alpha B} . \tag{103}$$

All fermionic exchange is contained within the exchange-diffusion functions

$$D_\alpha^\uparrow = \det(\rho_\alpha^\uparrow)\det(\rho_{\alpha A}^\uparrow)\det(\rho_{\alpha B}^\uparrow) , \tag{104}$$

$$D_\alpha^\downarrow = \det(\rho_\alpha^\downarrow)\det(\rho_{\alpha A}^\downarrow)\det(\rho_{\alpha B}^\downarrow) , \tag{105}$$

which constitute a product of the determinants of the free particle (diffusion) matrices between particles i and j on two adjacent time slices (not propagators)

$$\rho_\alpha^\uparrow(i,j) = \frac{1}{\lambda_{t_1\epsilon}^3} \sum_{\mathbf{n}} \exp\left(-\frac{\pi}{\lambda_{t_1\epsilon}^2}(\mathbf{r}_{\alpha,j}^\uparrow - \mathbf{r}_{\alpha A,i}^\uparrow + \mathbf{n}L)^2\right) , \tag{106}$$

$$\rho_{\alpha A}^\uparrow(i,j) = \frac{1}{\lambda_{t_1\epsilon}^3} \sum_{\mathbf{n}} \exp\left(-\frac{\pi}{\lambda_{t_1\epsilon}^2}(\mathbf{r}_{\alpha A,j}^\uparrow - \mathbf{r}_{\alpha B,i}^\uparrow + \mathbf{n}L)^2\right) , \tag{107}$$

$$\rho_{\alpha B}^\uparrow(i,j) = \frac{1}{\lambda_{2t_0\epsilon}^3} \sum_{\mathbf{n}} \exp\left(-\frac{\pi}{\lambda_{2t_0\epsilon}^2}(\mathbf{r}_{\alpha B,j}^\uparrow - \mathbf{r}_{\alpha+1,i}^\uparrow + \mathbf{n}L)^2\right) , \tag{108}$$

with an analogous definition for the spin-down electrons. Note that we have again exploited the idempotency property of the antisymmetrization operator to introduce determinants on all the ancilla time slices as well. The reason for this choice becomes obvious by closely examining the new configuration space, which is illustrated in the right panel of Fig. 7. Shown is a configuration of two particles in the τ-x-plane and beads on different types of time slices are distinguished by the different colors. For standard PIMC, a typical configuration would be given by the two red paths, which would correspond to two separate paths without a pair exchange. In addition, one would also have to consider all configurations with the same positions of the individual beads, but different connections between beads on adjacent slices, which would lead to contributions with different signs. By introducing the determinants within the PB-PIMC scheme, we combine all $N!$ possible connections between beads on adjacent slices into a single configuration weight. As explained in the beginning of this section, this analytic blocking of configurations with different signs results in a drastically less severe sign problem and, therefore, to perform simulations in substantial parts of the WDM regime.

This is further illustrated in Fig. 8, where we show a random screenshot from a PB-PIMC simulation with $P = 4$ fourth-order propagators and $N = 33$ spin-polarized electrons at $r_s = 1$ and $\theta = 1$. Again, the beads of different color correspond to different kind of time slices. The different line width of the red connections between some beads on adjacent slices symbolize the magnitude of the diffusion matrix elements, Eq. (106). Without the determinants, each bead would have exactly two connections. Hence, beads with more than two visible links in Fig. 8 significantly contribute to the permutation blocking, which, in stark contrast to standard PIMC, makes simulations feasible under such conditions.

As explained in Sec. 5.1, we use the Metropolis Monte Carlo algorithm [269] to generate all possible paths $\tilde{\mathbf{X}}$ according to the appropriate configuration weight defined by Eq. (100). Let us now discuss how we can compute physical expectation values from this Markov chain of configurations. For example, the total energy of the system can be computed from the partition function via the well-known relation

$$E = -\frac{1}{Z}\frac{\partial Z}{\partial \beta} , \tag{109}$$

and plugging in the PB-PIMC expression for Z, Eq. (100), into (109) gives the desired Monte Carlo estimator (for N spin-polarized electrons, the generalization to an arbitrary degree of spin polarization is obvious),

$$E = \frac{1}{P}\sum_{\alpha=0}^{P-1}\left(\tilde{V}_\alpha + 3\epsilon^2 u_0 \tilde{F}_k\right) + \frac{3DN}{2\epsilon} - \frac{\pi}{\beta}\sum_{\alpha=0}^{P-1}\sum_{i=1}^{N}\sum_{k=1}^{N}\left(\eta_{k,i}^\alpha \lambda_{t_1\epsilon}^{-2} + \eta_{k,i}^{\alpha A}\lambda_{t_1\epsilon}^{-2} + \eta_{k,i}^{\alpha B}\lambda_{2t_0\epsilon}^{-2}\right) , \tag{110}$$

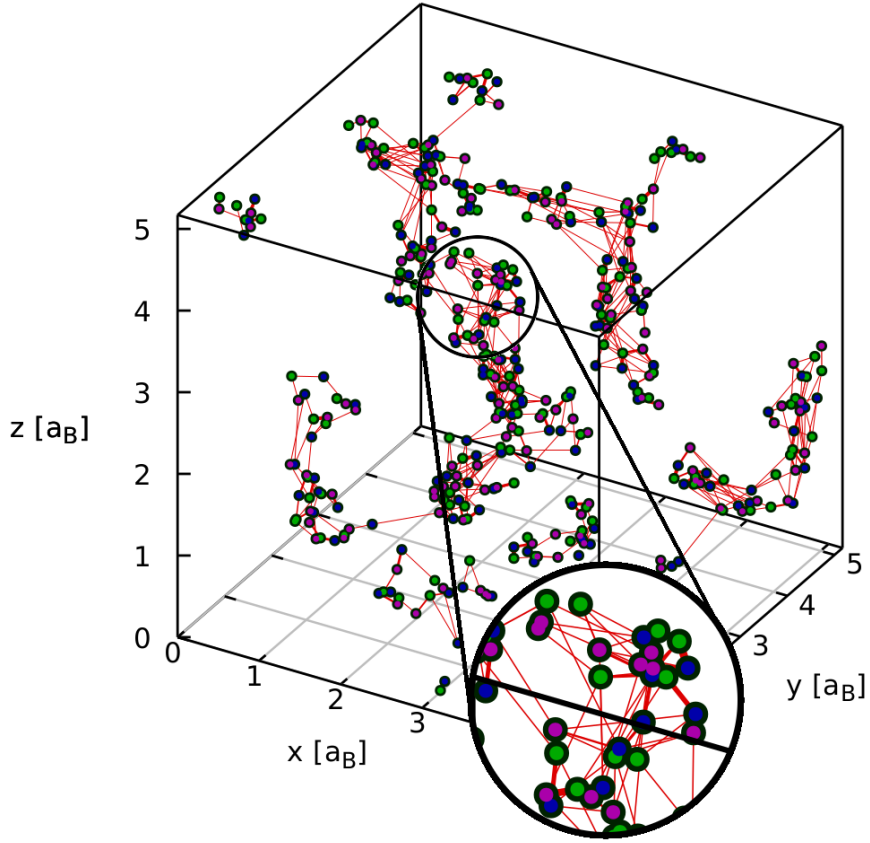Figure 8: Screenshot of a PB-PIMC simulation of the spin-polarized UEG with $N = 33$, $P = 4$, $r_s = 1$, and $\theta = 1$. The green, blue, and purple beads correspond to main, ancilla A, and ancilla B slices, respectively. The different width of the red connections symbolizes the magnitude of the diffusion matrix elements, cf. Eq. (106). Beads with more than two visible links significantly contribute to the permutation blocking.
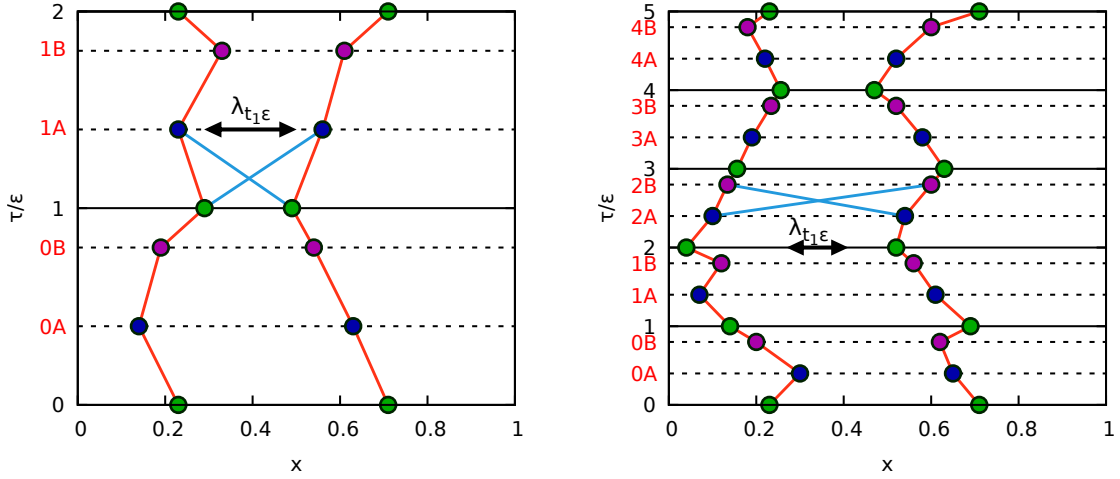
Figure 9: Effect of an increasing number of imaginary time slices on the permutation blocking – Shown are configurations with two spin-polarized electrons in the τ-x-plane with $P = 2$ (left) and $P = 5$ (right) fourth-order propagators. For $P = 2$, the thermal wavelength of a single time slice, $\lambda_{t_1\epsilon} = \sqrt{2\pi t_1\epsilon}$, is comparable to the average particle distance. Therefore, the off-diagonal (blue) diffusion matrix elements [cf. Eq. (106)] are comparable in magnitude to the diagonal (red) elements, and the permutation blocking within the determinants is efficient. In contrast, for $P = 5$ there are either large diagonal (as in the depicted configuration) or large off-diagonal elements, but not both simultaneously, and the permutation blocking will have almost no effect.

with the definitions

$$\eta_{k,i}^{\alpha} = \frac{(\rho_\alpha^{-1})_{k,i}}{\lambda_{t_1\epsilon}^3} \sum_{\mathbf{n}} \left(e^{-\frac{\pi}{\lambda_{t_1\epsilon}^2}(\mathbf{r}_{\alpha,k} - \mathbf{r}_{\alpha A,i} + L\mathbf{n})^2} (\mathbf{r}_{\alpha,k} - \mathbf{r}_{\alpha A,i} + L\mathbf{n})^2 \right) \tag{111}$$

$$\eta_{k,i}^{\alpha A} = \frac{(\rho_{\alpha A}^{-1})_{k,i}}{\lambda_{t_1\epsilon}^3} \sum_{\mathbf{n}} \left(e^{-\frac{\pi}{\lambda_{t_1\epsilon}^2}(\mathbf{r}_{\alpha A,k} - \mathbf{r}_{\alpha B,i} + L\mathbf{n})^2} (\mathbf{r}_{\alpha A,k} - \mathbf{r}_{\alpha B,i} + L\mathbf{n})^2 \right) \tag{112}$$

$$\eta_{k,i}^{\alpha B} = \frac{(\rho_{\alpha B}^{-1})_{k,i}}{\lambda_{2t_0\epsilon}^3} \sum_{\mathbf{n}} \left(e^{-\frac{\pi}{\lambda_{2t_0\epsilon}^2}(\mathbf{r}_{\alpha B,k} - \mathbf{r}_{\alpha+1,i} + L\mathbf{n})^2} (\mathbf{r}_{\alpha B,k} - \mathbf{r}_{\alpha+1,i} + L\mathbf{n})^2 \right) \quad . \tag{113}$$

Here the notation $(\rho_\alpha^{-1})_{k,i}$ indicates the (k,i)-element of the inverse diffusion matrix. Interestingly, the contribution of the force-terms to E in Eq. (110) splits to both the kinetic and potential energy, see Refs. [307, 219] for more details.

Finally, let us consider the effect on the permutation blocking of an increasing number of imaginary time propagators P, which is illustrated in Fig. 9. In the left panel, we show a configuration of two spin-polarized electrons in the τ-x-plane with $P = 2$ fourth-order propagators. In this case, the thermal wavelength of a single time slice, $\lambda_{t_1\epsilon} = \sqrt{2\pi t_1\epsilon}$, is comparable to the average particle distance. Hence, the off-diagonal diffusion matrix elements (blue connections) are similar in magnitude to the diagonal elements (red connections) and the permutation blocking within the determinants is effective. However, this situation is drastically changed for increasing P, cf. the right panel where a similar configuration is depicted for $P = 5$. Evidently, in this case $\lambda_{t_1\epsilon}$ is much smaller than the particle distance and there are either large diagonal [which is the case in the depicted configuration] or off-diagonal diffusion matrix elements, but not both simultaneously. Therefore, the permutation blocking will be ineffective and for $P \to \infty$ the original sign problem from standard PIMC will be recovered. In a nutshell, the introduction of antisymmetric imaginary time propagators allows to significantly alleviate the FSP and therefore to extend standard PIMC towards more degenerate systems. However, since this effect vanishes with increasing P, it is vital to combine the permutation blocking with a sophisticated factorization of the density matrix that allows for sufficient accuracy with only few propagators.

Let us conclude this section with a more quantitative discussion of the fermion sign problem within PB-PIMC simulations of the spin-polarized UEG at warm dense matter conditions. In the left panel of Fig. 10, we show the dependence of the average sign on the density parameter r_s for PB-PIMC simulations of $N = 33$ spin-polarized electrons with $P = 2$ imaginary time propagators at $\theta = 1$ (red), $\theta = 2$ (blue), and $\theta = 4$ (black). All three curves exhibit a qualitatively similar behavior, i.e., a decreasing sign towards higher density, see also the discussion of Fig. 6 above. However, in stark contrast to standard PIMC (green curve for $\theta = 1$), the sign stays finite for all r_s. Thus, it has been demonstrated that, for the present conditions, PB-PIMC simulations are feasible over the
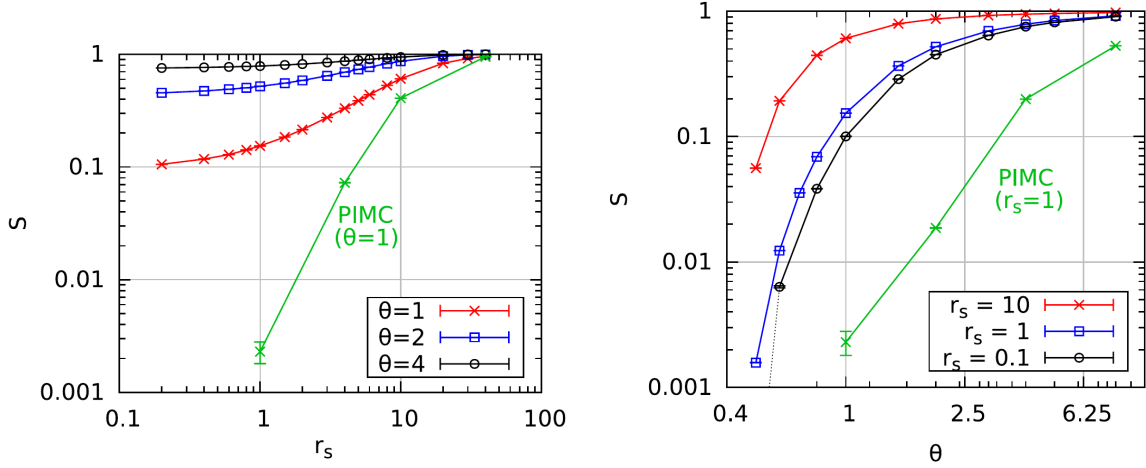
Figure 10: Average sign in PB-PIMC simulations of $N = 33$ spin-polarized electrons at warm dense matter conditions – Left panel: Density-dependence of S for $P = 2$ propagators for $\theta = 1$ (red), $\theta = 2$ (blue), and $\theta = 4$ (black). Right panel: Temperature-dependence of S for $P = 2$ for $r_s = 10$ (red), $r_s = 1$ (blue), and $r_s = 0.1$ (black). All standard PIMC results for S (green curves) have been taken from the Supplemental Material of Ref. [211]. Both panels are reproduced with the permissions of the authors of Ref. [220].

entire density range. In the right panel, the dependence of the average sign on θ is shown for the same system for $r_s = 10$ (red), $r_s = 1$ (blue), and $r_s = 0.1$ (black). For large temperatures, the sign is nearly equal to unity and the computational effort is small. With decreasing θ, both the diagonal and off-diagonal diffusion matrix elements become larger and both positive and negative determinants appear within the PB-PIMC simulations, eventually leading to a steep drop of S, which is more pronounced at weak coupling. Still, we stress that it is precisely at such conditions that the permutation blocking is most effective as well. Therefore, the sign problem is much less severe compared to standard PIMC (green curve). Overall, it can be seen that for warm dense matter conditions, i.e., for $r_s = 1, \ldots, 6$, PB-PIMC simulations are feasible down to $\theta = 0.5$.

5.5. Configuration Path Integral Monte Carlo

Another PIMC variant that has been proven to be highly valuable for the simulation of the UEG is the Configuration PIMC (CPIMC) method [215, 216, 218, 227]. It belongs to the class of continuous time world line Monte Carlo algorithms (CTWL-MC), which avoid the imaginary time discretization error by switching to the interaction picture with respect to a suitable part of the Hamiltonian. The basic idea of CTWL-MC stems from the works of Prokofev *et al.* [309] and Beard and Wiese [310]. Subsequently, many system specific CTWL-MC algorithms had been developed and highly optimized for fermionic as well as bosonic lattice models, most importantly for different variants of Hubbard and impurity models. A comprehensive review of the existing CTWL-MC algorithms and their applications can be found in Ref. [311]. However, until the development of CPIMC, continuous fermionic systems with long range Coulomb interactions have not been tackled with the CTWL-MC formalism mainly for two reasons: 1) the long range Coulomb interaction causes a severe sign problem and 2) it introduces new complex classes of diagrams which require a significantly more elaborate Monte-Carlo algorithm.

Essentially, CPIMC can be viewed as performing Metropolis Monte Carlo with the complete (infinite) perturbation expansion of the partition function with respect to the coupling strength of the system. As such, this method is most efficient at weak coupling and becomes infeasible at strong coupling where it suffers from a severe sign problem; yet, the critical coupling parameter lies well beyond the failure of analytical approaches. Moreover, CPIMC is practically applicable over the entire temperature range, even down to the ground state. Thus, regarding the range of applicability with respect to density and temperature, CPIMC is highly complementary to the PB-PIMC approach discussed in Sec. 5.4.

5.5.1. CPIMC representation of the partition function

For the derivation of both the standard PIMC and the PB-PIMC expansion of the partition function we started with utilizing $N-$particle states in coordinate representation to perform the trace over the density operator in Eq. (63). The correct Fermi statistics are then taken into account via a subsequent anti-symmetrization of the density operator, which causes the weight function to alter the sign with each pair exchange and, hence, can be regarded as the source of the FSP. To avoid this particular source, in CPIMC, we switch gears by making use of the second quantization representation of quantum mechanics for the UEG, which has been introduced in Sec. 2.3.

Here, the N-particle states, Eq. (13), are given by Slater determinants, which form a complete basis set of the N-particle states in Fock space. Thus, we can compute the partition function, Eq. (63), by carrying out the trace over the density operator with these states, yielding

$$Z = \sum_{\{n\}} \langle \{n\} | e^{-\beta \hat{H}} | \{n\} \rangle \ . \tag{114}$$

Unfortunately, the evaluation of the matrix elements of the density operator is not straightforward since the Slater determinants of plane waves are no eigenstates of the interacting UEG Hamiltonian, Eq. (11), but only of the ideal UEG. One solution to this problem is to use the series expansion of the exponential function

$$\begin{aligned}
Z &= \sum_{K=0}^{\infty} \sum_{\{n\}} \langle \{n\} | \frac{(-\beta)^K}{K!} \hat{H}^K | \{n\} \rangle \\
&= \sum_{K=0}^{\infty} \sum_{\{n\}^{(0)}} \sum_{\{n\}^{(1)}} \cdots \sum_{\{n\}^{((K-1))}} \frac{(-\beta)^K}{K!} \langle \{n\}^{(0)} | \hat{H} | \{n\}^{(1)} \rangle \langle \{n\}^{(1)} | \hat{H} | \{n\}^{(2)} \rangle \cdot \ldots \cdot \langle \{n\}^{(K-1)} | \hat{H} | \{n\}^{(K)} \rangle \ , \quad (115)
\end{aligned}$$

where we have inserted $K-1$ unities of the form $\hat{1} = \sum_{\{n\}^{(i)}} | \{n\}^{(i)} \rangle \langle \{n\}^{(i)} |$ so that $\{n\}^{(0)} = \{n\}^{(K)}$ holds implicitly. Applying the Slater-Condon rules to the UEG Hamiltonian we readily compute its matrix elements according to

$$\langle \{n\} | \hat{H} | \{\bar{n}\} \rangle = \begin{cases} D_{\{n\}} = \frac{1}{2} \sum_l \mathbf{k}_l^2 n_l + \frac{1}{2} \sum_{l<k} w_{lklk}^- n_l n_k, & \{n\} = \{\bar{n}\} \ , \\ Y_{\{n\},\{\bar{n}\}} = w_{pqrs}^- (-1)^{\alpha_{\{n\},pq} + \alpha_{\{\bar{n}\},rs}}, & \{n\} = \{\bar{n}\}_{r<s}^{p<q} \ , \end{cases} \tag{116}$$

with the phase factor

$$\alpha_{\{n\},pq} = \sum_{l=\min(p,q)+1}^{\max(p,q)-1} n_l \ , \tag{117}$$

and the two-particle integrals being defined in Eq. (12). In this notation, $|\{\bar{n}\}_{r<s}^{p<q}\rangle$ refers to the Slater determinant that is obtained by exciting two electrons from the orbitals r and s to p and q in $|\{\bar{n}\}\rangle$. Performing Metropolis Monte Carlo with the derived expression for the partition function, Eq. (115), has been termed the Stochastic Series Expansion (SSE) method. In particular, this approach has been successfully used for the simulation of the Heisenberg model [312, 313, 314, 315, 316], for which Eq. (115) can be recast into a form that has solely positive addends, thereby completely avoiding the sign problem. However, this is not possible for the UEG and, in addition to the factor $(-\beta)^K$, we observe that the matrix elements can also attain both positive and negative values, which causes a serious sign problem. In CPIMC, we therefore follow a different strategy and separate the diagonal part $\hat{D}$ of the Hamiltonian by exploiting the following identity of the density operator

$$e^{-\beta \hat{H}} = e^{-\beta \hat{D}} \hat{T}_\tau e^{-\int_0^\beta \hat{Y}(\tau) \mathrm{d}\tau} = e^{-\beta \hat{D}} \sum_{K=0}^{\infty} \int_0^\beta d\tau_1 \int_{\tau_1}^\beta d\tau_2 \ldots \int_{\tau_{K-1}}^\beta d\tau_K (-1)^K \hat{Y}(\tau_K) \hat{Y}(\tau_{K-1}) \cdot \ldots \cdot \hat{Y}(\tau_1) \ , \tag{118}$$

where $\hat{T}_\tau$ denotes the time-ordering operator and the time-dependence of the off-diagonal operator $\hat{Y}$ refers to the interaction picture in imaginary time with respect to the diagonal operator $\hat{D}$,

$$\hat{Y}(\tau) = e^{\tau \hat{D}} \hat{Y} e^{-\tau \hat{D}} \ . \tag{119}$$

Note that, independent of the underlying one-particle basis of the quantization, according to the Slater-Condon rules the Hamiltonian can always be split into a diagonal and off-diagonal contribution such that $\hat{H} = \hat{D} + \hat{Y}$. After inserting Eq. (118) into Eq. (115) and re-ordering some terms, the partition function becomes

$$Z = \sum_{\substack{K=0 \\ K \neq 1}}^{\infty} \sum_{\{n\}^{(0)}} \sum_{\{n\}^{(1)}} \cdots \sum_{\{n\}^{(K-1)}} \int_0^\beta d\tau_1 \int_{\tau_1}^\beta d\tau_2 \ldots \int_{\tau_{K-1}}^\beta d\tau_K (-1)^K e^{-\sum_{i=0}^K D_{\{n^{(i)}\}} (\tau_{i+1} - \tau_i)} \prod_{i=1}^K Y_{\{n^{(i)}\},\{n^{(i-1)}\}} \ . \tag{120}$$
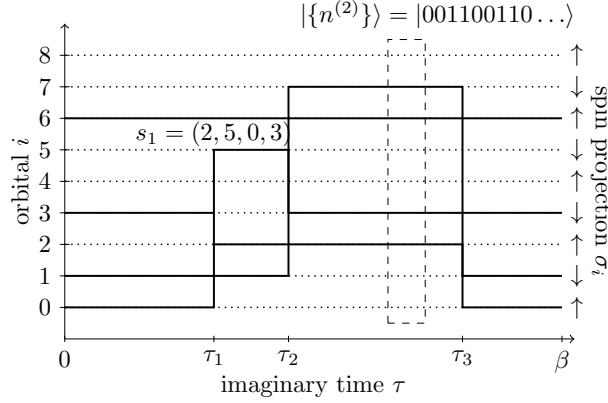
Figure 11: Sketch of a typical CPIMC path of $N = 4$ unpolarized electrons in Slater determinant (Fock) space in imaginary time. The starting determinant $\{n\}^{(0}$ at $\tau = 0$ undergoes three two-particle excitations at times τ_1, τ_2, and τ_3, where the last excitation defined by the involved orbitals $s_3 = (0, 1, 2, 7)$ must always ensure that the last state $\{n\}^{(3)}$ is equivalent to $\{n\}^{(0)}$. Reproduced from Ref. [221] with permission of the authors.

Taking into account that the off-diagonal matrix elements do not vanish only if the occupation numbers of the left and right state, i.e. $\{n\}^{(i)}$ and $\{n\}^{(i-1)}$, differ in exactly four orbitals p,q,r,s, cf. Eq. (116), we may introduce a multi-index $s_i = (pqrs)$ defining these four orbitals and re-write the summation as follows

$$Z = \sum_{\substack{K=0 \\ K \neq 1}}^{\infty} \sum_{\{n\}} \sum_{s_1 \ldots s_{K-1}} \int_0^\beta d\tau_1 \int_{\tau_1}^\beta d\tau_2 \ldots \int_{\tau_{K-1}}^\beta d\tau_K (-1)^K e^{-\sum_{i=0}^K D_{\{n^{(i)}\}}(\tau_{i+1}-\tau_i)} \prod_{i=1}^K Y_{\{n^{(i)}\},\{n^{(i-1)}\}}(s_i) , \qquad (121)$$

where $\{n\} = \{n\}^{(0)} = \{n\}^{(K)}$ always holds. This is the exact CPIMC expansion of the partition function. Regarding the application of the Metropolis algorithm, the benefit of Eq. (121) over the SSE, Eq. (115), is obvious: by switching to the interaction picture we got rid of all sign changes that are caused by the diagonal matrix elements since in Eq. (121) these solely enter in the exponential function, which is always positive. Nevertheless, the sign changes due to the off-diagonal matrix elements are still present and are the source of the sign problem in the CPIMC method.

Similar to the standard PIMC and PB-PIMC approach, each contribution to the CPIMC expansion of the partition function, Eq. (121), can be interpreted as a path in imaginary time, $\mathbf{X}$, that is entirely defined by the starting set of occupation numbers $\{n\}$ and all subsequent excitations $\{s_1, s_2 \ldots, s_K\}$ with their corresponding times $\{\tau_1, \tau_2 \ldots, \tau_K\}$, i.e.,

$$\mathbf{X} = (K, \{n\}, s_1, \ldots, s_{K-1}, \tau_1, \ldots, \tau_K) . \qquad (122)$$

In contrast to the standard PIMC formulation, these paths now evolve in the discrete Fock space instead of the continuous coordinate space. Moreover, there is no time discretization in the CPIMC formulation as the excitations occur at continuous times τ_i. Hence, unlike PIMC in coordinate space, there is no time discretization error. A sketch of a typical path occurring in the simulation of $N = 4$ unpolarized electrons is depicted in Fig. 11, where we chose the ordering of the spin orbitals such that even (odd) numbers correspond to up (down) spin projections. In correspondence to their visual appearance in these paths we refer to the excitations as "kinks". According to Eq. (121), the corresponding weight of each paths is given by

$$W(\mathbf{X}) = (-1)^K e^{-\sum_{i=0}^K D_{\{n^{(i)}\}}(\tau_{i+1}-\tau_i)} \prod_{i=1}^K Y_{\{n^{(i)}\},\{n^{(i-1)}\}}(s_i) . \qquad (123)$$

Note that, as discussed in detail in Sec. 5.2.3, the Metropolos algorithm can only be applied when using the modulus of the weight function. As usual, the Monte Carlo estimator of an observable, cf. Eq. (78), is derived from its thermodynamic relation to the partition function. For example, for the energy we have

$$\langle \hat{H} \rangle = -\frac{\partial}{\partial \beta} \ln Z = \sum_{\substack{K=0 \\ K \neq 1}}^{\infty} \sum_{\{n\}} \sum_{s_1 \ldots s_{K-1}} \int_0^\beta d\tau_1 \int_{\tau_1}^\beta d\tau_2 \ldots \int_{\tau_{K-1}}^\beta d\tau_K \left(\frac{1}{\beta} \sum_{i=0}^K D_{\{n^{(i)}\}}(\tau_{i+1} - \tau_i) - \frac{K}{\beta} \right) W(\mathbf{X}) . \qquad (124)$$

33
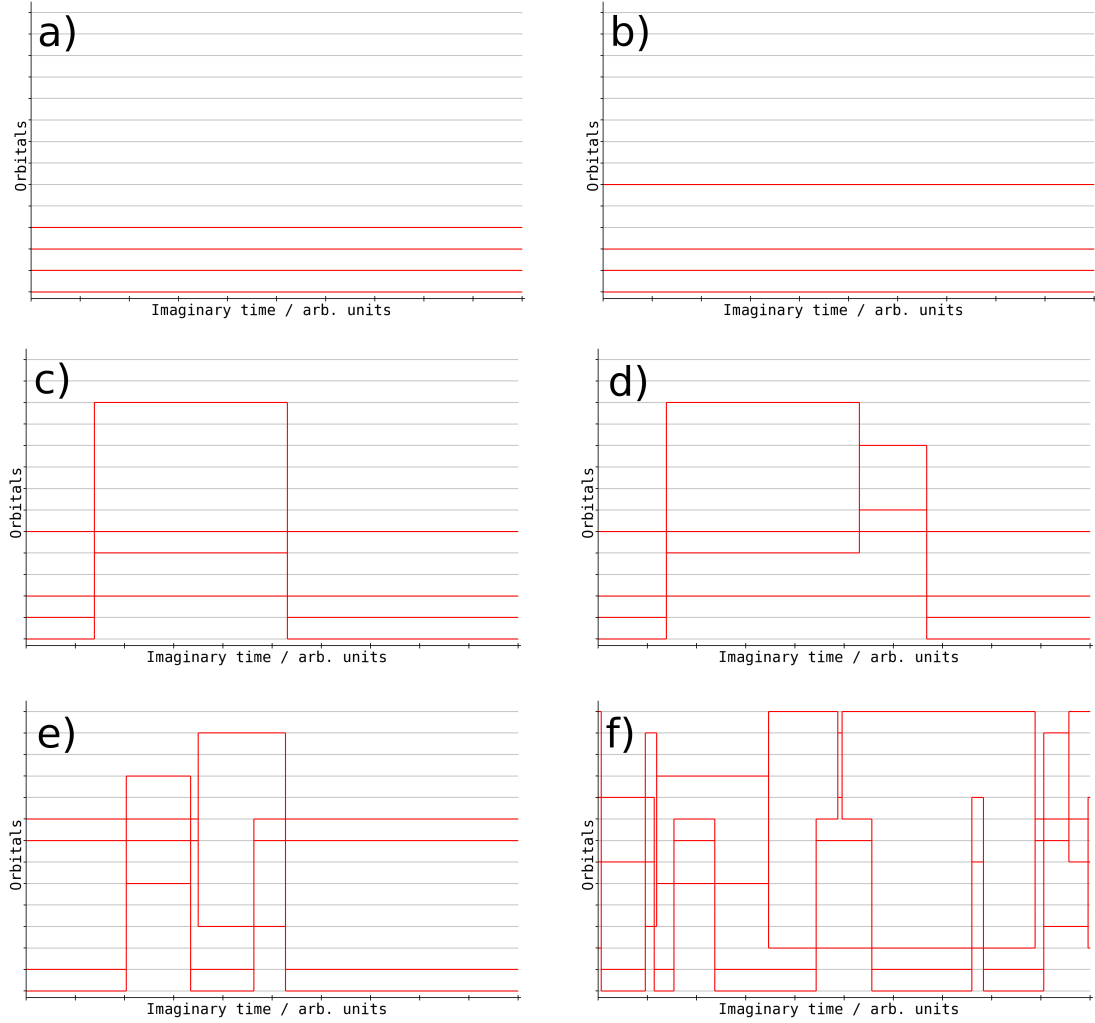
Figure 12: Snap shots of CPIMC paths from the simulation of $N = 4$ unpolarized electrons at $r_s = 1$ ant $\theta = 1$ in $N_B = 14$ plane wave spin-orbitals (indicated by the grey lines). The orbitals are ordered according to their corresponding kinetic energy $\mathbf{k}_i^2/2$. Depicted are the occupied orbitals (red lines) in dependence of the imaginary time, which sum up to 4 at any specific time $\tau \in [0, \beta]$. Panel **a)** shows the initial path that is used as the starting configuration in the Markov chain: no kinks with the lowest orbitals being occupied. In panel **b)** an entire orbital is excited, after which a pair of kinks is added in panel **c)**. Only then is it possible add single kinks by changing another kink in the path, which is depicted in panel **d)**. This way, depending on the density and temperature, the CPIMC algorithm eventually generates paths with more complicated structures as shown in panels **e)** and **d)**.
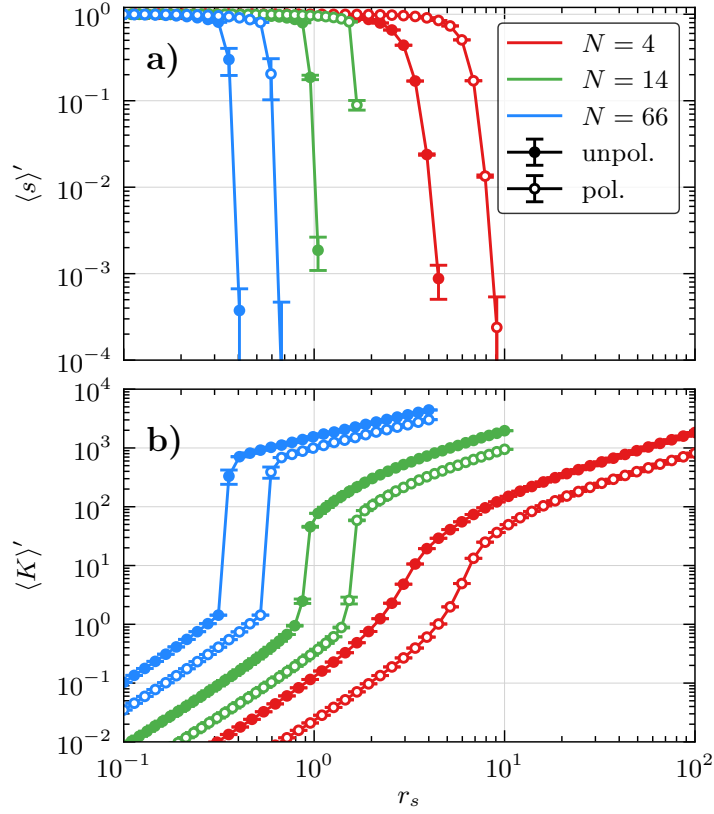
Figure 13: Average sign **a)** and average number of kinks **b)** in CPIMC simulation in dependence on the density parameter for $N = 4, 14, 66$ at $\theta = 1$. Shown are the results from the simulation of the spin-polarized (circles) and unpolarized (dots) UEG. Reproduced from Ref. [221] with permission of the authors.

In practice, in CPIMC simulations, we start the generation of the Markov chain from an initial path without kinks and with the lowest N plane wave spin-orbitals being occupied, where we choose the ordering of the orbitals in accordance to their kinetic energy $\mathbf{k}_i^2/2$. Fig. 12 a) shows a snap shot of such a starting path from a CPIMC simulation of $N = 4$ unpolarized electrons in $N_B = 14$ spin orbitals. Due to the fact that there are no $\beta-$periodic (closed) paths containing only a single kink, only two possible changes can be proposed to proceed: either an entire occupied orbital can be excited to an unoccupied orbital, see Fig. 12 b), or a symmetric pair of kinks can be added at once, see Fig. 12 c). These proposed changes are accepted or rejected with the corresponding Metropolis acceptance probability, cf. Eq. (62), which is computed using the modulus of the weight function $|W(\mathbf{X})|$. Only after a symmetric pair of kinks has been successfully added is it possible to add single kinks by changing another as demonstrated in Fig. 12 d). Depending on the temperature and density parameter in the simulation, the CPIMC algorithm eventually generates paths containing more kinks and more complex structures, see Figs. 12 e) and f).

5.5.2. The sign problem in the CPIMC approach

As discussed in Sec. 5.2.3, we can only apply the Metropolis algorithm to a partition function that has a weight function with alternating signs by simulating a modified system defined by the modulus of the weight function, cf. Eq. (82). Yet, this procedure comes at the cost of introducing the FSP. It is important to note that each kink enters the CPMC weight function, Eq. (121), with three possible sign changes: 1) the factor $(-1)^K$, 2) the sign of the corresponding two-particle integral, Eq. (12), and 3) the phase factor, Eq. (117), that depends on the set of occupation numbers at the time of the kink. To investigate the FSP in the CPIMC approach, Fig. 13 shows the average sign, a), and the average number of kinks, b), of all sampled paths in the generated Markov chain for simulations of $N = 4$ (red), $N = 14$ (green), and $N = 66$ (blue) electrons at $\theta = 1$ in dependence of the density parameter r_s, both for the polarized (circles) and unpolarized (dots) UEG. Since simulations with an average sign below $\sim 10^{-3}$ are not feasible, these quantities determine the applicable regime of the basic CPIMC method in the density-temperature plane. Independent from the number of electrons, the average sign is always unity in the ideal limit $r_s \to 0$, since here the UEG Hamiltonian is diagonal in the utilized plane wave basis. Hence, there cannot be
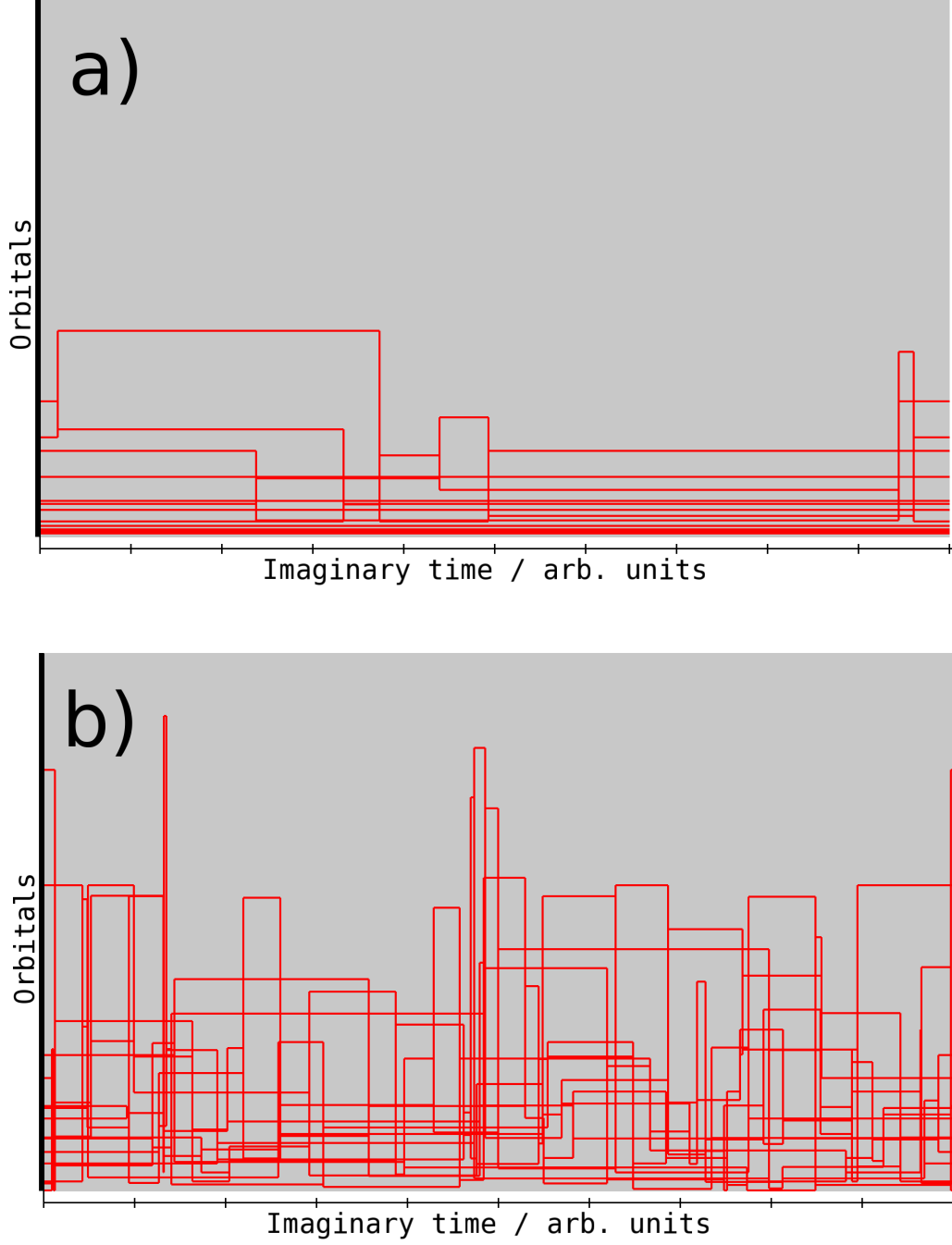
Figure 14: Snapshot of a typical path occurring in a CPIMC simulation of $N = 14$ unpolarized electrons at $r_s = 0.7$ (panel **a)**) and $r_s = 1$ (panel **b)**), both at $\theta = 1$ in $N_B = 778$ plane wave spin-orbitals, which are ordered according to their corresponding kinetic energy $\mathbf{k}_i^2/2$. Plotted is the occupation of each orbital (red and grey indicate occupied and unoccupied orbitals, respectively) in dependence on the imaginary time. Note that the density of the 778 orbitals (grey lines) appears to be continuous on this scale but when further zooming into the path it is of course discrete like in Fig. 12 where $N_B = 14$.
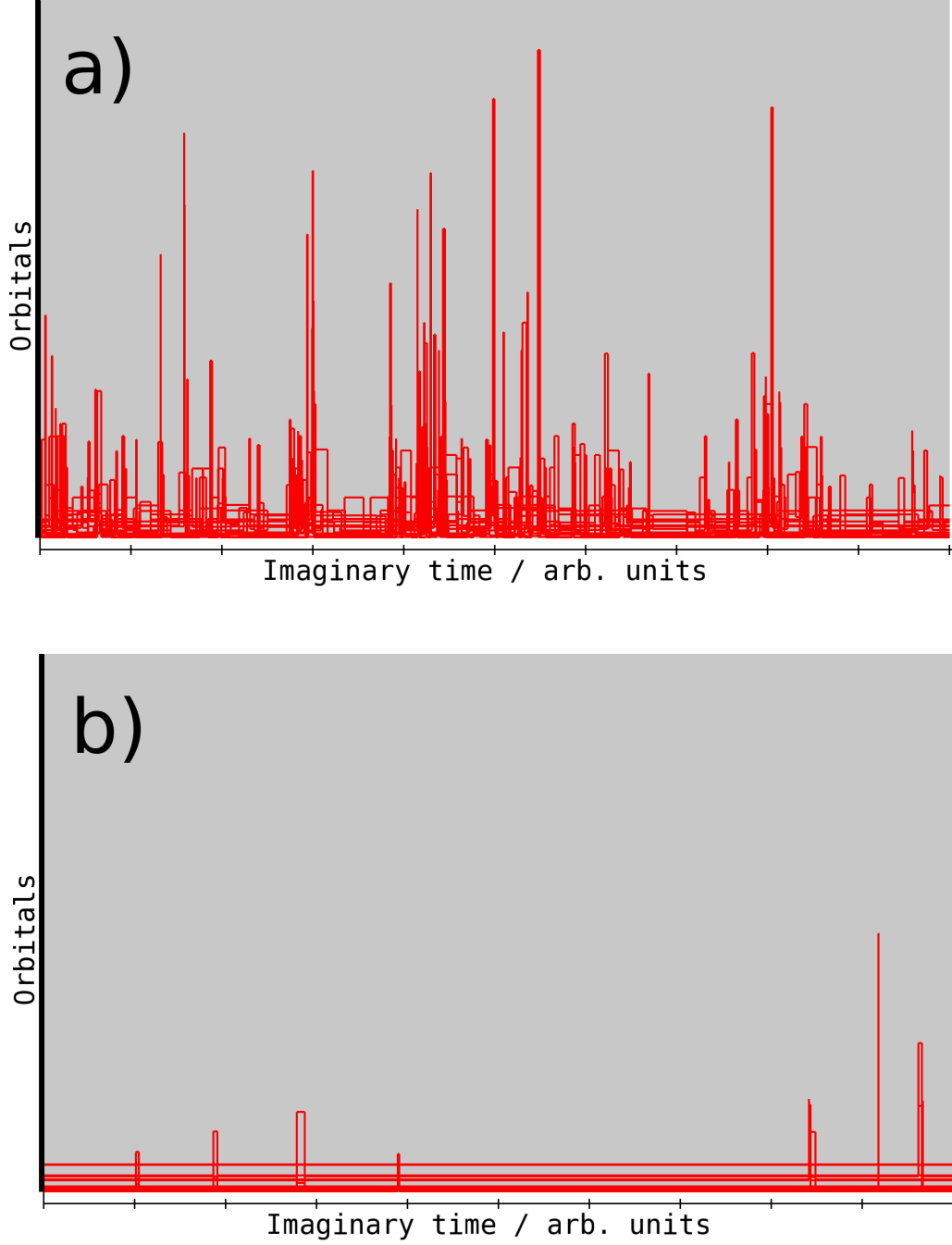
Figure 15: Snapshot of a typical path occurring in a CPIMC simulation of $N = 14$ unpolarized electrons at $r_s = 0.7$ (panel **a)**) and $r_s = 0.4$ (panel **b)**) both at $\theta = 0.01$ in $N_B = 778$ plane wave spin-orbitals, which are ordered according to their corresponding kinetic energy $\mathbf{k}_i^2/2$. Plotted is the occupation of each orbital (red and grey indicate occupied and unoccupied orbitals, respectively) in dependence on the imaginary time.
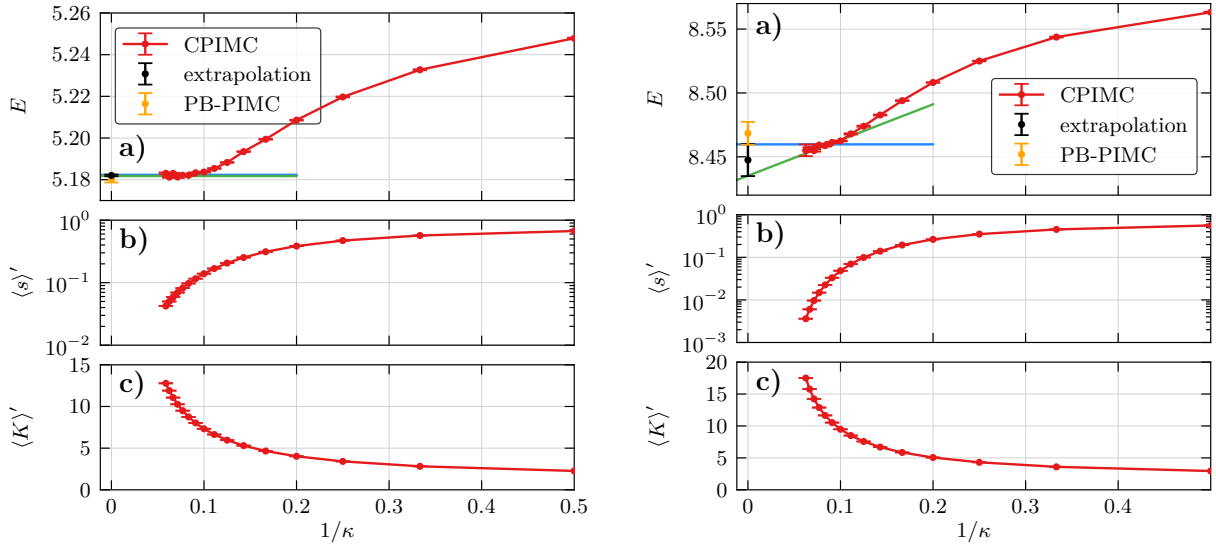
Figure 16: Convergence of **a)** the internal energy, **b)** the average sign and **c)** the average number of kinks with the kink potential parameter κ. Each point results from a complete CPIMC simulation of $N = 66$ unpolarized electrons at $r_s = 2$ and $\theta = 4$ (left) and $r_s = 0.8$ and $\theta = 1$ (right). The blue (green) line shows a horizontal (linear) fit to the last points. The asymptotic value (black point) in the limit $1/\kappa \to 0$ is enclosed between the blue and green lines and, within error bars, coincides with the PB-PIMC result (orange points). Left (right) graphic reproduced (modified) from Ref. [221] with permission of the authors.

any kinks in the paths and their weight is always positive.

However, with decreasing density, i.e., increasing r_s, we observe that the average sign drops drastically at some critical density that strongly depends on the number of electrons, temperature, as well as the spin-polarization. This drop is caused by an enormous increment of the average number of kinks at this critical density (note the logarithmic scale). For example, in case of $N = 14$ unpolarized electrons (green), at this temperature, the critical density is at $r_s \sim 0.8$. In Fig. 14, we further explore this case by showing snap shots of typical CPIMC paths occurring in the simulation of $N = 14$ electrons in $N_B = 778$ basis functions at $r_s = 0.7$, a), and $r_s = 1$, b), both at $\theta = 1$. While at $r_s = 0.7$ the paths contain only very few kinks, at $r_s = 1$, many paths contain ~ 100 kinks which are highly entangled and thereby induce many sign changes. When lowering the temperature while keeping the other system parameters constant this critical value of r_s becomes even smaller, wich is illustrated by the two simulation snap shots in Fig. 15 for $r_s = 0.7$, a), and $r_s = 0.4$, b), now at $\theta = 0.01$. At these low temperatures close to the ground state, even a density parameter of $r_s = 0.7$ is clearly not feasible with the basic CPIMC method as the paths typically contain about 500 kinks, while, at $r_s = 0.4$, the average number of kinks is reduced by two orders of magnitude so that simulations pose no problem here. Further, we point out that the structure of the generated CPIMC paths changes significantly with the temperature: at high temperature, see Fig. 14, the average occupation of higher orbitals is much larger due to the increased kinetic energy of the electrons, while at low temperatures, see Fig. 15, most of the kinks tend to occur in symmetric pairs with only very short imaginary time in between, so that theses structures appear as needles in the paths. Interestingly, the overall sign change of these symmetric pairs always exactly compensates to one and thus they do not worsen the FSP.

Finally, we stress that the linear dependence of the average number of kinks in Fig. 13 b) before and after the critical density is not an artefact due to the inevitable practical restriction to a finite number of basis functions in the simulation. In particular, this demonstrates that the modified CPIMC partition function with the modulus weight function is actually a convergent sum for any finite system parameters of the UEG. Mathematically this must not necessarily be the case, since if a sum with alternating signs of its summands converges, of course, the same sum with the modulus of the summands can be divergent. Nevertheless, the fact that the FSP in the basic CPIMC approach has a "hard-wall-like" character is rather unsatisfactory: there is either none when there are on average less than ~ 2 kinks in the paths or it is so strong that simulations are not feasible due to hundreds or even thousands of kinks. A problem which we will strongly mitigate in the next section.

5.5.3. Reduction of the FSP with an auxiliary kink potential

The restriction of the CPIMC approach to the nearly ideal regime, i.e. very large densities, due to a severe FSP at some critical value of r_s can be significantly alleviated by the use of a Fermi-like auxiliary kink potential

$$V_\kappa(K) = \frac{1}{e^{-(\kappa - K + 0.5)} + 1} \ , \tag{125}$$

by replacing the modulus of the weight function $|W(\mathbf{X})|$, cf. Eq. (123), by the modified weight

$$|W_\kappa(\mathbf{X})| = |W(\mathbf{X}) \cdot V_\kappa(K)| \ . \tag{126}$$

When performing simulations for fixed values of κ, this potential acts as a smoothly increasing penalty of paths with a large number of kinks K, thereby effectively suppressing the occurrence of these paths in the simulation. Since it is $\lim_{\kappa \to \infty} V_\kappa(K) = 1$, we can extrapolate the results from CPIMC simulation with different values of κ to the exact limit $1/\kappa \to 0$, which is illustrated in in the left panel of Fig. 16 for $N = 66$ electrons at $r_s = 2$ and $\theta = 4$. Indeed we observe that the total energy, a), is well converged at $\kappa \sim 10$ while the average sign, b), and the average number of kinks, c), are clearly not. In fact, for these parameters, the basic CPIMC simulation without the kink potential equilibrates at an average number of several hundreds of kinks. This fortunate behavior can be explained by a complete cancellation of all contributions to the energy of all paths that contain a larger number of kinks than about 10. In other words, the simulated modified partition function with the modulus of the weight function converges at much larger values of K than the physical partition function due to a complete cancellation of the weights. In this sense one may also call this circumstance a "sign blessing" rather than a "sign problem".

Since the convergence with the potential parameter $1/\kappa$ is monotonic, we can obtain a highly accurate upper and lower bound of the exact result even in those cases where convergence is not entirely reached, which is shown in the right panel of Fig. 16 for the example of $N = 66$ electrons at $r_s = 0.8$ and $\theta = 1$. For these parameters the bare CPIMC method generates paths that contain about a thousand kinks [see solid blue points in Fig. 13 b)]. Nevertheless, within the given error bars, the resulting value (black) agrees well with that from the PB-PIMC simulation (orange). Overall, at a fixed number of electrons N and temperature θ, the usage of the kink potential, Eq. (125), increases the feasible r_s parameter in CPIMC simulations by at least a factor of two. Thus, the applicability of the method is pushed into density regimes where common analytical perturbation theories break down.

5.6. Density Matrix Quantum Monte Carlo

The density matrix quantum Monte Carlo (DMQMC) approach developed by Foulkes, Malone, and co-workers [224, 222, 223] is similar to the CPIMC method from the previous section in so far as both are formulated in antisymmetrized Fock space. As we shall see, this leads to a similar range of applicability (see Sec. 5.7). However, in contrast to the path integral Monte Carlo paradigm, in DMQMC we directly sample the unnormalized thermal density matrix (expanded in a basis of Slater determinants). Therefore, it constitutes a direct extension of the full configuration interaction quantum Monte Carlo (FCIQMC) method [317, 19, 18, 20], which has proven to be highly successful in the ground state [318], to finite temperature. Furthermore, it can be viewed as the diffusion Monte Carlo analogue of CPIMC.

Following Ref. [222], we write the Bloch equation [cf. Eq. (87)] in a symmetrized form,

$$\frac{\mathrm{d}\hat{\rho}}{\mathrm{d}\beta} = -\frac{1}{2}(\hat{H}\hat{\rho} + \hat{\rho}\hat{H}) \ . \tag{127}$$

Thus, propagating the density matrix in imaginary time by an amount of $\Delta\beta$ using a simple (explicit) Euler scheme gives

$$\hat{\rho}(\beta + \Delta\beta) = \hat{\rho}(\beta) - \frac{\Delta\beta}{2}(\hat{H}\hat{\rho}(\beta) + \hat{\rho}(\beta)\hat{H}) + \mathcal{O}(\Delta\beta^2) \ . \tag{128}$$

The basic idea of the density matrix QMC method is to stochastically solve Eq. (128) by evolving a *population* of positive and negative walkers (sometimes denoted as "particles", "psi-particles", or "psips") in the operator space spanned by tensor products of Slater determinants. Writing down Eq. (128) in terms of matrix elements $\rho_{ij} = \langle i | \hat{\rho} | j \rangle$ (with $|i\rangle$ being a Slater determinant of plane waves) leads to

$$\rho_{ij}(\beta + \Delta\beta) = \rho_{ij}(\beta) - \frac{\Delta\beta}{2}\sum_k [(H_{ik} - S\delta_{ik})\rho_{kj} - \rho_{ik}(H_{kj} - S\delta_{kj})] \ , \tag{129}$$

with S being an, in principle, arbitrary shift that can be used to control the population of walkers [319, 317, 222]. Furthermore, it is convenient to introduce the *update matrix*

$$T_{ij} = -(H_{ij} - S\delta_{ij}) \, , \tag{130}$$

which allows us to write Eq. (129) as

$$\rho_{ij}(\beta + \Delta\beta) = \rho_{ij}(\beta) + \frac{\Delta\beta}{2} \sum_k (T_{ik}\rho_{kj} + \rho_{ik}T_{kj}) \, . \tag{131}$$

The update scheme governing the stochastic evolution of the walkers can be summarized in three straightforward rules:

1. *Spawning* – A walker can spawn from matrix element ρ_{ik} to ρ_{ij} with the probability $p_{\mathrm{spawn}}(ik \to ij) = \Delta\beta|T_{kj}|/2$ (the spawning process from ρ_{kj} to ρ_{ij} is similar).
2. *Clone/Die* – Walkers on ρ_{ij} can clone or die, leading to an increase or decrease of the population with the probability $p_{\mathrm{d}}(ij) = \Delta\beta|T_{ii}+T_{jj}|/2$. In particular, the population is increased if $\mathrm{sign}(T_{ii}+T_{jj})\times\mathrm{sign}(\rho_{ij}) > 0$ and decreased otherwise.
3. *Annihilation* – Walkers on the same matrix elements, but with an opposite sign, are annihilated. This drastically improves the efficiency of the algorithm.

Starting at $\beta = 0$ (where $\rho_{ij} = \delta_{ij}$, realized by populating the diagonal density matrix elements with uniform probability), the above algorithm is used to propagate ρ to the desired (inverse) temperature of interest. The full DMQMC simulation, i.e., the computation of thermodynamic expectation values, is then given by averaging over many independent of such "β-loops".

Regarding simulations of the electron gas using this basic version of DMQMC there appear two practical problems: (i) the distribution within the thermal density matrix changes rapidly with β and (ii) important determinants are often not present in the initial configuration. To overcome these obstacles, Malone and co-workers [222] proposed to solve a different differential equation, describing the evolution of a mean-field density matrix to the exact, fully correlated density matrix, both at inverse temperature β. This so-called *interaction picture* DMQMC method has turned out to be dramatically more efficient and was used to obtain all DMQMC data shown in Sec. 5.7.

As a final note, we mention that the fermion sign problem in DMQMC manifests as an exponential growth of the number of walkers needed to resolve the exact thermal density matrix, eventually rendering even a stochastical approach unfeasible. To delay this "exponential wall", the exact DMQMC simulation scheme can be used as a starting point for approximations. In particular, one can exploit the extreme degree of sparsity of the thermal density matrix to reduce the computational demands [223]. This, in turn, allows to significantly increase the range of applicability in terms of coupling strength, similar to the controlled kink extrapolation in the CPIMC method, see Sec. 5.5. The basic idea of this *initiator approximation* [223] is to prevent walkers on density matrix elements with a comparatively small weight from spawning off-spring on other small elements. Spawning events to unpopulated matrix elements are only possible from the set of so-called *initiator determinants*, which are occupied by a number of walkers above a certain threshold n_{init}, or if they result from multiple sign-coherent spawning events from other determinants. It is important to note that the bias due to the initiator approximation can be reduced by increasing the total number of walkers within the simulation, N_{walker}, and vanishes completely in the limit $N_{\mathrm{walker}} \to \infty$. Therefore, this "i-DMQMC" algorithm can be viewed as a controlled approximation, although a non-monotonic convergence towards the exact result with N_{walker} is possible. Furthermore, the accuracy for any finite number N_{walker} is significantly reduced for quantities that do not commute with the Hamiltonian.

5.7. Comparison of QMC methods

In this section, we present comparisons between data from different QMC methods in a chronological order, starting with the investigation by Schoof *et al.* [218] and finishing with the most recent comparison in Ref. [225], where all four methods had been included into the same plot. It is important to note that all results in this section have been obtained for a finite model system of $N = 33$ (spin-polarized) or $N = 66$ (unpolarized) electrons. An exhaustive introduction, explanation and discussion of finite-size errors, i.e., the extrapolation to the thermodynamic limit, can be found in section 6.
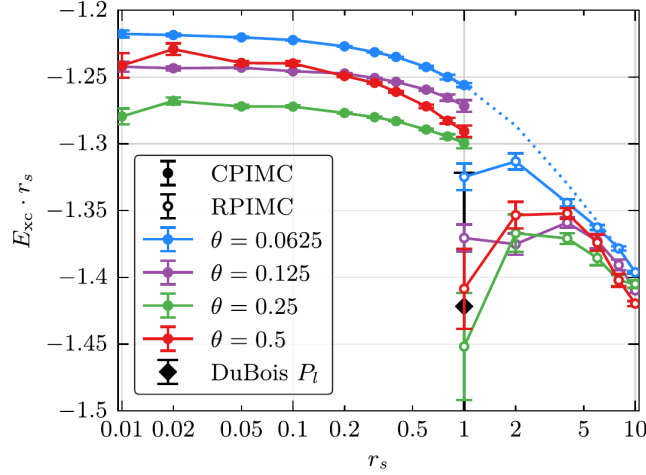
Figure 17: Low-temperature results for the exchange-correlation energy of the spin-polarized UEG with $N = 33$ electrons. The filled circles correspond to the configuration PIMC data by Schoof *et al.* [218] and the empty circles have been obtained by subtracting the finite-size correction from the restricted PIMC data in the Supplemental Material of Ref. [211]. The black diamond corresponds to $\theta = 0.0625$ and has been obtained via an approximation based on the extrapolation of permutation cycles introduced by DuBois *et al.* [320]. Reproduced from Ref. [218] with the permission of the authors.

5.7.1. The limits of the fixed node approximation

In 2013, Brown and co-workers [211] published the first QMC data for the UEG using the restricted PIMC method both for $\xi = 0$ and $\xi = 1$ covering substantial parts of the warm dense matter regime ($\theta = 0.0625, 0.125, 0.25, \ldots, 8$ and $1 \le r_s \le 40$). It is well known that employing a nodal constraint (using the free particle nodes) constitutes an uncontrolled approximation so that the accuracy of the RPIMC data was not clear. However, the remarkably high accuracy of the fixed node approximation in ground state calculations [16, 38, 17] lead to a high confidence in their results, which were subsequently used as input for various applications, e.g., Refs. [213, 212, 214, 321, 185]. In their seminal 2015 paper, Schoof *et al.* [218] were able to obtain *exact* CPIMC data for the spin-polarized electron gas up to $r_s = 1, \ldots, 4$ (depending on temperature), thus enabling them to gauge the bias in the RPIMC data. The results are shown in Fig. 17, where the exchange-correlation energy $E_{\text{xc}} = E - U_0$ (with U_0 being the energy of the ideal system) is plotted versus r_s for $N = 33$ electrons and four different temperatures in the low temperature regime, $\theta = 0.0625, 0.125, 0.25, 0.5$. The filled and empty circles correspond to the CPIMC and RPIMC data, respectively. For completeness, we mention that the black diamond corresponds to a single data point for $\theta = 0.0625$ from Ref. [320], which was obtained by performing an approximate extrapolation over the permutation cycles in the PIMC simulation; yet, it is not relevant in the present context. Although the sign problem is practically absent in the CPIMC simulations at $r_s < 0.1$, the statistical uncertainty (error bars) increases towards even higher density. The explanation for this behaviour is simple: with decreasing r_s the system becomes more similar to the ideal case, thereby making E_{xc} the difference between two large numbers, which naturally leads to an increased relative error. On the other hand, the relative CPIMC errors also increase in magnitude for $r_s \ge 0.6$ due to the fermion sign problem, which eventually leads to an exponential wall at some critical value of r_s, at which CPIMC simulations are no longer feasible. However, at $r_s = 1$ the error bars in the CPIMC data is clearly an order of magnitude smaller than those of the RPIMC data.

The most interesting feature of Fig. 17 is the striking disagreement between the exact CPIMC and RPIMC points where the data overlap. In particular, the fixed node approximation leads to an unphysical drop towards high density and the bias in E_{xc} exceeds 10%. This is in stark contrast to ground state results, where already the data by Ceperley and Alder from 1980 [16] had an accuracy of the order of 0.1%. Furthermore, the decreasing quality of the RPIMC data towards high density and weaker coupling contradicts the usual assumption that the systematic error due to the free particle nodes should be most pronounced at stronger nonideality, but vanish for $r_s = 0$ (ideal case). While we do not have a definitive explanation of this finding, a possible answer might be a lack of ergodicity within the RPIMC simulation due to the reference point freezing, see Sec. 5.3, an explanation that would be in good agreement with the observed increment of the RPIMC error bars towards higher density. Finally, we mention that Filinov [322, 323] called into question the validity of the fixed node approximation even for the ideal case.
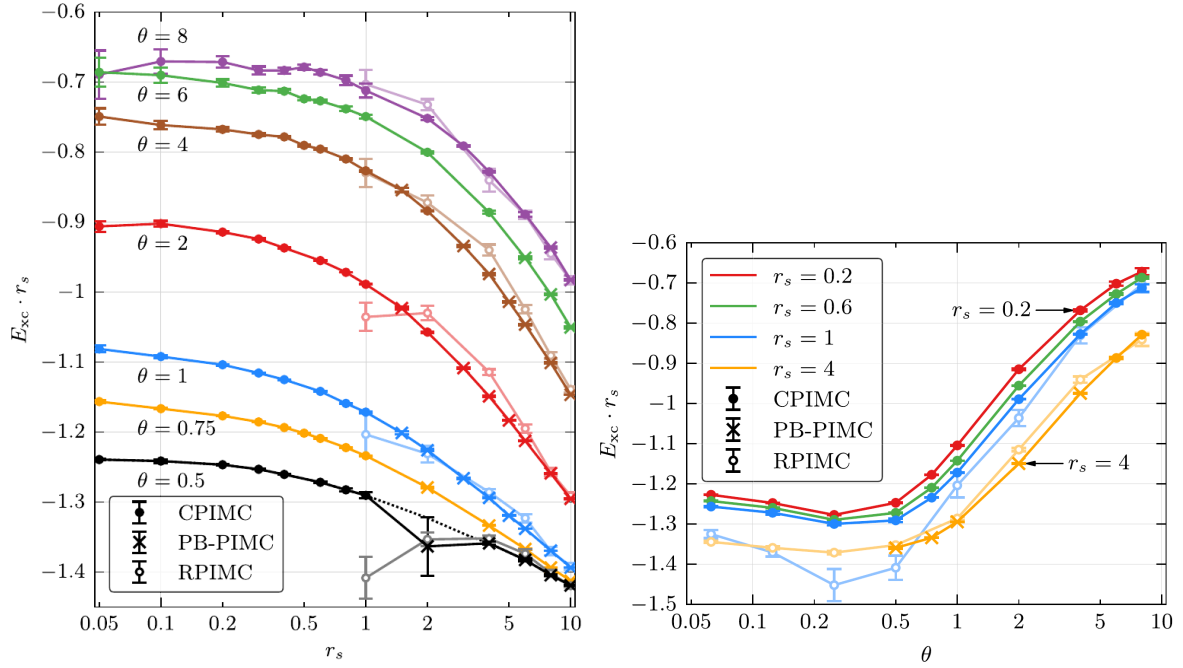
Figure 18: Combination of the configuration PIMC and permutation blocking PIMC methods. Shown is the exchange-correlation energy of $N = 33$ spin-polarized electrons in dependence of the density parameter r_s (left) and the reduced temperature θ (right). The colored filled circles and crosses correspond to the CPIMC and PB-PIMC data, respectively, and the faded empty circles to the RPIMC data by Brown *et al.* [211]. Reproduced from Ref. [217] with the permission of the authors.

5.7.2. Combining CPIMC and PB-PIMC

The important findings by Schoof *et al.* [218] from the previous section seriously called into question the utility of the RPIMC data as a basis for density functional theory or other applications at warm dense matter conditions (even more so when considering the additional need for a sufficiently accurate finite-size correction, see Sec. 6). The problem is that the exact CPIMC method (see Sec. 5.5), due to its formulation as an infinite perturbation expansion around the ideal system, is limited to moderate coupling (around $r_s = 1$, depending on temperature) and, therefore, cannot be used over substantial parts of the relevant WDM regime. To overcome this issue, Dornheim *et al.* [219] introduced the permutation blocking PIMC idea (see Sec. 5.4 for a detailed introduction) and subsequently demonstrated its utility for simulation of the electron gas [220]. In particular, it was suggested that the combination of CPIMC and PB-PIMC at complementary parameters could be used to obtain highly accurate results over the entire density range [217, 221].

This is demonstrated in the left panel of Fig. 18, where the exchange-correlation energy is shown in dependence of the density parameter r_s [217]. The faded empty circles correspond to the RPIMC data by Brown *et al.* [211], the filled circles to CPIMC and the crosses to PB-PIMC data. Note that we show either a CPIMC or a PB-PIMC point, depending on which method provides the smaller statistical uncertainty at a given r_s-θ-combination. Again, we mention that the comparatively large error bars in E_{xc} at small r_s and high temperature are due to its nature as the difference between two large numbers, the total and ideal energies E and U_0, respectively. Evidently, the PB-PIMC data is in excellent agreement with and smoothly connects to the CPIMC results for all depicted temperatures. This means that the combination allows for a highly accurate description down to $\theta = 0.5$. While CPIMC is also available for lower temperature, cf. Fig. 17, the permutation blocking PIMC approach eventually becomes infeasible due to the FSP, which is the reason for the relatively large error bar at $r_s = 2$ and $\theta = 0.5$. For completeness, we mention that the interaction energy V, which is sufficient to construct a parametrization of the exchange-correlation free energy f_{xc} (see Sec. 8), can be obtained with a significantly higher accuracy at $\theta = 0.5$, see Refs. [220, 221, 226].

The RPIMC data, on the other hand, exhibit an unphysical behavior even at moderate to high temperature. In particular, both for $\theta = 0.5$ and $\theta = 1$ there occurs a drop in E_{xc}, while for $\theta = 2$ and $\theta = 4$ there are pronounced bumps in the region $1 \leq r_s \leq 6$.

In the right panel of Fig. 18, we show the temperature dependence of E_{xc} for four different values of the density parameter, $r_s = 0.2, 0.6, 1, 4$. The RPIMC data are available for the two largest r_s-values, but again there appears a substantial disagreement to the combined CPIMC and PB-PIMC data. While all methods find a minimum in
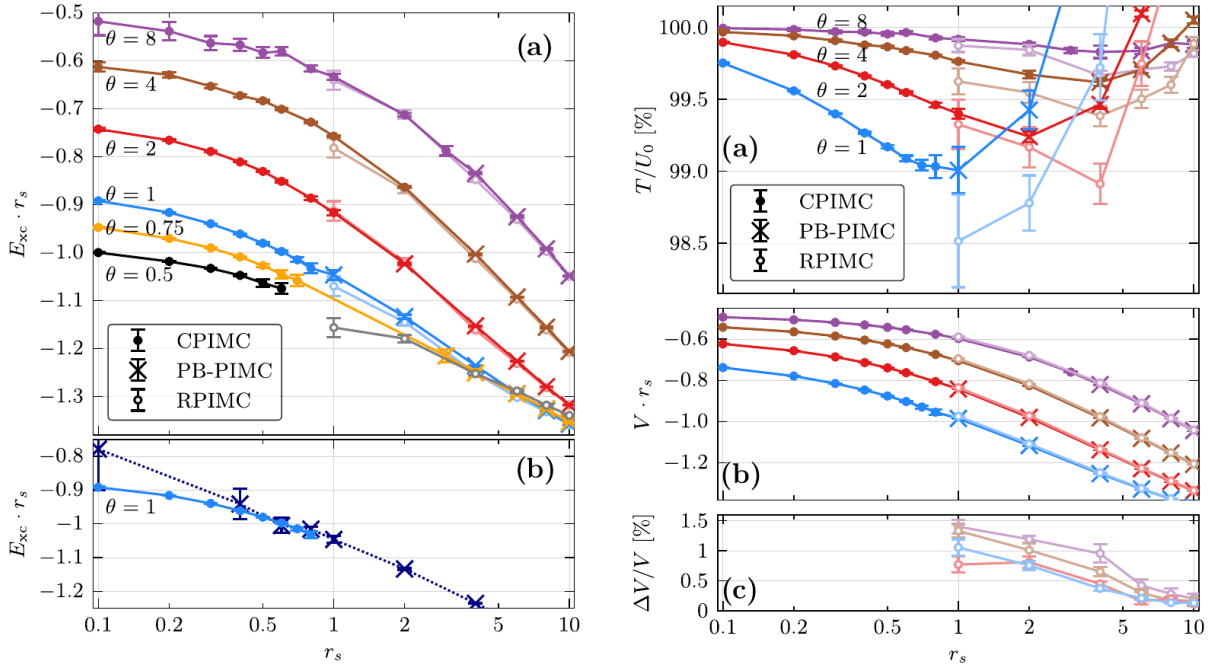
Figure 19: Combination of the configuration PIMC and permutation blocking PIMC methods for the unpolarized electron gas with $N = 66$ electrons. In the top left panel, we show results for the density-dependence of the exchange-correlation energy from configuration PIMC (filled circles), permutation blocking PIMC (crosses), and restricted PIMC (empty circles, taken from Ref. [211]). The bottom left panel shows all E_{xc} data for $\theta = 1$ both from PB-PIMC and CPIMC, where they are available. In the top right and center right panel, we show the kinetic energy (in units of the ideal result, U_0) and interaction energy from all three methods. Finally, the bottom right panel shows the relative deviation between RPIMC and our data for V. Reproduced from Ref. [221] with the permission of the authors.

$E_{\rm xc}$ around $\theta = 0.3$ for all depicted densities, the fixed node approximation leads to a drastically deeper minimum for $r_s = 1$ (see also Fig. 17 above). Groth and co-workers [217] gave a possible explanation of this non-monotonic behavior as the competition of two effects: on the one hand, thermal broadening of the particle density leads to a reduction of the interaction energy with temperature, while, on the other hand, Coulomb interactions might be partly increased as the thermal deBroglie wavelength (see Sec. 5.2) decreases with increasing θ. Note that a similar trend has been predicted in the vicinity of Wigner crystallization in $2D$, see Ref. [324].

Up to this point, all depicted results had been obtained for the spin-polarized case, i.e., $\xi = 1$. However, as real systems are found predominantly in an unpolarized state, the $\xi = 0$ case is arguably even more important for real applications. For this reason, in the left panel of Fig. 19, we show the r_s-dependence of $E_{\rm xc}$ for $N = 66$ unpolarized electrons. Again, we show either a CPIMC or PB-PIMC data point, depending on the statistical uncertainty. Due to the two-fold increase in system size (it is conventional to use a closed momentum shell, i.e., $N_\uparrow = N_\downarrow = 33$ spin-up and -down electrons), PB-PIMC results for the exchange-correlation energy are only available above half the Fermi temperature. Regarding the CPIMC approach, there is an additional issue which further reduces the feasible r_s parameter: electrons with opposite spin do not exchange which leads to an increased weight of kinks between those electrons (compared to the same corresponding to two electrons of equal spin) [221]. The bottom left panel of Fig. 19 shows data for $\theta = 1$ only, but both from PB-PIMC and CPIMC where they are available. Again, we stress the excellent agreement between the two independent methods as all data agree within error bars and no systematic deviations can be resolved. The comparion to the RPIMC data by Brown and co-workers [211] reveals that, for the unpolarized case and for moderate temperatures, there is no systematic bias of the same order as for the spin-polarized case. Only for the lowest depicted temperature, $\theta = 0.5$, there seems to appear a systematic drop of the RPIMC data towards high density.

In the right part of Fig. 19, we consider separately both the kinetic and the potential (interaction) contribution to the total energy. Specifically, in the top right panel, we plot the r_s-dependence of the kinetic energy (here labelled T and given in units of the ideal energy U_0) for $\theta = 1, 2, 4, 8$. Surprisingly, we find significantly larger disagreement than in $E_{\rm xc}$ for all depicted temperatures as the RPIMC data are systematically too small. Furthermore, these deviations do not vanish entirely even for large r_s.

The center right panel of the same figure shows the same information for the Ewald interaction energy V,

43
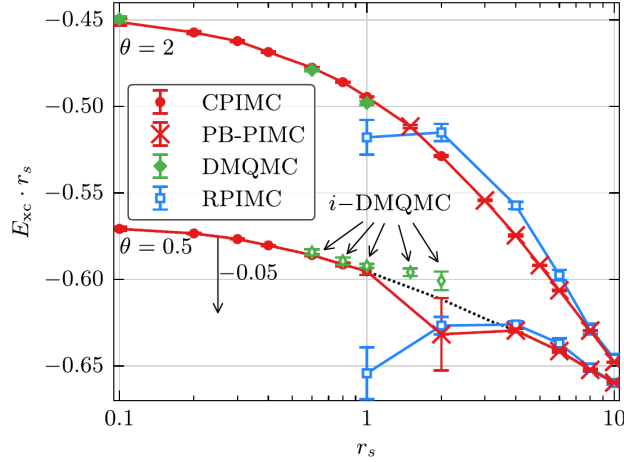
Figure 20: Comparison of all QMC methods for the spin-polarized electron gas at warm dense matter conditions. Shown are results for the r_s-dependence of the exchange-correlation energy for $N = 33$ electrons from CPIMC (red circles, data taken from Ref. [217]), PB-PIMC (red crosses, data taken from Ref. [217]), DMQMC (filled green diamonds) and initiator DMQMC (empty green diamonds, data taken from Ref. [223]) and RPIMC (blue squares, data taken from Ref. [211]). For $\theta = 0.5$, all data have been shifted by 0.05 Hartree. Reproduced from Ref. [225] with the permission of the authors.

although, on the given scale, no deviations are visible with the naked eye. For this reason, in the bottom right panel, we show the relative deviation between our data and RPIMC in V. Unsurprisingly, we find deviations of a similar magnitude than in the kinetic part, but of an opposite sign, i.e., here the RPIMC data are always too large.

In a nutshell, our analysis of the unpolarized electron gas has revealed that (i) the fixed node approximation gives significantly more accurate results for the exchange-correlation energy than for the spin-polarized case, but (ii) the separate kinetic and potential contributions are systematically biased for all temperatures, even for large r_s. Finding (ii) is a common property of approximations in quantum Monte Carlo methods for quantities that do not commute with the Hamiltonian. Similar behaviors have been reported in ground state diffusion Monte Carlo calculations using the fixed node approximation[4], e.g., Refs. [325, 326], or in finite-temperature DMQMC calculations employing the initiator approximation [223].

5.7.3. Emerging consensus of QMC methods

Shortly after the findings of the previous subsections had been reported, Malone and co-workers [223] achieved major breakthroughs regarding the application of the density matrix QMC method to the electron gas at WDM conditions. Their valuable set of additional, independent data has been included in Fig. 20 (green diamonds), where the r_s-dependence of E_{xc} is shown for all four QMC methods introduced above [225]. Note that the $\theta = 2$ data corresponds to the exact DMQMC algorithm whereas, for $\theta = 0.5$, the initiator approximation was employed. Evidently, the green points fully confirm our data up to $r_s = 1$ within error bars, although, at larger values of r_s, the initiator approximation apparently cause E_{xc} to be systematically to large.

We thus conclude that over the last two years there has emerged a consensus between different, independent QMC methods regarding the simulation of the UEG for a finite number of electrons. Naturally, the next step that had to be accomplished was the extrapolation of these results to the thermodynamic limit without a significant loss of accuracy. This turned out to be a surprisingly challenging task, which will be discussed and explained in detail in the next section.

Finally, in Fig. 21, we show the density-temperature combinations where the different QMC methods are feasible. Evidently, standard PIMC is only available at high temperature and strong coupling (due to the FSP). Our recent PB-PIMC method extends this regime significantly towards lower temperature and high density, i.e., towards strong degeneracy. In contrast, both the CPIMC and DMQMC methods, which are formulated in Fock space, excel at weak coupling but break down when correlation effects start to dominate. Observe that the apparent advantage of DMQMC over CPIMC at low temperature and intermediate r_s is due to the utilized initiator approximation that can lead to a significant bias for quantities that do not commute with the Hamiltonian, see Sec. 5.6 for details.

---

[4]In DMC, the bias can be removed by the *Hellmann-Feynman* operator sampling [325].
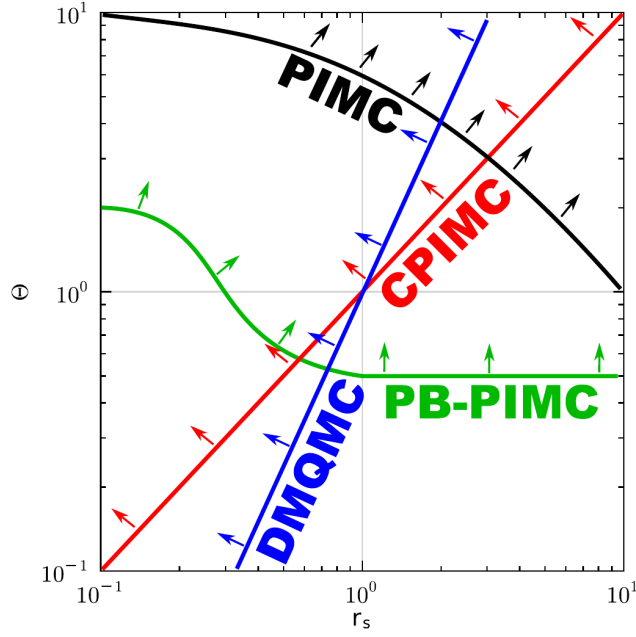
Figure 21: Density-temperature plane around the warm dense matter regime. Shown are the parameter ranges where standard PIMC (black), DMQMC (blue), CPIMC (red) and PB-PIMC (green) are feasible. Reproduced from Ref. [225] with the permission of the authors.

6. Finite-size correction of QMC data

6.1. Introduction and problem statement

The big advantage of using the quantum Monte Carlo methods introduced in Sec. 5 is that they – in stark contrast to the dielectric approximations or quantum classical mappings – allow to obtain an exact solution to the UEG Hamiltonian, Eq. (7). However, this is only possible for a model system with a finite number of particles N and a finite box length L. In practice, we are interested in the thermodynamic limit [327], i.e., the limit where both L and N go to infinity while the density n (and, therefore, the density parameter r_s) remain constant. To mimic as closely as possible the infinite electron gas in our QMC simulations, we employ periodic boundary conditions and incorporate the interaction of a single electron with an infinite array of periodic images via the Ewald interaction. Nevertheless, the interaction energy per particle, V_N/N, does not remain constant for different N and is not equal to the thermodynamic limit, which is defined as

$$\nu = \lim_{N \to \infty} \left. \frac{V_N}{N} \right|_{r_s=\text{const}} . \tag{132}$$

The difference between ν and V/N is the so-called finite-size error

$$\frac{\Delta V_N}{N} = \nu - \frac{V_N}{N} , \tag{133}$$

which needs to be compensated for by adding a so-called finite-size correction to the QMC results, i.e., an estimation for $\Delta V_N/N$. This is illustrated in Fig. 22, where, in the left panel, we plot the interaction energy per particle of the unpolarized electron gas with $\theta = 2$ and $r_s = 0.5$ versus the inverse number of particles $1/N$. The green crosses correspond to the bare QMC results and, obviously, are not converged with respect to N. More precisely, for $N = 38$ particles, there appears a finite-size error exceeding 10%. For a higher density, $r_s = 0.1$ (see the right panel), things appear to be even more dire and, for $N = 38$, $\Delta V_N/N$ is comparable in magnitude to ν and V/N themselves. In this situation it might seem natural to perform a a direct extrapolation to the TDL by performing a fit to the QMC data. However, the problem is that the exact functional form of the finite-size error in dependence of N is not known. The solid black and dashed yellow lines correspond to two fits with different functional forms,
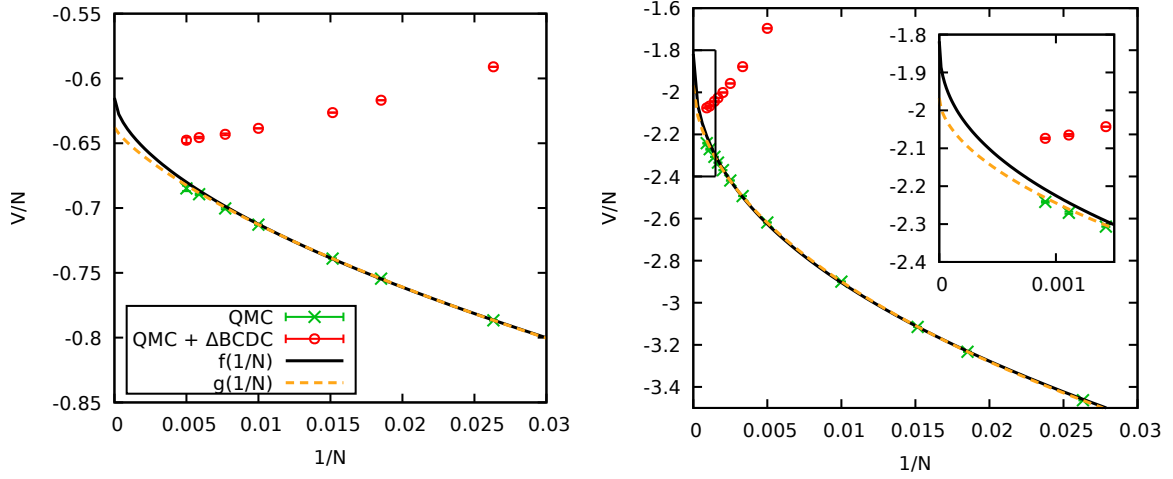
Figure 22: System size dependence of the potential energy per particle of the unpolarized UEG at $\theta = 2$ and $r_s = 0.5$ (left) and $r_s = 0.1$ (right) – Shown are bare QMC (CPIMC) results (green crosses) and the QMC results plus the finite-size correction proposed by Brown *et al.* [211] (ΔBCDC, red circles). The solid black and dashed yellow curves correspond to two equally reasonable fits to the QMC data of the form $f(x) = a + bx^c$ and $g(x) = a + bx + cx^d$, respectively. The left panel has been adapted from Ref. [226] with the permission of the authors.

specifically

$$f(N^{-1}) \;\; = \;\; a + \frac{b}{N^c} \; , \tag{134}$$

$$g(N^{-1}) \;\; = \;\; a + \frac{b}{N} + \frac{c}{N^d} \; , \tag{135}$$

with a, b, c and d being the free parameters. Evidently, for $r_s = 0.5$ both fit functions are equally appropriate and reproduce the QMC data quite well. Still, the estimation of the value in the TDL differs by several per cent. This clearly demonstrates that a reliable extrapolation of the QMC data is not possible without knowing the exact N-dependence of the finite-size error, which is not the case. Therefore, we need to derive a readily evaluable approximation to Eq. (133). In the ground state, finite-size effects are relatively well understood, see, e.g., Refs. [231, 328, 329, 330, 331]. In their pioneering work, Brown *et al.* [211] introduced a straightforward extension of the finite-size correction for the interaction energy by Chiesa *et al.* [329] to finite temperature [cf. Eq. (142)]. Adding this correction to the QMC results leads to the red circles in Fig. 22. Obviously, the finite-size errors are overestimated and the remaining bias is of the same order as the original one. Even worse, for $r_s = 0.1$ and $N < 100$ the corrected data exhibit a larger N-dependence than the bare QMC results. Hence, we conclude that in order to obtain accurate interaction energies in the thermodynamic limit we need to derive an improved finite-size correction. This requires us to analyze and understand the source of the finite-size error and find an accurate estimation for it.

6.2. Theory of finite-size effects

To derive an expression for the finite-size error due to the final simulation box [329, 330, 226, 225], it is convenient to express V/N in terms of the static structure factor $S(\mathbf{k})$

$$\frac{V_N}{N} = \frac{1}{2L^3} \sum_{\mathbf{G} \neq \mathbf{0}} [S_N(\mathbf{G}) - 1] \frac{4\pi}{G^2} + \frac{\xi_{\mathrm{M}}}{2} \; , \tag{136}$$

where the subscripts 'N' denote quantities computed for a finite number of particles, and the sum is to be carried out over the discrete reciprocal lattice vectors $\mathbf{G}$. In the thermodynamic limit, the Madelung constant vanishes, $\xi_{\mathrm{M}} \to 0$, and the potential energy per particle, Eq. (132), can be written as a continuous integral

$$\nu = \frac{1}{2} \int_{k < \infty} \frac{d\mathbf{k}}{(2\pi)^3} [S(k) - 1] \frac{4\pi}{k^2} \; , \tag{137}$$

where we have made use of the fact that for a uniform system the static structure factor solely depends on the modulus of the wave vector, $S(\mathbf{k}) = S(k)$. Obviously, the finite-size error is given by the difference of Eqs. (137)

46

and (136),

$$\frac{\Delta V_N}{N}[S(k), S_N(k)] = \nu - \frac{V_N}{N} \tag{138}$$

$$= \underbrace{\frac{1}{2}\int_{k<\infty}\frac{d\mathbf{k}}{(2\pi)^3}[S(k)-1]\frac{4\pi}{k^2}}_{v} - \underbrace{\left(\frac{1}{2L^3}\sum_{\mathbf{G}\neq\mathbf{0}}[S_N(\mathbf{G})-1]\frac{4\pi}{G^2}+\frac{\xi_M}{2}\right)}_{V_N/N},$$

and, thus, is a functional of the SFs of the infinite and finite systems, respectively. To derive a more easily workable expression for Eq. (138), we approximate the Madelung energy by [330]

$$\xi_M \approx \frac{1}{L^3}\sum_{\mathbf{G}\neq\mathbf{0}}\frac{4\pi}{G^2}e^{-\epsilon G^2} - \frac{1}{(2\pi)^3}\int_{k<\infty}d\mathbf{k}\,\frac{4\pi}{k^2}e^{-\epsilon k^2}\ , \tag{139}$$

which becomes exact for $\epsilon \to 0$. Inserting Eq. (139) into (138) gives

$$\frac{\Delta V_N}{N}[S(k), S_N(k)] = \frac{1}{2}\int_{k<\infty}\frac{d\mathbf{k}}{(2\pi)^3}S(k)\frac{4\pi}{k^2} - \frac{1}{2L^3}\sum_{\mathbf{G}\neq\mathbf{0}}S_N(\mathbf{G})\frac{4\pi}{G^2}\ . \tag{140}$$

Evidently, in Eq. (140) there are two possible sources for the finite-size error of V: (i) the difference between the SFs of the finite and infinite system, i.e., a finite-size effect in the actual functional form of $S(k)$ itself, or (ii) the approximation of the continuous integral from Eq. (137) by a discrete sum. Chiesa *et al.* [329] pointed out that, in the ground state, the SF converges remarkably fast with system size (this also holds at finite temperature, see Refs. [226, 225] and the discussion of Fig. 23), leaving (ii) as the sole explanation. In fact, the same authors suggested that the main contribution to Eq. (140) is the $\mathbf{G}=\mathbf{0}$ term, which is completely omitted from the sum. To derive an analytic expression of this term, one makes use of the fact that the random phase approximation becomes exact in the long wave length limit, $k \to 0$, which is valid at finite temperatures as well [332]. In particular, an expansion of the RPA static structure factor around $k = 0$ gives a parabolic expression,

$$S_0^{\mathrm{RPA}}(k) = \frac{k^2}{2\omega_p}\coth\left(\frac{\beta\omega_p}{2}\right)\ , \tag{141}$$

with $\omega_p = \sqrt{3}/r_s^{3/2}$ being the plasma frequency. These considerations lead to the finite-T extension of the FSC from Ref. [329], hereafter labelled as 'BCDC' [211]

$$\Delta V_{\mathrm{BCDC}}(N) = \lim_{k\to 0}\frac{S_0^{\mathrm{RPA}}(k)}{2L^3}\frac{4\pi}{k^2} \tag{142}$$

$$= \frac{\omega_p}{4N}\coth\left(\frac{\beta\omega_p}{2}\right)\ .$$

Thus, the first order finite-size correction used by Brown and co-workers predicts a finite-size error with a simple $1/N$ behavior. However, this ansatz is not appropriate for the conditions encountered in Fig. 22, as we shall now explain in detail.

In Fig. 23, we show the static structure factor for the unpolarized UEG at $\theta = 2$ and $r_s = 0.5$, i.e., the same conditions as in the left panel of Fig. 22 above. The blue, green, and yellow crosses correspond to QMC results for $N = 100$, $N = 66$, and $N = 38$ electrons, respectively and the grey solid line to a cubic spline fit to the largest depicted particle number. Due to momentum quantization in a finite simulation cell, data for $S_N(k)$ are available on an N-dependent discrete k-grid, and restricted to $k \geq k_{\min} = 2\pi/L$. Nevertheless, the functional form of $S_N(k)$ is remarkably well converged with system size for as few as $N = 38$ electrons, see also the inset. This means that the finite-size errors in the interaction energy are indeed the consequence of a discretization error as explained above. The light blue curve in Fig. 23 corresponds to the RPA expansion around $k = 0$, i.e., Eq. (141). Evidently, the parabola does not connect to the QMC data even for the largest particle number. Therefore, Eq. (142) is not sufficient to correct for the finite size error. In sum, the construction of a more accurate FSC requires accurate knowledge of $S(k)$ for $k < 2\pi/L$, i.e., for those wave vectors that are not accessible within the QMC simulations.
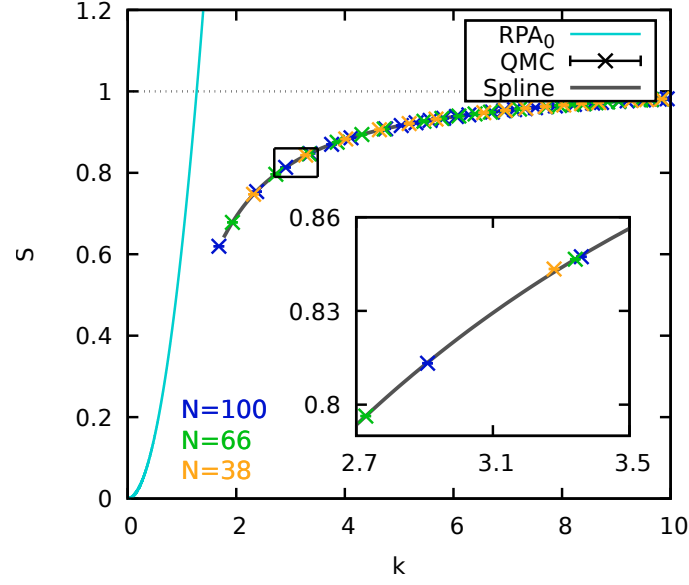
Figure 23: Static structure factor of the unpolarized UEG at $\theta = 2$ and $r_s = 0.5$ – Shown are QMC data for $N = 100$ (blue), $N = 66$ (green), and $N = 38$ (yellow) particles and the parabolic RPA expansion around $k = 0$ (light blue), cf. Eq. (141). The solid grey line corresponds to a cubic spline fit to the $N = 100$ data and the inset shows a magnified segment. Adapted from Ref. [226] with the permission of the authors.
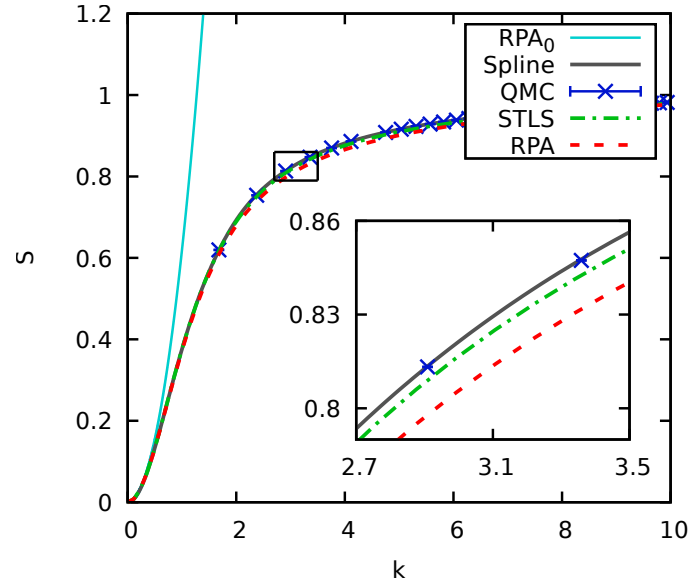
Figure 24: Static structure factor of the unpolarized UEG at $\theta = 2$ and $r_s = 0.5$ – Shown are QMC data for $N = 100$ particles (blue crosses), the parabolic RPA expansion around $k = 0$ (light blue), cf. Eq. (141), full STLS and RPA data (green dash-dotted and red dashed lines, respectively), and a spline connecting STLS for small k with QMC elsewhere (solid grey). The inset shows a magnified segment. Adapted from Ref. [226] with the permission of the authors.
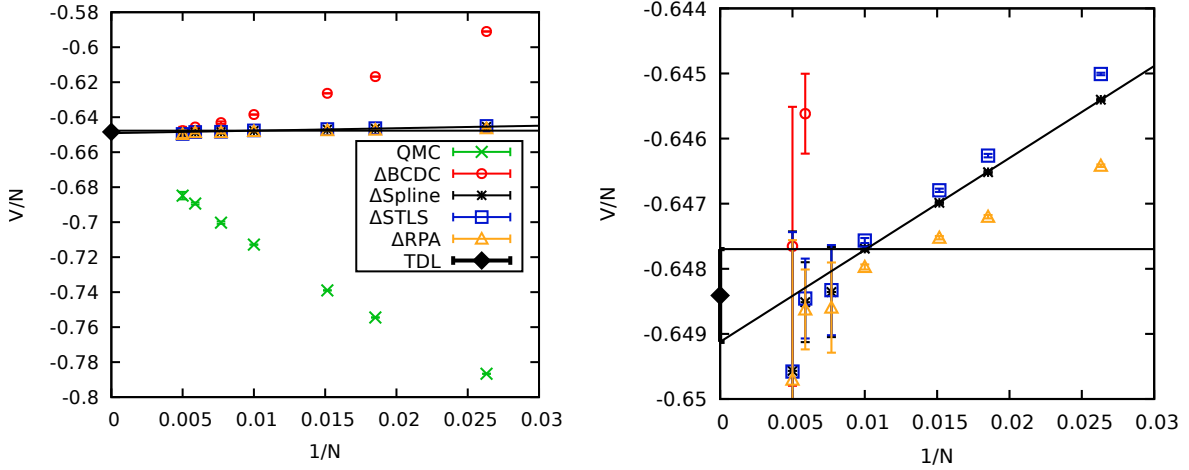
Figure 25: Improved finite-size correction for the interaction energy per particle of the unpolarized electron gas at $\theta = 2$ and $r_s = 0.5$ – Shown are the bare QMC data (green crosses) and the QMC data plus different finite-size corrections, namely Δ_{BCDC} [red circles, see Eq. (142)], and our new FSC from Eq. (143) evaluated using the static structure factors from the spline (black stars), STLS (blue squares) and full RPA (yellow triangles). The solid black lines correspond to a linear and a constant fit to the black stars and the black diamond depicts our result for V/N in the thermodynamic limit. The right panel shows a magnified inset around the results obtained by adding our new FSCs and the subsequent extrapolation. Evidently, using the static SFs solely from full STLS or RPA is sufficient to accurately estimate the finite-size error. Adapted from Ref. [226] with the permission of the authors.

6.3. Improved finite-size correction of the interaction energy

To obtain accurate data for the static structure factor for small k, we carry out full calculations within RPA and also with a static local field correction from the STLS formalism [204, 213], see Sec. 3. The results are shown in Fig. 24, where $S(k)$ is shown for the same conditions as in Fig. 23. The dashed red and dash-dotted green lines correspond to the full RPA and STLS data, respectively, and the blue crosses to the exact QMC results for $N = 100$. In the limit $k \to 0$, both the RPA and STLS curves are in perfect agreement with the parabolic form from Eq. (141), but strongly deviate for $k \gtrsim 0.5$. Further, both dielectric approximations exhibit a fairly good agreement with the QMC point at $k_{\min}$ and the STLS result is within the statistical uncertainty. Therefore, the combination of STLS at small k with the exact QMC data elsewhere allows for exact, unbiased structure factor over the entire k-range. In practice, this is realized by a (cubic) spline, cf. the solid grey line in Fig. 24. Further, we note that the accuracy of both STLS and RPA decreases for larger k, see the inset, although the static local field correction from STLS constitutes a significant improvement. This complementarity of QMC and the dielectric approximations allows for a rather vivid interpretation: Quantum Monte Carlo methods provide an exact treatment of all short-range exchange and correlation effects within the finite simulation box. However, due to the finite number of particles, the long-range limit cannot be resolved. In contrast, both RPA and STLS are formulated in the thermodynamic limit. Since the effect of correlations decreases for large distances, the small k-behavior is described accurately, whereas short-range XC effects are treated insufficiently. For completeness, we note that an accurate knowledge of $S(k)$ would allow to obtain an unbiased result for the interaction energy per particle in the TDL by directly evaluating Eq. (137). However, as we will see below, the detour over the finite-size corrections turns out to be advantageous for multiple reasons.

The thusly obtained model function for the static structure factor [i.e., the spline, $S_{\text{Spline}}(k)$] allows us to accurately estimate the finite-size error by straightforwardly evaluating Eq. (138) as

$$\Delta V_N \left[S_{\text{model}}(k) \right] = \frac{\Delta V_N}{N} \left[S_{\text{model}}(k), S_{\text{model}}(k) \right], \tag{143}$$

which we compute numerically. The resulting FSC is shown in Fig. 25, where we again show the N-dependence of the interaction energy per particle for the same conditions as above. Let us first consider the black stars, which have been obtained by adding to the bare QMC results $\Delta V_N[S_{\text{spline}}(k)]$. Evidently, the dependence on system size has been decreased by two orders of magnitude. The right panel shows a magnified segment around the new corrected results and we detect a small remaining finite-size error with a linear behavior. The main source of this residual error is the small N-dependence of $S_N(k)$ itself. However, even for as few as $N = 38$ particles, this bias is of the order of $\Delta V/V \sim 10^{-3}$. In practice, we always remove any residual errors by performing an additional extrapolation

of the corrected data. In particular, we perform a linear fit over all N and a constant fit to the last few points that are converged with N within twice the error bars (the latter corresponds to the assumption that the small system size dependence in $S_N(k)$ vanishes for large N, which it might), see the solid black lines. Our final estimation of the interaction energy per particle in the thermodynamic limit is then obtained as the mean of both fits, and the difference between the two constitutes the remaining uncertainty interval. Let us now consider the blue squares and yellow triangles, which have been obtained by evaluating Eq. (143) solely using the static structure factors from STLS and RPA, respectively, over the entire k-range. Surprisingly, both data sets are in good agreement with the black stars. This means that – despite the rather significant bias for intermediate k – both the full RPA and STLS SFs are sufficient model functions to estimate the discretization error in the interaction energy per particle. Therefore, it is not necessary to perform a spline interpolation for each case, and, in the following, we will compute ΔV_N using STLS. It is important to note that while the dielectric approximations allow to accurately estimate the discretization error in V_N/N, we still need a QMC result for V_N/N itself, i.e.,

$$\nu = \frac{V_N^{\mathrm{QMC}}}{N} + \Delta V_N \left[S_{\mathrm{STLS}}(k) \right] . \tag{144}$$

Replacing V_N/N by the STLS value, which is equivalent to evaluating Eq. (137) using $S_{\mathrm{STLS}}(k)$, would neglect the short-range exchange-correlation effects and induce a systematic bias of the order of $\Delta V/V \sim 10^{-2}$, see Sec. 7.

6.4. Examples of finite-size corrections of QMC data

6.4.1. Coupling strength dependence of the finite-size correction of QMC data

To demonstrate the universal applicability of the improved finite-size correction, in Fig. 26 we show results both for the static structure factor and the interaction energy per particle for the unpolarized UEG over three orders of magnitude of the coupling parameter r_s at $\theta = 2$. In the top row, results are depicted for $r_s = 10$, i.e., a relatively strongly coupled system. The left panel shows the static structure factor, where the QMC results for $N = 140$ electrons are depicted by the black crosses. Furthermore, the dashed blue line corresponds to the parabolic RPA expansion around $k = 0$ [see Eq. (141)], the dash-dotted green and dotted yellow lines to the full STLS and RPA results, respectively, and the solid red line to the spline connecting STLS for small k with QMC data elsewhere. For such parameters, QMC results for $S(k)$ range down to small S and for k_{min} all depicted data sets – even the RPA expansion – are in excellent agreement. Therefore, the finite-size correction proposed by Brown *et al.* [211] is appropriate, cf. the right panel. Overall, we observe substantial errors in the RPA curve for intermediate k starting around $k \gtrsim 0.1$. The STLS curve is in much better agreement to the QMC data everywhere, although it is too large for $k \lesssim 0.35$ and too small for larger k. The inset shows a magnified segment where, in addition to the QMC data for $N = 140$, we also show results for $N = 80$ (squares) and $N = 66$ (circles). Evidently, no system size dependence of $S_N(k)$ can be resolved within the given statistical uncertainty. Let us now consider the interaction energy per particle, which is depicted as a function of $1/N$ in the right panel. As usual, the green crosses correspond to the bare QMC results and, even for as few as $N = 34$ electrons, the finite-size error does not exceed $\Delta V/V = 1\%$. This can be explained by recalling the interpretation of finite-size effects as a discretization error in the integration of $S(k)$, which is densely sampled by the QMC points down to small values of S, cf. the left panel. Further, we note that the QMC points seem to exhibit a linear behavior as predicted by the BCDC-FSC, Eq. (142). Consequently, adding Δ_{BCDC} to the QMC data (red circles) removes the finite-size error and no system size dependence can be resolved within the given statistical uncertainty. Furthermore, we note that the improved FSC [Eq. (143)] using S_{STLS} as a model function leads to the same results.

In the center row, we show results for intermediate coupling, $r_s = 1$. Here, in contrast to the previous case, the RPA expansion does clearly not connect to the QMC results, which are not available down to such small S-values as above. Furthermore, we note that both the full RPA and STLS curves exhibit much smaller deviation to the QMC data, as it is expected. In fact, the STLS curve is only seldom not within twice the statistical uncertainty of the QMC points. For completeness, we mention that again no difference between QMC data for different particle numbers can be resolved, see the inset. The interaction energy per particle exhibits a rather peculiar behavior. First and foremost, we note that the finite-size error for $N = 34$ is of the order of 10% and, thus, larger than for the strong coupling case. Again this comes as no surprise when comparing the static structure factors and re-calling the discretization error. In addition, the bare QMC results seem to exhibit a linear dependence in $1/N$. This is further substantiated by a linear fit, cf. the solid green line, which reproduces all points within error bars. Interestingly, however, the calculated slope is not equal to the BCDC prediction by Eq. (142). Consequently, the red circles exhibit a distinct system size dependence and are not in agreement with the linear extrapolation. Finally, the improved FSC leads to significantly reduced finite-size errors, which we subsequently remove by an additional extrapolation as explained in the discussion of Fig. 25. The thusly obtained final result for the TDL significantly

Figure 26: Coupling dependence of static structure factors (left) and interaction energies per particle (right) of the unpolarized electron gas at $\theta = 2$ – Top row: $r_s = 10$, center row: $r_s = 1$, bottom row: $r_s = 0.1$. Shown are results for the static SF from QMC simulations with three different particle numbers (black symbols, the data for the two smallest N appear in the inset only), the RPA expansion around $k = 0$ (dashed blue), cf. Eq. (141), and full RPA and STLS data (dotted yellow and dashed dotted green lines, respectively). The solid red line corresponds to a spline connecting STLS for small k with QMC data elsewhere and the insets depict a magnified segment. The interaction energies per particle correspond to the bare QMC results (green crosses), and finite-size corrected data using Δ_{BCDC} (red circles) and the new improved FSC by Dornheim *et al.* [226] using S_{STLS} (blue squares). The solid black line corresponds to an extrapolation of the residual finite-size error and the black diamond depicts the extrapolated result for V/N in the TDL.

deviates from the linear extrapolation as well, which again demonstrates the problems with a direct extrapolation without knowing the exact functional form of the N-dependence.

Finally, in the bottom row we show results for $r_s = 0.1$, which corresponds to weak coupling and high density. Even for as many as $N = 700$ electrons, the QMC results are not available for the k-range where S is small. Hence, the RPA expansion does come nowhere near the QMC point at k_{min} and the BCDC-FSC is not expected to work. Further, both the full RPA and STLS curves are in good agreement with the QMC data and each other over the entire k-range. Again, we note that $S_N(k)$ converges remarkably fast with system size, see the inset. The large value of $S_N(k)$ at k_{min} indicates that the wave vector range where S varies most is not sampled sufficiently, or not accessed by QMC points at all. Consequently, the finite-size errors are substantially increased compared to $r_s = 10$ and $r_s = 1$ and, for $N = 38$ particles, are comparable in magnitude to V_N/N itself. Furthermore, the BCDC-FSC is not useful and severely overestimates the discretization error. In particular, for $N \lesssim 100$, the thusly 'corrected' data exhibit a larger system size dependence than the original bare QMC data. The improved FSC computed from S_{STLS} again works remarkably well even for small N, and reduces the system-size dependence by two orders of magnitude.

6.4.2. Temperature dependence of the finite-size correction of QMC data

As a second demonstration of the versatility of the improved finite-size correction, in Fig. 27 we investigate the temperature dependence of the static structure factor and the interaction energy per particle of the spin-polarized UEG at $r_s = 0.3$. The top row shows results for $\theta = 0.5$, which is the lowest temperature considered in the recent QMC simulations by Dornheim, Groth, and co-workers [226, 227]. The QMC results for $S(k)$ range down to intermediate values of S, but do not connect to the RPA expansion. Further, we note that both the full RPA and STLS curves are in good agreement with each other and the QMC data over the entire k-range. As usual, the largest deviations occur for intermediate k but are of the order of 0.1%. The bare QMC results for the interaction energy per particle seem to exhibit a linear behavior, but, similar to the observation in the center row of Fig. 26, not with the slope predicted by Eq. (142). Consequently, adding the BCDC-FSC does not remove the system-size dependence, as expected from the discussion of the static structure factors. The improved FSC from Eq. (143) using S_{STLS} as a model function to estimate the discretization error immediately improves the system size dependence by two orders of magnitude and no residual errors can be resolved with the naked eye.

The center and bottom rows show the same information for $\theta = 1$ and $\theta = 4$, respectively. First and foremost, we observe that the decline of $S(k)$ becomes steeper for increasing temperatures. This means that more QMC points are needed to accurately sample S, which, in turn, leads to increased discretization errors. In particular, for $\theta = 4$ and $N = 33$, the finite-size error is comparable in magnitude to V_N/N itself, and, even for $N = 1000$ electrons, no QMC results are available for $S \lesssim 0.6$. Further, we note that both the full RPA and STLS results for the static structure factor become increasingly accurate for large θ. This is, of course, expected as large temperatures render correlation effects less important. Finally, we mention that, while the BCDC-FSC becomes significantly less accurate, the improved FSC from Eq. (143) works well for all temperatures (and densities).

7. Benchmarks of other methods

The improved finite-size correction introduced in this section has subsequently been used to obtain an exhaustive and very accurate data set for the interaction energy for different temperature-density combinations and four different spin-polarizations ($\xi = 0$, $\xi = 1/3$, $\xi = 0.6$, and $\xi = 1$), see Refs. [226, 227]. This puts us, for the first time, in a position to gauge the accuracy of previously developed theories and approximations, most importantly that of the dielectric methods from Sec. 3.

7.1. Benchmarks of the interaction energy

In Fig. 28, we show the r_s-dependence of the interaction energy per particle of the unpolarized electron gas at two relevant temperatures, $\theta = 0.5$ (left) and $\theta = 1$ (right). The red diamonds correspond to our recent finite-size corrected QMC data and the solid red lines to simple fits at constant temperature θ, see Ref. [226] for details. Let us start our investigation by considering the most simple dielectric approach, i.e., the random phase approximation (brown dots). As expected, RPA only allows for a qualitative description at weak coupling, and even at extreme densities, $r_s = 0.1$, there appear deviations exceeding 2% in v. At moderate coupling, $r_s = 1$, we find relative errors of $\Delta v / v \approx 9\%$ for both depicted temperatures, indicating that RPA is of limited use for the description of electrons in the warm dense matter regime. The same applies for both depicted finite-temperature Green function data sets, where the Montroll-Ward approximation (MW, dotted pink line) closely follows RPA and the e^4-approximation

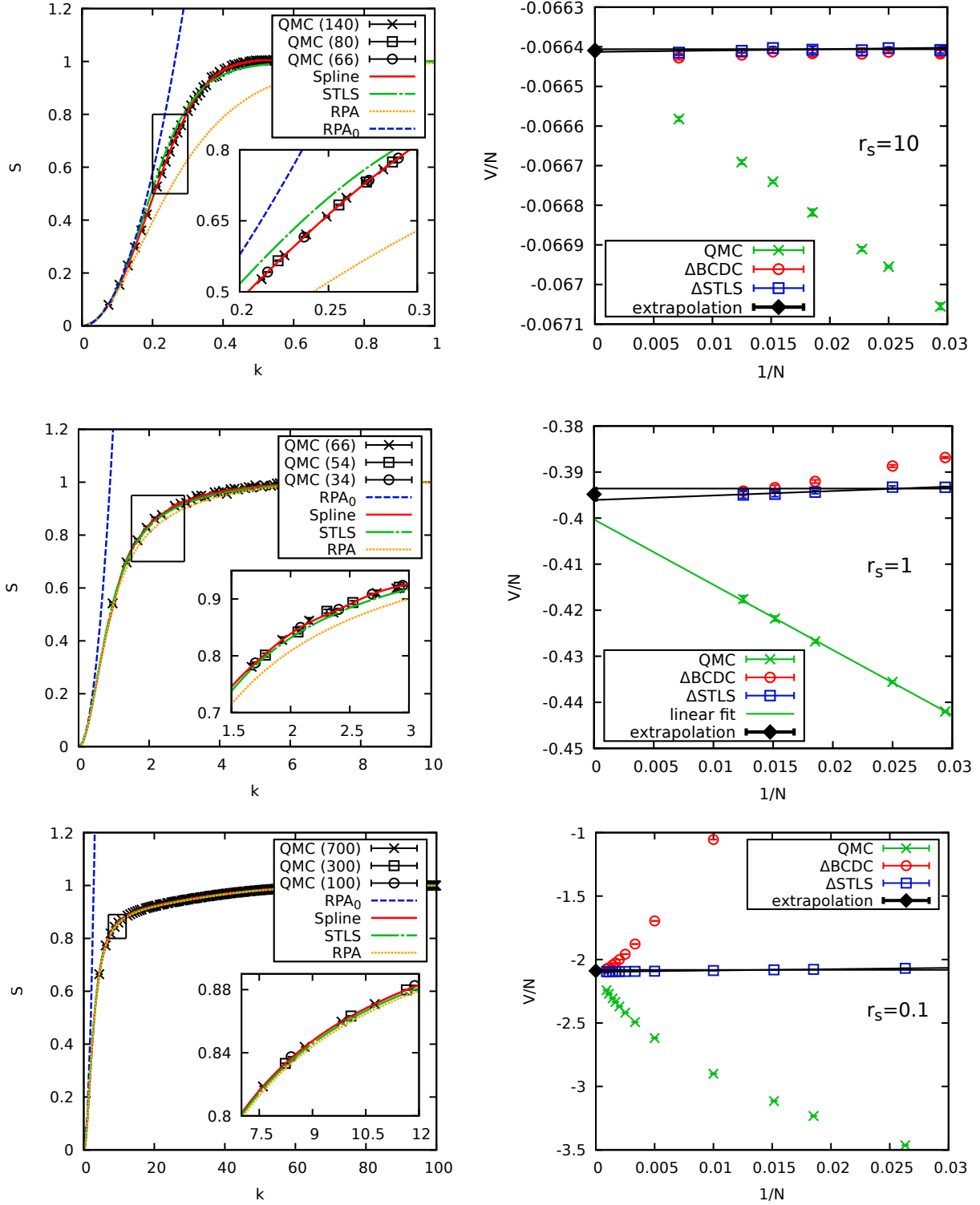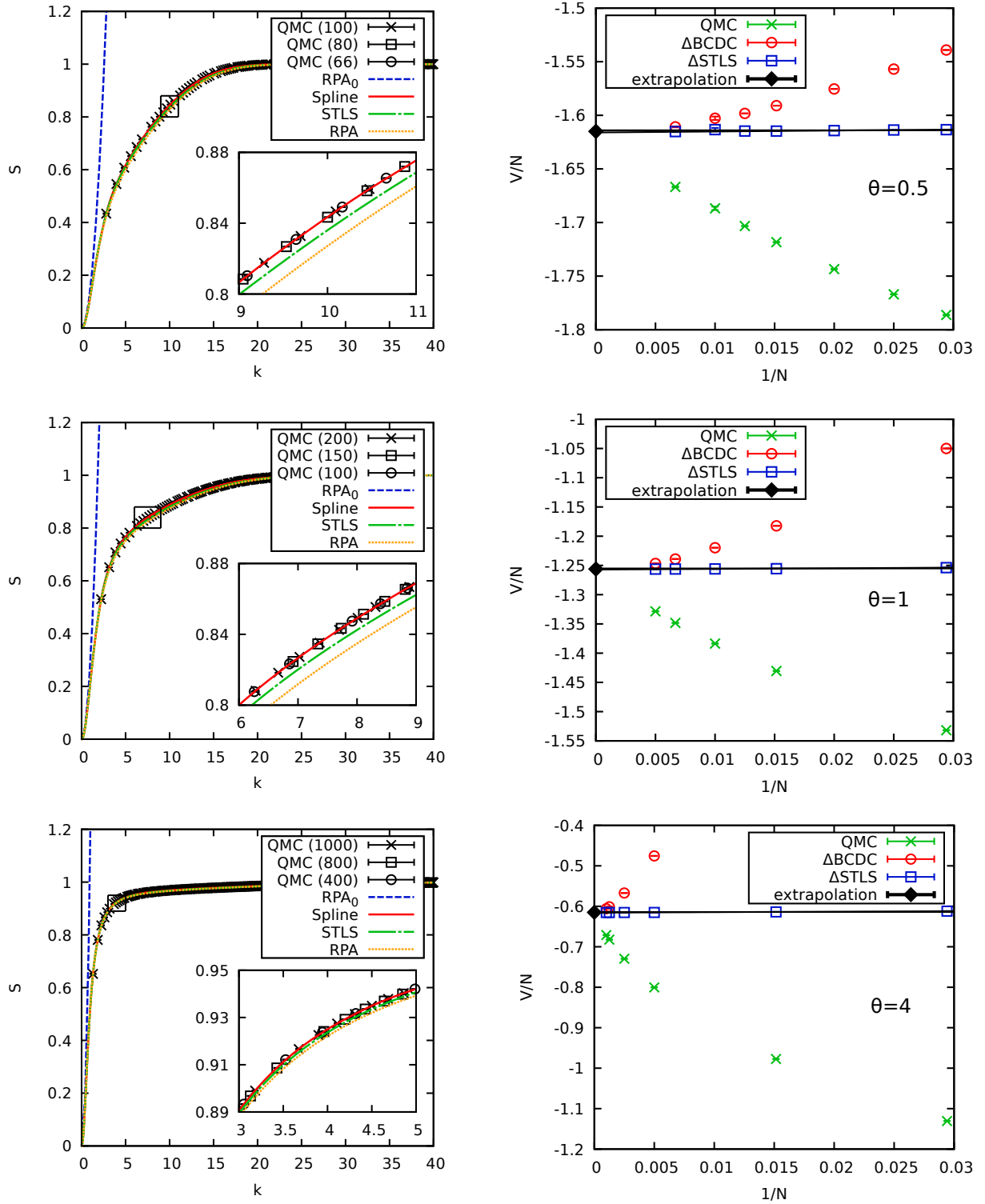Figure 27: Temperature dependence of static structure factors (left) and interaction energies per particle (right) of the spin-polarized electron gas at $r_s = 0.3$ – Top row: $\theta = 0.5$, center row: $\theta = 1$, bottom row: $\theta = 4$. Shown are results for the static SF from QMC simulations with three different particle numbers (black symbols, the data for the two smallest N appear in the inset only), the RPA expansion around $k = 0$ (dashed blue), cf. Eq. (141), and full RPA and STLS data (dotted yellow and dashed dotted green lines, respectively). The solid red line corresponds to a spline connecting STLS for small k with QMC data elsewhere and the insets depict a magnified segment. The interaction energies per particle correspond to the bare QMC results (green crosses), and finite-size corrected data using Δ_{BCDC} (red circles) and the new improved FSC from Ref. [226] using S_{STLS} (blue squares). The solid black line corresponds to an extrapolation of the residual finite-size error and the black diamond depicts the extrapolated result for V/N in the TDL.

53
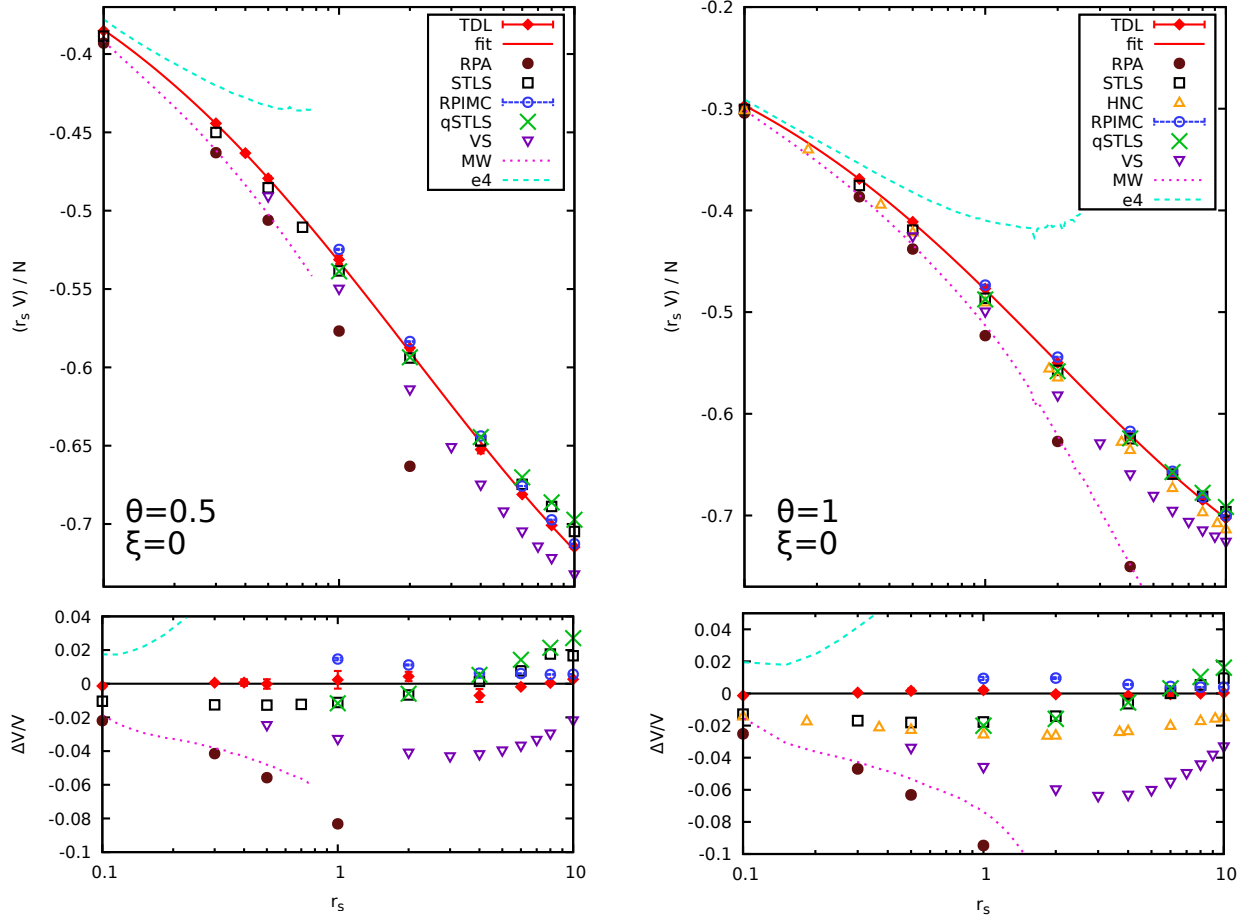
Figure 28: Comparison of the interaction energies for the unpolarized electron gas at $\theta = 0.5$ (left) and $\theta = 1$ (right). The red diamonds correspond to the finite-size corrected QMC data by Dornheim, Groth and co-workers [226] and the red lines depict fits to these data (see Ref. [226]). Further shown are the RPIMC data by Brown *et al.* [211] (blue circles), finite-temperature Green function data computed in the Montroll-Ward (MW, dotted pink) and e^4-approximation (dashed light blue), cf. Sec. 4, and various dielectric approximations, specifically RPA (brown dots), STLS (black squares), quantum STLS (green crosses, data obtained via integration of structure factors provided in Ref. [252]), Vashista-Singwi (VS, purple downward triangles) [213], and the recent static local field correction based on the hypernetted chain (HNC) equation by Tanaka [242].

exhibits a similar systematic error of the opposite sign (for more details on MW and e^4, see the Supplemental Material of Ref. [218]).

Let us next consider the STLS approximation, both using the static (black squares) and dynamic (so-called quantum STLS or qSTLS, green crosses) versions of the local field correction. Obviously, this inclusion of correlation effects via $G(q)$ leads to a remarkable improvement in the interaction energy even up to relatively strong coupling, $r_s = 10$. In particular, we find a maximum deviation of $\Delta v/v \approx 2\%$, which, for $\theta = 1$, are most pronounced around $r_s = 1$. This might seem surprising as the STLS closure relation for the LFC is expected to worsen towards increasing correlation effects. This is indeed the case both for the local field correction [and thus for the static density response function $\chi(q)$] as well as for the static structure factor. However, the interaction energy per particle is obtained from $S(k)$ via integration, cf. Eq. (37), and benefits from an error cancellation. For more details, see the investigation of the static structure factor in the next section. Furthermore, we note that the inclusion of the frequency dependency of the STLS local field correction has only a minor effect on v and even leads to slightly worse results compared to the static version introduced in Ref. [204]. At $\theta = 1$, we can also investigate the performance of a recently introduced (static) local field correction that is based on the hypernetted chain equation [242]. The results for the interaction energy are shown as the yellow triangles in the right panel of Fig. 28. For weak coupling, $r_s < 1$, the results are similar to both STLS versions, whereas for stronger coupling there appear differences between these dielectric methods of up to $\delta v/v = 3\%$. However, while the SLTS results for v intersect with the exact QMC results, the HNC data are always too low by up to 3%, making STLS the dielectric approximation of choice for the interaction energy. Again, this is in contrast to $S(k)$ and $G(k)$, where the new HNC-based formalism turns out to be superior, cf. Figs. 31 and 43. The purple downwards triangles correspond to the Vashista-Singwi formalism computed by Sjostrom and Dufty [213], which, for the present conditions, constitutes the least accurate dielectric approximation (excluding RPA) regarding v. Finally, let us consider the restricted PIMC results by Brown *et al.* [211] (blue circles), which are available down to $r_s = 1$. For the two depicted temperatures, these data are more accurate than the dielectric approximations with a maximum deviation of $\Delta v/v \approx 1.5\%$ at $r_s = 1$ and $\theta = 0.5$.

Next, we consider the spin-polarized case, which is shown in Fig. 29. While RPA turns out to be similarly inaccurate as for the unpolarized case, we find a slightly worse performance of both STLS variants in this case. In particular, there appear maximum deviations of around $\Delta v/v = 4\%$ at $r_s = 2$, and the curves do not intersect with the exact results. Again, both STLS and qSTLS lead to almost indistinguishable results in the interaction energy, although at $\xi = 1$ the qSTLS is slightly superior to STLS at large r_s. The RPIMC data from Ref. [211] are also slightly worse with a maximum deviation of $\Delta v/v \approx 3.5\%$ at $r_s = 4$ and $\theta = 1$. In fact, this point constitutes an outlier, which has already been reported for the investigation of the finite model system [220].

Let us conclude this section with the investigation of the electron gas at high temperature, $\theta = 8$, which is shown in Fig. 30. Both for the paramagnetic (left panel) and ferromagnetic (right panel) case, STLS and qSTLS lead to systematically too small results over the entire depicted density-range (the same is true for the VS data shown for $\xi = 0$) with a maximum deviation slightly exceeding 2% around $r_s = 4$ for $\xi = 1$. For completeness, we mention that coupling effects decrease with increasing θ, leading to a large ratio of kinetic and interaction contribution to the total energy. However, this does not necessarily have to result in an improved relative accuracy in v of the dielectric approximations, although, obviously, the total energy will be more accurate in this case. The random phase approximation exhibits a significantly improved performance compared to the previous figures, although there still appear errors of $\Delta v/v \approx 4\%$ at $r_s = 1$, which are rapidly increasing towards stronger coupling. In contrast to the lower temperature case, the finite-temperature Green function data, exhibits a pronounced unphysical bump in v around $r_s = 0.7$ with a maximum deviation of 7% and 10% for MW and e^4, respectively. Finally, the RPIMC data are considerably less accurate at high temperature and exhibit an increasing systematic bias towards high density with a maxium error of $\Delta v/v \approx 12\%$ at $r_s = 1$ and $\xi = 1$. This is mainly a consequence of the inappropriate finite-size correction, which becomes more severe both towards high density and temperature. The effect is more pronounced for the ferromagnetic case, since (i) $\theta = 8$ constitutes a higher temperature than for $\xi = 0$ due to the different Fermi energies, cf. Eq. (4), and (ii) only $N = 33$ electrons were simulated in contrast to $N = 66$ for the paramagnetic case.

7.2. Static structure factor

Finally, let us evaluate the accuracy of different theories regarding the static structure factor $S(k)$, which is of central importance for the dielectric approximations introduced in Sec. 3. In the left panel of Fig. 31, we show $S(k)$ for the unpolarized electron gas at $\theta = 1$ and $r_s = 1$. The solid black line corresponds to a cubic basis spline connecting the STLS data for the limit of small k with our QMC data elsewhere, see Ref. [333] and the explanation of finite-size effects in v above. At these conditions, all dielectric approximations give the correct qualitative description of the SSF. The most pronounced systematic deviations occur for intermediate k, with a
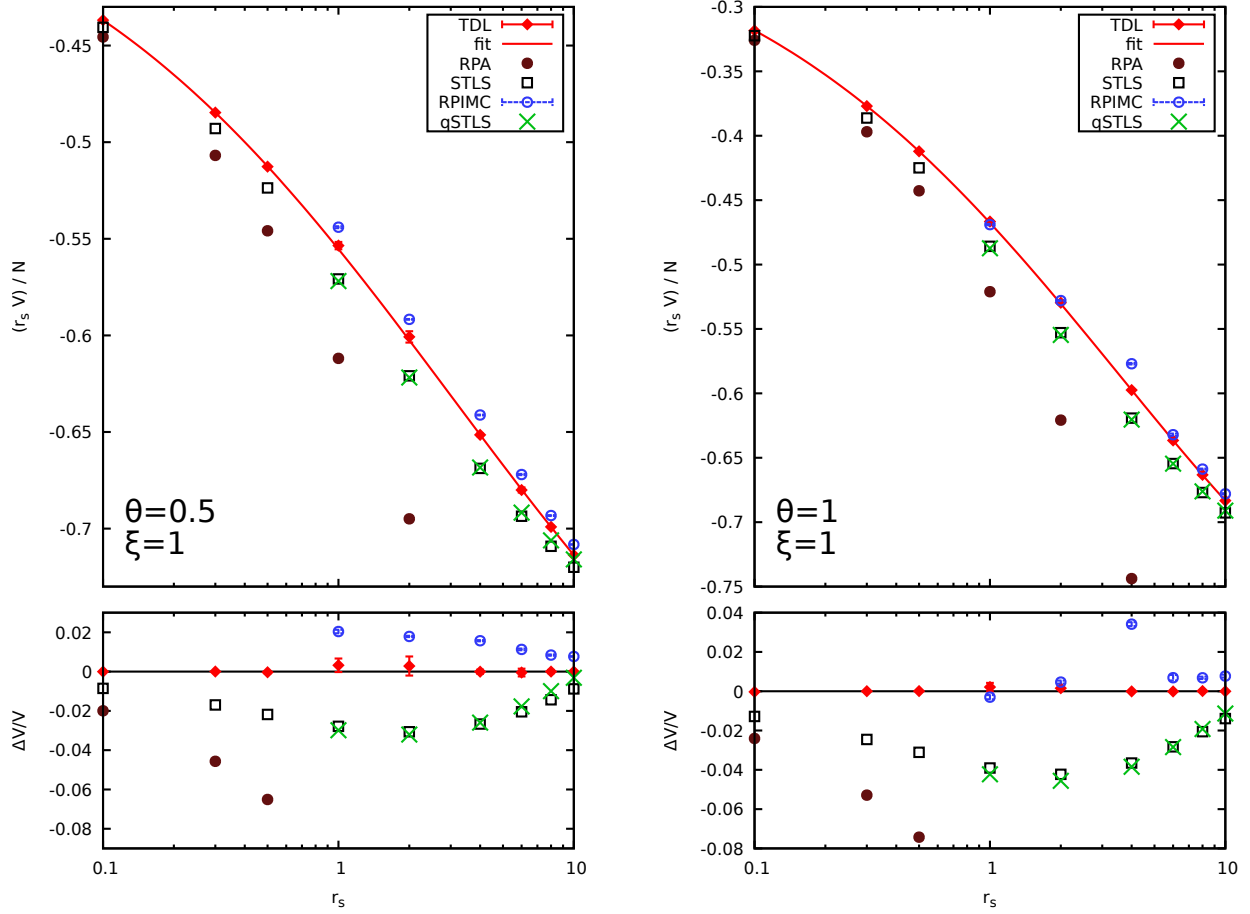
Figure 29: Gauging the accuracy of the interaction energy (per particle) of different approximations for the spin-polarized electron gas at $\theta = 0.5$ (left) and $\theta = 1$ (right). The red diamonds correspond to the finite-size corrected QMC data by Groth, Dornheim and co-workers [227] and the red lines depict corresponding fits to these data (see the Supplemental Material of Ref. [226] for more details). Further shown are the RPIMC data by Brown *et al.* [211] (blue circles) and various dielectric approximations, specifically RPA (brown dots), STLS (black squares), and quantum STLS (green crosses, data obtained via integration of structure factors provided in Ref. [252]).
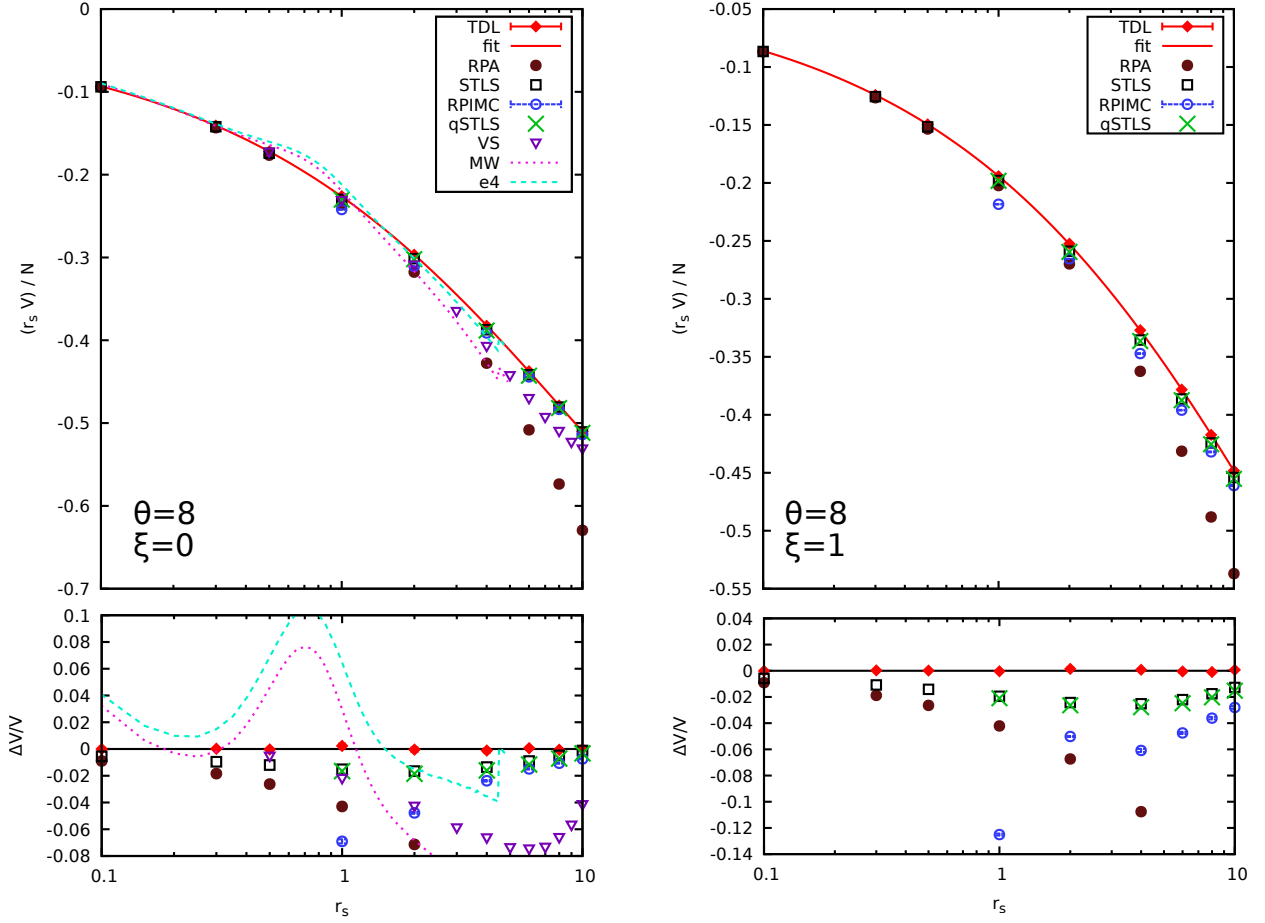
Figure 30: Gauging the accuracy of the interaction energy (per particle) of different approximations for the unpolarized (left) and spin-polarized (right) electron gas at $\theta = 8$. The red diamonds correspond to the finite-size corrected QMC data by Dornheim, Groth and co-workers [226, 227] and the red lines depict corresponding fits to these data (see the Supplemental Material of Ref. [226] for more details). Further shown are the RPIMC data by Brown *et al.* [211] (blue circles), finite-temperature Green function data computed in the Montroll-Ward (MW, dotted pink) and e^4-approximation (dashed light blue), cf. Sec. 4, and various dielectric approximations, specifically RPA (brown dots), STLS (black squares), quantum STLS (green crosses, data obtained via integration of structure factors provided in Ref. [252]), and, for $\xi = 0$, recent Vashista-Singwi based data by Sjostrom and Dufty [213] (purple downward triangles).
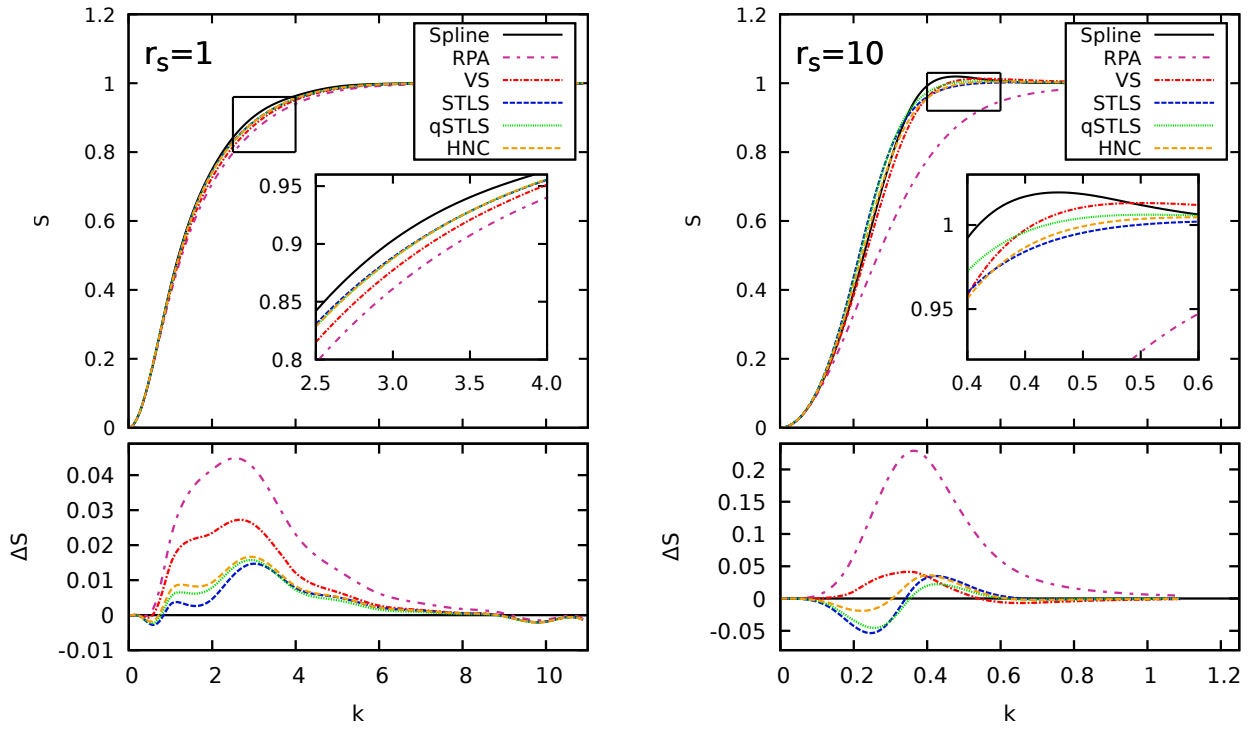
Figure 31: Gauging the accuracy of different approximations for the static structure factor of the unpolarized electron gas at $\theta = 1$ and $r_s = 1$ (left) and $r_s = 10$ (right). The solid black line corresponds to cubic spline fits connecting STLS at small k with our QMC data elsewhere [333], the double-dashed purple line to RPA, the dash-dotted red line to Vashista-Singwi (VS) [213], the dashed blue line to STLS, the dotted green line to qSTLS [252], and the dashed orange line to the recent local field correction based on the hypernetted-chain (HNC) approximation by Tanaka [242]. The bottom panels depict the relative deviations to our spline.

maximum deviation of $\Delta S/S \approx 10\%$ for RPA. On the other hand, STLS, qSTLS, and HNC exhibit a very similar behavior with maximum inaccuracies of 2%, and standard STLS being the most accurate approximation in this case. Further, the VS curve is significantly less accurate, albeit the overall behavior resembles the other LFC-based data.

In the right panel of Fig. 31, the same information is shown for stronger coupling, $r_s = 10$. In this case, our QMC-based spline exhibits a pronounced maximum around $k = 0.45$, which is due to Coulomb correlation effects, and cannot be accurately resolved by any of the dielectric methods. The random phase approximation breaks down, with a systematically too small structure factor over the entire k-range and deviations exceeding 25%. Again, STLS and qSTLS are very similar and give too large results for $k \lesssim 0.35$ and too small results elsewhere. The maximum deviations occur around $k = 0.2$ with $\Delta S/S \approx 10\%$, although qSTLS performs slightly better everywhere. The observed deviation ΔS (bottom panel) towards our spline is of high importance to understand the observed high performance of STLS in the interaction energy v. Since the latter is, for a uniform system, simply given by a one-dimensional integral over $S(k) - 1$, the area under the ΔS curve is directly proportional to the error in v. Evidently, the negative area for small k is of a similar magnitude as the positive one for larger k, which leads to a beneficial cancellation of errors and, thus, accurate results in v. In contrast, the recent HNC results for $S(k)$ by Tanaka [242] are significantly better than STLS almost over the entire k-range. Nevertheless, the corresponding results for v do not enjoy the error cancellation to the same degree. Finally, let us consider the VS curve from Ref. [213], which exhibits a qualitatively different behavior from the other dielectric approximations. More specifically, the results for $S(k)$ are too low for small k and slightly too large in the vicinity of large wave vectors. While the overall accuracy is again better than for STLS, there is almost no cancellation of errors when one is interested in v or, via an additional coupling-constant integration, in f_{xc}.

8. Parametrizations of the XC free energy

8.1. Introduction

In the ground state, the first parametrization of the exchange-correlation energy, $e_{\mathrm{xc}}(r_s)$, of the unpolarized UEG on the basis of QMC data (by Ceperley and Alder [15, 16]) has been obtained in 1981 by Perdew and Zunger [29]. Shortly afterwards, Vosko, Wilk, and Nusair [28] extended the parametrization to arbitrary spin-polarizations ξ, and provided a functional for $e_{\mathrm{xc}}(r_s, \xi)$ in the entire parameter regime relevant to DFT calculations in the LSDA.

At finite temperature, a parametrization of the exchange-correlation free energy, $f_{\mathrm{xc}}(rs, \theta, \xi)$, in dependence of density, temperature and spin-polarization is required. In lieu of accurate finite temperature QMC data, in 1982, Ebeling *et al.* [198, 199, 200, 201, 202] carried out first attempts to obtain such a functional for the unpolarized case in terms of Pade approximations that interpolate between the known limits, i.e., the ground state limit, $\lim_{\theta \to 0} f_{\mathrm{xc}}(r_s, \theta) = e_{\mathrm{xc}}(r_s, 0)$, and the Debye-Hückel limit [334], $\lim_{\theta \to \infty} f_{\mathrm{xc}}(r_s, \theta) = -\frac{1}{\sqrt{3}} r_s^{-3/2} T^{-1/2}$. After that, various approximate functionals have been obatained on the basis of the results from different dielectric approaches (see Sec. 3). Starting in the mid 1980s, Ichimaru, Tanaka and co-workers constructed a functional of $f_{\mathrm{xc}}(r_s, \theta)$ by fitting a complex Pade approximation to the finite temperature STLS data [203], which has subsequently been improved (IIT) by incorporating the exact ground state limit via a suitable bridge function [206]. Only very recently, this functional has been extended to arbitrary polarizations [249]. In addition to the STLS approach, the Vashishta-Singwi [213], hypernetted chain [242] (HNC), and the modified convolution approximation [205] (MCA) have been successfully explored in the construction of parametrizations of the exchange correlation free energy. However, a suitable spin-interpolation function has only been deduced from the MCA results. This MCA spin-interpolation function is also utilized for the generalization of the IIT and HNC functionals to arbititrary spin-polarizations.

Further, Dharama-wardana and Perrot presented [210, 209] another widely used functional [181, 182, 183] based on data from their classical mapping approximation (see Sec. 4.2.1). Then, after the first finite temperature QMC data by Brown *et al.* [211] became available in 2013, several attempts have been made to obtain functionals from these [213, 214, 212]. Among these, the most refined parametrization has been presented by Karasiev *et al.* [212] (KSDT), who, following the IIT functional, incorporated all known limits: ground state, Debye-Hückel and the high-density Hartree-Fock limit [248]. Yet, since Brown applied the RPIMC method solely to the fully polarized and unpolarized cases, the spin-interpolation of the KSDT functional has been constructed from the classical mapping data, for intermediate spin-polarizations. In addition, even for $\xi = 0$ and $\xi = 1$ the RPIMC data has turned out to be unreliable, as was shown in Sec. 7.

Only recently, Groth, Dornheim *et al.* [227] presented a complete *ab initio* parametrization of the exchange-correlation free energy, $f_{\mathrm{xc}}(rs, \theta, \xi)$, that is based on highly accurate data obtained from two novel finite temperature QMC methods, CPIMC and PB-PIMC see Sec. 5.5 and Sec. 5.4 and references therein.

8.2. Parametrizations

In the following, we will provide the concrete functional form of all parametrizations, which are shown in the comparison plots in Sec. 8.4. Further, the precise way in which these were constructed as well as the included limits are discussed in detail. To be as concise as possible, we have restricted ourselves to the 5 most accurate functionals: IIT, HNC, PDW, KSDT, and GDB. For a discussion of the accuracy of the parametrization by Ebeling and co-workers, see Ref. [335].

8.2.1. IIT parametrization

Since the dielectric methods are based on a self-consistency loop for the static structure factor and the local field correction, the natural thermodynamic quantity within this framework is given by the interaction energy computed from the static structure factor according to Eq. (37). For fixed spin-polarization $\xi = (n_\uparrow - n_\downarrow)/n$ with the total electron density $n = (n_\uparrow + n_\downarrow)$, the interaction energy is linked to the exchange-correlation free energy via the well-known coupling constant integration formula

$$f_{\text{xc}}^\xi(r_s, \theta) = \frac{1}{r_s^2} \int_0^{r_s} d\bar{r}_s \, \bar{r}_s \, v^\xi(\bar{r}_s, \theta) \, . \tag{145}$$

In the literature, the classical coupling parameter $\Gamma = 1/(r_s a_{\text{B}} T)$ is often utilized, so that Eq. (145) reads

$$f_{\text{xc}}^\xi(r_s, \theta) = \frac{1}{\Gamma^2} \int_0^\Gamma d\bar{\Gamma} \, \bar{\Gamma} \, v^\xi(\bar{\Gamma}, \theta) \, . \tag{146}$$

For the unpolarized ($\xi = 0$) and polarized ($\xi = 1$) case, Ichimaru, Tanaka and co-workers [206, 249] proposed the following Pade fit function for the interaction energy:

$$v^\xi(\Gamma, \theta) = -\frac{1}{r_s} \frac{\omega_\xi a(\theta/\omega_\xi^2) + b^\xi(\theta)\sqrt{\theta}\sqrt{\Gamma} + c^\xi(\theta)\theta\Gamma}{1 + d^\xi(\theta)\sqrt{\theta}\sqrt{\Gamma} + e^\xi(\theta)\theta\Gamma} \, , \tag{147}$$

with the spin-factor $\omega_\xi = (1 + \xi)^{1/3}$ and

$$a(\theta) = 0.610887 \tanh\left(\theta^{-1}\right) \frac{0.75 + 3.04363\theta^2 - 0.09227\theta^3 + 1.7035\theta^4}{1 + 8.31051\theta^2 + 5.1105\theta^4} \tag{148}$$

ensures that the correct Hartree-Fock limit, i.e., $\lim_{r_s \to 0} v^\xi = -\frac{1}{r_s}\omega_\xi a(\theta/\omega_\xi^2)$, as parametrized in Ref. [248] is fulfilled. The remaining functions b, c, d, and e are of the form

$$b^\xi(\theta) = \tanh\left(\frac{1}{\sqrt{\theta}}\right) \frac{b_1^\xi + b_2^\xi\theta^2 + b_3^\xi\theta^4}{1 + b_4^\xi\theta^2 + b_5^\xi\theta^4}$$

$$c^\xi(\theta) = \left[c_1^\xi + c_2^\xi \cdot \exp\left(-\theta^{-1}\right)\right] e^\xi(\theta)$$

$$d^\xi(\theta) = \tanh\left(\frac{1}{\sqrt{\theta}}\right) \frac{d_1^\xi + d_2^\xi\theta^2 + d_3^\xi\theta^4}{1 + d_4^\xi\theta^2 + d_5^\xi\theta^4}$$

$$e^\xi(\theta) = \tanh\left(\frac{1}{\theta}\right) \frac{e_1^\xi + e_2^\xi\theta^2 + e_3^\xi\theta^4}{1 + e_4^\xi\theta^2 + e_5^\xi\theta^4} \, ,$$

where the constants $b_1^\xi, \ldots, e_5^\xi$ are determined by a fit to the modified STLS data for the interaction energy. These modified results have been obtained by correcting the raw STLS interaction energy such that the exact ground state limit ($\theta = 0$), that is known from the QMC simulations by Ceperly and Alder [15, 16, 28], and the classical limit ($\theta \to \infty$) are restored. This is achieved via a hypothetically assumed interpolation function that interpolates between these two limits [249], so that the accuracy for intermediate values of θ is naturally unclear. Once the fitting constants in Eq. (147) are known (for their concrete values see Ref. [249]), the corresponding exchange-correlation free energy is immediately computed by analytically carrying out the coupling constant integration in Eq. (146),

yielding

$$
\begin{aligned}
f_{xc}^{\xi}(r_s, \theta) = \;\; & - \;\; \frac{1}{r_s} \frac{c(\theta)}{e(\theta)} \\
& - \;\; \frac{\theta}{2e(\theta)r_s^2\lambda^2} \left[\left(\omega_\xi a(\theta/\omega_\xi^2) - \frac{c(\theta)}{e(\theta)} \right) - \frac{d(\theta)}{e(\theta)} \left(b(\theta) - \frac{c(\theta)d(\theta)}{e(\theta)} \right) \right] \\
& \times \;\; \log \left| \frac{2e(\theta)\lambda^2 r_s}{\theta} + \sqrt{2}d(\theta)\lambda r_s^{1/2}\theta^{-1/2} + 1 \right| \\
& - \;\; \frac{\sqrt{2}}{e(\theta)} \left(b(\theta) - \frac{c(\theta)d(\theta)}{e(\theta)} \right) \frac{\theta^{1/2}}{r_s^{1/2}\lambda} \\
& + \;\; \frac{\theta}{r_s^2\lambda^2 e(\theta)\sqrt{4e(\theta) - d^2(\theta)}} \left[d(\theta) \left(\omega_\xi a(\theta/\omega_\xi^2) - \frac{c(\theta)}{e(\theta)} \right) \right. \\
& + \;\; \left. \left(2 - \frac{d^2(\theta)}{e(\theta)} \right) \left(b(\theta) - \frac{c(\theta)d(\theta)}{e(\theta)} \right) \right] \\
& \times \;\; \left[\arctan \left(\frac{2^{3/2}e(\theta)\lambda r_s^{1/2}\theta^{-1/2} + d(\theta)}{\sqrt{4e(\theta) - d^2(\theta)}} \right) - \arctan \left(\frac{d(\theta)}{\sqrt{4e(\theta) - d^2(\theta)}} \right) \right] ,
\end{aligned}
\tag{149}
$$

where the relation $\Gamma\theta = 2\lambda^2 r_s$ with $\lambda = (4/(9\pi))^{1/3}$ may be used to recast this into a modified function $f_{xc}^{\xi}(\Gamma, \theta)$. We mention that although the IIT parametrization for the unpolarized case ($\xi = 0$) has been provided long ago [206], the polarized case ($\xi = 1$) became available only recently [249]. Furthermore, we again stress that the IIT functional exactly fulfills all three know limits: classical, ground state and Hartree-Fock.

It is important to note that there are two different definitions of the degeneracy parameter for polarizations other than the fully unpolarized case. First, regardless of the polarization ξ, one may always use $\bar{\theta} = 2k_B T m_e/\hbar^2 k_F^2$ with $k_F = (3\pi^2 n)^{1/3}$ where $n = n_\uparrow + n_\downarrow$ is the total density of the system. This way, the parameter $\bar{\theta}$ is independent of the spin-polarization at constant values of r_s, but its physical meaning is somewhat unclear. The second possibility, which we employ, is to define the Fermi vector as $k_F^\uparrow = (6\pi^2 n_\uparrow)$, corresponding to the particle species with the higher density, $n_\uparrow \geq n_\downarrow$, cf. Eq. (4). Naturally, in the unpolarized case, where $n_\uparrow = n_\downarrow = n/2$, both definitions are equal, whereas at arbitrary polarizations the relation $\bar{\theta} = \theta(1 + \xi)^{2/3} = \theta\omega_\xi^2$ holds. Since the authors of the IIT parametrizations chose the definition of $\bar{\theta}$ for the degeneracy parameter in the determination of the fitting constants[5], we must evaluate Eq. (149) at $\theta(1+\xi)^{2/3}$. For completeness, we mention that Sjostrom and Dufty [213] used the same Pade ansatz for the interaction energy, Eq. (147), to obtain a functional of f_{xc} both from the VS scheme (see Sec. 3) and the RPIMC data by Brown *et al.* [211].

8.2.2. PDW parametrization

Perrot and Dharma-wardana [210] came up with a different idea to parametrize $f_{xc}^0(r_s, \theta)$ that is more suitable for their classical mapping approach, see Sec. 4.2.1, which allows for the direct computation of the exchange-correlation free energy. These values have been directly fitted to the following parametrization

$$
\begin{aligned}
f_{xc}^0(r_s, \theta) &= \frac{e_{xc}(r_s, 0) - P_1(r_s, \theta)}{P_2(r_s, \theta)}, \\
P_1(r_s, \theta) &= (A_2(r_s)u_1(r_s) + A_3(r_s)u_2(r_s))\,\theta^2 Q^2(r_s) + A_2(r_s)u_2(r_s)\theta^{5/2}Q^{5/2}(r_s), \\
P_2(r_s, \theta) &= 1 + A_1(r_s)\theta^2 Q^2(r_s) + A_3(r_s)\theta^{5/2}Q^{5/2}(r_s) + A_2(r_s)\theta^3 Q^3(r_s), \\
Q(r_s) &= \left(2r_s^2\lambda^2\right)^{-1} , \quad n(r_s) = \frac{3}{4\pi r_s^3} , \quad u_1(r_s) = \frac{\pi n(r_s)}{2} , \quad u_2(r_s) = \frac{2\sqrt{\pi n(r_s)}}{3}, \\
A_k(r_s) &= \exp\left(\frac{y_k(r_s) + \beta_k(r_s)z_k(r_s)}{1 + \beta_k(r_s)}\right) , \quad \beta_k(r_s) = \exp\left(5(r_s - r_k)\right), \\
y_k(r_s) &= \nu_k \log(r_s) + \frac{a_{1,k} + b_{1,k}r_s + c_{1,k}r_s^2}{1 + r_s^2/5} , \quad z_k(r_s) = r_s\frac{a_{2,k} + b_{2,k}r_s}{1 + c_{2,k}r_s^2} ,
\end{aligned}
\tag{150}
$$

---

[5]Note that the authors of Ref. [248] also chose the definition of θ that is used here, which is the reason for the temperature scaling factor ω_ξ^{-2} in the Hartree-Fock parametrization a.

where the fitting constants are provided in Ref. [210]. This functional recovers the correct QMC ground state limit, $e_{\text{xc}}(r_s, 0)$, as $\theta \to 0$ and the Debye-Hückel limit as $\theta \to \infty$. However, the Hartree-Fock limit at $r_s \to 0$ has not been included even though it were the very same authors who presented the Hartree-Fock parametrization [248] 16 years earlier. For completeness, we mention that an ansatz of the form Eq. (150) has also been utilized by Brown *et al.* [214] to obtain the first parametrization from a fit to their RPIMC data [211], yet, the overall functional behavior of this parametrization has later been shown to be unsatisfactory [212].

8.2.3. HNC parametrization

In the recently proposed HNC functional [242], Tanaka exploited the same Pade ansatz for the r_s-dependency of the HNC interaction energy as the IIT parametrization, cf. Eq. (147):

$$v^\xi(r_s, \theta) = -\frac{1}{r_s} \frac{\bar{a}^\xi(\theta) + \bar{b}^\xi(\theta)\sqrt{r_s} + \bar{c}^\xi(\theta)r_s}{1 + \bar{d}^\xi(\theta)\sqrt{r_s} + \bar{e}^\xi(\theta)r_s} , \tag{151}$$

but slightly modified the θ-dependence by using the general form

$$g(\theta) = G(\theta)\frac{1 + x_2\theta^2 + x_3\theta^3 + x_4\theta^4}{1 + y_2\theta^2 + y_3\theta^3 + y_4\theta^4} , \tag{152}$$

for all functions $\bar{b}^\xi, \bar{c}^\xi, \bar{d}^\xi, \bar{e}^\xi$. The major difference is that also terms with θ^3 are included in the fit. The Hartree-Fock limit of the HNC parametrizations is incorporated in $\bar{a}^\xi(\theta)$. After fitting Eq. (151) to the interaction energy from the HNC scheme (values of the fitting constants can be found in Ref. [242]), the functional for the exchange-correlation free energy is again obtained by analytically carrying out the coupling constant integration, Eq. (145), which leads to a very similar expression as Eq. (149). While the thus constructed HNC functional properly fulfills the classical Debye-Hückel limit, it does of course not include the exact QMC ground state limit.

8.2.4. KSDT parametrization

The KSDT functional is based on the RPIMC data by Brown *et al.* [214]. These data have been obtained for the interaction, kinetic, and exchange-correlation energy covering the relevant warm dense matter regime of the UEG. Therefore, Karasiev *et al.* came up with a slightly different strategy to construct a parametrization by utilizing the IIT Pade anastz, Eq. (147), directly for the exchange-correlation free energy instead of the interaction energy, i.e.,

$$f_{\text{xc}}^\xi(r_s, \theta) = -\frac{1}{r_s} \frac{\omega_\xi a(\theta) + b^\xi(\theta)\sqrt{r_s} + c^\xi(\theta)r_s}{1 + d^\xi(\theta)\sqrt{r_s} + e^\xi(\theta)r_s} , \tag{153}$$

with the temperature Pade functions $b - e$ of Eq. (149) and the Hartree-Fock parametrization, a, Eq. (148). First, they fitted the ground state limit of Eq. (153)

$$\lim_{\theta \to 0} f_{\text{xc}}^\xi(r_s, \theta) = e_{\text{xc}}^\xi(r_s, 0) = -\frac{1}{r_s} \frac{\omega_\xi a_1 + b_1^\xi\sqrt{r_s} + c_1^\xi e_1^\xi r_s}{1 + d_1^\xi\sqrt{r_s} + e_1^\xi r_s} , \tag{154}$$

to the most recent QMC data by Spink *et al.* [38], separately for $\xi = 0$ and $\xi = 1$, which determines the four ground state coefficients $b_1^\xi, c_1^\xi, d_1^\xi, e_1^\xi$. The exchange-correlation free energy, f_{xc}^ξ, is linked to the interaction (v^ξ), kinetic, (k^ξ), and exchange-correlation energy e_{xc}^ξ via the standard thermodynamic relations

$$v^\xi(r_s, \theta) = 2f_{\text{xc}}^\xi(r_s, \theta) + r_s \left.\frac{\partial f_{\text{xc}}^\xi(r_s, \theta)}{\partial r_s}\right|_\theta \tag{155}$$

$$e_{\text{xc}}^\xi(r_s, \theta) = f_{\text{xc}}^\xi(r_s, \theta) - \theta \left.\frac{\partial f_{\text{xc}}^\xi(r_s, \theta)}{\partial \theta}\right|_{r_s} \tag{156}$$

$$k^\xi(r_s, \theta) = k_s^\xi(r_s, \theta) - \theta \left.\frac{\partial f_{\text{xc}}^\xi(r_s, \theta)}{\partial \theta}\right|_{r_s} - f_{\text{xc}}^\xi(r_s, \theta) - r_s \left.\frac{\partial f_{\text{xc}}^\xi(r_s, \theta)}{\partial r_s}\right|_\theta , \tag{157}$$

with $k_s^\xi(r_s, \theta)$ being the ideal kinetic energy. Therefore, the RPIMC data sets for each of these quantities can be used for a fit of the right hand sides to these data, thereby determining the remaining coefficients in Eq. (153) that contain the temperature dependency. By carrying out all three of these fits both for $\xi = 0$ and $\xi = 1$, the authors of Ref. [212] found that using RPIMC data for e_{xc}^ξ results in the smallest average and maximum deviation of the fit function to the data. Moreover, they performed the consistency checks of re-computing the two thermodynamic

quantities from f_{xc}^{ξ} that have not been used for the fit, and then compared the result to the corresponding RPIMC data. Again, the deviations were smallest when using e_{xc}^{ξ} as input for the fit. In addition to the exact Hartree-Fock and ground state limit, the KSDT functional also fulfills the Debey-Hückel limit as $\theta \to \infty$ by simply fixing b_5 to $(3/2)^{1/2}\lambda^{-1}b_3$ for $\xi = 0$ and to $(3/2)^{1/2}2^{1/3}\lambda^{-1}b_3$ with $\lambda = (4/(9\pi))^{1/3}$ for $\xi = 1$. Finally, we mention that one of the temperature Pade functions, $c^{\xi}(\theta)$ [cf. Eq. (149)], had to be modified in the KSDT functional to reproduce the RPIMC data sufficiently well. Naturally, this has been accomplished by adding an additional parameter c_3 in the exponent, i.e.,

$$c^{\xi}(\theta) = \left[c_1^{\xi} + c_2^{\xi} \cdot \exp\left(-c_3\theta^{-1}\right) \right] e^{\xi}(\theta) . \tag{158}$$

The concrete values of all fitting constants of the KSDT functional are to be found in Ref. [212].

8.2.5. GDB Parametrization

In the construction of the GDB parametrization [227], we followed the same strategy as the previously discussed KSDT functional (Sec. 8.2.4), but instead used our new finite size corrected QMC data for the interaction energy (see Sec. 6), which, due to the fermion sign problem, are available down to $\theta = 0.5$. To close the remaining gap to the ground state, we computed a small temperature correction

$$\Delta_{\theta}^{STLS}(r_s, \theta, \xi) = v^{STLS}(r_s, \theta, \xi) - v^{STLS}(r_s, 0, \xi), \tag{159}$$

from the STLS method, (see Sec. 3), and added this onto the most accurate ground state QMC data by Spink *et al.* [38] for temperatures $\theta \leq 0.25$. Thereby, we obtained a highly accurate data set for the interaction energy over the entire relevant warm dense matter regime, which we fitted to the right hand side of Eq. (155) with the Pade ansatz, Eq. (153) for the exchange-correlation free energy. However, we found that the additional parameter c_3 in Eq. (158) is not necessary for a smooth fit through our data set. The values of the fitting constants in Eq. (153) can be found in Ref. [227].

8.3. Spin-interpolation

8.3.1. Spin-interpolation of the KSDT and GDB functional

To obtain an accurate parametrization of f_{xc} at arbitrary spin polarization $0 \leq \xi \leq 1$, the KSDT and GDB functional employ the ansatz [210]

$$f_{xc}(r_s, \theta, \xi) = f_{xc}^0(r_s, \bar{\theta}) + \left[f_{xc}^1(r_s, \bar{\theta} \cdot 2^{-2/3}) - f_{xc}^0(r_s, \bar{\theta}) \right] \Phi(r_s, \bar{\theta}, \xi) , \tag{160}$$

with $\bar{\theta} = \theta(1 + \xi)^{2/3}$ ensuring that the right hand side is evaluated at the same temperature T for the given density parameter r_s. Knowing that the exact ground state spin-interpolation function in the ideal limit, $r_s \to 0$, is given by

$$\Phi(r_s = 0, \theta = 0, \xi) = \frac{(1 + \xi)^{4/3} + (1 - \xi)^{4/3} - 2}{2^{4/3} - 2}, \tag{161}$$

Perrot and Dharama-wardana [210] proposed to extend this to the correlated system at finite temperature with the ansatz:

$$\Phi(r_s, \theta, \xi) = \frac{(1 + \xi)^{\alpha(r_s,\theta)} + (1 - \xi)^{\alpha(r_s,\theta)} - 2}{2^{\alpha(r_s,\theta)} - 2}, \tag{162}$$

$$\alpha(r_s, \theta) = 2 - h(r_s)e^{-\theta\lambda(r_s,\theta)},$$

$$h(r_s) = \frac{2/3 + h_1 r_s}{1 + h_2 r_s},$$

$$\lambda(r_s, \theta) = \lambda_1 + \lambda_2 \theta r_s^{1/2} ,$$

which fulfills the ground state limit of the ideal system, Eq. (161). Both in the GDB and KSDT functional the parameters h_1 and h_2 are obtained by fitting $f_{xc}(r_s, 0, \xi)$ to the ground state data of Ref. [38] for $\xi = 0.34$ and $\xi = 0.66$. Then, in the case of the KSDT functional, the remaining two parameters λ_1 and λ_2, which carry the temperature dependent information of the interpolation function, had to be determined by a subsequent fit to the approximate hypernetted chain data [210] of f_{xc} at intermediate spin-polarization ξ since Brown *et al.* did not provide these data. Whereas in case of the GDB functional [227], we performed vast additional QMC simulations to obtain *ab initio* data for the interaction energy $v^{\xi}(r_s, \theta)$ at $\xi = 1/3$ and $\xi = 0.66$, which we utilized to determine the parameters λ_1 and λ_2 via Eq. (155). Interestingly, we find that the spin interpolation depends only very weakly on θ, and in contrast to KSDT, λ_2 in fact vanishes within the accuracy of the fit and, thus, we set $\lambda_2 = 0$.

8.3.2. Spin-interpolation of the IIT and HNC functional

In 1989, Tanaka and Ichimaru [205] introduced a different spin-interpolation for the warm dense electron gas on the basis of the modified convolution approximation (MCA) (see Sec. 3). Specifically, their ansatz for the interaction energy is given by

$$v(r_s, \theta, \xi) = (1 - \xi^6)v^0(r_s, \theta) + \xi^6 v^1(r_s, \theta) + \left(\frac{1}{2}\xi^2 + \frac{5}{108}\xi^4 - \frac{59}{108}\xi^6\right) \frac{s(r_s, \theta)}{r_s} \quad , \tag{163}$$

with the definition

$$s(r_s, \theta) = -\frac{a_s(\theta) + b_s(\theta)r_s}{1 + c_s(\theta)r_s + d_s(\theta)r_s^2} \quad . \tag{164}$$

Note that the temperature-dependent coefficients $a_s(\theta), b_s(\theta), c_s(\theta), d_s(\theta)$ are of the same form as Eq. (152), see Ref. [205] for the appropriate fitting constants. This, in turn, leads to the spin-interpolation for the exchange-correlation free energy

$$f_{\mathrm{xc}}(r_s, \theta, \xi) = (1 - \xi^6)f_{\mathrm{xc}}^0(r_s, \theta) + \xi^6 f_{\mathrm{xc}}^1(r_s, \theta) + \left(\frac{1}{2}\xi^2 + \frac{5}{108}\xi^4 - \frac{59}{108}\xi^6\right) \Sigma(r_s, \theta) \quad , \tag{165}$$

and plugging Eq. (163) into (145) immediately gives

$$\Sigma(r_s, \theta) = \frac{1}{r_s^2} \int_0^{r_s} \mathrm{d}\overline{r}_s \ s(\overline{r}_s, \theta) \quad , \tag{166}$$

which (up to moderate temperature, see the discussion of Fig. 39 below) can be evaluated analytically as

$$\Sigma(r_s, \theta) = \begin{cases} \Sigma_<(r_s, \theta), & \text{if } c_s^2 < 4d_s \\ \Sigma_=(r_s, \theta), & \text{if } c_s^2 = 4d_s \\ \Sigma_>(r_s, \theta), & \text{otherwise} \end{cases} \quad , \tag{167}$$

with

$$\Sigma_<(r_s, \theta) = -\frac{1}{r_s^2}\left[\frac{b_s}{2d_s}\log\left|1 + c_s r_s + d_s r_s^2\right|\right. \tag{168}$$

$$\left.+\frac{2a_s d_s - b_s c_s}{d_s\sqrt{4d_s - c_s^2}}\left[\mathrm{atan}\left(\frac{2d_s r_s + c_s}{\sqrt{4d_s - c_s^2}}\right) - \mathrm{atan}\left(\frac{c_s}{\sqrt{4d_s - c_s^2}}\right)\right]\right] \quad ,$$

$$\Sigma_=(r_s, \theta) = -\frac{1}{r_s^2}\left[\frac{b_s}{2d_s}\log\left|1 + c_s r_s + d_s r_s^2\right| - \frac{2a_s d_s - b_s c_s}{d_s(2d_s r_s + c_s)}\right] \quad , \tag{169}$$

$$\Sigma_>(r_s, \theta) = -\frac{1}{r_s^2}\left[\frac{b_s}{2d_s}\log\left|1 + c_s r_s + d_s r_s^2\right|\right. \tag{170}$$

$$\left.+\frac{2a_s d_s - b_s c_s}{2d_s\sqrt{c_s^2 - 4d_s}}\left(\log\left|\frac{2d_s r_s + c_s - \sqrt{c_s^2 - 4d_s}}{2d_s r_s + c_s + \sqrt{c_s^2 - 4d_s}}\right| - \log\left|\frac{c_s - \sqrt{c_s^2 - 4d_s}}{c_s + \sqrt{c_s^2 - 4d_s}}\right|\right)\right] \quad .$$

As the spin-dependence of MCA is expected to be similar both to STLS and also the recent HNC-based LFC by Tanaka, Eqs. (163) and (165) are used for both of these parametrization with the same fitting constants as in the original reference [205].

8.4. Comparison of parametrizations

8.4.1. Interaction energy

In Fig. 32, we compare various results for the temperature-dependence of the interaction energy per particle of the unpolarized electron gas for different densities. The red crosses correspond to the finite-size corrected (using our new, improved finite-size correction, see Sec. 6) thermodynamic QMC results by Groth, Dornheim and co-workers [226, 227] and the red diamonds to the ground state QMC data [38] with an STLS temperature correction obtained from Eq. (159). Observe the smooth connection between the two data sets over the entire density-range. Thus, in combination, these constitute the most accurate existing data for the interaction energy over the entire warm dense matter regime and have subsequently been used as input for our recent parametrization, i.e., the red

Figure 32: Temperature dependence of the interaction energy of the unpolarized electron gas for $r_s = 0.1, 1, 4, 10$ – Shown are the recent QMC results from Refs. [226, 227] (red crosses), STLS temperature-corrected ground state QMC data (see Eq. (159), red diamonds), the parametrization by Groth, Dornheim and co-workers (GDB, red line) [227], RPIMC data (blue circles, BCDC, Ref. [211]) and the corresponding parametrization by Karasiev and co-workers (blue line, KSDT, Ref. [212]), data from an improved local field correction based on the hypernetted-chain approximation (green squares, HNC, Ref. [242]) and a corresponding parametrization (green line), the improved STLS parametriprzation by Ichimaru and co-workers (black line, IIT, Ref. [206, 249]), and the parametrization by Perrot and Dharma-wardana (yellow line, PDW, Ref. [210]). The bottom panels depict the relative deviation towards the GDB curve and the insets correspond to magnified segments.

65

line (GDB, Ref. [227]). Evidently, the employed Pade ansatz is an appropriate fit function, as the input data are accurately reproduced with a mean and maximum deviation of 0.12% and 0.63%, see also the corresponding bottom panels where we show the relative deviations of all data sets to the GDB curve.

Although the parametrization of the interaction energy is, for the most part, just a means to obtain the exchange-correlation free energy f_{xc}, cf. Eq. (155), it is still worth to consider, at this point, v itself to gauge the accuracy of various previous approximations and XC-functionals. The blue circles correspond to the RPIMC data from Ref. [211] (BCDC) and the blue line to the corresponding parametrization by Karasiev *et al.* [212] (KSDT). First and foremost, we note that the BCDC data are available for low to moderate densities, $r_s \geq 1$, and exhibit the largest deviations for the smallest r_s-value. This is a combination of two different effects. At low temperature, the observed systematic bias is mostly a consequence of the employed fixed node approximation (and, possibly, related to ergodicity problems in the QMC algorithm, see Sec. 5.3), whereas at high temperature the effects of the inappropriate finite-size correction dominate (cf. Sec. 6), leading to a maximum error of $\Delta v/v \approx 7\%$ for the unpolarized case. In contrast, the BCDC data are substantially more accurate at stronger coupling, with maximum deviations of 2% and 1% for $r_s = 4$ and $r_s = 10$, respectively.

The KSDT parametrization has been obtained from a fit to the BCDC data for E_{xc}, i.e., the sum of v and the exchange-correlation part of the kinetic energy k_{xc}. However, the results for the interaction energy computed from f_{xc} [cf. Eq. (155)] do not agree with the blue circles, which means that the parametrization and input data are not consistent as the exact thermodynamic relations, Eqs. (155)-(157), are strongly violated. In particular, there appear pronounced deviations between the two at low temperature as the KSDT functional incorporates the correct ground state limit. The largest deviations ($\Delta V/V \approx 11\%$) between the KSDT and GDB curves appear at high density, $r_s = 0.1$. This is a consequence of the lack of input data for the former in this regime, which is bridged by an interpolation between the RPIMC data at $r_s \geq 1$ and the correct Hartree Fock limit at $r_s = 0$. Furthermore, we stress the surprisingly large errors at high temperature both for $r_s = 4$ and $r_s = 10$, and the unphysical bump at low temperature in the latter case.

The black line depicts the widely used improved STLS parametrization that is due to Ichimaru and co-workers (IIT, Ref. [206, 249]). Given the incorporation of the exact behavior for $r_s \to 0$, $\theta \to \infty$ and $\theta \to 0$, and the remarkable accuracy of the STLS formalism inbetween (cf. Sec.6), the overall good performance of this functional does not come as a surprise. In particular, the most severe systematic errors occur for intermediate density ($r_s = 1$) and temperature, but do not exceed $\Delta v/v \approx 4\%$.

Next, let us consider the green curve corresponding to a fit to the recent data based on the improved local field correction derived from the hypernetted-chain approximation (HNC, green squares) by Tanaka [242]. While this new LFC does constitute an improvement, both, for the static structure factor (see Sec. 7.2) and $G(q)$ itself (Sec. 9), the same does not apply for the interaction energy, as for this quantity STLS benefits from a fortunate error cancellation in the integration, in particular at large r_s, cf. Fig. 31. Furthermore, the HNC parametrization exhibits a pronounced minimum around $\theta = 0.5$, the origin of which is probably an artifact of the lack of HNC input data for these parameters, see the insets for $r_s = 4$ and $r_s = 10$. In addition, the ground state limit is obtained from the zero temperature HNC data and not from the more accurate QMC results, which leads to relative errors of around 1% towards $\theta = 0$. Hence, we conclude that the green curve does not improve the twenty years older IIT parametrization, although it exhibits an overall similar accuracy.

Finally, we include the interaction energy computed from the parametrization of classical-mapping data (cf. Sec. 4.2.1) by Perrot and Dharma-wardana (yellow line, PDW, Ref. [210]). This curve was constructed from input data in the range $1 \leq r_s \leq 10$, and, somewhat ironically, the Hartree-Fock limit that was parametrized by the same authors in 1984 [248], was not incorporated. For this reason, the functional exhibits large deviations at high density and should not be used below $r_s = 1$. While PDW did include the correct ground state limit, the lowest finite temperature values correspond to $\theta = 0.25$, which explains the unphysical behavior of the yellow curve at low temperature for $r_s = 1$. Overall, we find that the PDW parametrization exhibits the largest systematic errors (with $\Delta v/v \gtrsim 6\%$) at intermediate temperatures around $\theta = 1$, which is not surprsing given the employed interpolation of the quantum temperature parameter in the classical mapping formalism, cf. Eq. (53).

In Fig. 33, we show the same comparison but for the spin-polarized case, $\xi = 1$. While we do find similar trends as in the previous figure, the relative biases of the different approximations are, overall, increased. In particular, the KSDT curve exhibits a maximum deviation exceeding 15% at high density, and even at $r_s = 1$ we find $\Delta v/v \approx 8\%$ around $\theta = 5$. Furthermore, this parametrization exhibits an unphysical plateau-like behavior in the low-temperature regime both at $r_s = 4$ and $r_s = 10$. In addition, the BCDC data are substantially more biased both at low and high temperature, with a maximum deviation of $\Delta v/v \approx 14\%$ at $r_s = 1$ and $\theta = 8$. The increased deviation for the latter case is a consequence of the definition of the reduced temperature, resulting in a larger temperature at equal θ-values for the spin-polarized case. This, in turn, exacerbates the inaccuracy of the employed
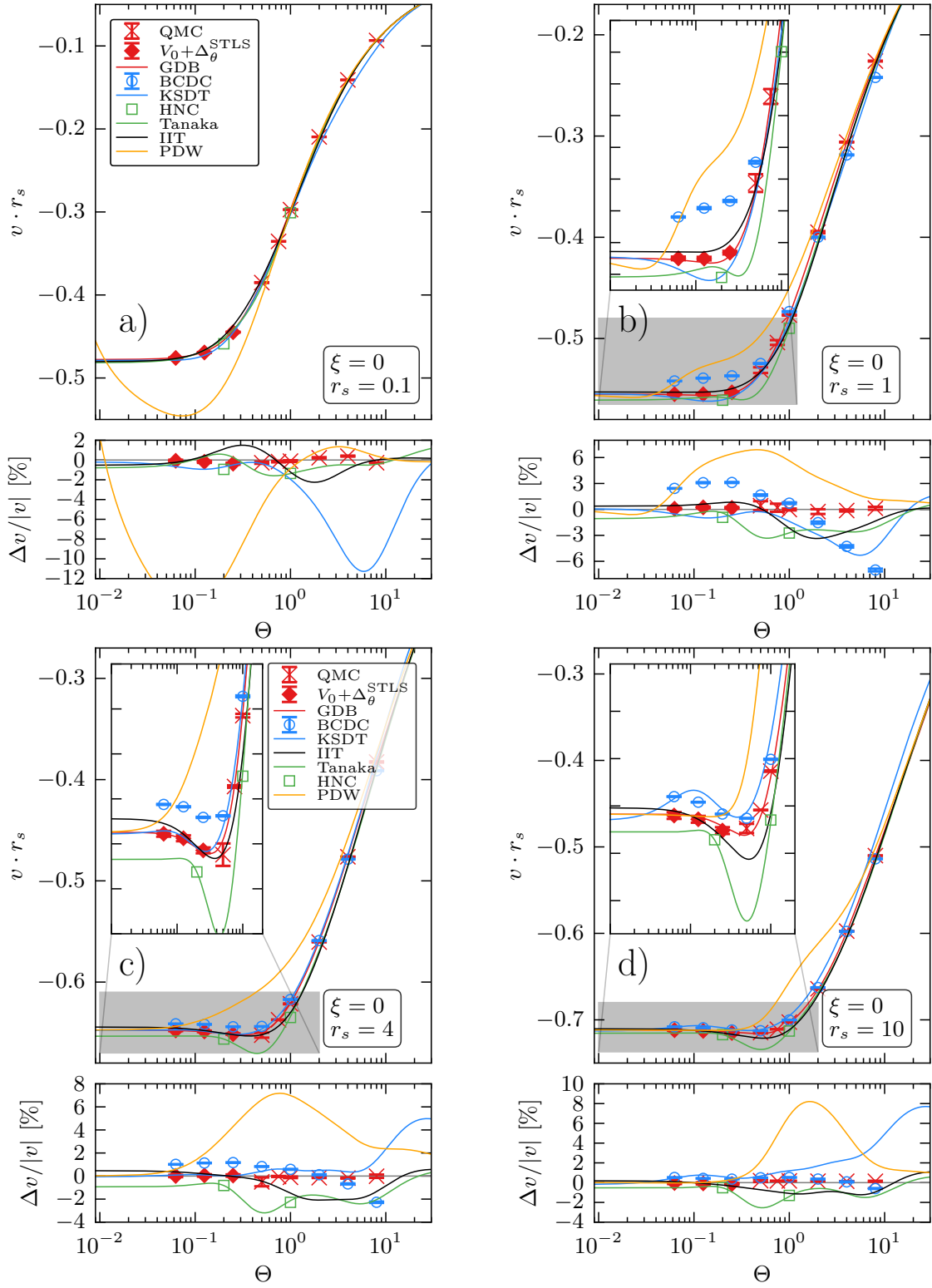
Figure 33: Temperature dependence of the interaction energy of the spin-polarized electron gas for $r_s = 0.1, 1, 4, 10$ – Shown are the recent QMC results from Refs. [226, 227] (red crosses), STLS temperature-corrected ground state QMC data (see Eq. (159), red diamonds), the parametrization by Groth, Dornheim and co-workers (GDB, red line) [227], RPIMC data (blue circles, BCDC, Ref. [211]) and the corresponding parametrization by Karasiev and co-workers (blue line, KSDT, Ref. [212]), data from an improved local field correction based on the hypernetted-chain approximation (green squares, HNC, Ref. [242]) and a corresponding parametrization (green line), and the improved STLS parametriprzation by Ichimaru and co-workers (black line, IIT, Ref. [206, 249]). The bottom panels depict the relative deviation towards the GDB curve and the insets correspond to magnified segments.

finite-size correction, cf. Sec. 6. At low temperature, the fixed node approximation exhibits a worse performance even for a finite model system [221]. The HNC and IIT parametrizations are of a similar quality, but the latter appears to be superior due to the incorporation of the correct ground state limit. The main difference compared to the unpolarized case is the significantly larger deviation for large temperature at $r_s = 10$. Interestingly, this is not a consequence of a worse performance of the STLS approximation itself, cf. Fig. 30 but, instead, of the *a posteriori* modification of the STLS data to incorporate the exact high and low temperatuere limit. Finally, we mention the excellent agreement between the GDB parametrization and its input data with a mean and maximum deviation of 0.17% and 0.63%, respectively.

8.4.2. Exchange-correlation free energy

Let us now consider the main quantity of interest, i.e., the exchange-correlation free energy f_{xc}. In Fig. 34, we compare the temperature dependence of the five most accurate functionals for the unpolarized case and at the same densities as in the previous section. All curves exhibit a qualitatively similar behavior except PDW at $r_s = 0.1$, which is again a consequence of the not incorporated Hartree-Fock limit and the density range of the input data ($1 \leq r_s \leq 10$). Overall, the KSDT parametrization is relatively accurate at low temperature ($\theta < 1$) although there appears a bump in both v and f_{xc} at large r_s, which leads to an unphysical slightly negative entropy [336]. In contrast, at intermediate to high temperature we find substantial systematic deviations (exceeding 10% at $r_s = 0.1$), which are a direct consequence of the utilized RPIMC input data. Again, the IIT and HNC curves exhibit a very similar performance, with the former being superior due to the correct ground state limit. More specifically, for the unpolarized case we find maximum deviations of around 3% at intermediate r_s-values and temperatures. Finally, the classical-mapping based PDW parametrization by Perrot and Dharma-wardana [210] exhibits deviations of up to $\Delta f_{xc}/f_{xc} \approx 5\%$ around the Fermi temperature.

For completeness, in Fig. 35 we show the same information for the spin-polarized electron gas. Again, we find an overall qualitatively similar behavior as for $\xi = 0$, but with increased systematic biases in the various approximations. The KSDT fit exhibits maximum deviations of up to 15% and 12% at the highest depicted densities, $r_s = 0.1$ and $r_s = 1$, respectively, around $\theta = 6$. With increasing coupling strength, these errors decrease with a maximum of $\Delta f_{xc}/f_{xc} \approx 2\%$ at $r_s = 10$ around $\theta = 0.4$. Moreover, there again appears an unphysical bump in the low temperature limit at low density. The IIT and HNC parametrizations roughly follow the same behavior as the interaction energy for the ferromagnetic case, cf. Fig. 33. Interestingly, the maximum deviation of the IIT curve does not appear at intermediate temperature, as for the paramagnetic case, but towards $\theta > 10$ at $r_s = 10$. Further, we note that the green curve also exhibits some unphysical behavior towards low θ and large r_s, which is similar to the KSDT function. Finally, let us consider the four PDW data points that are available at $r_s = 1$. Somewhat surprisingly, at the present conditions the employed classical mapping constitutes the most accurate of all depicted approximations with a maximum error of $\Delta f_{xc}/f_{xc} \approx 3\%$ around the Fermi temperature.

8.4.3. Exchange-correlation energy

Let us now consider another important thermodynamic quantity, i.e., the exchange-correlation energy e_{xc}, which is connected to f_{xc} via Eq. (156). Recall that the KSDT functional is actually based on the RPIMC data for e_{xc}, whereas our GDB parametrization was based on our QMC (and temperature corrected ground state QMC) data for the interaction energy alone. The main reason for our choice was the, in general, higher statistical uncertainty and greater difficulty of the finite-size correction for the kinetic contribution to the total energy. Nevertheless, for the ferromagnetic case we were able to obtain accurate QMC data for e_{xc} (using CPIMC for $\theta \leq 0.5$ and PB-PIMC elsewhere) over the entire temperature-range at $r_s = 1$. For completeness, we mention that we applied a twist-averaging procedure [328, 330] for $\theta \leq 0.5$ and added an additional finite-size correction onto the QMC data, see Ref. [227] for details. The results are depicted as the red points in Fig. 36 and are compared to the exchange-correlation energy that has been computed from the GDB parametrization via Eq. (156) (solid red line). Evidently, those independent data are in striking agreement over the entire temperature-range. This is an important cross-check for our functional and, in particular, for the temperature-corrected ground state data used for $\theta \leq 0.25$, see also the inset showing a magnified segments around the low-temperature regime. The blue circles correspond to the RPIMC data by Brown *et al.* [211] and are consistently too low over the entire depicted temperature range. The KSDT parametrization (blue solid line), which corresponds to a direct fit to these data, reproduces them for $\theta \geq 1$, leading to an unphysical dent for $4 \lesssim \theta \lesssim 20$ until the correct Debye-Hückel limit is attained. At low temperature, the KSDT curve does not reproduce the RPIMC input data, but performs significantly better, which is due to the incorporation of the exact ground state and high-density limits, which preclude this unphysically deep minimum at $r_s = 1$.

Next, we investigate the performance and consistency of the various parametrizations with respect to e_{xc} at $r_s = 10$, starting with the unpolarized case (Fig. 37, left panel). For these conditions, we were able to obtain
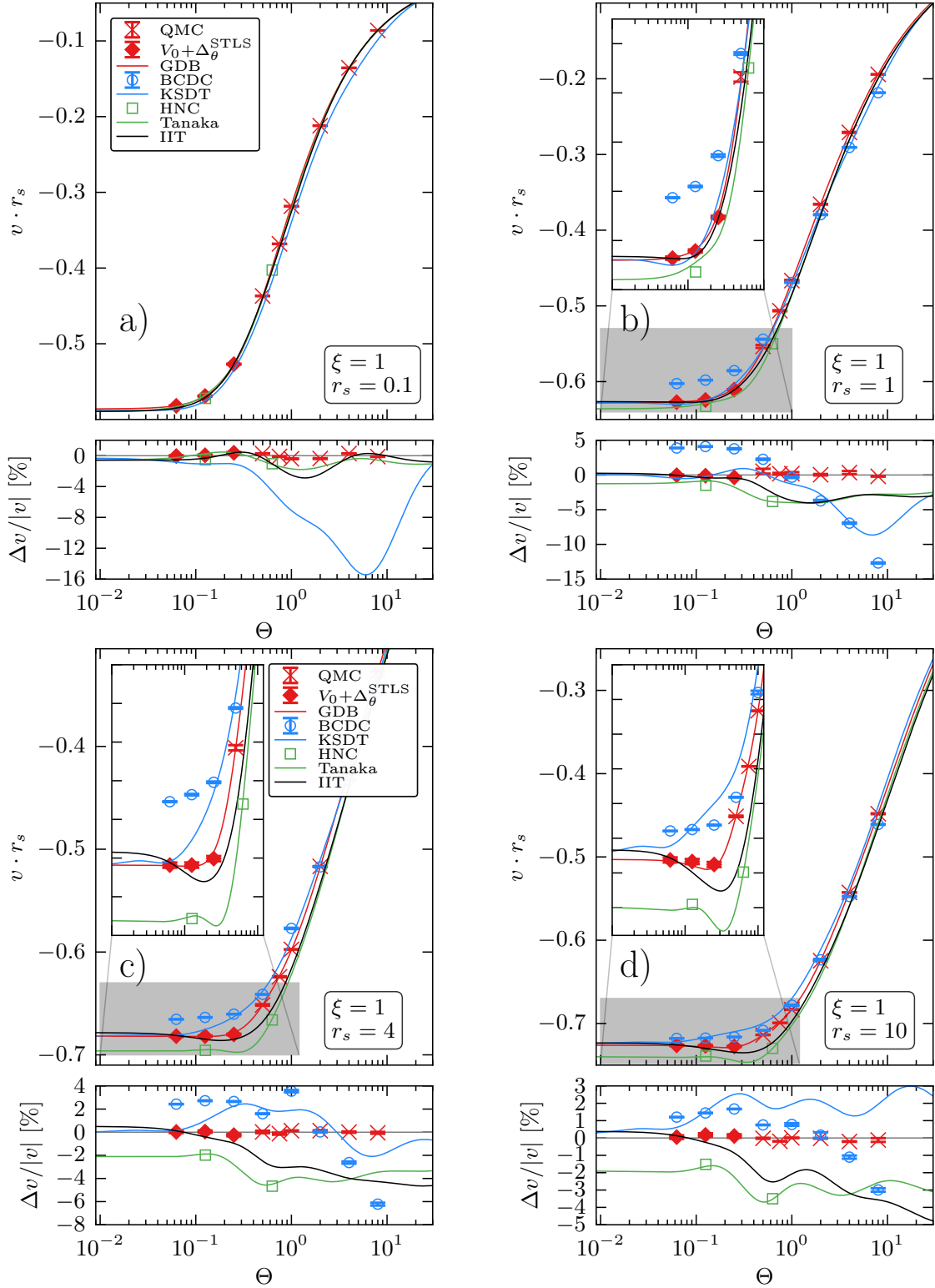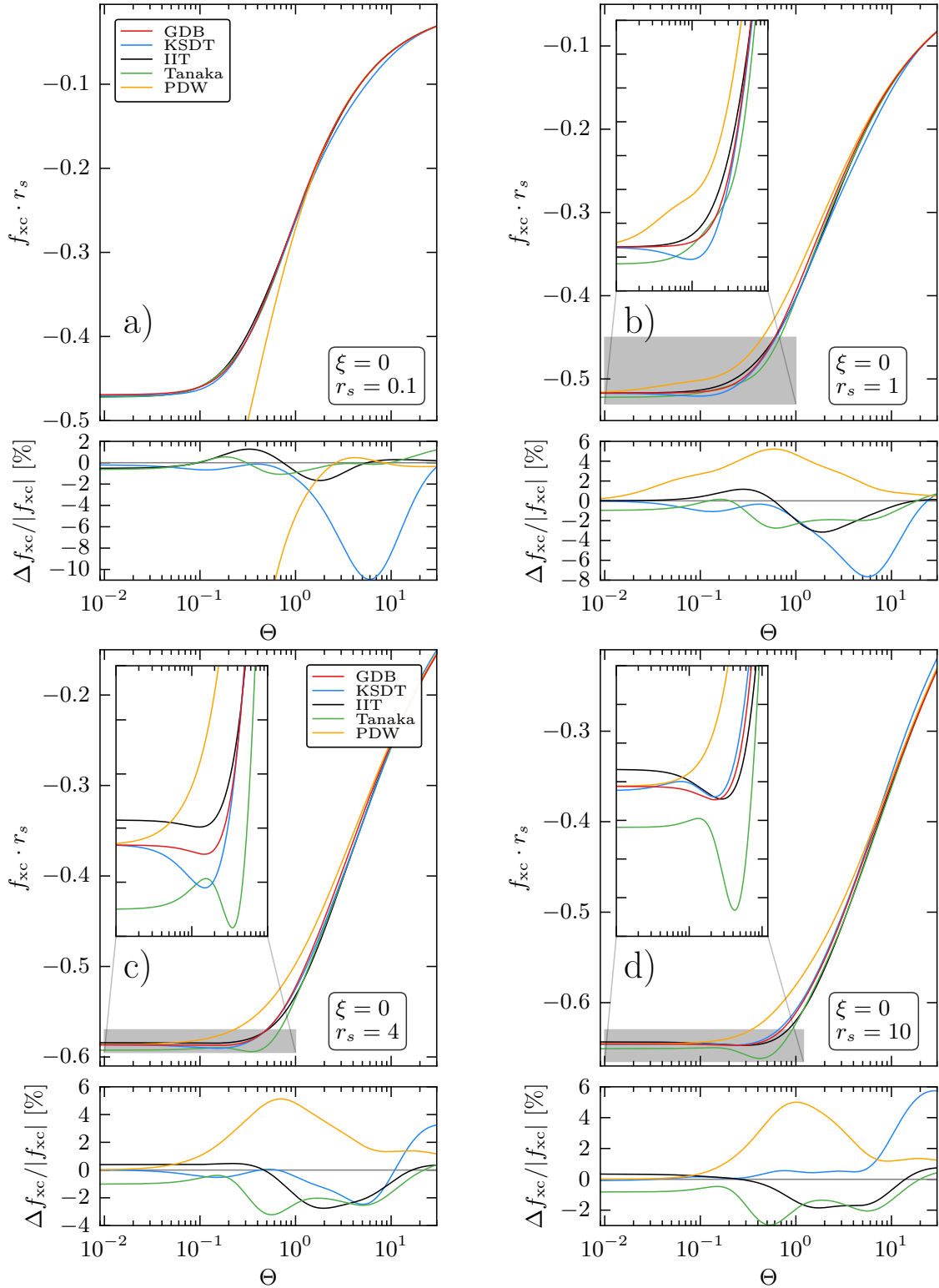
Figure 34: Temperature dependence of the exchange-correlation free energy of the unpolarized electron gas for $r_s = 0.1, 1, 4, 10$ – Shown are the parametrizations by Groth, Dornheim *et al.* (red line, GDB, Ref. [227]), Karasiev *et al.* (blue line, KSDT, Ref. [212]), Tanaka (green line, HNC, Ref. [242]), Ichimaru *et al.* (black line, IIT, Ref. [206, 249]) and Perrot and Dharma-wardana (yellow line, PDW, Ref. [210]). The bottom panels depict the relative deviation towards the GDB curve and the insets correspond to magnified segments.
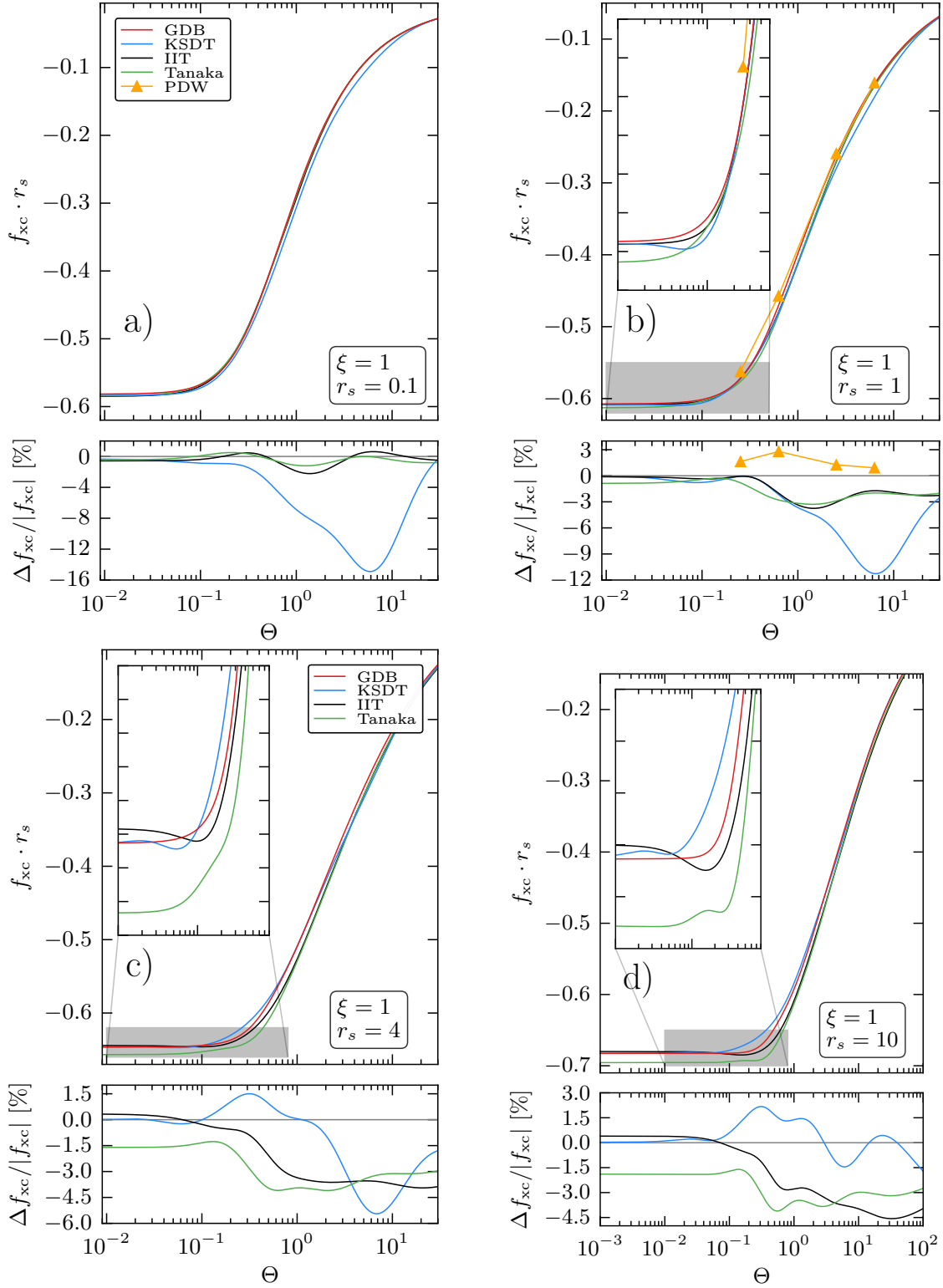
Figure 35: Temperature dependence of the exchange-correlation free energy of the spin-polarized electron gas for $r_s = 0.1, 1, 4, 10$ – Shown are the parametrizations by Groth, Dornheim *et al.* (red line, GDB, Ref. [227]), Karasiev *et al.* (blue line, KSDT, Ref. [212]), Tanaka (green line, HNC, Ref. [242]), and Ichimaru *et al.* (black line, IIT, Ref. [206, 249]) and, for $r_s = 1$, data points by Perrot and Dharma-wardana (yellow triangles, PDW, Ref. [210]). The bottom panels depict the relative deviation towards the GDB curve and the insets correspond to magnified segments.
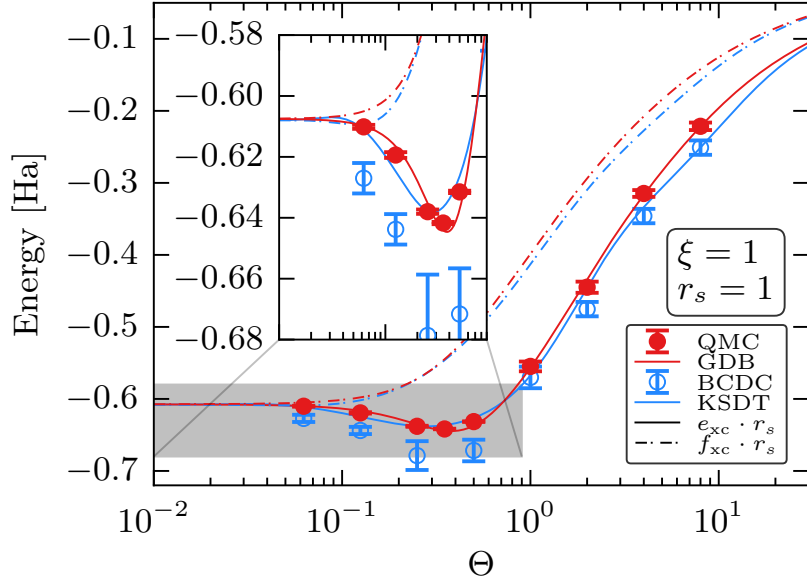
Figure 36: Cross-check of the GDB-parametrization via the exchange-correlation energy – Shown are the temperature dependence of e_{xc} (solid lines and points) and f_{xc} (dash-dotted lines) for the spin-polarized electron gas at $r_s = 1$. The red and blue lines correspond to the parametrizations by Groth, Dornheim *et al.* [227] and Karasiev *et al.* [212] and the red and blue points to our finite-size corrected QMC data (red) and the RPIMC data by Brown *et al.* [211]. Reproduced from Ref. [227] with the permission of the authors.
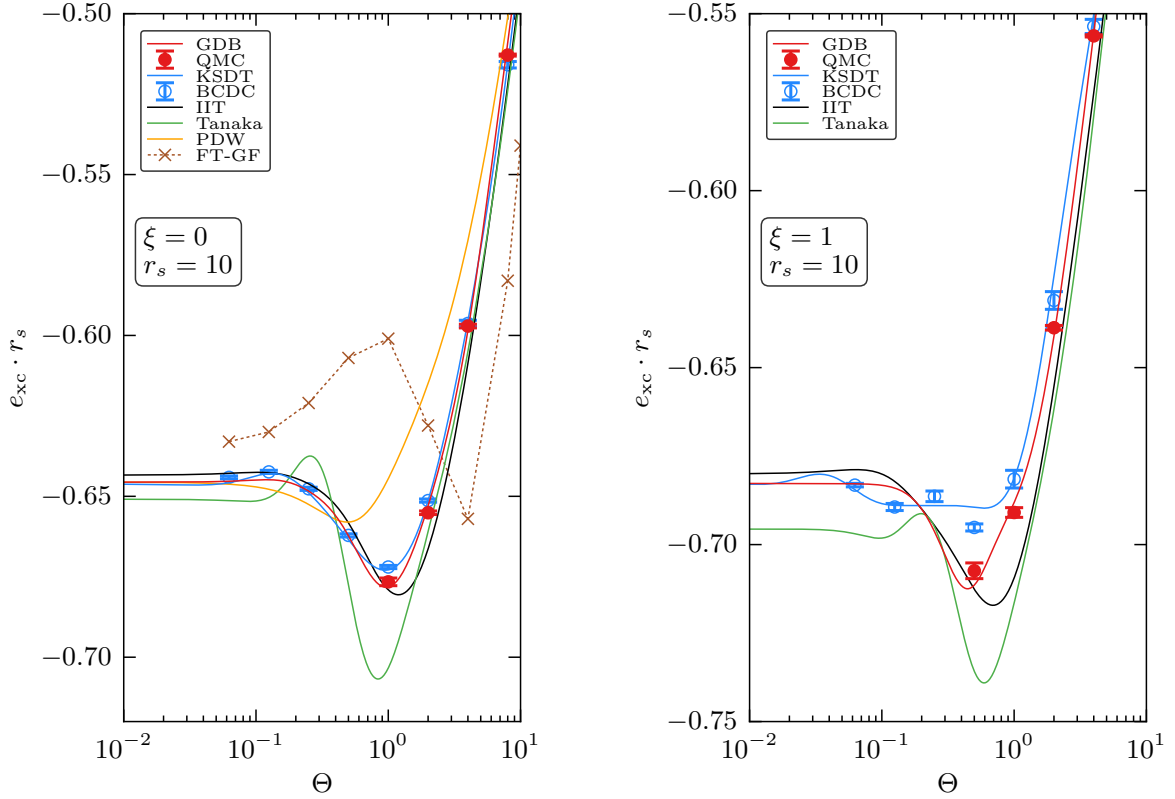
Figure 37: Temperature dependence of the exchange-correlation energy of the unpolarized (left) and spin-polarized (right) electron gas at $r_s = 10$ – Shown are results computed from the parametrizations by Groth, Dornheim *et al.* (red line, GDB, Ref. [227]), Karasiev *et al.* (blue line, KSDT, Ref. [212]), Tanaka (green line, HNC, Ref. [242]), Ichimaru *et al.* (black line, IIT, Ref. [206, 249]), and Perrot and Dharma-wardana (yellow line, PDW, Ref. [210]). In addition, we include the RPIMC data by Brown *et al.* [211] (BCDC, blue circles) and our recent finite-size corrected QMC results (red points, QMC). For completeness, we also compare with the very recent results of Kas and Rehr [197], which have been obtained from a refined finite temperature Green's function approach.

71

independent finite-size corrected QMC data down to $\theta = 0.5$ that has not been included in the construction of the functional. Again, the exchange-correlation energy computed from our GDB-parametrization via Eq. (156) is in perfect agreement with our QMC data for all temperatures. The RPIMC data (blue circles) and the KSDT fit to these data (blue line) are also in good agreement even at low temperature, which is in contrast to $r_s = 1$. Overall, there occur only small deviations to our data, although there does appear a small bump towards low temperature, which is connected to an unphysical negative entropy [336]. The improved STLS parametrization by Ichimaru *et al.* [206, 249] (black line) is of a similar quality to the KSDT curve and gives systematically too low results for $\theta \gtrsim 1$. In constrast, the green line, which corresponds to the recent parametrization of the HNC-LFC data by Tanaka [242], exhibits a substantially different behavior. While it is quite accurate for $\theta \gtrsim 2$, it shows a significantly too deep minimum around $\theta = 0.8$ followed by a pronounced unphysical bump at $\theta = 0.25$. The classical-mapping based parametrization by Perrot and Dharma-wardana [210] (yellow curve) clearly gives the least accurate data for $\theta \geq 1$.

In addition, for the exchange-corrlation energy, we can also compare with the very recent results by Kas and Rehr [197] (brown crosses), which have been computed via a refined finite temperature Green's function procedure (FT-GF). For the exchange-correlation energy of the unpolarized UEG, we can also perform the comparison for this quantity and thereby gauge the accuracy of this new approach. Surprisingly, at these parameters, the corresponding data exhibit a completely unphysical behavior with an additional local maximum in e_{xc} at $\theta \sim 1$, where both our *ab initio* functional and independent QMC data (red points) predict a minimum. Even at higher temperatures, the systematic bias of the FT-GF results is largest compared to all other depicted approaches.

Let us conclude this section with a brief discussion of the spin-polarized case, which is shown in the right panel of Fig. 37. Again, we observe perfect agreement between our QMC data and the GDB-parametrization for all temperatures. While the KSDT curve is also in good agreement with the underlying RPIMC data, there appear significantly larger deviations towards our results. In particular, there abruptly appears a plateau between $\theta \approx 0.9$ and $\theta = 0.1$, followed by an unphysical bump before the ground state limit is reached. In contrast, the IIT parametrization gives a qualitatively more similar behavior with respect to the red curve, although the overall accuracy is comparable to KSDT. Finally, the HNC parametrization again exhibits a too deep minimum and, in addition, does not incorporate the correct ground state limit.

8.4.4. Spin-dependency of the parametrizations

In Fig. 38, we show the spin-dependency of the interaction energy of the uniform electron gas for four different densities and six relevant temperatures. Note that we always define the Fermi energy entering the reduced temperature θ with respect to the spin-up electrons, cf. Eq. (4), which is different from definitions in parts of the relevant literature [205, 242, 210, 212]. The red points correspond to our recent finite-size corrected thermodynamic QMC data [226, 227], which is available at two intermediate spin-polarizations, $\xi = 1/3$ and $\xi = 0.6$. We stress that these data still constitute the only *ab initio* investigation of the ξ-dependency of the warm dense electron gas. The solid red line depicts our GDB-parametrization [227], which utilizes the spin-interpolation between the para- and ferromagnetic limits from Eq. (162). Surprisingly, we find that a single free parameter [λ_1 in Eq. (162)] is sufficient to accurately describe the temperature-dependence of the spin-interpolation, resulting in an average and maximum deviation between parametrization and QMC data of 0.15% and 0.8%, respectively, at intermediate ξ. The dotted blue curve corresponds to the functional by Karasiev *et al.* [212], who used the same functional form as the GDB-parametrization. However, due to the lack of RPIMC data for $0 < \xi < 1$, they determined the θ-dependent parameters in Eq. (162) from a fit to the sparse classical-mapping data from Perrot and Dharma-wardana [210] (12 values for f_{xc} at $r_s = 1, 3, 6$ and $\xi = 0.6$). At zero temperature, KSDT and GDB are in excellent agreement as both utilize the same ground state QMC data [38] to construct the ground state limit for all values of ξ. Towards higher temperatures, there occur increasing deviations that are most pronounced (in terms of the relative deviation) at $r_s = 0.1$ and $\theta = 4, 8$. This is again a consequence of the lack of input data for the KSDT functional for $r_s < 1$ at finite temperature, and the poor quality of the RPIMC data at $r_s = 1$ for the $\xi = 0, 1$ limits.

The dashed-dotted black and dashed green lines correspond to the improved STLS parametrization by Ichimaru, Tanaka, *et al.* [206, 205, 249] and the recent HNC-based parametriztion by Tanaka [242], respectively. Both use the finite-temperature spin-interpolation from Eq. (163) that has been constructed on the basis of the modified convolution approximation, see Ref. [205]. First and foremost, we note that the two curves do not agree, even in the ground state, since the $\xi = 0$ and $\xi = 1$ limits in IIT incorporate ground state QMC data, whereas the HNC limits have been constructed solely on the basis of the HNC data. Further, the IIT ground state limit for the ξ-dependence, at $r_s = 10$, is slightly non-monotonic, with a shallow minimum around $\xi \approx 0.8$. Towards high temperature, the deviations between the IIT and Tanaka parametrizations vanish, since both the STLS and HNC input data sets for the interaction energy eventually converge. At high density and temperature, we find an excellent agreement to our GDB curve, which is expected in this weak coupling regime. In contrast, towards lower density and temperature,
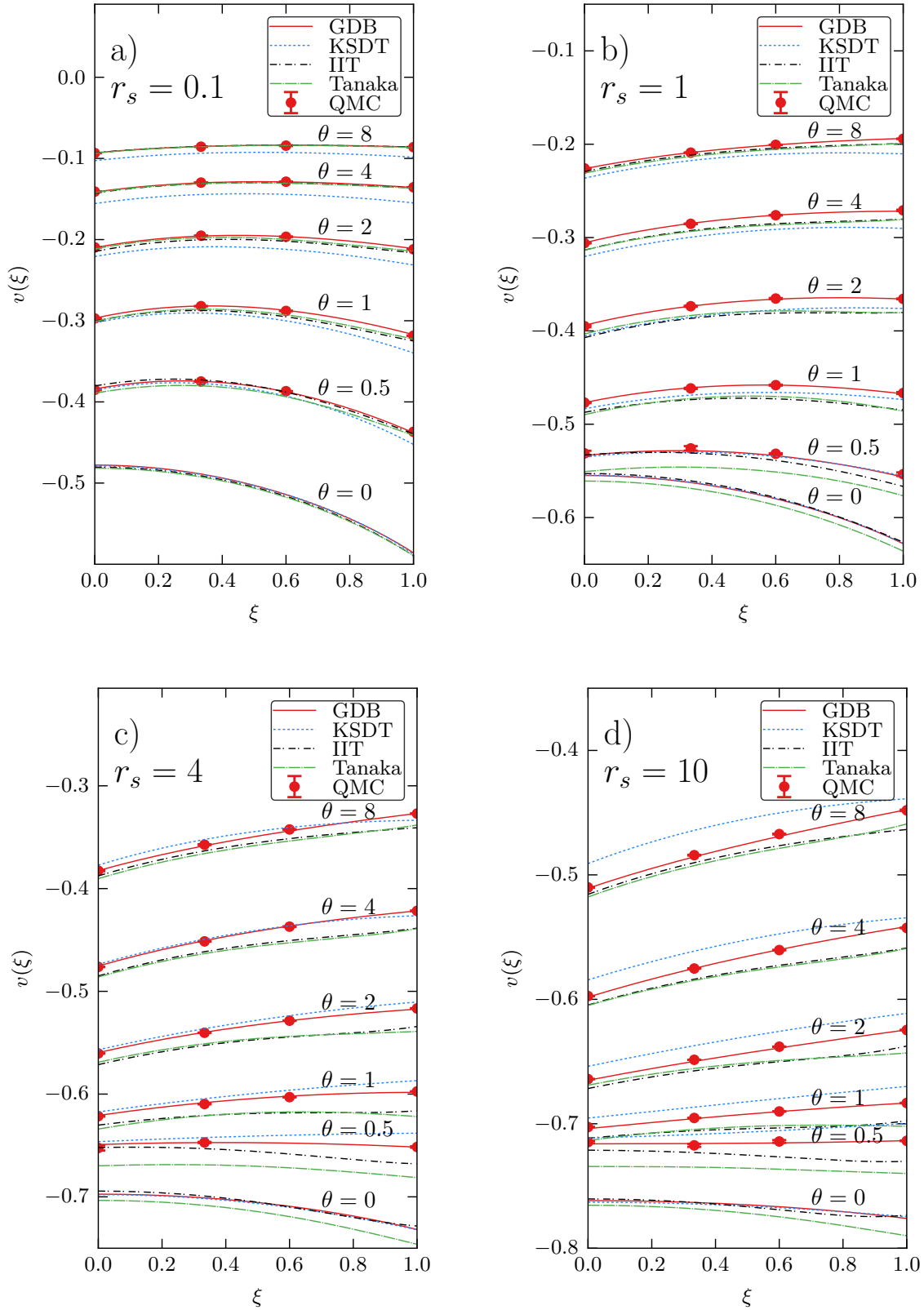
Figure 38: Spin-dependency of the interaction energy of the uniform electron gas – Shown are the parametrizations by Groth, Dornheim *et al.* (GDB, Ref. [227], red solid line), Karasiev *et al.* (KSDT, Ref. [212], blue dotted line), Ichimaru, Tanaka *et al.* (IIT, Refs. [206, 205, 249], black dash-dotted line), and the recent HNC-based function by Tanaka (Ref. [242], dashed green). The red points correspond to our finite-size corrected thermodynamic QMC data from Refs. [226, 227]. Note that we define the Fermi energy in the reduced temperature with respect to the spin-up electrons for all polarizations, cf. Eq. (4), which is different from the definitions in parts of the literature [205, 212, 210]. At $r_s = 4$ and $r_s = 10$, the $\theta = 0$ curves are shifted downward by 0.05 Hartree for better visibility.
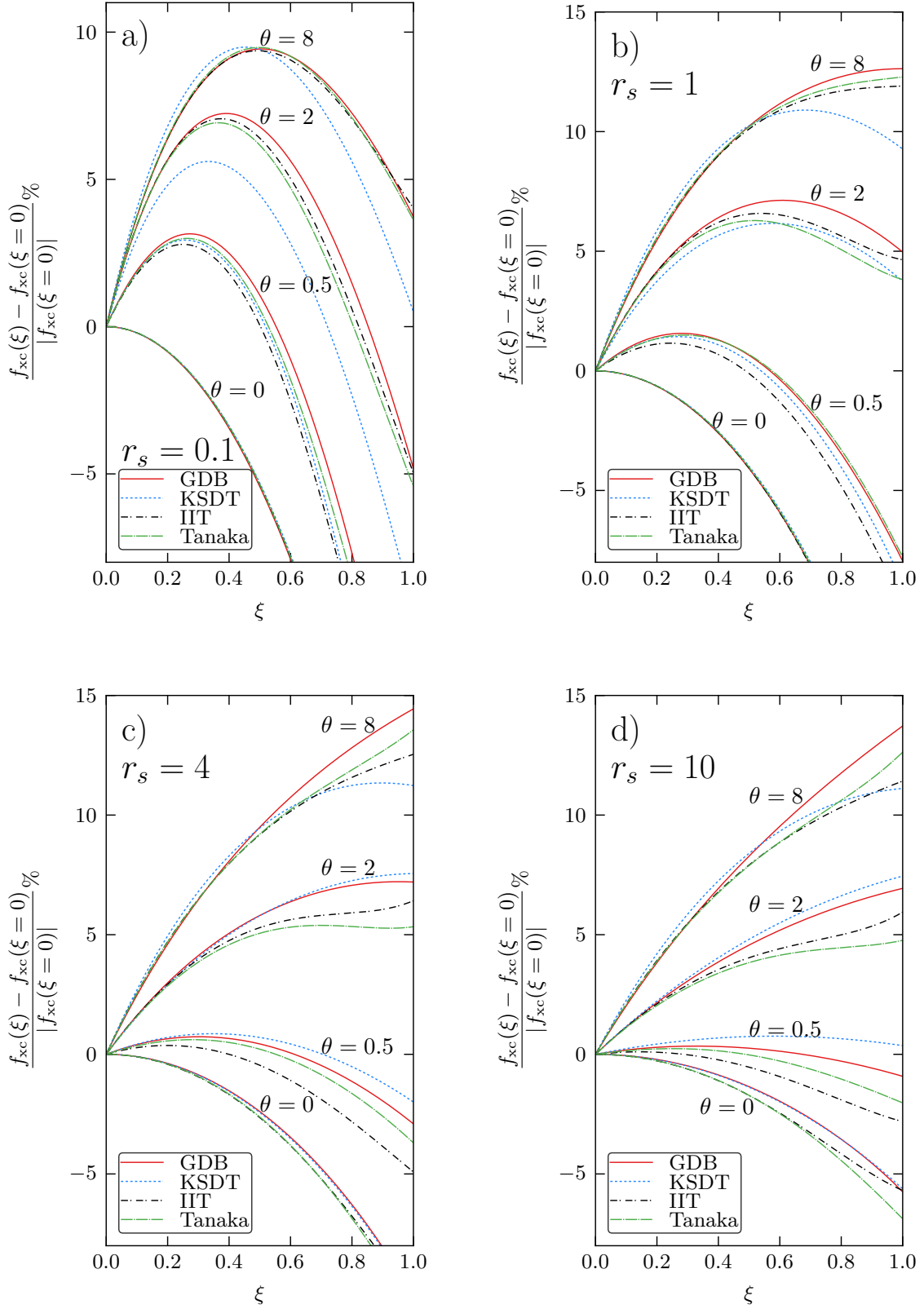
Figure 39: Spin-dependency of the exchange-correlation free energy of the uniform electron gas – Shown are the parametrizations by Groth, Dornheim *et al.* (GDB, Ref. [227], red solid line), Karasiev *et al.* (KSDT, Ref. [212], blue dotted line), Ichimaru, Tanaka *et al.* (IIT, Refs. [206, 205, 249], black dash-dotted line), and the recent HNC-based function by Tanaka (Ref. [242], dashed green). Note that we define the Fermi energy in the reduced temperature with respect to the spin-up electrons for all polarizations, cf. Eq. (4), which is different from the definitions in parts of the literature [205, 212, 210].

there occur substantial deviations and, in addition, unphysical dents around $\xi \approx 0.8$. In summary, we find that the KSDT, IIT and Tanaka curves exhibit, overall, a similar degree of accuracy.

Let us conclude the discussion of the different parametrizations with a comparison of the relative spin-dependency of the exchange-correlation free energy of the uniform electron gas at warm dense matter conditions which is presented in Fig. 39. In the ground state, all four depicted curves are close, although IIT and Tanaka substantially deviate from the other two at $r_s = 10$. In this case, IIT attains the correct limit for $\xi = 1$ due to the incorporation of ground state QMC data, which is lacking for Tanaka. Furthermore,, similar to our findings for the interaction energy in Fig. 38, there occur unphysical dents in f_{xc} for IIT and Tanaka around $\xi = 0.8$, even at $r_s = 1$, which are caused by the MCA-based spin-interpolation for f_{xc}, cf. Eq. (165). Finally, the KSDT results are best at $r_s = 10$, whereas there occur substantial deviations, both, towards high temperature and high density.

9. Inhomogeneous Electron Gas: QMC study of the static density response

9.1. Introduction

In Sec. 3, we gave a comprehensive introduction to the linear response theory of the uniform electron gas at warm dense matter conditions. In particular, we introduced several suitable approximations for the density response of the system to an external harmonic perturbation, which is fully characterized by the frequency-dependent response function $\chi(\mathbf{q}, \omega)$, cf. Eq. (19). The gist has been that the consideration of the perturbed system served as a means to an end, as complete knowledge of $\chi(\mathbf{q}, \omega)$ allows to compute all static properties of the unperturbed electron gas, such as the static structure factor, $S(\mathbf{k})$, or the interaction energy, v.

In contrast, in the following we will consider the calculation of the density response function as an end in itself, as this information is of high importance for many applications [1]. First and foremost, the local field correction, $G(\mathbf{q}, \omega)$, defined by Eq. (19) is directly related to the exchange-correlation kernel

$$K_{xc}(\mathbf{q}, \omega) = -\frac{4\pi}{q^2} G(\mathbf{q}, \omega) \quad , \tag{171}$$

which is the main input for density functional theory calculations in the adiabatic-connection fluctuation-dissipation formulation [337, 338, 339]. Albeit computationally demanding, this formulation of a true *non-local* XC-functional is a promising approach to go beyond widespread gradient approximations such as PBE [32] or its recent extension to finite temperature by Karasiev *et al.* [185]. In addition, accurate data for the LFCs of the warm dense electron gas are needed for the calculation of the dynamic structure factor $S(\mathbf{q}, \omega)$ of real systems (such as two-component plasmas), e.g. Refs. [340, 341, 342, 66]. We stress that the cutting-edge theoretical description of $S(\mathbf{q}, \omega)$ is among the most pressing goals of current warm dense matter research, as it is nowadays routinely obtained in experiments from x-ray Thomson scattering measurements for many systems, see Ref. [112] for a review. Further applications of $G(\mathbf{q}, \omega)$ include the calculation of electrical and optical conductivities [343, 344], energy transfer rates [345, 346], EOS models of ionized plasmas [195, 347, 189], and the construction of pseudo-potentials [348, 349, 350, 351, 352] that can be used, e.g., within simple molecular dynamics simulations.

In the following, we will explain how the static limit of the density response function,

$$\chi(\mathbf{q}) \equiv \lim_{\omega \to 0} \chi(\mathbf{q}, \omega) \quad , \tag{172}$$

can be obtained with high precision from *ab initio* quantum Monte Carlo simulations at warm dense matter conditions.

9.2. Theory

At zero temperature, the static density response function was computed from ground state QMC simulations of the harmonically perturbed (and, thus, inhomogeneous) electron gas [57, 58, 55, 56] back in the first half of the 1990s. Further, these accurate *ab initio* data have subsequently been parametrized by Corradini *et al.* [59]. In contrast, at warm dense matter conditions, until very recently, there were no *ab initio* data available, and one had to rely on interpolations between known limits, e.g. Ref. [353]. In the following, we will demonstrate how this gap was closed by extending the idea from Refs. [58, 57] to finite temperature, in the recent work by Dornheim and co-workers [354].

Consider a modified Hamiltonian of the form

$$\hat{H} = \hat{H}_0 + \hat{H}_{ext}(t) \quad , \tag{173}$$

where $\hat{H}_0$ corresponds to the standard Hamiltonian of the unperturbed uniform electron gas, cf. Eq. (7), and $\hat{H}_{\text{ext}}(t)$ denotes an, in general, time-dependent perturbation. In particular, we choose

$$\hat{H}_{\text{ext}}(t) = 2A \sum_{i=1}^{N} \cos\left(\mathbf{r}_i \cdot \mathbf{q} - \Omega\, t\right) \quad , \tag{174}$$

i.e., a sinusoidal external charge density (of perturbation wave vector $\mathbf{q}$ and frequency Ω) with the potential

$$\phi_{\text{ext}}(\mathbf{r}, t) = 2A \cos\left(\mathbf{r} \cdot \mathbf{q} - \Omega\, t\right) \quad . \tag{175}$$

Let us recall the standard definition of the density response function as [1]

$$\tilde{\chi}(\mathbf{q}, \tau) = \frac{-i}{\hbar} \left\langle [\rho(\mathbf{q}, \tau), \rho(-\mathbf{q}, 0)] \right\rangle_0 \Theta(\tau) \, , \tag{176}$$

with $\langle \dots \rangle_0$ indicating that the thermodynamic expectation value has to be carried out with respect to the unperturbed system. Naturally, Eq. (176) solely depends on the time difference, $\tau = t - t'$, and on the modulus of the wave vector, i.e. the wavenumber q. Further, it is often convenient to consider the Fourier transform of Eq. (176) with respect to the second argument,

$$\chi(\mathbf{q}, \omega) = \lim_{\eta \to 0} \int_{-\infty}^{\infty} \mathrm{d}\tau \; e^{(i\omega - \eta)\tau} \tilde{\chi}(\mathbf{q}, \tau) \, . \tag{177}$$

However, at the time of this writing, time-dependent QMC simulations are still severely limited by an additional *dynamical sign problem*, e.g. Refs. [355, 356, 357]. Therefore, in the present work, we restrict ourselves to the static limit $\chi(\mathbf{q})$ [cf. Eq. (172)], i.e., the density response to a constant (time-independent) perturbation,

$$\phi_{\text{ext}}(\mathbf{r}) = 2A \cos(\mathbf{r} \cdot \mathbf{q}) \, . \tag{178}$$

Still, we stress that the basic idea that is explained below can be applied within time-dependent simulations, such as the nonequilibrium Green functions technique [358, 259, 239], in exactly the same way. Note that all time-dependencies are, in the following, dropped for simplicity. In particular, $\chi(\mathbf{q})$ characterizes the linear relation between the induced and external charge densities,

$$\rho_{\text{ind}}(\mathbf{q}) = \frac{4\pi}{q^2} \chi(\mathbf{q}) \rho_{\text{ext}}(\mathbf{q}) \, . \tag{179}$$

The external density is straightforwardly obtained from the Poisson equation as

$$\rho_{\text{ext}}(\mathbf{q}) = \frac{q^2 A}{4\pi} \left(\delta_{\mathbf{k}, \mathbf{q}} + \delta_{\mathbf{k}, -\mathbf{q}}\right) \, , \tag{180}$$

and, by definition, the induced density is given by the difference between the densities of the perturbed and unperturbed systems,

$$\begin{aligned} \rho_{\text{ind}}(\mathbf{q}) &= \langle \hat{\rho}_{\mathbf{q}} \rangle_A - \langle \hat{\rho}_{\mathbf{q}} \rangle_0 \\ &= \frac{1}{V} \left\langle \sum_{j=1}^{N} e^{-i\mathbf{q} \cdot \mathbf{r}_j} \right\rangle_A \, . \end{aligned} \tag{181}$$

We note that the notation $\langle \dots \rangle_A$ indicates that the thermodynamic expectation value has to be computed in the perturbed system, and that, for the second equality in Eq. (181) we made use of the fact that $\langle \hat{\rho}_{\mathbf{q}} \rangle_0 = 0$. Finally, this gives a simple, direct expression for the static density response function,

$$\chi(\mathbf{q}) = \frac{1}{A} \langle \hat{\rho}_{\mathbf{q}} \rangle_A \quad . \tag{182}$$

In practice, we carry out several *ab initio* quantum Monte Carlo calculations of the harmonically perturbed electron gas for each perturbation wave vector $\mathbf{q} = 2\pi L^{-1}(a, b, c)^T$ (with $a, b, c \in \mathbb{Z}$), for a variety of amplitudes A. This allows us to compute the exact induced density for arbitrarily strong perturbations. In the small A-regime, linear response theory is accurate and, thus, Eq. (182) holds, implying that $\langle \rho_{\mathbf{q}} \rangle_A$ is linear in A, with $\chi(\mathbf{q})$ being the slope.
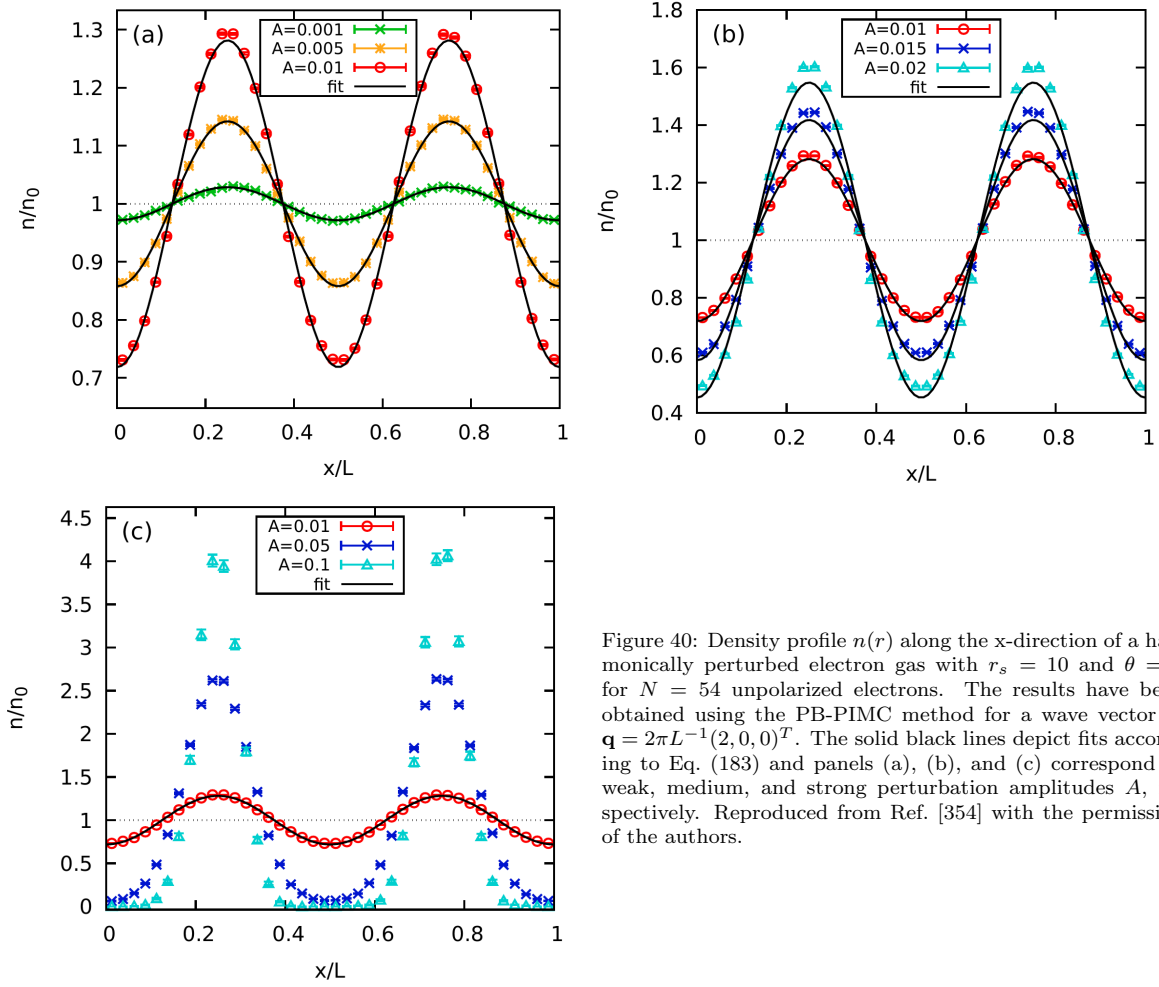
Figure 40: Density profile $n(r)$ along the x-direction of a harmonically perturbed electron gas with $r_s = 10$ and $\theta = 1$ for $N = 54$ unpolarized electrons. The results have been obtained using the PB-PIMC method for a wave vector of $\mathbf{q} = 2\pi L^{-1}(2,0,0)^T$. The solid black lines depict fits according to Eq. (183) and panels (a), (b), and (c) correspond to weak, medium, and strong perturbation amplitudes A, respectively. Reproduced from Ref. [354] with the permission of the authors.

For completeness, we mention a second, closely related way to estimate $\chi(\mathbf{q})$ from a QMC simulation of the inhomogeneous system. In linear response theory, the perturbed density profile is given by

$$\langle n(\mathbf{r}) \rangle_A = n_0 + 2A \cos(\mathbf{q} \cdot \mathbf{r}) \chi(\mathbf{q}) , \qquad (183)$$

with n_0 being the density of the unperturbed system. In particular, the LHS. of Eq. (183) is easily obtained within a QMC simulation in coordinate space (such as PB-PIMC, but also standard PIMC), and a subsequent cosinusoidal fit gives another estimation of the desired static density response function.

9.3. Ab initio QMC results for the static density response

In the following section, we will demonstrate the feasibility of computing *ab initio* data for the static density response using QMC methods. In particular, we will focus on two exemplary test cases at low and high density and moderate temperatures to illustrate the range of validity of linear response theory. We will discuss the necessity of finite-size corrections at certain parameters and demonstrate how this can be accomplished, and compare our new data for $\chi(\mathbf{q})$ to the dielectric approximations introduced in Sec. 3.

9.3.1. Strong coupling: PB-PIMC results

In Fig. 40, we show *ab initio* PB-PIMC results [354] for the density profile along the x direction (i.e., along the direction of the perturbation wave vector $\mathbf{q} = 2\pi L^{-1}(2,0,0)^T$). The simulation was carried out for $N = 54$ spin-unpolarized electrons at $r_s = 10$ and $\theta = 1$, which corresponds to moderate to strong coupling at a moderate temperature. The results for relatively weak perturbation amplitudes A are depicted in panel a). The solid black lines correspond to the cosinusoidal fits according to Eq. (183). Evidently, for the two smallest perturbations ($A = 0.001$, green crosses and $A = 0.005$, yellow asterisks) no deviations from linear response theory can be resolved.
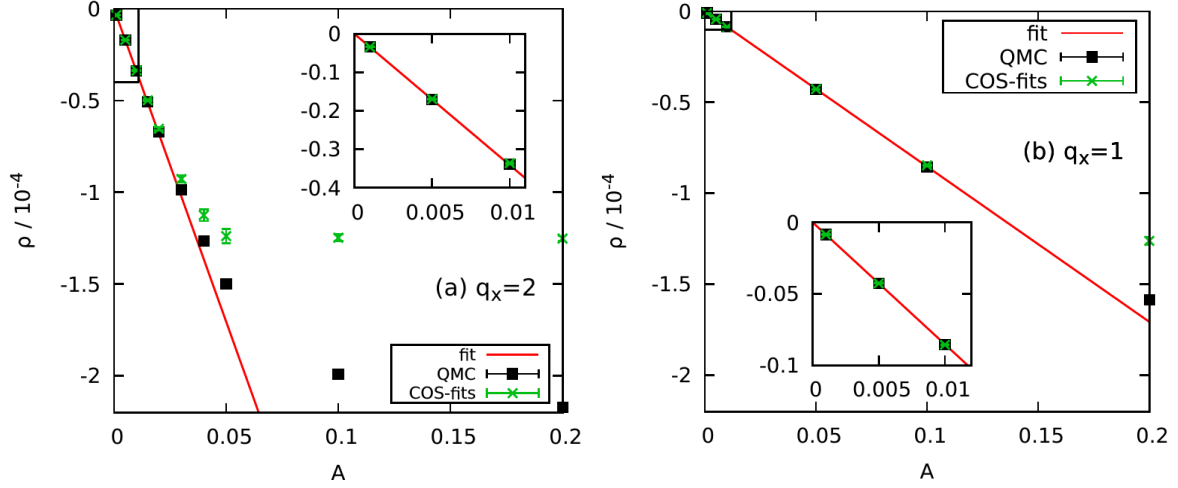
Figure 41: PB-PIMC results for the perturbation strength dependence of the induced density modulation ρ_q for $N = 54$ unpolarized electrons at $r_s = 10$ and $\theta = 1$. The panels (a) and (b) correspond to the perturbation wave vectors $\mathbf{q} = 2\pi L^{-1}(q_x, 0, 0)^T$ with $q_x = 2$ and $q_x = 1$, respectively. The black squares correspond to the direct evaluation of Eq. (182), the green crosses have been obtained from the cosine-fits, cf. Eq. (183), and the red lines depict linear fits to the QMC points. Reproduced from Ref. [354] with the permission of the authors.

This is a rather remarkable result, as the yellow points exhibit maximum deviations from the mean value, n_0, of more than 10%, i.e., the system is already moderately inhomogeneous. A doubling of the perturbation amplitude to $A = 0.01$ (red circles) leads to density modulations of the order of 25%, and deviations from the cosine-fit are clearly visible around the maxima and minima. Still, these differences between data and fit are of the order of 1%. In panel b), we show density profiles for further increased perturbation amplitudes, $A = 0.015$ (blue crosses) and $A = 0.02$ (light blue triangles). Evidently, the observed shell structure further departs from the cosinusoidal prediction from LRT, as it is expected. Nevertheless, even at strong inhomogeneity, with density modulations exceeding 50% of the mean value, LRT provides a good quantitative description as the maximum error around the maxima does still not exceed 10%. Finally, in panel c) of Fig. 40, we show results for strong perturbations, namely $A = 0.05$ (blue crosses) and $A = 0.1$ (light blue triangles). Eventually, the system is dominated by the external potential and, for the strongest depicted perturbation amplitude, two distinct shells with negligible overlap are formed. Obviously, Eq. (183) is no longer appropriate and LRT does not capture the dominant physical effects. For completeness, we mention that the relatively large statistical uncertainty in the light blue triangles, in particular around the maxima, is a consequence of the fact that the fermion sign problem becomes more severe towards increasing inhomogeneity, see Ref. [354] for a more detailed explanation.

In Fig. 41, we show a comparison of the QMC results for the static density response function $\chi(\mathbf{q})$ as obtained from cosinusoidal fits to the density profile (green crosses), cf. Fig. 40, or via the direct evaluation of Eq. (182) (black squares). More specifically, we show the perturbation strength dependence of the induced density $\rho_{\text{ind}}(\mathbf{q})$ for two different wave vectors ($\mathbf{q} = 2\pi L^{-1}(2, 0, 0)^T$, panel a) and $\mathbf{q} = 2\pi L^{-1}(1, 0, 0)^T$, panel b). Further, the solid red line corresponds to a linear fit of the black squares in the small A regime ($A < 0.01$). Let us start by considering the same $\mathbf{q}$-vector as in the previous figure, i.e., with panel a). We note the perfect agreement between the cosine-fit and direct results for ρ_{ind} for weak perturbations. Interestingly, this still holds for $A = 0.01$, where we found visible deviations between density profile and fit, cf. Fig. 40 a). With increasing A, both sets of data differ from the linear fit, although the deviations of the black squares are significantly smaller. In panel b), the same information is shown for a smaller wave vector, $\mathbf{q} = 2\pi L^{-1}(1, 0, 0)^T$. Overall, we observe the same trends as in panel a), although the density response is considerably smaller. This is a consequence of screening effects inherent to the uniform electron gas, e.g. Ref. [332]. As a consequence, the system is less inhomogeneous, and linear response theory holds up to larger A-values than in the former case.

Let us now continue the discussion of the PB-PIMC results for the static density response function by considering the full wave vector dependence of $\chi(\mathbf{q})$, which is depicted in Fig. 42 for the same parameters as in the previous figures. The different symbols correspond to $N = 54$ (blue crosses), $N = 34$ (light blue circles), $N = 20$ (yellow squares), $N = 14$ (black triangles) and $N = 8$ (green diamonds) unpolarized electrons. The main effect of the different system size is the unique $\mathbf{q}$-grid for each N, which is a direct consequence of the momentum quantization in the finite simulation cell, cf. Sec. 6. The functional form of $\chi(\mathbf{q})$ itself, however, is, for the current set of parameters, remarkably well converged with system size. Even in the right panel, where a magnified segment

Figure 42: PB-PIMC results for the wave vector dependence of the static density response function χ for the unpolarized electron gas at $r_s = 10$ and $\theta = 1$. Shown are QMC results [cf. Eq. (182)] for different particle numbers N (symbols), and results from dielectric approximations, namely RPA (grey line) and STLS (red line). Further, the black arrow indicated the Fermi wave vector, $k_\mathrm{F} = (9\pi/4)^{1/3}/r_s$. Panel (b) shows a magnified segment. Reproduced from Ref. [354] with the permission of the authors.

around the smallest **q**-values is shown, no finite-size effects in the density response function can be resolved (note that this changes for higher densities, see Sec. 9.3.2). Furthermore, we note that the increased error bars towards large wave vectors are a consequence of the quickly oscillating nature of the external potential in this regime, see Ref. [354] for more details. The solid grey and red lines correspond to dielectric approximations, namely RPA and STLS, respectively. In the small q-regime, both curves are in excellent agreement with each other and the parabolic asymptotic behavior known from the literature [332]. With increasing q, however, they substantially deviate with a maximum difference of $\Delta\chi \sim 50\%$ around twice the Fermi vector k_F. In particular, we find that the inclusion of an appropriate local field correction is crucial to account for the pronounced coupling effects at these parameters. Consequently, the STLS approximation (see Sec. 3) gives significantly improved data for the static density response function, although the agreement with the QMC data is still only qualitative.

We conclude this section with a discussion of the *static local field correction*, $G(\mathbf{q})$, which is readily computed from $\chi(\mathbf{q})$, cf. Eq. (185) below. The results are shown in Fig. 43, where we compare the QMC data for $N = 34$ (light blue circles) and $N = 54$ (blue crosses) to the static local field correction from STLS theory (solid black line). First and foremost, we note that no system-size dependence can be resolved within the given statistical uncertainty, as expected. Furthermore, the systematic bias in the STLS results is substantially larger than in the total density response function, since $G(\mathbf{q})$ is dominated by exchange-correlation effects. In addition, we note that the recent LFC based on the hypernetted chain equation by Tanaka [242] is significantly more accurate than STLS, which is in stark contrast to the corresponding results for the interaction energy v, cf. Sec. 6. Moreover, the solid purple curve depicts the LFC obtained in the Vashista-Singwi scheme [213] and, overall, exhibits a similar accuracy as the HNC curve. The dotted yellow and dash-dotted green lines are predictions for the asymptotic behavior of the local field correction based on the compressibility sum-rule, cf. Eq. (39), using as input the parametrization of $f_\mathrm{xc}(r_s, \theta)$ by Groth, Dornheim *et al.* [227] or Karasiev *et al.* [212], respectively (for a review on sum rules in classical and quantum mechanical charged fluids, see Ref. [359]).

For completeness, we mention that it is well known that the local field correction from STLS (and also from HNC) does not fulfill Eq. (39) and, thus, does not give the correct long-range behavior [in contrast to the total static density response function $\chi(\mathbf{q})$]. In stark contrast, the VS curve is in perfect agreement to the asymptotic expansion, which is somewhat surprising given the systematic bias in the interaction energy itself. Although both utilized parametrizations for f_xc deviate by less than four percent, at the present conditions, the pre-factors of the parabolic behavior of G differ by more than a factor of two. The reason for this striking deviation is that the compressibility sum-rule is not sensitive to f_xc itself, but to its second derivative with respect to the density (or the density parameter r_s). Evidently, the yellow curve is consistent with the QMC results for the smallest wave vectors, whereas the KSDT prediction does not appear to be better than the STLS curve. Therefore, this investigation of the compressibility sum-rule convincingly demonstrates that a highly accurate parametrization of f_xc is not only important as input to finite-temperature DFT calculations in the local density approximation. These data are equally important for observables that are related to derivatives of f_xc, e.g., Ref. [360].
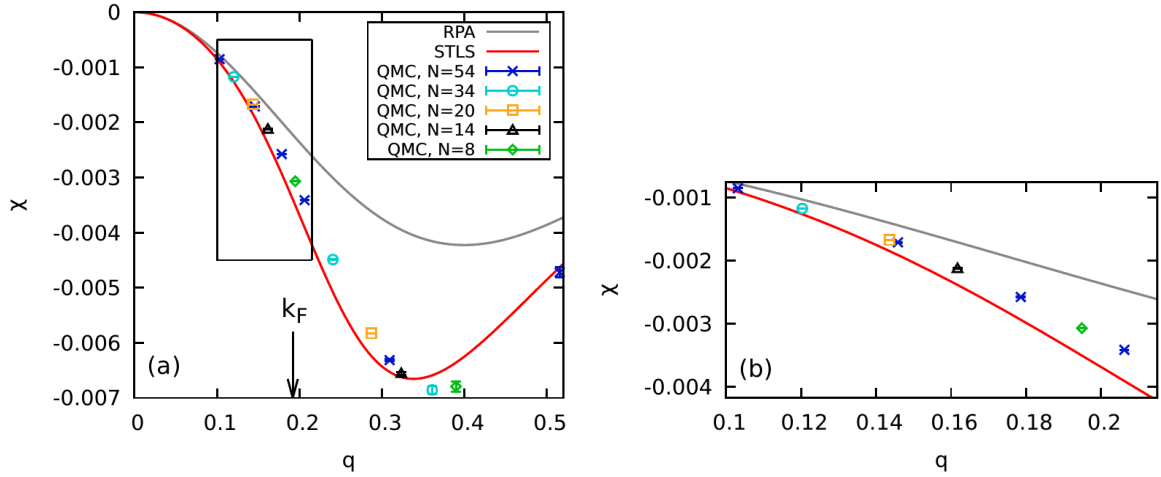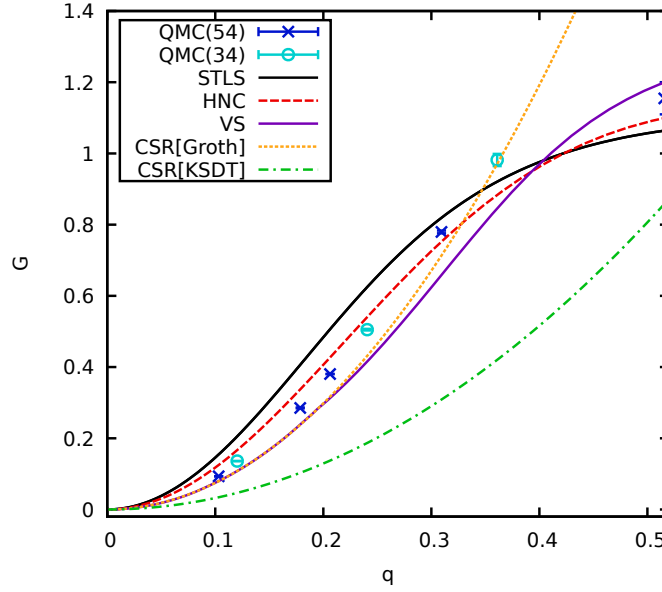
Figure 43: PB-PIMC results for the wave vector dependence of the static local field correction G for the unpolarized electron gas at $r_s = 10$ and $\theta = 1$. Shown are QMC results [cf. Eq. (185)] for $N = 54$ (blue crosses) and $N = 34$ (light blue circles), data from STLS (solid black line), the recent LFC based on the HNC equation by Tanaka [242] (red dashed line) and Vashista-Singwi (solid purple line, Ref. [213]), and asymptotic long-range predictions from the compressibility sum-rule [cf. Eq. (39)] using the exchange-correlation functionals by Groth, Dornheim *et al.* [227] (yellow dotted) and Karasiev *et al.* [212] (green dash-dotted, KSDT).

9.3.2. Moderate coupling: CPIMC results

To obtain highly accurate data for the static density response function of the UEG at high densities, we also extended the CPIMC method to the simulation of the inhomogeneous electron gas, which leads to a significantly more complicated algorithm, compared to the unifrom electron gas. This is due to the substantially larger number of possible diagrams that have to be taken into account. Most importantly, in addition to the two-partical excitations (so-called type-4 kinks) in the CPIMC simulation paths, which are already present in the homogeneous case (see Sec. 5.5), there also occur one-partical excitations (type-2 kinks). For more details on the specific changes of the CPIMC algorithm we refer to Ref. [361].

In the top panel of Fig. 44, we show CPIMC results for the induced density, $\rho_{ind}(\mathbf{q})$, for $N = 14$ unpolarized electrons at moderate coupling and temperature, $r_s = 0.5$ and $\theta = 0.5$ (red crosses), for the perturbation wave vector $\mathbf{q} = 2\pi L^{-1}(1,0,0)^T$. The solid grey line corresponds to the linear response prediction for an ideal system and the dashed black line to a linear fit according to Eq. (182). Clearly, linear response theory provides a remarkably accurate description of the static density response over the entire depicted A-range. The bottom panel of Fig. 44 shows the corresponding simulation results for the average sign and the numbers of type-2 and type-4 kinks. First, we observe that the sign (yellow dash-dotted line) attains an almost constant value for $A < 0.5$ and does not drop below $S = 0.3$, even for the largest considered perturbation amplitude, explaining the small statistical uncertainty in the results for ρ_{ind}. The average number of type-4 kinks (green dotted line) exhibits a qualitatively similar behavior, although with a slight increase towards increasing A. In stark contrast, the average number of type-2 kinks (red solid line) distinctly increases with the perturbation strength, as expected. Further, we note that, for weak inhomogeneity, the CPIMC simulation is dominated by Coulomb interaction effects, which manifests itself in the occurrence of type-4 kinks. With increasing A (around $A \sim 0.8$), there are on average more type-2 kinks present as the system becomes increasingly altered by the external potential.

As we have seen above (cf. Fig. 42), at $r_s = 10$ no system size dependence has been resolved for as few as four electrons. However, it is well known that finite-size effects become more pronounced at higher densities. This is investigated in Fig. 45, where we show the wave vector dependence of the static density response function for the same conditions as in Fig. 44. The red circles, blue diamonds, yellow squares, and purple crosses correspond to the raw CPIMC simulation results for $N = 38$, $N = 20$, $N = 14$, and $N = 4$ electrons, respectively. Further, we show results from RPA (dashed black) and STLS (solid brown), as well as the static response function of the corresponding noninteracting system (solid black line). The dielectric approximations exhibit the same exact parabolic behavior for small $\mathbf{q}$ values [332], whereas the ideal function attains a maximum at $q = 0$. This contrast is a consequence of the absence of Coulomb screening effects in the latter case. Further, we note that the inclusion of the static local
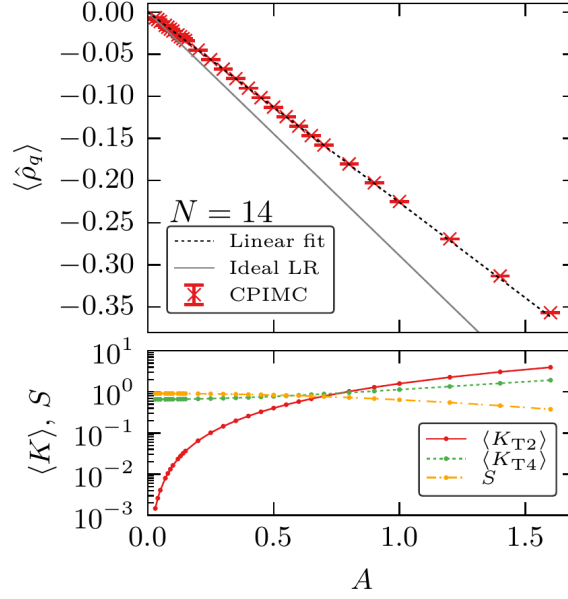
Figure 44: In the top panel, we show CPIMC results for the perturbation strength dependence of the induced density modulation, ρ_q, for $N = 14$ unpolarized electrons at $r_s = 0.5$ and $\theta = 0.5$ with the perturbation wave vector $\mathbf{q} = 2\pi L^{-1}(1,0,0)^T$. The red crosses depict the CPIMC data and the dotted black line depicts a corresponding linear fit. Also shown is the linear response of ideal fermions at the same parameters (solid grey line). In the bottom panel, we show data for the average numbers of type-2 (red) and type-4 (green) kinks and the average sign (yellow) corresponding to the CPIMC simulations from the top panel. Reproduced from Ref. [361] with the permission of the authors.

field correction from STLS theory leads to differences in $\chi(\mathbf{q})$ of around 5%, which are most pronounced around the Fermi wave vector k_{F}. Let us now consider the uncorrected CPIMC simulation results. Evidently, these data are not converged with respect to system size (see in particular the bottom panel where we show a magnified segment) and, without further improvement, no systematic errors in the STLS curve can be resolved.

At the same time, it is well known from ground state QMC calculations of the static density response function [55, 56] that the *static local field correction*, G, which contains all information about short-range exchange-correlation effects, can be accurately obtained from simulations of few electrons in a small box, i.e., $G_N(\mathbf{q}) \approx G(\mathbf{q})$. Therefore, the bulk of the system size dependence observed in Fig. 45 is due to finite-size effects in the ideal density response function, i.e., $\chi_0^N(\mathbf{q}) \neq \chi_0(\mathbf{q})$. In the following, we will exploit this fact to compute the density response function, $\chi^{\mathrm{TDL}}(\mathbf{q})$, in the thermodynamic limit from the QMC result for a specific, finite number of electrons N, $\chi^N(\mathbf{q})$. For this purpose, we rewrite Eq. (19) in terms of finite-size quantities,

$$\chi^N(\mathbf{q}) = \frac{\chi_0^N(\mathbf{q})}{1 - 4\pi/q^2[1 - G^N(\mathbf{q})]\chi_0^N(\mathbf{q})} \quad , \tag{184}$$

and solve Eq. (184) for the local field correction,

$$G^N(\mathbf{q}) = 1 + \frac{q^2}{4\pi}\left(\frac{1}{\chi^N(\mathbf{q})} - \frac{1}{\chi_0^N(\mathbf{q})}\right) \quad . \tag{185}$$

The finite-size corrected result for the density response function is then obtained by plugging the QMC result for the static local field correction, Eq. (185), into Eq. (19),

$$\chi^{\mathrm{TDL}}(\mathbf{q}) = \frac{\chi_0(\mathbf{q})}{1 + \frac{q^2}{4\pi}\left(\frac{1}{\chi^N(\mathbf{q})} - \frac{1}{\chi_0^N(\mathbf{q})}\right)\chi_0(\mathbf{q})} \quad . \tag{186}$$

Let us now verify the underlying assumption of this finite-size correction procedure, i.e., that $G^N(\mathbf{q})$ does not depend on system size. In Fig. 46, we show the wave vector dependence of the local field correction computed from the QMC results for $\chi^N(\mathbf{q})$ depicted in Fig. 45. The black symbols correspond to the direct evaluation of Eq. (186). Evidently, no finite-size effects can be resolved within the statistical uncertainty over the entire depicted q-range. We note that the increasing error bars towards large wave vectors are a consequence of the reduced impact
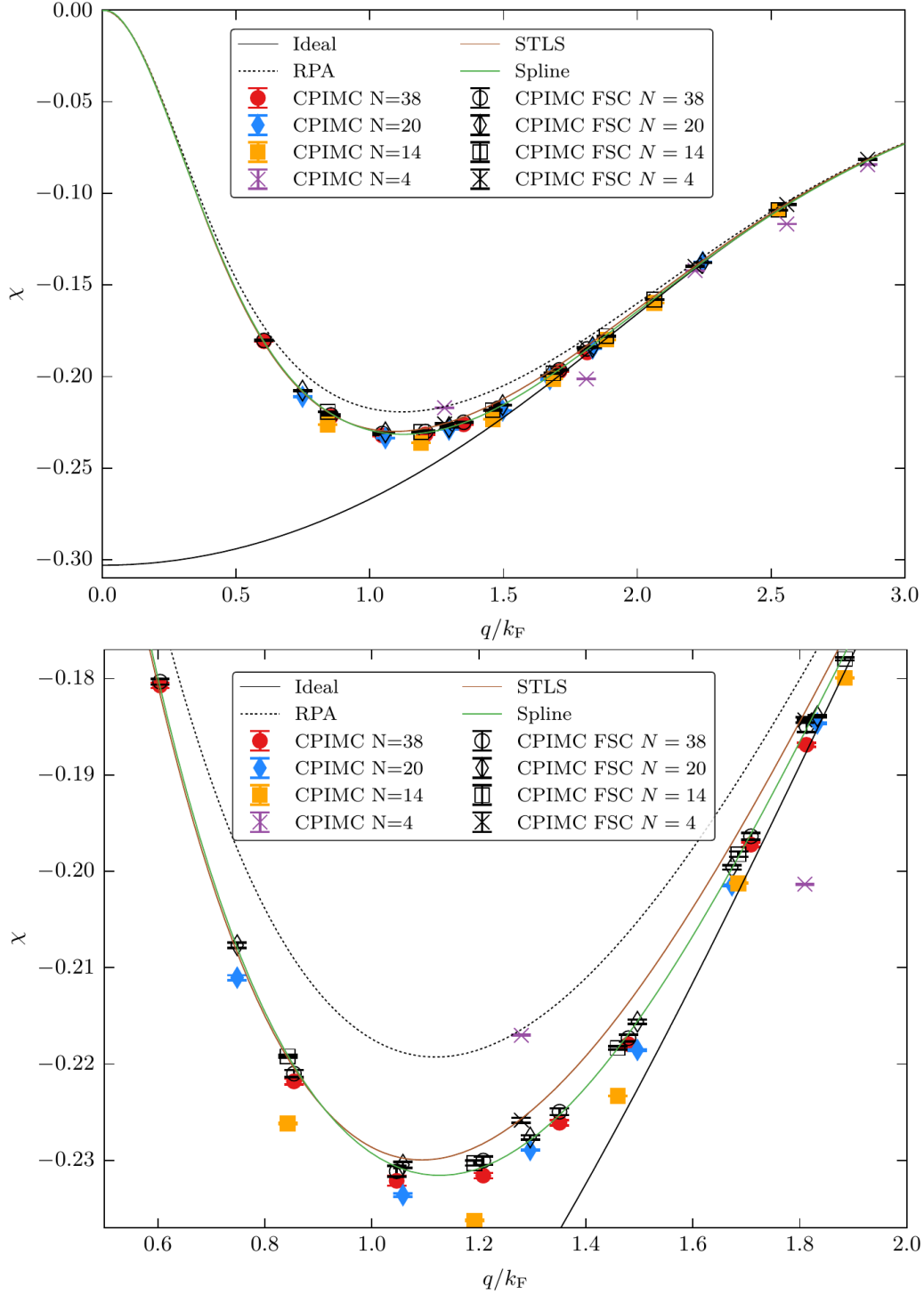
Figure 45: Wave vector dependence of the static density response function χ of the unpolarized electron gas at $r_s = 0.5$ and $\theta = 0.5$. The colored circles, diamonds, squared and crosses depict the bare CPIMC data for $N = 38$, $N = 20$, $N = 14$, and $N = 4$ electrons, respectively, and the corresponding black symbols have been obtained by applying the finite-size correction using the N-consistent data for the ideal density response function as explained in the text. The solid green line depicts a spline fit to the black points. Further shown are the ideal response function $\chi_0(q)$ (solid black), and dielectric approximations in RPA (dotted black) and STLS (solid brown). The bottom panel shows a magnified segment. Reproduced from Ref. [361] with the permission of the authors.
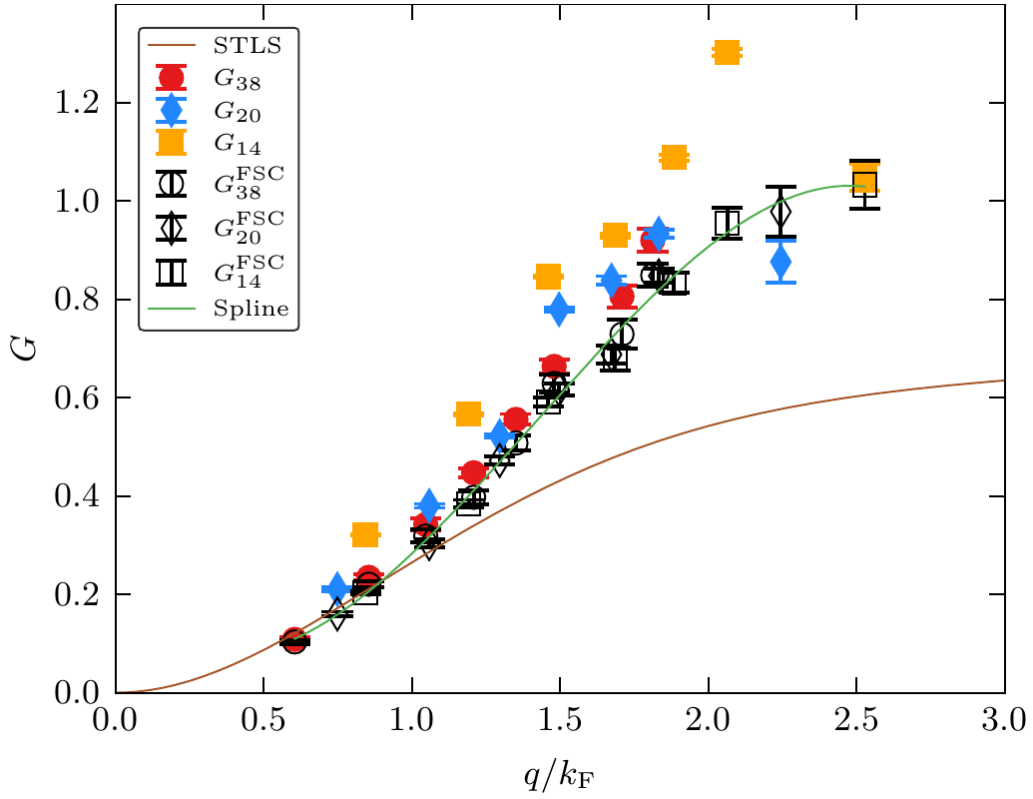
Figure 46: Wave vector dependence of the static local field correction $G(q)$ for the unpolarized electron gas at $\theta = 0.5$ and $r_s = 0.5$. The circles, diamonds, and squares have been obtained from CPIMC calculations with $N = 38$, $N = 20$, and $M = 14$ electrons, respectively. The colored symbols correspond to the results using the ideal response function in the thermodynamic limit [i.e., by replacing in Eq. (185) χ_0^N by χ_0] whereas the black symbols were computed directly from Eq. (185) in a consistent manner by using the ideal response function with the same finite number of electrons as the CPIMC simulations. Reproduced from Ref. [361] with the permission of the authors.

of $G(\mathbf{q})$ on the total density response function, as it becomes the decreasing difference between two almost equal, large numbers, amplified by the factor of q^2. The green line corresponds to a spline fitted to the black symbols and the brown line depicts the local field correction from the STLS formalism. Again, note that the STLS theory does not give the correct asymptotic behavior for G [in contrast to $\chi(\mathbf{q})$] as the compressibility sum-rule is violated, cf. Sec. 3. In addition, we observe increasing deviations between the green and brown curves that start around the Fermi wave vector, k_F, and reach values of the order of 50%. Despite the good quality of STLS data for, e.g., interaction energies and static structure factors, this is not surprising since $G(\mathbf{q})$ constitutes one of the quantities in many-body theory that is most sensitive to exchange-correlation effects. For completeness, we mention that the colored symbols in Fig. 46 were obtained by replacing in Eq. (184) the size-consistent ideal density response function, $\chi_0^N(\mathbf{q})$, by the analogue in the thermodynamic limit, $\chi_0(\mathbf{q})$. This inconsistency results in significantly biased data for the local field correction, which highlights the necessity to use $\chi_0^N(\mathbf{q})$. We point out that the calculation of the latter is surprisingly involved at finite temperature as, to the best of our knowledge, no readily computable expression (such as the usual spectral representation in the ground state) exists. However, a detailed discussion of this issue is beyond the scope of the present work, for a comprehensive analysis, we refer to Ref. [361].

Finally, let us examine the thus finite-size corrected data for the static density response function itself, i.e., the black symbols in Fig. 45. Evidently, no system size dependence can be resolved for $N \geq 14$, over the entire wave vector range. This allows us to construct a smooth spline fit of these data, which is depicted by the solid green line. In addition, we note that even the results obtained from a CPIMC simulation of as few as four electrons exhibit only minor deviations for intermediate q-values. We conclude this discussion with a brief comparison of our new accurate data for the static density response function to dielectric theories, namely the above mentioned RPA and STLS curves. Specifically, all curves (apart from the ideal result) exhibit the correct behavior for the limits $q \to 0$ and $q \to \infty$, as it is expected. Further, neglecting correlation effects causes substantial errors in the RPA results over a broad range of wave vectors, whereas the STLS data exhibit a maximum bias of around one percent between one and two Fermi wave vectors.

10. Summary and Outlook

10.1. Summary and Discussion

The present work has been devoted to the thermodynamic description of the uniform electron gas at warm dense matter conditions – a topic of high current interest in many fields including astrophysics, laser plasmas and material science. Accurate thermodynamic data for these systems are crucial for comparison with experiments and for the development of improved theoretical methods. Of particular importance are such data as input for many-body simulations such as the ubiquitous density functional theory. Our data are also highly valuable as input for other models such as quantum hydrodynamics, e.g. [362, 193], in order to study screening effects and effective potentials, e.g. [363] and transport and wave phenomena. We have discussed a variety of theoretical approaches that are broadly used to compute the static properties of the electron gas, which include the dielectric formalism (Sec. 3), various quantum Monte Carlo methods (Sec. 5), quantum-classical mappings, and finite-temperature Green functions (Sec. 4). Among these approaches, the most accurate results are provided by path integral Monte Carlo (PIMC) calculations (Sec. 5), which, for the UEG, however, are severely limited by the fermion sign problem. For this reason, over the last years, much effort has been undertaken to develop improved fermionic QMC simulations at finite temperature that were reviewed in Sec. 5.2. Particular progress was achieved by the present authors which we summarize in the following:

1. We introduced two novel QMC methods – CPIMC (Configuration PIMC, Sec. 5.5) and PB-PIMC (Permutation blocking PIMC, Sec. 5.4) – that are accurate and efficient in complementary parameter regions.
2. We have demonstrated in detail that the combination of CPIMC and PB-PIMC allows for a highly accurate description of electrons in the warm dense matter regime over the entire density range, down to half the Fermi temperature without the use of uncontrolled approximations such as the fixed node approximation (RPIMC, see Sec. 5.3).
3. Our results have been fully confirmed by a third, independent new method—DMQMC (Density matrix QMC, Sec. 5.6), thereby leading to a consensus regarding the thermodynamic properties of the warm dense UEG for a finite number N of electrons.
4. The next natural step has been the extrapolation of the finite N-simulations to the thermodynamic limit (Sec. 6) – a task that turned out to be surprisingly nontrivial. We have shown that the previously used finite-size correction is not appropriate over substantial parts of the WDM regime. Further, we demonstrated that the major finite-size error is due to the missing long-range contribution, which cannot be accessed directly within QMC simulations of a finite number of electrons in a finite simulation cell.

5. To compensate for this, we combined the exact treatment of short-range exchange-correlation effects from QMC with the dielectric formalism (specifically, with the STLS approximation), that is known to be exact precisely in the long wavelength limit, $q \to 0$. This combination of QMC and STLS data allows (i) for a highly accurate description of the static structure factor, $S(q)$, in the thermodynamic limit over the entire q-range, and (ii) for an improved finite-size correction that is efficient over the entire WDM regime.

6. Applying this scheme, we have performed extensive simulations for a broad parameter range and, thus, obtained the first *ab initio* thermodynamic results for the warm dense UEG in the thermodynamic limit, with an unprecedented accuracy of 0.3%.

7. Using these new data, for the first time, it became possible to benchmark previous approximations, including RPIMC and dielectric methods such as RPA, STLS, and the recent improved HNC-scheme by Tanaka (Sec. 7).

8. For practical applications, we constructed – based on an exhaustive QMC data set – a new parametrization (*GDB parametrization*) of the exchange-correlation free energy of the warm dense UEG with respect to density, temperature, and spin-polarization, i.e., $f_{\mathrm{xc}}(r_s, \theta, \xi)$, that bridges the gap to the well-known ground state limit, see Sec. 8.

9. Based on the new GDB parametrization we performed unambiguous tests of the accuracy and applicatbility limits of earlier parametrizations and fits.

10. Finally, we have outlined strategies how to extend our *ab initio* approach to the *inhomogeneous* electron gas. This was achieved by performing, both, PB-PIMC and the CPIMC simulations for harmonically perturbed systems (Sec. 9).

11. These simulations were utilized to compute the first *ab inito* results for the static density response function, $\chi(q)$, and for the static local field correction, $G(q)$.

Even though the results for the inhomogeneous electron gas are still preliminary they demonstrate that the present approach is very promising. They also demonstrate that accurate QMC data are not only important for the exchange correlation free energy. Of possibly even greater importance is their use for quantities that are derivatives of the free energy that are much more sensitive to incaccuracies. This includes the compressibility and the local field corrections.

10.2. Outlook

A natural extension of our work is given by the thorough investigation of the static density response of the warm dense electron gas as outlined in Sec. 9. Similar to the parametrization of f_{xc}, the construction of a complete parametrization of the static local field correction with respect to density, temperature, and wave vector, $G(\mathbf{q}, r_s, \theta)$, constitutes a highly desirable goal, since it allows, e.g., for the computation of a true nonlocal exchange-correlation functional within the adiabatic connection fluctuation dissipation formulation of density functional theory [339, 337, 338]. Interesting open questions in this direction include the large q-behavior of G and the possible existence of charge- and spin-density waves [1, 251].

A further topic of high importance is the investigation of the *dynamic properties* of warm dense electrons such as the single-particle spectrum [364, 197], $A(\mathbf{q}, \omega)$, the single-particle dispersion, $\omega(\mathbf{q})$, or the density of states. The spectral function $A(\mathbf{q}, \omega)$ is a key quantity of many-body theories such as Matsubara and nonequilibrium Green functions theory, e.g. [365, 195], that are extensively applied to describe the properties of correlated macroscopic systems [366], atoms and molecules [367], Hubbard clusters [368], or ultracold atoms in traps [369]. Unbiased QMC results may play a crucial role to test and improve selfenergy approximations. Moreover, to probe the collective properties of correlated electrons, the dynamic structure factor, $S(\mathbf{q}, \omega)$, plays a key role. It is of particular importance, e.g., for the description of collective excitations of realistic warm dense matter within the Chihara decomposition [370, 112]. Furthermore, the dynamic structure factor is directly linked to other dynamic and optical properties such as the dielectric function or the dynamic conductivity and reflectivity. Also, the dynamic structure factor yields the plasmon spectrum which is an important experimental diagnostic of warm dense matter. For correlated charged particles in traps, the plasmon spectrum transforms into discrete normal modes that contain important information on the state of the system. Of particular importance are the center of mass (dipole or Kohn) mode e.g. [371], and the breathing (monopole) mode [372, 373], and may serve as a diagnostic tool for electrons in quantum dots or ultracold atoms in traps, e.g. [374, 375] and references therein. Here, exact solutions of the Schrödinger equation are limited to a few particles, and QMC may provide the necessary *ab initio results*.

In principle, dynamical properties and spectra of correlated electrons in equilibrium and nonequilibrium can be directly computed via *time-propagation*, as demonstrated with nonequilibrium Green functions in Ref. [358, 376], calling for similar approaches using Monte Carlo methods. Unfortunately, time-dependent QMC simulations are severely hampered by the so-called dynamical sign problem [356, 357] that permits only very short simulations that are not suitable to generate spectra. An alternative strategy is given by the approximate method of moments [377],

where the possibility to include our *ab initio* results for the static structure factor is currently being investigated. In addition, it is straightforward to utilize our QMC methods to compute *imaginary-time correlation functions* [378]. These can be used as the basis for the reconstruction of dynamic quantities [379], such as $S(\mathbf{q}, \omega)$, which is a well established procedure for the investigation of bosons, e.g., Refs. [380, 288, 289]. A particular advantage of this strategy is the exact treatment of correlation effects, which allows to benchmark other approaches including the above mentioned method of moments, (dynamic) RPA and STLS, or the interpolation between various limits proposed by Gregori *et al.* [353]. For completeness, we note that a similar strategy has recently been explored by Motta *et al.* [381, 382] for the $2D$ electron gas in the ground state, and the recent remarkable progress in the field of reconstruction, in general, Refs. [383, 384, 385, 386, 387].

Another important quantity is the *momentum distribution*, $n(k)$, of warm dense matter which is directly accessible experimentally via photoionization of atoms and molecules [388, 389] or photoemission from solids and liquids, e.g. [390]. The tail of $n(k)$ is crucial for impact excitation and ionization processes and directly reflects correlation and quantum effects in the system. Knowledge of the exact large-k asymptotics of $n(k)$ is crucial for accurate predictions of impact excitation and ionization rates of chemical reactions and of nuclear fusion rates in a dense plasma environment, such as in the solar interior [46], in compact stars or in laser fusion experiments. The momentum distribution of the UEG has been extensively investigated at zero temperature, e.g., Refs. [34, 35, 43, 44, 45, 46, 47, 48, 49, 50, 51, 52, 53, 54, 391]. However, at warm dense matter conditions, to our knowledge, no similar studies exist. Due to its formulation in momentum space, the CPIMC method is perfectly suited to compute highly accurate results for the momentum distribution in dense quantum systems.

We further note that, in many ultracompact astrophysical objects such as dwarf stars or neutron stars, densities are so high (small r_s values), that *relativistic effects* become important [207, 208]. For this task, one can extend our CPIMC method to the simulation of the relativistic Hamiltonian of the UEG (i.e., by using the appropriate modified dispersion relation).

Finally, aside from its relevance as a model system in many-body physics and a benchmark tool for approximations and simulations, the warm dense electron gas constitutes the key contribution to real warm dense matter that contains, in addition, heavy particle species. The extension to realistic multi-component simulations can be done in various ways. One is to use the UEG data as an input to finite-temperature DFT simulations. Here the ab initio data for the exchange-correlation free energy of the warm dense electron gas and the analytical parametrization presented in this review are of direct importance. On the other hand, dense two-component plasmas have been successfully investigated by path integral Monte Carlo methods by Ceperley amd Militzer and co-workers (RPIMC), e.g. [164, 135, 86] and by Filinov and co-workers (direct fermionic PIMC), e.g. [392, 127]. The problems analyzed include the thermodynamic functions, the pair distribution functions [393] and proton crystallization at high density [394, 129]. For two-component plasmas, of course, the fermion sign problem is even more severe than for the UEG. So the accuracy of the commonly used fixed node approximation remains to be verified against unbiased methods. A powerful tool for these simulations is the use of effective quantum pair potentials, that incorporate many-body and quantum effects and have been derived by Kelbg [395, 396, 397], Ebeling and co-workers and many others, see e.g. refs. [398, 399] and references therein. Another promising strategy is to extend the coupled electron-ion Monte Carlo method [166] to finite temperatures. Yet the high complexity and the vast parameter space of warm dense matter requires the parallel development of independent theoretical and computational methods that can be used to benchmark one against the other. The present *ab initio* data is expected to be a valuable reference for these developments.

10.3. Open resources

Finally, we mention the paramount value of the UEG as a test bed for the development of simulation techniques, as it requires an accurate treatment of (i) fermionic exchange, (ii) Coulomb correlation, and (iii) thermal excitations at the same time. For this reason, our extensive QMC data set (for various energies and the static structure factor) and the GDB parametrization of the free energy are openly available [400].

Acknowledgements

11. References

References

[1] G. Giuliani, G. Vignale, Quantum Theory of the Electron Liquid, Masters Series in Physics and Astronomy, Cambridge University Press, 2005.
URL https://books.google.de/books?id=kFkIKRfgUpsC

[2] T. Ott, H. Thomsen, J. Abraham, T. Dornheim, M. Bonitz, Recent progress in the theory and simulation of strongly correlated plasmas: phase transitions, transport, quantum, and magnetic field effects, Eur. Phys. J. D (in print).

[3] P.-F. Loos, P. M. W. Gill, The uniform electron gas, Comp. Mol. Sci. 6 (4) (2016) 410–429. doi:10.1002/wcms.1257.
URL http://onlinelibrary.wiley.com/doi/10.1002/wcms.1257/abstract

[4] G. Mahan, Many-Particle Physics, Physics of Solids and Liquids, Springer US, 1990.
URL https://books.google.de/books?id=v8du6cp0vUAC

[5] J. Bardeen, L. N. Cooper, J. R. Schrieffer, Theory of Superconductivity, Phys. Rev. 108 (5) (1957) 1175–1204. doi:10.1103/PhysRev.108.1175.
URL http://link.aps.org/doi/10.1103/PhysRev.108.1175

[6] G. Baym, C. Pethick, Landau Fermi-Liquid Theory: Concepts and Applications, Wiley, 2008.
URL https://books.google.de/books?id=xmiV4YSEjE4C

[7] D. Pines, D. Bohm, A Collective Description of Electron Interactions: II. Collective vs Individual Particle Aspects of the Interactions, Phys. Rev. 85 (2) (1952) 338–353. doi:10.1103/PhysRev.85.338.
URL http://link.aps.org/doi/10.1103/PhysRev.85.338

[8] D. Bohm, D. Pines, A Collective Description of Electron Interactions: III. Coulomb Interactions in a Degenerate Electron Gas, Phys. Rev. 92 (3) (1953) 609–625. doi:10.1103/PhysRev.92.609.
URL http://link.aps.org/doi/10.1103/PhysRev.92.609

[9] K. S. Singwi, M. P. Tosi, R. H. Land, A. Sjölander, Electron Correlations at Metallic Densities, Phys. Rev. 176 (2) (1968) 589–599. doi:10.1103/PhysRev.176.589.
URL http://link.aps.org/doi/10.1103/PhysRev.176.589

[10] P. Vashishta, K. S. Singwi, Electron Correlations at Metallic Densities. V, Phys. Rev. B 6 (3) (1972) 875–887. doi:10.1103/PhysRevB.6.875.
URL http://link.aps.org/doi/10.1103/PhysRevB.6.875

[11] A. A. Kugler, Theory of the local field correction in an electron gas, J. Stat. Phys. 12 (1) (1975) 35–87. doi:10.1007/BF01024183.
URL http://link.springer.com/article/10.1007/BF01024183

[12] A. A. Kugler, Collective modes, damping, and the scattering function in classical liquids, J. Stat. Phys. 8 (2) (1973) 107–153. doi:10.1007/BF01008535.
URL http://link.springer.com/article/10.1007/BF01008535

[13] S. Ichimaru, Strongly coupled plasmas: high-density classical plasmas and degenerate electron liquids, Rev. Mod. Phys. 54 (4) (1982) 1017–1059. doi:10.1103/RevModPhys.54.1017.
URL http://link.aps.org/doi/10.1103/RevModPhys.54.1017

[14] P. Nozieres, D. Pines, Theory Of Quantum Liquids, Advanced Books Classics, Avalon Publishing, 1999.
URL https://books.google.de/books?id=q3wCwaV-gmUC

[15] D. Ceperley, Ground state of the fermion one-component plasma: A Monte Carlo study in two and three dimensions, Phys. Rev. B 18 (7) (1978) 3126–3138. doi:10.1103/PhysRevB.18.3126.
URL http://link.aps.org/doi/10.1103/PhysRevB.18.3126

[16] D. M. Ceperley, B. J. Alder, Ground State of the Electron Gas by a Stochastic Method, Phys. Rev. Lett. 45 (7) (1980) 566. doi:10.1103/PhysRevLett.45.566.
URL http://link.aps.org/doi/10.1103/PhysRevLett.45.566

[17] W. M. C. Foulkes, L. Mitas, R. J. Needs, G. Rajagopal, Quantum Monte Carlo simulations of solids, Rev. Mod. Phys. 73 (1) (2001) 33–83. doi:10.1103/RevModPhys.73.33.
URL http://link.aps.org/doi/10.1103/RevModPhys.73.33

[18] J. J. Shepherd, A. Grüneis, G. H. Booth, G. Kresse, A. Alavi, Convergence of many-body wave-function expansions using a plane-wave basis: From homogeneous electron gas to solid state systems, Phys. Rev. B 86 (3) (2012) 035111. doi:10.1103/PhysRevB.86.035111.
URL http://link.aps.org/doi/10.1103/PhysRevB.86.035111

[19] J. J. Shepherd, G. Booth, A. Grüneis, A. Alavi, Full configuration interaction perspective on the homogeneous electron gas, Phys. Rev. B 85 (8) (2012) 081103. doi:10.1103/PhysRevB.85.081103.
URL http://link.aps.org/doi/10.1103/PhysRevB.85.081103

[20] J. J. Shepherd, G. H. Booth, A. Alavi, Investigation of the full configuration interaction quantum Monte Carlo method using homogeneous electron gas models, J. Chem. Phys. 136 (24) (2012) 244101. doi:10.1063/1.4720076.
URL http://scitation.aip.org/content/aip/journal/jcp/136/24/10.1063/1.4720076

[21] P. López Ríos, A. Ma, N. D. Drummond, M. D. Towler, R. J. Needs, Inhomogeneous backflow transformations in quantum Monte Carlo calculations, Phys. Rev. E 74 (6) (2006) 066701. doi:10.1103/PhysRevE.74.066701.
URL http://link.aps.org/doi/10.1103/PhysRevE.74.066701

[22] M. Holzmann, D. M. Ceperley, C. Pierleoni, K. Esler, Backflow correlations for the electron gas and metallic hydrogen, Phys. Rev. E 68 (4) (2003) 046707. doi:10.1103/PhysRevE.68.046707.
URL http://link.aps.org/doi/10.1103/PhysRevE.68.046707

[23] W. Kohn, L. J. Sham, Self-Consistent Equations Including Exchange and Correlation Effects, Phys. Rev. 140 (4A) (1965) A1133–A1138. doi:10.1103/PhysRev.140.A1133.
URL http://link.aps.org/doi/10.1103/PhysRev.140.A1133

[24] P. Hohenberg, W. Kohn, Inhomogeneous Electron Gas, Phys. Rev. 136 (3B) (1964) B864–B871. doi:10.1103/PhysRev.136.B864.
URL http://link.aps.org/doi/10.1103/PhysRev.136.B864

[25] R. Jones, Density functional theory: Its origins, rise to prominence, and future, Rev. Mod. Phys. 87 (3) (2015) 897–923. doi:10.1103/RevModPhys.87.897.
URL http://link.aps.org/doi/10.1103/RevModPhys.87.897

[26] K. Burke, Perspective on density functional theory, J. Chem. Phys. 136 (15) (2012) 150901. doi:10.1063/1.4704546.
URL http://scitation.aip.org/content/aip/journal/jcp/136/15/10.1063/1.4704546

[27] R. O. Jones, O. Gunnarsson, The density functional formalism, its applications and prospects, Rev. Mod. Phys. 61 (3) (1989) 689–746. doi:10.1103/RevModPhys.61.689.
URL http://link.aps.org/doi/10.1103/RevModPhys.61.689

[28] S. H. Vosko, L. Wilk, M. Nusair, Accurate spin-dependent electron liquid correlation energies for local spin density calculations: a critical analysis, Can. J. Phys. 58 (8) (1980) 1200–1211. doi:10.1139/p80-159.
URL http://www.nrcresearchpress.com/doi/abs/10.1139/p80-159

[29] J. P. Perdew, A. Zunger, Self-interaction correction to density-functional approximations for many-electron systems, Phys. Rev. B 23 (10) (1981) 5048–5079. doi:10.1103/PhysRevB.23.5048.
URL http://link.aps.org/doi/10.1103/PhysRevB.23.5048

[30] T. Chachiyo, Communication: Simple and accurate uniform electron gas correlation energy for the full range of densities, J. Chem. Phys. 145 (2) (2016) 021101. `doi:10.1063/1.4958669`.
URL `http://aip.scitation.org/doi/10.1063/1.4958669`

[31] J. P. Perdew, K. Burke, Y. Wang, Generalized gradient approximation for the exchange-correlation hole of a many-electron system, Phys. Rev. B 54 (23) (1996) 16533–16539. `doi:10.1103/PhysRevB.54.16533`.
URL `https://link.aps.org/doi/10.1103/PhysRevB.54.16533`

[32] J. P. Perdew, K. Burke, M. Ernzerhof, Generalized Gradient Approximation Made Simple, Phys. Rev. Lett. 77 (18) (1996) 3865–3868. `doi:10.1103/PhysRevLett.77.3865`.
URL `http://link.aps.org/doi/10.1103/PhysRevLett.77.3865`

[33] G. Ortiz, P. Ballone, The Correlation Energy of the Spin-Polarized Uniform Electron Gas, Europhys. Lett. 23 (1) (1993) 7. `doi:10.1209/0295-5075/23/1/002`.
URL `http://stacks.iop.org/0295-5075/23/i=1/a=002`

[34] G. Ortiz, P. Ballone, Correlation energy, structure factor, radial distribution function, and momentum distribution of the spin-polarized uniform electron gas, Phys. Rev. B 50 (3) (1994) 1391–1405. `doi:10.1103/PhysRevB.50.1391`.
URL `http://link.aps.org/doi/10.1103/PhysRevB.50.1391`

[35] G. Ortiz, P. Ballone, Erratum: Correlation energy, structure factor, radial distribution function, and momentum distribution of the spin-polarized uniform electron gas [Phys. Rev. B 50, 1391 (1994)], Phys. Rev. B 56 (15) (1997) 9970–9970. `doi:10.1103/PhysRevB.56.9970`.
URL `https://link.aps.org/doi/10.1103/PhysRevB.56.9970`

[36] G. Ortiz, M. Harris, P. Ballone, Zero Temperature Phases of the Electron Gas, Phys. Rev. Lett. 82 (26) (1999) 5317–5320. `doi:10.1103/PhysRevLett.82.5317`.
URL `http://link.aps.org/doi/10.1103/PhysRevLett.82.5317`

[37] N. D. Drummond, Z. Radnai, J. R. Trail, M. D. Towler, R. J. Needs, Diffusion quantum Monte Carlo study of three-dimensional Wigner crystals, Phys. Rev. B 69 (8) (2004) 085116. `doi:10.1103/PhysRevB.69.085116`.
URL `http://link.aps.org/doi/10.1103/PhysRevB.69.085116`

[38] G. G. Spink, R. J. Needs, N. D. Drummond, Quantum Monte Carlo study of the three-dimensional spin-polarized homogeneous electron gas, Phys. Rev. B 88 (8) (2013) 085121. `doi:10.1103/PhysRevB.88.085121`.
URL `http://link.aps.org/doi/10.1103/PhysRevB.88.085121`

[39] A. W. Overhauser, Pair-correlation function of an electron gas, Can. J. Phys. 73 (11-12) (1995) 683–686. `arXiv:https://doi.org/10.1139/p95-101`, `doi:10.1139/p95-101`.
URL `https://doi.org/10.1139/p95-101`

[40] J. P. Perdew, Y. Wang, Pair-distribution function and its coupling-constant average for the spin-polarized electron gas, Phys. Rev. B 46 (20) (1992) 12947–12954. `doi:10.1103/PhysRevB.46.12947`.
URL `http://link.aps.org/doi/10.1103/PhysRevB.46.12947`

[41] P. Gori-Giorgi, F. Sacchetti, G. B. Bachelet, Analytic static structure factors and pair-correlation functions for the unpolarized homogeneous electron gas, Phys. Rev. B 61 (11) (2000) 7353–7363. `doi:10.1103/PhysRevB.61.7353`.
URL `http://link.aps.org/doi/10.1103/PhysRevB.61.7353`

[42] P. Gori-Giorgi, J. P. Perdew, Pair distribution function of the spin-polarized electron gas: A first-principles analytic model for all uniform densities, Phys. Rev. B 66 (16) (2002) 165118. `doi:10.1103/PhysRevB.66.165118`.
URL `http://link.aps.org/doi/10.1103/PhysRevB.66.165118`

[43] M. Holzmann, B. Bernu, C. Pierleoni, J. McMinis, D. M. Ceperley, V. Olevano, L. Delle Site, Momentum Distribution of the Homogeneous Electron Gas, Phys. Rev. Lett. 107 (11) (2011) 110402. `doi:10.1103/PhysRevLett.107.110402`.
URL `http://link.aps.org/doi/10.1103/PhysRevLett.107.110402`

[44] J. C. Kimball, Short-range correlations and the structure factor and momentum distribution of electrons, J. Phys. A 8 (9) (1975) 1513. `doi:10.1088/0305-4470/8/9/021`.
URL `http://stacks.iop.org/0305-4470/8/i=9/a=021`

[45] H. Yasuhara, Y. Kawazoe, A note on the momentum distribution function for an electron gas, Phys. A 85 (2) (1976) 416–424. `doi:10.1016/0378-4371(76)90060-1`.
URL `http://www.sciencedirect.com/science/article/pii/0378437176900601`

[46] A. N. Starostin, A. B. Mironov, N. L. Aleksandrov, N. J. Fisch, R. M. Kulsrud, Quantum corrections to the distribution function of particles over momentum in dense media, Phys. A 305 (12) (2002) 287–296. `doi:10.1016/S0378-4371(01)00677-X`.
URL `http://www.sciencedirect.com/science/article/pii/S037843710100677X`

[47] Y. Takada, H. Yasuhara, Momentum distribution function of the electron gas at metallic densities, Phys. Rev. B 44 (15) (1991) 7879–7887. `doi:10.1103/PhysRevB.44.7879`.
URL `https://link.aps.org/doi/10.1103/PhysRevB.44.7879`

[48] Y. Takada, T. Kita, New self-consistency relation between the correlation energy and the momentum distribution function with application to the one-dimensional hubbard model, J. Phys. Soc. Jpn. 60 (1991) 25.

[49] P. Ziesche, Momentum distribution and structure factors of a high-density homogeneous electron gas from its cumulant two-body reduced density matrix, Phys. Rev. A 86 (1) (2012) 012508. `doi:10.1103/PhysRevA.86.012508`.
URL `http://link.aps.org/doi/10.1103/PhysRevA.86.012508`

[50] P. Ziesche, The high-density electron gas: How momentum distribution $n(k)$ and static structure factor $s(q)$ are mutually related through the off-shell self-energy $\sum(k,\omega)$, Ann. Phys. 522 (10) (2010) 739–765. `doi:10.1002/andp.201000022`.
URL `http://onlinelibrary.wiley.com/doi/10.1002/andp.201000022/abstract`

[51] P. Ziesche, J. Cioslowski, The three-dimensional electron gas at the weak-correlation limit: how peculiarities of the momentum distribution and the static structure factor give rise to logarithmic non-analyticities in the kinetic and potential correlation energies, Phys. A 356 (24) (2005) 598–608. `doi:10.1016/j.physa.2005.04.006`.
URL `http://www.sciencedirect.com/science/article/pii/S0378437105003407`

[52] P. Gori-Giorgi, P. Ziesche, Momentum distribution of the uniform electron gas: Improved parametrization and exact limits of the cumulant expansion, Phys. Rev. B 66 (23) (2002) 235116. `doi:10.1103/PhysRevB.66.235116`.
URL `https://link.aps.org/doi/10.1103/PhysRevB.66.235116`

[53] H. Maebashi, Y. Takada, Analysis of exact vertex function for improving on the GWΓ scheme for first-principles calculation of electron self-energy, Phys. Rev. B 84 (24) (2011) 245134. `doi:10.1103/PhysRevB.84.245134`.
URL `https://link.aps.org/doi/10.1103/PhysRevB.84.245134`

[54] Y. Takada, Emergence of an excitonic collective mode in the dilute electron gas, Phys. Rev. B 94 (24) (2016) 245106. `doi:10.1103/PhysRevB.94.245106`.
URL `http://link.aps.org/doi/10.1103/PhysRevB.94.245106`

[55] S. Moroni, D. M. Ceperley, G. Senatore, Static response from quantum Monte Carlo calculations, Phys. Rev. Lett. 69 (13) (1992) 1837–1840. `doi:10.1103/PhysRevLett.69.1837`.
URL `http://link.aps.org/doi/10.1103/PhysRevLett.69.1837`

[56] S. Moroni, D. M. Ceperley, G. Senatore, Static Response and Local Field Factor of the Electron Gas, Phys. Rev. Lett. 75 (4) (1995) 689–692. `doi:10.1103/PhysRevLett.75.689`.
URL `http://link.aps.org/doi/10.1103/PhysRevLett.75.689`

[57] G. Sugiyama, C. Bowen, B. J. Alder, Static dielectric response of charged bosons, Phys. Rev. B 46 (20) (1992) 13042–13050. `doi:10.1103/PhysRevB.46.13042`.
URL `http://link.aps.org/doi/10.1103/PhysRevB.46.13042`

[58] C. Bowen, G. Sugiyama, B. J. Alder, Static dielectric response of the electron gas, Phys. Rev. B 50 (20) (1994) 14838–14848. `doi:10.1103/PhysRevB.50.14838`.
URL `https://link.aps.org/doi/10.1103/PhysRevB.50.14838`

[59] M. Corradini, R. Del Sole, G. Onida, M. Palummo, Analytical expressions for the local-field factor $G(q)$ and the exchange-correlation kernel $K_{xc}(r)$ of the homogeneous electron gas, Phys. Rev. B 57 (23) (1998) 14569–14571. `doi:10.1103/PhysRevB.57.14569`.
URL `http://link.aps.org/doi/10.1103/PhysRevB.57.14569`

[60] V. E. Fortov, Extreme states of matter on Earth and in space, Phys.-Usp. 52 (6) (2009) 615. `doi:10.3367/UFNe.0179.200906h.0653`.
URL `http://iopscience.iop.org/article/10.3367/UFNe.0179.200906h.0653/meta`

[61] U. S. Department of Energy, Basic research needs for high energy density laboratory physics, https://nnsa.energy.gov/sites/default/files/nnsa/01-13-inlinefiles/Basicoffice of Science and National Nuclear Security Administration (2009).

[62] E. Wigner, On the Interaction of Electrons in Metals, Phys. Rev. 46 (11) (1934) 1002–1011. `doi:10.1103/PhysRev.46.1002`.
URL `https://link.aps.org/doi/10.1103/PhysRev.46.1002`

[63] A. Filinov, M. Bonitz, Y. Lozovik, Wigner Crystallization in Mesoscopic 2d Electron Systems, Phys. Rev. Lett. 86 (17) (2001) 3851–3854. `doi:10.1103/PhysRevLett.86.3851`.
URL `http://link.aps.org/doi/10.1103/PhysRevLett.86.3851`

[64] A. Filinov, Y. Lozovik, M. Bonitz, Path integral simulations of crystallization of quantum confined electrons, phys. stat. sol. (b) 221 (2000) 231.

[65] M. Bonitz, C. Henning, D. Block, Complex plasmas: a laboratory for strong correlations, Reports on Progress in Physics 73 (6) (2010) 066501.
URL `http://stacks.iop.org/0034-4885/73/i=6/a=066501`

[66] F. Graziani, M. Desjarlais, R. Redmer, S. Trickey, Frontiers and Challenges in Warm Dense Matter, Lecture Notes in Computational Science and Engineering, Springer International Publishing, 2014.
URL `https://books.google.de/books?id=Hdm4BAAAQBAJ`

[67] R. Püstow, N. Nettelmann, W. Lorenzen, R. Redmer, H/He demixing and the cooling behavior of Saturn, Icarus 267 (Supplement C) (2016) 323–333. `doi:10.1016/j.icarus.2015.12.009`.
URL `http://www.sciencedirect.com/science/article/pii/S0019103515005606`

[68] N. Nettelmann, R. Püstow, R. Redmer, Saturn layered structure and homogeneous evolution models with different EOSs, Icarus 225 (1) (2013) 548–557. `doi:10.1016/j.icarus.2013.04.018`.
URL `http://www.sciencedirect.com/science/article/pii/S0019103513001784`

[69] N. Nettelmann, K. Wang, J. J. Fortney, S. Hamel, S. Yellamilli, M. Bethkenhagen, R. Redmer, Uranus evolution models with simple thermal boundary layers, Icarus 275 (Supplement C) (2016) 107–116. `doi:10.1016/j.icarus.2016.04.008`.
URL `http://www.sciencedirect.com/science/article/pii/S0019103516300537`

[70] B. Militzer, W. B. Hubbard, J. Vorberger, I. Tamblyn, S. A. Bonev, A Massive Core in Jupiter Predicted from First-Principles Simulations, Astrophys. J. Lett. 688 (1) (2008) L45. `doi:10.1086/594364`.
URL `http://iopscience.iop.org/1538-4357/688/1/L45`

[71] H. F. Wilson, B. Militzer, Sequestration of Noble Gases in Giant Planet Interiors, Phys. Rev. Lett. 104 (12) (2010) 121101. `doi:10.1103/PhysRevLett.104.121101`.
URL `https://link.aps.org/doi/10.1103/PhysRevLett.104.121101`

[72] F. Soubiran, B. Militzer, K. P. Driver, S. Zhang, Properties of hydrogen, helium, and silicon dioxide mixtures in giant planet interiors, Phys. Plasmas 24 (4) (2017) 041401. `doi:10.1063/1.4978618`.
URL `http://aip.scitation.org/doi/abs/10.1063/1.4978618`

[73] J. Vorberger, I. Tamblyn, B. Militzer, S. A. Bonev, Hydrogen-helium mixtures in the interiors of giant planets, Phys. Rev. B 75 (2) (2007) 024206. doi:10.1103/PhysRevB.75.024206.
URL https://link.aps.org/doi/10.1103/PhysRevB.75.024206

[74] J. Vorberger, I. Tamblyn, S. A. Bonev, B. Militzer, Properties of Dense Fluid Hydrogen and Helium in Giant Gas Planets, Contrib. Plasma Phys. 47 (4-5) (2007) 375–380. doi:10.1002/ctpp.200710050.
URL http://onlinelibrary.wiley.com/doi/10.1002/ctpp.200710050/abstract

[75] N. Nettelmann, B. Holst, A. Kietzmann, M. French, R. Redmer, D. Blaschke, Ab Initio Equation of State Data for Hydrogen, Helium, and Water and the Internal Structure of Jupiter, Astrophys. J. 683 (2) (2008) 1217. doi:10.1086/589806.
URL http://stacks.iop.org/0004-637X/683/i=2/a=1217

[76] M. French, T. R. Mattsson, N. Nettelmann, R. Redmer, Equation of state and phase diagram of water at ultrahigh pressures as in planetary interiors, Phys. Rev. B 79 (5) (2009) 054107. doi:10.1103/PhysRevB.79.054107.
URL https://link.aps.org/doi/10.1103/PhysRevB.79.054107

[77] M. D. Knudson, M. P. Desjarlais, R. W. Lemke, T. R. Mattsson, M. French, N. Nettelmann, R. Redmer, Probing the Interiors of the Ice Giants: Shock Compression of Water to 700 GPa and 3.8 g/cm^3, Phys. Rev. Lett. 108 (9) (2012) 091102. doi:10.1103/PhysRevLett.108.091102.
URL http://link.aps.org/doi/10.1103/PhysRevLett.108.091102

[78] D. Saumon, W. B. Hubbard, G. Chabrier, H. M. van Horn, The role of the molecular-metallic transition of hydrogen in the evolution of Jupiter, Saturn, and brown dwarfs, Astrophys. J. 391 (1992) 827–831. doi:10.1086/171391.

[79] W. B. Hubbard, T. Guillot, J. I. Lunine, A. Burrows, D. Saumon, M. S. Marley, R. S. Freedman, Liquid metallic hydrogen and the structure of brown dwarfs and giant planets, Phys. Plasmas 4 (5) (1997) 2011–2015. doi:10.1063/1.872570.
URL http://aip.scitation.org/doi/abs/10.1063/1.872570

[80] G. W. Collins, L. B. D. Silva, P. Celliers, D. M. Gold, M. E. Foord, R. J. Wallace, A. Ng, S. V. Weber, K. S. Budil, R. Cauble, Measurements of the Equation of State of Deuterium at the Fluid Insulator-Metal Transition, Science 281 (5380) (1998) 1178–1181. doi:10.1126/science.281.5380.1178.
URL http://science.sciencemag.org/content/281/5380/1178

[81] S. H. Glenzer, L. B. Fletcher, E. Galtier, B. Nagler, R. Alonso-Mori, B. Barbrel, S. B. Brown, D. A. Chapman, Z. Chen, C. B. Curry, F. Fiuza, E. Gamboa, M. Gauthier, D. O. Gericke, A. Gleason, S. Goede, E. Granados, P. Heimann, J. Kim, D. Kraus, M. J. MacDonald, A. J. Mackinnon, R. Mishra, A. Ravasio, C. Roedel, P. Sperling, W. Schumaker, Y. Y. Tsui, J. Vorberger, U Zastrau, A. Fry, W. E. White, J. B. Hasting, H. J. Lee, Matter under extreme conditions experiments at the Linac Coherent Light Source, J. Phys. B 49 (9) (2016) 092001. doi:10.1088/0953-4075/49/9/092001.
URL http://stacks.iop.org/0953-4075/49/i=9/a=092001

[82] G. Chabrier, P. Brassard, G. Fontaine, D. Saumon, Cooling Sequences and Color-Magnitude Diagrams for Cool White Dwarfs with Hydrogen Atmospheres, Astrophys. J. 543 (1) (2000) 216. doi:10.1086/317092.
URL http://iopscience.iop.org/article/10.1086/317092/meta

[83] J. Daligault, S. Gupta, Electron-Ion Scattering in Dense Multi-Component Plasmas: Application to the Outer Crust of an Accreting Neutron Star, Astrophys. J. 703 (1) (2009) 994. doi:10.1088/0004-637X/703/1/994.
URL http://stacks.iop.org/0004-637X/703/i=1/a=994

[84] P. K. Shukla, B. Eliasson, Colloquium, Rev. Mod. Phys. 83 (3) (2011) 885–906. doi:10.1103/RevModPhys.83.885.
URL https://link.aps.org/doi/10.1103/RevModPhys.83.885

[85] G. Brumfiel, Nuclear weapons physics: Welcome to the Atomic Weapons Establishment, Nature News 464 (7286) (2010) 156–157. doi:10.1038/464156a.
URL http://www.nature.com/news/2010/100310/full/464156a.html

[86] S. X. Hu, B. Militzer, V. N. Goncharov, S. Skupsky, First-principles equation-of-state table of deuterium for inertial confinement fusion applications, Phys. Rev. B 84 (22) (2011) 224109. `doi:10.1103/PhysRevB.84.224109`.
URL `http://link.aps.org/doi/10.1103/PhysRevB.84.224109`

[87] A. L. Kritcher, T. Döppner, C. Fortmann, T. Ma, O. L. Landen, R. Wallace, S. H. Glenzer, In-Flight Measurements of Capsule Shell Adiabats in Laser-Driven Implosions, Phys. Rev. Lett. 107 (1) (2011) 015002. `doi:10.1103/PhysRevLett.107.015002`.
URL `http://link.aps.org/doi/10.1103/PhysRevLett.107.015002`

[88] M. Gomez, S. Slutz, A. Sefkow, D. Sinars, K. Hahn, S. Hansen, E. Harding, P. Knapp, P. Schmit, C. Jennings, T. Awe, M. Geissel, D. Rovang, G. Chandler, G. Cooper, M. Cuneo, A. Harvey-Thompson, M. Herrmann, M. Hess, O. Johns, D. Lamppa, M. Martin, R. McBride, K. Peterson, J. Porter, G. Robertson, G. Rochau, C. Ruiz, M. Savage, I. Smith, W. Stygar, R. Vesey, Experimental Demonstration of Fusion-Relevant Conditions in Magnetized Liner Inertial Fusion, Phys. Rev. Lett. 113 (15) (2014) 155003. `doi:10.1103/PhysRevLett.113.155003`.
URL `http://link.aps.org/doi/10.1103/PhysRevLett.113.155003`

[89] P. Schmit, P. Knapp, S. Hansen, M. Gomez, K. Hahn, D. Sinars, K. Peterson, S. Slutz, A. Sefkow, T. Awe, E. Harding, C. Jennings, G. Chandler, G. Cooper, M. Cuneo, M. Geissel, A. Harvey-Thompson, M. Herrmann, M. Hess, O. Johns, D. Lamppa, M. Martin, R. McBride, J. Porter, G. Robertson, G. Rochau, D. Rovang, C. Ruiz, M. Savage, I. Smith, W. Stygar, R. Vesey, Understanding Fuel Magnetization and Mix Using Secondary Nuclear Reactions in Magneto-Inertial Fusion, Phys. Rev. Lett. 113 (15) (2014) 155004. `doi:10.1103/PhysRevLett.113.155004`.
URL `http://link.aps.org/doi/10.1103/PhysRevLett.113.155004`

[90] R. Nora, W. Theobald, R. Betti, F. Marshall, D. Michel, W. Seka, B. Yaakobi, M. Lafon, C. Stoeckl, J. Delettrez, A. Solodov, A. Casner, C. Reverdin, X. Ribeyre, A. Vallet, J. Peebles, F. Beg, M. Wei, Gigabar Spherical Shock Generation on the OMEGA Laser, Phys. Rev. Lett. 114 (4) (2015) 045001. `doi:10.1103/PhysRevLett.114.045001`.
URL `http://link.aps.org/doi/10.1103/PhysRevLett.114.045001`

[91] O. A. Hurricane, D. A. Callahan, D. T. Casey, E. L. Dewald, T. R. Dittrich, T. Döppner, S. Haan, D. E. Hinkel, L. F. Berzak Hopkins, O. Jones, A. L. Kritcher, S. Le Pape, T. Ma, A. G. MacPhee, J. L. Milovich, J. Moody, A. Pak, H.-S. Park, P. K. Patel, J. E. Ralph, H. F. Robey, J. S. Ross, J. D. Salmonson, B. K. Spears, P. T. Springer, R. Tommasini, F. Albert, L. R. Benedetti, R. Bionta, E. Bond, D. K. Bradley, J. Caggiano, P. M. Celliers, C. Cerjan, J. A. Church, R. Dylla-Spears, D. Edgell, M. J. Edwards, D. Fittinghoff, M. A. Barrios Garcia, A. Hamza, R. Hatarik, H. Herrmann, M. Hohenberger, D. Hoover, J. L. Kline, G. Kyrala, B. Kozioziemski, G. Grim, J. E. Field, J. Frenje, N. Izumi, M. Gatu Johnson, S. F. Khan, J. Knauer, T. Kohut, O. Landen, F. Merrill, P. Michel, A. Moore, S. R. Nagel, A. Nikroo, T. Parham, R. R. Rygg, D. Sayre, M. Schneider, D. Shaughnessy, D. Strozzi, R. P. J. Town, D. Turnbull, P. Volegov, A. Wan, K. Widmann, C. Wilde, C. Yeamans, Inertially confined fusion plasmas dominated by alpha-particle self-heating, Nat. Phys. advance online publication. `doi:10.1038/nphys3720`.
URL `http://www.nature.com/nphys/journal/vaop/ncurrent/full/nphys3720.html`

[92] E. I. Moses, R. N. Boyd, B. A. Remington, C. J. Keane, R. Al-Ayat, The National Ignition Facility: Ushering in a new age for high energy density science, Phys. Plasmas 16 (4) (2009) 041006. `doi:10.1063/1.3116505`.
URL `http://aip.scitation.org/doi/abs/10.1063/1.3116505`

[93] B. A. Hammel, S. W. Haan, D. S. Clark, M. J. Edwards, S. H. Langer, M. M. Marinak, M. V. Patel, J. D. Salmonson, H. A. Scott, High-mode Rayleigh-Taylor growth in NIF ignition capsules, High Energy Density Phys. 6 (2) (2010) 171–178. `doi:10.1016/j.hedp.2009.12.005`.
URL `http://www.sciencedirect.com/science/article/pii/S1574181809001323`

[94] S. Root, R. J. Magyar, J. H. Carpenter, D. L. Hanson, T. R. Mattsson, Shock Compression of a Fifth Period Element: Liquid Xenon to 840 GPa, Phys. Rev. Lett. 105 (8) (2010) 085501. `doi:10.1103/PhysRevLett.105.085501`.
URL `https://link.aps.org/doi/10.1103/PhysRevLett.105.085501`

[95] M. D. Knudson, D. L. Hanson, J. E. Bailey, C. A. Hall, J. R. Asay, Use of a Wave Reverberation Technique to Infer the Density Compression of Shocked Liquid Deuterium to 75 GPa, Phys. Rev. Lett. 90 (3) (2003) 035505. `doi:10.1103/PhysRevLett.90.035505`.
URL `https://link.aps.org/doi/10.1103/PhysRevLett.90.035505`

[96] M. D. Knudson, M. P. Desjarlais, A. Becker, R. W. Lemke, K. R. Cochrane, M. E. Savage, D. E. Bliss, T. R. Mattsson, R. Redmer, Direct observation of an abrupt insulator-to-metal transition in dense liquid deuterium, Science 348 (6242) (2015) 1455–1460. `doi:10.1126/science.aaa7471`.
URL `http://science.sciencemag.org/content/348/6242/1455`

[97] M. K. Matzen, M. A. Sweeney, R. G. Adams, J. R. Asay, J. E. Bailey, G. R. Bennett, D. E. Bliss, D. D. Bloomquist, T. A. Brunner, R. B. Campbell, G. A. Chandler, C. A. Coverdale, M. E. Cuneo, J.-P. Davis, C. Deeney, M. P. Desjarlais, G. L. Donovan, C. J. Garasi, T. A. Haill, C. A. Hall, D. L. Hanson, M. J. Hurst, B. Jones, M. D. Knudson, R. J. Leeper, R. W. Lemke, M. G. Mazarakis, D. H. McDaniel, T. A. Mehlhorn, T. J. Nash, C. L. Olson, J. L. Porter, P. K. Rambo, S. E. Rosenthal, G. A. Rochau, L. E. Ruggles, C. L. Ruiz, T. W. L. Sanford, J. F. Seamen, D. B. Sinars, S. A. Slutz, I. C. Smith, K. W. Struve, W. A. Stygar, R. A. Vesey, E. A. Weinbrecht, D. F. Wenger, E. P. Yu, Pulsed-power-driven high energy density phys. and inertial confinement fusion research, Phys. Plasmas 12 (5) (2005) 055503. `doi:10.1063/1.1891746`.
URL `http://aip.scitation.org/doi/10.1063/1.1891746`

[98] R. Magyar, Equations of state of mixtures: Density functional theory (DFT) simulations and experiments on Sandia's z machine, AIP Conf. Proc. 1426 (1) (2012) 1195–1198. `doi:10.1063/1.3686494`.
URL `http://aip.scitation.org/doi/abs/10.1063/1.3686494`

[99] Y. Ding, A. Brachmann, F.-J. Decker, D. Dowell, P. Emma, J. Frisch, S. Gilevich, G. Hays, P. Hering, Z. Huang, R. Iverson, H. Loos, A. Miahnahri, H.-D. Nuhn, D. Ratner, J. Turner, J. Welch, W. White, J. Wu, Measurements and Simulations of Ultralow Emittance and Ultrashort Electron Beams in the Linac Coherent Light Source, Phys. Rev. Lett. 102 (25) (2009) 254801. `doi:10.1103/PhysRevLett.102.254801`.
URL `https://link.aps.org/doi/10.1103/PhysRevLett.102.254801`

[100] L. B. Fletcher, H. J. Lee, T. Döppner, E. Galtier, B. Nagler, P. Heimann, C. Fortmann, S. LePape, T. Ma, M. Millot, A. Pak, D. Turnbull, D. A. Chapman, D. O. Gericke, J. Vorberger, T. White, G. Gregori, M. Wei, B. Barbrel, R. W. Falcone, C.-C. Kao, H. Nuhn, J. Welch, U. Zastrau, P. Neumayer, J. B. Hastings, S. H. Glenzer, Ultrabright X-ray laser scattering for dynamic warm dense matter physics, Nat. Photonics 9 (4) (2015) 274–279. `doi:10.1038/nphoton.2015.41`.
URL `https://www.nature.com/nphoton/journal/v9/n4/abs/nphoton.2015.41.html`

[101] P. Sperling, E. Gamboa, H. Lee, H. Chung, E. Galtier, Y. Omarbakiyeva, H. Reinholz, G. Röpke, U. Zastrau, J. Hastings, L. Fletcher, S. Glenzer, Free-Electron X-Ray Laser Measurements of Collisional-Damped Plasmons in Isochorically Heated Warm Dense Matter, Phys. Rev. Lett. 115 (11) (2015) 115001. `doi:10.1103/PhysRevLett.115.115001`.
URL `http://link.aps.org/doi/10.1103/PhysRevLett.115.115001`

[102] U. Zastrau, P. Sperling, M. Harmand, A. Becker, T. Bornath, R. Bredow, S. Dziarzhytski, T. Fennel, L. Fletcher, E. Förster, S. Göde, G. Gregori, V. Hilbert, D. Hochhaus, B. Holst, T. Laarmann, H. Lee, T. Ma, J. Mithen, R. Mitzner, C. Murphy, M. Nakatsutsumi, P. Neumayer, A. Przystawik, S. Roling, M. Schulz, B. Siemer, S. Skruszewicz, J. Tiggesbäumker, S. Toleikis, T. Tschentscher, T. White, M. Wöstmann, H. Zacharias, T. Döppner, S. Glenzer, R. Redmer, Resolving Ultrafast Heating of Dense Cryogenic Hydrogen, Phys. Rev. Lett. 112 (10) (2014) 105002. `doi:10.1103/PhysRevLett.112.105002`.
URL `https://link.aps.org/doi/10.1103/PhysRevLett.112.105002`

[103] T. Tschentscher, C. Bressler, J. Grünert, A. Madsen, A. P. Mancuso, M. Meyer, A. Scherz, H. Sinn, U. Zastrau, Photon Beam Transport and Scientific Instruments at the European XFEL, Appl. Sci. 7 (6) (2017) 592. `doi:10.3390/app7060592`.
URL `http://www.mdpi.com/2076-3417/7/6/592`

[104] V. E. Fortov, R. I. Ilkaev, V. A. Arinin, V. V. Burtzev, V. A. Golubev, I. L. Iosilevskiy, V. V. Khrustalev, A. L. Mikhailov, M. A. Mochalov, V. Y. Ternovoi, M. V. Zhernokletov, Phase Transition in a Strongly Nonideal Deuterium Plasma Generated by Quasi-Isentropical Compression at Megabar Pressures, Phys. Rev. Lett. 99 (18) (2007) 185001. `doi:10.1103/PhysRevLett.99.185001`.
URL `https://link.aps.org/doi/10.1103/PhysRevLett.99.185001`

[105] V. E. Fortov, I. V. Lomonosov, Shock waves and equations of state of matter, Shock Waves 20 (1) (2010) 53–71. doi:10.1007/s00193-009-0224-8.
URL https://link.springer.com/article/10.1007/s00193-009-0224-8

[106] S. H. Glenzer, O. L. Landen, P. Neumayer, R. W. Lee, K. Widmann, S. W. Pollaine, R. J. Wallace, G. Gregori, A. Höll, T. Bornath, R. Thiele, V. Schwarz, W.-D. Kraeft, R. Redmer, Observations of Plasmons in Warm Dense Matter, Phys. Rev. Lett. 98 (6) (2007) 065002. doi:10.1103/PhysRevLett.98.065002.
URL https://link.aps.org/doi/10.1103/PhysRevLett.98.065002

[107] C. Fortmann, C. Niemann, S. H. Glenzer, Theory of x-ray scattering in high-pressure electrides, Phys. Rev. B 86 (17) (2012) 174116. doi:10.1103/PhysRevB.86.174116.
URL https://link.aps.org/doi/10.1103/PhysRevB.86.174116

[108] J. Clerouin, G. Robert, P. Arnault, C. Ticknor, J. D. Kress, L. A. Collins, Evidence for out-of-equilibrium states in warm dense matter probed by x-ray Thomson scattering, Phys. Rev. E 91 (1) (2015) 011101. doi:10.1103/PhysRevE.91.011101.
URL https://link.aps.org/doi/10.1103/PhysRevE.91.011101

[109] A. L. Kritcher, P. Neumayer, J. Castor, T. Döppner, R. W. Falcone, O. L. Landen, H. J. Lee, R. W. Lee, E. C. Morse, A. Ng, S. Pollaine, D. Price, S. H. Glenzer, Ultrafast X-ray Thomson Scattering of Shock-Compressed Matter, Science 322 (5898) (2008) 69–71. doi:10.1126/science.1161466.
URL http://science.sciencemag.org/content/322/5898/69

[110] D. Kraus, A. Ravasio, M. Gauthier, D. O. Gericke, J. Vorberger, S. Frydrych, J. Helfrich, L. B. Fletcher, G. Schaumann, B. Nagler, B. Barbrel, B. Bachmann, E. J. Gamboa, S. Göde, E. Granados, G. Gregori, H. J. Lee, P. Neumayer, W. Schumaker, T. Döppner, R. W. Falcone, S. H. Glenzer, M. Roth, Nanosecond formation of diamond and lonsdaleite by shock compression of graphite, Nat. Commun. 7. doi:10.1038/ncomms10970.
URL https://www.ncbi.nlm.nih.gov/pmc/articles/PMC4793081/

[111] P. Davis, T. Döppner, J. R. Rygg, C. Fortmann, L. Divol, A. Pak, L. Fletcher, A. Becker, B. Holst, P. Sperling, R. Redmer, M. P. Desjarlais, P. Celliers, G. W. Collins, O. L. Landen, R. W. Falcone, S. H. Glenzer, X-ray scattering measurements of dissociation-induced metallization of dynamically compressed deuterium, Nat. Commun. 7. doi:10.1038/ncomms11189.
URL https://www.ncbi.nlm.nih.gov/pmc/articles/PMC4835540/

[112] S. H. Glenzer, R. Redmer, X-ray Thomson scattering in high energy density plasmas, Rev. Mod. Phys. 81 (4) (2009) 1625–1663. doi:10.1103/RevModPhys.81.1625.
URL http://link.aps.org/doi/10.1103/RevModPhys.81.1625

[113] A. Ng, Outstanding questions in electron–ion energy relaxation, lattice stability, and dielectric function of warm dense matter, Int. J. Quantum Chem. 112 (1) (2012) 150–160. doi:10.1002/qua.23197.
URL http://onlinelibrary.wiley.com/doi/10.1002/qua.23197/abstract

[114] Y. Ping, D. Hanson, I. Koslow, T. Ogitsu, D. Prendergast, E. Schwegler, G. Collins, A. Ng, Broadband Dielectric Function of Nonequilibrium Warm Dense Gold, Phys. Rev. Lett. 96 (25) (2006) 255003. doi:10.1103/PhysRevLett.96.255003.
URL https://link.aps.org/doi/10.1103/PhysRevLett.96.255003

[115] A. Ng, P. Sterne, S. Hansen, V. Recoules, Z. Chen, Y. Y. Tsui, B. Wilson, dc conductivity of two-temperature warm dense gold, Phys. Rev. E 94 (3) (2016) 033213. doi:10.1103/PhysRevE.94.033213.
URL https://link.aps.org/doi/10.1103/PhysRevE.94.033213

[116] Y. Ping, A. Fernandez-Panella, H. Sio, A. Correa, R. Shepherd, O. Landen, R. A. London, P. A. Sterne, H. D. Whitley, D. Fratanduono, T. R. Boehly, G. W. Collins, Differential heating: A versatile method for thermal conductivity measurements in high-energy-density matter, Phys. Plasmas 22 (9) (2015) 092701. doi:10.1063/1.4929797.
URL http://aip.scitation.org/doi/10.1063/1.4929797

[117] Z. Chen, B. Holst, S. E. Kirkwood, V. Sametoglu, M. Reid, Y. Y. Tsui, V. Recoules, A. Ng, Evolution of ac Conductivity in Nonequilibrium Warm Dense Gold, Phys. Rev. Lett. 110 (13) (2013) 135001. doi:10.1103/PhysRevLett.110.135001.
URL https://link.aps.org/doi/10.1103/PhysRevLett.110.135001

[118] Z. Chen, P. Hering, S. B. Brown, C. Curry, Y. Y. Tsui, S. H. Glenzer, A single-shot spatial chirp method for measuring initial AC conductivity evolution of femtosecond laser pulse excited warm dense matter, Rev. Sci. Instrum. 87 (11) (2016) 11E548. doi:10.1063/1.4962057.
URL http://aip.scitation.org/doi/10.1063/1.4962057

[119] N. J. Hartley, P. Belancourt, D. A. Chapman, T. Döppner, R. P. Drake, D. O. Gericke, S. H. Glenzer, D. Khaghani, S. LePape, T. Ma, P. Neumayer, A. Pak, L. Peters, S. Richardson, J. Vorberger, T. G. White, G. Gregori, Electron-ion temperature equilibration in warm dense tantalum, High Energy Density Phys. 14 (Supplement C) (2015) 1–5. doi:10.1016/j.hedp.2014.10.003.
URL http://www.sciencedirect.com/science/article/pii/S1574181814000639

[120] R. Ernstorfer, M. Harb, C. T. Hebeisen, G. Sciaini, T. Dartigalongue, R. J. D. Miller, The Formation of Warm Dense Matter: Experimental Evidence for Electronic Bond Hardening in Gold, Science 323 (5917) (2009) 1033–1037. doi:10.1126/science.1162697.
URL http://www.sciencemag.org/content/323/5917/1033

[121] W. Ebeling, V. Fortov, V. Filinov, Quantum Statistics of Dense Gases and Nonideal Plasmas, Springer Series in Plasma Science and Technology, Springer, 2017.

[122] A. W. DeSilva, J. D. Katsouros, Electrical conductivity of dense copper and aluminum plasmas, Phys. Rev. E 57 (5) (1998) 5945–5951. doi:10.1103/PhysRevE.57.5945.
URL https://link.aps.org/doi/10.1103/PhysRevE.57.5945

[123] A. N. Mostovych, Y. Chan, Reflective Probing of the Electrical Conductivity of Hot Aluminum in the Solid, Liquid, and Plasma Phases, Phys. Rev. Lett. 79 (25) (1997) 5094–5097. doi:10.1103/PhysRevLett.79.5094.
URL https://link.aps.org/doi/10.1103/PhysRevLett.79.5094

[124] V. S. Filinov, Construction of a Monte-Carlo method for calculating Feynman integrals, USSR Comput. Math. Math. Phys. 26 (1) (1986) 21–29. doi:10.1016/0041-5553(86)90176-X.
URL http://www.sciencedirect.com/science/article/pii/004155538690176X

[125] V. S. Filinov, M. Bonitz, W. Ebeling, V. E. Fortov, Thermodynamics of hot dense H-plasmas: path integral Monte Carlo simulations and analytical approximations, Plasma Phys. Contr. Fusion 43 (6) (2001) 743. doi:10.1088/0741-3335/43/6/301.
URL http://stacks.iop.org/0741-3335/43/i=6/a=301

[126] V. S. Filinov, V. E. Fortov, M. Bonitz, P. R. Levashov, Phase transition in strongly degenerate hydrogen plasma, JETP Lett. 74 (7) (2001) 384–387. doi:10.1134/1.1427127.
URL http://link.springer.com/article/10.1134/1.1427127

[127] V. S. Filinov, M. Bonitz, V. E. Fortov, W. Ebeling, P. Levashov, M. Schlanges, Thermodynamic Properties and Plasma Phase Transition in dense Hydrogen, Contrib. Plasma Phys. 44 (5-6) (2004) 388–394. doi:10.1002/ctpp.200410057.
URL http://onlinelibrary.wiley.com/doi/10.1002/ctpp.200410057/abstract

[128] V. S. Filinov, H. Fehske, M. Bonitz, V. E. Fortov, P. Levashov, Correlation effects in partially ionized mass asymmetric electron-hole plasmas, Phys. Rev. E 75 (3) (2007) 036401. doi:10.1103/PhysRevE.75.036401.
URL http://link.aps.org/doi/10.1103/PhysRevE.75.036401

[129] V. S. Filinov, M. Bonitz, H. Fehske, V. E. Fortov, P. R. Levashov, Proton Crystallization in a Dense Hydrogen Plasma, Contrib. Plasma Phys. 52 (3) (2012) 224–228. doi:10.1002/ctpp.201100085.
URL http://onlinelibrary.wiley.com/doi/10.1002/ctpp.201100085/abstract

[130] V. S. Filinov, V. E. Fortov, M. Bonitz, Z. Moldabekov, Fermionic path-integral Monte Carlo results for the uniform electron gas at finite temperature, Phys. Rev. E 91 (3) (2015) 033108. doi:10.1103/PhysRevE.91.033108.
URL http://link.aps.org/doi/10.1103/PhysRevE.91.033108

[131] V. Filinov, M. Bonitz, Y. Ivanov, E.-M. Ilgenfritz, V. Fortov, Thermodynamics of the Quark-Gluon Plasma at Finite Chemical Potential: Color Path Integral Monte Carlo Results, Contrib. Plasma Phys. 55 (2-3) (2015) 203–208. doi:10.1002/ctpp.201400056.
URL http://onlinelibrary.wiley.com/doi/10.1002/ctpp.201400056/abstract

[132] V. S. Filinov, V. E. Fortov, M. Bonitz, Z. Moldabekov, Total and correlation energy of the uniform polarized electron gas at finite temperature: Direct path integral simulations, J. Phys. Conf. Ser. 653 (1) (2015) 012113. doi:10.1088/1742-6596/653/1/012113.
URL http://stacks.iop.org/1742-6596/653/i=1/a=012113

[133] D. M. Ceperley, Fermion nodes, J. Stat. Phys. 63 (5-6) (1991) 1237–1267. doi:10.1007/BF01030009.
URL http://link.springer.com/10.1007/BF01030009

[134] D. M. Ceperley, Path-integral calculations of normal liquid ^{3}He, Phys. Rev. Lett. 69 (2) (1992) 331–334. doi:10.1103/PhysRevLett.69.331.
URL http://link.aps.org/doi/10.1103/PhysRevLett.69.331

[135] B. Militzer, D. M. Ceperley, Path Integral Monte Carlo Calculation of the Deuterium Hugoniot, Phys. Rev. Lett. 85 (9) (2000) 1890–1893. doi:10.1103/PhysRevLett.85.1890.
URL http://link.aps.org/doi/10.1103/PhysRevLett.85.1890

[136] N. D. Mermin, Thermal Properties of the Inhomogeneous Electron Gas, Phys. Rev. 137 (5A) (1965) A1441–A1443. doi:10.1103/PhysRev.137.A1441.
URL http://link.aps.org/doi/10.1103/PhysRev.137.A1441

[137] U. Gupta, A. K. Rajagopal, Density functional formalism at finite temperatures with some applications, Phys. Rep. 87 (6) (1982) 259–311. doi:10.1016/0370-1573(82)90077-1.
URL http://www.sciencedirect.com/science/article/pii/0370157382900771

[138] A. Pribram-Jones, S. Pittalis, E. K. U. Gross, K. Burke, Thermal Density Functional Theory in Context, Springer International Publishing, Cham, 2014, pp. 25–60. doi:10.1007/978-3-319-04912-0_2.
URL https://doi.org/10.1007/978-3-319-04912-0_2

[139] P. Balbuena, J. Seminario, Molecular Dynamics: From Classical to Quantum Methods, Theoretical and Computational Chemistry, Elsevier Science, 1999.
URL https://books.google.de/books?id=dpgXPzTLSpYC

[140] M. P. Desjarlais, Density-functional calculations of the liquid deuterium Hugoniot, reshock, and reverberation timing, Phys. Rev. B 68 (6) (2003) 064204. doi:10.1103/PhysRevB.68.064204.
URL https://link.aps.org/doi/10.1103/PhysRevB.68.064204

[141] B. Holst, R. Redmer, M. P. Desjarlais, Thermophysical properties of warm dense hydrogen using quantum molecular dynamics simulations, Phys. Rev. B 77 (18) (2008) 184201. doi:10.1103/PhysRevB.77.184201.
URL http://link.aps.org/doi/10.1103/PhysRevB.77.184201

[142] B. Holst, M. French, R. Redmer, Electronic transport coefficients from ab initio simulations and application to dense liquid hydrogen, Phys. Rev. B 83 (23) (2011) 235120. doi:10.1103/PhysRevB.83.235120.
URL http://link.aps.org/doi/10.1103/PhysRevB.83.235120

[143] B. Witte, L. Fletcher, E. Galtier, E. Gamboa, H. Lee, U. Zastrau, R. Redmer, S. Glenzer, P. Sperling, Warm Dense Matter Demonstrating Non-Drude Conductivity from Observations of Nonlinear Plasmon Damping, Phys. Rev. Lett. 118 (22) (2017) 225001. doi:10.1103/PhysRevLett.118.225001.
URL https://link.aps.org/doi/10.1103/PhysRevLett.118.225001

[144] R. C. Clay, J. Mcminis, J. M. McMahon, C. Pierleoni, D. M. Ceperley, M. A. Morales, Benchmarking exchange-correlation functionals for hydrogen at high pressures using quantum Monte Carlo, Phys. Rev. B 89 (18) (2014) 184106. doi:10.1103/PhysRevB.89.184106.
URL http://link.aps.org/doi/10.1103/PhysRevB.89.184106

[145] R. C. Clay, M. Holzmann, D. M. Ceperley, M. A. Morales, Benchmarking density functionals for hydrogen-helium mixtures with quantum Monte Carlo: Energetics, pressures, and forces, Phys. Rev. B 93 (3) (2016) 035121. doi:10.1103/PhysRevB.93.035121.
URL http://link.aps.org/doi/10.1103/PhysRevB.93.035121

[146] V. V. Karasiev, L. Calderín, S. B. Trickey, Importance of finite-temperature exchange correlation for warm dense matter calculations, Phys. Rev. E 93 (6) (2016) 063207. doi:10.1103/PhysRevE.93.063207.
URL http://link.aps.org/doi/10.1103/PhysRevE.93.063207

[147] M. W. C. Dharma-wardana, Current Issues in Finite-T Density-Functional Theory and Warm-Correlated Matter, Computation 4 (2) (2016) 16. doi:10.3390/computation4020016.
URL http://www.mdpi.com/2079-3197/4/2/16

[148] A. Pribram-Jones, D. A. Gross, K. Burke, DFT: A Theory Full of Holes?, Annu. Rev. Phys. Chem. 66 (1) (2015) 283–304. doi:10.1146/annurev-physchem-040214-121420.
URL https://doi.org/10.1146/annurev-physchem-040214-121420

[149] K. P. Driver, B. Militzer, All-Electron Path Integral Monte Carlo Simulations of Warm Dense Matter: Application to Water and Carbon Plasmas, Phys. Rev. Lett. 108 (11) (2012) 115502. doi:10.1103/PhysRevLett.108.115502.
URL http://link.aps.org/doi/10.1103/PhysRevLett.108.115502

[150] B. Militzer, K. P. Driver, Development of Path Integral Monte Carlo Simulations with Localized Nodal Surfaces for Second-Row Elements, Phys. Rev. Lett. 115 (17) (2015) 176403. doi:10.1103/PhysRevLett.115.176403.
URL http://link.aps.org/doi/10.1103/PhysRevLett.115.176403

[151] K. P. Driver, B. Militzer, First-principles equation of state calculations of warm dense nitrogen, Phys. Rev. B 93 (6) (2016) 064101. doi:10.1103/PhysRevB.93.064101.
URL https://link.aps.org/doi/10.1103/PhysRevB.93.064101

[152] S. Zhang, K. P. Driver, F. Soubiran, B. Militzer, First-principles equation of state and shock compression predictions of warm dense hydrocarbons, Phys. Rev. E 96 (1) (2017) 013204. doi:10.1103/PhysRevE.96.013204.
URL https://link.aps.org/doi/10.1103/PhysRevE.96.013204

[153] K. P. Driver, F. Soubiran, S. Zhang, B. Militzer, Comparison of path integral Monte Carlo simulations of helium, carbon, nitrogen, oxygen, water, neon, and silicon plasmas, High Energy Density Phys. 23 (2017) 81–89. doi:10.1016/j.hedp.2017.03.003.
URL https://www.sciencedirect.com/science/article/pii/S1574181817300228

[154] K. P. Driver, B. Militzer, First-principles simulations of warm dense lithium fluoride, Phys. Rev. E 95 (4) (2017) 043205. doi:10.1103/PhysRevE.95.043205.
URL https://link.aps.org/doi/10.1103/PhysRevE.95.043205

[155] F. Lambert, J. Clérouin, S. Mazevet, Structural and dynamical properties of hot dense matter by a Thomas-Fermi-Dirac molecular dynamics, Europhys. Lett. 75 (5) (2006) 681. doi:10.1209/epl/i2006-10184-7.
URL http://iopscience.iop.org/article/10.1209/epl/i2006-10184-7/meta

[156] F. Lambert, J. Clérouin, S. Mazevet, D. Gilles, Properties of Hot Dense Plasmas by Orbital-Free Molecular Dynamics, Contrib. Plasma Phys. 47 (4-5) (2007) 272–280. doi:10.1002/ctpp.200710037.
URL http://onlinelibrary.wiley.com/doi/10.1002/ctpp.200710037/abstract

[157] V. V. Karasiev, T. Sjostrom, S. B. Trickey, Generalized-gradient-approximation noninteracting free-energy functionals for orbital-free density functional calculations, Phys. Rev. B 86 (11) (2012) 115101. doi:10.1103/PhysRevB.86.115101.
URL http://link.aps.org/doi/10.1103/PhysRevB.86.115101

[158] T. Sjostrom, J. Daligault, Fast and Accurate Quantum Molecular Dynamics of Dense Plasmas Across Temperature Regimes, Phys. Rev. Lett. 113 (15) (2014) 155006. doi:10.1103/PhysRevLett.113.155006.
URL http://link.aps.org/doi/10.1103/PhysRevLett.113.155006

[159] V. V. Karasiev, T. Sjostrom, S. B. Trickey, Finite-temperature orbital-free DFT molecular dynamics: Coupling Profess and Quantum Espresso, Comp. Phys. Comm. 185 (12) (2014) 3240–3249. doi:10.1016/j.cpc.2014.08.023.
URL http://www.sciencedirect.com/science/article/pii/S001046551400304X

[160] C. Gao, S. Zhang, W. Kang, C. Wang, P. Zhang, X. T. He, Validity boundary of orbital-free molecular dynamics method corresponding to thermal ionization of shell structure, Phys. Rev. B 94 (20) (2016) 205115. doi:10.1103/PhysRevB.94.205115.
URL http://link.aps.org/doi/10.1103/PhysRevB.94.205115

[161] J. W. Dufty, S. B. Trickey, Scaling, bounds, and inequalities for the noninteracting density functionals at finite temperature, Phys. Rev. B 84 (12) (2011) 125118. `doi:10.1103/PhysRevB.84.125118`.
URL `https://link.aps.org/doi/10.1103/PhysRevB.84.125118`

[162] S. Zhang, S. Zhao, W. Kang, P. Zhang, X.-T. He, Link between k absorption edges and thermodynamic properties of warm dense plasmas established by an improved first-principles method, Phys. Rev. B 93 (11) (2016) 115114. `doi:10.1103/PhysRevB.93.115114`.
URL `http://link.aps.org/doi/10.1103/PhysRevB.93.115114`

[163] S. Zhang, H. Wang, W. Kang, P. Zhang, X. T. He, Extended application of Kohn-Sham first-principles molecular dynamics method with plane wave approximation at high energy – From cold materials to hot dense plasmas, Phys. Plasmas 23 (4) (2016) 042707. `doi:10.1063/1.4947212`.
URL `http://aip.scitation.org/doi/abs/10.1063/1.4947212`

[164] C. Pierleoni, D. M. Ceperley, Computational Methods in Coupled Electron-Ion Monte Carlo Simulations, Chem. Phys. Chem. 6 (9) (2005) 1872–1878. `doi:10.1002/cphc.200400587`.
URL `http://onlinelibrary.wiley.com/doi/10.1002/cphc.200400587/abstract`

[165] D. Ceperley, M. Dewing, C. Pierleoni, The Coupled Electronic-Ionic Monte Carlo Simulation Method, arXiv:physics/0207006ArXiv: physics/0207006.
URL `http://arxiv.org/abs/physics/0207006`

[166] C. Pierleoni, D. M. Ceperley, M. Holzmann, Coupled Electron-Ion Monte Carlo Calculations of Dense Metallic Hydrogen, Phys. Rev. Lett. 93 (14) (2004) 146402. `doi:10.1103/PhysRevLett.93.146402`.
URL `http://link.aps.org/doi/10.1103/PhysRevLett.93.146402`

[167] N. M. Tubman, E. Liberatore, C. Pierleoni, M. Holzmann, D. M. Ceperley, Molecular-Atomic Transition along the Deuterium Hugoniot Curve with Coupled Electron-Ion Monte Carlo Simulations, Phys. Rev. Lett. 115 (4) (2015) 045301. `doi:10.1103/PhysRevLett.115.045301`.
URL `http://link.aps.org/doi/10.1103/PhysRevLett.115.045301`

[168] R. P. Dias, I. F. Silvera, Observation of the Wigner-Huntington transition to metallic hydrogen, Science (2017) eaal1579`doi:10.1126/science.aal1579`.
URL `http://science.sciencemag.org/content/early/2017/01/25/science.aal1579`

[169] M. A. Morales, C. Pierleoni, D. M. Ceperley, Equation of state of metallic hydrogen from coupled electron-ion Monte Carlo simulations, Phys. Rev. E 81 (2) (2010) 021202. `doi:10.1103/PhysRevE.81.021202`.
URL `http://link.aps.org/doi/10.1103/PhysRevE.81.021202`

[170] C. Pierleoni, M. A. Morales, G. Rillo, M. Holzmann, D. M. Ceperley, Liquid-liquid phase transition in hydrogen by coupled electronion Monte Carlo simulations, Proc. Natl. Acad. Sci. U.S.A 113 (18) (2016) 4953–4957. `doi:10.1073/pnas.1603853113`.

[171] Y. Luo, S. Sorella, Ab initio molecular dynamics with quantum Monte Carlo, Mech. Mat. 2 (2015) 29. `doi:10.3389/fmats.2015.00029`.
URL `http://journal.frontiersin.org/article/10.3389/fmats.2015.00029/full`

[172] C. Attaccalite, S. Sorella, Stable Liquid Hydrogen at High Pressure by a Novel *Ab Initio* Molecular-Dynamics Calculation, Phys. Rev. Lett. 100 (11) (2008) 114501. `doi:10.1103/PhysRevLett.100.114501`.
URL `http://link.aps.org/doi/10.1103/PhysRevLett.100.114501`

[173] G. Mazzola, S. Sorella, Distinct Metallization and Atomization Transitions in Dense Liquid Hydrogen, Phys. Rev. Lett. 114 (10) (2015) 105701. `doi:10.1103/PhysRevLett.114.105701`.
URL `http://link.aps.org/doi/10.1103/PhysRevLett.114.105701`

[174] A. Zen, Y. Luo, G. Mazzola, L. Guidoni, S. Sorella, Ab initio molecular dynamics simulation of liquid water by quantum Monte Carlo, J. Chem. Phys. 142 (14) (2015) 144111. `doi:10.1063/1.4917171`.
URL `http://scitation.aip.org/content/aip/journal/jcp/142/14/10.1063/1.4917171`

[175] G. Mazzola, S. Yunoki, S. Sorella, Unexpectedly high pressure for molecular dissociation in liquid hydrogen by electronic simulation, Nat. Commun. 5 (2014) 3487. `doi:10.1038/ncomms4487`.
URL `http://www.nature.com/ncomms/2014/140319/ncomms4487/full/ncomms4487.html`

[176] G. Mazzola, A. Zen, S. Sorella, Finite-temperature electronic simulations without the Born-Oppenheimer constraint, J. Chem. Phys. 137 (13) (2012) 134112. `doi:10.1063/1.4755992`.
URL `http://scitation.aip.org/content/aip/journal/jcp/137/13/10.1063/1.4755992`

[177] C. Ullrich, Time-Dependent Density-Functional Theory: Concepts and Applications, Oxford Graduate Texts, OUP Oxford, 2012.
URL `https://books.google.de/books?id=hCNNsC4sEtkC`

[178] C. A. Ullrich, Time-Dependent Density-Functional Theory: Features and Challenges, with a Special View on Matter Under Extreme Conditions, Springer International Publishing, Cham, 2014, pp. 1–23. `doi:10.1007/978-3-319-04912-0_1`.
URL `https://doi.org/10.1007/978-3-319-04912-0_1`

[179] A. Baczewski, L. Shulenburger, M. Desjarlais, S. Hansen, R. Magyar, X-ray Thomson Scattering in Warm Dense Matter without the Chihara Decomposition, Phys. Rev. Lett. 116 (11) (2016) 115004. `doi:10.1103/PhysRevLett.116.115004`.
URL `http://link.aps.org/doi/10.1103/PhysRevLett.116.115004`

[180] R. J. Magyar, L. Shulenburger, A. D. Baczewski, Stopping of Deuterium in Warm Dense Deuterium from Ehrenfest Time-Dependent Density Functional Theory, Contrib. Plasma Phys. 56 (5) (2016) 459–466. `doi:10.1002/ctpp.201500143`.
URL `http://onlinelibrary.wiley.com/doi/10.1002/ctpp.201500143/abstract`

[181] M. W. C. Dharma-wardana, F. Perrot, Spin- and valley-dependent analysis of the two-dimensional low-density electron system in Si MOSFETs, Phys. Rev. B 70 (3) (2004) 035308. `doi:10.1103/PhysRevB.70.035308`.
URL `https://link.aps.org/doi/10.1103/PhysRevB.70.035308`

[182] M. W. C. Dharma-wardana, Static and dynamic conductivity of warm dense matter within a density-functional approach: Application to aluminum and gold, Phys. Rev. E 73 (3) (2006) 036401. `doi:10.1103/PhysRevE.73.036401`.
URL `https://link.aps.org/doi/10.1103/PhysRevE.73.036401`

[183] M. W. C. Dharma-wardana, M. S. Murillo, Pair-distribution functions of two-temperature two-mass systems: Comparison of molecular dynamics, classical-map hypernetted chain, quantum Monte Carlo, and Kohn-Sham calculations for dense hydrogen, Phys. Rev. E 77 (2) (2008) 026401. `doi:10.1103/PhysRevE.77.026401`.
URL `https://link.aps.org/doi/10.1103/PhysRevE.77.026401`

[184] M. W. C. Dharma-Wardana, The classical-map hyper-netted-chain (CHNC) method and associated novel density-functional techniques for warm dense matter, Int. J. Quantum Chem. 112 (1) (2012) 53–64. `doi:10.1002/qua.23170`.
URL `http://onlinelibrary.wiley.com/doi/10.1002/qua.23170/abstract`

[185] V. V. Karasiev, J. W. Dufty, S. B. Trickey, Nonempirical semi-local free-energy density functional for matter under extreme conditions, arXiv:1612.06266 [cond-mat]ArXiv: 1612.06266.
URL `http://arxiv.org/abs/1612.06266`

[186] D. Saumon, G. Chabrier, Fluid hydrogen at high density: Pressure dissociation, Phys. Rev. A 44 (8) (1991) 5122–5141. `doi:10.1103/PhysRevA.44.5122`.
URL `https://link.aps.org/doi/10.1103/PhysRevA.44.5122`

[187] D. Saumon, G. Chabrier, Fluid hydrogen at high density: Pressure ionization, Phys. Rev. A 46 (4) (1992) 2084–2100. `doi:10.1103/PhysRevA.46.2084`.
URL `http://link.aps.org/doi/10.1103/PhysRevA.46.2084`

[188] G. Chabrier, Quantum effects in dense Coulumbic matter - Application to the cooling of white dwarfs, Astrophys. J. 414 (1993) 695. `doi:10.1086/173115`.
URL `http://adsabs.harvard.edu/doi/10.1086/173115`

[189] G. Chabrier, A. Y. Potekhin, Equation of state of fully ionized electron-ion plasmas, Phys. Rev. E 58 (4) (1998) 4941–4949. `doi:10.1103/PhysRevE.58.4941`.
URL `https://link.aps.org/doi/10.1103/PhysRevE.58.4941`

[190] A. Y. Potekhin, G. Chabrier, Thermodynamic Functions of Dense Plasmas: Analytic Approximations for Astrophysical Applications, Contrib. Plasma Phys. 50 (1) (2010) 82–87. `doi:10.1002/ctpp.201010017`.
URL `http://onlinelibrary.wiley.com/doi/10.1002/ctpp.201010017/abstract`

[191] A. Y. Potekhin, G. Chabrier, Equation of state for magnetized Coulomb plasmas, Astron. Astrophys. 550 (2013) A43. `doi:10.1051/0004-6361/201220082`.
URL `http://dx.doi.org/10.1051/0004-6361/201220082`

[192] N. Crouseilles, P.-A. Hervieux, G. Manfredi, Quantum hydrodynamic model for the nonlinear electron dynamics in thin metal films, Phys. Rev. B 78 (15) (2008) 155412. `doi:10.1103/PhysRevB.78.155412`.
URL `http://link.aps.org/doi/10.1103/PhysRevB.78.155412`

[193] D. Michta, F. Graziani, M. Bonitz, Quantum Hydrodynamics for Plasmas a Thomas-Fermi Theory Perspective, Contrib. Plasma Phys. 55 (6) (2015) 437–443. `doi:10.1002/ctpp.201500024`.
URL `http://onlinelibrary.wiley.com/doi/10.1002/ctpp.201500024/abstract`

[194] A. Diaw, M. S. Murillo, A viscous quantum hydrodynamics model based on dynamic density functional theory, Sci. Rep. 7 (1) (2017) 15352. `doi:10.1038/s41598-017-14414-9`.
URL `https://www.nature.com/articles/s41598-017-14414-9`

[195] D. Kremp, M. Schlanges, W. Kraeft, Quantum Statistics of Nonideal Plasmas, Springer Series on Atomic, Optical, and Plasma Physics, Springer Berlin Heidelberg, 2006.
URL `https://books.google.de/books?id=savMPLWUFfkC`

[196] J. Vorberger, M. Schlanges, W. D. Kraeft, Equation of state for weakly coupled quantum plasmas, Phys. Rev. E 69 (4) (2004) 046407. `doi:10.1103/PhysRevE.69.046407`.
URL `http://link.aps.org/doi/10.1103/PhysRevE.69.046407`

[197] J. Kas, J. Rehr, Finite Temperature Green's Function Approach for Excited State and Thermodynamic Properties of Cool to Warm Dense Matter, Phys. Rev. Lett. 119 (17) (2017) 176403. `doi:10.1103/PhysRevLett.119.176403`.
URL `https://link.aps.org/doi/10.1103/PhysRevLett.119.176403`

[198] W. Ebeling, W. Richert, Thermodynamic Functions of Nonideal Hydrogen Plasmas, Ann. Phys. 494 (5) (1982) 362–370. `doi:10.1002/andp.19824940508`.
URL `http://onlinelibrary.wiley.com/doi/10.1002/andp.19824940508/abstract`

[199] W. Richert, W. Ebeling, Thermodynamic Functions of the Electron Fluid for a Wide Density-Temperature Range, physica status solidi (b) 121 (2) (1984) 633–639. `doi:10.1002/pssb.2221210222`.
URL `http://onlinelibrary.wiley.com/doi/10.1002/pssb.2221210222/abstract`

[200] W. Ebeling, W. Richert, Plasma phase transition in hydrogen, Phys. Lett. A 108 (2) (1985) 80–82. `doi:10.1016/0375-9601(85)90521-3`.
URL `http://www.sciencedirect.com/science/article/pii/0375960185905213`

[201] W. Ebeling, H. Lehmann, Nonideal Ionization in Plasmas with Higher Charges, Contrib. Plasma Phys. 29 (4-5) (1989) 365–371. `doi:10.1002/ctpp.2150290406`.
URL `http://onlinelibrary.wiley.com/doi/10.1002/ctpp.2150290406/abstract`

[202] W. Ebeling, Free Energy and Ionization in Dense Plasmas of the Light Elements, Contrib. Plasma Phys. 30 (5) (1990) 553–561. `doi:10.1002/ctpp.2150300502`.
URL `http://onlinelibrary.wiley.com/doi/10.1002/ctpp.2150300502/abstract`

[203] S. Tanaka, S. Mitake, S. Ichimaru, Parametrized equation of state for electron liquids in the Singwi-Tosi-Land-Sjölander approximation, Phys. Rev. A 32 (3) (1985) 1896–1899. `doi:10.1103/PhysRevA.32.1896`.
URL `http://link.aps.org/doi/10.1103/PhysRevA.32.1896`

[204] S. Tanaka, S. Ichimaru, Thermodynamics and Correlational Properties of Finite-Temperature Electron Liquids in the Singwi-Tosi-Land-Sjölander Approximation, J. Phys. Soc. Jpn. 55 (7) (1986) 2278–2289. `doi:10.1143/JPSJ.55.2278`.
URL `http://journals.jps.jp/doi/abs/10.1143/JPSJ.55.2278`

[205] S. Tanaka, S. Ichimaru, Spin-dependent correlations and thermodynamic functions for electron liquids at arbitrary degeneracy and spin polarization, Phys. Rev. B 39 (2) (1989) 1036–1051. `doi:10.1103/PhysRevB.39.1036`.
URL `http://link.aps.org/doi/10.1103/PhysRevB.39.1036`

[206] S. Ichimaru, H. Iyetomi, S. Tanaka, Statistical physics of dense plasmas: Thermodynamics, transport coefficients and dynamic correlations, Phys. Rep. 149 (2) (1987) 91–205. `doi:10.1016/0370-1573(87)90125-6`.
URL `http://www.sciencedirect.com/science/article/pii/0370157387901256`

[207] S. Ichimaru, Statistical Plasma Physics: Basic principles, Frontiers in physics, Westview Press, 2004.
URL `https://books.google.de/books?id=CWssAAAAYAAJ`

[208] S. Ichimaru, Statistical Plasma Physics: Condensed plasmas, Frontiers in physics, Westview Press, 2004.
URL `https://books.google.de/books?id=T2ssAAAAYAAJ`

[209] M. W. C. Dharma-wardana, F. Perrot, Simple Classical Mapping of the Spin-Polarized Quantum Electron Gas: Distribution Functions and Local-Field Corrections, Phys. Rev. Lett. 84 (5) (2000) 959–962. `doi:10.1103/PhysRevLett.84.959`.
URL `http://link.aps.org/doi/10.1103/PhysRevLett.84.959`

[210] F. Perrot, M. W. C. Dharma-wardana, Spin-polarized electron liquid at arbitrary temperatures: Exchange-correlation energies, electron-distribution functions, and the static response functions, Phys. Rev. B 62 (24) (2000) 16536–16548. `doi:10.1103/PhysRevB.62.16536`.
URL `http://link.aps.org/doi/10.1103/PhysRevB.62.16536`

[211] E. W. Brown, B. K. Clark, J. L. DuBois, D. M. Ceperley, Path-Integral Monte-Carlo Simulation of the Warm Dense Homogeneous Electron Gas, Phys. Rev. Lett. 110 (14) (2013) 146405. `doi:10.1103/PhysRevLett.110.146405`.
URL `http://link.aps.org/doi/10.1103/PhysRevLett.110.146405`

[212] V. V. Karasiev, T. Sjostrom, J. Dufty, S. Trickey, Accurate Homogeneous Electron Gas Exchange-Correlation Free Energy for Local Spin-Density Calculations, Phys. Rev. Lett. 112 (7) (2014) 076403. `doi:10.1103/PhysRevLett.112.076403`.
URL `http://link.aps.org/doi/10.1103/PhysRevLett.112.076403`

[213] T. Sjostrom, J. Dufty, Uniform electron gas at finite temperatures, Phys. Rev. B 88 (11) (2013) 115123. `doi:10.1103/PhysRevB.88.115123`.
URL `http://link.aps.org/doi/10.1103/PhysRevB.88.115123`

[214] E. W. Brown, J. L. DuBois, M. Holzmann, D. M. Ceperley, Exchange-correlation energy for the three-dimensional homogeneous electron gas at arbitrary temperature, Phys. Rev. B 88 (8) (2013) 081102. `doi:10.1103/PhysRevB.88.081102`.
URL `http://link.aps.org/doi/10.1103/PhysRevB.88.081102`

[215] T. Schoof, M. Bonitz, A. Filinov, D. Hochstuhl, J. Dufty, Configuration Path Integral Monte Carlo, Contrib. Plasma Phys. 51 (8) (2011) 687–697. `doi:10.1002/ctpp.201100012`.
URL `http://onlinelibrary.wiley.com/doi/10.1002/ctpp.201100012/abstract`

[216] T. Schoof, S. Groth, M. Bonitz, Towards ab Initio Thermodynamics of the Electron Gas at Strong Degeneracy, Contrib. Plasma Phys. 55 (2-3) (2015) 136–143. `doi:10.1002/ctpp.201400072`.
URL `http://onlinelibrary.wiley.com/doi/10.1002/ctpp.201400072/abstract`

[217] S. Groth, T. Schoof, T. Dornheim, M. Bonitz, *Ab initio* quantum Monte Carlo simulations of the uniform electron gas without fixed nodes, Phys. Rev. B 93 (8) (2016) 085102. `doi:10.1103/PhysRevB.93.085102`.
URL `http://link.aps.org/doi/10.1103/PhysRevB.93.085102`

[218] T. Schoof, S. Groth, J. Vorberger, M. Bonitz, *Ab Initio* Thermodynamic Results for the Degenerate Electron Gas at Finite Temperature, Phys. Rev. Lett. 115 (13) (2015) 130402. `doi:10.1103/PhysRevLett.115.130402`.
URL `http://link.aps.org/doi/10.1103/PhysRevLett.115.130402`

[219] T. Dornheim, S. Groth, A. Filinov, M. Bonitz, Permutation blocking path integral Monte Carlo: a highly efficient approach to the simulation of strongly degenerate non-ideal fermions, New J. Phys. 17 (7) (2015) 073017. `doi:10.1088/1367-2630/17/7/073017`.
URL `http://iopscience.iop.org/1367-2630/17/7/073017`

[220] T. Dornheim, T. Schoof, S. Groth, A. Filinov, M. Bonitz, Permutation blocking path integral Monte Carlo approach to the uniform electron gas at finite temperature, J. Chem. Phys. 143 (20) (2015) 204101. `doi:10.1063/1.4936145`.
URL `http://scitation.aip.org/content/aip/journal/jcp/143/20/10.1063/1.4936145`

[221] T. Dornheim, S. Groth, T. Schoof, C. Hann, M. Bonitz, *Ab initio* quantum Monte Carlo simulations of the uniform electron gas without fixed nodes: The unpolarized case, Phys. Rev. B 93 (20) (2016) 205134. `doi:10.1103/PhysRevB.93.205134`.
URL `http://link.aps.org/doi/10.1103/PhysRevB.93.205134`

[222] F. D. Malone, N. S. Blunt, J. J. Shepherd, D. K. K. Lee, J. S. Spencer, W. M. C. Foulkes, Interaction picture density matrix quantum Monte Carlo, J. Chem. Phys. 143 (4) (2015) 044116. `doi:10.1063/1.4927434`.
URL `http://scitation.aip.org/content/aip/journal/jcp/143/4/10.1063/1.4927434`

[223] F. D. Malone, N. Blunt, E. W. Brown, D. Lee, J. Spencer, W. Foulkes, J. J. Shepherd, Accurate Exchange-Correlation Energies for the Warm Dense Electron Gas, Phys. Rev. Lett. 117 (11) (2016) 115701. `doi:10.1103/PhysRevLett.117.115701`.
URL `http://link.aps.org/doi/10.1103/PhysRevLett.117.115701`

[224] N. S. Blunt, T. W. Rogers, J. S. Spencer, W. M. C. Foulkes, Density-matrix quantum Monte Carlo method, Phys. Rev. B 89 (24) (2014) 245124. `doi:10.1103/PhysRevB.89.245124`.
URL `http://link.aps.org/doi/10.1103/PhysRevB.89.245124`

[225] T. Dornheim, S. Groth, F. D. Malone, T. Schoof, T. Sjostrom, W. M. C. Foulkes, M. Bonitz, Ab initio quantum Monte Carlo simulation of the warm dense electron gas, Phys. Plasmas 24 (5) (2017) 056303. `doi:10.1063/1.4977920`.
URL `http://aip.scitation.org/doi/full/10.1063/1.4977920`

[226] T. Dornheim, S. Groth, T. Sjostrom, F. D. Malone, W. Foulkes, M. Bonitz, *Ab Initio* Quantum Monte Carlo Simulation of the Warm Dense Electron Gas in the Thermodynamic Limit, Phys. Rev. Lett. 117 (15) (2016) 156403. `doi:10.1103/PhysRevLett.117.156403`.
URL `http://link.aps.org/doi/10.1103/PhysRevLett.117.156403`

[227] S. Groth, T. Dornheim, T. Sjostrom, F. D. Malone, W. Foulkes, M. Bonitz, *Ab initio* exchange-correlation free energy of the uniform electron gas at warm dense matter conditions, Phys. Rev. Lett. 119 (13) (2017) 135001. `doi:10.1103/PhysRevLett.119.135001`.
URL `https://link.aps.org/doi/10.1103/PhysRevLett.119.135001`

[228] S. W. d. Leeuw, J. W. Perram, E. R. Smith, Simulation of electrostatic systems in periodic boundary conditions. I. Lattice sums and dielectric constants, Proc. R. Soc. Lond. A 373 (1752) (1980) 27–56. `doi:10.1098/rspa.1980.0135`.
URL `http://rspa.royalsocietypublishing.org/content/373/1752/27`

[229] V. Ballenegger, Communication: On the origin of the surface term in the Ewald formula, J. Chem. Phys. 140 (16) (2014) 161102. `doi:10.1063/1.4872019`.
URL `http://scitation.aip.org/content/aip/journal/jcp/140/16/10.1063/1.4872019`

[230] A. Y. Toukmaji, J. A. Board, Ewald summation techniques in perspective: a survey, Comp. Phys. Comm. 95 (2) (1996) 73–92. `doi:10.1016/0010-4655(96)00016-1`.
URL `http://www.sciencedirect.com/science/article/pii/0010465596000161`

[231] L. M. Fraser, W. M. C. Foulkes, G. Rajagopal, R. J. Needs, S. D. Kenny, A. J. Williamson, Finite-size effects and Coulomb interactions in quantum Monte Carlo calculations for homogeneous systems with periodic boundary conditions, Phys. Rev. B 53 (4) (1996) 1814–1832. `doi:10.1103/PhysRevB.53.1814`.
URL `http://link.aps.org/doi/10.1103/PhysRevB.53.1814`

[232] Z.-H. Duan, R. Krasny, An Ewald summation based multipole method, J. Chem. Phys. 113 (9) (2000) 3492–3495. `doi:10.1063/1.1289918`.
URL `http://aip.scitation.org/doi/abs/10.1063/1.1289918`

[233] V. Natoli, D. M. Ceperley, An Optimized Method for Treating Long-Range Potentials, J. Comp. Phys. 117 (1) (1995) 171–178. `doi:10.1006/jcph.1995.1054`.
URL `http://www.sciencedirect.com/science/article/pii/S0021999185710546`

[234] C. J. Fennell, J. D. Gezelter, Is the Ewald summation still necessary? Pairwise alternatives to the accepted standard for long-range electrostatics, J. Chem. Phys. 124 (23) (2006) 234104. `doi:10.1063/1.2206581`.
URL `http://aip.scitation.org/doi/abs/10.1063/1.2206581`

[235] E. Yakub, C. Ronchi, An efficient method for computation of long-ranged Coulomb forces in computer simulation of ionic fluids, J. Chem. Phys. 119 (22) (2003) 11556–11560. `doi:10.1063/1.1624364`.
URL `http://scitation.aip.org/content/aip/journal/jcp/119/22/10.1063/1.1624364`

[236] E. Yakub, C. Ronchi, A New Method for Computation of Long Ranged Coulomb Forces in Computer Simulation of Disordered Systems, J. Low Temp. Phys. 139 (5-6) (2005) 633–643. `doi:10.1007/s10909-005-5451-5`.
URL `http://link.springer.com/article/10.1007/s10909-005-5451-5`

[237] E. S. Yakub, Effective computer simulation of strongly coupled Coulomb fluids, J. Phys. A 39 (17) (2006) 4643. `doi:10.1088/0305-4470/39/17/S51`.
URL `http://stacks.iop.org/0305-4470/39/i=17/a=S51`

[238] G. Vernizzi, G. I. Guerrero-Garca, M. Olvera de la Cruz, Coulomb interactions in charged fluids, Phys. Rev. E 84 (1) (2011) 016707. `doi:10.1103/PhysRevE.84.016707`.
URL `http://link.aps.org/doi/10.1103/PhysRevE.84.016707`

[239] M. Bonitz, Quantum Kinetic Theory, Springer International Publishing, 2016.
URL `https://books.google.de/books?id=wW7_CgAAQBAJ`

[240] Y. Klimontovich, V. Silin, J. Exptl. Theor. Phys. (U.S.S.R.) 23 (1952) 151.

[241] M. Gell-Mann, K. A. Brueckner, Correlation Energy of an Electron Gas at High Density, Phys. Rev. 106 (2) (1957) 364–368. `doi:10.1103/PhysRev.106.364`.
URL `http://link.aps.org/doi/10.1103/PhysRev.106.364`

[242] S. Tanaka, Correlational and thermodynamic properties of finite-temperature electron liquids in the hypernetted-chain approximation, J. Chem. Phys. 145 (21) (2016) 214104. `doi:10.1063/1.4969071`.
URL `http://scitation.aip.org/content/aip/journal/jcp/145/21/10.1063/1.4969071`

[243] H. Hayashi, M. Shimizu, Electron Correlations at Metallic Densities. IV, J. Phys. Soc. Jpn. 48 (1) (1980) 16–23. `doi:10.1143/JPSJ.48.16`.
URL `http://journals.jps.jp/doi/abs/10.1143/JPSJ.48.16`

[244] T. Hasegawa, M. Shimizu, Electron Correlations at Metallic Densities, II. Quantum Mechanical Expression of Dielectric Function with Wigner Distribution Function, J. Phys. Soc. Jpn. 38 (4) (1975) 965–973. `doi:10.1143/JPSJ.38.965`.
URL `http://journals.jps.jp/doi/abs/10.1143/JPSJ.38.965`

[245] A. Holas, S. Rahman, Dynamic local-field factor of an electron liquid in the quantum versions of the Singwi-Tosi-Land-Sjölander and Vashishta-Singwi theories, Phys. Rev. B 35 (6) (1987) 2720–2731. `doi:10.1103/PhysRevB.35.2720`.
URL `http://link.aps.org/doi/10.1103/PhysRevB.35.2720`

[246] U. Gupta, A. K. Rajagopal, Inhomogeneous electron gas at nonzero temperatures: Exchange effects, Phys. Rev. A 21 (6) (1980) 2064–2068. `doi:10.1103/PhysRevA.21.2064`.
URL `https://link.aps.org/doi/10.1103/PhysRevA.21.2064`

[247] U. Gupta, A. K. Rajagopal, Exchange-correlation potential for inhomogeneous electron systems at finite temperatures, Phys. Rev. A 22 (6) (1980) 2792–2797. `doi:10.1103/PhysRevA.22.2792`.
URL `http://link.aps.org/doi/10.1103/PhysRevA.22.2792`

[248] F. Perrot, M. W. C. Dharma-wardana, Exchange and correlation potentials for electron-ion systems at finite temperatures, Phys. Rev. A 30 (5) (1984) 2619–2626. doi:10.1103/PhysRevA.30.2619.
URL http://link.aps.org/doi/10.1103/PhysRevA.30.2619

[249] S. Tanaka, Improved equation of state for finite-temperature spin-polarized electron liquids on the basis of Singwi-Tosi-Land-Sjölander approximation, Contrib. Plasma Phys. (2017) n/a–n/a. doi:10.1002/ctpp.201600096.
URL http://onlinelibrary.wiley.com/doi/10.1002/ctpp.201600096/abstract

[250] W. Stolzmann, M. Rösler, Static Local-Field Corrected Dielectric and Thermodynamic Functions, Contrib. Plasma Phys. 41 (2-3) (2001) 203–206. doi:10.1002/1521-3986(200103)41:2/3<203::AID-CTPP203>3.0.CO;2-S.
URL http://onlinelibrary.wiley.com/doi/10.1002/1521-3986(200103)41:2/3<203::AID-CTPP203>3.0.CO;2-S/abstract

[251] H. K. Schweng, H. M. Böhm, Finite-temperature electron correlations in the framework of a dynamic local-field correction, Phys. Rev. B 48 (4) (1993) 2037–2045. doi:10.1103/PhysRevB.48.2037.
URL http://link.aps.org/doi/10.1103/PhysRevB.48.2037

[252] P. Arora, K. Kumar, R. K. Moudgil, Spin-resolved correlations in the warm-dense homogeneous electron gas, Eur. Phys. J. B 90 (4) (2017) 76. doi:10.1140/epjb/e2017-70532-y.
URL https://link.springer.com/article/10.1140/epjb/e2017-70532-y

[253] H. Kählert, G. J. Kalman, M. Bonitz, Dynamics of strongly correlated and strongly inhomogeneous plasmas, Phys. Rev. E 90 (1) (2014) 011101. doi:10.1103/PhysRevE.90.011101.
URL https://link.aps.org/doi/10.1103/PhysRevE.90.011101

[254] H. Kählert, G. J. Kalman, M. Bonitz, Linear Fluid Theory for Weakly Inhomogeneous Plasmas with Strong Correlations, Contrib. Plasma Phys. 55 (5) (2015) 352–359. doi:10.1002/ctpp.201400085.
URL http://onlinelibrary.wiley.com/doi/10.1002/ctpp.201400085/abstract

[255] J. F. Springer, M. A. Pokrant, F. A. Stevens, Integral equation solutions for the classical electron gas, J. Chem. Phys. 58 (11) (1973) 4863–4867. doi:10.1063/1.1679070.
URL http://aip.scitation.org/doi/10.1063/1.1679070

[256] K.-C. Ng, Hypernetted chain solutions for the classical one-component plasma up to $\gamma = 7000$, J. Chem. Phys. 61 (7) (1974) 2680–2689. doi:10.1063/1.1682399.
URL http://scitation.aip.org/content/aip/journal/jcp/61/7/10.1063/1.1682399

[257] N. D. Mermin, Lindhard Dielectric Function in the Relaxation-Time Approximation, Phys. Rev. B 1 (5) (1970) 2362–2363. doi:10.1103/PhysRevB.1.2362.
URL https://link.aps.org/doi/10.1103/PhysRevB.1.2362

[258] A. Selchow, G. Röpke, A. Wierling, Extended Mermin-like Dielectric Function for a Two-Component Plasma, Contrib. Plasma Phys. 42 (1) (2002) 43–54. doi:10.1002/1521-3986(200201)42:1<43::AID-CTPP43>3.0.CO;2-3.
URL http://onlinelibrary.wiley.com/doi/10.1002/1521-3986(200201)42:1<43::AID-CTPP43>3.0.CO;2-3/abstract

[259] G. Stefanucci, R. van Leeuwen, Nonequilibrium Many-Body Theory of Quantum Systems: A Modern Introduction, Cambridge University Press, 2013.
URL https://books.google.de/books?id=6GsrjPFXLDYC

[260] E. W. Montroll, J. C. Ward, Quantum Statistics of Interacting Particles; General Theory and Some Remarks on Properties of an Electron Gas, Phys. Fluids 1 (1) (1958) 55–72. doi:10.1063/1.1724337.
URL http://scitation.aip.org/content/aip/journal/pof1/1/1/10.1063/1.1724337

[261] S. Dutta, J. Dufty, Uniform electron gas at warm, dense matter conditions, Europhys. Lett. 102 (6) (2013) 67005. doi:10.1209/0295-5075/102/67005.
URL http://iopscience.iop.org/0295-5075/102/6/67005

[262] S. Dutta, J. Dufty, Classical representation of a quantum system at equilibrium: Applications, Phys. Rev. E 87 (3) (2013) 032102. doi:10.1103/PhysRevE.87.032102.
URL http://link.aps.org/doi/10.1103/PhysRevE.87.032102

[263] J. Dufty, S. Dutta, Classical representation of a quantum system at equilibrium: Theory, Phys. Rev. E 87 (3) (2013) 032101. doi:10.1103/PhysRevE.87.032101.
URL http://link.aps.org/doi/10.1103/PhysRevE.87.032101

[264] K. Binder, Monte Carlo and Molecular Dynamics Simulations in Polymer Science, Oxford University Press, 1995.
URL https://books.google.de/books?id=NLJe2ypFM7IC

[265] Y. Liu, J. Wu, A bridge-functional-based classical mapping method for predicting the correlation functions of uniform electron gases at finite temperature, J. Chem. Phys. 140 (8) (2014) 084103. doi:10.1063/1.4865935.
URL http://scitation.aip.org/content/aip/journal/jcp/140/8/10.1063/1.4865935

[266] Y. Liu, J. Wu, An improved classical mapping method for homogeneous electron gases at finite temperature, J. Chem. Phys. 141 (6) (2014) 064115. doi:10.1063/1.4892587.
URL http://scitation.aip.org/content/aip/journal/jcp/141/6/10.1063/1.4892587

[267] J. W. Dufty, S. Dutta, Classical Representation of a Quantum System at Equilibrium, Contrib. Plasma Phys. 52 (1) (2012) 100–103. doi:10.1002/ctpp.201100066.
URL http://onlinelibrary.wiley.com/doi/10.1002/ctpp.201100066/abstract

[268] J. Wrighton, J. Dufty, S. Dutta, Finite-temperature quantum effects on confined charges, Phys. Rev. E 94 (5) (2016) 053208. doi:10.1103/PhysRevE.94.053208.
URL https://link.aps.org/doi/10.1103/PhysRevE.94.053208

[269] N. Metropolis, A. W. Rosenbluth, M. N. Rosenbluth, A. H. Teller, E. Teller, Equation of State Calculations by Fast Computing Machines, J. Chem. Phys. 21 (6) (1953) 1087–1092. doi:10.1063/1.1699114.
URL http://scitation.aip.org/content/aip/journal/jcp/21/6/10.1063/1.1699114

[270] C. H. Mak, R. Egger, H. Weber-Gottschick, Multilevel Blocking Approach to the Fermion Sign Problem in Path-Integral Monte Carlo Simulations, Phys. Rev. Lett. 81 (21) (1998) 4533–4536. doi:10.1103/PhysRevLett.81.4533.
URL http://link.aps.org/doi/10.1103/PhysRevLett.81.4533

[271] R. Egger, L. Mühlbacher, C. H. Mak, Path-integral Monte Carlo simulations without the sign problem: Multilevel blocking approach for effective actions, Phys. Rev. E 61 (5) (2000) 5961–5966. doi:10.1103/PhysRevE.61.5961.
URL http://link.aps.org/doi/10.1103/PhysRevE.61.5961

[272] R. Egger, C. H. Mak, Multilevel blocking monte carlo simulations for quantum dots, Int. J. Mod. Phys. B 15 (10n11) (2001) 1416–1425. doi:10.1142/S021797920100591X.
URL http://www.worldscientific.com/doi/abs/10.1142/S021797920100591X

[273] M. V. Dikovsky, C. H. Mak, Analysis of the multilevel blocking approach to the fermion sign problem: Accuracy, errors, and practice, Phys. Rev. B 63 (23) (2001) 235105. doi:10.1103/PhysRevB.63.235105.
URL http://link.aps.org/doi/10.1103/PhysRevB.63.235105

[274] L. Mühlbacher, R. Egger, Crossover from nonadiabatic to adiabatic electron transfer reactions: Multilevel blocking Monte Carlo simulations, J. Chem. Phys. 118 (1) (2003) 179–191. doi:10.1063/1.1523014.
URL http://scitation.aip.org/content/aip/journal/jcp/118/1/10.1063/1.1523014

[275] P. N. Vorontsov-Velyaminov, M. A. Voznesenski, D. V. Malakhov, A. P. Lyubartsev, A. V. Broukhno, Path integral method in quantum statistics problems: generalized ensemble Monte Carlo and density functional approach, J. Phys. A 39 (17) (2006) 4711. doi:10.1088/0305-4470/39/17/S62.
URL http://stacks.iop.org/0305-4470/39/i=17/a=S62

[276] M. A. Voznesenskiy, P. N. Vorontsov-Velyaminov, A. P. Lyubartsev, Path-integral-expanded-ensemble Monte Carlo method in treatment of the sign problem for fermions, Phys. Rev. E 80 (6) (2009) 066702. doi:10.1103/PhysRevE.80.066702.
URL http://link.aps.org/doi/10.1103/PhysRevE.80.066702

[277] M. F. Herman, E. J. Bruskin, B. J. Berne, On path integral Monte Carlo simulations, J. Chem. Phys. 76 (10) (1982) 5150–5155. doi:10.1063/1.442815.
URL http://aip.scitation.org/doi/abs/10.1063/1.442815

[278] D. M. Ceperley, Path integrals in the theory of condensed helium, Rev. Mod. Phys. 67 (2) (1995) 279–355. doi:10.1103/RevModPhys.67.279.
URL http://link.aps.org/doi/10.1103/RevModPhys.67.279

[279] D. Chandler, P. Wolynes, Exploiting the isomorphism between quantum theory and classical statistical mechanics of polyatomic fluids, J. Chem. Phys. 74 (1981) 4078. doi:10.1063/1.441588.
URL http://dx.doi.org/10.1063/1.441588

[280] E. Pollock, D. Ceperley, Simulation of quantum many-body systems by path-integral methods, Phys. Rev. B 30 (5) (1984) 2555–2568. doi:10.1103/PhysRevB.30.2555.
URL http://link.aps.org/doi/10.1103/PhysRevB.30.2555

[281] E. L. Pollock, D. M. Ceperley, Path-integral computation of superfluid densities, Phys. Rev. B 36 (16) (1987) 8343–8352. doi:10.1103/PhysRevB.36.8343.
URL http://link.aps.org/doi/10.1103/PhysRevB.36.8343

[282] P. Sindzingre, M. L. Klein, D. M. Ceperley, Path-integral Monte Carlo study of low-temperature ^{4}He clusters, Phys. Rev. Lett. 63 (15) (1989) 1601–1604. doi:10.1103/PhysRevLett.63.1601.
URL http://link.aps.org/doi/10.1103/PhysRevLett.63.1601

[283] Y. Kwon, F. Paesani, K. Whaley, Local superfluidity in inhomogeneous quantum fluids, Phys. Rev. B 74 (17). doi:10.1103/PhysRevB.74.174522.
URL http://link.aps.org/doi/10.1103/PhysRevB.74.174522

[284] T. Dornheim, A. Filinov, M. Bonitz, Superfluidity of strongly correlated bosons in two- and three-dimensional traps, Phys. Rev. B 91 (5) (2015) 054503. doi:10.1103/PhysRevB.91.054503.
URL http://link.aps.org/doi/10.1103/PhysRevB.91.054503

[285] P. Grüter, D. Ceperley, F. Lalo, Critical Temperature of Bose-Einstein Condensation of Hard-Sphere Gases, Phys. Rev. Lett. 79 (19) (1997) 3549–3552. doi:10.1103/PhysRevLett.79.3549.
URL https://link.aps.org/doi/10.1103/PhysRevLett.79.3549

[286] S. Pilati, S. Giorgini, M. Modugno, N. Prokof'ev, Dilute Bose gas with correlated disorder: a path integral Monte Carlo study, New J. Phys. 12 (7) (2010) 073003. doi:10.1088/1367-2630/12/7/073003.
URL http://stacks.iop.org/1367-2630/12/i=7/a=073003

[287] H. Saito, Path-Integral Monte Carlo Study on a Droplet of a Dipolar Bose–Einstein Condensate Stabilized by Quantum Fluctuation, J. Phys. Soc. Jpn. 85 (5) (2016) 053001. doi:10.7566/JPSJ.85.053001.
URL http://journals.jps.jp/doi/full/10.7566/JPSJ.85.053001

[288] A. Filinov, M. Bonitz, Collective and single-particle excitations in two-dimensional dipolar Bose gases, Phys. Rev. A 86 (4). doi:10.1103/PhysRevA.86.043628.
URL http://link.aps.org/doi/10.1103/PhysRevA.86.043628

[289] A. Filinov, Correlation effects and collective excitations in bosonic bilayers: Role of quantum statistics, superfluidity, and the dimerization transition, Phys. Rev. A 94 (1) (2016) 013603. doi:10.1103/PhysRevA.94.013603.
URL http://link.aps.org/doi/10.1103/PhysRevA.94.013603

[290] E. Loh, J. Gubernatis, R. Scalettar, S. White, D. Scalapino, R. Sugar, Sign problem in the numerical simulation of many-electron systems, Phys. Rev. B 41 (13) (1990) 9301–9307. doi:10.1103/PhysRevB.41.9301.
URL http://link.aps.org/doi/10.1103/PhysRevB.41.9301

[291] M. Troyer, U.-J. Wiese, Computational Complexity and Fundamental Limitations to Fermionic Quantum Monte Carlo Simulations, Phys. Rev. Lett. 94 (17). doi:10.1103/PhysRevLett.94.170201.
URL http://link.aps.org/doi/10.1103/PhysRevLett.94.170201

[292] H. Kleinert, Path Integrals in Quantum Mechanics, Statistics, Polymer Physics, and Financial Markets, World Scientific, 2009.

[293] H. F. Trotter, On the Product of Semi-Groups of Operators, Proc. Am. Math. Soc. 10 (4) (1959) 545–551. `doi:10.2307/2033649`.
URL `http://www.jstor.org/stable/2033649`

[294] H. De Raedt, B. De Raedt, Applications of the generalized Trotter formula, Phys. Rev. A 28 (6) (1983) 3575–3580. `doi:10.1103/PhysRevA.28.3575`.
URL `https://link.aps.org/doi/10.1103/PhysRevA.28.3575`

[295] D. Ceperley, Path integral monte carlo methods for fermions, in: K. Binder, G. Ciccotti (Eds.), Monte Carlo and Molecular Dynamics of Condensed Matter Systems, Italian Physical Society, Bologna, 1996.

[296] M. Boninsegni, N. Prokofev, B. Svistunov, Worm Algorithm for Continuous-Space Path Integral Monte-Carlo Simulations, Phys. Rev. Lett. 96 (7) (2006) 070601. `doi:10.1103/PhysRevLett.96.070601`.
URL `http://link.aps.org/doi/10.1103/PhysRevLett.96.070601`

[297] M. Boninsegni, N. V. Prokofev, B. V. Svistunov, Worm algorithm and diagrammatic Monte Carlo: A new approach to continuous-space path integral Monte Carlo simulations, Phys. Rev. E 74 (3) (2006) 036701. `doi:10.1103/PhysRevE.74.036701`.
URL `http://link.aps.org/doi/10.1103/PhysRevE.74.036701`

[298] W.-D. Kraeft, D. Kremp, W. Ebeling, G. Röpke, Quantum Statistics of Charged Particle Systems, Akademie-Verlag Berlin, 1986.

[299] T. Dornheim, H. Thomsen, P. Ludwig, A. Filinov, M. Bonitz, Analyzing Quantum Correlations Made Simple, Contrib. Plasma Phys. 56 (5) (2016) 371–379. `doi:10.1002/ctpp.201500120`.
URL `http://onlinelibrary.wiley.com/doi/10.1002/ctpp.201500120/abstract`

[300] V. M. Zamalin, G. E. Norman, V. S. Filinov, The Monte Carlo Method in Statistical Thermodynamics, Nauka, Moscow, 1977.

[301] M. Takahashi, M. Imada, Monte Carlo Calculation of Quantum Systems, J. Phys. Soc. Jpn. 53 (3) (1984) 963–974. `doi:10.1143/JPSJ.53.963`.
URL `http://journals.jps.jp/doi/abs/10.1143/JPSJ.53.963`

[302] A. P. Lyubartsev, Simulation of excited states and the sign problem in the path integral Monte Carlo method, J. Phys. A 38 (30) (2005) 6659. `doi:10.1088/0305-4470/38/30/003`.
URL `http://iopscience.iop.org/0305-4470/38/30/003`

[303] S. A. Chin, High-order path-integral Monte Carlo methods for solving quantum dot problems, Phys. Rev. E 91 (3) (2015) 031301. `doi:10.1103/PhysRevE.91.031301`.
URL `http://link.aps.org/doi/10.1103/PhysRevE.91.031301`

[304] M. Takahashi, M. Imada, Monte Carlo Calculation of Quantum Systems. II. Higher Order Correction, J. Phys. Soc. Jpn. 53 (11) (1984) 3765–3769. `doi:10.1143/JPSJ.53.3765`.
URL `http://journals.jps.jp/doi/abs/10.1143/JPSJ.53.3765`

[305] S. A. Chin, C. R. Chen, Gradient symplectic algorithms for solving the Schrödinger equation with time-dependent potentials, J. Chem. Phys. 117 (4) (2002) 1409–1415. `doi:10.1063/1.1485725`.
URL `http://scitation.aip.org/content/aip/journal/jcp/117/4/10.1063/1.1485725`

[306] L. Brualla, K. Sakkos, J. Boronat, J. Casulleras, Higher order and infinite Trotter-number extrapolations in path integral Monte Carlo, J. Chem. Phys. 121 (2) (2004) 636–643. `doi:10.1063/1.1760512`.
URL `http://scitation.aip.org/content/aip/journal/jcp/121/2/10.1063/1.1760512`

[307] K. Sakkos, J. Casulleras, J. Boronat, High order Chin actions in path integral Monte Carlo, J. Chem. Phys. 130 (20) (2009) 204109. `doi:10.1063/1.3143522`.
URL `http://scitation.aip.org/content/aip/journal/jcp/130/20/10.1063/1.3143522`

[308] R. E. Zillich, J. M. Mayrhofer, S. A. Chin, Extrapolated high-order propagators for path integral Monte Carlo simulations, J. Chem. Phys. 132 (4) (2010) 044103. `doi:10.1063/1.3297888`.
URL `http://scitation.aip.org/content/aip/journal/jcp/132/4/10.1063/1.3297888`

[309] N. V. Prokofev, B. V. Svistunov, I. S. Tupitsyn, Exact quantum Monte Carlo process for the statistics of discrete systems, JETP Lett. 64 (12) (1996) 911–916. `doi:10.1134/1.567243`.
URL `http://www.springerlink.com/content/613449m532p78470/`

[310] B. B. Beard, U.-J. Wiese, Simulations of discrete quantum systems in continuous euclidean time, Phys. Rev. Lett. 77 (1996) 5130–5133. `doi:10.1103/PhysRevLett.77.5130`.
URL `https://link.aps.org/doi/10.1103/PhysRevLett.77.5130`

[311] E. Gull, A. J. Millis, A. I. Lichtenstein, A. N. Rubtsov, M. Troyer, P. Werner, Continuous-time Monte Carlo methods for quantum impurity models, Rev. Mod. Phys. 83 (2) (2011) 349–404. `doi:10.1103/RevModPhys.83.349`.
URL `http://link.aps.org/doi/10.1103/RevModPhys.83.349`

[312] A. W. Sandvik, J. Kurkijärvi, Quantum monte carlo simulation method for spin systems, Phys. Rev. B 43 (1991) 5950–5961. `doi:10.1103/PhysRevB.43.5950`.
URL `https://link.aps.org/doi/10.1103/PhysRevB.43.5950`

[313] A. W. Sandvik, Finite-size scaling of the ground-state parameters of the two-dimensional heisenberg model, Phys. Rev. B 56 (1997) 11678–11690. `doi:10.1103/PhysRevB.56.11678`.
URL `https://link.aps.org/doi/10.1103/PhysRevB.56.11678`

[314] A. W. Sandvik, Stochastic series expansion method with operator-loop update, Phys. Rev. B 59 (1999) R14157–R14160. `doi:10.1103/PhysRevB.59.R14157`.
URL `https://link.aps.org/doi/10.1103/PhysRevB.59.R14157`

[315] A. W. Sandvik, Multichain mean-field theory of quasi-one-dimensional quantum spin systems, Phys. Rev. Lett. 83 (1999) 3069–3072. `doi:10.1103/PhysRevLett.83.3069`.
URL `https://link.aps.org/doi/10.1103/PhysRevLett.83.3069`

[316] P. V. Shevchenko, A. W. Sandvik, O. P. Sushkov, Double-layer Heisenberg antiferromagnet at finite temperature: Brueckner theory and quantum Monte Carlo simulations, Phys. Rev. B 61 (2000) 3475–3487. `doi:10.1103/PhysRevB.61.3475`.
URL `https://link.aps.org/doi/10.1103/PhysRevB.61.3475`

[317] G. H. Booth, A. J. W. Thom, A. Alavi, Fermion Monte Carlo without fixed nodes: A game of life, death, and annihilation in Slater determinant space, J. Chem. Phys. 131 (5) (2009) 054106. `doi:10.1063/1.3193710`.
URL `http://scitation.aip.org/content/aip/journal/jcp/131/5/10.1063/1.3193710`

[318] G. H. Booth, A. Grüneis, G. Kresse, A. Alavi, Towards an exact description of electronic wavefunctions in real solids, Nature 493 (7432) (2013) 365–370. `doi:10.1038/nature11770`.
URL `http://www.nature.com/nature/journal/v493/n7432/abs/nature11770.html`

[319] C. J. Umrigar, M. P. Nightingale, K. J. Runge, A diffusion Monte Carlo algorithm with very small timestep errors, J. Chem. Phys. 99 (4) (1993) 2865–2890. `doi:10.1063/1.465195`.
URL `http://aip.scitation.org/doi/abs/10.1063/1.465195`

[320] J. L. DuBois, E. W. Brown, B. J. Alder, Overcoming the fermion sign problem in homogeneous systems, arXiv:1409.3262 [cond-mat]ArXiv: 1409.3262.
URL `http://arxiv.org/abs/1409.3262`

[321] T. Sjostrom, J. Daligault, Gradient corrections to the exchange-correlation free energy, Phys. Rev. B 90 (15) (2014) 155109. `doi:10.1103/PhysRevB.90.155109`.
URL `http://link.aps.org/doi/10.1103/PhysRevB.90.155109`

[322] V. Filinov, Cluster expansion for ideal Fermi systems in the 'fixed-node approximation', J. Phys. A 34 (8) (2001) 1665. `doi:10.1088/0305-4470/34/8/312`.
URL `http://iopscience.iop.org/0305-4470/34/8/312`

[323] V. S. Filinov, Analytical contradictions of the fixed-node density matrix, High Temp. 52 (5) (2014) 615–620. doi:10.1134/S0018151X14040105.
URL http://link.springer.com/article/10.1134/S0018151X14040105

[324] B. Clark, M. Casula, D. Ceperley, Hexatic and Mesoscopic Phases in a 2d Quantum Coulomb System, Phys. Rev. Lett. 103 (5). doi:10.1103/PhysRevLett.103.055701.
URL http://link.aps.org/doi/10.1103/PhysRevLett.103.055701

[325] R. Gaudoin, J. M. Pitarke, Hellman-Feynman Operator Sampling in Diffusion Monte Carlo Calculations, Phys. Rev. Lett. 99 (12) (2007) 126406. doi:10.1103/PhysRevLett.99.126406.
URL https://link.aps.org/doi/10.1103/PhysRevLett.99.126406

[326] I. G. Gurtubay, R. Gaudoin, J. M. Pitarke, Benchmark quantum Monte Carlo calculations of the ground-state kinetic, interaction and total energy of the three-dimensional electron gas, J. Phys. Condens. Matter 22 (6) (2010) 065501. doi:10.1088/0953-8984/22/6/065501.
URL http://stacks.iop.org/0953-8984/22/i=6/a=065501

[327] E. H. Lieb, H. Narnhofer, The thermodynamic limit for jellium, J. Stat. Phys. 12 (4) (1975) 291–310. doi:10.1007/BF01012066.
URL https://link.springer.com/article/10.1007/BF01012066

[328] C. Lin, F. H. Zong, D. M. Ceperley, Twist-averaged boundary conditions in continuum quantum Monte Carlo algorithms, Phys. Rev. E 64 (1) (2001) 016702. doi:10.1103/PhysRevE.64.016702.
URL http://link.aps.org/doi/10.1103/PhysRevE.64.016702

[329] S. Chiesa, D. M. Ceperley, R. M. Martin, M. Holzmann, Finite-Size Error in Many-Body Simulations with Long-Range Interactions, Phys. Rev. Lett. 97 (7) (2006) 076404. doi:10.1103/PhysRevLett.97.076404.
URL http://link.aps.org/doi/10.1103/PhysRevLett.97.076404

[330] N. D. Drummond, R. J. Needs, A. Sorouri, W. M. C. Foulkes, Finite-size errors in continuum quantum Monte Carlo calculations, Phys. Rev. B 78 (12) (2008) 125106. doi:10.1103/PhysRevB.78.125106.
URL http://link.aps.org/doi/10.1103/PhysRevB.78.125106

[331] M. Holzmann, R. C. Clay, M. A. Morales, N. M. Tubman, D. M. Ceperley, C. Pierleoni, Theory of finite size effects for electronic quantum Monte Carlo calculations of liquids and solids, Phys. Rev. B 94 (3) (2016) 035126. doi:10.1103/PhysRevB.94.035126.
URL http://link.aps.org/doi/10.1103/PhysRevB.94.035126

[332] A. A. Kugler, Bounds for Some Equilibrium Properties of an Electron Gas, Phys. Rev. A 1 (6) (1970) 1688–1696. doi:10.1103/PhysRevA.1.1688.
URL http://link.aps.org/doi/10.1103/PhysRevA.1.1688

[333] T. Dornheim, S. Groth, M. Bonitz, Ab initio results for the static structure factor of the warm dense electron gas, Contrib. Plasma Phys. 57 (10) (2017) 468–478. doi:10.1002/ctpp.201700096.
URL http://dx.doi.org/10.1002/ctpp.201700096

[334] H. E. DeWitt, Statistical Mechanics of HighTemperature Quantum Plasmas Beyond the Ring Approximation, J. Math. Phys. 7 (4) (1966) 616–626. doi:10.1063/1.1704974.
URL http://scitation.aip.org/content/aip/journal/jmp/7/4/10.1063/1.1704974;jsessionid=8AjO6DUAODnHhlQ1CPoUsjbY.x-aip-live-03

[335] S. Groth, T. Dornheim, M. Bonitz, Free energy of the uniform electron gas: Testing analytical models against first-principles results, Contrib. Plasma Phys. 57 (3) (2017) 137–146. doi:10.1002/ctpp.201600082.
URL http://onlinelibrary.wiley.com/doi/10.1002/ctpp.201600082/abstract

[336] K. Burke, J. C. Smith, P. E. Grabowski, A. Pribram-Jones, Exact conditions on the temperature dependence of density functionals, Phys. Rev. B 93 (19) (2016) 195132. doi:10.1103/PhysRevB.93.195132.
URL http://link.aps.org/doi/10.1103/PhysRevB.93.195132

[337] D. Lu, Evaluation of model exchange-correlation kernels in the adiabatic connection fluctuation-dissipation theorem for inhomogeneous systems, J. Chem. Phys. 140 (18) (2014) 18A520. doi:10.1063/1.4867538.
URL http://scitation.aip.org/content/aip/journal/jcp/140/18/10.1063/1.4867538

[338] C. E. Patrick, K. S. Thygesen, Adiabatic-connection fluctuation-dissipation DFT for the structural properties of solids – The renormalized ALDA and electron gas kernels, J. Chem. Phys. 143 (10) (2015) 102802. `doi:10.1063/1.4919236`.
URL `http://scitation.aip.org/content/aip/journal/jcp/143/10/10.1063/1.4919236`

[339] A. Pribram-Jones, P. E. Grabowski, K. Burke, Thermal Density Functional Theory: Time-Dependent Linear Response and Approximate Functionals from the Fluctuation-Dissipation Theorem, Phys. Rev. Lett. 116 (23) (2016) 233001. `doi:10.1103/PhysRevLett.116.233001`.
URL `http://link.aps.org/doi/10.1103/PhysRevLett.116.233001`

[340] P. Neumayer, C. Fortmann, T. Döppner, P. Davis, R. W. Falcone, A. L. Kritcher, O. L. Landen, H. J. Lee, R. W. Lee, C. Niemann, S. Le Pape, S. H. Glenzer, Plasmons in Strongly Coupled Shock-Compressed Matter, Phys. Rev. Lett. 105 (7) (2010) 075003. `doi:10.1103/PhysRevLett.105.075003`.
URL `http://link.aps.org/doi/10.1103/PhysRevLett.105.075003`

[341] K.-U. Plagemann, P. Sperling, R. Thiele, M. P. Desjarlais, C. Fortmann, T. Döppner, H. J. Lee, S. H. Glenzer, R. Redmer, Dynamic structure factor in warm dense beryllium, New J. Phys. 14 (5) (2012) 055020. `doi:10.1088/1367-2630/14/5/055020`.
URL `http://stacks.iop.org/1367-2630/14/i=5/a=055020`

[342] C. Fortmann, A. Wierling, G. Röpke, Influence of local-field corrections on Thomson scattering in collision-dominated two-component plasmas, Phys. Rev. E 81 (2) (2010) 026405. `doi:10.1103/PhysRevE.81.026405`.
URL `http://link.aps.org/doi/10.1103/PhysRevE.81.026405`

[343] H. Reinholz, G. Röpke, S. Rosmej, R. Redmer, Conductivity of warm dense matter including electron-electron collisions, Phys. Rev. E 91 (4) (2015) 043105. `doi:10.1103/PhysRevE.91.043105`.
URL `https://link.aps.org/doi/10.1103/PhysRevE.91.043105`

[344] M. Veysman, G. Röpke, M. Winkel, H. Reinholz, Optical conductivity of warm dense matter within a wide frequency range using quantum statistical and kinetic approaches, Phys. Rev. E 94 (1) (2016) 013203. `doi:10.1103/PhysRevE.94.013203`.
URL `https://link.aps.org/doi/10.1103/PhysRevE.94.013203`

[345] J. Vorberger, D. O. Gericke, T. Bornath, M. Schlanges, Energy relaxation in dense, strongly coupled two-temperature plasmas, Phys. Rev. E 81 (4) (2010) 046404. `doi:10.1103/PhysRevE.81.046404`.
URL `https://link.aps.org/doi/10.1103/PhysRevE.81.046404`

[346] L. X. Benedict, M. P. Surh, L. G. Stanton, C. R. Scullard, A. A. Correa, J. I. Castor, F. R. Graziani, L. A. Collins, O. Certík, J. D. Kress, M. S. Murillo, Molecular dynamics studies of electron-ion temperature equilibration in hydrogen plasmas within the coupled-mode regime, Phys. Rev. E 95 (4) (2017) 043202. `doi:10.1103/PhysRevE.95.043202`.
URL `https://link.aps.org/doi/10.1103/PhysRevE.95.043202`

[347] J. Vorberger, D. O. Gericke, W. D. Kraeft, The equation of state for hydrogen at high densities, High Energy Density Phys. 9 (3) (2013) 448–456. `doi:10.1016/j.hedp.2013.04.011`.
URL `http://www.sciencedirect.com/science/article/pii/S1574181813000517`

[348] C. E. Starrett, D. Saumon, A simple method for determining the ionic structure of warm dense matter, High Energy Density Phys. 10 (2014) 35–42. `doi:10.1016/j.hedp.2013.12.001`.
URL `http://www.sciencedirect.com/science/article/pii/S1574181813001900`

[349] A. N. Souza, D. J. Perkins, C. E. Starrett, D. Saumon, S. B. Hansen, Predictions of x-ray scattering spectra for warm dense matter, Phys. Rev. E 89 (2) (2014) 023108. `doi:10.1103/PhysRevE.89.023108`.
URL `https://link.aps.org/doi/10.1103/PhysRevE.89.023108`

[350] G. Senatore, S. Moroni, D. M. Ceperley, Local field factor and effective potentials in liquid metals, J. Non-Cryst. Solids 205 (1996) 851–854. `doi:10.1016/S0022-3093(96)00316-X`.
URL `http://www.sciencedirect.com/science/article/pii/S002230939600316X`

[351] S. Gravel, N. W. Ashcroft, Nonlinear response theories and effective pair potentials, Phys. Rev. B 76 (14) (2007) 144103. `doi:10.1103/PhysRevB.76.144103`.
URL `https://link.aps.org/doi/10.1103/PhysRevB.76.144103`

111

[352] Z. Moldabekov, S. Groth, T. Dornheim, M. Bonitz, T. Ramazanov, Ion potential in non-ideal dense quantum plasmas, Contrib. Plasma Phys. 57 (10) (2017) 532–538. `doi:10.1002/ctpp.201700109`.
URL `http://dx.doi.org/10.1002/ctpp.201700109`

[353] G. Gregori, A. Ravasio, A. Höll, S. H. Glenzer, S. J. Rose, Derivation of the static structure factor in strongly coupled non-equilibrium plasmas for X-ray scattering studies, High Energy Density Phys. 3 (12) (2007) 99–108. `doi:10.1016/j.hedp.2007.02.006`.
URL `http://www.sciencedirect.com/science/article/pii/S157418180700016X`

[354] T. Dornheim, S. Groth, J. Vorberger, M. Bonitz, Permutation-blocking path-integral Monte Carlo approach to the static density response of the warm dense electron gas, Phys. Rev. E 96 (2) (2017) 023203. `doi:10.1103/PhysRevE.96.023203`.
URL `https://link.aps.org/doi/10.1103/PhysRevE.96.023203`

[355] L. Mühlbacher, E. Rabani, Real-Time Path Integral Approach to Nonequilibrium Many-Body Quantum Systems, Phys. Rev. Lett. 100 (17) (2008) 176403. `doi:10.1103/PhysRevLett.100.176403`.
URL `https://link.aps.org/doi/10.1103/PhysRevLett.100.176403`

[356] M. Schiró, M. Fabrizio, Real-time diagrammatic Monte Carlo for nonequilibrium quantum transport, Phys. Rev. B 79 (15) (2009) 153302. `doi:10.1103/PhysRevB.79.153302`.
URL `https://link.aps.org/doi/10.1103/PhysRevB.79.153302`

[357] M. Schiró, Real-time dynamics in quantum impurity models with diagrammatic Monte Carlo, Phys. Rev. B 81 (8) (2010) 085126. `doi:10.1103/PhysRevB.81.085126`.
URL `https://link.aps.org/doi/10.1103/PhysRevB.81.085126`

[358] N.-H. Kwong, M. Bonitz, Real-Time Kadanoff-Baym Approach to Plasma Oscillations in a Correlated Electron Gas, Phys. Rev. Lett. 84 (8) (2000) 1768–1771. `doi:10.1103/PhysRevLett.84.1768`.
URL `https://link.aps.org/doi/10.1103/PhysRevLett.84.1768`

[359] P. A. Martin, Sum rules in charged fluids, Rev. Mod. Phys. 60 (4) (1988) 1075–1127. `doi:10.1103/RevModPhys.60.1075`.
URL `https://link.aps.org/doi/10.1103/RevModPhys.60.1075`

[360] F. G. Eich, M. Holzmann, G. Vignale, Effective mass of quasiparticles from thermodynamics, Phys. Rev. B 96 (3) (2017) 035132. `doi:10.1103/PhysRevB.96.035132`.
URL `https://link.aps.org/doi/10.1103/PhysRevB.96.035132`

[361] S. Groth, T. Dornheim, M. Bonitz, Configuration path integral Monte Carlo approach to the static density response of the warm dense electron gas, J. Chem. Phys. 147 (16) (2017) 164108. `doi:10.1063/1.4999907`.
URL `http://aip.scitation.org/doi/10.1063/1.4999907`

[362] M. Bonitz, E. Pehlke, T. Schoof, Attractive forces between ions in quantum plasmas: Failure of linearized quantum hydrodynamics, Phys. Rev. E 87 (2013) 033105. `doi:10.1103/PhysRevE.87.033105`.
URL `https://link.aps.org/doi/10.1103/PhysRevE.87.033105`

[363] Z. Moldabekov, T. Schoof, P. Ludwig, M. Bonitz, T. Ramazanov, Statically screened ion potential and bohm potential in a quantum plasma, Phys. Plasmas 22 (10) (2015) 102104. `arXiv:https://doi.org/10.1063/1.4932051`, `doi:10.1063/1.4932051`.
URL `https://doi.org/10.1063/1.4932051`

[364] A. L. Kutepov, G. Kotliar, One-electron spectra and susceptibilities of the three-dimensional electron gas from self-consistent solutions of Hedin's equations, Phys. Rev. B 96 (3) (2017) 035108. `doi:10.1103/PhysRevB.96.035108`.
URL `https://link.aps.org/doi/10.1103/PhysRevB.96.035108`

[365] K. Balzer, M. Bonitz, Nonequilibrium Green's Functions Approach to Inhomogeneous Systems, Springer, 2013.

[366] D. Semkat, D. Kremp, M. Bonitz, Kadanoff-Baym equations and non-Markovian Boltzmann equation in generalized T-matrix approximation, Journal of Mathematical Physics 41 (11) (2000) 7458–7467. `arXiv:https://doi.org/10.1063/1.1286204`, `doi:10.1063/1.1286204`.
URL `https://doi.org/10.1063/1.1286204`

[367] K. Balzer, S. Bauch, M. Bonitz, Efficient grid-based method in nonequilibrium Green's function calculations: Application to model atoms and molecules, Phys. Rev. A 81 (2010) 022510. `doi:10.1103/PhysRevA.81.022510`.
URL `https://link.aps.org/doi/10.1103/PhysRevA.81.022510`

[368] N. Schlünzen, M. Bonitz, Nonequilibrium Green functions approach to strongly correlated fermions in lattice systems, Contrib. Plasma Phys. B 56 (2016) 5–91. `doi:10.1002/ctpp.201610003`.

[369] N. Schlünzen, S. Hermanns, M. Bonitz, C. Verdozzi, Dynamics of strongly correlated fermions: *Ab initio* results for two and three dimensions, Phys. Rev. B 93 (2016) 035107. `doi:10.1103/PhysRevB.93.035107`.
URL `https://link.aps.org/doi/10.1103/PhysRevB.93.035107`

[370] J. Chihara, Difference in X-ray scattering between metallic and non-metallic liquids due to conduction electrons, J. Phys. F 17 (2) (1987) 295. `doi:10.1088/0305-4608/17/2/002`.
URL `http://stacks.iop.org/0305-4608/17/i=2/a=002`

[371] M. Bonitz, K. Balzer, R. van Leeuwen, Invariance of the Kohn center-of-mass mode in a conserving theory, Phys. Rev. B 76 (2007) 045341. `doi:10.1103/PhysRevB.76.045341`.
URL `https://link.aps.org/doi/10.1103/PhysRevB.76.045341`

[372] S. Bauch, K. Balzer, C. Henning, M. Bonitz, Quantum breathing mode of trapped bosons and fermions at arbitrary coupling, Phys. Rev. B 80 (2009) 054515. `doi:10.1103/PhysRevB.80.054515`.
URL `https://link.aps.org/doi/10.1103/PhysRevB.80.054515`

[373] C. Henning, K. Fujioka, P. Ludwig, A. Piel, A. Melzer, M. Bonitz, Existence and vanishing of the breathing mode in strongly correlated finite systems, Phys. Rev. Lett. 101 (2008) 045002. `doi:10.1103/PhysRevLett.101.045002`.
URL `https://link.aps.org/doi/10.1103/PhysRevLett.101.045002`

[374] C. R. McDonald, G. Orlando, J. W. Abraham, D. Hochstuhl, M. Bonitz, T. Brabec, Theory of the quantum breathing mode in harmonic traps and its use as a diagnostic tool, Phys. Rev. Lett. 111 (2013) 256801. `doi:10.1103/PhysRevLett.111.256801`.
URL `https://link.aps.org/doi/10.1103/PhysRevLett.111.256801`

[375] R. Schmitz, S. Krönke, L. Cao, P. Schmelcher, Quantum breathing dynamics of ultracold bosons in one-dimensional harmonic traps: Unraveling the pathway from few- to many-body systems, Phys. Rev. A 88 (2013) 043601. `doi:10.1103/PhysRevA.88.043601`.
URL `https://link.aps.org/doi/10.1103/PhysRevA.88.043601`

[376] K. Balzer, S. Hermanns, M. Bonitz, Electronic double excitations in quantum wells: Solving the two-time Kadanoff-Baym equations, EPL (Europhysics Letters) 98 (6) (2012) 67002.
URL `http://stacks.iop.org/0295-5075/98/i=6/a=67002`

[377] Y. V. Arkhipov, A. B. Ashikbayeva, A. Askaruly, A. E. Davletov, I. M. Tkachenko, Dielectric function of dense plasmas, their stopping power, and sum rules, Phys. Rev. E 90 (5) (2014) 053102. `doi:10.1103/PhysRevE.90.053102`.
URL `http://link.aps.org/doi/10.1103/PhysRevE.90.053102`

[378] B. J. Berne, Path integral Monte Carlo methods: Static- and time-correlation functions, J. Stat. Phys. 43 (5-6) (1986) 911–929. `doi:10.1007/BF02628319`.
URL `https://link.springer.com/article/10.1007/BF02628319`

[379] M. Jarrell, J. E. Gubernatis, Bayesian inference and the analytic continuation of imaginary-time quantum Monte Carlo data, Phys. Rep. 269 (3) (1996) 133–195. `doi:10.1016/0370-1573(95)00074-7`.
URL `http://www.sciencedirect.com/science/article/pii/0370157395000747`

[380] G. Ferré, J. Boronat, Dynamic structure factor of liquid ^{4}He across the normal-superfluid transition, Phys. Rev. B 93 (10) (2016) 104510. `doi:10.1103/PhysRevB.93.104510`.
URL `https://link.aps.org/doi/10.1103/PhysRevB.93.104510`

[381] M. Motta, D. E. Galli, S. Moroni, E. Vitali, Imaginary time correlations and the phaseless auxiliary field quantum Monte Carlo, J. Chem. Phys. 140 (2) (2014) 024107. `doi:10.1063/1.4861227`.
URL `http://scitation.aip.org/content/aip/journal/jcp/140/2/10.1063/1.4861227`

[382] M. Motta, D. E. Galli, S. Moroni, E. Vitali, Imaginary time density-density correlations for two-dimensional electron gases at high density, J. Chem. Phys. 143 (16) (2015) 164108. `doi:10.1063/1.4934666`.
URL `http://scitation.aip.org/content/aip/journal/jcp/143/16/10.1063/1.4934666`

[383] R. Levy, J. P. F. LeBlanc, E. Gull, Implementation of the maximum entropy method for analytic continuation, Comp. Phys. Comm. 215 (Supplement C) (2017) 149–155. `doi:10.1016/j.cpc.2017.01.018`.
URL `http://www.sciencedirect.com/science/article/pii/S0010465517300309`

[384] N. V. Prokofev, B. V. Svistunov, Spectral analysis by the method of consistent constraints, JETP Letters 97 (11) (2013) 649–653. `doi:10.1134/S002136401311009X`.
URL `https://link.springer.com/article/10.1134/S002136401311009X`

[385] E. Vitali, M. Rossi, L. Reatto, D. E. Galli, Ab initio low-energy dynamics of superfluid and solid ^{4}He, Phys. Rev. B 82 (17). `doi:10.1103/PhysRevB.82.174510`.
URL `http://link.aps.org/doi/10.1103/PhysRevB.82.174510`

[386] J. Otsuki, M. Ohzeki, H. Shinaoka, K. Yoshimi, Sparse modeling approach to analytical continuation of imaginary-time quantum Monte Carlo data, Phys. Rev. E 95 (6) (2017) 061302. `doi:10.1103/PhysRevE.95.061302`.
URL `https://link.aps.org/doi/10.1103/PhysRevE.95.061302`

[387] J. Schött, E. G. C. P. van Loon, I. L. M. Locht, M. I. Katsnelson, I. Di Marco, Comparison between methods of analytical continuation for bosonic functions, Phys. Rev. B 94 (24) (2016) 245140. `doi:10.1103/PhysRevB.94.245140`.
URL `https://link.aps.org/doi/10.1103/PhysRevB.94.245140`

[388] D. Hochstuhl, M. Bonitz, Two-photon ionization of helium studied with the multiconfigurational time-dependent Hartree-Fock method, The Journal of Chemical Physics 134 (8) (2011) 084106. `arXiv:https://doi.org/10.1063/1.3553176`, `doi:10.1063/1.3553176`.
URL `https://doi.org/10.1063/1.3553176`

[389] D. Hochstuhl, C. Hinz, M. Bonitz, Time-dependent multiconfiguration methods for the numerical simulation of photoionization processes of many-electron atoms, The European Physical Journal Special Topics 223 (2) (2014) 177–336. `doi:10.1140/epjst/e2014-02092-3`.
URL `https://doi.org/10.1140/epjst/e2014-02092-3`

[390] W. Schattke, M. van Howe (Eds.), Solid-State Photoemission and Related Methods: Theory and Experiment, Wiley-VCH, 2003.

[391] W. D. Kraeft, M. Schlanges, J. Vorberger, H. E. DeWitt, Kinetic and correlation energies and distribution functions of dense plasmas, Phys. Rev. E 66 (2002) 046405. `doi:10.1103/PhysRevE.66.046405`.
URL `https://link.aps.org/doi/10.1103/PhysRevE.66.046405`

[392] V. S. Filinov, M. Bonitz, V. E. Fortov, High-density pheomena in hydrogen plasma, JETP Lett. 72 (5) (2000) 361–365.
URL `http://link.springer.com/article/10.1134/1.1427127`

[393] V. S. Filinov, V. E. Fortov, M. Bonitz, D. Kremp, Pair distribution functions of dense partially ionized hydrogen plasma, Phys. Lett. A 72 (5) (2000) 228–235.
URL `http://link.springer.com/article/10.1134/1.1427127`

[394] M. Bonitz, V. S. Filinov, V. E. Fortov, P. R. Levashov, H. Fehske, Crystallization in two-component coulomb systems, Phys. Rev. Lett. 95 (2005) 235006. `doi:10.1103/PhysRevLett.95.235006`.
URL `https://link.aps.org/doi/10.1103/PhysRevLett.95.235006`

[395] G. Kelbg, Theorie des Quanten-Plasmas, Ann. Phys., Lpz. 467 (3-4) (1963) 219–224. `doi:10.1002/andp.19634670308`.
URL `http://dx.doi.org/10.1002/andp.19634670308`

[396] G. Kelbg, Quantenstatistik der Gase mit Coulomb-Wechselwirkung, Ann. Phys., Lpz. 467 (7-8) (1963) 354–360. `doi:10.1002/andp.19634670703`.
URL `http://dx.doi.org/10.1002/andp.19634670703`

[397] G. Kelbg, Klassische statistische Mechanik der Teilchen-Mischungen mit sortenabhngigen weitreichenden zwischenmolekularen Wechselwirkungen, Ann. Phys., Lpz. 469 (7-8) (1964) 394–403. `doi:10.1002/andp.19644690705`.
URL `http://dx.doi.org/10.1002/andp.19644690705`

[398] A. V. Filinov, M. Bonitz, W. Ebeling, Improved Kelbg potential for correlated Coulomb systems, J. Phys. A: Math. General 36 (2003) 5957–5962.

[399] A. V. Filinov, V. O. Golubnychiy, M. Bonitz, W. Ebeling, J. W. Dufty, Temperature-dependent quantum pair potentials and their application to dense partially ionized hydrogen plasmas, Phys. Rev. E 70 (2004) 046411. `doi:10.1103/PhysRevE.70.046411`.
URL `https://link.aps.org/doi/10.1103/PhysRevE.70.046411`

[400] Git-repository: Ab-initio thermodynamic description of the warm dense electron gas (2017).
URL `https://github.com/agbonitz/xc_functional`

Chapter 3

Method Development

3.1 Introduction of Permutation Blocking PIMC

The beginning of my PhD thesis in November 2014 coincided with a spike in fermionic QMC simulations at finite temperature, see, e.g., Refs. [74, 157, 170–172]. Beforehand, it used to be common wisdom that path integral Monte Carlo simulations would become infeasible as soon as fermionic exchange effects become important, i.e., in the most interesting regime. For this reason, back in 2013, Brown and co-workers published the first thermodynamic QMC results for the uniform electron gas at warm dense matter conditions [157] using the fixed-node approximation [48]. While formally avoiding the fermion sign problem, they utilized the nodal structure of the ideal system for all coupling parameters, so that the accuracy of these data had remained unclear.

Independently, Tim Schoof and Simon Groth were developing a new approach to fermionic QMC simulations at finite temperature as part of their PhD and Master theses [75, 76, 173]. Their so-called configuration PIMC approach [73, 74, 59] is formulated in the antisymmetric Fock space and can be interpreted as a Monte Carlo simulation on the exact, infinite perturbation expansion around the ideal system. In contrast to the standard PIMC methods in coordinate space, CPIMC excels at weak coupling and strong degeneracy and has no sign problem for the ideal system. Instead, it eventually breaks down with increasing coupling strength. Therefore, it was clear that CPIMC was complementary to standard PIMC, and, due to its exact nature, is capable to provide valuable benchmark data for other methods. In their seminal paper, Schoof *et al.* [59] managed to obtain highly accurate data for $N = 33$ spin-polarized electrons up to $r_{\mathrm{s}} = 1$, which made it possible to evaluate the quality of the available RPIMC data. Surprisingly, they found deviations of up to 10% in the exchange–correlation energy towards low temperature and high density, which is in stark contrast to the ground state, where the fixed-node approximation is known

to provide a highly accurate description of the electron gas [46, 111, 174]. Therefore, it was clear that a new method was needed that, on the one hand, could extend standard PIMC towards lower temperature and higher densities, while, on the other hand, being sufficiently accurate to allow for a smooth connection with the CPIMC data in the weak coupling regime: the development of such an approach—PB-PIMC—is the first central goal of this thesis.

In theory, it was known since the late 70s and early 80s that the application of antisymmetric imaginary-time propagators, i.e., determinants, leads to a significant reduction of the fermion sign problem in standard PIMC simulations [41, 60, 61, 66]. This is due to a grouping together of terms of different signs into a single term—a strategy that is often denoted as *blocking* in the QMC community [175]. In particular, Filinov and co-workers have successfully pursued this strategy within their QMC simulations of various systems, see, e.g., Refs. [63–71]. However, there is a catch-22: for an increasing number of imaginary-time slices, which are needed for a sufficient description towards low temperature and strong degeneracy, the advantage due to the determinants vanishes. In other words, the determinants do not work when they are needed most.

The basic idea of the permutation blocking PIMC scheme is to combine said antisymmetric propagators with a higher-order factorization of the density matrix [176–178] that allows for sufficient accuracy with a small number of time slices. In this way, the onset of the sign problem, compared to standard PIMC, is delayed both towards lower temperature and weaker coupling. For completeness, I mention that in early 2015, Chin [62] proposed a similar strategy, although his aim was the approximation of the ground-state energy of electrons in a quantum dot.

The development and implementation of the PB-PIMC method constitutes the foundation of this thesis. As a proof of principle, I initially implemented it for electrons in a harmonic trap, where a comparison to exact CPIMC and standard PIMC[1] data is possible at weak and strong coupling, respectively. As it turns out, the introduction of the determinants leads to a significantly more complicated configuration space without any fixed trajectories or paths. To still have an efficient sampling procedure, I developed a new update scheme based on the temporary construction of artificial trajectories, which is inspired by the continuous-space worm algorithm paradigm by Boninsegni *et al.* [35, 36]. The underlying equations, derivation of Monte Carlo estimators and a comprehensive discussion of said update scheme can be found in the following paper[2], Ref. [72], together with a concise discussion of numerical results. In particular, it was found that, indeed, PB-PIMC is capable to provide accurate

---

[1]The standard PIMC results for electrons in the trap were obtained using the PIMC code that I implemented as part of my Master thesis [43].

[2]T. Dornheim, S. Groth, A. Filinov, and M. Bonitz, New J. Phys. **17**, 073017 (2015), reproduced under the Creative Commons 3.0 license.

data where no other *ab initio* methods are available, and that the optimal choice of two free parameters in the factorization scheme allows for a significantly improved accuracy for only two or three imaginary-time propagators.

New Journal of Physics

The open access journal at the forefront of physics

CrossMark

PAPER

Permutation blocking path integral Monte Carlo: a highly efficient approach to the simulation of strongly degenerate non-ideal fermions

Tobias Dornheim[1], Simon Groth[1], Alexey Filinov[1,2] and Michael Bonitz[1]

[1] Institut für Theoretische Physik und Astrophysik, Christian-Albrechts-Universität, Leibnizstraße 15, Kiel D-24098, Germany
[2] Joint Institute for High Temperatures RAS, Izhorskaya Str. 13, 125412 Moscow, Russia

E-mail: dornheim@theo-physik.uni-kiel.de

Abstract

Correlated fermions are of high interest in condensed matter (Fermi liquids, Wigner molecules), cold atomic gases and dense plasmas. Here we propose a novel approach to path integral Monte Carlo (PIMC) simulations of strongly degenerate non-ideal fermions at finite temperature by combining a fourth-order factorization of the density matrix with antisymmetric propagators, i.e., determinants, between all imaginary time slices. To efficiently run through the modified configuration space, we introduce a modification of the widely used continuous space worm algorithm, which allows for an efficient sampling at arbitrary system parameters. We demonstrate how the application of determinants achieves an effective blocking of permutations with opposite signs, leading to a significant relieve of the fermion sign problem. To benchmark the capability of our method regarding the simulation of degenerate fermions, we consider multiple electrons in a quantum dot and compare our results with other *ab initio* techniques, where they are available. The present permutation blocking PIMC approach allows us to obtain accurate results even for $N = 20$ electrons at low temperature and arbitrary coupling, where no other *ab initio* results have been reported, so far.

1. Introduction

The *ab initio* simulation of strongly degenerate nonideal fermions at finite temperature is of high current importance for many fields. The numerous physical applications include electrons in a quantum dot [1–4], fermionic bilayer systems [5–7], the homogeneous electron gas [8–10], dense two-component plasmas [11–13] in stellar interiors and modern laser compression experiments (warm dense matter) [14, 15] and inertial fusion [16]. Despite remarkable recent progress, existing simulation methods face serious problems.

The widely used path integral Monte Carlo (PIMC) method, e.g. [17], is a highly successful tool for the *ab initio* simulation of both distinguishable particles ('boltzmannons', e.g. [18, 19]) and bosons [17] and allows for the calculation of quasi-exact results for up to $N \sim 10^3$ particles [20] at finite temperature. However, the application of PIMC to fermions is hampered by the notorious sign problem [21], which renders even small systems unfeasible for state of the art techniques and has been revealed to be *NP*-complete for a given representation [22]. With increasing exchange effects, permutation cycles with opposite signs appear with nearly equal frequency and the statistical error increases exponentially. For this reason, standard PIMC is applicable to fermions only at weak degeneracy, that is, at relatively high temperature or low density.

The recently introduced configuration path integral Monte Carlo (CPIMC) method [9, 23, 24] exhibits a complementary behavior. This conceptually different approach can be interpreted as a Monte Carlo simulation on a perturbation expansion around the ideal quantum system and, therefore, CPIMC excels at weak nonideality and strong degeneracy. Unfortunately, the physically most interesting region, where both fermionic exchange and interactions are strong simultaneously, remains out of reach.
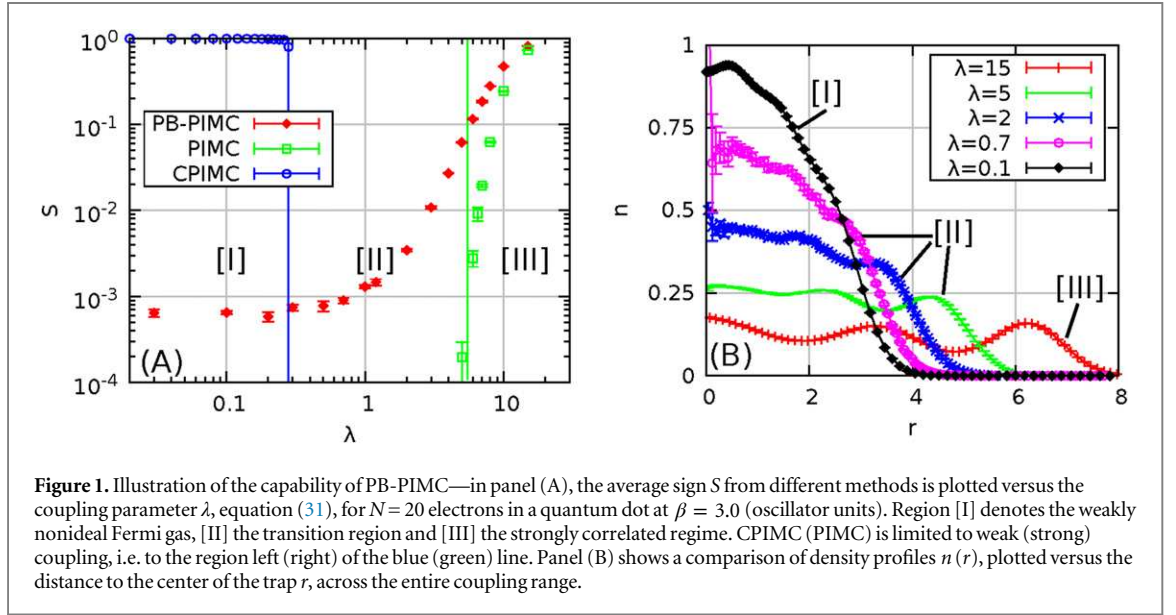
Figure 1. Illustration of the capability of PB-PIMC—in panel (A), the average sign *S* from different methods is plotted versus the coupling parameter λ, equation (31), for $N = 20$ electrons in a quantum dot at $\beta = 3.0$ (oscillator units). Region [I] denotes the weakly nonideal Fermi gas, [II] the transition region and [III] the strongly correlated regime. CPIMC (PIMC) is limited to weak (strong) coupling, i.e. to the region left (right) of the blue (green) line. Panel (B) shows a comparison of density profiles $n(r)$, plotted versus the distance to the center of the trap *r*, across the entire coupling range.

A popular approach to extend standard PIMC to higher degeneracy is Restricted PIMC (RPIMC) [25], also known as fixed node approximation. This idea requires explicit knowledge of the nodal surfaces of the density matrix, which are, in general, unknown and one has to rely on approximations, thereby introducing an uncontrollable systematic error. In addition, it has been shown analytically [26, 27] that RPIMC does not reproduce the exact density matrix in the limit of the ideal Fermi gas and, therefore, the results become unreliable at increasing degeneracy [9].

Recently, DuBois *et al* [28] have suggested that, at least for homogeneous systems, the individual exchange probabilities in PIMC are independent of the configuration of other permutations present and that permutation frequencies of large exchange cycles can be extrapolated from few-particle permutations. This would allow for a significant reduction of the configuration space and a drastic reduction of the sign problem. While first simulation results with this approximation for the short-range interacting ^{3}He are in good agreement with experimental data [28], the existing comparison [9] for long-range Coulomb interaction is insufficient to assess the accuracy and, in addition, inhomogeneous systems remain out of reach.

Another possibility to relieve the sign problem in fermionic PIMC without introducing any approximations is the usage of antisymmetric imaginary time propagators, i.e., determinants [10, 29–31]. It is well known that the sign problem becomes more severe with an increasing number of propagators arising from the Trotter-type factorization of the density operator. Consequently, it has been proposed to combine the antisymmetric propagators with a higher order factorization [32–35] of the density matrix. This has recently allowed to obtain an accurate estimate of the ground state energy of degenerate, strongly nonideal electrons in a quantum dot [36].

In the present work, we extend this idea to finite temperature. For this purpose, we combine a fourth-order propagator derived in [37], which has already been succesfully applied to PIMC by Sakkos *et al* [38], with a full antisymmetrization on all time slices to simulate fermions in the canonical ensemble. We demonstrate that the introduction of determinants effectively allows for the combination of *N*! configurations from usual PIMC into a single configuration weight, thereby reducing the complexity of the problem and blocking both positive and negative weights to drastically increase the sign. To efficiently exploit the resulting configuration space with the Metropolis algorithm [39] at arbitrary parameters, we develop a set of Monte Carlo updates similar to the usual continuous space worm algorithm (WA) [20, 40].

To demonstrate the capability of our permutation blocking (PB-PIMC) method, we consider Coulomb interacting fermions in a 2D harmonic confinement, cf equation (30), which can be experimentally realized e.g. by spin-polarized electrons in a quantum dot [1–4]. Figure 1(A) shows the average sign *S* for $N = 20$ electrons, plotted versus the coupling strength λ, cf equation (31). CPIMC is applicable in the weakly nonideal regime [I], where the system is predominantly shaped by the Fermi statistics. In contrast, standard PIMC allows one to accurately simulate systems in the strongly coupled regime [III], where exchange effects are not yet dominating, and bosons and fermions exhibit a very similar behavior. The PB-PIMC method, as will be shown in this work, is applicable over the entire coupling range yielding reasonably accurate results with acceptable computational effort. Interestingly, this includes the physically most interesting transition region [II], where both the Coulomb repulsion and quantum statistics govern the system. Here no *ab initio* results have been reported to this date, except for very small particle numbers, since PIMC and CPIMC fail, due to the sign problem. In panel (B), we

show density profiles from all three regimes. Evidently, the transition from the strongly coupled system with a pronounced shell structure ($\lambda = 15$) to the nearly ideal Fermi gas with the characteristic weak density modulations ($\lambda = 0.1$) can be resolved.

In the remainder of this work, we introduce the PB-PIMC method in detail. We show that the optimal choice of two free parameters of the fourth-order factorization allows for a calculation of energies and densities with an accuracy of the order of 0.1% with as few as two or three propagators, even in the low temperature regime. We calculate energies and densities from PB-PIMC for $N = 20$ electrons at low temperature over the entire coupling range. We find excellent agreement with both PIMC and CPIMC in the limiting cases of strong and weak coupling, respectively, and perform simulations in the transition regime, where no other *ab initio* results are available. Finally, we investigate the performance behavior of our method when the system size is varied.

2. Theory

2.1. Idea of PB-PIMC

We consider the canonical ensemble (the particle number N, volume V and inverse temperature $\beta = 1/k_B T$ are fixed) and write the partition function in coordinate representation as

$$Z = \frac{1}{N!} \sum_{\sigma \in S_N} \text{sgn}(\sigma) \int d\mathbf{R} \, \langle \mathbf{R} | \, e^{-\beta \hat{H}} \, | \hat{\pi}_\sigma \mathbf{R} \rangle, \tag{1}$$

where $\mathbf{R} = \{\mathbf{r}_1, ..., \mathbf{r}_N\}$ contains the coordinates of all particles and $\hat{\pi}_\sigma$ denotes the exchange operator corresponding to a particular element σ from the permutation group S_N. The Hamiltonian is given by the sum of the kinetic ($\hat{K}$) and potential ($\hat{V}$) energy, $\hat{H} = \hat{K} + \hat{V}$. For the next step, we use the group property of the density operator

$$\hat{\rho} = e^{-\beta \hat{H}} = \prod_{\alpha=0}^{P-1} e^{-\epsilon \hat{H}}, \tag{2}$$

with $\epsilon = \beta/P$, and insert $P - 1$ unities of the form $\hat{1} = \int d\mathbf{R}_\alpha \, |\mathbf{R}_\alpha\rangle\langle\mathbf{R}_\alpha|$. This gives

$$Z = \int d\mathbf{R}_0 ... d\mathbf{R}_{P-1} \prod_{\alpha=0}^{P-1} \left(\frac{1}{N!} \sum_{\sigma \in S_N} \text{sgn}(\sigma) \langle \mathbf{R}_\alpha | \, e^{-\epsilon \hat{H}} \, | \hat{\pi}_\sigma \mathbf{R}_{\alpha+1} \rangle \right). \tag{3}$$

Note that we have exploited the permutation operator's idempotency property in equation (3) to introduce antisymmetry on all P imaginary time slices. Following Sakkos *et al* [38], we introduce the factorization from [37],

$$e^{-\epsilon \hat{H}} \approx e^{-v_1 \epsilon \hat{W}_{a_1}} e^{-t_1 \epsilon \hat{K}} e^{-v_2 \epsilon \hat{W}_{1-2a_1}} e^{-t_1 \epsilon \hat{K}} e^{-v_1 \epsilon \hat{W}_{a_1}} e^{-2t_0 \epsilon \hat{K}}, \tag{4}$$

for each of the exponential functions in equation (3). By including double commutator terms of the form

$$\left[\left[\hat{V}, \hat{K} \right], \hat{V} \right] = \frac{\hbar^2}{m} \sum_{i=1}^{N} |\mathbf{F}_i|^2, \tag{5}$$

we have to evaluate the total force on each particle, $\mathbf{F}_i = -\nabla_i V(\mathbf{R})$, and equation (4) is accurate to fourth order in ϵ. The explicit form of the modified potential terms $\hat{W}$ is given by

$$\hat{W}_{a_1} = \hat{V} + \frac{u_0}{v_1} a_1 \epsilon^2 \left(\frac{\hbar^2}{m} \sum_{i=1}^{N} |\mathbf{F}_i|^2 \right) \quad \text{and}$$

$$\hat{W}_{1-a_1} = \hat{V} + \frac{u_0}{v_2} (1 - a_1) \epsilon^2 \left(\frac{\hbar^2}{m} \sum_{i=1}^{N} |\mathbf{F}_i|^2 \right). \tag{6}$$

There are two free parameters in equation (4), namely $0 \leqslant a_1 \leqslant 1$, which controls the relative weight of the forces on a particular slice, and $0 \leqslant t_0 \leqslant (1 - 1/\sqrt{3})/2$, which determines the ratio of the, in general, non-equidistant time steps between 'daughter' slices, cf figure 2. All other factors are calculated from these choices:

Figure 2. Illustration of the configuration space—in the left panel, the imaginary time is plotted versus the (arbitrary) spatial coordiante *x*. Each time step of length ϵ is further divided into three non-equidistant subintervals, with two 'daughter' slices *A* and *B*. The right panel illustrates the combination of all $3PN!$ possible trajectories into a single configuration weight $W(\mathbf{X})$. Between each two adjacent time slices, both the connection between beads from the same particle (diagonal elements of the diffusion matrix, the blue and red lines) and between beads from different particles (off-diagonal elements, the green lines) are efficiently grouped together to improve the average sign.

$$u_0 = \frac{1}{12}\left(1 - \frac{1}{1-2t_0} + \frac{1}{6\left(1-2t_0\right)^3}\right),$$

$$v_1 = \frac{1}{6\left(1-2t_0\right)^2},$$

$$v_2 = 1 - 2v_1 \quad \text{and}$$

$$t_1 = \frac{1}{2} - t_0. \tag{7}$$

The fourth-order approximation of the imaginary time propagator $e^{-\epsilon \hat{H}}$ is visualized in figure 2. The inverse temperature β has been split into $P = 4$ intervals of length ϵ, which are further divided into three, in general, non-equidistant sub-intervals. Thus, for each main 'bead' τ_α, there exist two daughter beads, $\tau_{\alpha A}$ and $\tau_{\alpha B}$.

Let us for a moment ignore the antisymmetry in equation (3) and evaluate the imaginary time propagator in a straightforward way [38]:

$$\langle \mathbf{R}_\alpha| \ e^{-\epsilon \hat{H}} \ |\mathbf{R}_{\alpha+1}\rangle = \int d\mathbf{R}_{\alpha A} d\mathbf{R}_{\alpha B} \left[e^{-\epsilon \tilde{V}_\alpha} e^{-u_0 \epsilon^3 \frac{\hbar^2}{m} \tilde{F}_\alpha} \right.$$

$$\left. \prod_{i=1}^{N} \rho_\alpha(i, i) \rho_{\alpha, A}(i, i) \rho_{\alpha B}(i, i) \right], \tag{8}$$

with the definitions of the potential terms

$$\tilde{V}_\alpha = v_1 V\left(\mathbf{R}_\alpha\right) + v_2 V\left(\mathbf{R}_{\alpha A}\right) + v_1 V\left(\mathbf{R}_{\alpha B}\right),$$

$$\tilde{F}_\alpha = \sum_{i=1}^{N} \left(a_1 |\mathbf{F}_{\alpha,i}|^2 + \left(1 - 2a_1\right) |\mathbf{F}_{\alpha A,i}|^2 + a_1 |\mathbf{F}_{\alpha B,i}|^2 \right), \tag{9}$$

and the diffusion matrices

$$\rho_\alpha(i, j) = \lambda_{t_1\epsilon}^{-D} \exp\left(-\frac{\pi}{\lambda_{t_1\epsilon}^2} (\mathbf{r}_{\alpha,j} - \mathbf{r}_{\alpha A,i})^2 \right),$$

$$\rho_{\alpha A}(i, j) = \lambda_{t_1\epsilon}^{-D} \exp\left(-\frac{\pi}{\lambda_{t_1\epsilon}^2} (\mathbf{r}_{\alpha A,j} - \mathbf{r}_{\alpha B,i})^2 \right),$$

$$\rho_{\alpha B}(i, j) = \lambda_{2t_0\epsilon}^{-D} \exp\left(-\frac{\pi}{\lambda_{2t_0\epsilon}^2} (\mathbf{r}_{\alpha B,j} - \mathbf{r}_{\alpha+1,i})^2 \right), \tag{10}$$

where λ_β denotes the thermal wavelength $\lambda_\beta^2 = 2\pi\hbar^2\beta/m$ and D is the dimensionality of the system. Thus, the matrix elements of equation (10) are equal to the free particle density matrix, $\rho_\alpha(i, j) = \rho_0(\mathbf{r}_{\alpha,j}, \mathbf{r}_{\alpha A,i}, t_1\epsilon)$.

The permutation operator commutes with both $\hat{\rho}$ and $\hat{H}$ and we are, therefore, allowed to artificially introduce the antisymmetrization between all $3P$ slices without changing the result. This transforms equation (8) to

$$
\frac{1}{N!} \sum_{\sigma \in S_N} \mathrm{sgn}(\sigma) \langle \mathbf{R}_\alpha | \, e^{-\epsilon \hat{H}} \, |\hat{\pi}_\sigma \mathbf{R}_{\alpha+1}\rangle
$$

$$
= \left(\frac{1}{N!}\right)^3 \int d\mathbf{R}_{\alpha A} d\mathbf{R}_{\alpha B} \left[e^{-\epsilon \tilde{V}_\alpha} e^{-\epsilon^3 u_0 \frac{\hbar^2}{m} \tilde{F}_\alpha} \det(\rho_\alpha) \det(\rho_{\alpha A}) \det(\rho_{\alpha B}) \right]. \tag{11}
$$

Finally, this gives the partition function

$$
Z = \frac{1}{(N!)^{3P}} \int d\mathbf{X} \prod_{\alpha=0}^{P-1} e^{-\epsilon \tilde{V}_\alpha} e^{-\epsilon^3 u_0 \frac{\hbar^2}{m} \tilde{F}_\alpha} \det(\rho_\alpha) \det(\rho_{\alpha A}) \det(\rho_{\alpha B}), \tag{12}
$$

and the integration is carried out over all coordinates on all $3P$ slices:

$$
d\mathbf{X} = d\mathbf{R}_0 \ldots d\mathbf{R}_{P-1} d\mathbf{R}_{0A} \ldots d\mathbf{R}_{P-1A} d\mathbf{R}_{0B} \ldots d\mathbf{R}_{P-1B}. \tag{13}
$$

The benefits of the partition function equation (12) are illustrated in the right panel of figure 2 where the beads of two particles are plotted in the τ–x-plane. In the usual PIMC formulation (without the determinants), each of the particles would correspond to a single closed trajectory as visualized by the blue and red connections. To take into account the antisymmetry of fermions, one would also need to sample all configurations with the same positions of the individual beads but different connections between adjacent time slices, which have both positive and negative weights. By indroducing determinants between all slices, we include all $N!$ possible connections between beads on adjacent slices (the green lines) into a single configuration weight and the usual interpretation of mapping a quantum system onto an ensemble of interacting ringpolymers [41] is no longer appropriate. Therefore, a large number of sign changes, due to different permutations, are grouped together resulting in an efficient compensation of many terms (blocking), and the average sign (cf equation (22)) in our simulations is significantly increased [31].

2.2. Energy estimator

The total energy E follows from the partition function via the familiar relation

$$
E = -\frac{1}{Z}\frac{\partial Z}{\partial \beta}. \tag{14}
$$

Substituting the expression from equation (12) into (14) and performing a lengthy but straightforward calculation gives the final result for the thermodynamic (TD) estimator

$$
E = \frac{3\,DN}{2\epsilon} - \sum_{k=0}^{P-1}\sum_{\kappa=1}^{N}\sum_{\xi=1}^{N}\left(\frac{\pi \Psi_{\kappa\xi}^k}{\epsilon P \lambda_{t_1\epsilon}^2}(\mathbf{r}_{k,\kappa} - \mathbf{r}_{kA,\xi})^2 \right.
$$

$$
\left. + \frac{\pi \Psi_{\kappa\xi}^{kA}}{\epsilon P \lambda_{t_1\epsilon}^2}(\mathbf{r}_{kA,\kappa} - \mathbf{r}_{kB,\xi})^2 + \frac{\pi \Psi_{\kappa\xi}^{kB}}{\epsilon P \lambda_{2t_0\epsilon}^2}(\mathbf{r}_{kB,\kappa} - \mathbf{r}_{k+1,\xi})^2 \right)
$$

$$
+ \frac{1}{P}\sum_{k=0}^{P-1}\left(\tilde{V}_k + 3\epsilon^2 u_0 \frac{\hbar^2}{m}\tilde{F}_k \right), \tag{15}
$$

with the definitions

$$
\Psi_{\kappa\xi}^k = \left(\rho_k^{-1}\right)_{\kappa\xi}(\rho_k)_{\xi\kappa}
$$

$$
\Psi_{\kappa\xi}^{kA} = \left(\rho_{kA}^{-1}\right)_{\kappa\xi}(\rho_{kA})_{\xi\kappa}
$$

$$
\Psi_{\kappa\xi}^{kB} = \left(\rho_{kB}^{-1}\right)_{\kappa\xi}(\rho_{kB})_{\xi\kappa}. \tag{16}
$$

To split the total energy into a kinetic and a potential part, we evaluate

$$
K = \frac{m}{\beta Z}\frac{\partial}{\partial m}Z, \tag{17}
$$

and find the TD estimator of the kinetic energy

$$K = \frac{3ND}{2\epsilon} - \sum_{k=0}^{P-1}\sum_{\kappa=1}^{N}\sum_{\xi=1}^{N}\left[\frac{\pi\Psi_{\kappa\xi}^{k}}{\epsilon P\lambda_{t_1\epsilon}^{2}}(\mathbf{r}_{k,\kappa} - \mathbf{r}_{kA,\xi})^2 + \frac{\pi\Psi_{\kappa\xi}^{kA}}{\epsilon P\lambda_{t_1\epsilon}^{2}}(\mathbf{r}_{kA,\kappa} - \mathbf{r}_{kB,\xi})^2 \right.$$
$$\left. + \frac{\pi\Psi_{\kappa\xi}^{kB}}{\epsilon P\lambda_{2t_0\epsilon}^{2}}(\mathbf{r}_{kB,\kappa} - \mathbf{r}_{k+1,\xi})^2 \right] + \frac{1}{P}\sum_{k=0}^{P-1}\left(\epsilon^2 u_0 \frac{\hbar^2}{m}\tilde{F}_k \right). \tag{18}$$

Thus, the estimator of the potential energy is given by

$$V = E - K = \frac{1}{P}\sum_{k=0}^{P-1}\left(\tilde{V}_k + 2\epsilon^2 u_0 \frac{\hbar^2}{m}\tilde{F}_k \right). \tag{19}$$

We notice that the forces contribute to both the kinetic and the potential energy. For completeness, we mention that, for an increasing number of propagators, $P \to \infty$, the first and second terms in equation (15) diverge, which leads to a growing variance and, therefore, statistical uncertainty of both E and K. To avoid this problem, one might derive a virial estimator, e.g. [42], which requires the evaluation of the derivative of the potential terms instead. However, since we are explicitly interested in performing simulations with few propagators to relieve the fermion sign problem, the estimator from equation (15) is sufficient.

3. Monte Carlo algorithm

In section 2, we have derived an expression for the partition function Z, equation (12), which incorporates determinants of the diffusion matrices between all $3P$ time slices, thereby combining $3PN!$ different configurations from the usual PIMC into a single weight $W(\mathbf{X})$. However, each determinant can still be either positive or negative, depending on the relative magnitude of diagonal and off-diagonal elements. Hence, we apply the Metropolis algorithm [39] to the modified partition function

$$Z' = \int d\mathbf{X} \ |W(\mathbf{X})|, \tag{20}$$

and calculate fermionic expectation values as

$$\langle O \rangle_f = \frac{\langle OS \rangle'}{\langle S \rangle'}, \tag{21}$$

with the definition of the average sign

$$\langle S \rangle' = \frac{1}{Z'}\int d\mathbf{X} \ |W(\mathbf{X})| \, S(\mathbf{X}), \tag{22}$$

and the signum of the configuration $\mathbf{X}$,

$$S(\mathbf{X}) = \prod_{\alpha=0}^{P-1}\left[\text{sgn}\left(\det(\rho_\alpha)\right)\text{sgn}\left(\det(\rho_{\alpha A})\right)\text{sgn}\left(\det(\rho_{\alpha B})\right) \right]. \tag{23}$$

Let us summarize some important facts about the configuration space defined by equation (20):

(i) With increasing number of propagators P, the effect of the blocking decreases and, for $P \to \infty$, the sign converges to the sign of standard PIMC. Blocking is maximal if $\lambda_{t_1\epsilon}$ and $\lambda_{2t_0\epsilon}$ are comparable to the average interparticle distance d, cf figure 3. Only in such a case, there can be both large diagonal and off-diagonal elements in the diffusion matrices.

(ii) Configuration weights $|W(\mathbf{X})|$ can only be large, when at least one element in each row of each diffusion matrix is large. Therefore, we sample either large diagonal or large off-diagonal elements. Blocking happens naturally as a by-product and does not have to be specifically included into the sampling. This also means that we have to implement a mechanism to sample exchange, i.e., to switch between large diagonal and off-diagonal diffusion matrix elements.

(i) There are no fixed trajectories. Therefore, beads do not have a previous or a next bead, as in standard PIMC. For an efficient and flexible sampling algorithm, we temporarily construct artificial trajectories and choose the included beads randomly.

The most efficient mechanism for the sampling of exchange cycles in standard PIMC is the so-called worm algorithm [20, 40], where macroscopic trajectories are naturally realized by a small set of local updates which

Figure 3. Influence of the imaginary time step ϵ on the efficiency of the permutation blocking—two configurations of $N = 2$ particles are visualized in the τ–x-plane. In the left and right panel, there are $P = 2$ and $P = 5$ time slices, respectively (daughter slices are neglected for simplicity). Only with few propagators, the thermal wavelength λ_ϵ of a single propagator is comparable to the mean interparticle distance d, which is crucial for an efficient grouping of permutations into a single configuration weight. With increasing P, diagonal (red and blue lines) and off-diagonal (green lines) distances are no longer of the same order and the permutation blocking is inefficient.

enjoy a high acceptance probability. In the rest of the section, we modify this algorithm to be applicable to the new configuration space without any fixed connections between individual beads.

3.1. Sampling scheme

To take advantage of the main benefits from the usual continuous space WA, we will temporarily construct artificial trajectories and sample new beads according to standard PIMC techniques, e.g. [43]. The initial situation for our considerations is illustrated in the left panel of figure 4, where a pre-existing trajectory (pink curve) with four missing beads in the middle is shown in the τ–x-plane. We choose the sampling probability to close the configuration as

$$T_{\text{sample}} = \frac{\prod_{i=0}^{M-1} \rho_0(\mathbf{r}_i, \mathbf{r}_{i+1}, \tau_{i+1} - \tau_i)}{\rho_0(\mathbf{r}_0, \mathbf{r}_M, \tau_M - \tau_0)}, \tag{24}$$

which results in the consecutive generation of $M - 1$ new coordinates $\mathbf{r}_i$, $i \in [1, M - 1]$, according to

$$P(\mathbf{r}_i) = \frac{\rho_0(\mathbf{r}_{i-1}, \mathbf{r}_i, \tau_i - \tau_{i-1})\rho_0(\mathbf{r}_i, \mathbf{r}_M, \tau_M - \tau_i)}{\rho_0(\mathbf{r}_{i-1}, \mathbf{r}_M, \tau_M - \tau_{i-1})}$$

$$= \left(\frac{1}{\sqrt{2\pi\sigma_i^2}}\right)^D \exp\left(-\frac{(\mathbf{r}_i - \boldsymbol{\xi}_i)^2}{2\sigma_i^2}\right), \tag{25}$$

which is a Gaussian (cf the blue curves in figure 4) with the variance

$$\sigma_i^2 = \frac{\hbar^2}{m} \frac{(\tau_i - \tau_{i-1})(\tau_M - \tau_i)}{\tau_M - \tau_{i-1}}, \tag{26}$$

around the intersection of the connection between the previous coordinate, $\mathbf{r}_{i-1}$, with the end point $\mathbf{r}_M$ and the time slice τ_i

$$\boldsymbol{\xi}_i = \frac{\tau_M - \tau_i}{\tau_M - \tau_{i-1}}\mathbf{r}_{i-1} + \frac{\tau_i - \tau_{i-1}}{\tau_M - \tau_{i-1}}\mathbf{r}_M. \tag{27}$$

3.2. Artificial worm algorithm

In the usual WA-PIMC, the configuration space is defined by the Matsubara Green function (e.g. [44]) which implies that the algorithm does not only allow for the change of the particle number N (grand canonical ensemble) but, in addition, requires the generation of configurations with a single open path, the so-called worm. However, in the PB-PIMC configuration space defined by equation (12), there are no trajectories and, therefore, no direct realization of a worm is possible. Instead, we consider an extended ensemble, which

Figure 4. Illustration of the sampling scheme (left) and the extended configuration space (right)—in the left panel, an artificial trajectory (pink curve) with four missing beads is plotted in the τ–x-plane. The new coordinates (green circles) are sampled according to a Gaussian (blue curves) around the intersection of the connecting straight lines between the previous and last bead with the current time slice (black crosses). The right panel gives an example for an open configuration in the extended configuration space with two special beads which are denoted as 'head' and 'tail'. There are only $N - 1$ beads on eight time slices, going forward in imaginary time starting from $\tau_{\text{head}} = \tau_{2A}$. The circles, triangles and squares distinguish beads from three different particles and the empty symbols at the right boundary indicate the missing beads on a particular slice.

combines closed configurations with a total of $3NP$ beads and open configurations, where on some consecutive time slices the number of beads is reduced by one, to $N - 1$. Such a configuration is illustrated in the right panel of figure 4. There are two special beads which are denoted as 'head' and 'tail' and the triangles, circles and squares symbolize beads from three different particles. There are eight beads from different particles missing (indicated by the empty symbols at the right boundary) between $\tau_{\text{head}} = \tau_{2A}$ and $\tau_{\text{tail}} = \tau_{1A}$, going forward in imaginary time.

For most slices, the computation of the diffusion matrix allows for no degree of freedom in the extended ensemble. We define the latter in a way, that the head bead does not serve as a starting point for the elements but is treated as if it was missing. This is justified because, otherwise, there does not necessarily exist a large matrix element in this particular row because no artificial connection has been sampled on the next slice. For the configuration from figure 4, the diffusion matrix of the head's time slice is given by

$$
\rho_{2A} = \begin{pmatrix} \rho_0\left(\mathbf{r}_{1,2A}, \mathbf{r}_{1,2B}, t_1\epsilon\right) & \rho_0\left(\mathbf{r}_{1,2A}, \mathbf{r}_{2,2B}, t_1\epsilon\right) & 0 \\ 1 & 1 & 1 \\ \rho_0\left(\mathbf{r}_{3,2A}, \mathbf{r}_{1,2B}, t_1\epsilon\right) & \rho_0\left(\mathbf{r}_{3,2A}, \mathbf{r}_{2,2B}, t_1\epsilon\right) & 0 \end{pmatrix}
$$

$$
\Rightarrow \det(\rho_{2A}) = \det\begin{pmatrix} \rho_0\left(\mathbf{r}_{1,2A}, \mathbf{r}_{1,2B}, t_1\epsilon\right) & \rho_0\left(\mathbf{r}_{1,2A}, \mathbf{r}_{2,2B}, t_1\epsilon\right) \\ \rho_0\left(\mathbf{r}_{3,2A}, \mathbf{r}_{1,2B}, t_1\epsilon\right) & \rho_0\left(\mathbf{r}_{3,2A}, \mathbf{r}_{2,2B}, t_1\epsilon\right) \end{pmatrix}. \tag{28}
$$

All diffusion matrices with $N - 1$ beads on their slices are computed in the same way. The other degree of freedom for which the extended ensemble allows is the choice whether the tail will be included as the final coordinate in the diffusion matrix or not. Here, it makes sense to allow for this possibility, because there does exist at least a single large element in this particular row anyway. The corresponding matrix for the configuration from figure 4 looks like

$$
\rho_{2A} = \begin{pmatrix} \rho_0\left(\mathbf{r}_{1,1}, \mathbf{r}_{1,1A}, t_1\epsilon\right) & \rho_0\left(\mathbf{r}_{1,1}, \mathbf{r}_{2,1A}, t_1\epsilon\right) & \rho_0\left(\mathbf{r}_{1,1}, \mathbf{r}_{3,1A}, t_1\epsilon\right) \\ \rho_0\left(\mathbf{r}_{2,1}, \mathbf{r}_{1,1A}, t_1\epsilon\right) & \rho_0\left(\mathbf{r}_{2,1}, \mathbf{r}_{2,1A}, t_1\epsilon\right) & \rho_0\left(\mathbf{r}_{2,1}, \mathbf{r}_{3,1A}, t_1\epsilon\right) \\ 1 & 1 & 1 \end{pmatrix}. \tag{29}
$$

However, we emphasize that the particular choice of the extended ensemble does not influence the extracted canonical expectation values as long as detailed balance is fulfilled in all updates. We have developed a simulation scheme which consists of four different types of moves that ensure detailed balance and ergodicity. The updates are presented in detail in the appendix.

4. Simulation results

As a test system to benchmark our method, we consider N spin-polarized electrons in a quantum dot [1–4], which can be described approximately by a harmonic confinement with a frequency Ω. We use oscillator units, i.e., the characteristic energy scale $E_0 = \hbar\Omega$ and oscillator length $l = \sqrt{\hbar/\Omega m}$, and obtain the dimensionless Hamiltonian

$$\hat{H} = -\frac{1}{2}\sum_{i=1}^{N}\nabla_i^2 + \frac{1}{2}\sum_{i=1}^{N}\mathbf{r}_i^2 + \sum_{i<j}^{N}\frac{\lambda}{|\mathbf{r}_i - \mathbf{r}_j|}, \tag{30}$$

with the coupling parameter

$$\lambda = \frac{e^2}{l_0\hbar\Omega}, \tag{31}$$

being defined as the ratio of Coulomb and oscillator energy. For large λ, the electrons are strongly coupled and exchange effects become negligible (region [III] in figure 1), while, for $\lambda \ll 1$, the ideal Fermi gas will be approached and the system is governed by the fermionic exchange (region [I] in figure 1). To confirm the quality of our simulations, we compare the results at weak and strong coupling with CPIMC and standard PIMC, respectively, where they are available.

4.1. Optimal choice of a_1 and t_0

We start the discussion of the simulation results by investigating the effects of the two free parameters a_1 and t_0 on the convergence of two different observables, namely the energy E and radial density $n(r)$.

In figure 5, results are summarized for $N = 4$ electrons with $\lambda = 1.3$ and $\beta = 5$, i.e., moderate coupling and low temperature, and panel (A) shows the convergence of the total energy as a function of the inverse number of propagators which is proportional to the imaginary time step, $\epsilon \propto 1/P$. The red diamonds [(a) $t_0 = 0.04$, $a_1 = 0.0$] and blue circles [(b) $t_0 = 0.13$, $a_1 = 0.33$] denote two different combinations of free parameters and exhibit a clearly different convergence behavior towards the exact result known from CPIMC, i.e., the black line. For $P = 2$, the energy with parameter set (a) is too low by almost one percent. With increasing P, E increases and reaches a maximum around $P = 5$, until the curves approach the exact energy from above. For parameter set (b), the energy converges monotonically from above and, even for $P = 2$, the deviation from the CPIMC result is as small as 0.2%. The selected energies which are listed in table 1 reveal that the total energy is converged for $P = 14$ within the statistical uncertainty. For the panels (C) and (D), the energy has been split into a potential (V) and kinetic (K) contribution. For both parameter combinations, V converges monotonically, although from different directions. In addition, parameter set (b) gives a much better result for small P. Panel (D) reveals, that the kinetic energy K is responsible for the non-monotonous convergence of E for parameter set (a), which again delivers worse results for $P = 2$, as compared to the blue circles. Finally, panel (B) shows the average sign S as a function of $1/P$. Both curves exhibit a similar decrease with an increasing number of propagators, as it is expected. However, parameter set (a) always allows for a better sign than (b). The reason for this behavior is the free parameter t_0, which controls the relative spacing between the three time slices of an imaginary time step ϵ. For $t_0 = 0.04$, there are a single small and two large steps. The latter allow for more blocking, since the corresponding decay length $\lambda_{t_i\epsilon}$ in the diffusion matrices is large as well. For $t_0 = 0.13$, on the other hand, there are three nearly equal steps, each of which with a smaller decay length than the two large ones for parameter set (a). Therefore, less blocking is possible and more determinants with a negative sign appear in the Markov chain.

The different convergence behaviors of the two free parameter combinations for small P leads to the question how to choose t_0 and a_1 for optimal results. To provide an answer, we consider the same system as in figure 5, and investigate the accuracy of the total energy as a function of t_0, for a fixed $a_1 = 0.33$. The simulation results are shown in the left panel of figure 6 for $P = 2$ (red squares), $P = 3$ (blue circles) and $P = 4$ (green diamonds). All three curves exhibit a similar decay towards the exact value starting from small t_0, followed by a minimum around $t_0 = 0.14$ and finally an increasing error for larger values. We note that as few as two propagators allow for an accuracy of $|\Delta E|/E < 2 \times 10^{-3}$ for the best choice of the free parameters. Figure 6(B) shows the dependency of the average sign S on t_0. Again, we observe that S decreases with increasing t_0 as explained during the discussion of figure 5. In addition, it is revealed that the combination of $P = 4$ and $t_0 = 0.01$ leads to a larger sign than $P = 3$ and $t_0 > 0.10$. However, the optimum free parameters allow for a higher accuracy even for $P = 2$, compared to small t_0 with more propagators. Therefore, it turns out to be advantagous to use the fourth order factorization with the two free parameters despite the smaller average sign for the same P compared to the factorization with only a single daughter slice for each propagator, i.e., $t_0 = 0.0$.

Finally, we mention that the optimal choice of a_1 and t_0 depends on the observable of interest. In figure 7, we investigate the effects of the free parameters on the convergence of the radial density distribution $n(r)$ for the

Figure 5. Convergence of the energy for $N = 4$, $\lambda = 1.3$ and $\beta = 5.0$—panel (A) shows the convergence of the total energy versus the inverse number of propagators $P^{-1} \propto \epsilon$. Shown are the results for two different choices of the parameters, (a) $t_0 = 0.04$, $a_1 = 0.0$ and (b) $t_0 = 0.13$, $a_1 = 0.33$, and the correct energy from CPIMC with the corresponding confidence interval. Panel (B) shows the decay of the average sign S with increasing P and panels (C) and (D) display the potential and kinetic energy V and K, respectively, where $E = V + K$.

Table 1. Convergence of the energy for $N = 4$, $\lambda = 1.3$ and $\beta = 5.0$ for selected parameter combinations shown in figure 5.

Simulation	E	V	K	S
$P = 2^a$	12.1924(3)	9.0283(3)	3.1641(3)	0.4907(3)
$P = 2^b$	12.3186(2)	9.0927(2)	3.2258(2)	0.3771(2)
$P = 14^a$	12.293(4)	9.083(1)	3.210(4)	0.02664(1)
$P = 14^b$	12.292(2)	9.0831(6)	3.209(2)	0.020600(7)
CPIMC	12.293(3)	—	—	—

[a] $t_0 = 0.04$, $a_1 = 0.0$

[b] $t_0 = 0.13$, $a_1 = 0.33$

same system as in figures 5 and 6. The left panel shows n as a function of the distance to the center of the trap, r, for four different P and the parameter combination $a_1 = 0.33$ and $t_0 = 0.13$, which has been proven to allow for nearly optimum energy values at $P = 2$, cf figure 6. The black curve corresponds to $P = 10$ and is converged within statistical uncertainty. For $P = 2$ (red diamonds), there appear significant deviations to the latter, in particular n is too large around the maximum $r \approx 1.25$ and too small at the boundary of the system. The $P = 3$ results (blue squares) exhibit the same trends although the differences towards the black curve are reduced. Finally, the density for $P = 4$ (green circles) can hardly be distinguished from the converged data. The right panel compares the density for $P = 2$ with two different combinations of free parameters. The red diamonds (parameter set (a)) correspond to the curve from the left panel and the green circles (parameter set (b)) to $a_1 = 0.0$ and $t_0 = 0.04$. The latter parameters clearly allow for a density distribution which is much closer to the exact results than the a_1 and t_0 values which provide the optimal energy.
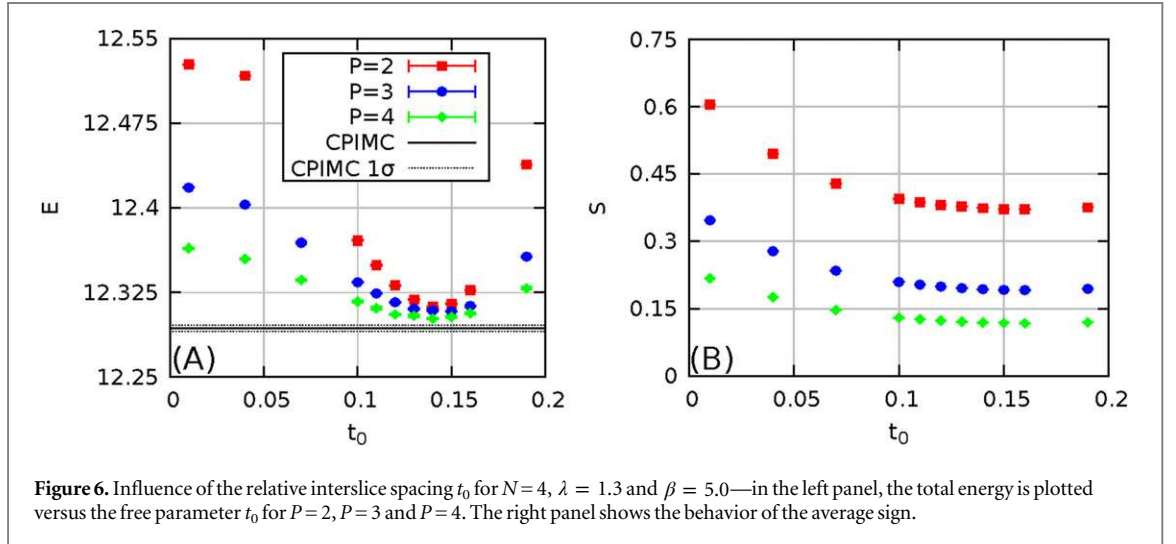
Figure 6. Influence of the relative interslice spacing t_0 for $N = 4$, $\lambda = 1.3$ and $\beta = 5.0$—in the left panel, the total energy is plotted versus the free parameter t_0 for $P = 2$, $P = 3$ and $P = 4$. The right panel shows the behavior of the average sign.

Figure 7. Convergence of the radial density for $N = 4$, $\lambda = 1.3$ and $\beta = 5.0$—the radial density n is plotted versus the distance to the center of the trap, r. In panel (A), the free parameters are chosen as $t_0 = 0.13$ and $a_1 = 0.33$ and the convergence with P is illustrated. Panel (B) compares two different sets of free parameters, (a) $t_0 = 0.13$ and $a_1 = 0.33$ and (b) $t_0 = 0.04$ and $a_1 = 0.0$, for $P = 2$.

4.2. Temperature dependence

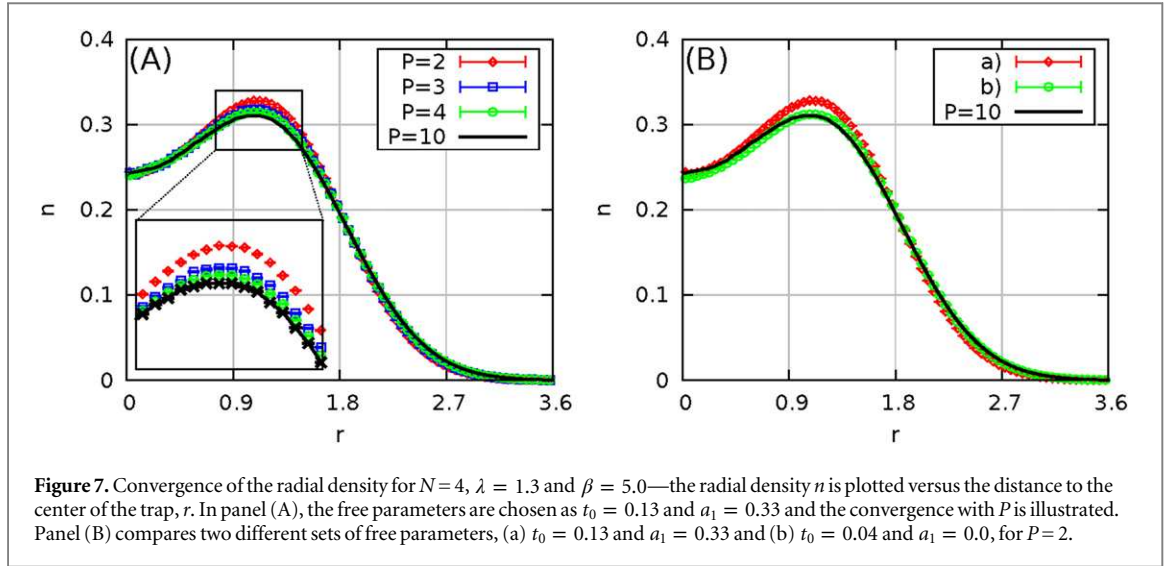In the last section, we have demonstrated that the optimal choice of the free parameters a_1 and t_0 allows for the calculation of energies with an accuracy of 0.1% with as few as two propagators, even at a relatively low temperature, $\beta = 5.0$. However, with decreasing T (i.e., increasing β) the number of required propagators must be increased to keep the commutator error fixed. In figure 8, we investigate the effect of a decreasing temperature on the accuracy provided by a few propagators P for $N = 4$ electrons at indermediate coupling, $\lambda = 1.3$. The left panel shows the total energy E as a function of the inverse temperature β. We compare results for $P = 2$ (green circles), $P = 3$ (red diamonds) and $P = 4$ (blue triangles) to exact results from CPIMC (black stars). At larger temperature, $\beta \leqslant 7.0$, all four datasets nearly coincide and exhibit the expected decrease towards the energy of the ground state. With increasing β, the $P = 2$ results exhibit an unphysical drop because two propagators are not sufficient and the commutator errors become more significant. The red and blue curves exhibit a qualitatively similar trend, however, the energy drop is weaker and shifted to lower temperature. Even at $\beta = 10.0$, which is already very close to the ground state, three propagators allow for an accurate description of the system.

In the right panel of figure 8, the average sign S is plotted versus the inverse temperature. At small β, the wavefunctions of the electrons do not overlap and, hence, the system is not degenerate. With decreasing temperature, exchange effects become increasingly important which leads to a decrease of S. However, while for standard PIMC the sign is expected to exponentially decrease with β, S seems to converge for PB-PIMC with $P = 3$ and $P = 4$ and exhibits an even slightly non-monotonous behavior for $P = 2$. The application of antisymmetric propagators leads to a competition with respect to S and β. On the one hand, with increasing inverse temperature off-diagonal matrix elements are increased, which leads to more negative determinants and, therefore, more negative weights in the Markov chain. On the other hand, the thermal wavelengths $\lambda_{t_1\epsilon}$ and $\lambda_{2t_0\epsilon}$
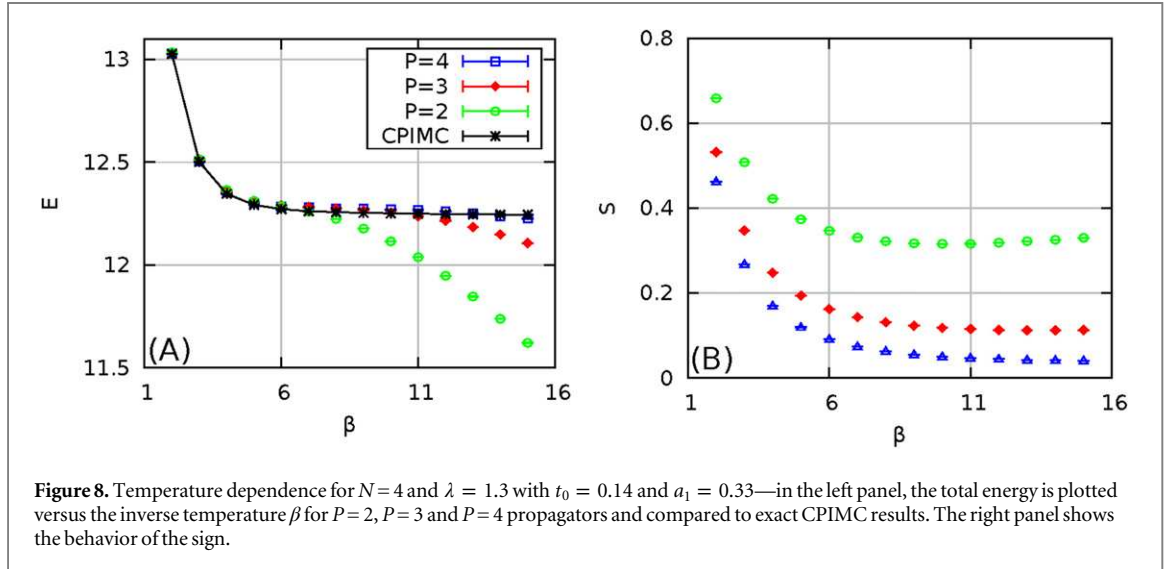
Figure 8. Temperature dependence for $N = 4$ and $\lambda = 1.3$ with $t_0 = 0.14$ and $a_1 = 0.33$—in the left panel, the total energy is plotted versus the inverse temperature β for $P = 2$, $P = 3$ and $P = 4$ propagators and compared to exact CPIMC results. The right panel shows the behavior of the sign.
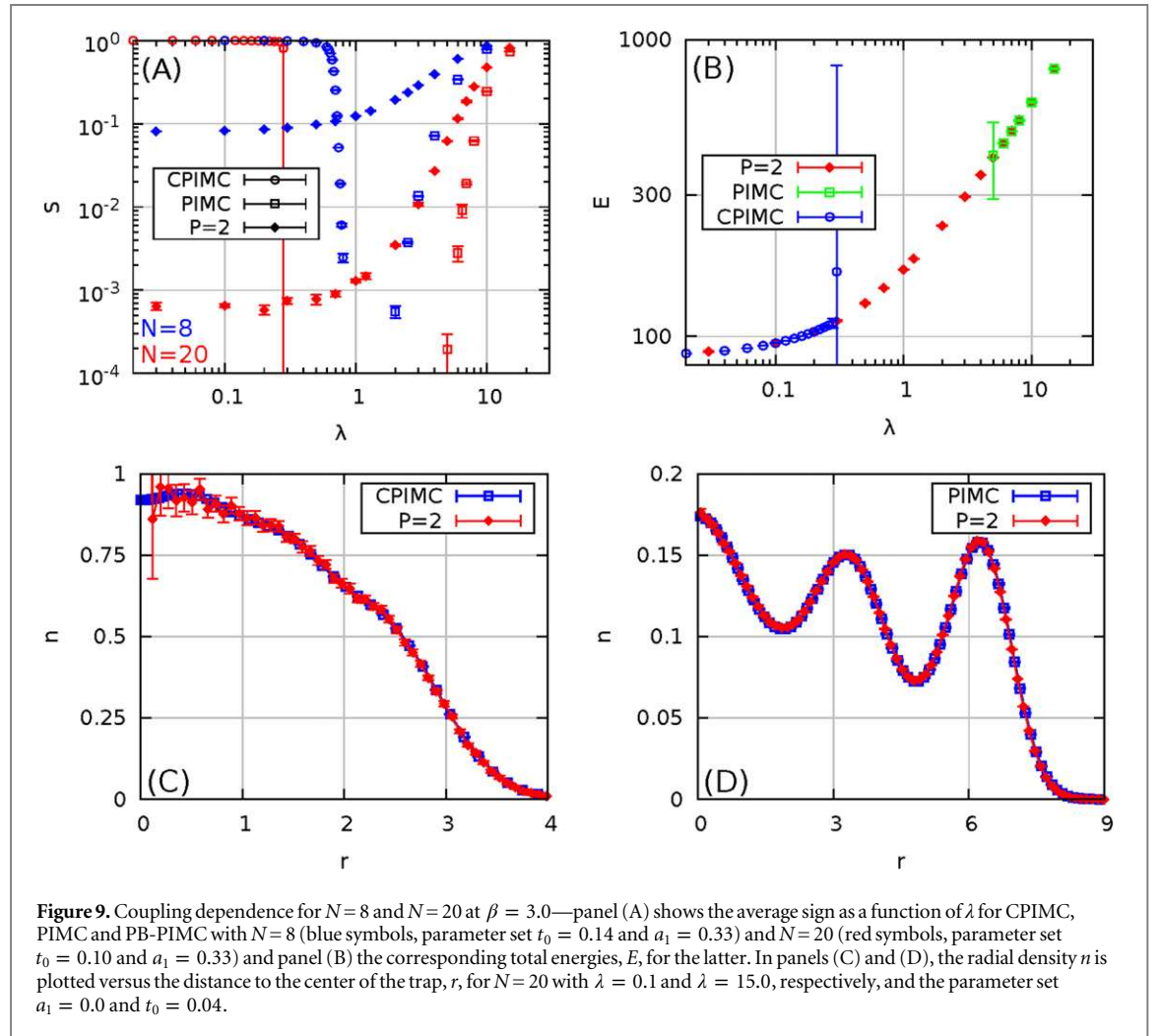
are increasing with β, which makes the blocking of large diagonal and off-diagonal elements more effective. Hence, the sign can even become larger with β once the system has reached the ground state, because the particle distribution remains constant while more elements in the diffusion matrix compensate each other in the determinants.

We conclude that few propagators allow for the calculation of accurate results up to low temperature, $\beta \lesssim 10.0$. For higher β, the system is in its ground state and finite temperature PIMC is no longer the method of choice.

4.3. Dependence on the coupling strength

In the previous sections, we have restricted ourselves to the investigation of small systems to illustrate the convergence and sign behavior depending on relevant parameters. In this section, we demonstrate that PB-PIMC allows for the calculation of accurate results at parameters where no other *ab initio* results have been reported, so far. Figure 9 shows results for $N = 8$ and $N = 20$ electrons at $\beta = 3.0$ over a wide range of coupling parameters, λ. In panel (A), the average sign S is plotted versus λ for standard PIMC (squares), CPIMC (circles) and the present PB-PIMC (diamonds) with $P = 2$ and the parameter sets $t_0 = 0.14$ and $a_1 = 0.33$ ($N = 8$, blue symbols) and $t_0 = 0.10$ and $a_1 = 0.33$ ($N = 20$, red symbols), which are known to allow for accurate energies, cf figure 6. It is well understood that PIMC allows for the simulation of strongly coupled fermions, where exchange effects do not play a dominant role. With decreasing λ, the sign exhibits a sharp drop and the sign problem prevents the simulation within feasible computation time for $\lambda \lesssim 2.0$ and $\lambda \lesssim 5.0$, respectively. Evidently, larger systems lead to a more severe decrease of S at larger coupling strength. CPIMC, on the other hand, can be interpreted as a Monte Carlo simulation on a perturbation expansion around the ideal quantum system, i.e., $\lambda = 0.0$. Hence, the method efficiently provides exact results for small coupling, where the system is close to an ideal one. For $N = 20$ around $\lambda \approx 0.3$, the sign almost instantly drops from $S \approx 0.97$ towards zero, and CPIMC is no longer applicable, without further approximation. This means that, in particular for larger systems, there have only been results for systems that are (a) almost ideal or (b) so strongly coupled that fermions and bosons lead to nearly equal physical properties. The physically particularly interesting regime where Coulomb correlations and Fermi statistics are significant simultaneously, has remained out of reach.

However, the average sign from PB-PIMC exhibits a much less severe drop with decreasing λ than standard PIMC and saturates for $\lambda \lesssim 0.7$. For $N = 8$, the average sign remains above $S = 0.08$, which allows for good accuracy with relatively low effort. The small sign, $S \sim 10^{-3}$, for $N = 20$ indicates that the simulations are computationally involved but, in contrast to PIMC and CPIMC, still feasible. In panel (B) of figure 9, the total energy E for $N = 20$ is plotted versus λ over the entire coupling range and the statistical uncertainty from the PB-PIMC results is smaller than the size of the data points. Both, at small and large λ, the $P = 2$ results are in excellent agreement with the exact energy known from the other methods and, in addition, results are obtained for the particularly interesting transition region (region [II] in figure 1). In panel (C), we show the radial density for $N = 20$ and low coupling, $\lambda = 0.10$, calculated with the parameter set $t_0 = 0.04$ and $a_1 = 0.0$, which has been proven effective for accurate densities $n(r)$. The PB-PIMC results (red diamonds) are in excellent agreement with the exact CPIMC data (blue squares) over the entire r-range. For completeness, we mention that this combination of parameters allows for an approximately three times as high sign as the choice from panels (A) and (B), which was choosen to allow for a good energy, and the results have been obtained within $t_{\text{CPU}} \sim 10^3$

Figure 9. Coupling dependence for $N = 8$ and $N = 20$ at $\beta = 3.0$—panel (A) shows the average sign as a function of λ for CPIMC, PIMC and PB-PIMC with $N = 8$ (blue symbols, parameter set $t_0 = 0.14$ and $a_1 = 0.33$) and $N = 20$ (red symbols, parameter set $t_0 = 0.10$ and $a_1 = 0.33$) and panel (B) the corresponding total energies, E, for the latter. In panels (C) and (D), the radial density n is plotted versus the distance to the center of the trap, r, for $N = 20$ with $\lambda = 0.1$ and $\lambda = 15.0$, respectively, and the parameter set $a_1 = 0.0$ and $t_0 = 0.04$.

core hours. Panel (D) shows the density of a strongly coupled system, $\lambda = 15.0$, and $N = 20$. Again, the two propagators already provide very good agreement with the exact curve. In figure 1(B), we have shown density profiles for coupling parameters over the entire coupling range. At $\lambda = 15$ (red pluses), there are three distinct shells and the physical behavior is dominated by the strong Coulomb repulsion. Decreasing the coupling to $\lambda = 5$ (green bars) leads to a reduced extension of the system, and the three shells exhibit a much larger overlap. At intermediate coupling, $\lambda = 2$ (blue crosses), both the interaction and fermionic exchange govern the system. The density profile is still significantly more extended than the ideal pendant, but n exhibits modulations instead of a flat curve. Decreasing the repulsion further to $\lambda = 0.7$ (pink circles) leads to a further reduction of the extension. However, n does not approach a Gaussian-like profile as for ideal boltzmannons or bosons, but continues to exhibit the density modulations which are characteristic for fermions. For $\lambda = 0.1$, the system is almost ideal and the density is completely dominated by the quantum statistics.

Finally, in figure 10 we compare density profiles for $N = 20$ particles at $\beta = 3.0$ with Fermi-, Bose- and Boltzmann statistics. Panel (A) shows results for intermediate coupling, $\lambda = 2.0$. The distinguishable boltzmannons (blue diamonds) exhibit a nearly flat profile without any shell structure, i.e., a liquid-like behavior. The bosonic particles (green circles) lead to an even smoother curve, with a slightly reduced extension of the system. For fermions (red squares), on the other hand, the exchange already plays a significant role, as the particles exhibit an additional repulsion due to the Pauli principle, and n decays only at larger r. In addition, the fermionic density profile exhibits distinct modulations. In panel (B), we show a comparison for smaller coupling, $\lambda = 0.7$. Again, the boltzmannons and bosons lead to smooth density profiles which are very similar, despite a reduced extension of the Bose-system and an increased density around the center of the trap. The fermions exhibit a different behavior as the system is significantly more extended and the density profile again features distinct modulations.

In conclusion, we have presented *ab initio* results for the energy and the density for up to 20 electrons over the entire coupling range. A comparison with standard PIMC and CPIMC has revealed excellent agreement in

Figure 10. Influence of quantum statistics for $N = 20$ and $\beta = 3.0$—we show the radial density $n(r)$ for Fermi-, Bose- and Boltzmann-statistics in the transition region for $\lambda = 2.0$ (A) and $\lambda = 0.7$ (B).

Figure 11. Particle number dependence of the average sign for $\lambda = 0.1$ and $\beta = 3.0$ and two different combinations of the simulation parameters.
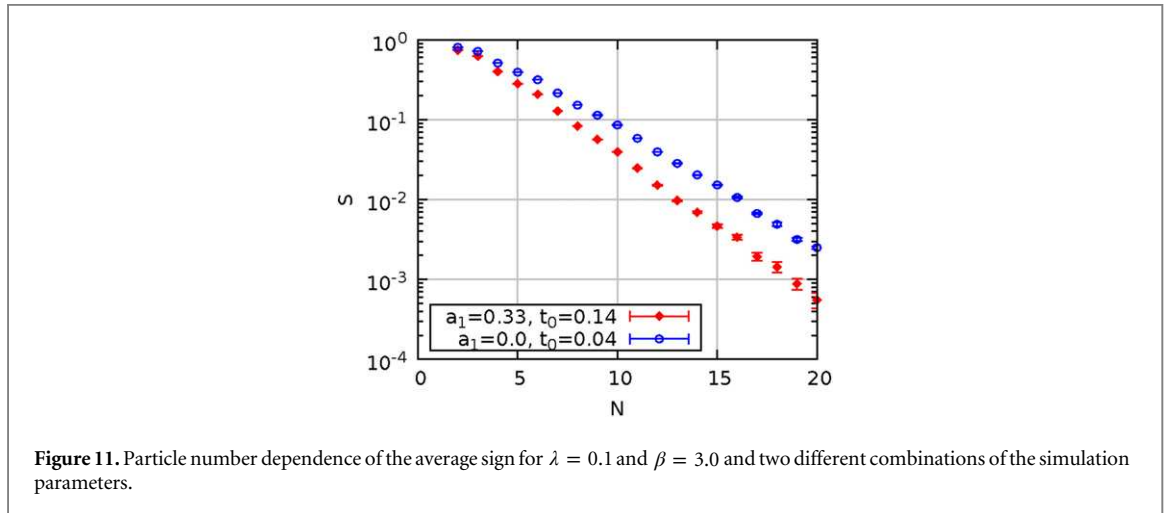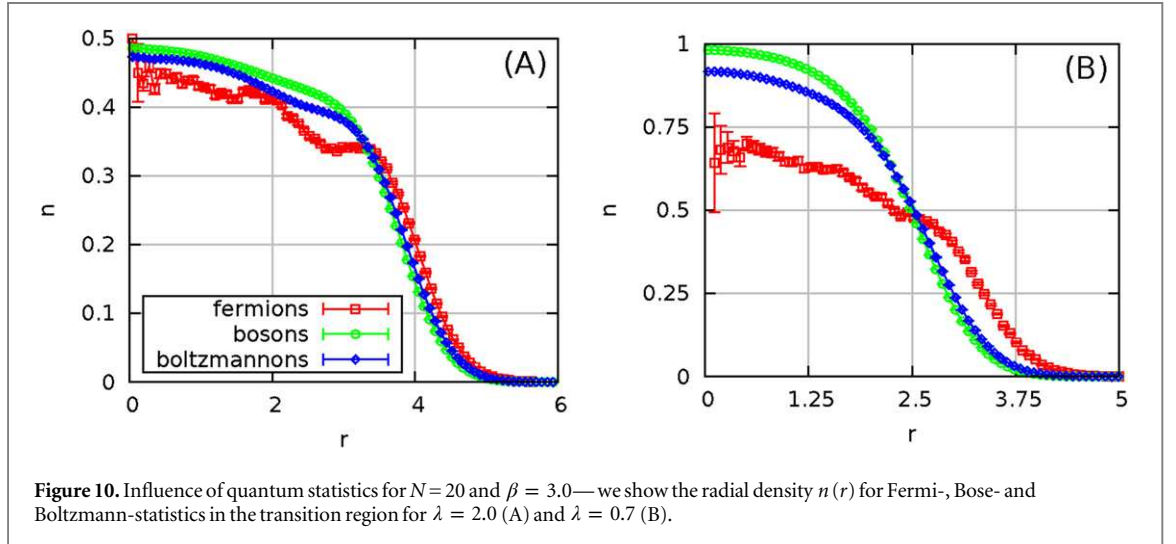
both the limits of weak and strong coupling. A more detailed investigation of the transition from the classical to the degenerate regime, including systematic comparisons with bosons and boltzmannons, is beyond the scope of this work and will be published elsewhere.

4.4. Particle number dependence
In the last section, we have shown that the sign problem is more severe for larger systems, cf figure 9(A). Here, we provide a more detailed investigation of the performance of our method in dependence on the particle number. In figure 11, the average sign S is plotted versus N for $\lambda = 0.1$ and $\beta = 3.0$, i.e., a very degenerate system, with two different combinations of free parameters. It is revealed that S exhibits an exponential decay with the system size and, as usual, the smaller t_0 leads to a more effective blocking. Therefore, the PB-PIMC approach still suffers from the fermion sign problem, and feasible system sizes for 2D quantum dots at weak coupling are limited to $N \leqslant 30$. This is a remarkable result since standard PIMC simulations for $\lambda = 0.1$ and $\beta = 3.0$ are possible only for $N \leqslant 4$.

5. Discussion

In summary, we have presented a novel approach to the PIMC simulation of degenerate fermions at finite temperature by combining a fourth-order factorization of the density matrix with a full antisymmetrization between all imaginary time slices. The latter allows to merge $3PN!$ configurations from the standard PIMC formulation into a single configuration weight, thereby efficiently grouping together permutations of opposite

signs which leads to a significant relieve of the fermion sign problem. To efficiently run through the resulting configuration space at arbitrary system parameters, we have modified the widely used continuous space WA by introducing an extended ensemble with open configurations and by temporarily constructing artificial trajectories. We have demonstrated the capabilities of our method by simulating up to $N = 20$ electrons in a quantum dot. It has been revealed that the (empirical) optimal choice of the free parameters a_1 and t_0 from the fourth order factorization allows for the calculation of energies with an accuracy of 0.1% even for just two propagators. For completeness, we mention that different observables lead to different optimal parameters. We have concluded, that it appears to be favourable to use two instead of a single daughter time slice for each time step ϵ, despite the reduced sign for the same number of propagators.

The investigation of the temperature dependence of the convergence with respect to the number of time steps P has revealed, that as few as three propagators are sufficient to accurately simulate fermions, up to $\beta \leqslant 10.0$. For larger inverse temperatures, the system approaches its ground state and finite temperature PIMC techniques are no longer the methods of choice.

To demonstrate that our PB-PIMC approach allows for the calculation of accurate results for systems beyond the capability of any other quantum Monte Carlo technique, we have simulated $N = 20$ electrons at relatively low temperature, $\beta = 3.0$, and arbitrary coupling strength. CPIMC excells at weak coupling and provides exact results for $\lambda < 0.3$, i.e., in the region where the systems are still close to the ideal case. Standard PIMC, on the other hand, is applicable at strong coupling $\lambda \geqslant 5.0$ where exchange effects are not yet dominating, until the rapid decrease of the sign renders any simulation unfeasible. For PB-PIMC, the sign converges for $\lambda \leqslant 0.7$ and, hence, computations are possible at arbitrary degeneracy, in particular, in the physically most interesting transition region between classical and ideal quantum behavior. We find excellent agreement with both PIMC and CPIMC in both the limits of strong and weak coupling. Finally, we have demonstrated that PB-PIMC still suffers from the fermion sign problem, since, as expected, S decreases exponentially with the particle number.

A possible future application of PB-PIMC to the quantum dot system might include the investigation of the transition from the classical to the degenerate quantum regime, in particular a systematic comparison of fermions to bosons and boltzmannons. To describe realistic quantum dots, it will be important to include the spin degrees of freedom into the simulation. In particular, this should allow us to recover, for weak coupling, Hund's rules physics and also to address the spin contamination problem [45, 46]. Furthermore, it could be interesting to extend the considerations to 3D confinements, e.g. [47, 48], and study the impact of quantum statistics on structural transitions [49]. In addition, we expect our method to be of interest for the future investigation of numerous Fermi systems, including the finite temperature homogeneous electron gas [8–10], two-component plasmas [11–13] and fermionic bilayer systems [5–7].

Acknowledgments

Appendix. Monte Carlo updates

In this appendix, we present an ergodic set of Monte Carlo updates which are based on the usual continuous space WA [20, 40] from standard PIMC.

(i) *Deform*: this update is similar to standard PIMC techniques, e.g. [43], and deforms a randomly constructed artificial trajectory.

- Select a start time τ_s uniformly from all $3P$ slices.
- Select a 'start' bead on τ_s.
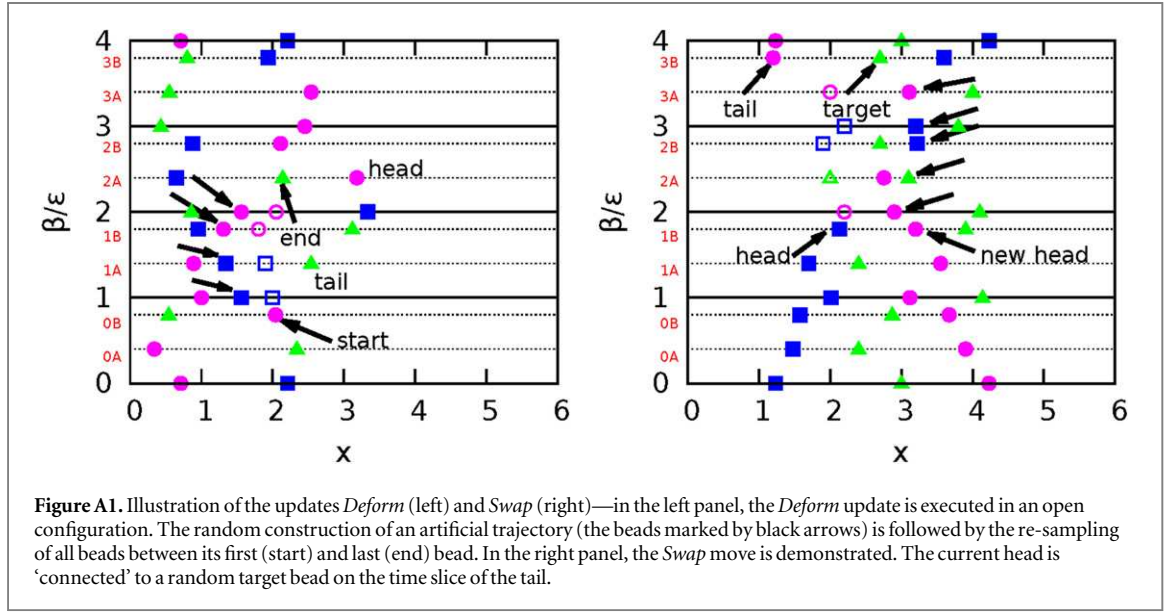- Select the number of beads to be changed, $m \in [1, \tilde{M}]$.

Figure A1. Illustration of the updates *Deform* (left) and *Swap* (right)—in the left panel, the *Deform* update is executed in an open configuration. The random construction of an artificial trajectory (the beads marked by black arrows) is followed by the re-sampling of all beads between its first (start) and last (end) bead. In the right panel, the *Swap* move is demonstrated. The current head is 'connected' to a random target bead on the time slice of the tail.

- Select $m + 1$ beads on the next slices according to

$$T_{\text{select}} = \prod_{i=0}^{m} \frac{\rho_0\left(\mathbf{r}_i^{\text{old}}, \mathbf{r}_{i+1}^{\text{old}}, \epsilon_i\right)}{\Sigma_i^{\text{old}}}, \tag{A.1}$$

with Σ_i^{old} being the normalization and the label 'old' indicates the configuration before the update.

- Resample m beads in the middle according to equation (24):

$$T_{\text{resample}} = \frac{\prod_{i=0}^{m} \rho_0\left(\mathbf{r}_i^{\text{new}}, \mathbf{r}_{i+1}^{\text{new}}, \epsilon_i\right)}{\rho_0\left(\mathbf{r}_0, \mathbf{r}_{m+1}, \epsilon_{\text{tot}}\right)}, \tag{A.2}$$

and ϵ_{tot} denotes the imaginary time difference between the fixed endpoints. The constant $\tilde{M}$ is a free parameter and can be optimized to enhance the performance. The update is self-balanced and the Metropolis solution for the acceptance probability is given by

$$A_{\text{Deform}}\left(\mathbf{X} \to \tilde{\mathbf{X}}\right) = \min\left(1, \ e^{-\epsilon \Delta \Phi} \prod_{i=0}^{m} \left| \frac{\Sigma_i^{\text{old}}}{\Sigma_i^{\text{new}}} \frac{\det\rho_i^{\text{new}}}{\det\rho_i^{\text{old}}} \right| \right), \tag{A.3}$$

with Φ containing both the change in the potential energy and all forces. *Deform* is illustrated in the left panel of figure A1 .

(ii) *Open/ Close*: this update pair constitutes the only possibility to switch between open and closed configurations. The *Open* move is executed as follows:

- Select the time slice of the new head, τ_{head}, uniformly from all $3P$ slices.

- Select the bead of the new head, $\mathbf{r}_{\text{head}}$.

- Select the total number of links to be erased as $m \in [1, \tilde{M}]$.

- Select m beads on the next slices from

$$T_{\text{select}} = \prod_{i=0}^{m-1} \frac{\rho_0\left(\mathbf{r}_i, \mathbf{r}_{i+1}, \epsilon_i\right)}{\Sigma_i}, \tag{A.4}$$

the last one will be the new tail after the update.

- Delete $m - 1$ beads between the new head and tail. The reverse move closes an open configuration. Let m denote the number of missing links between head and tail. If $m > \tilde{M}$, the update is rejected.

- Sample $m - 1$ new beads according to equation (24) with head and tail being the fixed endpoints:

$$T_{\text{sample}} = \frac{\prod_{i=0}^{m-1} \rho_0(\mathbf{r}_i, \mathbf{r}_{i+1}, \epsilon_i)}{\rho_0(\mathbf{r}_{\text{head}}, \mathbf{r}_{\text{tail}}, \epsilon_{\text{tot}})}. \tag{A.5}$$

The acceptance ratios are computed as

$$A_{\text{Open}}\left(\mathbf{X} \rightarrow \tilde{\mathbf{X}}\right) = \min\left(1, \Gamma e^{-\epsilon \Delta \Phi} e^{-\epsilon_{\text{tot}} \mu} \prod_{i=0}^{m-1} \left| \Sigma_i \frac{\det \rho_i^{\text{new}}}{\det \rho_i^{\text{old}}} \right| \right)$$

$$A_{\text{Close}}\left(\mathbf{X} \rightarrow \tilde{\mathbf{X}}\right) = \min\left(1, \frac{e^{-\epsilon \Delta \Phi} e^{\epsilon_{\text{tot}} \mu}}{\Gamma} \prod_{i=0}^{m-1} \left| \frac{1}{\Sigma_i} \frac{\det \rho_i^{\text{new}}}{\det \rho_i^{\text{old}}} \right| \right), \tag{A.6}$$

with the definition

$$\Gamma = \frac{3CP\tilde{M}N}{\rho_0(\mathbf{r}_{\text{tail}}, \mathbf{r}_{\text{head}}, \epsilon_{\text{tot}})}. \tag{A.7}$$

The parameter μ is another degree of freedom of the algorithm and plays the same role as the chemical potential in the usual WA-PIMC scheme.

(iii) *Swap*: the *Swap* move very efficiently generates exchange, i.e., allows for a switch between large off-diagonal or diagonal diffusion matrix elements as it is illustrated in the right panel of figure A1. Let m denote the number of missing beads between head and tail.

- Choose a target bead on the slice τ_{tail} according to

$$T_{\text{target}} = \frac{\rho_0(\mathbf{r}_{\text{head}}, \mathbf{r}_t, \epsilon_{\text{tot}})}{\Sigma_{\text{forward}}}, \tag{A.8}$$

with Σ_{forward} being the normalization. The tail itself cannot be chosen.

- Choose backwards $m + 1$ beads according to

$$T_{\text{select}} = \prod_{i=0}^{m} \frac{\rho_0\left(\mathbf{r}_{i+1}^{\text{old}}, \mathbf{r}_i^{\text{old}}, \epsilon_i\right)}{\Sigma_i^{\text{old}}}. \tag{A.9}$$

The head itself cannot be selected on the last slice and the last bead will be the new head after the update.

- 'Connect' the old head with the target bead by re-sampling the m beads between the slices of head and tail according to

$$T_{\text{sample}} = \frac{\prod_{i=0}^{m} \rho_0\left(\mathbf{r}_i^{\text{new}}, \mathbf{r}_{i+1}^{\text{new}}, \epsilon_i\right)}{\rho_0(\mathbf{r}_{\text{head}}, \mathbf{r}_{\text{target}}, \epsilon_{\text{tot}})}. \tag{A.10}$$

The update is self-balanced and the acceptance ratio is calculated as

$$A_{\text{Swap}}\left(\mathbf{X} \rightarrow \tilde{\mathbf{X}}\right) = \min\left(1, \eta \prod_{i=0}^{m} \left| \frac{\Sigma_i^{\text{old}}}{\Sigma_i^{\text{new}}} \frac{\det \rho_i^{\text{new}}}{\det \rho_i^{\text{old}}} \right| \right), \tag{A.11}$$

with the abbreviation

$$\eta = e^{-\epsilon \Delta \Phi} \frac{\Sigma_{\text{forward}}}{\Sigma_{\text{reverse}}}, \tag{A.12}$$

and Σ_{reverse} being the normalization of the selection of the target bead from the reverse move.

(iv) *Advance/ Recede:* these updates move the head forward (backward) in the imaginary time. However, they are optional and, in principle, not needed for ergodicity. The *Advance* move is executed as follows:

- Calculate the number of missing beads between head and tail, α. If $\alpha = 0$, the update is rejected.

- Select the number of new beads to be sampled, $m \in [1, \alpha]$.

- Sample the position of the new head from $\rho_0(\mathbf{r}_{\text{head}}, \mathbf{r}_{\text{head}}^{\text{new}}, \epsilon_{\text{tot}})$.

- Sample the $m - 1$ beads between old and new head according to equation (24)

$$T_{\text{sample}} = \frac{\prod_{i=0}^{m-1} \rho_0\left(\mathbf{r}_i^{\text{new}}, \mathbf{r}_{i+1}^{\text{new}}, \epsilon_i\right)}{\rho_0\left(\mathbf{r}_{\text{head}}, \mathbf{r}_{\text{head}}^{\text{new}}, \epsilon_{\text{tot}}\right)}. \tag{A.13}$$

The reverse move is given by *Recede*. Let κ denote the total number of beads which can be removed. If $\kappa = 0$, the update is rejected.

- Select the total number of beads to be removed as $m \in [1, \kappa]$.

- Select m beads backwards starting from the old head from

$$T_{\text{select}} = \prod_{i=0}^{m-1} \frac{\rho_0\left(\mathbf{r}_i^{\text{new}}, \mathbf{r}_{i+1}^{\text{new}}, \epsilon_i\right)}{\Sigma_i^{\text{new}}}, \tag{A.14}$$

with Σ_i^{new} being the normalization. The last one will be the new head after the update. Here 'new' denotes new with respect to *Advance*, since the coordinates are pre-existing for the *Recede* move. Delete the m beads between the new head and tail.

This gives the acceptance ratios

$$A_{\text{Advance}}\left(\mathbf{X} \to \tilde{\mathbf{X}}\right) = \min\left(1, \theta e^{-\epsilon \Delta \Phi} \prod_{i=0}^{m-1} \left| \frac{1}{\Sigma_i^{\text{new}}} \frac{\det \rho_i^{\text{new}}}{\det \rho_i^{\text{old}}} \right| \right)$$

$$A_{\text{Recede}}\left(\mathbf{X} \to \tilde{\mathbf{X}}\right) = \min\left(1, \frac{e^{-\epsilon \Delta \Phi}}{\theta} \prod_{i=0}^{m-1} \left| \Sigma_i^{\text{new}} \frac{\det \rho_i^{\text{new}}}{\det \rho_i^{\text{old}}} \right| \right), \tag{A.15}$$

with the definition

$$\theta = \frac{\alpha}{\kappa} e^{\epsilon_{\text{tot}} \mu}. \tag{A.16}$$

The presented list of Monte Carlo moves constitutes an ergodic set of local updates, which allows for an efficient sampling of both the extended configuration space and a canonical Markov chain.

References

[1] Egger R, Häusler W, Mak C H and Grabert H 1999 Crossover from Fermi liquid to Wigner molecule behavior in quantum dots *Phys. Rev. Lett.* **82** 3320

[2] Filinov A V, Bonitz M and Lozovik Y E 2001 Wigner crystallization in mesoscopic 2D electron systems *Phys. Rev. Lett.* **86** 3851

[3] Rontani M, Cavazzoni C, Bellucci D and Goldoni G 2006 Full configuration interaction approach to the few-electron problem in artificial atoms *J. Chem. Phys.* **124** 124102

[4] Ghosal A, Güçlü A D, Umrigar C J, Ullmo D and Baranger H U 2007 Incipient Wigner localization in circular quantum dots *Phys. Rev. B* **76** 085341

[5] Filinov A, Bonitz M, Ludwig P and Lozovik Y E 2006 Path integral Monte Carlo results for Bose condensation of mesoscopic indirect excitons *Phys. Status Solidi* **3** 2457–60

[6] Ludwig P, Balzer K, Filinov A, Stolz H and Bonitz M 2008 On the Coulomb-dipole transition in mesoscopic classical and quantum electron–hole bilayers *New J. Phys.* **10** 083031

[7] Matveeva N and Giorgini S 2014 Fixed-node diffusion Monte Carlo study of the BCS-BEC crossover in a bilayer system of fermionic dipoles *Phys. Rev. A* **90** 053620

[8] Brown E W, Clark B K, DuBois J L and Ceperley D M 2013 Path-Integral Monte Carlo simulation of the warm dense homogeneous electron gas *Phys. Rev. Lett.* **110** 146405

[9] Schoof T, Groth S, Vorberger J and Bonitz M 2015 *Ab initio* thermodynamic results for the degenerate electron gas at finite temperature (arXiv: 1502.04616)

[10] Filinov V S, Fortov V E, Bonitz M and Moldabekov Z 2015 Fermionic path integral Monte Carlo results for the uniform electron gas at finite temperature *Phys. Rev. E* **91** 033108

[11] Bonitz M, Filinov V S, Fortov V E, Levashov P R and Fehske H 2005 Crystallization in two-component coulomb systems *Phys. Rev. Lett.* **95** 235006

[12] Morales M A, Pierleoni C and Ceperley D 2010 Equation of state of metallic hydrogen from coupled electron–ion Monte Carlo simulations *Phys. Rev. E* **81** 021202

[13] Filinov V S, Bonitz M, Fehske H, Fortov V E and Levashov P R 2012 Proton crystallization in a dense hydrogen plasma *Contrib. Plasma Phys.* **52** 224–8

[14] Fletcher L B *et al* 2014 Observations of continuum depression in warm dense matter with x-ray Thomson scattering *Phys. Rev. Lett.* **112** 145004

[15] Kraus D *et al* 2013 Probing the complex ion structure in liquid carbon at 100 GPa *Phys. Rev. Lett.* **111** 255501

[16] Hurricane O A *et al* 2014 *Nature* **506** 343–8

[17] Ceperley D M 1995 Path integrals in the theory of condensed helium *Rev. Mod. Phys.* **67** 279–355

[18] Militzer B and Pollock E L 2005 Equilibrium contact probabilities in dense plasmas *Phys. Rev. B* **71** 134303

[19] Clark B K, Casula M and Ceperley D M 2009 Hexatic and mesoscopic phases in a 2D quantum Coulomb system *Phys. Rev. Lett.* **103** 055701

[20] Boninsegni M, Prokof'ev N and Svistunov B 2006 Worm algorithm for continuous-space path integral Monte Carlo simulations *Phys. Rev. Lett.* **96** 070601

[21] Loh E Y, Gubernatis J E, Scalettar R T, White S R, Scalapino D J and Sugar R L 1990 Sign problem in the numerical simulation of many-electron systems *Phys. Rev.* B **41** 9301–7

[22] Troyer M and Wiese U J 2005 Computational complexity and fundamental limitations to fermionic quantum Monte Carlo simulations *Phys. Rev. Lett.* **94** 170201

[23] Schoof T, Bonitz M, Filinov A V, Hochstuhl D and Dufty J W 2011 Configuration path integral Monte Carlo *Contrib. Plasma Phys.* **51** 687–97

[24] Schoof T, Groth S and Bonitz M 2015 Towards *ab initio* thermodynamics of the electron gas at strong degeneracy *Contrib. Plasma Phys.* **55** 136–43

[25] Ceperley D M 1991 Fermion nodes *J. Stat. Phys.* **63** 1237–67

[26] Filinov V S 2001 Cluster expansion for ideal Fermi systems in the fixed-node approximation *J. Phys. A: Math. Gen.* **34** 1665–77

[27] Filinov V S 2014 Analytical contradictions of the fixed-node density matrix *High Temp.* **52** 615–20

[28] DuBois J L, Alder B J and Brown E W 2014 Overcoming the fermion sign problem in homogeneous systems arXiv:1409.3262

[29] Takahashi M and Imada M 1984 Monte Carlo calculation of quantum systems *J. Phys. Soc. Japan* **53** 963–74

[30] Filinov V S, Bonitz M, Fortov V E, Ebeling W, Levashov P and Schlanges M 2004 Thermodynamic properties and plasma phase transition in dense hydrogen *Contrib. Plasma Phys.* **44** 388–94

[31] Lyubartsev A P 2005 Simulation of excited states and the sign problem in the path integral Monte Carlo method *J. Phys. A: Math. Gen.* **38** 6659–74

[32] Suzuki M 1990 Fractal decomposition of exponential operators with applications to many-body theories and Monte Carlo simulations *Phys. Lett.* A **146** 319–23

[33] Suzuki M 1995 Hybrid exponential product formulas for unbounded operators with possible applications to Monte Carlo simulations *Phys. Lett.* A **201** 425–8

[34] Chin S A 1997 Sympletic integrators from composite operator factorizations *Phys. Lett.* A **226** 344–8

[35] Takahashi M and Imada M 1984 Monte Carlo of quantum systems: II. Higher order correction *J. Phys. Soc. Japan* **53** 3765–9

[36] Chin S A 2015 High-order path integral Monte Carlo methods for solving quantum dot problems *Phys. Rev.* E **91** 031301(R)

[37] Chin S A and Chen C R 2002 Gradient symplectic algorithms for solving the Schrödinger equation with time-dependent potentials *J. Chem. Phys.* **117** 1409

[38] Sakkos K, Casulleras J and Boronat J 2009 High order chin actions in path integral Monte Carlo *J. Chem. Phys.* **130** 204109

[39] Metropolis N, Rosenbluth A W, Rosenbluth M N, Teller A H and Teller E 1953 Equation of state calculations by fast computing machines *J. Chem. Phys.* **21** 1087

[40] Boninsegni M, Prokov'ev N V and Svistunov B V 2006 Worm algorithm and diagrammatic Monte Carlo: a new approach to continuous-space path integral Monte Carlo simulations *Phys. Rev.* E **74** 036701

[41] Chandler D and Wolynes P G 1981 Exploiting the isomorphism between quantum theory and classical statistical mechanics of polyatomic fluids *J. Chem. Phys.* **74** 4078

[42] Janke W and Sauer T 1997 Optimal energy estimation in path-integral Monte Carlo simulations *J. Chem. Phys.* **107** 5821

[43] Filinov A V, Böning J and Bonitz M 2007 Path integral Monte Carlo simulation of charged particles in traps *Computational Many-Particle Physics (Lecture Notes in Physics* vol 739) ed H Fehske, R Schneider and A Weiße (Heidelberg: Springer)

[44] Fetter A L and Walecka J D 2003 *Quantum Theory of Many-Particle Systems* (New York: Dover)

[45] Egger R, Häusler W, Mak C H and Grabert H 1999 Erratum: Crossover from Fermi liquid to Wigner molecule behavior in quantum dots *Phys. Rev. Lett.* **83** 462(E)

[46] Weiss S and Egger R 2005 Path-integral Monte Carlo simulations for interacting few-electron quantum dots with spin–orbit coupling *Phys. Rev.* B **72** 245301

[47] Ludwig P, Kosse S and Bonitz M 2005 Structure of spherical three-dimensional Coulomb crystals *Phys. Rev.* E **71** 046403

[48] Dornheim T, Filinov A and Bonitz M 2015 Superfluidity of strongly correlated bosons in two- and three-dimensional traps *Phys. Rev.* B **91** 054503

[49] Thomsen H and Bonitz M 2015 Resolving structural transitions in spherical dust clusters *Phys. Rev.* E **91** 043104

3.2 Resolving Correlation and Exchange Effects using Reduced Correlation Functions

In early 2015, Thomsen and Bonitz [179] were able to report remarkable progress regarding a notoriously hard topic in computational statistical physics: the accurate estimation and interpretation of phase transitions[3] in finite systems, see, e.g., Ref. [180]. In particular, they exploited various symmetries (e.g., the spherical symmetry in a harmonic trap) to define a reduced correlation function, which can subsequently be used to compute a reduced entropy[4]. Unsurprisingly, abrupt peaks in said reduced entropy can be identified with different phase transitions, for example, angular melting within a shell or radial melting between different ones [181]. A further advantage of this strategy is that all required quantities can be obtained within thermodynamic Monte Carlo simulations (such as PIMC in the quantum case), as no dynamic information like for the Lindemann parameter [182] is required.

Being motivated by the promising capability of PB-PIMC regarding the simulation of electrons in a $2D$ quantum dot that was demonstrated in Ref. [72] (Sec. 3.1), I implemented such a reduced correlation function—specifically the so-called center-two particle correlation function, for a definition, see the following paper[5], Ref. [38]—into the PB-PIMC code (and, in addition, into the standard PIMC program from my master thesis [43]). Subsequently, I carried out simulations of $N = 13$ charged quantum particles in a $2D$ harmonic trap at moderately low temperature over two orders of coupling strength ($\lambda = 0.1, 1, 10$ in oscillator units). In particular, standard PIMC was used to simulate bosons and boltzmannons (i.e., distinguishable particles without any exchange effects, see, e.g., Refs. [20, 37]) and PB-PIMC to simulate fermions (i.e., electrons). Thereby, we were able to spatially resolve the resulting nontrivial interplay of Coulomb repulsion and exchange effects.

In the context of the present thesis, the following Ref. [163] should be viewed as an excursion into a topic of potential interest for future research and as a first proof of principle regarding the utility of reduced correlation functions for the investigation of quantum systems. Possible future investigations might include the spatial distribution of superfluidity within trapped bosons [28, 26] or Wigner crystallization of electrons in quantum dots, see, e.g., Refs. [183–185].

---

[3]In finite systems, these are often denoted as *crossovers* as *real* phase transitions only occur in the bulk.

[4]Note that the term entropy here refers to its definition from information theory but, for a quantum system, is not equal to the physical entropy.

[5]T. Dornheim, H. Thomsen, P. Ludwig, A. Filinov, and M. Bonitz, Contrib. Plasma Phys. (2016), **56**, p. 371-379, Copyright Wiley-VCH Verlag GmbH & Co. KGaA. Reproduced with permission.

Analyzing Quantum Correlations Made Simple

T. Dornheim[1], **H. Thomsen**[1], **P. Ludwig**[1]*, **A. Filinov**[1,2], and **M. Bonitz**[1]

[1] Institut für Theoretische Physik und Astrophysik, Christian-Albrechts-Universität zu Kiel, Leibnizstraße 15, 24098 Kiel, Germany

[2] Joint Institute for High Temperatures RAS, Izhorskaya str. 13, 125412 Moscow, Russia

The understanding of correlations in degenerate nonideal many-particle systems is complex and theoretically challenging. Using the recently proposed permutation blocking path integral Monte Carlo (PB-PIMC) scheme, which allows for an exact treatment of many-body correlations, we study the influence of quantum statistics in a confined few-particle Coulomb (quantum dot) system. As a versatile tool to gain insight into the internal structure of correlated many-body systems, the application of triple correlation functions is extended to quantum systems.

Self-organized structure formation of interacting particles is one of the most fundamental processes in nature [1]. The basic theoretical understanding and analysis of this cooperative phenomena requires (i) sophisticated simulation techniques that allow us to solve the basic equations of many-particle physics on first principles, and (ii) advanced tools for the analysis of the details of collective behaviour in these interacting systems such as structure formation, spatial correlations and melting (phase) transitions. However, even simple models used to describe interacting quantum systems in the regime where strong Coulomb correlations and quantum exchange effects are present are computationally very demanding. Therefore, trapped few-particle systems such as electrons in quantum dots [2] ("artificial atoms") serve as a suitable laboratory for the investigation of fundamental many-body interaction phenomena without requiring undesirable (uncontrollable) simplifications of the fundamental physics.

Path integral Monte Carlo (PIMC) is a finite temperature simulation technique for an ab-initio description of correlated quantum systems with arbitrarily strong Coulomb and quantum exchange (spin) effects [3, 4]. Furthermore, it provides a high flexibility with respect to trap geometry or the inclusion of defects et cetera, and quasi exact simulations with up to $N \sim 10^4$ bosons and boltzmannons are feasible [5, 6]. However, a rigorous and exact treatment of fermionic quantum exchange with standard PIMC is strongly limited by the fermion sign problem [7, 8]. For that reason, the permutation blocking path integral Monte Carlo (PB-PIMC) scheme [9, 10] has been recently introduced which allows us to significantly reduce this issue and to extend the range of application of the PIMC method towards stronger degeneracy, i.e., lower temperature and higher densities. Therefore, we are able to obtain approximation-free data for Bose, Boltzmann and Fermi statistics on the footing of first principle quantum Monte Carlo simulations.

Apart from an accurate computation, a central aspect of this contribution concerns the analysis of quantum correlations. To this end, we will extend the application of the recently derived triple-correlation functions [11–13] in order to resolve the influence of different quantum statistics on spatial correlations in degenerate 2D Coulomb (quantum dot) systems. While the (radial) pair distribution function–as a widely used tool for the structural analysis–is well suited for the investigation of the structure in homogeneous macroscopic systems with isotropic pair interaction potentials, in confined systems, where translational symmetry is lost, the distribution of pairs may depend on the position within the trap and a function that solely depends on the modulus of the pair distance does not allow for a local differentiation (e.g. between shells). For that reason, we utilize an appropriate generalized, angle resolved quantity to visualize complex spatial correlations in confined systems with an inhomogeneous density profile. The concept of such a many-body correlation function has possible applications over wide ranges:

---

from finite quantum systems such as electronic structures, classical systems like dusty plasma Coulomb crystals in confining potentials [11–15] or self-organized barrier discharges [16, 17], to the constellation of extragalactic objects in astrophysics [18, 19].

1   System of study

As a representative model of a strongly correlated electronic system, we consider a single quantum dot consisting of $N = 13$ charged particles in a (concentric) $2D$ harmonic confinement of frequency Ω, which is described by the dimensionless Hamiltonian

$$\hat{H} = -\frac{1}{2} \sum_{k=1}^{N} \nabla_k^2 + \frac{1}{2} \sum_{k=1}^{N} \mathbf{r}_k^2 + \sum_{k<l}^{N} \frac{\lambda}{|\mathbf{r}_k - \mathbf{r}_l|} \; . \tag{1}$$

Oscillator units (i.e., the characteristic length $l_0 = \sqrt{\hbar/m\Omega}$ and energy scale $E_0 = \hbar\Omega$) are used throughout this work. The coupling constant $\lambda = q^2/(l_0\hbar\Omega)$ (with q being the particle's charge) characterizes the strength of the Coulomb repulsion and can be controlled (experimentally) by the variation of the trap frequency. In order to analyze the characteristics of quantum exchange, we study fermions (e.g. spin-polarized electrons in a quantum dot [20–22]), bosons (e.g. indirect excitons [23, 24]), and distinguishable particles referred to as "boltzmannons", see e.g. [25]. To simulate the system at finite temperature, we are using rigorous path integral Monte Carlo methods as outlined in section 2. Here, we consider a relatively low temperature, i.e., inverse temperature $\beta = 1/k_\mathrm{B}T = 3$ and vary the coupling strength λ over two orders of magnitude.

2   Finite temperature quantum Monte Carlo simulations

The Path Integral Monte Carlo (PIMC) method [3] is one of the most powerful available tools for the treatment of strongly correlated and degenerate quantum systems yielding direct results for the particle density distributions that are free from any approximations or fit parameters. The only simulation input data involved are the fundamental pair (e.g. Coulomb) interaction potentials as well as the boundary (confinement) conditions allowing for a high flexibility regarding to specific setups (system's geometry, defects, external fields, etc.). PIMC is based on the Metropolis algorithm [26], which allows to generate configurations from the canonical distribution and, therefore, yields direct thermodynamic averages, i.e., finite temperature results. Despite the complexity of a physical system, the PIMC method achieves excellent performance, as long as the particles obey Boltzmann[1] or Bose statistics. In the path integral picture (i.e., the imaginary time path integral representation of the density matrix), quantum statistics requires the additional sampling of the particle permutations, which significantly increases the dimensionality of the configuration space. These permutations can be decomposed into a sequence of two-particle exchanges along the imaginary timeline. In the case of fermions, the superposition of all $N!$ permutations of N identical particles leads to the inherent[2] *fermionic sign problem*, since an alternating sign of the prefactor of the many-body density matrix causes an essential cancellation of positive and negative contributions corresponding to even and odd permutations, respectively [7]. Thus, an accurate calculation of these vanishing differences is exponentially aggravated [8] with the increase of quantum degeneracy arising at low temperatures and high densities, where all permutations appear with nearly equal probability. The recently introduced Permutation Blocking PIMC (PB-PIMC) scheme employed in this contribution allows us to overcome these severe limitations of standard PIMC and thereby to significantly extend the accessible parameter ranges of fermions towards higher degeneracy [9, 10].

---

[1] PIMC runs most efficient if quantum statistics is neglected and distinguishable spinless (Boltzmann) particles are considered [1].

[2] One has to distinguish between the cancellation of contributions inherent to the Metropolis Monte Carlo sampling scheme and the limited numerical precision due to a finite number of bits, which can be neglected here.

2.1 Standard PIMC

We consider the canonical ensemble (with fixed particle number N, trap frequency Ω and inverse temperature $\beta = 1/k_\mathrm{B}T$) and write the partition function for N distinguishable particles in coordinate representation as

$$Z = \int \mathrm{d}\mathbf{R} \langle \mathbf{R}| \, e^{-\beta \hat{H}} \, |\mathbf{R}\rangle \,, \tag{2}$$

with $\mathbf{R} = \{\mathbf{r}_1, \ldots, \mathbf{r}_N\}$ containing all particle coordinates. To simulate the system using the standard path integral Monte Carlo method, e.g. [3,4], we exploit a group property of the density matrix

$$e^{-\beta \hat{H}} = \left(e^{-\epsilon \hat{H}} \right)^P \,, \tag{3}$$

with $\epsilon = \beta/P$, and insert $P-1$ unities of the form $\hat{1} = \int \mathrm{d}\mathbf{R}_\alpha \, |\mathbf{R}\rangle_\alpha \langle \mathbf{R}|_\alpha$ to transform Eq. (2) to

$$Z = \int \mathrm{d}\mathbf{X} \, \langle \mathbf{R}_0| \, e^{-\epsilon \hat{H}} \, |\mathbf{R}_1\rangle \langle \mathbf{R}_1| \, \cdots \, |\mathbf{R}_{P-1}\rangle \langle \mathbf{R}_{P-1}| \, e^{-\epsilon \hat{H}} \, |\mathbf{R}_0\rangle \,, \tag{4}$$

with the integration being carried out over P sets of coordinates, $\mathrm{d}\mathbf{X} = \mathrm{d}\mathbf{R}_0 \ldots \mathrm{d}\mathbf{R}_{P-1}$. Eq. (4) is exact and constitutes an integral over P density matrices at P times the temperature. This allows one to use the *primitive approximation* $e^{-\epsilon \hat{H}} \approx e^{-\epsilon \hat{K}} e^{-\epsilon \hat{V}}$, with $\hat{K}$ and $\hat{V}$ being the kinetic and potential contribution to the Hamiltonian, respectively, which yields exact results for $P \to \infty$. The separate matrix elements of $e^{-\epsilon \hat{V}}$ and $e^{-\epsilon \hat{K}}$ are known, and the resulting high-dimensional integral can be evaluated using the Metropolis algorithm [26]. To simulate bosons or fermions, one has to extend the partition function by the sum over all permutations

$$Z = \frac{1}{N!} \sum_{\sigma \in S_N} \mathrm{sgn}(\sigma) \int \mathrm{d}\mathbf{R} \, \langle \mathbf{R}| \, e^{-\beta \hat{H}} \, |\hat{\pi}_\sigma \mathbf{R}\rangle \,, \tag{5}$$

with $\hat{\pi}_\sigma$ being the exchange operator which corresponds to a particular element σ from the permutation group S_N. Hence, Eq. (5) requires the employed PIMC approach to generate exchange cycles, which can be very efficiently accomplished using the worm algorithm [5,6]. For bosons and boltzmannons, all terms are strictly positive. However, the sign of fermionic contributions depends on the parity of the particular permutation. With increasing exchange effects, towards high density and low temperature, permutation cycles with positive and negative signs appear with nearly equal probability and, therefore, the statistical error increases exponentially. This numerical issue is known as the *fermion sign problem* [7] and limits standard PIMC to weak degeneracy, i.e., strong coupling and/or high temperature, where exchange effects play only a minor role.

2.2 Permutation Blocking PIMC

PB-PIMC is basically a combination of (i) antisymmetric imaginary time propagators, i.e., determinants [27–29], which allow for an analytic cancellation of positive and negative permutations within a single configuration weight (permutation blocking), (ii) a higher-order factorization of the density matrix [30–32], and (iii) a highly efficient Monte Carlo sampling scheme based on artificial trajectories [9]. While the blocking of permutations can lead to a significant reduction of the fermion sign problem, with an increasing number of propagators P this advantage quickly vanishes. Therefore, instead of the *primitive approximation*, the PB-PIMC implementation utilizes the *fourth order factorization* [31,32]

$$e^{-\epsilon \hat{H}} \approx e^{-v_1 \epsilon \hat{W}_{a_1}} e^{-t_1 \epsilon \hat{K}} e^{-v_2 \epsilon \hat{W}_{1-2a_1}} e^{-t_1 \epsilon \hat{K}} e^{-v_1 \epsilon \hat{W}_{a_1}} e^{-2t_0 \epsilon \hat{K}} \quad, \tag{6}$$

of the density matrix, which allows for sufficient accuracy with only a few high temperature factors. The $\hat{W}$ operators in Eq. (6) denote a modified potential, which combines $\hat{V}$ with double commutator terms of the form [32]

$$[[\hat{V}, \hat{K}], \hat{V}] = \frac{\hbar^2}{m} \sum_{i=1}^N |\mathbf{F}_i|^2 \,. \tag{7}$$

Therefore, PB-PIMC requires the evaluation of the force acting on each particle $\mathbf{F}_i = -\nabla_i V(\mathbf{R})$. The final result for the partition function is given by

$$Z = \frac{1}{(N!)^{3P}} \int d\mathbf{X} \prod_{\alpha=0}^{P-1} e^{-\epsilon \tilde{V}_\alpha} e^{-\epsilon^3 u_0 \frac{\hbar^2}{m} \tilde{F}_\alpha} \det(\rho_\alpha) \det(\rho_{\alpha A}) \det(\rho_{\alpha B}) , \tag{8}$$

with $\tilde{V}_\alpha$ and $\tilde{F}_\alpha$ containing the contributions of the potential and the forces, respectively, and the diffusion matrix

$$\rho_\alpha(i,j) = \lambda_{t_1\epsilon}^{-D} \exp\left(-\frac{\pi}{\lambda_{t_1\epsilon}^2}(\mathbf{r}_{\alpha,j} - \mathbf{r}_{\alpha A,i})^2 \right) , \tag{9}$$

with $\lambda_{t_1\epsilon} = \sqrt{2\pi\epsilon t_1 \hbar^2/m}$ being the thermal wavelength of a single time slice. Instead of explicitly sampling each permutation cycle as in standard PIMC, we combine configuration weights of both positive and negative sign in the determinants, which leads to a cancellation of terms and, therefore, a highly effective blocking of permutations. When the wavelength $\lambda_{t_1\epsilon}$ is comparable to the mean inter-particle distance, the blocking is most effective and the average sign in the Monte Carlo simulations is significantly increased. However, with an increasing P, $\lambda_{t_1\epsilon}$ decreases and, eventually, the average sign converges towards the sign from standard PIMC. Hence, it is crucial to employ the fourth order factorization from Eq. (6), which allows for sufficient accuracy with as few as two or three propagators. To ensure an ergodic and highly efficient sampling procedure for this modified configuration space, we have combined the worm algorithm idea [6] with the temporary construction of artificial trajectories where blocking happens automatically as a by-product. For a detailed description of PB-PIMC, we refer to [9].

For the sake of completeness, we mention that the recently introduced Configuration PIMC (CPIMC) approach [33–35] exhibits a complementary range of applicability ($\lambda \lesssim 1$). CPIMC can be interpreted as a Monte Carlo simulation on an expansion around the ideal system and, therefore, excels at weak coupling and strong degeneracy. Unfortunately, the physically most interesting transition region remains out of reach. A popular extension of standard PIMC towards higher degeneracy is Restricted PIMC (RPIMC), often denoted as fixed node approximation [36]. However, this approach requires explicit knowledge of the nodal structure of the density matrix, which is a priori unknown. Therefore, one has to rely on approximations which introduce an uncontrolled systematic error [37, 38]. To circumvent these issues, here we pursue the above introduced permutation blocking idea which allows us to simulate the system over the entire coupling range.

3 Particle distribution functions

Microscopic phase-space information, and in particular the distribution of particles and particle pairs are central quantities in statistical physics. While the radial pair distribution function $g(r) = g(|\mathbf{r}_2 - \mathbf{r}_1|)$ is well suited for the analysis of the structure in homogeneous isotropic systems, see e.g. [39], an advanced quantity is required for confined systems. In the homogeneous system, the two-particle distribution $\rho_2(\mathbf{r}_1, \mathbf{r}_2)$ must not depend on the position of the particle pair or on its orientation due to the symmetry. Hence, the pair correlations can be described solely as a function of the absolute pair distance r.

3.1 Two-particle density

For a harmonically trapped system, ρ_2 is not invariant under translation, but under rotation with respect to the trap center. Consequently, an appropriate pair correlation function requires three coordinates: r_{I} and r_{II} as the radial position of the first and the second particle of the pair, respectively, and the enclosed angle ϑ with respect to the trap center, cf. Fig. 1. The two-particle density in generalized coordinates $\rho_2(r_{\mathrm{I}}, r_{\mathrm{II}}, \vartheta)$ is sampled as a three-dimensional histogram in the PIMC simulation. This quantity is referred to as *center-two-particle* (c2p) density and can be interpreted as the probability of measuring a pair of particles of which the first (second) has a distance r_{I} (r_{II}) from the trap center and where both particles enclose an angle ϑ with the trap center, cf. Fig. 1.
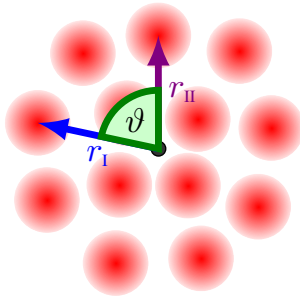
Fig. 1 Generalized coordinates of the center-two-particle correlation function $\rho_2(r_\mathrm{I}, r_\mathrm{II}, \vartheta)$ for a harmonically confined 2D Coulomb cluster. All possible positions of two particles are sampled and compiled with respect to three parameters: distance r_I of the first particle from the trap center, distance r_II of the second particle from the trap center, and their connecting angle ϑ. In the *center-two-particle* distribution function, the trap center serves as a third reference point. The classical particle positions serve as an example, where the $N = 13$ particles arrange themselves on two concentric shells.

3.2   Two-particle correlations

In order to emphasize angular correlations, it has proven reasonable to define the *center-two-particle* (c2p) correlation function

$$g_{\mathrm{c2p}}(r_\mathrm{I}, r_\mathrm{II}, \vartheta) = \frac{\rho_2(r_\mathrm{I}, r_\mathrm{II}, \vartheta)}{\rho_2^{\mathrm{id}}(r_\mathrm{I}, r_\mathrm{II}, \vartheta)}, \tag{10}$$

which is normalized by the *ideal two-particle density* ρ_2^{id} of a corresponding system with the same radial density profile but without any angular modulations. This allows one to compensate for the non-correlation related effects that are solely caused by the inhomogeneous density profile. For 2D systems, this density is given by[3] $\rho_2^{\mathrm{id}} = \frac{N-1}{N} 4\pi r_\mathrm{I} r_\mathrm{II} n(r_\mathrm{I}) n(r_\mathrm{II})$ as the product of the radial density $n(r)$ at both particle radii [11–13].

While $g_{\mathrm{c2p}}(r_\mathrm{I}, r_\mathrm{II}, \vartheta)$ is a function of three coordinates, a two-dimensional distribution function $g_{\mathrm{c2p}}^{\mathrm{int}}(r_\mathrm{II}, \vartheta)$ is extracted by the integration over a particular r_I range. Here, we have integrated over an r_I range that corresponds to the outer (inner) shell or region when the shell structure has vanished. For classical or localized quantum particles, this can be interpreted as choosing one reference particle from the outer (inner) shell.

Being derived from the concept of a many-particle correlation function, the c2p function takes explicitly into account the concentric symmetry of the harmonically confined system. It provides local insight into the structure and allows one to resolve the radial and relative angular distribution of two particles with respect to the trap center. In particular, it is sensitive to the mutual orientation of particle pairs, but not affected by a rotation of the particle cluster as a whole (e.g. during the simulation run). The c2p function is well defined and robust yielding reliable information also in the case of partially incomplete data sets, e.g. from experiments. As this quantity relies only on the statistical distribution of particle positions, it does neither require explicitly labeled particles nor dynamical information such as particle trajectories, which makes the c2p function well suited for equilibrium Monte Carlo simulations.

4   Analysis of spatial quantum correlations

Considering Bose, Boltzmann and Fermi statistics for a system of $N = 13$ particles, we investigate the influence of quantum statistics on the spatial correlations over a wide range of the coupling parameter λ covering two orders of magnitude.

Figure 2 shows the integrated c2p-density where we have carried out the r_I-integration over the outer region of the system (shaded area in the inset density profile). The first column shows a strongly coupled system ($\lambda = 10$). Due to the strong Coulomb repulsion, the particles are quasi localized and the quantum statistics has only a small influence on the structure because of the negligible overlap of the wave function. The radial density (top panel and black line in the insets) is virtually the same for all three particle types and exhibits two distinct shells. In parts (a), (d) and (g) of Fig. 2, the c2p correlation function reveals no significant differences between the three systems as well. The most prominent feature is the correlation hole at a radial coordinate $r_\mathrm{II} \approx 4$ and small angular pair distances $\vartheta \lesssim 30°$.

---

[3] The factor $(N-1)/N$ is conventional and ensures that the normalization of both ρ_2 and ρ_2^{id} is the number of particle pairs. The factor has only minor influence on the result especially for large particle numbers. It has no qualitative impact on the structures which are found in the plots. For small particle numbers, one finds that with the factor included, g_{c2p} approaches a value slightly above unity for large distances and weak correlations, cf. bottom row of Fig. 2. This can be understood since the correlation hole at small distances has to be compensated.
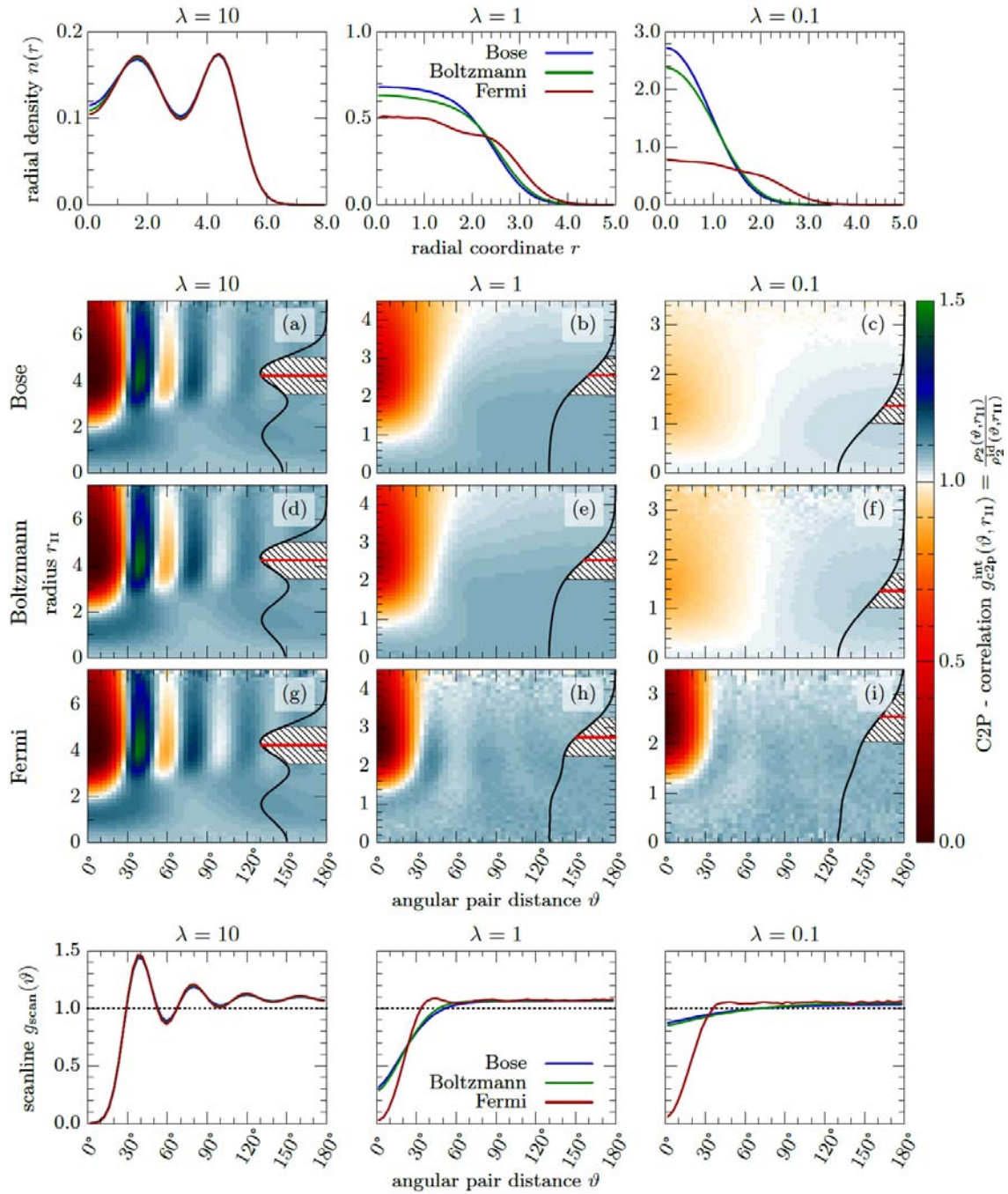
Fig. 2 Effect of quantum statistics in the outer shell: Center panel: center-two-particle correlation function for a system of $N = 13$ bosons, boltzmannons, and fermions at strong ($\lambda = 10$), moderate ($\lambda = 1$) and weak ($\lambda = 0.1$) coupling strength. The radial density is shown as an inset where the shaded area indicates the r_{I} integration range. The red line indicates the angular density cut (scanline) through the outer shell which is shown in the lower panel. Top panel: comparison of the radial density profiles for the three different statistics. Bottom panel: scanlines through the r_{II}-ϑ plane as indicated by the red line in (a-i) at constant r_{II}.

This hole is followed by a sequence of maxima and minima in ϑ direction which correspond to angular pair correlations within the outer shell. These correlations are found even for distant particles with $\vartheta \approx 180°$, i.e.,

the particles are located at opposite sides of the trap. Since it is difficult to meter the absolute height in color maps, we show a scanline at the middle of the outer shell in the bottom panel. This scanline $g_{\text{scan}}(\vartheta)$ confirms that virtually the same intra-shell angular correlations are found for bosons, boltzmannons and fermions at strong coupling. As a further interesting feature in panels (a), (d) and (g), we find angular correlations with the particles on the inner shell, which appear as–less pronounced–maxima and minima at a radius $r_{\text{II}} \approx 1.5$ that corresponds to the inner shell. This means that orientations of inner and outer shell are not independent.
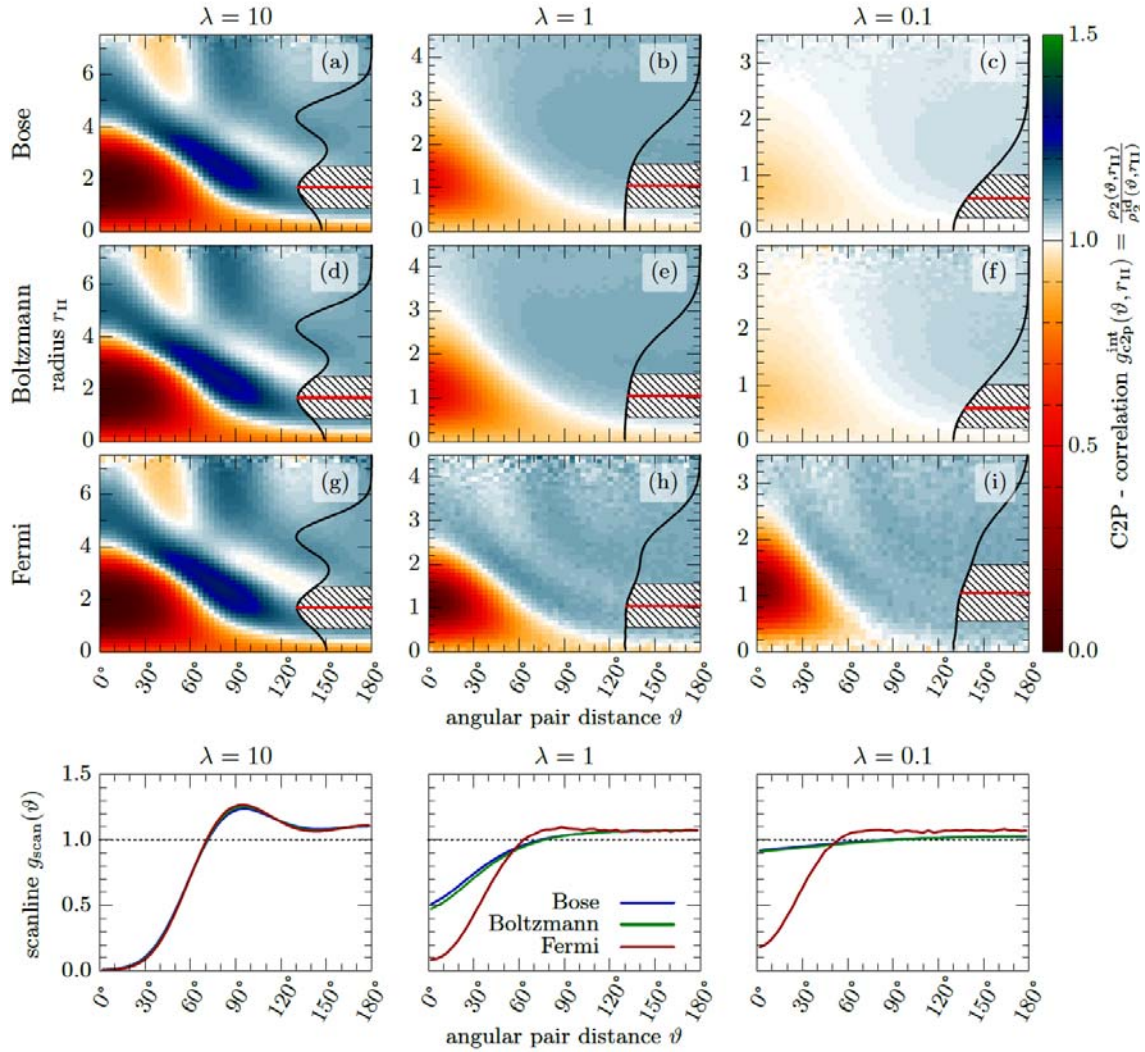
Fig. 3 Effect of quantum statistics in the inner shell: Center-two-particle correlation function (top panel) as in Fig. 2 but with r_{I} being integrated over the inner region (shaded area in the inset). The scanlines (bottom panel) at the r_{II} value which is marked by the red line show the intra-shell angular correlations within the inner shell.

At a ten times lower coupling parameter ($\lambda = 1$) shown in the central column of Fig. 2, the quantum statistics has a noticeable impact on the spatial structure of the systems. In the radial density shown at the top panel, we find that the cluster of fermions is enlarged compared to bosons and boltzmannons because of the degeneration pressure. In parts (b), (e) and (h), the c2p correlation function again shows the correlation hole[4] around $r_{\text{II}} = 3$ and small angular pair distances ϑ for all three quantum statistics. As a unique feature, the fermionic system exhibits angular correlations also at larger distances. These appear as a sequence of dark and bright areas along

---

[4] For fermions, the correlation hole is caused by both quantum exchange effects and the Coulomb repulsion. In this case, one might refer to this as an exchange correlation hole.

the direction of ϑ. In the scanline (bottom panel), the angular correlations beyond the correlation hole at $\vartheta = 0°$ are reflected as a maximum around $\vartheta = 40°$ followed by a minimum around $\vartheta = 60°$[5]. This feature is a manifestation of the Pauli blocking which leads to an effective 'hard-core' repulsion. The 'hard-core' interaction separates the fermions in addition to the Coulomb repulsion that is present for all three types of particles.

The right column of Fig 2 shows the three systems at weak coupling ($\lambda = 0.1$). Here, the radial density (top panel) shows that both bosons and boltzmannons concentrate at the trap center while the radial profile of the fermionic system does not change significantly compared with $\lambda = 1.0$. For bosons and boltzmannons, hardly any angular correlations are visible at weak coupling. Solely the correlation hole at small pair angles remains as a shallow minimum in parts (c) and (f) of Fig. 2. The scanline (bottom panel) reveals that the total variation of the pair density is below 20%. In contrast, the fermionic system in part (i) of the figure exhibits clear angular correlations although these are weaker than in part (h) at moderate coupling. The scanline clearly indicates the difference between fermions on the one hand and bosons and boltzmannons on the other hand. Only the fermionic system has a pronounced (exchange) correlation hole where the correlation function drops almost down to zero which is due to the governing effect of Fermi repulsion[6].

Figure 3 displays, as a supplement for Fig. 2, the analogous function with an r_{I} integration that corresponds to the radial range of the inner instead of the outer shell. In that case, the angular correlations within the inner shell are visible as pronounced peaks around $r_{\mathrm{II}} \approx 1.5$ while very weak inter-shell angular correlations are found as weaker peaks around $r_{\mathrm{II}} \approx 5$. The inner shell is populated by $N_1 = 4$ particles on average which explains why the peak for nearest on-shell neighbors appears at $\vartheta = 90°$. For classical particles at zero temperature with such a configuration, one would expect another maximum around $r_{\mathrm{II}} \approx 1.5$ and $\vartheta = 180°$ caused by the opposite particle within the inner shell, cf. Fig. 1. Both to the quantum mechanical delocalization and the finite temperature cause the maximum to be smeared out. For this reason, the minimum at $\vartheta = 135°$ in the scanline (bottom panel) as well as the maximum at $180°$ are both very weak. Overall, we again find a crossover from a nearly classical system at strong coupling ($\lambda = 10$) towards a degenerate quantum system, where for fermions the Pauli blocking dominates. This leads to a significantly different behaviour in comparison to bosons and boltzmannons.

5   Conclusion

As a main goal, in this contribution we have investigated the influence of quantum statistics on spatial correlations in a degenerate 2D quantum dot system. Using state of the art quantum Monte Carlo techniques to simulate bosons, boltzmannons and fermions from first principles, we have studied the crossover from a nearly classical system with governing repulsive Coulomb interaction towards a density (coupling) regime that is dominated by quantum exchange effects. To resolve this effect in great detail, we have used the recently introduced center two-particle correlation function [13] which allows to study spatial many-body correlations on a level widely beyond the standard radial pair distribution function $g(r)$. A future application of this quantity may include the investigation of the spatial distribution of superfluidity in finite systems [40–42]. Furthermore, we note that a reduced entropy can be directly computed from the proposed correlation function, which is well suited to determine various kinds of phase boundaries (such as multistage intra-shell, inter-shell, and radial melting transitions) in both finite and macroscopic systems [12, 13]. In contrast to the Lindemann parameter, it is a thermodynamic quantity and therefore directly accessible to equilibrium Monte Carlo simulations as it does not require any dynamical information [1, 43].

---

[5] Two further maxima around $\vartheta = 80°$ and $\vartheta = 120°$ as well as a minimum around $\vartheta = 105°$ are clearly visible only in Fig. 2 (h). The reason for this is that the color map offers a wider overview which is missing in the scanline that includes only one bin in r_{II} direction.

[6] The reason why $g_{\mathrm{scan}}(\vartheta)$ is not exactly zero at small ϑ is the finite integration range for r_{I}. Therefore, two particles can be aligned in radial direction, i.e. $\vartheta = 0°$ and still have finite distance.

References

[1] P. Ludwig, Structure Formation in Strongly Correlated Few-Particle Systems in Traps, PhD Thesis, Universität Rostock (2008).

[2] S. Reimann, and M. Manninen, Rev. Mod. Phys. **74**, 1283 (2002).

[3] D.M. Ceperley, Rev. Mod. Phys. **67**, 279 (1995).

[4] A.V. Filinov, J. Böning and M. Bonitz, Path integral Monte Carlo simulation of charged particles in traps, in "Computational Many-Particle Physics", H. Fehske, R. Schneider and A. Weiße (Eds.), Lecture Notes in Physics **739**, Springer Heidelberg (2007).

[5] M. Boninsegni, N. Prokof'ev and B. Svistunov, Phys. Rev. Lett. **96**, 070601 (2006).

[6] M. Boninsegni, N.V. Prokov'ev and B.V. Svistunov, Phys. Rev. E **74**, 036701 (2006).

[7] E.Y. Loh, J.E. Gubernatis, R.T. Scalettar, S.R. White, D.J. Scalapino, and R.L. Sugar, Phys. Rev. B **41**, 9301 (1990).

[8] M. Troyer and U.J. Wiese, Phys. Rev. Lett. **94**, 170201 (2005).

[9] T. Dornheim, S. Groth, A. Filinov and M. Bonitz, New J. Phys. **17**, 073017 (2015).

[10] T. Dornheim, T. Schoof, S. Groth, A. Filinov, and M. Bonitz, J. Chem. Phys. **143**, 204101 (2015).

[11] H. Thomsen, J. Schablinski, and M. Bonitz, Phase Transitions in Dusty Plasmas, in "Complex Plasmas", M. Bonitz, J. Lopez, K. Becker and H. Thomsen (Eds.), Springer Series on Atomic; Optical and Plasma Physics **82**, 3 (2014).

[12] H. Thomsen and M. Bonitz, Phys. Rev. E **91**, 043104 (2015).

[13] H. Thomsen, Melting Processes and Laser Manipulation of Strongly Coupled Yukawa Systems, PhD Thesis, Christian-Albrechts-Universität zu Kiel (2015).

[14] P. Ludwig, H. Thomsen, K. Balzer, A. Filinov, and M. Bonitz, New J. Phys. **52**, 124013 (2010).

[15] A. Schella, , T. Miksch, A. Melzer, J. Schablinski, D. Block, A. Piel, H. Thomsen, P. Ludwig, and M. Bonitz, Phys. Rev. E **84**, 056402 (2011).

[16] R. Wild and L. Stollenwerk, EPJ D **66**, 214 (2012).

[17] M. Bogaczyk, S. Nemschokmichal, R. Wild, L. Stollenwerk, R. Brandenburg, J. Meichsner, and H.-E. Wagner, Contrib. Plas. Phys. **52**, 847 (2012).

[18] Edward J. Groth, and P.J. E. Peebles, ApJ **217**, 385 (1977).

[19] J.N. Fry and P.J.E. Peebles, ApJ **221**, 19 (1978).

[20] R. Egger, W. Häusler, C.H. Mak, and H. Grabert, Phys. Rev. Lett. **82**, 3320 (1999).

[21] A.V. Filinov, M. Bonitz, and Y.E. Lozovik, Phys. Rev. Lett. **86**, 3851 (2001).

[22] A. Ghosal, A.D. Güçlü, C.J. Umrigar, D. Ullmo, and H.U. Baranger, Phys. Rev. B **76**, 085341 (2007).

[23] J. Böning, A. Filinov, and M. Bonitz, Phys. Rev. B **84**, 075130 (2011).

[24] K. Sperlich, P. Ludwig, A. Filinov, M. Bonitz, H. Stolz, D. Hommel, and A. Gust, phys. stat. sol. (c) **6**, 551 (2009).

[25] B.K. Clark, M. Casula, and D.M. Ceperley, Phys. Rev. Lett. **103**, 055701 (2009).

[26] N. Metropolis, A.W. Rosenbluth, M.N. Rosenbluth, A.H. Teller, and E. Teller, J. Chem. Phys. **21**, 1087 (1953).

[27] M. Takahashi and M. Imada, J. Phys. Soc. Jpn. **53**, 963 (1984).

[28] V.S. Filinov, M. Bonitz, V.E. Fortov, W. Ebeling, P. Levashov, and M. Schlanges, Contrib. Plasma Phys. **44**, 388 (2004).

[29] A.P. Lyubartsev, J. Phys. A: Math. Gen. **38**, 6659 (2005).

[30] S.A. Chin, Phys. Rev. E **91**, 031301(R) (2015).

[31] S.A. Chin and C.R. Chen, J. Chem. Phys. **117**, 1409 (2002).

[32] K. Sakkos, J. Casulleras, and J. Boronat, J. Chem. Phys. **130**, 204109 (2009).

[33] T. Schoof, M. Bonitz, A.V. Filinov, D. Hochstuhl, and J.W. Dufty, Contrib. Plasma Phys. **51**, 687 (2011).

[34] T. Schoof, S. Groth, and M. Bonitz, Optical and Plasma Physics **82**, 153 (2014).

[35] T. Schoof, S. Groth, J. Vorberger, and M. Bonitz, Phys. Rev. Lett. **115**, 130402 (2015).

[36] D.M. Ceperley, J. Stat. Phys. **63**, 1237 (1991).

[37] V.S. Filinov, J. Phys. A: Math. Gen. **34**, 1665 (2001).

[38] V.S. Filinov, High Temp. **52**, 615 (2014).

[39] P. Gori-Giorgi, F. Sacchetti, and G.B. Bachelet, Phys. Rev. B **61**, 7353 (2000).

[40] Y. Kwon, F. Paesani, and K. Whaley, Phys. Rev. B **74**, 174522 (2006).

[41] A. Filinov, J. Böning, M. Bonitz, and Yu. Lozovik, Phys. Rev. B **77**, 214527 (2008).

[42] T. Dornheim, A. Filinov, and M. Bonitz, Phys. Rev. B **91**, 054503 (2015).

[43] J. Böning, A. Filinov, P. Ludwig, H. Baumgartner, M. Bonitz, and Yu.E. Lozovik, Phys. Rev. Lett. **100**, 113401 (2008).

3.3   Application of PB-PIMC to the Uniform Electron Gas

The high current interest and experimental progress in warm dense matter research lead to a surge of fermionic QMC simulations of the uniform electron gas at finite temperature. As mentioned in Sec. 3.1, Brown's RPIMC data [157] were seriously called into question by the new, exact CPIMC data obtained by our group [59]. In addition, Filinov and co-workers [69] published a third, independent set of QMC data, although the comparability to the other results has remained unclear due to (i) the different treatment of the positive homogeneous background and (ii) the absence of reliable benchmarks. Given the observed ability of PB-PIMC to strongly alleviate the FSP, an extension to the UEG was highly desirable.

To make this happen, the underlying equations that are governing the PB-PIMC formalism had to be adjusted to include periodic boundary conditions[6], which requires the modification both of the Monte Carlo estimators (for example, for the energy, see Eq. (8) in the following paper, Ref. [77]) and the acceptance probabilities of the updates. In addition, the sampling procedure itself had to be adapted to the periodicity inherent to the UEG. Furthermore, the long-range nature of the Coulomb interaction requires one to consider the interaction not only between different electrons in the simulation cell, but also with the infinite array of periodic images (the same applies to the positive uniform background). This is achieved by employing the so-called Ewald summation [186, 187], which corresponds to the solution of Poisson's equation in periodic boundary conditions [188, 189]. In particular, one splits the infinite sum over all images into two separate parts in real and reciprocal space, which are rapidly converging[7].

In the following paper [77], the application of PB-PIMC to the warm dense electron gas is demonstrated for the spin-polarized case. More specifically, we discuss the modifications of the PB-PIMC partition function, as well as the resulting changes in the Monte Carlo estimator for the energy. A brief demonstration of the convergence with the number of propagators is followed by the exhaustive investigation of $N = 33$ spin-polarized electrons at warm dense matter conditions.

In a nutshell, we found that PB-PIMC does again significantly extend standard PIMC towards both lower temperature and higher density and, for $\theta > 0.5$, simulations are feasible over the entire density range. The comparison with previous results revealed excellent agreement to the exact CPIMC data, where they are available, whereas the RPIMC data by Brown *et al.* [157] exhibit significant deviations, which increase with density.

---

[6]In practice, the ideal density matrix is implemented as a periodic sum over Gaussians [41, 21].

[7]Given the appropriate choice of a free parameter.

Overall, this paper constitutes the proof of principle regarding the utility of PB-PIMC for the simulation of warm dense electrons and regarding its complementary nature with respect to CPIMC.

Permutation blocking path integral Monte Carlo approach to the uniform electron gas at finite temperature

Tobias Dornheim,[1,a)] Tim Schoof,[1] Simon Groth,[1] Alexey Filinov,[1,2] and Michael Bonitz[1]

[1]*Institut für Theoretische Physik und Astrophysik, Christian-Albrechts-Universität, Leibnizstrasse 15,*
Kiel D-24098, Germany
[2]*Joint Institute for High Temperatures RAS, Izhorskaya Str. 13, 125412 Moscow, Russia*

The uniform electron gas (UEG) at finite temperature is of high current interest due to its key relevance for many applications including dense plasmas and laser excited solids. In particular, density functional theory heavily relies on accurate thermodynamic data for the UEG. Until recently, the only existing first-principle results had been obtained for $N = 33$ electrons with restricted path integral Monte Carlo (RPIMC), for low to moderate density, $r_s = \overline{r}/a_B \gtrsim 1$. These data have been complemented by configuration path integral Monte Carlo (CPIMC) simulations for $r_s \leq 1$ that substantially deviate from RPIMC towards smaller r_s and low temperature. In this work, we present results from an independent third method—the recently developed permutation blocking path integral Monte Carlo (PB-PIMC) approach [T. Dornheim *et al.*, New J. Phys. **17**, 073017 (2015)] which we extend to the UEG. Interestingly, PB-PIMC allows us to perform simulations over the entire density range down to half the Fermi temperature ($\theta = k_B T/E_F = 0.5$) and, therefore, to compare our results to both aforementioned methods. While we find excellent agreement with CPIMC, where results are available, we observe deviations from RPIMC that are beyond the statistical errors and increase with density. © *2015 AIP Publishing LLC.* [http://dx.doi.org/10.1063/1.4936145]

I. INTRODUCTION

Over the last years, there has been an increasing interest in the thermodynamic properties of degenerate electrons in the quantum mechanical regime. Such information is vital for the description of highly compressed matter,[1–3] including plasmas in laser fusion experiments[4–9] and in compact stars and planet cores.[10–12] In addition, the widespread density functional theory (DFT) approach crucially depends on the availability of accurate quantum Monte Carlo (QMC) data for the exchange correlation energy of the uniform electron gas (UEG), hitherto at zero temperature.[13–17] However, in recent years more and more applications with highly excited electrons have emerged, which require to go beyond ground state DFT. Hence, there exists a high current need for an *ab initio* thermodynamic description of the UEG at finite T.

The widely used path integral Monte Carlo (PIMC) method, e.g., Ref. 18, is a powerful tool for the *ab initio* simulation of both distinguishable particles (often referred to as "boltzmannons," e.g., Refs. 19 and 20) and bosons and allows for quasi exact results for up to $N \sim 10^3$ particles at finite temperature.[21,22] However, the application of PIMC to fermions is hampered by the notorious fermion sign problem (FSP), e.g., Ref. 23, which might render even small systems unfeasible for state of the art QMC methods and is known to be NP-hard for a given representation.[24] With increasing degeneracy effects, permutation cycles with opposite signs nearly cancel each other and the statistical uncertainty grows exponentially. Hence, standard PIMC cannot provide the

desired results without further improvement. Brown *et al.*[25] have presented the first finite temperature results for the UEG down to $r_s = 1$ using restricted PIMC (RPIMC),[26] a popular approach to extend PIMC to higher degeneracy, that is, lower temperature and higher density. To avoid the FSP, this method requires explicit knowledge of the nodal surface of the density matrix, which is, in general, unknown and one has to rely on approximations. The use of the ideal nodes for a nonideal system appears to be problematic, as has been shown for the case of hydrogen.[27,28] In addition, it has been shown analytically that RPIMC does not reproduce the exact limit of the ideal Fermi gas ($r_s \rightarrow 0$).[29,30] Therefore, the quality of the RPIMC data remains unclear. Indeed, recent configuration PIMC (CPIMC)[31,32] results for the highly degenerate UEG by Schoof *et al.*[33] have revealed a significant disagreement between the two methods at small r_s and low temperature. While the first application of a novel density matrix QMC (DMQMC) approach[34] to the UEG for four particles reports excellent agreement with CPIMC,[35] additional simulations of larger systems are needed to resolve the discrepancy towards RPIMC. For completeness, we mention that QMC results by Filinov *et al.*[36] cannot be used as a benchmark due to the different treatment of the homogeneous positive background and a different account of the long-range Coulomb interaction[37,38] than the usual Ewald summation. In this situation, an independent third first-principle method, capable to treat warm dense matter (WDM) parameters, would be highly desirable.

In this work we, therefore, investigate the applicability of the recently developed permutation blocking PIMC (PB-PIMC) approach[39] to the uniform electron gas. We note

that PB-PIMC is essentially standard PIMC but combines two well known concepts: (1) antisymmetric imaginary time propagators,[40–42] i.e., determinants, between all "time slices" and (2) a higher order factorization of the density matrix.[43–46] This means that each particle is represented by a "path" consisting of $3 \times P$ coordinates ("beads"), where P is the number of high-temperature factors (or propagators). (3) To efficiently sample this more complicated configuration space, PB-PIMC uses a novel Monte Carlo update scheme which combines the worm algorithm idea[21,22] with the temporary construction of artificial trajectories, cf. Ref. 39. The application of determinants leads to a relieve of the FSP by an effective cancellation of positive and negative terms in the partition function, which belong to permutation cycles of different parity in standard PIMC. However, since the blocking is most effective if the thermal wavelength of a single propagator is of the same order as the mean interparticle distance, it is crucial to employ a higher order factorization scheme which allows for sufficient accuracy with only a few time slices. Therefore, it is the combination of the above three ingredients that allows us to significantly extend the range of applicability of standard PIMC towards stronger degeneracy, see also Fig. 1.

The details of our PB-PIMC scheme, for the UEG, are described in Section II B, after a brief introduction of the employed model in Section II A. In Section III A, we present our simulation results starting with a detailed investigation of the convergence behavior with respect to the factorization of the density matrix. We proceed by simulating $N = 33$ spin-polarized electrons, which is a commonly used model system of the UEG, see Section III B. Interestingly, our PB-PIMC approach allows us to obtain accurate results over the entire density range and, therefore, to make a comparison with the pre-existing RPIMC and CPIMC results for the UEG. Finally, in Section III C we investigate the applicability of our method with respect to the temperature. We find that PB-PIMC, in combination with CPIMC, allows for the simulation of

FIG. 1. Density-temperature plain around the warm dense matter (WDM) regime. PB-PIMC significantly extends the range of applicability of standard PIMC (qualitatively shown by the red dashed line, see also Figs. 5 and 7) towards lower temperature and higher density while CPIMC is applicable to the highly degenerate and weakly nonideal UEG.[33] RPIMC data[25] are available for $r_s \geq 1$. The orange area marks the conditions of WDM and inertial confinement fusion (ICF).[5]

the UEG over a broad parameter range, which includes the physically most interesting regime of warm dense matter, cf. Fig. 1.

II. THEORY

A. Model Hamiltonian

The uniform electron gas, often referred to as "Jellium," is a model description of Coulomb interacting electrons with a neutralizing background of positive charges which are uncorrelated and homogeneously distributed. To describe an infinite system based on a finite number of particles, one implements periodic boundary conditions and includes the interaction of the N electrons in the main cell with all their images via Ewald summation. Following the notation from Ref. 47, we express the Hamiltonian of the N electron UEG (in atomic units) as

$$\hat{H} = -\frac{1}{2} \sum_{i=1}^{N} \nabla_i^2 + \frac{1}{2} \sum_{i=1}^{N} \sum_{j \neq i}^{N} e^2 \Psi(\mathbf{r}_i, \mathbf{r}_j) + \frac{Ne^2}{2} \xi,$$

with ξ being the Madelung constant and the periodic Ewald pair potential

$$\Psi(\mathbf{r}, \mathbf{s}) = \frac{1}{V} \sum_{\mathbf{G} \neq 0} \frac{e^{-\pi^2 \mathbf{G}^2/\kappa^2} e^{2\pi i \mathbf{G}(\mathbf{r}-\mathbf{s})}}{\pi \mathbf{G}^2}$$
$$- \frac{\pi}{\kappa^2 V} + \sum_{\mathbf{R}} \frac{\text{erfc}(\kappa|\mathbf{r} - \mathbf{s} + \mathbf{R}|)}{|\mathbf{r} - \mathbf{s} + \mathbf{R}|}. \quad (1)$$

Here, $\mathbf{R} = \mathbf{n}_1 L$ and $\mathbf{G} = \mathbf{n}_2/L$ denote the real and reciprocal space lattice vectors, respectively, with the box length L and volume $V = L^3$. The specific choice of the Ewald parameter κ does not influence the outcome of Eq. (1) and, therefore, can be used to optimize the convergence. PB-PIMC requires explicit knowledge of all forces in the system, and the force between the electrons i and j can be obtained from

$$\mathbf{F}_{ij} = -\nabla_i \Psi(\mathbf{r}_i, \mathbf{r}_j). \quad (2)$$

The evaluation of Eq. (2) is relatively straightforward and we find

$$\mathbf{F}_{ij} = \frac{2}{V} \sum_{\mathbf{G} \neq 0} \left(\frac{\mathbf{G}}{\mathbf{G}^2} \sin\left[2\pi \mathbf{G}(\mathbf{r}_i - \mathbf{r}_j)\right] e^{-\pi^2 \mathbf{G}^2/\kappa^2} \right)$$
$$+ \sum_{\mathbf{R}} \frac{\mathbf{r}_i - \mathbf{r}_j + \mathbf{R}}{\alpha^3} \left(\text{erfc}(\kappa\alpha) + \frac{2\kappa\alpha}{\sqrt{\pi}} e^{-\kappa^2\alpha^2} \right),$$

with the definition $\alpha = |\mathbf{r}_i - \mathbf{r}_j + \mathbf{R}|$.

B. Simulation method

To calculate canonical expectation values with the PB-PIMC approach,[39] we write the partition function in coordinate representation as

$$Z = \frac{1}{N!} \sum_{\sigma \in S_N} \text{sgn}(\sigma) \int d\mathbf{R} \, \langle \mathbf{R} | e^{-\beta \hat{H}} | \hat{\pi}_\sigma \mathbf{R} \rangle, \quad (3)$$

with $\mathbf{R} = \mathbf{r}_1, \ldots, \mathbf{r}_N$ containing the coordinates of all electrons, $\hat{\pi}_\sigma$ denoting the exchange operator which corresponds to a specific element σ from the permutation group S_N and
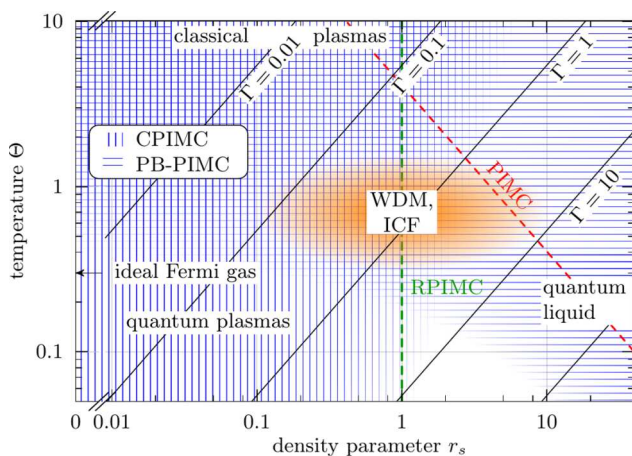
$\beta = 1/k_{\rm B}T$. For the next step, we make use of the usual group property of the density matrix in Eq. (3) and arrive at an expression for Z which requires the evaluation of P density matrices at P times higher temperature. However, instead of the primitive approximation $e^{-\epsilon \hat{H}} \approx e^{-\epsilon \hat{K}} e^{-\epsilon \hat{V}}$, with $\epsilon = \beta/P$ being the imaginary time step of a single propagator and the kinetic and potential contributions to the Hamiltonian $\hat{K}$ and $\hat{V}$, respectively, we use the fourth order factorization,[44,45]

$$e^{-\epsilon \hat{H}} \approx e^{-v_1 \hat{W}_{a_1}} e^{-t_1 \epsilon \hat{K}} e^{-v_2 \hat{W}_{1-2a_1}} e^{-t_1 \epsilon \hat{K}} e^{-v_1 \hat{W}_{a_1}} e^{-2t_0 \epsilon \hat{K}}. \quad (4)$$

The $\hat{W}$ operators in Eq. (4) denote a modified potential, which combines $\hat{V}$ with double commutator terms of the form

$$[[\hat{V}, \hat{K}], \hat{V}] = \frac{\hbar^2}{m} \sum_{i=1}^{N} |\mathbf{F}_i|^2 \quad (5)$$

and, therefore, requires the evaluation of all forces on each particle, $\mathbf{F}_i = -\nabla_i V(\mathbf{R})$. Our final result for the partition function is given by

$$Z = \frac{1}{(N!)^{3P}} \int d\mathbf{X} \prod_{\alpha=0}^{P-1} e^{-\epsilon \tilde{V}_\alpha} e^{-\epsilon^3 u_0 \frac{\hbar^2}{m} \tilde{F}_\alpha}$$
$$\times \det(\rho_\alpha) \det(\rho_{\alpha A}) \det(\rho_{\alpha B}), \quad (6)$$

with the definition of the potential and force terms

$$\tilde{V}_\alpha = v_1 V(\mathbf{R}_\alpha) + v_2 V(\mathbf{R}_{\alpha A}) + v_1 V(\mathbf{R}_{\alpha B}),$$
$$\tilde{F}_\alpha = \sum_{i=1}^{N} \left(a_1 |\mathbf{F}_{\alpha,i}|^2 + (1 - 2a_1) |\mathbf{F}_{\alpha A,i}|^2 + a_1 |\mathbf{F}_{\alpha B,i}|^2 \right), \quad (7)$$

and the diffusion matrices

$$\rho_\alpha(i,j) = \lambda_{t_1 \epsilon}^{-D} \sum_{\mathbf{n}} \exp\left(-\frac{\pi}{\lambda_{t_1 \epsilon}^2} (\mathbf{r}_{\alpha,j} - \mathbf{r}_{\alpha A,i} + \mathbf{n}L)^2 \right),$$

with D being the dimensionality, see, e.g., Ref. 40. Eq. (6) contains two free coefficients, t_0 and a_1, which can be used for optimization, cf. Fig. 2, and the integration is carried out over $3P$ sets of coordinates, $d\mathbf{X} = d\mathbf{R}_0 \ldots d\mathbf{R}_{P-1} d\mathbf{R}_{0A} \ldots d\mathbf{R}_{P-1A} d\mathbf{R}_{0B} \ldots d\mathbf{R}_{P-1B}$. Instead of explicitly sampling each permutation individually, as in standard PIMC, we combine configuration weights of both
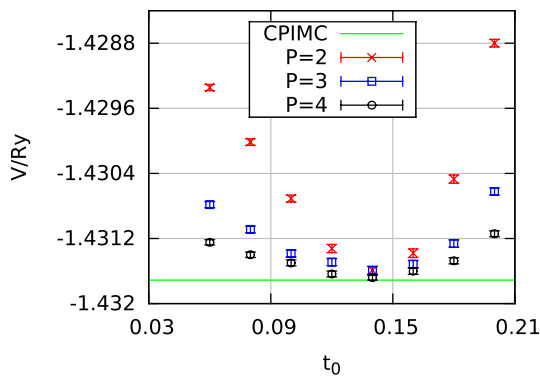

FIG. 2. Influence of the relative interslice spacing t_0 for $N = 4$, $r_s = 4$, and $\theta = 0.5$ on the convergence of the propagator. The exact result known from CPIMC (green line) is compared to the PB-PIMC results for $P = 2$, $P = 3$, and $P = 4$ for the fixed free parameter $a_1 = 0.33$ over the entire t_0 range. The optimal value is located around $t_0 = 0.14$.

positive and negative signs in the determinants, which leads to a cancellation of terms and, therefore, an effective blocking of permutations. When the thermal wavelength of a single time slice, $\lambda_{t_1 \epsilon} = \sqrt{2\pi \epsilon t_1 \hbar^2/m}$, is comparable to the mean interparticle distance, the effect of the blocking is most pronounced and the average sign in our simulations is significantly increased. However, with an increasing number of propagators P, $\lambda_{t_1 \epsilon}$ decreases and, eventually, the blocking will have no effect and the sign converges towards the sign from standard PIMC. Hence, it is crucial to employ the high order factorization from Eq. (4), which allows for reasonable accuracy even for only two or three propagators. We simulate the canonical probability distribution defined by Eq. (6) using the Metropolis algorithm.[48] For this purpose, we have introduced a set of efficient Monte Carlo updates that combine the worm algorithm idea[21,22] with the temporary construction of artificial trajectories, see Ref. 39 for a more detailed description.

C. Energy estimator

The consideration of periodicity in the diffusion matrices requires minor modifications in the energy estimator presented in Ref. 39, which can be derived from the partition function via the familiar relation

$$E = -\frac{1}{Z} \frac{\partial Z}{\partial \beta}. \quad (8)$$

Inserting the expression from Eq. (6) into (8) and performing a lengthy but straightforward calculation leads to

$$E = \frac{1}{P} \sum_{k=0}^{P-1} \left(\tilde{V}_k + 3\epsilon^2 u_0 \frac{\hbar^2}{m} \tilde{F}_k \right) + \frac{3DN}{2\epsilon}$$
$$- \sum_{k=0}^{P-1} \sum_{\kappa=1}^{N} \sum_{\xi=1}^{N} \left(\frac{\pi \eta_{\kappa\xi}^k}{\epsilon P \lambda_{t_1\epsilon}^2} + \frac{\pi \eta_{\kappa\xi}^{kA}}{\epsilon P \lambda_{t_1\epsilon}^2} + \frac{\pi \eta_{\kappa\xi}^{kB}}{\epsilon P \lambda_{2t_0\epsilon}^2} \right),$$

with the definition

$$\eta_{\kappa\xi}^k = \frac{(\rho_k^{-1})_{\kappa\xi}}{\lambda_{t_1\epsilon}^D} \sum_{\mathbf{n}} \exp\left[-\frac{\pi}{\lambda_{t_1\epsilon}^2} (\mathbf{r}_{k,\kappa} - \mathbf{r}_{kA,\xi} + L\mathbf{n})^2 \right]$$
$$\times (\mathbf{r}_{k,\kappa} - \mathbf{r}_{kA,\xi} + L\mathbf{n})^2. \quad (9)$$

For completeness, we note that the total energy E splits into the kinetic and potential contributions, K and V, in precisely the same way as before.[39]

III. RESULTS

A. Convergence

We begin the discussion of our simulation results by investigating the convergence of the energy with the number of imaginary time propagators P. To enhance the performance, the free parameters from the propagator, a_1 and t_0, can be optimized. In Fig. 2, we choose $a_1 = 0.33$, which corresponds to equally weighted forces on all time slices, and plot potential energy V, calculated with $P = 2$, $P = 3$, and $P = 4$, versus t_0 over the entire possible range for a benchmark system of $N = 4$ spin-polarized electrons with $\theta = 0.5$ and

$r_s = 4$. To assess the accuracy, we compare these results with the exact energy known from CPIMC (green line). Evidently, the optimal choice for this free parameter is located around $t_0 = 0.14$, which is consistent with previous findings by Sakkos *et al.*[45] and the application of PB-PIMC to electrons in a quantum dot.[39] For completeness, we mention that the kinetic energy K exhibits the same behavior. Hence, we use the combination $a_1 = 0.33$ and $t_0 = 0.14$ for all presented simulations in this work. However, it should be noted that our method converges for all possible choices of the free parameters. In Fig. 3, we demonstrate the convergence of the energy with respect to the number of propagators for the same system as in Fig. 2. However, since V and K nearly cancel for this particular combination of r_s, θ, and N, we investigate the convergence of both contributions separately. The top panel shows the potential energy versus the inverse number of propagators $P^{-1} \propto \epsilon$ and we compare the PB-PIMC results to the exact value (with the corresponding confidence interval) from CPIMC. We find that as few as two propagators allow for a relative accuracy $\Delta V/|V| \sim 10^{-4}$ and with $P = 4$ the potential energy is converged within error bars. In the bottom panel, we show the same information for the kinetic energy K. The variance of K is one order of magnitude larger than that of V and, for two propagators, we find the relative time step error $\Delta K/K \sim 10^{-3}$. With increasing P, the PB-PIMC results are fluctuating around the exact value, within error bars.

Finally, we address the r_s–dependence of the time step error by comparing PB-PIMC results for V with $P = 2$
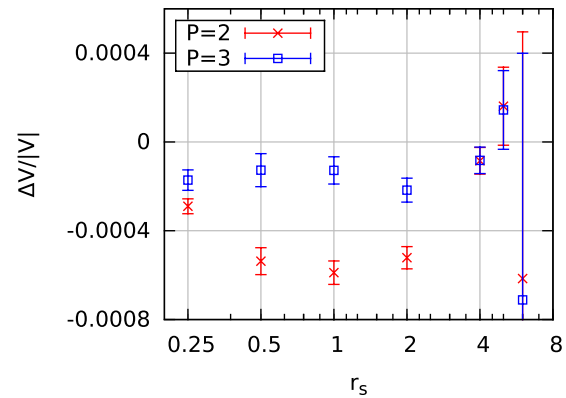
FIG. 4. Accuracy of two and three propagators over a broad r_s range for $N = 4$ and $\theta = 0.5$ with $t_0 = 0.14$ and $a_1 = 0.33$. We show the relative difference between the potential energy from PB-PIMC and CPIMC, $\Delta V/|V|$, for the optimal parameters from the fourth order propagator.

(red crosses) and $P = 3$ (blue squares) to the exact values from CPIMC. In Fig. 4, the relative error of the potential energy $\Delta V/|V|$ is plotted versus r_s for $N = 4$ spin-polarized electrons at $\theta = 0.5$. The increased errorbars for larger r_s are a manifestation of the sign problem from CPIMC,[32] while for the rest the statistical uncertainty from PB-PIMC predominates. The time step error is smaller for three propagators over the entire r_s–range, as it is expected, and adopts a maximum around $r_s = 1$. This can be understood by recalling the source of the systematic error in PB-PIMC. For $r_s \to 0$, the UEG approaches an ideal system and the commutator error from $\hat{K}$ and $\hat{V}$ vanishes. For $r_s \to \infty$, on the other hand, the particles are more separated and the system becomes more classical. Therefore, the neglected commutator terms are most important at intermediate r_s, which is the case for the results in Fig. 4.

We conclude that as few as two or three propagators provide sufficient accuracy to assess the discrepancy between CPIMC and RPIMC observed in previous studies.[33] In particular, the selected benchmark temperature, $\theta = 0.5$, is even lower than for all other simulations to be presented in this work. Hence, the observed time step error constitutes an upper bound for the accuracy of our results in the remainder of the paper.

B. Density parameter dependence

Among the most interesting questions regarding the implementation of PB-PIMC for the UEG is the range of applicability with respect to the density parameter r_s. To address this issue, we simulate $N = 33$ spin-polarized electrons, which corresponds to a closed momentum shell and is often used as a starting point for finite size corrections. In Fig. 5, we show the average sign S versus r_s for three different temperatures over a broad density range. All PB-PIMC data exhibit a qualitatively similar behavior, that is, a smooth decrease of S towards smaller r_s until it saturates. At large r_s, the coupling induced particle separation mostly exceeds the extension of the single particle wavefunctions and quantum exchange effects do not play a dominant role. With decreasing r_s, the UEG approaches an ideal system and the particles begin to overlap, which leads to sign changes in
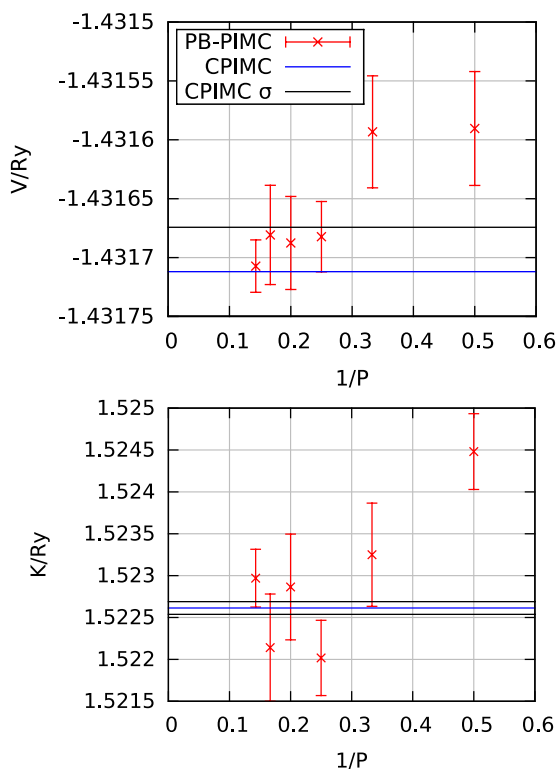

FIG. 3. Convergence of the potential (top) and kinetic (bottom) energy for $N = 4$, $r_s = 4$, and $\theta = 0.5$ with $t_0 = 0.14$ and $a_1 = 0.33$. In the top panel, the potential energy V is plotted versus the inverse number of propagators $P^{-1} \propto \epsilon$ and the PB-PIMC results are compared to the exact value known from CPIMC. The bottom panel shows the same information for the kinetic energy K.
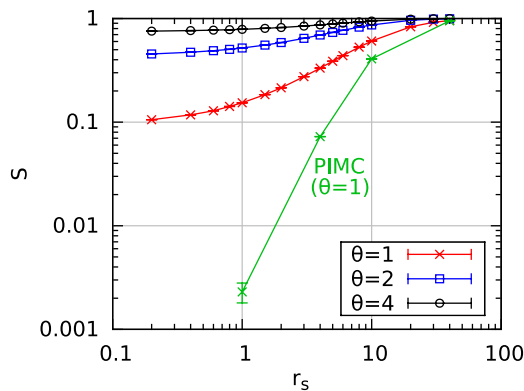
FIG. 5. The average sign of PB-PIMC is plotted versus the density parameter r_s for three different temperatures and $N = 33$ spin-polarized electrons with $P = 2$, $a_1 = 0.33$, and $t_0 = 0.14$. The standard PIMC data (green crosses) are taken from the supplement of Ref. 25.

the determinants. However, due to the blocking, the average sign, instead of dropping exponentially, remains finite which implies that, for the three depicted temperatures, PB-PIMC is applicable over the entire density range. This is in stark contrast to standard PIMC (cf. the green curve), which exhibits a significantly smaller average sign and, for $\theta = 1$, is not feasible for $r_s \lesssim 3$. Nevertheless, with decreasing temperature the sign of PB-PIMC drops and the FSP makes the simulations more involved, cf. Section III C.

In Fig. 6, we compare the corresponding energies with RPIMC[49] and CPIMC,[33] where they are available. The top row displays the relative difference in the potential energy towards PB-PIMC with two propagators. For $\theta = 4$ and $\theta = 2$, we find excellent agreement with CPIMC. For the lowest temperature, $\theta = 1$, the CPIMC values are systematically lower by $\Delta V/|V| \lesssim 10^{-3}$. However, this discrepancy can be
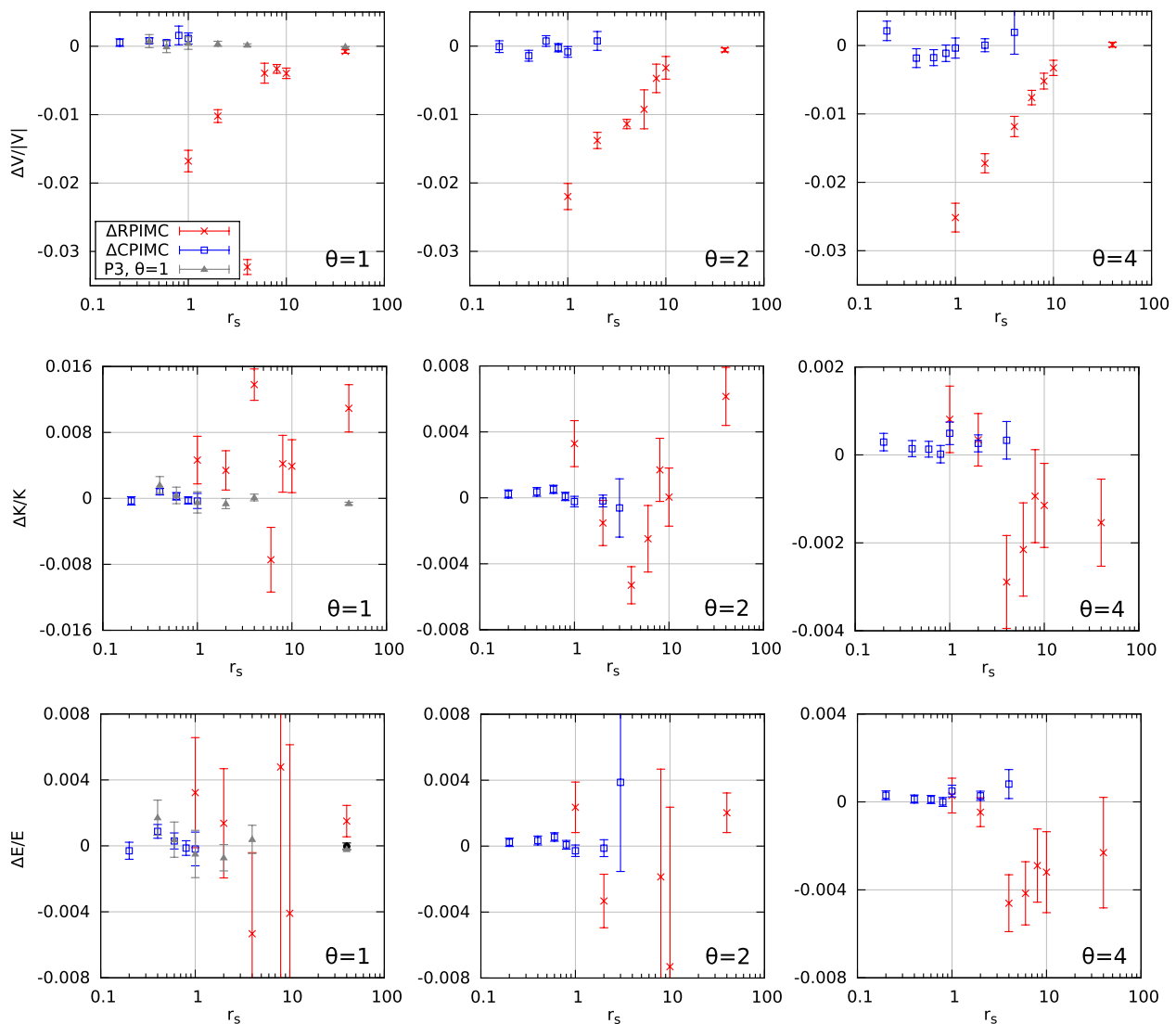
FIG. 6. Comparison of PB-PIMC with CPIMC and RPIMC for $N = 33$ spin-polarized electrons and three temperatures. In the top row, the relative deviation of the potential energy from PB-PIMC with $P = 2$, $t_0 = 0.14$ and $a_1 = 0.33$ is plotted versus r_s. The center and bottom rows display the same information for the kinetic and total energy, respectively. The black dot in the bottom left panel ($\Delta E/E$ for $\theta = 1$) corresponds to standard PIMC and is taken from the supplement of Ref. 25.

explained by the convergence behavior of the propagator, cf. Fig. 4, since the potential (and kinetic) energy is expected to converge from above towards the exact result. To confirm this assumption, we also plot results for $P = 3$ and $\theta = 1$, visualized by the grey triangles. Evidently, these points coincide with the CPIMC data everywhere within the errorbars and, thus, can be regarded as quasi-exact. The RPIMC data for V, on the other hand, exhibit a systematic discrepancy with respect to PB-PIMC and CPIMC.[33] At $r_s = 1$, the energies approximately differ by $\Delta V/|V| \sim 0.02$, but the difference decreases with increasing r_s. In the center row, we display the relative difference in the kinetic energy. Again, all PB-PIMC results are in good agreement with CPIMC. On the other hand, there is no clear systematic deviation between the PB-PIMC and RPIMC data, although most RPIMC-values for $\theta = 1$ are lower while the opposite holds for most values for $\theta = 4$. Finally, the bottom row displays the relative difference in the total energy. Interestingly, for $\theta = 1$ the difference of RPIMC in V and K towards PB-PIMC nearly cancels, so that E appears to be in good agreement. In particular, even the value for $\theta = 1$ and $r_s = 4$, where the potential energy is an outlier, and both V and K exhibit a maximum deviation, is almost within single error bars. For completeness, we have also included the total energy for $\theta = 1$ and $r_s = 40$ from standard PIMC,[49] cf. the black circle, which is in excellent agreement with PB-PIMC as well. For $\theta = 2$ and $\theta = 4$, most RPIMC values for E are higher than PB-PIMC, although the deviation hardly exceeds twice the error bars.

C. Temperature dependence

Finally, we investigate the performance of PB-PIMC with respect to the temperature. In Fig. 7, the average sign of PB-PIMC is plotted versus θ for $N = 33$ spin-polarized electrons at $r_s = 10$, $r_s = 1$, and $r_s = 0.1$. All three curves exhibit a similar behavior, that is, a large sign S at high temperature and a monotonous decay for $T \to 0$. However, for $r_s = 10$, the system is significantly less degenerate than for both other density parameters, and even at $\theta = 0.5$, the
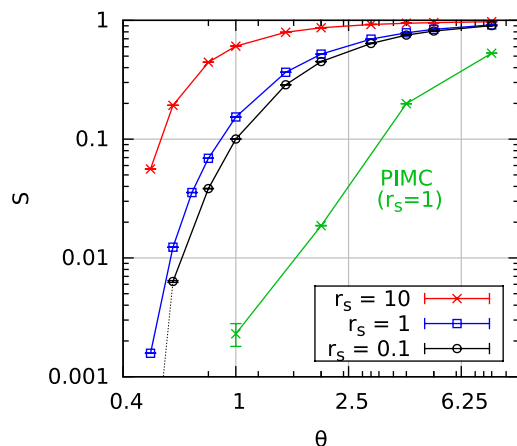
average sign of $S \approx 0.056$ indicates that the simulations are feasible. For $r_s = 1$ and $r_s = 0.1$, the decay of S is more rapid and, at low temperature, the simulations are more involved. In particular, half the Fermi temperature seems to constitute the current limit down to which reasonable results can be achieved for such r_s–values (and this particle number) and, for $r_s = 0.1$, the sign is zero within error bars, cf. the dashed line. For completeness, we also show the average sign of standard PIMC for $r_s = 1$, cf. the green curve. Evidently, these simulations are significantly more severely affected by the FSP and simulations are feasible only for $\theta \gtrsim 2$. Finally, we note that the average signs of PB-PIMC for the two smaller depicted r_s parameters are more similar to each other than to $r_s = 10$. We characterize the temperature in units of the ideal Fermi temperature, which is appropriate for weak coupling. However, for large r_s, the system becomes increasingly nonideal and, therefore, θ does not constitute an adequate measure for the degeneracy.

In Fig. 8, we compare the energies of the $N = 33$ electrons at $r_s = 1$ from PB-PIMC both to RPIMC[49] and CPIMC. The top panel displays the relative difference in the potential energy versus θ. The CPIMC results for V are in good agreement with PB-PIMC, while the RPIMC data are systematically higher, by about 2%. Interestingly, this behavior appears to be almost independent of the temperature. In the bottom panel, the same information is shown for the kinetic energy and, again, PB-PIMC agrees with CPIMC over the entire

FIG. 7. The average sign of PB-PIMC is plotted versus the temperature θ for $r_s = 10$, $r_s = 1$, and $r_s = 0.1$ and $N = 33$ spin-polarized electrons with $P = 2$ and the free parameters $t_0 = 0.14$ and $a_1 = 0.33$. The standard PIMC data (green crosses) are taken from the supplement of Ref. 25.

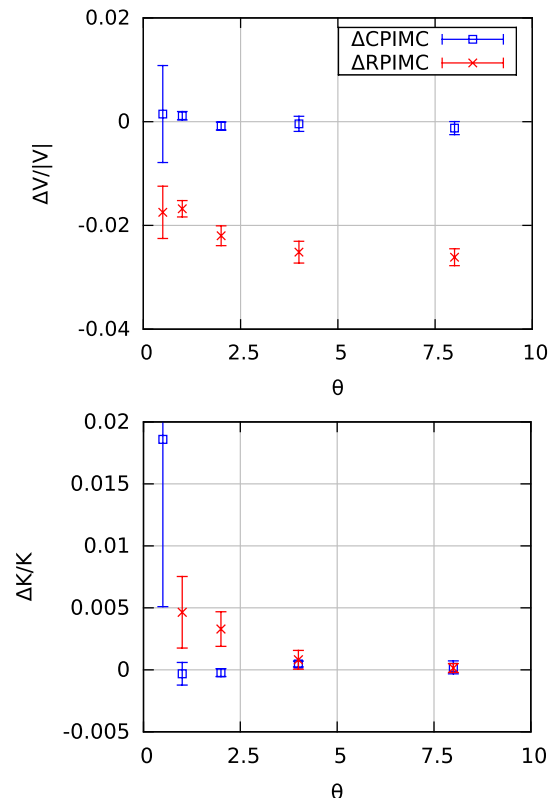FIG. 8. Comparison with CPIMC and RPIMC as a function of temperature. In the top panel, the relative deviation of the potential energy from the PB-PIMC result is plotted versus θ for $N = 33$ spin-polarized electrons and $r_s = 1$. The bottom panel displays the same information for the kinetic contribution.

temperature range. The large statistical uncertainty at $\theta = 0.5$ is a manifestation of the FSP in PB-PIMC, which prevents us from obtaining more precise kinetic energies with feasible computational effort. The RPIMC data for K are slightly lower, at low temperature, which confirms the trend observed by Schoof *et al.*,[33] and seems to converge towards the other methods for large θ.

IV. DISCUSSION

In summary, we have successfully extended the PB-PIMC approach[39] to the uniform electron gas at finite temperature. We have started the discussion with a brief introduction of our simulation scheme, which combines a fourth-order factorization of the density matrix with the application of antisymmetric imaginary time propagators, i.e., determinants. This allows us to combine permutations, which appear as individual configurations with positive and negative sign in standard PIMC, into a single configuration weight (hence the label permutation blocking). Furthermore, we employ an efficient set of Monte Carlo updates which is based on the temporary construction of artificial trajectories. Due to the combination of these three concepts, the average sign in our simulations is significantly increased.

To assert the quality of our numerical results, we have investigated the optimization of the free parameters of our propagator and demonstrated the convergence of both the potential and kinetic energies with respect to the number of imaginary time steps. We have found that even for the lowest considered temperature, $\theta = 0.5$, as few as two propagators allow for a relative accuracy of 0.1% and 0.01% in the kinetic and potential energies, respectively. After this preparatory work, we have shown results for $N = 33$ spin-polarized electrons, which is a commonly used model system as it is well suited to be a starting point for the extrapolation to the macroscopic limit (finite size corrections). In striking contrast to previous implementations of standard PIMC, PB-PIMC is feasible over the entire density range and, therefore, allows us to compare our results to both CPIMC and RPIMC data, where they are available. Our PB-PIMC data exhibit a very good agreement with CPIMC, for both the potential and kinetic energies, for all three investigated temperatures. On the other hand, we observe deviations between PB-PIMC and RPIMC of up to 3% in the potential energy, which decrease towards strong coupling. For the kinetic energy, we find no systematic trend although, for $\theta = 1$, most of the RPIMC-values are smaller while, for $\theta = 4$, most are larger than the PB-PIMC results. However, for both temperatures this deviation hardly exceeds twice the RPIMC errorbars.

Finally, we have investigated the applicability of PB-PIMC to the $N = 33$ spin-polarized electrons with respect to the temperature. With decreasing θ, exchange effects lead to more negative determinants in the configuration weights and, therefore, a smaller average sign. For the physically most interesting density regime, $r_s \sim 1$, simulations are feasible above $\theta = 0.5$ while for larger r_s even lower temperatures are possible. Therefore, it has once more been demonstrated that the range of applicability of standard PIMC has been significantly extended. A comparison of the energies for

$r_s = 1$ over the entire applicable temperature range has again revealed an excellent agreement with CPIMC. On the other hand, we observe a nearly θ-independent relative deviation between PB-PIMC and RPIMC in the potential energy of approximately 2%, whereas differences in the kinetic energy are observed only towards low temperature.

We conclude that our permutation blocking PIMC approach is capable to provide accurate results for the UEG over a broad parameter range. This approach is efficient above a minimum temperature of about $0.5T_F$ and, thus, complements CPIMC. Even though PB-PIMC carries a small systematic error (which is controllable and depends only on the number of time slices), we expect it to be useful for the development and test of other new techniques such as DMQMC[34,35] and other novel versions of fermionic PIMC, such as the approximate treatment of exchange cycles by DuBois *et al.*[50] or a variational approach to the RPIMC nodes, e.g., Ref. [51].

A natural follow-up of this work will be the extension of PB-PIMC to unpolarized systems which, in combination with CPIMC, should allow for a nearly complete description of the finite temperature UEG over the entire density range. In addition, we aim for the application or derivation of finite size corrections in order to extrapolate our results to the macroscopic limit[47,52,53] which could be followed by the construction of a new analytical fit formula for the UEG at finite temperature, e.g., Refs. [54] and [55]. Finally, since PB-PIMC allows for efficient simulations in the warm dense matter regime, applications to two-component plasmas, such as dense hydrogen,[56–58] are within reach.

[1]L. B. Fletcher *et al.*, "Observations of continuum depression in warm dense matter with x-ray Thomson scattering," Phys. Rev. Lett. **112**, 145004 (2014).

[2]D. Kraus *et al.*, "Probing the complex ion structure in liquid carbon at 100 GPa," Phys. Rev. Lett. **111**, 255501 (2013).

[3]S. P. Regan *et al.*, "Inelastic x-ray scattering from shocked liquid deuterium," Phys. Rev. Lett. **109**, 265003 (2012).

[4]J. D. Lindl *et al.*, "The physics basis for ignition using indirect-drive targets on the National Ignition Facility," Phys. Plasmas **11**, 339 (2004).

[5]S. X. Hu, B. Militzer, V. N. Goncharov, and S. Skupsky, "First-principles equation-of-state table of deuterium for inertial confinement fusion applications," Phys. Rev. B **84**, 224109 (2011).

[6]O. A. Hurricane *et al.*, "Fuel gain exceeding unity in an inertially confined fusion implosion," Nature **506**, 343-348 (2014).

[7]R. Nora *et al.*, "Gigabar spherical shock generation on the OMEGA laser," Phys. Rev. Lett. **114**, 045001 (2015).

[8]M. R. Gomez *et al.*, "Experimental demonstration of fusion-relevant conditions in magnetized liner inertial fusion," Phys. Rev. Lett. **113**, 155003 (2014).

[9]P. F. Schmit *et al.*, "Understanding fuel magnetization and mix using secondary nuclear reactions in magneto-inertial fusion," Phys. Rev. Lett. **113**, 155004 (2014).

[10] M. D. Knudson *et al.*, "Probing the interiors of the ice giants: Shock compression of water to 700 GPa and 3.8 **g**/cm³," Phys. Rev. Lett. **108**, 091102 (2012).

[11] B. Militzer *et al.*, "A massive core in Jupiter predicted from first-principles simulations," Astrophys. J. **688**, L45 (2008).

[12] N. Nettelmann, A. Becker, B. Holst, and R. Redmer, "Jupiter models with improved *ab initio* hydrogen equation of state (H-REOS.2)," Astrophys. J. **750**, 52 (2012).

[13] D. M. Ceperley and B. J. Alder, "Ground state of the electron gas by a stochastic method," Phys. Rev. Lett. **45**, 566 (1980).

[14] For completeness, we mention that improved ground state methods have been developed, the most accurate apparently being the full configuration interaction QMC method.[15–17]

[15] J. J. Shepherd, G. Booth, A. Grüneis, and A. Alavi, "Full configuration interaction perspective on the homogeneous electron gas," Phys. Rev. B **85**, 081103(R) (2012).

[16] J. J. Shepherd, G. H. Booth, and A. Alavi, "Investigation of the full configuration interaction quantum Monte Carlo method using homogeneous electron gas models," J. Chem. Phys. **136**, 244101 (2012).

[17] J. J. Shepherd, A. Grüneis, G. H. Booth, G. Kresse, and A. Alavi, "Convergence of many-body wave-function expansions using a plane-wave basis: From homogeneous electron gas to solid state systems," Phys. Rev. B **86**, 035111 (2012).

[18] D. M. Ceperley, "Path integrals in the theory of condensed helium," Rev. Mod. Phys. **67**, 279-355 (1995).

[19] B. Militzer and E. L. Pollock, "Equilibrium contact probabilities in dense plasmas," Phys. Rev. B **71**, 134303 (2005).

[20] B. K. Clark, M. Casula, and D. M. Ceperley, "Hexatic and mesoscopic phases in a 2D quantum Coulomb system," Phys. Rev. Lett. **103**, 055701 (2009).

[21] M. Boninsegni, N. Prokof'ev, and B. Svistunov, "Worm algorithm for continuous-space path integral Monte Carlo simulations," Phys. Rev. Lett. **96**, 070601 (2006).

[22] M. Boninsegni, N. V. Prokov'ev, and B. V. Svistunov, "Worm algorithm and diagrammatic Monte Carlo: A new approach to continuous-space path integral Monte Carlo simulations," Phys. Rev. E **74**, 036701 (2006).

[23] E. Y. Loh, J. E. Gubernatis, R. T. Scalettar, S. R. White, D. J. Scalapino, and R. L. Sugar, "Sign problem in the numerical simulation of many-electron systems," Phys. Rev. B **41**, 9301-9307 (1990).

[24] M. Troyer and U. J. Wiese, "Computational complexity and fundamental limitations to fermionic quantum Monte Carlo simulations," Phys. Rev. Lett. **94**, 170201 (2005).

[25] E. W. Brown, B. K. Clark, J. L. DuBois, and D. M. Ceperley, "Path-integral Monte Carlo simulation of the warm dense homogeneous electron gas," Phys. Rev. Lett. **110**, 146405 (2013).

[26] D. M. Ceperley, "Fermion nodes," J. Stat. Phys. **63**, 1237-1267 (1991).

[27] B. Militzer and E. L. Pollock, "Variational density matrix method for warm, condensed matter: Application to dense hydrogen," Phys. Rev. E **61**, 3470-3482 (2000).

[28] B. Militzer, Ph.D. dissertation, University of Illinois at Urbana-Champaign (2000).

[29] V. S. Filinov, "Cluster expansion for ideal Fermi systems in the 'fixed-node approximation,'" J. Phys. A: Math. Gen. **34**, 1665-1677 (2001).

[30] V. S. Filinov, "Analytical contradictions of the fixed-node density matrix," High Temp. **52**, 615-620 (2014).

[31] T. Schoof, M. Bonitz, A. V. Filinov, D. Hochstuhl, and J. W. Dufty, "Configuration path integral Monte Carlo," Contrib. Plasma Phys. **51**, 687-697 (2011).

[32] T. Schoof, S. Groth, and M. Bonitz, "Towards *ab initio* thermodynamics of the electron gas at strong degeneracy," Contrib. Plasma Phys. **55**, 136-143 (2015).

[33] T. Schoof, S. Groth, J. Vorberger, and M. Bonitz, "*Ab initio* thermodynamic results for the degenerate electron gas at finite temperature," Phys. Rev. Lett. **115**, 130402 (2015).

[34] N. S. Blunt, T. W. Rogers, J. S. Spencer, and W. M. Foulkes, "Density-matrix quantum Monte Carlo method," Phys. Rev. B **89**, 245124 (2014).

[35] F. D. Malone *et al.*, "Interaction picture density matrix quantum Monte Carlo," J. Chem. Phys. **143**, 044116 (2015).

[36] V. S. Filinov, V. E. Fortov, M. Bonitz, and Zh. Moldabekov, "Fermionic path integral Monte Carlo results for the uniform electron gas at finite temperature," Phys. Rev. E **91**, 033108 (2015).

[37] E. Yakub and C. Ronchi, "An efficient method for computation of long-ranged Coulomb forces in computer simulation of ionic fluids," J. Chem. Phys. **119**, 11556-11560 (2003).

[38] E. Yakub and C. Ronchi, "A new method for computation of long ranged Coulomb forces in computer simulation of disordered systems," J. Low Temp. Phys. **139**, 633-643 (2005).

[39] T. Dornheim, S. Groth, A. Filinov, and M. Bonitz, "Permutation blocking path integral Monte Carlo: A highly efficient approach to the simulation of strongly degenerate non-ideal fermions," New J. Phys. **17**, 073017 (2015).

[40] M. Takahashi and M. Imada, "Monte Carlo calculation of quantum systems," J. Phys. Soc. Jpn. **53**, 963-974 (1984).

[41] V. S. Filinov *et al.*, "Thermodynamic properties and plasma phase transition in dense hydrogen," Contrib. Plasma Phys. **44**, 388-394 (2004).

[42] A. P. Lyubartsev, "Simulation of excited states and the sign problem in the path integral Monte Carlo method," J. Phys. A: Math. Gen. **38**, 6659-6674 (2005).

[43] M. Takahashi and M. Imada, "Monte Carlo of quantum systems. II. Higher order correction," J. Phys. Soc. Jpn. **53**, 3765-3769 (1984).

[44] S. A. Chin and C. R. Chen, "Gradient symplectic algorithms for solving the Schrödinger equation with time-dependent potentials," J. Chem. Phys. **117**, 1409 (2002).

[45] K. Sakkos, J. Casulleras, and J. Boronat, "High order Chin actions in path integral Monte Carlo," J. Chem. Phys. **130**, 204109 (2009).

[46] S. A. Chin, "High-order path integral Monte Carlo methods for solving quantum dot problems," Phys. Rev. E **91**, 031301(R) (2015).

[47] L. M. Fraser *et al.*, "Finite-size effects and Coulomb interactions in quantum Monte Carlo calculations for homogeneous systems with periodic boundary conditions," Phys. Rev. B **53**, 1814 (1996).

[48] N. Metropolis, A. W. Rosenbluth, M. N. Rosenbluth, A. H. Teller, and E. Teller, "Equation of state calculations by fast computing machines," J. Chem. Phys. **21**, 1087 (1953).

[49] We take the energy values from the supplement of Ref. 25 and substract the finite size corrections. This allows for a meaningful comparison with the same model system of $N = 33$ spin-polarized electrons.

[50] J. L. DuBois, B. J. Alder, and E. W. Brown, "Overcoming the fermion sign problem in homogeneous systems," e-print arXiv:1409.3262 (2014).

[51] E. W. Brown, Ph.D. dissertation, University of Illinois at Urbana-Champaign (2014).

[52] N. D. Drummond, R. J. Needs, A. Sorouri, and W. M. C. Foulkes, "Finite-size errors in continuum quantum Monte Carlo calculations," Phys. Rev. B **78**, 125106 (2008).

[53] C. Lin, F. H. Zong, and D. M. Ceperley, "Twist-averaged boundary conditions in continuum quantum Monte Carlo algorithms," Phys. Rev. E **64**, 016702 (2001).

[54] E. W. Brown, J. L. DuBois, M. Holzmann, and D. M. Ceperley, "Exchange-correlation energy for the three-dimensional homogeneous electron gas at arbitrary temperature," Phys. Rev. B **88**, 081102(R) (2013).

[55] V. V. Karasiev, T. Sjostrom, J. Dufty, and S. B. Trickey, "Accurate homogeneous electron gas exchange-correlation free energy for local spin-density calculations," Phys. Rev. Lett. **112**, 076403 (2014).

[56] M. Bonitz, V. S. Filinov, V. E. Fortov, P. R. Levashov, and H. Fehske, "Crystallization in two-component Coulomb systems," Phys. Rev. Lett. **95**, 235006 (2005).

[57] M. A. Morales, C. Pierleoni, and D. Ceperley, "Equation of state of metallic hydrogen from coupled electron-ion Monte Carlo simulations," Phys. Rev. E **81**, 021202 (2010).

[58] V. S. Filinov, M. Bonitz, H. Fehske, V. E. Fortov, and P. R. Levashov, "Proton crystallization in a dense hydrogen plasma," Contrib. Plasma Phys. **52**, 224-228 (2012).

Chapter 4

Combination of PB-PIMC and CPIMC

4.1 The Spin-polarized Case

The successful application of the PB-PIMC approach to the uniform electron gas shown in the previous section 3.3 demonstrated (i) the complementary nature to CPIMC, (ii) the utility of CPIMC to provide exact benchmark data at high density, and (iii) that the combination of both methods allows for a highly accurate description of the UEG over the entire density range down to half the Fermi temperature *without the fixed-node approximation*. Indeed, the final point constitutes a reoccurring theme throughout the rest of this thesis and was explored in detail in the next paper[1], Ref. [162], for the case of $N = 33$ spin-polarized electrons.

First of all, I carried out extensive PB-PIMC simulations and obtained new data for the total, kinetic, and interaction energy for four additional temperatures ($\theta = 0.5, 0.75, 6$ and 8). The combined data from PB-PIMC and CPIMC was made available in a data table, for example, as a benchmark for future method development. Secondly, the comparison of the exchange–correlation energy between PB-PIMC, CPIMC, and the RPIMC data from Ref. [157] (Fig. 7 in the following paper, Ref. [162]) again revealed the excellent agreement between the first two methods everywhere and the significant systematic bias of the latter even at intermediate to high temperatures.

A further achievement of this paper is the systematic investigation of the so-called *kink extrapolation* procedure that extends the CPIMC method to larger r_s values (approximately by a factor of two), to which, however, I did not contribute.

---

[1]S. Groth, T. Schoof, T. Dornheim, and M. Bonitz, Phys. Rev. B **93**, 085102 (2016). Copyright by the American Physical Society (2016).

Ab initio quantum Monte Carlo simulations of the uniform electron gas without fixed nodes

S. Groth, T. Schoof, T. Dornheim, and M. Bonitz

Institut für Theoretische Physik und Astrophysik, Christian-Albrechts-Universität zu Kiel, D-24098 Kiel, Germany

(Received 12 November 2015; revised manuscript received 14 January 2016; published 1 February 2016)

The uniform electron gas (UEG) at finite temperature is of key relevance for many applications in the warm dense matter regime, e.g., dense plasmas and laser excited solids. Also, the quality of density functional theory calculations crucially relies on the availability of accurate data for the exchange-correlation energy. Recently, results for $N = 33$ spin-polarized electrons at high density, $r_s = \bar{r}/a_B \lesssim 4$, and low temperature have been obtained with the configuration path integral Monte Carlo (CPIMC) method [T. Schoof *et al.*, Phys. Rev. Lett. **115**, 130402 (2015)]. To achieve these results, the original CPIMC algorithm [T. Schoof *et al.*, Contrib. Plasma Phys. **51**, 687 (2011)] had to be further optimized to cope with the fermion sign problem (FSP). It is the purpose of this paper to give detailed information on the manifestation of the FSP in CPIMC simulations of the UEG and to demonstrate how it can be turned into a controllable convergence problem. In addition, we present new thermodynamic results for higher temperatures. Finally, to overcome the limitations of CPIMC towards strong coupling, we invoke an independent method—the recently developed permutation blocking path integral Monte Carlo approach [T. Dornheim *et al.*, J. Chem. Phys. **143**, 204101 (2015)]. The combination of both approaches is able to yield *ab initio* data for the UEG over the entire density range, above a temperature of about one half of the Fermi temperature. Comparison with restricted path integral Monte Carlo data [E. W. Brown *et al.*, Phys. Rev. Lett. **110**, 146405 (2013)] allows us to quantify the systematic error arising from the free particle nodes.

DOI: 10.1103/PhysRevB.93.085102

I. INTRODUCTION

The uniform electron gas (UEG) constitutes a well-known simple model for metals [1]. At finite temperature, the spin-polarized UEG is described by the density parameter $r_s = \bar{r}/a_B$ [$\bar{r}$ is the mean interparticle distance related to the density by $n^{-1} = 4\pi\bar{r}^3/3$, and a_B is the Bohr radius] and the dimensionless temperature (degeneracy parameter) $\Theta = k_B T/E_F$, with the Fermi energy E_F. Besides being an interesting theoretical model system for studying correlated fermionic many-body systems, exact data for the exchange-correlation energy of the UEG is essential for the construction of exchange correlation functionals [2,3] for density functional theory (DFT) calculations of more realistic systems, e.g. atoms, molecules, and novel materials. For the ground state this data has been provided many years ago by Ceperley and Alder [4] utilizing the fixed node diffusion Monte Carlo approach. Based on these calculations, Perdew and Zunger computed the density functionals [5], which have been the basis for countless DFT applications.

Often one is interested in properties of chemical systems or condensed matter at low temperature, not exceeding room temperature, for which it is justified to use ground state results. However, in recent years more and more applications have emerged where the electrons are highly excited, e.g., by compression of the material or by electromagnetic radiation. Examples are dense plasmas in compact stars or planet cores, e.g., [6–8], and laser fusion experiments at the National Ignition Facility, e.g. [9–11], at Rochester [12], or Sandia [13,14]. It is now widely agreed upon that the theoretical description of these experiments requires to go beyond ground state DFT. This leads to a high demand for exact data for the UEG at finite temperature and high to moderate density where fermionic exchange and correlation effects play an important role simultaneously, namely the warm dense matter (WDM) regime, where both r_s and Θ are of order one.

Quantum Monte Carlo (QMC) simulations are the method of choice for the computation of exact thermodynamic quantities at finite temperature. However, it is well known that, when applied to fermions, path integral Monte Carlo (PIMC) methods suffer the fermion sign problem (FSP), which may render the simulation even of small fermionic systems impossible and was shown to be NP hard [15]. In the standard PIMC formulation in coordinate space, e.g. [16], the FSP causes an exponential loss of accuracy with increasing degeneracy, i.e., towards low temperature and high density of the system. For this reason, standard fermionic PIMC calculations of the commonly used $N = 33$ spin-polarized UEG are not feasible in the warm dense matter regime [17]. Presently, the search for accurate and efficient strategies to weaken the FSP is one of the most important questions in condensed matter and dense plasma theory.

A popular approach to avoid the FSP is the restricted (fixed-node) PIMC (RPIMC) method [18], which is claimed to be exact if the true nodal surface of the density matrix would be known. Usually this is not the case, and one has to rely on approximations, thereby introducing an uncontrolled systematic error. Brown *et al.* [17] performed RPIMC calculations with ideal nodes of the UEG in a broad density-temperature range down to $r_s = 1$ and $\Theta = 0.0625$. These results have been used by many groups, e.g., for the construction of analytical fits for the exchange-correlation free energy [2,3] and as benchmarks for models and simulations [19,20].

In a recent paper [21], we applied the configuration path integral Monte Carlo (CPIMC) approach to the uniform electron gas and were able to obtain *ab initio* simulation results for finite temperatures and high degeneracy. These results also showed that the RPIMC data of Ref. [17] are inaccurate for high densities, $r_s \lesssim 4$. As any fermionic PIMC approach, CPIMC as well suffers from the FSP. But, being formulated in Fock space of Slater determinants [22,23], CPIMC experiences an increasing FSP with decreasing quantum degeneracy,
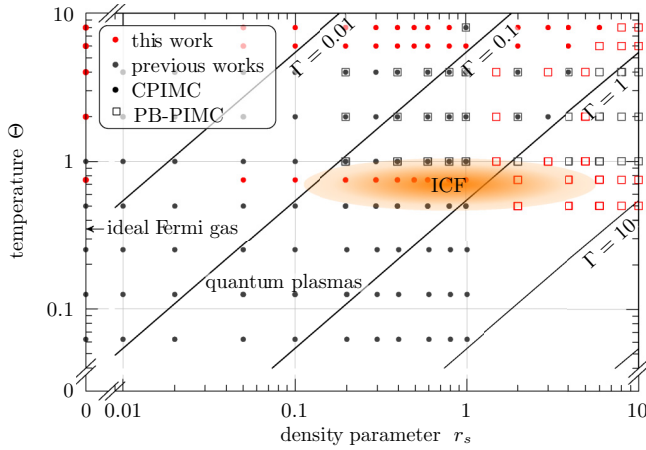
FIG. 1. Available *ab initio* quantum Monte Carlo data in the warm dense matter range for $N = 33$ spin-polarized electrons. Dots: CPIMC. Squares: PB-PIMC. Red: Additional combined CPIMC and PB-PIMC results of this paper. Gray: Previous results from CPIMC [21] and PB-PIMC [25], respectively. ICF: Typical inertial confinement fusion parameters [10]. Quantum (classical) behavior dominates below (above) the line $\Theta = 1$. $\Gamma = e^2/\bar{r}k_B T$ is the classical coupling parameter.

i.e., towards low density. In the case of the UEG with $N = 33$ particles, direct CPIMC simulations were possible only for $r_s \lesssim 0.4$. Nevertheless, in Ref. [21] an extension to substantially larger r_s was achieved by introducing an auxiliary kink potential which leads to a complication of the original CPIMC algorithm.

For this reason, the present paper aims at giving a comprehensive explanation of the modified CPIMC approach, in particular of the details of the kink potential and the issues of convergence and accuracy. In order to give a systematic analysis of these concepts and their capabilities, we concentrate on the simplest situation—the polarized UEG. Also, we restrict ourselves to finite particle numbers, deferring the issues of finite size effects and extrapolation to the thermodynamics limit to a future publication. Here, we explore in detail how the algorithm performs with varying particle number and what range of densities and temperatures is accessible. This allows us to extend the range of *ab initio* CPIMC data presented in Ref. [21] to temperatures as high as $\Theta = 8$ and to larger r_s values, where the maximum accessible value is found to be on the order of $r_s^{\max} \sim \Theta$. However, we demonstrate that it is possible to access the entire r_s range without fixed nodes. To this end, we invoke another *ab initio* approach—the recently developed permutation blocking PIMC method (PB-PIMC) [24,25] which has a complementary FSP, restricting the simulations from the side of low temperatures. For $N = 33$ spin-polarized particles, the combination of CPIMC and PB-PIMC allows us to present exact results for $\Theta \geqslant 0.5$, for all densities, without fixed nodes, see Fig. 1.

The paper is organized as follows. After introducing the model Hamiltonian of the UEG in Sec. II A, we start with a brief but self-contained derivation of the CPIMC expansion of the partition function in Sec. II B and, in Sec. II C, explain the interpretation of the latter as being a sum over closed paths in Fock space, in imaginary time. In Sec. III A, we proceed

with addressing the FSP in direct CPIMC simulations, where we find an abrupt drop of the average sign at a certain critical value of r_s depending on particle number and temperature. Then, in Sec. III B, we demonstrate how the applicable region of the CPIMC method can be extended to significantly lower densities by the use of an auxiliary kink potential and an appropriate extrapolation scheme. In Sec. IV, the main ideas of PB-PIMC and its differences compared to standard PIMC are explained. Finally, in Sec. V, we combine the two complementary methods, CPIMC and PB-PIMC, to obtain results for $N = 33$ spin-polarized particles over the whole density range for several degeneracy parameters reaching from $\theta = 0.5$ to $\theta = 8$.

II. THEORY

A. The Jellium Hamiltonian

In second quantization with respect to plane waves, $\langle \mathbf{r} | \mathbf{k} \rangle = \frac{1}{L^{3/2}} e^{i\mathbf{k} \cdot \mathbf{r}}$ with $\mathbf{k} = \frac{2\pi}{L} \mathbf{m}$, $\mathbf{m} \in \mathbf{Z}^3$, the Hamiltonian of the finite simulation-cell 3D uniform electron gas consisting of N electrons on a uniform neutralizing background in a periodic box of length L takes the familiar form (Rydberg units)

$$\hat{H} = \sum_i \mathbf{k}_i^2 \hat{a}_i^\dagger \hat{a}_i + 2 \sum_{\substack{i<j,k<l \\ i \neq k, j \neq l}} w_{ijkl}^- \hat{a}_i^\dagger \hat{a}_j^\dagger \hat{a}_l \hat{a}_k + E_M, \quad (1)$$

with the antisymmetrized two-electron integrals, $w_{ijkl}^- = w_{ijkl} - w_{ijlk}$, where

$$w_{ijkl} = \frac{4\pi e^2}{L^3(\mathbf{k}_i - \mathbf{k}_k)^2} \delta_{\mathbf{k}_i + \mathbf{k}_j, \mathbf{k}_k + \mathbf{k}_l}, \quad (2)$$

and the delta function ensuring momentum conservation. The first (second) term in the Hamiltonian Eq. (1) describes the kinetic (interaction) energy. The Madelung energy E_M accounts for the self-interaction of the Ewald summation in periodic boundary conditions [26], for which we found $E_M \approx -2.837297 \cdot (3/4\pi)^{\frac{1}{3}} N^{\frac{2}{3}} r_s^{-1}$. The operator $\hat{a}_i^\dagger$ ($\hat{a}_i$) creates (annihilates) a particle in the orbital $|\mathbf{k}_i\rangle$. The diverging contributions in the interaction term, i.e., for $\mathbf{k}_i = \mathbf{k}_k$ and $\mathbf{k}_j = \mathbf{k}_l$, cancel with the contributions due to the positive background. Note that choosing the plane wave basis, which is the ideal, natural, and Hartree-Fock basis at the same time, has the major advantage of having two-electron integrals that can be computed analytically according to Eq. (2). In an arbitrary basis one generally has to compute the two-electron integrals prior to the simulation and store them in computer memory, limiting the number of basis functions that can be taken into account. Yet, it is well-known that plane waves badly describe the Coulomb interaction, making a large number of basis functions necessary to obtain converged results.

B. CPIMC expansion of the partition function

In equilibrium many-body quantum statistics the central quantity is the partition function, which is given by the trace over the density operator

$$Z = \text{Tr} \, \hat{\rho} , \quad (3)$$

where, in the canonical ensemble,

$$\hat{\rho} = e^{-\beta \hat{H}}, \tag{4}$$

with the inverse temperature $\beta = [k_B T]^{-1}$. In standard PIMC, the trace in Eq. (3) is evaluated in coordinate space expressing the density operator in terms of a product of M density operators at M-times higher temperature, which is justified by the Trotter formula. To correctly take into account Fermi statistics, one then has to antisymmetrize the density operator thereby introducing a sign change in the weight function for odd particle permutations. This is the source of the FSP in standard PIMC. In CPIMC instead we perform the trace in Eq. (3) directly with antisymmetrized N-particle states (Slater determinants)

$$|\{n\}\rangle = |n_1, n_2, \dots \rangle, \tag{5}$$

which form a complete basis of the Fock space. Here, the n_i denote the fermionic occupation numbers ($n_i = 0, 1$) of the orbitals $|\mathbf{k}_i\rangle$.

To bring the partition function into a form suitable for a Monte Carlo algorithm, one can split the Hamiltonian into a diagonal and off-diagonal part, i.e., $\hat{H} = \hat{D} + \hat{Y}$, which is always possible for any arbitrary basis. In the interaction picture in imaginary time with respect to the diagonal operator $\hat{D}$, i.e.,

$$\hat{Y}(\tau) = e^{\tau \hat{D}} \hat{Y} e^{-\tau \hat{D}}, \quad \tau \in (0, \beta), \tag{6}$$

the density operator can be written in terms of a perturbation expansion in orders of $\hat{Y}$

$$
\begin{aligned}
e^{-\beta \hat{H}} &= e^{-\beta \hat{D}} \hat{T}_\tau e^{-\int_0^\beta \hat{Y}(\tau) \mathrm{d}\tau} \\
&= e^{-\beta \hat{D}} \sum_{K=0}^{\infty} \int_0^\beta d\tau_1 \int_{\tau_1}^\beta d\tau_2 \dots \int_{\tau_{K-1}}^\beta d\tau_K \\
&\quad \times (-1)^K \hat{Y}(\tau_K) \hat{Y}(\tau_{K-1}) \cdot \dots \cdot \hat{Y}(\tau_1),
\end{aligned} \tag{7}
$$

where $\hat{T}_\tau$ denotes the time-ordering operator. Inserting Eq. (7) into Eq. (3), evaluating the trace and rearranging terms, yields the following expansion of the partition function

$$
\begin{aligned}
Z = \sum_{\substack{K=0, \\ K \neq 1}}^{\infty} \sum_{\{n\}} \sum_{s_1 \dots s_{K-1}} \int_0^\beta d\tau_1 \int_{\tau_1}^\beta d\tau_2 \dots \int_{\tau_{K-1}}^\beta d\tau_K \\
\times (-1)^K e^{-\sum_{i=0}^K D_{\{n^{(i)}\}} (\tau_{i+1} - \tau_i)} \prod_{i=1}^K Y_{\{n^{(i)}\}, \{n^{(i-1)}\}}(s_i),
\end{aligned} \tag{8}
$$

where s_i denotes a multi-index defining the orbitals in which the two sets of occupation numbers $\{n^{(i)}\}$ and $\{n^{(i-1)}\}$ differ. Due to the trace in Eq. (3) it has to be $\{n\} = \{n^{(0)}\} = \{n^{(K)}\}$. According to the Slater-Condon rules the Fock space matrix elements of the UEG Hamiltonian do not vanish only if the states differ in no (diagonal part) or exactly four occupation numbers (off-diagonal part) so that

$$D_{\{n^{(i)}\}} = \sum_l \mathbf{k}_l^2 n_l^{(i)} + \sum_{l < k} w_{lklk}^- n_l^{(i)} n_k^{(i)}, \tag{9}$$

$$Y_{\{n^{(i)}\}, \{n^{(i-1)}\}}(s_i) = w_{s_i}^- (-1)^{\alpha_{s_i}} \tag{10}$$

with $s_i = (pqrs)$ defining the four occupation numbers in which $\{n^{(i)}\}$ and $\{n^{(i-1)}\}$ differ, where it is $p < q$ and $r < s$.

In this notation, the exponent of the fermionic phase factor is given by

$$\alpha_{s_i} = \alpha_{pqrs}^{(i)} = \sum_{l=p}^{q-1} n_l^{(i-1)} + \sum_{l=r}^{s-1} n_l^{(i)}.$$

Monte Carlo estimators of observables are readily computed as derivatives of the partition function Eq. (8), e.g., for the internal energy one obtains

$$\langle \hat{H} \rangle = -\frac{\partial}{\partial \beta} \ln Z \tag{11}$$

$$
\begin{aligned}
= \sum_{\substack{K=0, \\ K \neq 1}}^{\infty} \sum_{\{n\}} \sum_{s_1 \dots s_{K-1}} \int_0^\beta d\tau_1 \int_{\tau_1}^\beta d\tau_2 \dots \int_{\tau_{K-1}}^\beta d\tau_K \\
\times \left(\frac{1}{\beta} \sum_{i=0}^K D_{\{n^{(i)}\}} (\tau_{i+1} - \tau_i) - \frac{K}{\beta} \right) W.
\end{aligned} \tag{12}
$$

We point out that the expansion (8) is exact and system independent. Monte Carlo methods using this expansion belong to the so-called continuous time QMC methods (in the interaction picture) since there is no imaginary time discretization left. This concept has been developed by Prokofev *et al.* [27,28] and extensively applied to lattice models, e.g., [27–30]. We have presented an alternative derivation of Eq. (8) by starting from the Trotter formula and developed an algorithm for continuous systems [23] requiring more involved Monte Carlo steps compared to lattice models.

C. Closed path in Fock space

A contribution to the partition function Eq. (8) can be interpreted as a $\beta-$ periodic path in Fock space, in imaginary time, that is uniquely defined by the initial determinant $\{n\} = \{n^{(0)}\}$ at $\beta = 0$ and the K two-particle excitations of type $s_i = (pqrs)$ at times τ_i, where two particles are excited from the orbitals r and s to p and q. An example of such a path is illustrated in Fig. 2. Due to their visual appearance, the excitations are called "kinks." The weight of each path is determined by the weight function which, according to Eqs. (8)
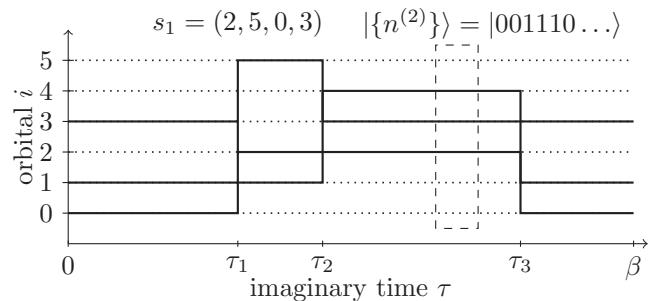
FIG. 2. Typical closed path in Slater determinant (Fock) space. The state with three occupied orbitals $|\vec{k}_0\rangle, |\vec{k}_1\rangle, |\vec{k}_3\rangle$ undergoes a two-particle excitation s_1 at time τ_1 replacing the occupied orbitals $|\vec{k}_0\rangle, |\vec{k}_3\rangle$ by $|\vec{k}_2\rangle, |\vec{k}_5\rangle$. Two further excitations occur at τ_2 and τ_3. The states at the "imaginary times" $\tau = 0$ and $\tau = \beta$ coincide. All possible paths contribute to the partition function Z, Eq. (8). (Figure from Ref. [21].)

and (10), reads

$$W(K,\{n\},s_1,\ldots,s_{K-1},\tau_1,\ldots,\tau_K)$$

$$= (-1)^K e^{-\sum_{i=0}^K D_{\{n^{(i)}\}}(\tau_{i+1}-\tau_i)} \prod_{i=1}^K w_{s_i}^- (-1)^{\alpha_{s_i}}. \quad (13)$$

The set of occupation numbers of a determinant between kinks contributes to the exponential function with its corresponding diagonal matrix element, cf. Eq. (9), weighted with the length of the time interval on which the determinant is realized in the path. On the other hand, each kink enters the product over all kinks in the path with its corresponding antisymmetrized two-electron integral and phase factor of the involved orbitals. Since the two-electron integrals can be both positive and negative, there are altogether three sources of sign changes in the weight function.

III. SIGN PROBLEM OF CPIMC

A. Sign problem of the direct CPIMC method

Since the weight function W takes both positive and negative values, it is not a probability density. Therefore, the Metropolis algorithm can only be used to generate a Markov chain of paths distributed according to the modulus of the weight. This is achieved with an ergodic set of six Monte Carlo steps in which single or paired kinks are added or changed. A detailed description of these steps can be found in Ref. [22]. By generating a Markov chain of paths according to the modulus of the weight, we actually simulate a system described by

$$Z' = \sum_{\substack{K=0, \\ K\neq 1}}^{\infty} \sum_{\{n\}} \sum_{s_1\ldots s_{K-1}} \int_0^\beta d\tau_1 \int_{\tau_1}^\beta d\tau_2 \ldots \int_{\tau_{K-1}}^\beta d\tau_K$$

$$\times |W(K,\{n\},s_1,\ldots,s_{K-1},\tau_1,\ldots,\tau_K)| \quad (14)$$

rather than the true physical system described by the partition function Eq. (8). Physical expectation values of observables are then obtained via

$$\langle O \rangle = \frac{\langle Os \rangle'}{\langle s \rangle'}, \quad (15)$$

where O is the Monte Carlo estimator, e.g., for the internal energy the term in brackets in Eq. (12), $\langle \cdot \rangle'$ denotes the expectation value with respect to the modified partition function, Eq. (14), and $s = \text{sign}(W)$ measures the sign of each path. For the expectation value of s, which is called the *average sign*, it holds

$$\langle s \rangle' = \frac{Z}{Z'} = e^{-\beta N(f-f')} \quad (16)$$

with f being the free energy per particle. It is straightforward to show that the relative statistical error of quantities computed with Monte Carlo methods via Eq. (15) is inversely proportional to the average sign. Therefore, it grows exponentially with particle number and inverse temperature, while it can only be reduced by the square root of the number of Monte Carlo samples. Depending on the available computational resources acceptable statistical errors can be obtained for average signs larger than about 10^{-4}. This is the FSP.

Figure 3(a) shows the dependency of the average sign in CPIMC simulations of the UEG on the density parameter
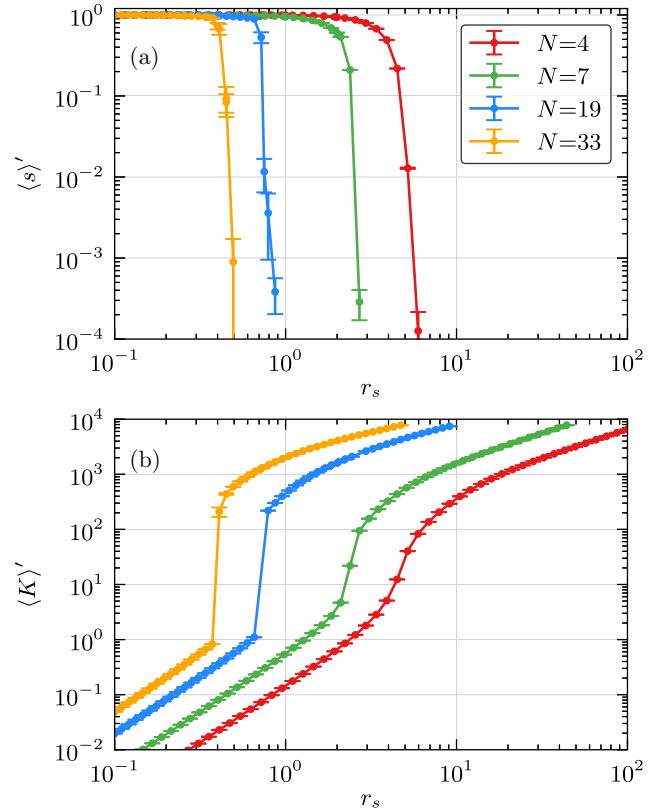
FIG. 3. Average sign (a) and average number of kinks (b) of direct CPIMC, plotted versus the density parameter for different particle numbers in $N_B = 2109$ basis functions at $\theta = 0.125$.

at a fixed degeneracy parameter $\theta = 0.125$ for different particle numbers. The number of basis functions is fixed to $N_B = 2109$, which is sufficient to obtain converged results (within reasonable statistical errors) for all data points. We generally observe a rather sharp drop of the average sign from almost 1 to about 10^{-3}. This effect clearly increases and shifts towards smaller r_s with particle number. Consequently, for $N = 33$ particles at this temperature we obtain negligible small statistical errors for $r_s \lesssim 0.4$, whereas for slightly larger values of r_s direct simulations are not feasible. To investigate this behavior in more detail, in Fig. 3(b) we plot the average number of kinks in the simulations for the same parameters. This quantity is closely connected to the average sign since each additional kink in the paths comes with three potential sources of sign changes, cf. Sec. II C. In CPIMC simulations with on average more than 30 kinks we find that, depending on the temperature, the average sign is too small to obtain results with reasonable statistical errors.

In the high density regime, the average number of kinks grows linearly with r_s, see Fig. 3(b), then at some critical value of r_s it starts growing exponentially. The slope of this exponential growth increases with particle number so that for $N = 33$ it appears to be rather a jump from below 1 to about 200 kinks at $r_s \sim 0.4$ explaining the sudden drop of the average sign in Fig. 3(a). Interestingly, for further reduced density, the average number of kinks grows again linearly with r_s. We have carefully checked that this is not an effect of the finite
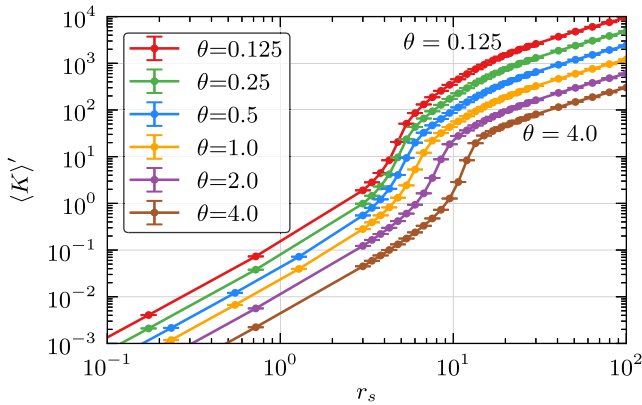
FIG. 4. Average number of kinks of direct CPIMC, plotted versus the density parameter for $N = 4$ particles in $N_B = 5575$ basis functions at different temperatures.

number of basis functions. However, in this regime, even for $N = 4$ particles the average number of kinks is larger than 1000 resulting in a practically vanishing average sign. For $N = 4$ particles, Fig. 4 shows the average number of kinks in dependence on r_s for different degeneracy parameters. In the linear regimes (both at very large and small values of r_s), the average number of kinks depends also linearly on the degeneracy parameter while the onset of the exponential growth shifts towards smaller r_s, for increasing degeneracy, i.e., for decreasing θ. Further, at lower temperatures, the transition from the exponential to the linear r_s dependency is smoother, cf. red and brown curve in Fig. 4. Summarizing, the direct CPIMC method suffers an abrupt drop of the average sign in particular for larger systems and lower temperature caused by a strong increase of the average number of kinks in the simulated paths.

B. Extending CPIMC towards lower density

In this section, the use of the auxiliary kink potentials is explained, and its influence on the CPIMC method is investigated in detail. These kink potentials have been introduced in Ref. [21] to obtain the results for $r_s > 0.4$.

The average number of kinks in the simulation is only connected to the number of kinks K necessary for the partition function of the primed system to be converged, cf. Eq. (14). However, to obtain correct physical observables via Eq. (15) it is sufficient to include only those paths in the simulation that actually contribute to the physical partition function Eq. (8), which, due to cancellations of contributions with opposite sign, may converge for a much smaller value of K than the primed partition function. In other words, if this cancellation applies, then we can restrict the simulation paths to a certain number of kinks and thereby strongly reduce the sign problem while still obtaining exact results for the observables. In addition, since both Eqs. (8) and (14) are exact perturbation series in orders of the number of kinks K, it is reasonable to investigate the convergence of this series with respect to K. For this purpose, we have introduced an auxiliary Fermi-like kink potential

$$V_{\delta,\kappa}(K) = \frac{1}{e^{-\delta(\kappa - K + 0.5)} + 1}, \tag{17}$$
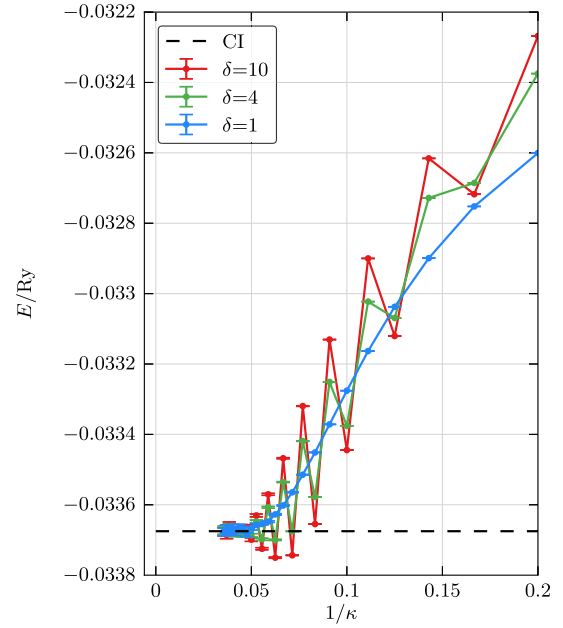
FIG. 5. Convergence of the internal energy with respect to the kink potential parameter κ, using different parameters δ. The system consists of $N = 4$ particles in $N_B = 19$ basis functions at $\theta = 0.5$ and $r_s = 40$ for which the energy can be computed with an exact configuration interaction (CI) method (dashed black line). Each point is the result of a whole CPIMC simulation, where integer numbers from 5 to 28 have been used for κ.

which becomes a step function at $K = \kappa + 0.5$ in the limit $\delta \to \infty$. We add this potential as an auxiliary factor in the primed partition function so that it acts as a penalty, depending on the values of δ and κ, for paths with a large number of kinks. Hence, the simulated partition function is now parametrized by δ and κ reading

$$Z'(\delta,\kappa) = \sum_{\substack{K=0,\\K\neq1}}^{\infty} \sum_{\{n\}} \sum_{s_1\ldots s_{K-1}} \int_0^\beta d\tau_1 \int_{\tau_1}^\beta d\tau_2 \ldots \int_{\tau_{K-1}}^\beta d\tau_K$$

$$\times V_{\delta,\kappa}(K) |W(K,\{n\},s_1,\ldots,s_{K-1},\tau_1,\ldots,\tau_K)|. \tag{18}$$

Obviously, for any non-negative value of δ, we recover the original primed partition function in the limit $\kappa \to \infty$

$$Z' = \lim_{\kappa \to \infty} Z'(\delta,\kappa), \quad \forall \, \delta \geqslant 0. \tag{19}$$

Therefore, performing CPIMC simulations for different values of κ at fixed δ converges to the exact result in the limit $1/\kappa \to 0$.

This is demonstrated in Fig. 5, where the convergence of the internal energy is shown for three different values of δ. The system size has been chosen to be very small, i.e., $N = 4$ particles in $N_B = 19$ basis functions at $\theta = 0.5$ and $r_s = 40$, so that the energy can be computed with an exact diagonalization method (dashed black line). For the parameter κ integer values have been used from $\kappa = 5$ to 28. At $\delta = 10$ (red points), the kink potential practically resembles a step function restricting paths in the simulation to a maximum of $K_{\max} = \kappa$ kinks. Interestingly, in this case the energy converges not
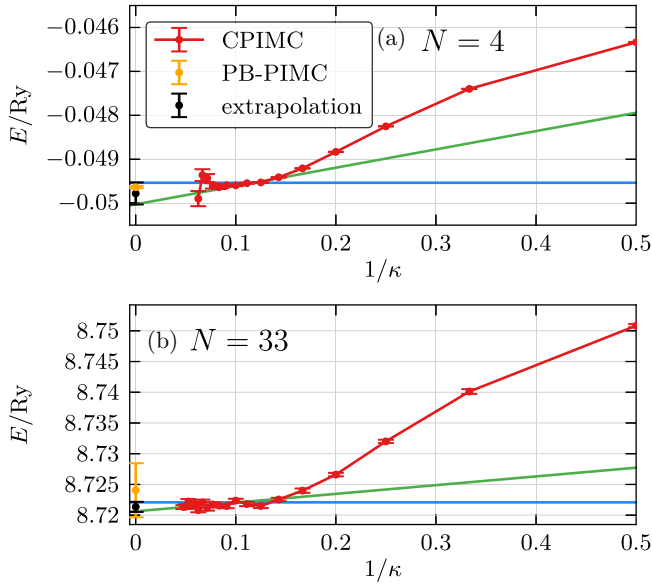
FIG. 6. Convergence of the internal energy with respect to the kink potential parameter κ and extrapolation to $1/\kappa \to 0$, corresponding to $K \to \infty$, at $\theta = 1.0$. (a) $N = 4$ particles and $r_s = 10.0$ in $N_B = 5575$ basis functions. (b) $N = 33$ and $r_s = 1.0$ in $N_B = 4169$ basis functions. The asymptotic values (black points) are enclosed between the blue and green lines and, within error bars, coincide with the PB-PIMC result (orange points).

monotonically towards the exact result but oscillates with even and odd numbers of κ. Strictly speaking, for only odd numbers of κ the energy does converge monotonically while for even numbers it first drops below the exact value before eventually converging. This behavior may be explained by the factor $(-1)^K$ in the weight function, c.f. Eq. (13), dominating the other two sign changing sources of the phase factor and the two-electron integrals. Nevertheless, these oscillations render a reliable extrapolation to the exact limit $1/\kappa \to 0$ difficult and hence, simply restricting the number of kinks is not a good choice. For smaller values of δ (green points in Fig. 5) where we, to a larger extent, allow paths with a larger number of kinks than κ, the oscillations are significantly reduced. At $\delta = 1$ (blue points), the oscillations finally vanish completely and the energy converges monotonically towards the exact result. In fact, we always observe an s-shaped convergence behavior with $1/\kappa$ for Fermi potentials with $\delta \lesssim 1$. This allows for a very robust extrapolation scheme to the exact result in the limit $1/\kappa \to \infty$ after the onset of convergence that is clearly indicated by the change in curvature (at $\kappa \sim 17$ in Fig. 5).

In Fig. 6(a), we demonstrate this extrapolation scheme for a more difficult system of $N = 4$ particles in $N_B = 5575$ basis functions at $\theta = 1$ and $r_s = 10$, for which the direct CPIMC method without the kink potential is not applicable due to on average more than 50 kinks, cf. orange curve in Fig. 4, and a resulting vanishing sign. To obtain an upper bound of the exact energy, we perform a horizontal fit (blue line) to those points after the onset of the convergence, while for the lower bound a linear fit is performed to those points (green line). The concrete fitting procedure is explained in Appendix. For comparison the result for the energy of the likewise exact PB-PIMC method

(cf. Sec. IV) is shown (orange point), which is well enclosed by the horizontal and linear fit and hence perfectly confirms our approach. Note that for the $N = 4$ particles in only $N_B = 19$ basis functions in Fig. 5 the energy is entirely converged for $\kappa = 20$ so that all points for $\kappa > 20$ lie on the horizontal line of the CI energy. This is because here the direct CPIMC algorithm converges to an average number of 20 kinks. In contrast, in Fig. 6(a), after the change in curvature at approximately $\kappa = 8$, the energy is not entirely converged and still slowly decreasing. In this regime a near cancellation of all contributions for increasing κ occurs. However, in the limit $\kappa \to \infty$ the energy does not converge linearly towards the exact value, because the direct CPIMC algorithm always converges at a finite value of $\langle K \rangle'$, cf. Fig. 3(b) and Fig. 4. Therefore, from some value of κ onwards, depending on the average number of kinks in the direct CPIMC algorithm, the points will be on a horizontal line getting no further contributions for increasing κ. For this reason, the linear fit (green line) is indeed a true lower bound of the exact energy for the used number of basis function. Our extrapolation scheme also works well for larger systems, which is illustrated in Fig. 6(b) for the example of $N = 33$ particles at $\theta = 1$ and $r_s = 1$ in $N_B = 4169$ basis functions. Here, the extrapolated value (black point) also agrees with the PB-PIMC result (orange point), which has a larger statistical error than in Fig. 6(a), due to the larger density. For a convergence plot for the same system at a lower temperature of $\theta = 0.0625$, where no other results are available, we refer to Ref. [21].

In general, the use of the kink potential combined with the extrapolation scheme actually more than doubles the accessible density parameter within the CPIMC approach at fixed other system parameters. Nevertheless, our procedure is still limited by the FSP, which is indicated by the increasing error bars of the last points in Fig. 6(a). For example, at $\kappa = 10$ there are on average $\langle K \rangle' \sim 9.4$ kinks with a corresponding average sign $\langle s \rangle' \sim 0.05$, while at $\kappa = 16$ (last point) there are $\langle K \rangle' \sim 15.3$ kinks with a corresponding average sign $\langle s \rangle' \sim 5 \times 10^{-3}$ causing a large statistical error. Of course, if the sign problem becomes too severe before the onset of convergence (indicated by the change in curvature), our procedure is not applicable.

IV. BASIC IDEA OF PB-PIMC

In contrast to CPIMC, our permutation blocking PIMC approach is essentially standard PIMC in coordinate space but combines two well-known concepts: (1) antisymmetric imaginary time propagators, i.e., determinants [31–33], and (2) a fourth-order factorization of the density matrix [34–36]. In addition, to sample this more complicated configuration space, one of us has developed an efficient set of Monte Carlo updates based on the temporary construction of artificial trajectories. Since PB-PIMC and its application to the UEG have been introduced in detail in Refs. [24] and [25], here we shall restrict ourselves to a brief overview.

We start from the coordinate representation of the canonical partition function (3) describing a system of N spin-polarized fermions at inverse temperature β

$$Z = \frac{1}{N!} \sum_{\sigma \in S_N} \text{sgn}(\sigma) \int d\mathbf{R} \; \langle \mathbf{R} | e^{-\beta \hat{H}} | \hat{\pi}_\sigma \mathbf{R} \rangle, \qquad (20)$$

with $\hat{\pi}_\sigma$ being the exchange operator that corresponds to a particular element σ from the permutation group S_N with associated sign sgn(σ). However, since the low-temperature matrix elements of $\hat{\rho}$ are not known, we use the group property $\hat{\rho}(\beta) = \prod_{\alpha=0}^{P-1} \hat{\rho}(\epsilon)$, with $\epsilon = \beta/P$, and approximate each of the P factors at a P times higher temperature by the fourth-order factorization [35,36]

$$e^{-\epsilon\hat{H}} \approx e^{-v_1\epsilon\hat{W}_{a_1}} e^{-t_1\epsilon\hat{K}} e^{-v_2\epsilon\hat{W}_{1-2a_1}}$$
$$\times e^{-t_1\epsilon\hat{K}} e^{-v_1\epsilon\hat{W}_{a_1}} e^{-2t_0\epsilon\hat{K}}, \qquad (21)$$

which allows for sufficient accuracy, for small P. The $\hat{W}$ operators in Eq. (21) denote a modified potential that combines the usual potential energy $\hat{V}$ with double commutator terms of the form

$$[[\hat{V},\hat{K}],\hat{V}] = \frac{\hbar^2}{m}\sum_{i=1}^{N}|\mathbf{F}_i|^2, \quad \mathbf{F}_i = -\nabla_i V(\mathbf{R}), \qquad (22)$$

where $\hat{K}$ denotes the operator of the kinetic energy. Therefore, PB-PIMC requires the additional evaluation of all forces, and the final result for the partition function is given by

$$Z = \frac{1}{(N!)^{3P}} \int d\mathbf{X} \prod_{\alpha=0}^{P-1} \left(e^{-\epsilon\tilde{V}_\alpha} e^{-\epsilon^3 u_0 \frac{\hbar^2}{m}\tilde{F}_\alpha} \right. \qquad (23)$$

$$\left. \det(\rho_\alpha)\det(\rho_{\alpha A})\det(\rho_{\alpha B}) \right). \qquad (24)$$

Here, $\tilde{V}_\alpha$ and $\tilde{F}_\alpha$ contain all contributions of the potential energy and the forces, respectively, and the diffusion matrix is given by

$$\rho_\alpha(i,j) = \lambda_{t_1\epsilon}^{-D} \exp\left(-\frac{\pi}{\lambda_{t_1\epsilon}^2}(\mathbf{r}_{\alpha,j} - \mathbf{r}_{\alpha A,i})^2\right), \qquad (25)$$

with $\lambda_{t_1\epsilon} = \sqrt{2\pi\epsilon t_1\hbar^2/m}$ being the thermal wavelength of a single "time slice."

Instead of explicitly sampling each permutation cycle, as in standard PIMC, we combine both positively and negatively signed configuration weights in the determinants, which leads to a cancellation of terms and, therefore, a significantly increased average sign in our simulations. However, this "permutation blocking" is only effective when $\lambda_{t_1\epsilon}$ is comparable to the mean interparticle distance. With increasing P, $\lambda_{t_1\epsilon}$ decreases and the average sign eventually converges towards that of standard PIMC. Hence, it is crucial to combine the determinants with the fourth order factorization from Eq. (21), which allows for sufficient accuracy with as few as two or three propagators and thereby maximizes the benefit of the blocking by the determinants.

V. CPIMC AND PB-PIMC BENCHMARK RESULTS FOR THE POLARIZED UEG

Due to the complementary character of the FSP the CPIMC and PB-PIMC approaches are well suited to be combined and, thereby, to circumvent the sign problem. Concerning the $N = 33$ spin-polarized UEG, CPIMC is applicable practically over the entire temperature range from $\theta = 0.01$ to 10 and suffers an increasing sign problem for increasing r_s. The critical region at which the FSP becomes severe is around $r_s \sim 1$ for $\theta \lesssim 0.5$
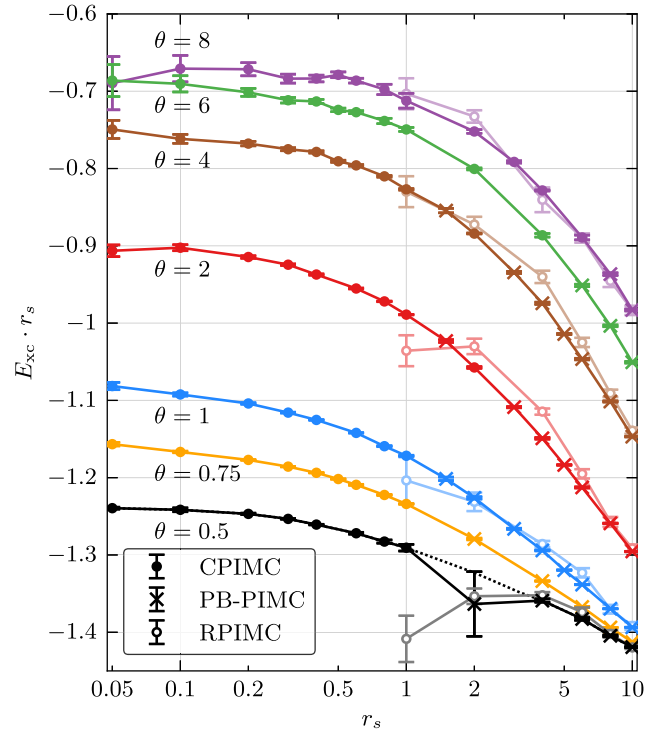
FIG. 7. Exchange-correlation energy E_{xc} times r_s of the $N = 33$ particle spin-polarized UEG over the density parameter r_s for different degeneracy parameters θ. Results have been obtained by combining the CPIMC (dots) and PB-PIMC (crosses) approach taking the most accurate values of each method (connected by the solid line). In addition, RPIMC results from Ref. [17] are plotted for comparison (open circles).

and $r_s \sim \theta$ for $\theta \gtrsim 1$. On the other hand, the PB-PIMC method suffers a weak increase of the FSP for decreasing r_s, yet it is in principle capable of providing results over the entire density range for degeneracy parameters $\theta \gtrsim 0.75$. At temperatures $\theta < 0.5$, PB-PIMC is not feasible at high density.

For the construction of density functionals the exchange-correlation energy E_{xc} (per particle) of the UEG is of particular importance, which is obtained by subtracting the ideal energy U_0 from the total internal energy

$$E_{xc} = E - U_0. \qquad (26)$$

In Fig. 7, we show our results for the exchange-correlation energy. Note that we plot $E_{xc} \cdot r_s$ which converges towards the finite Hartree-Fock energy in the limit $r_s \to 0$. We always took the most accurate value of CPIMC (solid dots) or PB-PIMC (crosses), in cases where both are available. These data complement our earlier results that are included here as well, to have a complete set (for CPIMC, data for four isotherms $\theta = 0.5, 1, 2, 4$ have been reported in Ref. [21], while for PB-PIMC, the internal energy for the three isotherms $\theta = 1, 2, 4$ has been presented in Ref. [25], where the application of the method to the UEG is explained in detail). At $\theta = 0.5$, CPIMC can provide data up to $r_s = 1$, while PB-PIMC suffers a too strong FSP below $r_s = 2$ leaving a gap between both approaches. We have fitted a spline of order 4 to the available points and are thereby able to accurately close the gap (dotted

TABLE I. Energies per particle for $N = 33$ polarized electrons: ideal energy U_0, kinetic energy E_{kin}, potential energy E_{pot}, and exchange-correlation energy E_{xc}. An a marks CPIMC results that have been obtained by an extrapolation as explained in Appendix. For these values, the error given in parenthesis includes systematic effects. All other errors correspond to a 1σ standard deviation. A b marks results from PB-PIMC calculations. For CPIMC results, the number of basis functions N_B is given in the last column. Energies in units of Ryd.

θ	r_s	U_0	E_{kin}	E_{pot}	E_{xc}	N_B
0.50	0.05	2380.191(6)	2376.036(25)	−20.63427(16)	−24.789(26)	2109
	0.10	595.0477(16)	593.041(25)	−10.40869(32)	−12.416(25)	4169
	0.20	148.7619(4)	147.818(5)	−5.29077(12)	−6.234(5)	4169
	0.30	66.11641(18)	65.5186(17)	−3.57994(9)	−4.1777(17)	4169
	0.40	37.19048(10)	36.7599(10)	−2.72121(13)	−3.1518(11)	4169
	0.60	16.52910(5)	16.2673(14)^a	−1.8577(8)^a	−2.1198(21)^a	2109
	0.80	9.297620(25)	9.1196(30)^a	−1.424(4)^a	−1.6034(26)^a	2109
	1.00	5.950477(16)	5.823(6)^a	−1.162(6)^a	−1.291(4)^a	2109
	2.00	1.487619(4)	1.426(22)^b	−0.6202(23)^b	−0.682(21)^b	
					−0.661^c	
	4.00	0.3719050(10)	0.3618(6)^b	−0.32970(8)^b	−0.3398(5)^b	
	6.00	0.1652910(5)	0.16355(30)^b	−0.22873(6)^b	−0.23047(29)^b	
	8.00	0.09297600(25)	0.09356(14)^b	−0.176150(30)^b	−0.17557(13)^b	
	10.00	0.05950500(16)	0.06130(8)^b	−0.143718(17)^b	−0.14192(7)^b	
0.75	0.05	3147.466(12)	3143.18(4)	−18.84333(19)	−23.13(5)	4169
	0.10	786.8665(31)	784.718(10)	−9.51839(8)	−11.667(11)	4169
	0.20	196.7166(8)	195.6818(24)	−4.85031(4)	−5.8851(26)	4169
	0.30	87.42961(35)	86.7672(12)	−3.289850(30)	−3.9523(12)	4169
	0.40	49.17916(19)	48.7016(4)	−2.506603(22)	−2.9842(5)	4169
	0.50	31.47466(12)	31.10585(31)	−2.034685(20)	−2.40349(34)	4169
	0.60	21.85740(9)	21.5612(7)^a	−1.71865(16)^a	−2.0154(11)^a	4169
	0.80	12.29479(5)	12.0878(5)^a	−1.32039(10)^a	−1.5280(8)^a	4169
	1.00	7.868665(31)	7.7140(5)^a	−1.0793(6)^a	−1.2340(5)^a	4169
	2.00	1.967166(8)	1.9097(6)^b	−0.58218(7)^b	−0.6397(6)^b	
	4.00	0.4917920(19)	0.47535(10)^b	−0.316986(20)^b	−0.33343(10)^b	
	6.00	0.2185740(9)	0.21257(13)^b	−0.221880(28)^b	−0.22788(13)^b	
	8.00	0.1229480(5)	0.120659(29)^b	−0.171940(11)^b	−0.174229(29)^b	
	10.00	0.07868700(31)	0.078268(32)^b	−0.140854(9)^b	−0.141272(31)^b	
1.00	0.05	3957.262(19)	3953.20(9)	−17.56511(21)	−21.63(9)	4169
	0.10	989.316(5)	987.269(20)	−8.87662(10)	−10.923(21)	4169
	0.20	247.3289(12)	246.337(5)	−4.52798(5)	−5.520(5)	4169
	0.30	109.9239(5)	109.2790(18)	−3.07450(4)	−3.7194(19)	4169
	0.40	61.83222(30)	61.3643(11)	−2.345237(22)	−2.8132(11)	4169
	0.60	27.48099(13)	27.1891(4)	−1.611535(18)	−1.9034(4)	4169
	0.80	15.45805(8)	15.2540(7)	−1.2450(15)	−1.4491(8)	4169
	1.00	9.89316(5)	9.7381(10)^a	−1.01625(29)^a	−1.1717(7)^a	4169
	1.50	4.396958(21)	4.3066(15)^b	−0.71068(17)^b	−0.8010(15)^b	
	2.00	2.473289(12)	2.4136(8)^b	−0.55337(12)^b	−0.6131(8)^b	
	3.00	1.099239(5)	1.06770(26)^b	−0.39052(5)^b	−0.42206(26)^b	
	4.00	0.6183220(30)	0.59980(14)^b	−0.305012(33)^b	−0.32353(15)^b	
	5.00	0.3957260(19)	0.38361(7)^b	−0.251795(19)^b	−0.26392(8)^b	
	6.00	0.2748100(13)	0.26690(5)^b	−0.215138(13)^b	−0.22305(5)^b	
	8.00	0.1545810(8)	0.150966(20)^b	−0.167579(7)^b	−0.171193(22)^b	
	10.00	0.0989320(5)	0.097380(13)^b	−0.137806(5)^b	−0.139358(13)^b	
2.00	0.05	7335.15(4)	7331.95(15)	−14.93186(20)	−18.13(15)	5575
	0.10	1833.788(11)	1832.30(4)	−7.54095(11)	−9.02(4)	5575
	0.20	458.4470(26)	457.718(8)	−3.84305(5)	−4.572(8)	5575
	0.30	203.7542(12)	203.2810(32)	−2.60821(4)	−3.0815(34)	5575
	0.40	114.6118(7)	114.2583(20)	−1.989454(30)	−2.3429(21)	5575
	0.60	50.93856(29)	50.7147(9)	−1.368155(19)	−1.5920(10)	5575
	0.80	28.65294(16)	28.4931(5)	−1.055120(15)	−1.2149(5)	5575
	1.00	18.33788(11)	18.21454(30)	−0.865709(17)	−0.98905(31)	5575
	1.50	8.15017(5)	8.0775(12)^b	−0.60945(21)^b	−0.6821(12)^b	
	2.00	4.584470(26)	4.5339(4)^a	−0.4780(5)^a	−0.5287(6)^a	5575
	3.00	2.037542(12)	2.00917(27)^b	−0.34120(8)^b	−0.36958(28)^b	

TABLE I. (*Continued*).

θ	r_s	U_0	E_{kin}	E_{pot}	E_{xc}	N_B
	4.00	1.146118(7)	1.12840(27)[b]	−0.26956(9)[b]	−0.28727(28)[b]	
	5.00	0.733515(4)	0.72143(9)[b]	−0.224617(35)[b]	−0.23670(10)[b]	
	6.00	0.5093860(29)	0.50075(11)[b]	−0.19347(5)[b]	−0.20210(13)[b]	
	8.00	0.2865290(16)	0.28185(4)[b]	−0.152706(18)[b]	−0.15739(4)[b]	
	10.00	0.1833790(11)	0.180676(18)[b]	−0.126841(10)[b]	−0.129543(21)[b]	
4.00	0.05	14258.10(14)	14256.29(19)	−13.17459(10)	−14.99(23)	24405
	0.10	3564.525(35)	3563.55(5)	−6.63750(5)	−7.62(6)	24405
	0.20	891.131(9)	890.660(12)	−3.367889(23)	−3.839(14)	24405
	0.30	396.058(4)	395.752(5)	−2.277115(17)	−2.583(7)	24405
	0.40	222.7828(22)	222.5676(30)	−1.731134(13)	−1.946(4)	24405
	0.50	142.5810(14)	142.4029(24)	−1.403167(13)	−1.5812(27)	24405
	0.60	99.0146(10)	98.8721(13)	−1.184072(9)	−1.3265(16)	24405
	0.80	55.6957(5)	55.5925(13)	−0.909464(11)	−1.0126(14)	24405
	1.00	35.64525(35)	35.5622(10)	−0.743926(12)	−0.8269(10)	24405
	1.50	15.84233(15)	15.7935(18)[b]	−0.5208(4)[b]	−0.5696(19)[b]	
	2.00	8.91131(9)	8.87718(18)	−0.407967(8)	−0.44210(20)	24405
	3.00	3.96058(4)	3.9409(4)[b]	−0.29176(17)[b]	−0.3115(5)[b]	
	4.00	2.227828(22)	2.21563(34)[b]	−0.23140(14)[b]	−0.2436(4)[b]	
	5.00	1.425810(14)	1.41669(16)[b]	−0.19370(8)[b]	−0.20282(18)[b]	
	6.00	0.990146(10)	0.98344(14)[b]	−0.16772(8)[b]	−0.17442(17)[b]	
	8.00	0.556957(5)	0.55306(9)[b]	−0.13378(5)[b]	−0.13767(10)[b]	
	10.00	0.3564530(35)	0.35389(4)[b]	−0.112127(25)[b]	−0.11469(4)[b]	
6.00	0.05	21232.56(31)	21231.34(28)	−12.50240(7)	−13.7(4)	38911
	0.10	5308.14(8)	5307.53(7)	−6.28885(4)	−6.90(11)	38911
	0.20	1327.035(19)	1326.709(17)	−3.181308(18)	−3.507(26)	38911
	0.30	589.793(9)	589.566(8)	−2.145065(12)	−2.372(12)	38911
	0.40	331.759(5)	331.602(5)	−1.626612(9)	−1.783(7)	38911
	0.50	212.3256(31)	212.1926(34)	−1.315274(9)	−1.448(5)	38911
	0.60	147.4484(21)	147.3440(24)	−1.107473(8)	−1.2118(32)	38911
	0.80	82.9397(12)	82.864(4)	−0.847318(17)	−0.923(4)	38911
	1.00	53.0814(8)	53.0227(25)	−0.690775(17)	−0.7494(26)	38911
	2.00	13.27035(19)	13.2448(6)	−0.374712(10)	−0.4003(6)	38911
	4.00	3.31759(5)	3.3074(5)[a]	−0.21107(8)[a]	−0.2216(6)[a]	38911
	6.00	1.474484(21)	1.46893(21)[b]	−0.15299(14)[b]	−0.15854(26)[b]	
	8.00	0.829397(12)	0.82618(12)[b]	−0.12223(8)[b]	−0.12544(15)[b]	
	10.00	0.530814(8)	0.52859(9)[b]	−0.10284(7)[b]	−0.10507(11)[b]	
8.00	0.05	28224.1(5)	28222.5(4)	−12.14740(7)	−13.8(7)	44473
	0.10	7056.03(14)	7055.43(10)	−6.103529(32)	−6.71(17)	44473
	0.20	1764.009(34)	1763.732(25)	−3.081446(15)	−3.36(4)	44473
	0.30	784.004(15)	783.799(12)	−2.073757(12)	−2.279(19)	44473
	0.40	441.002(9)	440.863(7)	−1.569731(9)	−1.709(11)	44473
	0.50	282.241(5)	282.151(5)	−1.267116(9)	−1.358(8)	44473
	0.60	196.001(4)	195.9224(35)	−1.065252(7)	−1.144(5)	44473
	0.80	110.2505(21)	110.191(8)	−0.812627(18)	−0.872(8)	44473
	1.00	70.5603(14)	70.509(9)	−0.660769(30)	−0.712(10)	44473
	2.00	17.64009(34)	17.6191(11)	−0.355004(10)	−0.3760(12)	44473
	3.00	7.84004(15)	7.8274(5)	−0.251192(7)	−0.2638(5)	44473
	4.00	4.41002(9)	4.40107(15)	−0.198143(7)	−0.20709(17)	44473
	6.00	1.96001(4)	1.95532(32)[a]	−0.14327(8)[a]	−0.1482(5)[a]	44473
	8.00	1.102505(21)	1.09990(18)[b]	−0.11447(13)[b]	−0.11708(22)[b]	
	10.00	0.705603(14)	0.70369(11)[b]	−0.09639(7)[b]	−0.09830(13)[b]	

line). With this, we are able to present *ab initio* results for this system for the entire density range, for all temperatures $\Theta > 0.5$.

In Table I, we present all CPIMC and PB-PIMC data points shown in Fig. 7. In addition to the exchange-correlation energy, the ideal, kinetic, and potential energy are listed. Note that even the ideal energy in the canonical ensemble cannot be calculated analytically. Further, we added the number of basis functions N_B that have been used in the corresponding CPIMC simulation, where we have carefully checked convergence of the energy (within statistical errors) with respect to N_B. The origin of the fluctuations at the highest temperature
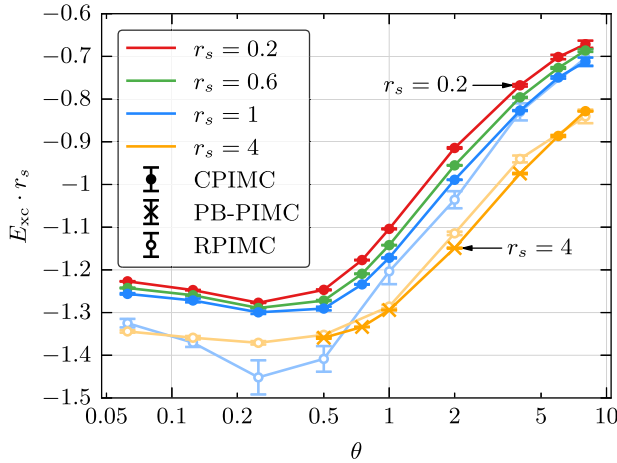
FIG. 8. Exchange-correlation energy E_{xc} times r_s of the $N = 33$ particle spin-polarized UEG over the degeneracy parameter θ for different density parameters r_s. Shown are results from CPIMC (dots) and PB-PIMC (crosses) calculations. In addition, RPIMC results from Ref. [17] are plotted for comparison (lines with light colors and open circles, for $r_s = 1$ and $r_s = 4$).

are easily understood: At $\theta = 8$, the relative contribution of the exchange-correlation energy to the internal energy becomes very small since the kinetic energy dominates for increasing temperature. Hence, E_{xc} is obtained by subtracting two large numbers of similar size which, of course, is ill-conditioned and, therefore, increases the statistical error of E_{xc}. The same applies in the limit $r_s \to 0$. Nevertheless, our exchange-correlation energies represent the most accurate results published to date.

For comparison we also plot the RPIMC data from Ref. [17]. It is evident that they not only have a significantly larger statistical error, but they clearly deviate systematically from our results. Interestingly, the deviations increase from $\theta = 1$ to $\theta = 2$, and even at $\theta = 4$, there is a significant discrepancy. This observation stands in contrast to the assumption that the systematic error due to the fixed node approximation vanishes for increasing temperature.

Finally, Fig. 8 shows the dependence of the exchange-correlation energy on temperature for four fixed densities. We again show the most accurate points of either CPIMC and PB-PIMC. CPIMC allows for calculations practically down to the ground state, for $r_s \lesssim 1$. On the other hand, PB-PIMC is limited, at larger densities, to temperatures $\theta \geqslant 0.5$. We observe that all isochores are nearly parallel and do not cross. An interesting feature is the existence of a minimum around $\Theta \sim 0.25$, for all densities (some uncertainty remains for the lowest density, $r_s = 4$, as our simulations are confined to $\Theta \geqslant 0.5$). Similar observations have been made in the fit results of Ref. [2] and in the computation of the screened potential of an ion in a streaming quantum plasma [37].

The origin of this nonmonotonic behavior is a competition of two effects. The governing trend is a decrease of the (modulus of the) interaction energy with temperature arising from a thermal broadening of the particle density. At low temperatures there exists a second trend arising from quantum diffraction

effects: The thermal DeBroglie wavelength is reduced with temperature increase which increases the Coulomb interaction. A similar trend of an intermediate increase of correlations with temperature has been predicted for Wigner crystallization in 2D [38].

In addition to the *ab initio* data, Fig. 8 also includes the fixed node RPIMC data of Ref. [17] which are available for the two lowest densities, $r_s = 1$ and $r_s = 4$. For the case $r_s = 4$ the RPIMC results are systematically too high by a few percent. More severe deviations are observed for $r_s = 1$ where the energies are too low. Particularly strong deviations are seen for low temperatures, $\theta \lesssim 1$ where the error exceeds 10%, giving even rise to a crossing of two isochores.

VI. SUMMARY AND DISCUSSION

This paper was devoted to a detailed discussion of the CPIMC simulation results for the uniform electron gas reported in a recent paper [21]. We presented a systematic analysis of the fermion sign problem of direct CPIMC for the polarized UEG. For increasing particle number, a sharp drop of the average sign, at a certain critical value of $r_s^{cr}(\Theta, N)$, has been observed and was shown to be connected to a strong increase in the average number of kinks in the simulation paths in Fock space. By introducing an auxiliary Fermi-like kink potential we introduced a modified CPIMC approach for which the accessible r_s range could be increased by more than a factor 2, for a fixed particle number and temperature [21]. When restricting the number of kinks to a maximum number $K_{\max}$, it turned out that the energy does not converge monotonically but rather oscillates towards the exact result with increasing $K_{\max}$, which renders a reliable extrapolation scheme difficult. However, by choosing the kink potential parameter δ such that it acts as a smooth penalty for paths with a larger number of kinks, a monotonic convergence of the energy could be achieved. We have developed a robust extrapolation scheme that provides strict upper and lower bounds thereby yielding an accurate value for the thermodynamic quantities of the UEG.

An independent confirmation of our extrapolation procedure could be obtained by a comparison to accurate PB-PIMC results. Interestingly, utilizing the kink potential, the energy of the simulation typically converges at about 20–30 kinks (on average in the simulation paths), whereas the direct CPIMC approach (without the potential) equilibrates at several thousand kinks. This is explained by an almost complete cancellation of contributions of paths with a large number of kinks in the partition function, which sets the limitation of the auxiliary kink potential method: It works only if we are able to reach the onset of this near cancellation, before the sign problem becomes too severe. This is clearly detectable from the convergence behavior of the energy, cf. Fig. 6: Only when the energy approaches the horizontal asymptote, as a function of $1/\kappa$, the method is applicable.

The second goal of this paper was to extend the available *ab initio* results for the exchange-correlation energy of the polarized electron gas to higher temperatures and lower densities. This was achieved by combining two complementary independent methods—CPIMC and PB-PIMC. With this we were able to avoid the sign problem for $N = 33$ electrons over

the entire density range, for all temperatures $\theta \geqslant 0.5$, and we presented data up to $\theta = 8$, completely avoiding fixed nodes or similar approximations. In all cases where both methods overlap we observed perfect agreement (within error bars), allowing for extremely valuable cross-checks.

Below $\theta = 0.5$, the present combination of two methods accesses only parts of the density range. Within the current implementations (and reasonable numerical effort) PB-PIMC is not applicable, for high densities, whereas CPIMC can only provide accurate results up to a minimum density around $r_s \sim 1$, leaving open a gap in the density which further increases with the particle number. Work is presently underway to access larger particle numbers and, eventually, perform an extrapolation to the thermodynamic limit, as was successfully demonstrated for very high densities in Ref. [21].

The present results should be useful for the development of improved quantum Monte Carlo simulations including density matrix QMC [39,40] and tests of improved fermionic nodes for RPIMC. The present scheme of combining CPIMC and PB-PIMC should also be suitable to produce first-principle results for the paramagnetic electron gas for which an increased sign problem of CPIMC was observed [21].

APPENDIX: EXTRAPOLATION WITH RESPECT TO THE NUMBER OF KINKS

To obtain an upper bound for the energy from CPIMC calculations utilizing the kink potential (see, e.g., Fig. 6) a horizontal (constant) fit is performed as follows: First, all data points with a relative error exceeding 1% are discarded defining a maximum value of κ, denoted κ_{max} (minimum of $1/\kappa_{max}$), satisfying this condition. Second, all data points are upshifted by 1σ standard deviation. Then, horizontal fits are performed to the next $6, 7, 8 \ldots, n_h$ points with $\kappa < \kappa_{max}$, where we add additional points as long as these deviate no more than 4σ from the constant fit. This procedure ensures that we only fit to those points belonging to the onset of convergence (indicated by the change in curvature in Fig. 6).

A lower bound of the energy is obtained by starting with a linear fit to the last n_h points with $\kappa < \kappa_{max}$. But instead of the prior upshift of the data by 1σ we now perform a downshift of the data points by 1σ prior to the fit. We proceed with adding points included in the linear fit as long as there are less than 3 points deviating by 2σ and less than 1 point deviating by 3σ from the fit. The lower bound of the energy is given by the lowest value of all linear fits at $1/\kappa = 0$. The result for the energy is then computed as the mean value of the lower and upper bounds with the error estimated (from above) as their difference.

[1] G. D. Mahan, *Many-Particle Physics*, 3rd ed. (Springer, New York, 2000).

[2] V. V. Karasiev, T. Sjostrom, J. Dufty, and S. B. Trickey, Accurate Homogeneous Electron Gas Exchange-Correlation Free Energy for Local Spin-Density Calculations, Phys. Rev. Lett. **112**, 076403 (2014) and Supplemental Material.

[3] E. W. Brown, J. L. DuBois, M. Holzmann, and D. M. Ceperley, Exchange-correlation energy for the three-dimensional homogeneous electron gas at arbitrary temperature, Phys. Rev. B **88**, 081102(R) (2013); Exchange-correlation energy for the three-dimensional homogeneous electron gas at arbitrary temperature, **88**, 199901(E) (2013).

[4] D. M. Ceperley and B. J. Alder, Ground State of the Electron Gas by a Stochastic Method, Phys. Rev. Lett. **45**, 566 (1980).

[5] J. P. Perdew and A. Zunger, Self-interaction correction to density-functional approximations for many-electron systems, Phys. Rev. B **23**, 5048 (1981).

[6] M. D. Knudson, M. P. Desjarlais, R. W. Lemke, T. R. Mattsson, M. French, N. Nettelmann, and R. Redmer, Probing the Interiors of the Ice Giants: Shock Compression of Water to 700 GPa and 3.8 g/cm³, Phys. Rev. Lett. **108**, 091102 (2012).

[7] B. Militzer, W. B. Hubbard, J. Vorberger, I. Tamblyn, and S. A. Bonev, A Massive Core in Jupiter predicted from first-principles simulations, Astrophys. J. **688**, L45 (2008).

[8] N. Nettelmann, A. Becker, B. Holst, and R. Redmer, Jupiter models with improved ab initio hydrogen equation of state (H-REOS.2), Astrophys. J. **750**, 52 (2012).

[9] J. D. Lindl *et al.*, The physics basis for ignition using indirect-drive targets on the National Ignition Facility, Phys. Plasmas **11**, 339 (2004).

[10] S. X. Hu, B. Militzer, V. N. Goncharov, and S. Skupsky, First-principles equation-of-state table of deuterium for inertial confinement fusion applications, Phys. Rev. B **84**, 224109 (2011).

[11] O. Hurricane *et al.*, Fuel gain exceeding unity in an inertially confined fusion implosion, Nature (London) **506**, 343 (2014).

[12] R. Nora, W. Theobald, R. Betti, F. J. Marshall, D. T. Michel, W. Seka, B. Yaakobi, M. Lafon, C. Stoeckl, J. Delettrez, A. A. Solodov, A. Casner, C. Reverdin, X. Ribeyre, A. Vallet, J. Peebles, F. N. Beg, and M. S. Wei, Gigabar Spherical Shock Generation on the OMEGA Laser, Phys. Rev. Lett. **114**, 045001 (2015).

[13] M. R. Gomez, S. A. Slutz, A. B. Sefkow, D. B. Sinars, K. D. Hahn, S. B. Hansen, E. C. Harding, P. F. Knapp, P. F. Schmit, C. A. Jennings, T. J. Awe, M. Geissel, D. C. Rovang, G. A. Chandler, G. W. Cooper, M. E. Cuneo, A. J. Harvey-Thompson, M. C. Herrmann, M. H. Hess, O. Johns, D. C. Lamppa, M. R. Martin, R. D. McBride, K. J. Peterson, J. L. Porter, G. K. Robertson, G. A. Rochau, C. L. Ruiz, M. E. Savage, I. C. Smith, W. A. Stygar, and R. A. Vesey, Experimental Demonstration of Fusion-Relevant Conditions in Magnetized Liner Inertial Fusion, Phys. Rev. Lett. **113**, 155003 (2014).

[14] P. F. Schmidt, P. F. Knapp, S. B. Hansen, M. R. Gomez, K. D. Hahn, D. B. Sinars, K. J. Peterson, S. A. Slutz, A. B. Sefkow,

T. J. Awe, E. Harding, C. A. Jennings, G. A. Chandler, G. W. Cooper, M. E. Cuneo, M. Geissel, A. J. Harvey-Thompson, M. C. Herrmann, M. H. Hess, O. Johns, D. C. Lamppa, M. R. Martin, R. D. McBride, J. L. Porter, G. K. Robertson, G. A. Rochau, D. C. Rovang, C. L. Ruiz, M. E. Savage, I. C. Smith, W. A. Stygar, and R. A. Vesey, Understanding Fuel Magnetization and Mix Using Secondary Nuclear Reactions in Magneto-Inertial Fusion, Phys. Rev. Lett. **113**, 155004 (2014).

[15] M. Troyer and U.-J. Wiese, Computational Complexity and Fundamental Limitations to Fermionic Quantum Monte Carlo simulations, Phys. Rev. Lett. **94**, 170201 (2005).

[16] D. M. Ceperley, Path integrals in the theory of condensed helium, Rev. Mod. Phys. **67**, 279 (1995).

[17] E. W. Brown, B. K. Clark, J. L. DuBois, and D. M. Ceperley, Path-Integral Monte Carlo Simulation of the Warm Dense Homogeneous Electron Gas, Phys. Rev. Lett. **110**, 146405 (2013).

[18] D. M. Ceperley, Fermion nodes, J. Stat. Phys. **63**, 1237 (1991).

[19] V. S. Filinov, V. E. Fortov, M. Bonitz, and Zh. Moldabekov, Fermionic path-integral Monte Carlo results for the uniform electron gas at finite temperature, Phys. Rev. E **91**, 033108 (2015).

[20] J. L. DuBois, E. W. Brown, and B. J. Alder, arXiv:1409.3262.

[21] T. Schoof, S. Groth, J. Vorberger, and M. Bonitz, *Ab Initio* Thermodynamic Results for the Degenerate Electron Gas at Finite Temperature, Phys. Rev. Lett. **115**, 130402 (2015).

[22] T. Schoof, S. Groth, and M. Bonitz, Towards ab initio thermodynamics of the electron gas at strong degeneracy, Contrib. Plasma Phys. **55**, 136 (2015).

[23] T. Schoof, M. Bonitz, A. Filinov, D. Hochstuhl, and J. W. Dufty, Configuration Path integral Monte Carlo, Contrib. Plasma Phys. **51**, 687 (2011).

[24] T. Dornheim, S. Groth, A. Filinov, and M. Bonitz, Permutation blocking path integral Monte Carlo: a highly efficient approach to the simulation of strongly degenerate non-ideal fermions, New J. Phys. **17**, 073017 (2015).

[25] T. Dornheim, T. Schoof, S. Groth, A. Filinov, and M. Bonitz, Permutation blocking path integral Monte Carlo approach to the uniform electron gas at finite temperature, J. Chem. Phys. **143**, 204101 (2015).

[26] L. M. Fraser, W. M. C. Foulkes, G. Rajagopal, R. J. Needs, S. D. Kenny, and A. J. Williamson, Finite-size effects and Coulomb interactions in quantum Monte Carlo calculations for homogeneous systems with periodic boundary conditions, Phys. Rev. B **53**, 1814 (1996).

[27] N. V. Prokofev, B. V. Svistunov, and I. S. Tupitsyn, Exact quantum Monte Carlo process for the statistics of discrete systems, JETP Lett. **64**, 911 (1996).

[28] N. V. Prokofev, B. V. Svistunov, and I. S. Tupitsyn, Exact, complete, and universal continuous-time worldline Monte Carlo approach to the statistics of discrete quantum systems, JETP **87**, 310 (1998).

[29] K. Van Houcke, S. M. A. Rombouts, and L. Pollet, Quantum Monte Carlo simulation in the canonical ensemble at finite temperature, Phys. Rev. E **73**, 056703 (2006).

[30] S. M. A. Rombouts, K. Van Houcke, and L. Pollet, Loop Updates for Quantum Monte Carlo Simulations in the Canonical Ensemble, Phys. Rev. Lett. **96**, 180603 (2006).

[31] M. Takahashi and M. Imada, Monte Carlo calculation of quantum systems, J. Phys. Soc. Jpn. **53**, 963 (1984).

[32] V. S. Filinov, M. Bonitz, V. E. Fortov, W. Ebeling, P. Levashov, and M. Schlanges, Thermodynamic properties and plasma phase transition in dense hydrogen, Contrib. Plasma Phys. **44**, 388 (2004).

[33] A. P. Lyubartsev, Simulation of excited states and the sign problem in the path integral Monte Carlo method, J. Phys. A: Math. Gen. **38**, 6659 (2005).

[34] S. A. Chin, High-order path integral Monte Carlo methods for solving quantum dot problems, Phys. Rev. E **91**, 031301(R) (2015).

[35] S. A. Chin and C. R. Chen, Gradient symplectic algorithms for solving the Schrödinger equation with time-dependent potentials, J. Chem. Phys. **117**, 1409 (2002).

[36] K. Sakkos, J. Casulleras, and J. Boronat, High order Chin actions in path integral Monte Carlo, J. Chem. Phys. **130**, 204109 (2009).

[37] Z. Moldabekov, P. Ludwig, M. Bonitz, and T. Ramazanov, Ion potential in warm dense matter: Wake effects due to streaming degenerate electrons, Phys. Rev. E **91**, 023102 (2015).

[38] B. K. Clark, M. Casula, and D. M. Ceperley, Hexatic and Mesoscopic Phases in a 2D Quantum Coulomb System, Phys. Rev. Lett. **103**, 055701 (2009).

[39] N. S. Blunt, T. W. Rogers, J. S. Spencer, and W. M. C. Foulkes, Density-matrix quantum Monte Carlo method, Phys. Rev. B **89**, 245124 (2014).

[40] Fionn D. Malone, N. S. Blunt, James J. Shepherd, D. K. K. Lee, J. S. Spencer, and W. M. C. Foulkes, Interaction picture density matrix quantum Monte Carlo, J. Chem. Phys. **143**, 044116 (2015).

4.2   The Unpolarized Case

Up to this point, we had limited our investigations to the spin-polarized (ferromagnetic) case. However, as naturally occurring plasmas tend to be mostly unpolarized (i.e., paramagnetic), this case certainly is of even higher interest for warm dense matter applications. For this reason, with the aid of the Daad–Rise exchange student Connor Hann, I extended PB-PIMC to the simulation of multiple particle species. In this case, these were given by spin-up and -down electrons, although the future investigation of other scenarios like electrons and holes [67] is easily possible.

The details regarding the modification of the underlying equations and the adaption of the free parameters in the fourth-order factorization of the density matrix, which is necessary due to the absence of the Pauli exclusion principle between spin-up and -down electrons, are discussed in detail in the following paper[2], Ref. [163]. Further, we investigated the fermion sign problem for this case and, again, found a significant extension of the range of accessible parameters compared to standard PIMC. However, the FSP tends to be in general more severe than in the spin-polarized case. A similarly detailed discussion was given regarding the extension of the CPIMC method to this system, although I did not contribute to it.

In addition, we performed extensive simulations of the unpolarized UEG and made the combined data from both methods available for future method development. Overall, we found that RPIMC delivers improved results for the exchange–correlation energy as compared to the spin-polarized case, although both the kinetic and interaction contribution still substantially deviate. In contrast, the independent PB-PIMC and CPIMC data are in excellent agreement everywhere, as it is expected. Finally, we presented, for the first time, a comparison to RPIMC for a quantity that is not some kind of energy, namely the pair correlation function $g(r)$.

---

[2]T. Dornheim, S. Groth, T. Schoof, C. Hann, and M. Bonitz, Phys. Rev. B **93**, 205134 (2016). Copyright by the American Physical Society (2016).

Ab initio quantum Monte Carlo simulations of the uniform electron gas without fixed nodes: The unpolarized case

T. Dornheim,[1] S. Groth,[1] T. Schoof,[1] C. Hann,[1,2] and M. Bonitz[1,*]

[1]*Institut für Theoretische Physik und Astrophysik, Christian-Albrechts-Universität zu Kiel, D-24098 Kiel, Germany*
[2]*Department of Physics, Duke University, Durham, North Carolina 27708, USA*

In a recent publication [S. Groth *et al.*, Phys. Rev. B **93**, 085102 (2016)], we have shown that the combination of two complementary quantum Monte Carlo approaches, namely configuration path integral Monte Carlo [T. Schoof *et al.*, Phys. Rev. Lett. **115**, 130402 (2015)] and permutation blocking path integral Monte Carlo [T. Dornheim *et al.*, New J. Phys. **17**, 073017 (2015)], allows for the accurate computation of thermodynamic properties of the spin-polarized uniform electron gas over a wide range of temperatures and densities without the fixed-node approximation. In the present work, we extend this concept to the unpolarized case, which requires nontrivial enhancements that we describe in detail. We compare our simulation results with recent restricted path integral Monte Carlo data [E. W. Brown *et al.*, Phys. Rev. Lett. **110**, 146405 (2013)] for different energy contributions and pair distribution functions and find, for the exchange correlation energy, overall better agreement than for the spin-polarized case, while the separate kinetic and potential contributions substantially deviate.

I. INTRODUCTION

Quantum Monte Carlo (QMC) simulations of fermions are of paramount importance to describe manifold aspects of nature. In particular, recent experimental progress with highly compressed matter [1–3] such as plasmas in laser fusion experiments [4–9] and solids after laser irradiation [10], but also the need for an appropriate description of compact stars and planet cores [11–13], has lead to a high demand for accurate simulations of electrons in the warm dense matter (WDM) regime (i.e., density parameter $r_s = \bar{r}/a_B \sim 1$ and degeneracy temperature $\theta = k_B T/E_F \sim 1$). Unfortunately, the application of all QMC methods to fermions is severely hampered by the fermion sign problem (FSP) [14,15]. A popular approach to circumvent this issue is the restricted path integral Monte Carlo (RPIMC) [16] method, which, however, is afflicted with an uncontrollable error due the fixed node approximation [17–20]. Therefore, until recently, the quality of the only available QMC results for the uniform electron gas (UEG) in the WDM regime [21] has remained unclear.

To address this issue, in a recent publication (paper I, Ref. [22]) we have combined two complementary approaches: our configuration path integral Monte Carlo (CPIMC) method [23–25] excels at high to medium density and arbitrary temperature, while our permutation blocking path integral Monte Carlo (PB-PIMC) approach [26,27] significantly extends standard fermionic PIMC [28,29] towards lower temperature and higher density. Surprisingly, it has been found that existing RPIMC results are inaccurate even at high temperatures.

However, although the spin-polarized systems that have been investigated in our previous works are of relevance for the description of, e.g., ferromagnetic materials or strongly magnetized systems, they constitute a rather special case, since most naturally occurring plasmas are predominantly

unpolarized. Therefore, in the present work we modify both our implementations of PB-PIMC and CPIMC to simulate the unpolarized UEG. So far only a single data set for a small system ($N = 14$ electrons, one isotherm) could be obtained in our previous work [25] because the paramagnetic case turns out to be substantially more difficult than the ferromagnetic one. Therefore, we have developed nontrivial enhancements of our CPIMC algorithm that are discussed in detail. With these improvements, we are able to present accurate results for different energies for the commonly used case of $N = 66$ unpolarized electrons over a broad range of parameters.

Since many details of our approach have been presented in our paper I [22], in the remainder of this paper we restrict ourselves to a brief, but self-contained introduction to CPIMC and PB-PIMC. We set the focus on the differences arising from their application to the unpolarized UEG, compared to the spin-polarized case and, therefore, the present investigation complements our previous results [22,27] for the latter. In Sec. II, we introduce the model Hamiltonian, both in coordinate space (II A) and second quantization (II B) and, subsequently, provide a brief introduction to the employed QMC approaches (Sec. III), namely PB-PIMC (III A) and CPIMC (III B). Finally, in Sec. IV, we present combined results from both methods for the exchange correlation, kinetic, and potential energy (IV A), as well as the pair distribution function (IV B). Further, we compare our data to those from RPIMC [21], where available. While we find better agreement than for the spin-polarized case [22,27], there nevertheless appear significant deviations towards lower temperature.

II. HAMILTONIAN OF THE UNIFORM ELECTRON GAS

The uniform electron gas ("Jellium") is a model system of Coulomb interacting electrons in a neutralizing homogeneous background. As such, it explicitly allows one to study effects due to the correlation and exchange of the electrons, whereas

those due to the positive ions are neglected. Furthermore, the widespread density functional theory (DFT) crucially depends on *ab initio* results for the exchange correlation energy of the uniform electron gas (UEG), hitherto at zero temperature [30]. However, it is widely agreed that the appropriate treatment of matter under extreme conditions requires one to go beyond ground state DFT, which, in turn, needs accurate results for the finite temperature UEG. While the electron gas itself is defined as an infinite macroscopic system, QMC simulations are possible only for a finite number of particles N. Hence we always assume periodic boundary conditions and include the interaction of the N electrons in the main simulation cell with all their images via Ewald summation and defer any additional finite-size corrections [31–33] to a future publication.

A. Coordinate representation of the Hamiltonian

Following Refs. [27,31], we express the Hamiltonian (we measure energies in Rydberg and distances in units of the Bohr radius a_0) for $N = N_\uparrow + N_\downarrow$ unpolarized electrons in coordinate space as

$$\hat{H} = -\sum_{i=1}^{N} \nabla_i^2 + \sum_{i=1}^{N} \sum_{j\neq i}^{N} e^2 \Psi(\mathbf{r}_i, \mathbf{r}_j) + N e^2 \xi, \quad (1)$$

with the well-known Madelung constant ξ and the periodic Ewald pair interaction

$$\Psi(\mathbf{r}, \mathbf{s}) = \frac{1}{V} \sum_{\mathbf{G}\neq 0} \frac{e^{-\pi^2 \mathbf{G}^2/\kappa^2} e^{2\pi i \mathbf{G}(\mathbf{r}-\mathbf{s})}}{\pi \mathbf{G}^2} - \frac{\pi}{\kappa^2 V} + \sum_{\mathbf{R}} \frac{\text{erfc}(\kappa|\mathbf{r} - \mathbf{s} + \mathbf{R}|)}{|\mathbf{r} - \mathbf{s} + \mathbf{R}|}. \quad (2)$$

Here $\mathbf{R} = \mathbf{n}_1 L$ and $\mathbf{G} = \mathbf{n}_2/L$ denote the real and reciprocal space lattice vectors, respectively, with the box length L, volume $V = L^3$, and the usual Ewald parameter κ. Furthermore, PB-PIMC simulations require the evaluation of all forces within the system, where the force between two electrons i and j is given by

$$\mathbf{F}_{ij} = \frac{2}{V} \sum_{\mathbf{G}\neq 0} \left(\frac{\mathbf{G}}{\mathbf{G}^2} \sin[2\pi \mathbf{G}(\mathbf{r}_i - \mathbf{r}_j)] e^{-\pi^2 \mathbf{G}^2/\kappa^2} \right) + \sum_{\mathbf{R}} \frac{\mathbf{r}_i - \mathbf{r}_j + \mathbf{R}}{\alpha^3} \left(\text{erfc}(\kappa\alpha) + \frac{2\kappa\alpha}{\sqrt{\pi}} e^{-\kappa^2\alpha^2} \right), \quad (3)$$

with the definition $\alpha = |\mathbf{r}_i - \mathbf{r}_j + \mathbf{R}|$.

B. Hamiltonian in second quantization

In second quantization with respect to spin orbitals of plane waves, $\langle \mathbf{r}\sigma | \mathbf{k}_i \sigma_i \rangle = \frac{1}{L^{3/2}} e^{i\mathbf{k}_i \cdot \mathbf{r}} \delta_{\sigma,\sigma_i}$ with $\mathbf{k}_i = \frac{2\pi}{L} \mathbf{m}_i$, $\mathbf{m}_i \in \mathbb{Z}^3$, and $\sigma_i \in \{\uparrow, \downarrow\}$, the model Hamiltonian, Eq. (1), takes the form

$$\hat{H} = \sum_i \mathbf{k}_i^2 \hat{a}_i^\dagger \hat{a}_i + 2 \sum_{\substack{i < j, k < l \\ i \neq k, j \neq l}} w_{ijkl}^- \hat{a}_i^\dagger \hat{a}_j^\dagger \hat{a}_l \hat{a}_k + N e^2 \xi, \quad (4)$$

with the antisymmetrized two-electron integrals, $w_{ijkl}^- = w_{ijkl} - w_{ijlk}$, where

$$w_{ijkl} = \frac{4\pi e^2}{L^3 (\mathbf{k}_i - \mathbf{k}_k)^2} \delta_{\mathbf{k}_i + \mathbf{k}_j, \mathbf{k}_k + \mathbf{k}_l} \delta_{\sigma_i, \sigma_k} \delta_{\sigma_j, \sigma_l}, \quad (5)$$

and the Kronecker δ's ensuring both momentum and spin conservation. The first (second) term in the Hamiltonian Eq. (4) describes the kinetic (interaction) energy. The operator $\hat{a}_i^\dagger$ ($\hat{a}_i$) creates (annihilates) a particle in the spin orbital $|\mathbf{k}_i \sigma_i\rangle$.

III. FERMIONIC QUANTUM MONTE CARLO WITHOUT FIXED NODES

Throughout the entire work, we consider the canonical ensemble, i.e., the volume V, particle number N, and inverse temperature $\beta = 1/k_B T$ are fixed. In equilibrium statistical mechanics, all thermodynamic quantities can be derived from the partition function

$$Z = \text{Tr}\hat{\rho}, \quad (6)$$

which is of central importance for any QMC formulation and defined as the trace over the canonical density operator

$$\hat{\rho} = e^{-\beta\hat{H}}. \quad (7)$$

The expectation value of an arbitrary operator $\hat{A}$ is given by

$$\langle \hat{A} \rangle = \frac{\text{Tr}(\hat{A}\hat{\rho})}{\text{Tr}\hat{\rho}} = \frac{1}{Z} \text{Tr}(\hat{A}\hat{\rho}). \quad (8)$$

However, for an appropriate description of fermions, Eqs. (6) and (8) must be extended either by antisymmetrizing $\hat{\rho} \to \hat{\rho}^-$ or the trace itself [23], $\text{Tr} \to \text{Tr}^-$. Therefore, it holds that

$$Z = \text{Tr}\hat{\rho}^- = \text{Tr}^- \hat{\rho}. \quad (9)$$

While defining the trace in Eq. (9) as either expression does not change the well-defined thermodynamic expectation values, it does lead to rather different formulations of the same problem. The combination of antisymmetrizing the density matrix and evaluating the trace in coordinate space is the first step towards both standard PIMC and PB-PIMC, cf. Sec. III A, but also RPIMC. All these approaches share the fact that they are efficient when fermionic quantum exchange does not yet dominate a system, but they will become increasingly costly towards low temperature and high density. Switching to second quantization and carrying out the trace in antisymmetrized Fock space, on the other hand, is the basic idea behind our CPIMC method, cf. Sec. III B, and, in a different way, behind the likewise density matrix QMC method [34]. The latter approach has recently been applied to the case of $N = 4$ spin-polarized electrons [35], where complete agreement with our CPIMC results [24] was reported. These QMC approaches tend to excel at high density, i.e., weak nonideality, and become eventually unfeasible towards stronger coupling strength.

Therefore, it is a natural strategy to combine different representations at complementary parameter ranges as this does effectively allow one to circumvent the numerical shortcomings with which every single fermionic QMC method is necessarily afflicted [22,27].

A. Permutation blocking PIMC

1. Basic idea

In this section, we will briefly introduce our permutation blocking PIMC approach. A more detailed description of the method itself and its application to the spin-polarized UEG can be found in Refs. [26,27].

The basic idea behind PB-PIMC is essentially equal to standard PIMC in coordinate space, e.g., Ref. [29], but, in addition, combines two well-known concepts: (1) antisymmetric imaginary time propagators, i.e., determinants [36–38], and (2) a fourth-order factorization of the density matrix [39–42]. Furthermore, since this leads to a significantly more complicated configuration space without any fixed paths, one of us has developed an efficient set of Metropolis Monte Carlo [43] updates that utilize the temporary construction of artificial trajectories [26]. As mentioned above, we evaluate the trace within the canonical partition function for $N = N_\uparrow + N_\downarrow$ unpolarized electrons in coordinate representation

$$
Z = \frac{1}{N_\uparrow! N_\downarrow!} \sum_{\sigma_\uparrow \in S_{N_\uparrow}} \sum_{\sigma_\downarrow \in S_{N_\downarrow}} \operatorname{sgn}(\sigma_\uparrow) \operatorname{sgn}(\sigma_\downarrow)
$$

$$
\times \int d\mathbf{R} \, \langle \mathbf{R} | \, e^{-\beta \hat{H}} \, | \hat{\pi}_{\sigma_\uparrow} \hat{\pi}_{\sigma_\downarrow} \mathbf{R} \rangle \,, \tag{10}
$$

with $\hat{\pi}_{\sigma_{\uparrow,\downarrow}}$ being the exchange operator that corresponds to a particular element $\sigma_{\uparrow,\downarrow}$ from the permutation group $S_{N_{\uparrow,\downarrow}}$ with associated sign $\operatorname{sgn}(\sigma_{\uparrow,\downarrow})$ and $\uparrow (\downarrow)$ denoting spin-up (spin-down) electrons. However, since the kinetic and potential contributions to the Hamiltonian, $\hat{K}$ and $\hat{V}$, do not commute, the low-temperature matrix elements of $\hat{\rho}$ are not known. To overcome this issue, we use the common group property $\hat{\rho}(\beta) = \prod_{\alpha=0}^{P-1} \hat{\rho}(\epsilon)$ of the density matrix, with $\epsilon = \beta/P$, and approximate each of the P factors at a P times higher temperature by the fourth-order factorization [40,41]

$$
e^{-\epsilon \hat{H}} \approx e^{-v_1 \epsilon \hat{W}_{a_1}} e^{-t_1 \epsilon \hat{K}} e^{-v_2 \epsilon \hat{W}_{1-2a_1}}
$$

$$
\times e^{-t_1 \epsilon \hat{K}} e^{-v_1 \epsilon \hat{W}_{a_1}} e^{-2t_0 \epsilon \hat{K}} \,. \tag{11}
$$

The $\hat{W}$ operators in Eq. (11) combine the usual potential energy $\hat{V}$ with double commutator terms of the form

$$
[[\hat{V}, \hat{K}], \hat{V}] = \frac{\hbar^2}{m} \sum_{i=1}^{N} |\mathbf{F}_i|^2, \quad \mathbf{F}_i = -\nabla_i V(\mathbf{R}), \tag{12}
$$

and, therefore, require the evaluation of all forces [44] within the system; cf. Eq. (3). The explicit expressions of these modified potential terms are given by

$$
\hat{W}_{a_1} = \hat{V} + \frac{u_0}{v_1} a_1 \epsilon^2 \left(\frac{\hbar^2}{m} \sum_{i=1}^{N} |\mathbf{F}_i|^2 \right),
$$

$$
\hat{W}_{1-2a_1} = \hat{V} + \frac{u_0}{v_2}(1-2a_1)\epsilon^2 \left(\frac{\hbar^2}{m} \sum_{i=1}^{N} |\mathbf{F}_i|^2 \right). \tag{13}
$$

Furthermore, we note that there are two free parameters in Eq. (11) that can be used for optimization, namely $0 \leqslant a_1 \leqslant 1$ and $0 \leqslant t_0 \leqslant (1 - 1/\sqrt{3})/2$. All other coefficients (u_0, v_1, v_2, and t_1) are subsequently calculated from these choices; see Refs. [26,41].

The final result for the PB-PIMC partition function is given by

$$
Z = \frac{1}{(N_\uparrow! N_\downarrow!)^{3P}} \int d\mathbf{X}
$$

$$
\times \prod_{\alpha=0}^{P-1} \left(e^{-\epsilon \tilde{V}_\alpha} e^{-\epsilon^3 u_0 \frac{\hbar^2}{m} \tilde{F}_\alpha} D_{\alpha,\uparrow} D_{\alpha,\downarrow} \right), \tag{14}
$$

with $\tilde{V}_\alpha$ and $\tilde{F}_\alpha$ containing all contributions of the potential energy and the forces, respectively. For each propagator α, there are N particle coordinates on the "main time slice," $\mathbf{R}_\alpha$, and, in addition, on two "daughter slices," $\mathbf{R}_{\alpha A}$ and $\mathbf{R}_{\alpha B}$, with the integration in Eq. (14) being carried out over all of them. The exchange-diffusion functions are defined as

$$
D_{\alpha,\uparrow} = \det(\rho_{\alpha,\uparrow}) \det(\rho_{\alpha A,\uparrow}) \det(\rho_{\alpha B,\uparrow}),
$$

$$
D_{\alpha,\downarrow} = \det(\rho_{\alpha,\downarrow}) \det(\rho_{\alpha A,\downarrow}) \det(\rho_{\alpha B,\downarrow}) \tag{15}
$$

and contain the determinants of the diffusion matrices

$$
\rho_{\alpha,\uparrow}(i,j) = \lambda_{t_1\epsilon}^{-3} \sum_{\mathbf{n}} e^{-\frac{\pi}{\lambda_{t_1\epsilon}^2}(\mathbf{r}_{\alpha,\uparrow,j} - \mathbf{r}_{\alpha A,\uparrow,i} + \mathbf{n}L)^2}, \tag{16}
$$

with $\lambda_{t_1\epsilon} = \sqrt{2\pi\epsilon t_1 \hbar^2/m}$ being the thermal wavelength of a single "time slice."

In contrast to standard PIMC, where each permutation cycle has to be explicitly sampled, we combine both positively and negatively signed configuration weights in the determinants both for the spin-up and spin-down electrons. This leads to a cancellation of many terms and, consequently, a significantly increased average sign in our Monte Carlo simulations. Yet, this "permutation blocking" is only effective when $\lambda_{t_1\epsilon}$ is comparable to the mean interparticle distance, i.e., when there are both large diagonal and off-diagonal elements in the diffusion matrices. With an increasing number of high-temperature factors P, $\lambda_{t_1\epsilon}$ decreases and, eventually, when there is only but a single large element in each row of the $\rho_{\alpha,\uparrow}$, the average sign converges towards that of standard PIMC. For this reason, it is crucial to combine the determinants from the antisymmetric propagators with an appropriate factorization of the density matrix that allows for sufficient (though finite) accuracy with as few as two or three propagators, thereby maximizing the benefit of the blocking within the determinants. This requirement is met by the factorization scheme Eq. (11) which, in the limit of large P, leads to a convergence behavior with $1/P^4$ as was shown in Ref. [41]. However, even though this asymptotic limit is not reached (which is the case for all simulations presented in this work), the empirical choice of the two free parameters t_0 and a_1 allows for significantly improved accuracy with only two or three propagators (compared to the primitive factorization $e^{-\epsilon \hat{H}} \approx e^{-\epsilon \hat{K}} e^{-\epsilon \hat{V}}$) [41].

Furthermore, we note that since electrons with different spin projections do not exchange at all, PB-PIMC simulations of the unpolarized UEG with $N = N_\uparrow + N_\downarrow$ do suffer from a significantly less severe sign problem than for $N = 2N_\uparrow$ spin-polarized electrons.

2. Application to the unpolarized UEG

The accuracy of our PB-PIMC simulations crucially depends on the systematic factorization error for small P [26,27].
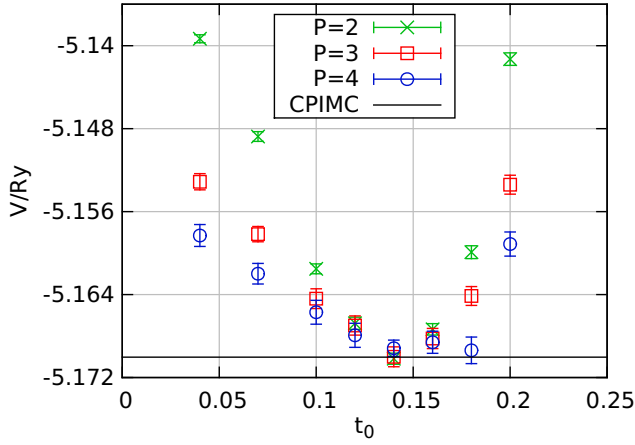
FIG. 1. Influence of the relative interslice spacing t_0 on the convergence—the potential energy from PB-PIMC simulations of $N = 4$ unpolarized electrons at $\theta = 0.5$ and $r_s = 1$ is plotted versus t_0 for the fixed choice $a_1 = 0.33$.

Thus we begin the investigation of the unpolarized electron gas with the analysis of the empirical optimization of the two free parameters from Eq. (11), namely a_1 (weighting the contributions of the forces on different time slices) and t_0 (controlling the relative interslice spacing). In Fig. 1, we fixed $a_1 = 0.33$ fixed, which corresponds to equally weighted forces on all slices, and plot the potential energy V for $P = 2,3,4$ over the entire t_0 range for a benchmark system of $N = 4$ unpolarized electrons at $r_s = 1$ and $\theta = 0.5$. Evidently, for all t_0 values V approaches the exact result, which has been obtained with CPIMC, monotonically from above. The optimum value for t_0 is located around $t_0 = 0.14$, where all three PB-PIMC values are within single error bars with the black line. For completeness, we mention that this particular set of the optimum free parameters for the energy is consistent with the previous findings for different systems [26,27,41]. A detailed investigation of the convergence properties of the employed fourth-order factorization including the asymptotic behavior for large P is beyond the scope of this work and can be found in Ref. [41].

A natural follow-up question is how the factorization error for few propagators behaves as a function of the density parameter r_s in the WDM regime, $\theta = 1$. In Fig. 2, we show results for the relative error of the potential [$\Delta V/|V|$, panel (a)] and kinetic energy [$\Delta K/K$, panel (b)], where the reference values are again obtained from CPIMC (see Fig. 12 for a similar plot for $N = 66$ electrons). The statistical uncertainty is mainly due to PB-PIMC, except for $r_s = 4$ where the CPIMC error bar predominates. For the kinetic energy, even for $P = 3$ there are no clear systematic deviations from the exact result over the entire r_s range. Only with two propagators, our results for K appear to be slightly too large for $r_s \in (0.5,1,2)$, although this trend hardly exceeds $\Delta K/K = 5 \times 10^{-4}$. For the potential energy, the factorization error behaves quite differently. For $r_s \geqslant 1$, even with two propagators the accuracy is better than 0.1%, while towards higher density ($r_s < 1$), the convergence significantly deteriorates. In particular, at $r_s = 0.25$ even with $P = 5$ there is a deviation of $\Delta V/|V| \approx$
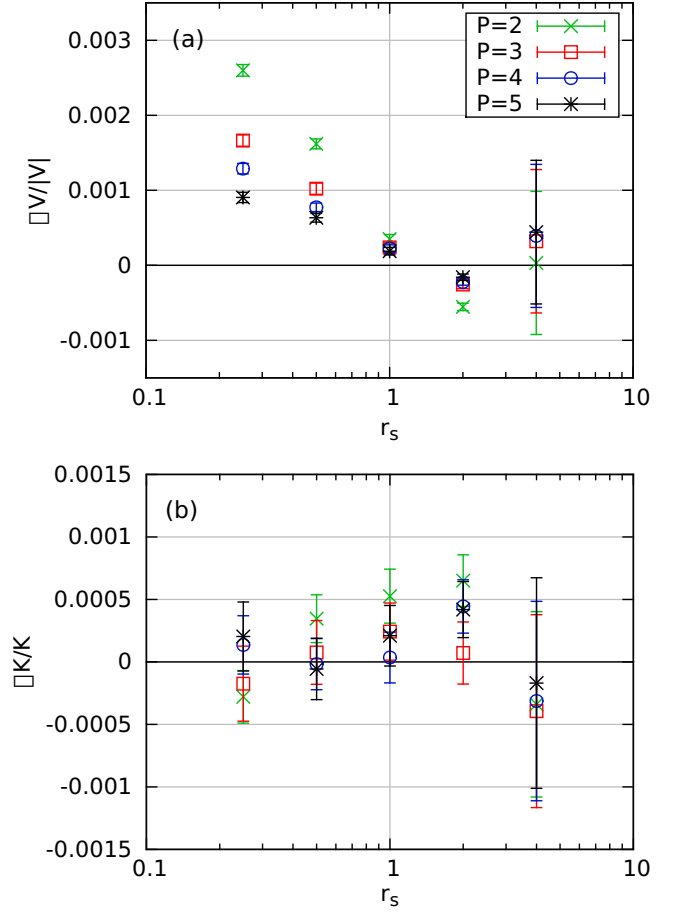

FIG. 2. Density dependence of the relative time step error from PB-PIMC with $a_1 = 0.33$ and $t_0 = 0.14$—the relative differences between PB-PIMC results with $P = 2,3,4,5$ and reference data from CPIMC are plotted versus r_s for the potential energy (a) and the kinetic energy (b), with $\theta = 1$.

0.1%. This observation is in striking contrast to our previous investigation of the polarized UEG, where the relative error in both K and V decreased towards $r_s \to 0$. The reason for this trend lies in the presence of two different particle species which do not exchange with each other, namely $N_\uparrow$ spin-up and $N_\downarrow$ spin-down electrons. Even at high density, two electrons from the same species are effectively separated by their overlapping kinetic density matrices that cancel in the determinants, which is nothing else than the Pauli blocking. Yet, a spin-up and a spin-down electron do not experience such a repulsion and, at weak coupling (small r_s), can be separated by much smaller distances r from each other. With decreasing r the force terms in Eq. (11) that scale as $F(r) \propto 1/r^2$ will eventually exceed the Coulomb potential $V(r) \propto 1/r$, i.e., the higher order correction predominates. This trend must be compensated by an increasing number of propagators P. Hence the fermionic nature of the electrons that manifests as the Pauli blocking significantly enhances the performance of our factorization scheme, which means that the simulation of unpolarized systems is increasingly hampered towards high density. In addition to the Monte Carlo inherent sign problem,

this is a further reason to combine PB-PIMC with CPIMC, since the latter excels just in this regime.

In our recent analysis of PB-PIMC for electrons in a two-dimensional (2D) harmonic trap [26], it was found that, while the combination $a_1 = 0.33$ and $t_0 = 0.14$ [parameter set (a)] is favorable for a fast convergence of the energy, it does not perform so well for other properties like, in that case, the density profile. To address this issue, we again simulate a benchmark system of $N = 4$ unpolarized electrons and compute the pair distribution function $g(r)$; see, e.g., Ref. [45] for a comprehensive discussion. In Fig. 3, we show results for the above combination of free parameters (a) and $P = 2,3,4,5$. Panel (a) displays the data for the interspecies distribution function $g_{\uparrow\downarrow}$. We note that, for the infinite UEG, this quantity approaches unity at large distances, but the small simulation box for $N = 4$ restricts us to the depicted r range. All four curves deviate from each other for $r \lesssim 0.5$, which indicates that $g_{\uparrow\downarrow}$ is not yet converged even for $P = 5$ at small distances, and are equal otherwise. This is again a clear indication of the shortcomings of our fourth-order factorization, which overestimates the Coulomb repulsion at short ranges. The

intraspecies distribution function $g_{\uparrow\uparrow} = g_{\downarrow\downarrow}$, which is shown in panel (b), does not exhibit such a clear trend since only the green curve that corresponds to $P = 2$ can be distinguished from the rest. This is, of course, expected and a consequence of the Pauli blocking as explained above.

Evidently, our propagator with the employed choice of free parameters (a) does not allow for an accurate description of the Coulomb repulsion at short distances. To understand this issue, we repeat the simulations with a different combination $a_1 = 0$ and $t_0 = 0.04$ [parameter set (b)], which has already proven to be superior to parameter set (a) for the radial density in the 2D harmonic trap. The results are shown in Fig. 4 for different numbers of propagators. The data with $P = 2$ are nearly equal to the results from parameters (a) and $P = 5$. The data for $P = 4$ and $P = 5$ almost coincide and are significantly increased with respect to the other curves. The main reason for the improved accuracy of parameter set (b) is the choice $a_1 = 0$, which means that the forces are only taken into account on intermediate time slices. Due to the diagonality of the pair distribution function in coordinate space, it is measured exclusively on the main slices, for whose distribution the force

FIG. 3. Convergence of the pair distribution function for $N = 4$ unpolarized electrons at $\theta = 1$ and $r_s = 4$—shown are PB-PIMC results for the inter- [$g_{\uparrow\downarrow}$, panel (a)] and intraspecies [$g_{\uparrow\uparrow}$, panel (b)] distribution function for different numbers of propagators P and the fixed free parameters $a_1 = 0.33$ and $t_0 = 0.14$.

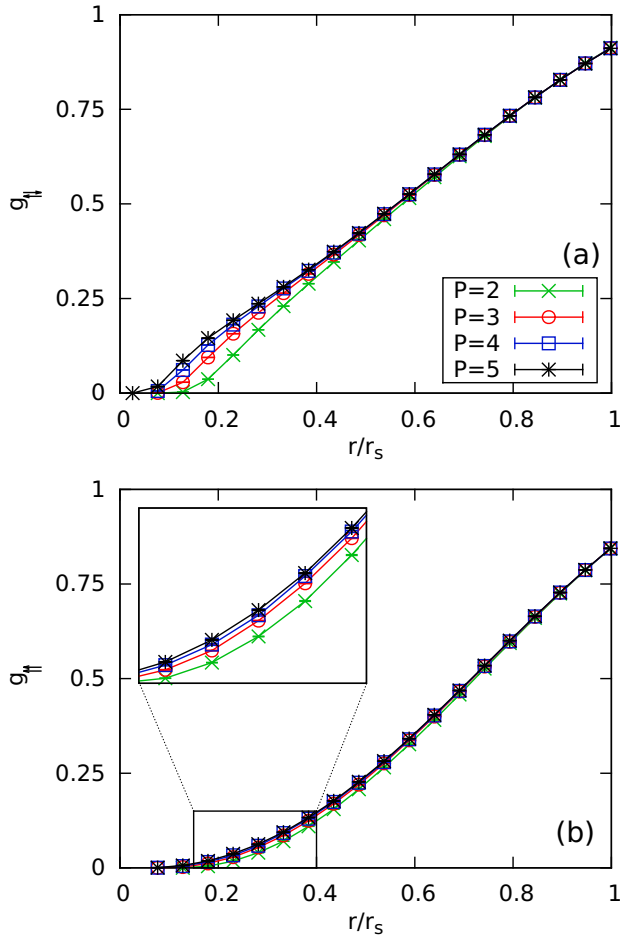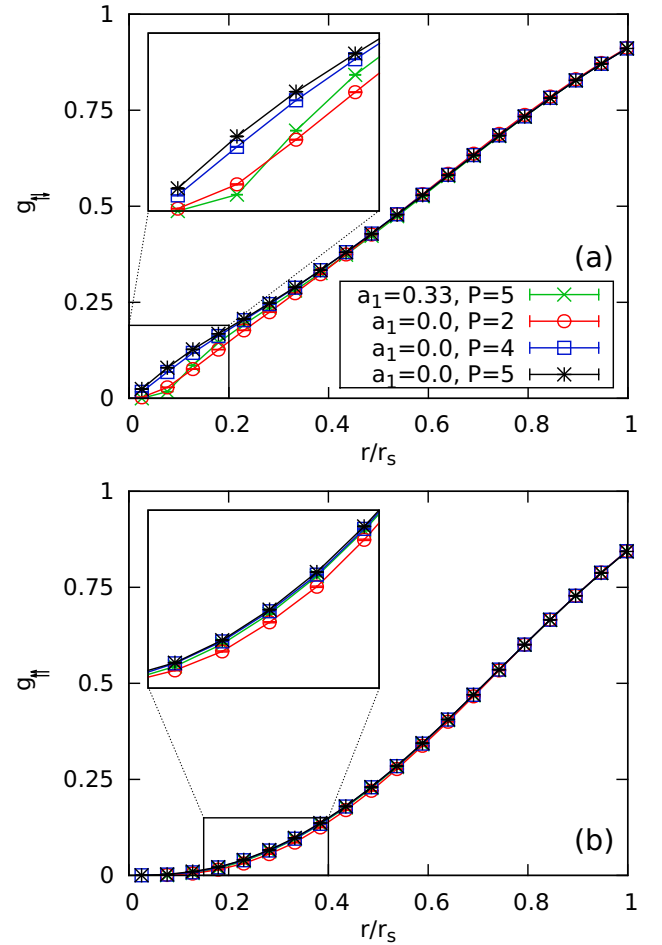FIG. 4. Convergence of the pair distribution function for $N = 4$ unpolarized electrons at $\theta = 1$ and $r_s = 4$—shown is the same information as in Fig. 3, but for a different combination of free parameters, i.e., $a_1 = 0$ and $t_0 = 0.04$.

terms do not directly enter. For this reason, the interspecies pair distribution function is not as drastically affected by the divergence of the $F(r) \propto 1/r^2$ terms at small r and the convergence of this quantity is significantly improved. For completeness, in panel (b) we again show results for $g_{\uparrow\uparrow}$, which, for parameter set (b), are almost converged even for two propagators. It is important to note that a relatively large factorization error in the pair distribution function does not necessarily imply a similar inaccuracy of the potential energy, since the latter is not directly computed as the integral of the pair potential $\Psi(\mathbf{r}, \mathbf{s})$ over $g(r)$. Instead, our estimator is derived as the derivative of Z, which leads to the explicit inclusion of force terms [26,27]. Furthermore, it should be understood that, while the description of the Coulomb repulsion at very short ranges is particularly challenging, this does not predominate in larger systems since the average number of particles within distance $r \in [\tilde{r}, \tilde{r} + \Delta\tilde{r})$ increases as $N(\tilde{r}) \propto \tilde{r}^2$. For $N = 66$ unpolarized electrons, which is the standard system size within this work, these effects are by far not as important and, for the same combination of r_s and θ as in Fig. 4, both the inter- and intraspecies distribution function are of much higher quality; cf. Fig. 13.

Up to this point, only data for small benchmark systems with $N = 4$ electrons have been presented. To obtain meaningful results for the UEG, we simulate $N = 66$ unpolarized electrons, which is a commonly used model system since it corresponds to a closed momentum shell and, therefore, is well suited as a starting point for an extrapolation to the thermodynamic limit (finite size corrections). In Fig. 5, the average sign, cf. Eq. (21), is plotted versus the density parameter r_s for five different temperatures. For $\theta = 2, 4, 8$, $\langle s \rangle'$ is almost equal to unity for $r_s = 40$ and decreases just a trifle towards higher density, until it saturates at $r_s \sim 0.5$. Consequently, simulations are possible over the entire density range with relatively small computational effort. The slight increase of $\langle s \rangle'$ around $r_s \in [1,10]$ is a nonideality effect:

at high density, the system is approximately ideal and the Fermi temperature θ_F is an appropriate measure for quantum degeneracy. With increasing r_s, coupling effects become more important, which leads to a stronger separation of the electrons. Thus there is less overlap of the kinetic density matrices and the determinants become exclusively positive. For $\theta = 1$, the average sign already significantly deviates from unity at $r_s = 40$ and exhibits a more severe decrease towards smaller r_s. Nevertheless, it attains a finite value $\langle s \rangle' \approx 0.01$ even at high density $r_s = 0.1$, which means that simulations are more involved but still manageable over the entire coupling range. This is in stark contrast to standard PIMC without the permutation blocking (red circles), for which the sign exhibits a sharp drop and simulations become unfeasible below $r_s \approx 5$. Finally, the green curve corresponds to $\theta = 0.75$, where PB-PIMC is capable of providing accurate results for $r_s \geqslant 3$.

B. Configuration PIMC

1. Basic idea

In this section, the main aspects of our CPIMC approach are explained. A detailed derivation of the CPIMC expansion of the partition function and the utilized Monte Carlo steps for the polarized UEG can be found in Refs. [22,24].

For CPIMC, instead of evaluating the trace of the partition function Eq. (6) in coordinate representation, we switch to second quantization and perform the trace with antisymmetrized N-particle states (Slater determinants)

$$|\{n\}\rangle = |n_1, n_2, \dots\rangle, \qquad (17)$$

with n_i being the fermionic occupation number ($n_i \in \{0,1\}$) of the ith spin orbital $|\mathbf{k}_i \sigma_i\rangle$, where we choose the ordering of orbitals such that even (odd) orbital numbers have spin-up (spin-down) $\sigma = \uparrow(\downarrow)$. In this representation, fermionic antisymmetry is automatically taken into account via the anticommutation relations of the creation and annihilation operators, and thus, an explicit antisymmetrization of the density operator is not needed. The expansion of the partition function is based on the concept of continuous time QMC, e.g., Refs. [46,47], where the Hamiltonian is split into a diagonal and off-diagonal part $\hat{H} = \hat{D} + \hat{Y}$ with respect to the chosen basis. Summing up the entire perturbation series of the density operator $e^{-\beta\hat{H}}$ in terms of $\hat{Y}$ finally yields

$$Z = \sum_{\substack{K=0, \\ K \neq 1}}^{\infty} \sum_{\{n\}} \sum_{s_1 \dots s_{K-1}} \int_0^\beta d\tau_1 \int_{\tau_1}^\beta d\tau_2 \dots \int_{\tau_{K-1}}^\beta d\tau_K$$

$$\times (-1)^K e^{-\sum_{i=0}^K D_{\{n^{(i)}\}}(\tau_{i+1} - \tau_i)} \prod_{i=1}^K Y_{\{n^{(i)}\}, \{n^{(i-1)}\}}(s_i), \quad (18)$$

with the Fock space matrix elements of the diagonal and off-diagonal operator

$$D_{\{n^{(i)}\}} = \sum_l \mathbf{k}_l^2 n_l^{(i)} + \sum_{l<k} w_{lklk}^- n_l^{(i)} n_k^{(i)}, \qquad (19)$$

$$Y_{\{n^{(i)}\}, \{n^{(i-1)}\}}(s_i) = w_{s_i}^- (-1)^{\alpha_{s_i}}. \qquad (20)$$

Here, $s_i = (pqrs)$ defines the four occupation numbers in which $\{n^{(i)}\}$ and $\{n^{(i-1)}\}$ differ, where it is $p < q$ and $r < s$.
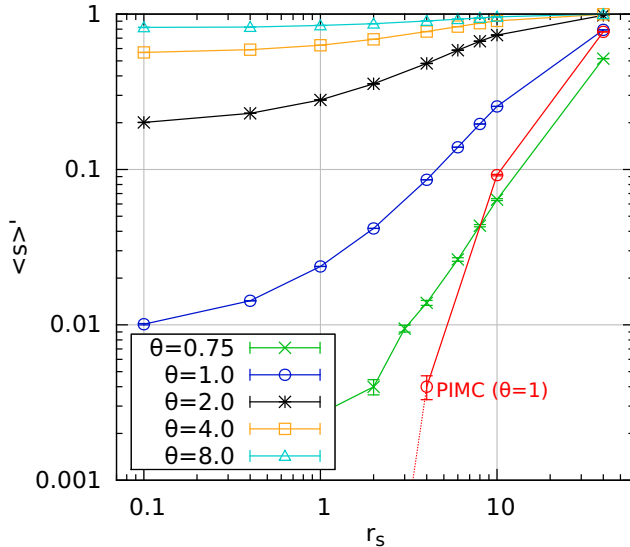

FIG. 5. Average sign for PB-PIMC simulations of $N = 66$ unpolarized electrons at different temperatures—all PB-PIMC data have been obtained for $P = 2$ with $a_1 = 0.33$ and $t_0 = 0.14$ and the standard PIMC data (red curve) have been taken from Ref. [21].
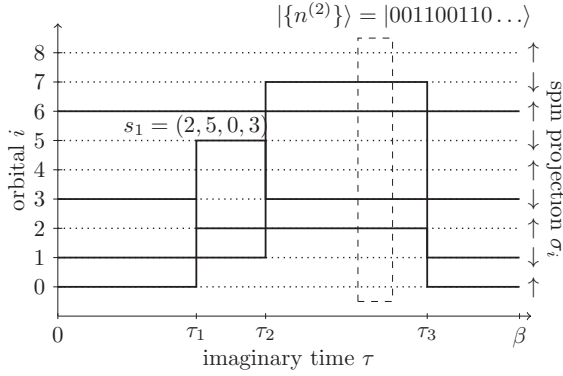
FIG. 6. Typical closed path of $N = 4$ unpolarized particles in Slater determinant (Fock) space. The state with four occupied orbitals $|\mathbf{k}_0\uparrow\rangle, |\mathbf{k}_1\downarrow\rangle, |\mathbf{k}_3\downarrow\rangle, |\mathbf{k}_6\uparrow\rangle$ undergoes a two-particle excitation s_1 at time τ_1 replacing the occupied orbitals $|\mathbf{k}_0\uparrow\rangle, |\mathbf{k}_3\downarrow\rangle$ by $|\mathbf{k}_2\uparrow\rangle, |\mathbf{k}_5\downarrow\rangle$. Two further excitations occur at τ_2 and τ_3. The states at the "imaginary times" $\tau = 0$ and $\tau = \beta$ coincide. In addition, the total spin projection is conserved at any time. All possible paths contribute to the partition function Z, Eq. (18).

In this notation, the exponent of the fermionic phase factor is given by

$$\alpha_{s_i} = \alpha_{pqrs}^{(i)} = \sum_{l=p}^{q-1} n_l^{(i-1)} + \sum_{l=r}^{s-1} n_l^{(i)}.$$

Due to the trace, each addend in Eq. (18) fulfills $\{n\} = \{n^{(0)}\} = \{n^{(K)}\}$ and hence can be interpreted as a β-periodic path in Fock space. An example of such a path for the case of an unpolarized UEG is depicted in Fig. 6. The starting determinant $\{n\}$ at $\tau = 0$ undergoes K excitations of type s_i at time τ_i, which we refer to as "kinks." The weight of each path is computed according to the second line of Eq. (18), which can be both positive and negative. Since the Metropolis algorithm [43] can only be applied to strictly positive weights, we have to take the modulus of the weights in our MC procedure and compute expectation values according to

$$\langle O \rangle = \frac{\langle Os \rangle'}{\langle s \rangle'}, \qquad (21)$$

where O is the corresponding Monte Carlo estimator of the observable, $\langle \cdot \rangle'$ denotes the expectation value with respect to the modulus weights, and s measures the sign of each path. Therefore, $\langle s \rangle'$ is the *average sign* of all sampled paths during the MC simulation. It is straightforward to show that the relative statistical error of observables computed according to Eq. (21) is inversely proportional to the average sign. As a consequence, in practice, reliable expectation values can be obtained if the average sign is larger than about 10^{-4}.

2. Application to the unpolarized UEG

The difference between CPIMC simulations of the polarized and unpolarized UEG enters basically in two ways. First, in addition to the particle number N, the total spin projection in the summation over the starting determinant $\{n^{(0)}\}$ in Eq. (18) has to be fixed, i.e., the number of spin-up $N_\uparrow$ and spin-down electrons $N_\downarrow$. Thus, if a whole occupied orbital is excited

during the MC procedure (for details, see Ref. [24]), it can only be excited to an orbital with the same spin projection. For example, orbital 6 in Fig. 6 could only be excited to orbital 8 or some higher unoccupied orbital with spin up (not pictured). Moreover, when adding a kink or changing two kinks via some two-particle excitation, it is most effective to include spin conservation in the choice of the four involved orbitals, since all other proposed excitations would be rejected due to a vanishing weight.

For the second aspect, we have to explicitly consider the modulus weight of some kink $s_i = (pqrs)$, which is given by the modulus of Eq. (20)

$$
\begin{aligned}
&|Y_{\{n^{(i)}\},\{n^{(i-1)}\}}(s_i)| \\
&= \left| \frac{1}{(\mathbf{k}_p - \mathbf{k}_r)^2} \delta_{\sigma_p,\sigma_r} \delta_{\sigma_q,\sigma_s} - \frac{1}{(\mathbf{k}_p - \mathbf{k}_s)^2} \delta_{\sigma_p,\sigma_s} \delta_{\sigma_q,\sigma_r} \right| \\
&\quad \times \frac{4\pi e^2}{L^3} \delta_{\mathbf{k}_p + \mathbf{k}_q, \mathbf{k}_r + \mathbf{k}_s},
\end{aligned} \qquad (22)
$$

where we have used the definition of the antisymmetrized two-electron integrals from Sec. II B. If all of the involved spin orbitals have the same spin projection, the Kronecker δ's due to the spin obviously equal one, and the two-electron integrals are efficiently blocked, i.e., in most (momentum conserving) cases it is $|w_{pqrs}^-| < |w_{pqrs}|$ and $|w_{pqrs}^-| < |w_{pqsr}|$. However, if the involved orbitals have different spin projections, one of the two terms in Eq. (22) is always zero and $|w_{pqrs}^-| = |w_{pqsr}|$ or $|w_{pqrs}^-| = |w_{pqrs}|$. Hence, for otherwise fixed system parameters, the average weight of kinks in the unpolarized system is significantly larger. Since the diagonal matrix elements, cf. Eq. (19), are independent of the spin, there ought to be more kinks in simulations of the unpolarized system, which in turn results in a smaller sign, because each kink enters the partition function with three possible sign changes.

We address this issue in Fig. 7, where we plot the average sign (a) and the average number of kinks (b) for the polarized (circles) and unpolarized (dots) UEG of $N = 4, 14$, and 66 electrons at $\theta = 1$. Coming from small values of r_s, the average number of kinks grows linearly with r_s. Depending on the particle number, at some critical value of r_s, it starts growing exponentially, until it eventually turns again into a linear dependency. The onset of the exponential growth is connected to a drop of the average sign due to the combinatorial growth of potential sign changes in the sampled paths with increasing number of kinks. This behavior becomes more extreme the larger the particle number, both for the polarized and unpolarized system, so that for $N = 66$ electrons (blue lines), the average number of kinks suddenly increases from less than about two to a couple of hundred, which corresponds to a drop of the average sign from almost one to below 10^{-3}. However, for the unpolarized system, the critical value of r_s at which the average sign starts dropping drastically is approximately half of that of the polarized system containing the same number of electrons. In practice, this means that for $N = 66$ polarized electrons at $\theta = 1$ direct CPIMC calculations are feasible up to $r_s \sim 0.6$, whereas for $N = 66$ unpolarizd electrons direct CPIMC is applicable only up to $r_s \sim 0.3$.
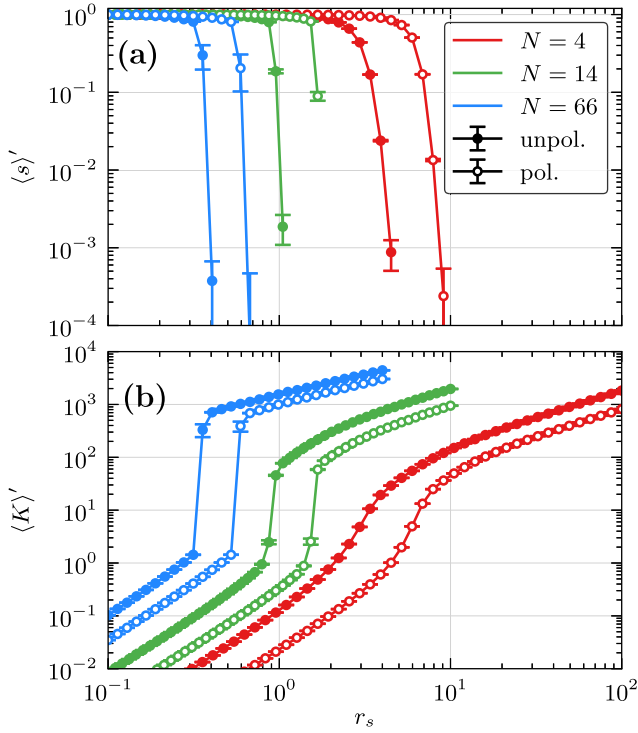
FIG. 7. Average sign (a) and average number of kinks (b) of direct CPIMC, plotted versus the density parameter for three different particle numbers $N = 4, 14, 66$ in $N_B = 2109, 4169, 5575$ plane wave basis functions, respectively, at $\theta = 1$. Shown are the results from the simulation of the polarized (circles) and unpolarized (dots) UEG, where for the unpolarized case $2N_B$ spin orbitals have been used.

3. Auxiliary kink potential

In Ref. [22], it has been shown that the use of an auxiliary kink potential of the form

$$V_{\delta,\kappa}(K) = \frac{1}{e^{-\delta(\kappa - K + 0.5)} + 1} \tag{23}$$

significantly extends the applicability range of our CPIMC method towards larger values of r_s. This is achieved by adding the potential to the second line of the partition function Eq. (18), i.e., multiplying the weight of each path with the potential. Obviously, since $V_{\delta,\kappa}(K) \to 1$ in the limit $\kappa \to \infty$, performing CPIMC simulations for increasing values of κ at fixed δ always converges to the exact result. Yet, to ensure a monotonic convergence of the energy, it turned out that the value of δ has to be sufficiently small. Both for the polarized and unpolarized system, choosing $\delta = 1$ is sufficient. In fact, the potential is nothing but a smooth penalty for paths with a larger number of kinks than κ.

In Fig. 8, we show the convergence of (a) the internal energy (per particle), (b) the average sign, and (c) the average number of kinks with respect to the kink potential parameter κ of $N = 66$ unpolarized electrons at $r_s = 2$ and $\theta = 4$. We have performed independent CPIMC simulations for different κ, using integer values from 2 to 17. While the energy almost remains constant for $\kappa \geqslant 10$ with a corresponding average sign larger than 0.1, the average sign and number of kinks themselves clearly are not converged. Further, the

FIG. 8. Convergence of (a) the internal energy, (b) the average sign, and (c) the average number of kinks with respect to the kink potential parameter κ of $N = 66$ unpolarized electrons at $r_s = 2$ and $\theta = 4$ in $N_B = 88\,946$ spin orbitals. The potential parameter δ has been fixed to one. The blue (green) line show a horizontal (linear) fit to the last converged points. The asymptotic value (black point) in the limit $1/\kappa \to 0$ is enclosed between the blue and green lines and, within error bars, coincides with the PB-PIMC result (orange points).

direct CPIMC algorithm (without the kink potential) would give a couple of thousand kinks with a practically vanishing sign. However, for the convergence of observables like the energy, apparently, a significantly smaller number of kinks is sufficient. This can be explained by a near cancellation of all additional contributions of the sampled paths with increasing number of kinks. For a detailed analysis, see Ref. [22].

We generally observe an s-shaped convergence of observables with $1/\kappa$, where the onset of the cancellation and near convergence are clearly indicated by the change in curvature. This allows for a robust extrapolation scheme to the asymptotic limit $1/\kappa \to \infty$, which is explained in detail in Ref. [22]. An upper (lower) bound of the asymptotic value is obtained by a horizontal (linear) fit to the last points after the onset of convergence. The extrapolated result is then computed as the mean value of the lower and upper bounds with the uncertainty estimated as their difference. In Fig. 8, both, the horizontal (blue line) and linear fit (green line) almost coincide due to the complete convergence (within statistical errors) of the last points. The asymptotic CPIMC result (black dot) perfectly agrees (within error bars) with the PB-PIMC result (orange dot). This confirms the validity of using the kink potential also for the unpolarized UEG.

4. Further enhancement of the kink potential

It turns out that, in case of the unpolarized UEG, even with the use of a kink potential with $\delta = 1$, the simulation may approach paths with an extremely large number of kinks. This is demonstrated by the turquoise data points in Fig. 9(c), where
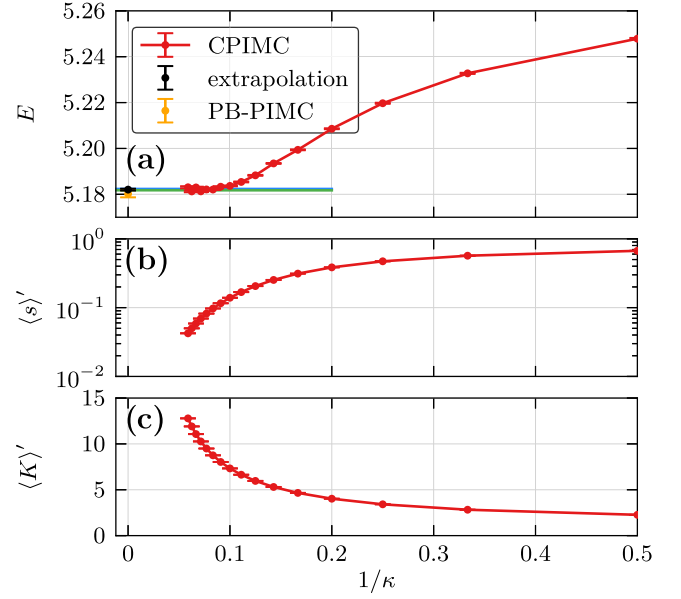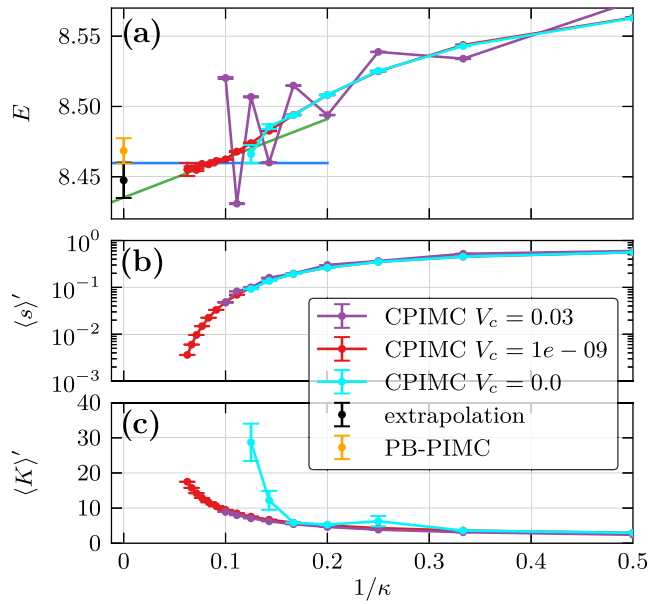
FIG. 9. Convergence of (a) the internal energy, (b) the average sign, and (c) the average number of kinks with respect to the kink potential parameter κ of $N = 66$ unpolarized electrons at $r_s = 0.8$ and $\theta = 1$ in $N_B = 11\,150$ spin orbitals. The potential parameter δ has been fixed to one. The three curves correspond to CPIMC calculations where the kink potential has been cut off at different values V_c, i.e., $V_{1,\kappa}(K)$ [cf. Eq. (23)] is set to zero if it takes values smaller than V_c. The blue (green) line shows a horizontal (linear) fit to the last converged red points. The asymptotic value (black point) in the limit $1/\kappa \rightarrow 0$ is enclosed between the blue and green lines and, within error bars, coincides with the PB-PIMC result (orange points).

the average number of kinks is shown for $N = 66$ unpolarized electrons at $\theta = 1$ and $r_s = 0.8$. For example, at $\kappa = 8$, there are on average about 30 kinks. However, increasing the penalty for paths with a number of kinks larger than κ, by increasing δ, is not a solution, since this would cause a nonmonotonic convergence, oscillating with even and odd numbers of κ, as has been demonstrated in Ref. [22]. Therefore, we choose a different strategy which is justified by the fact that paths with a very large number of kinks do not contribute to physical observables; cf. Sec. III B 3 and Ref. [22]: we cut off the potential once it has dropped below some critical value V_c, thereby completely prohibiting paths where $V_{1,\kappa}(K) < V_c$. If the cutoff value is too large, we again recover an oscillating convergence behavior of the energy with even and odd numbers of κ rendering an extrapolation difficult. This is shown by the purple data points in Fig. 9(a), where the simulations have been performed with $V_c = 0.03$ so that paths with a number of kinks larger than $\kappa + 3$ are prohibited. On the other hand, if we set $V_c = 10^{-9}$, so that paths with up to $\kappa + 20$ kinks are allowed, the oscillations vanish (within statistical errors) and we can again apply our extrapolation scheme. Indeed, even with the additional cutoff the extrapolated value (black dot) coincides with that of the PB-PIMC simulation (orange dot) within error bars. In all simulations presented below we have carefully verified that the cutoff value is sufficiently small to guarantee converged results.

To summarize, as for the polarized UEG [22], the accessible range of density parameters r_s of our CPIMC method can be extended by more than a factor two by the use of a suitable kink potential, in simulations of the unpolarized UEG as well. For example, at $\theta = 1$ direct CPIMC simulations are feasible up to $r_s \sim 0.3$, see Fig. 7, whereas the kink potential allows us to obtain accurate energies up to $r_s = 0.8$, as demonstrated in Fig. 9. In addition to the extrapolation scheme that has been introduced before for the spin-polarized case [22], we have cut off the potential at a sufficiently small value to prevent the simulation paths from approaching extremely large numbers of kinks. We expect this enhancement of CPIMC to be useful for arbitrary systems. In particular, it will allow us to further extend our previous results for the polarized UEG to larger r_s values.

IV. COMBINED CPIMC AND PB-PIMC RESULTS

A. Exchange-correlation energy

The exchange-correlation energy per particle, E_{xc}, of the uniform electrons gas is of central importance for the construction of density functionals and, therefore, has been the subject of numerous previous studies, e.g., Refs. [21,22,25,48–50]. It is defined as the difference between the total energy of the correlated system and the ideal energy U_0,

$$E_{\text{xc}} = E - U_0 . \tag{24}$$

In Fig. 10(a), we show results for this quantity for six different temperatures in dependence on the density parameter r_s. All data are also available in Table I in the Appendix. In order to fully exploit the complementary nature of our two approaches, we always present the most accurate data from either CPIMC (dots) or PB-PIMC (crosses). This allows us to cover the entire density range for $\theta \geqslant 1$, since here, the two methods allow for an overlap with respect to r_s. For completeness, we mention that the apparently larger statistical uncertainty for $\theta = 8$ in comparison to lower temperature is not a peculiar manifestation of the FSP, but, instead, an artifact due to the definition (24). At high temperature, the system becomes increasingly ideal and, therefore, the total energy E approaches U_0. To obtain E_{xc} at $\theta = 8$, a large part of E is subtracted, which, obviously, means that the comparatively small remainder is afflicted with a larger relative statistical uncertainty.

To illustrate the overlap between PB-PIMC and CPIMC, we show all available data points for $\theta = 1$ for both methods in panel (b). This is the lowest temperature for which this is possible and, therefore, the most difficult example, because the systematic propagator error from PB-PIMC at small r_s is most significant here. Evidently, both data sets are in excellent agreement with each other and the deviations are well within the error bars. Although we do expect that the increase of the PB-PIMC factorization error for small r_s, cf. Fig. 2, should become less severe for larger systems, any systematic trend is masked by the sign problem anyway and cannot clearly be resolved for the given statistical uncertainty.

Let us now consider temperatures below $\theta = 1$. For $\theta = 0.75$, CPIMC is applicable only for $r_s \leqslant 0.7$, while PB-PIMC delivers accurate results for $r_s \geqslant 3$. Thus the intermediate regime remains, without further improvements, out of reach
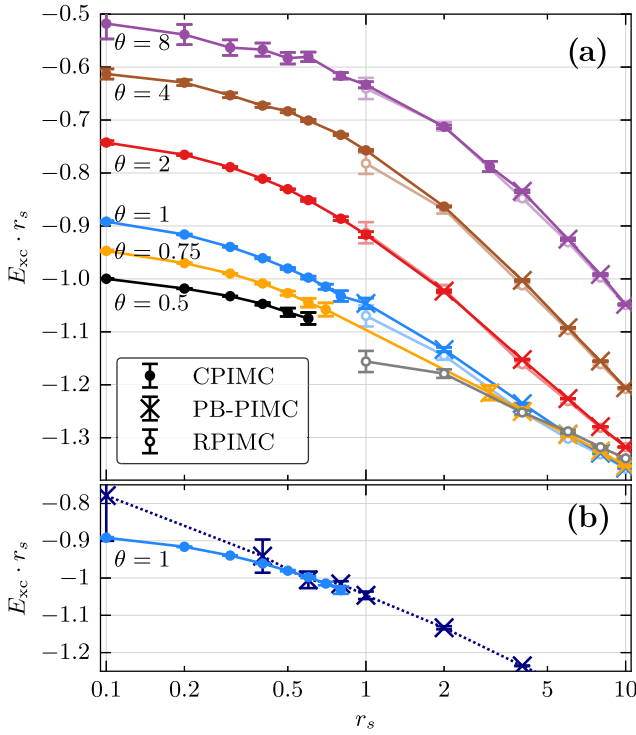
FIG. 10. Exchange-correlation energy E_{xc} times r_s of the unpolarized $N = 66$ particle UEG over the density parameter r_s for different temperatures. In graphic (a), only the best results from CPIMC (dots) or PB-PIMC (crosses) calculations are shown; cf. Table I in the Appendix. In addition, RPIMC results by Brown *et al.* [21,51] are plotted for comparison (lines with light colors and open circles). Graphic (b) also shows PB-PIMC data for $r_s < 1$ at $\theta = 1$.

FIG. 11. Kinetic (a) and potential (b) energy of the unpolarized $N = 66$ particle UEG over the density parameter r_s for different temperatures. Panel (c) shows the relative difference between our results and RPIMC data by Brown *et al.* [21,51].

and, for $\theta = 0.5$, PB-PIMC is not applicable for $N = 66$ unpolarized electrons in this density regime at all.

The comparison of our combined results to the RPIMC data by Brown *et al.* [21], which are available for $r_s \geqslant 1$, reveals excellent agreement for the three highest temperatures, $\theta = 2, 4, 8$. For $\theta = 1$, all results are still within single error bars, but the RPIMC data appear to be systematically too low. This observation is confirmed for $\theta = 0.5$, where the fixed node approximation seems to induce an even more significant drop of E_{xc}. For completeness, we mention that although a similar trend has been found for the spin-polarized UEG as well [22,25,27], the overall agreement between RPIMC and our independent results is a little better for the unpolarized case.

Finally, we consider the kinetic and potential contribution, K and V, to the total energy separately. In Fig. 11(a), the kinetic energy in units of the ideal energy U_0 is plotted versus r_s and we again observe a smooth connection of the PB-PIMC (crosses) and CPIMC (dots) data for all four shown temperatures. The RPIMC data (circles), on the other hand, exhibit clear deviations and are systematically too low even for $r_s = 10$. In panel (b), we show the same information for the potential energy, but the large V range prevents us from resolving any differences between the different data sets. For this reason, in panel (c), we explicitly show the relative differences
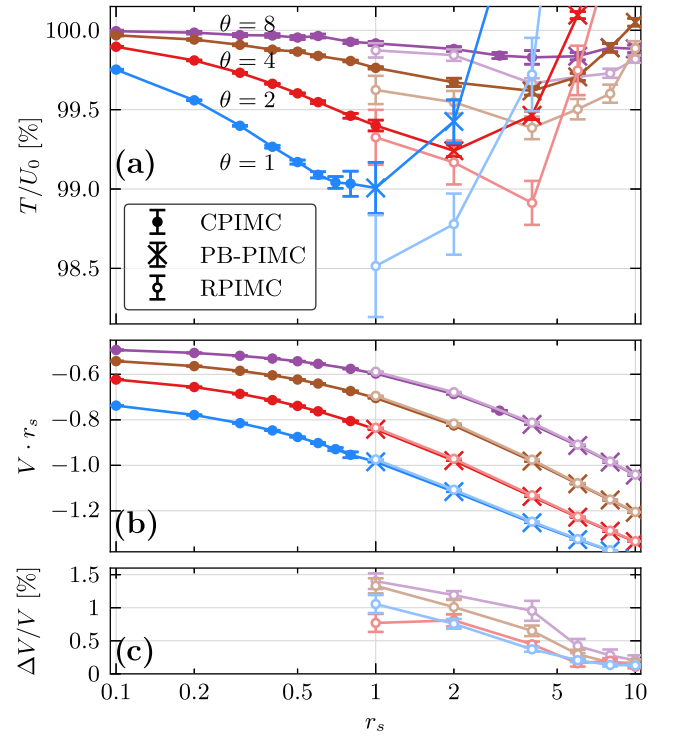
between our results and those from RPIMC. Evidently, the latter are systematically too high and the relative deviations increase with density exceeding $\Delta V/V = 1\%$. Curiously, $\Delta V/V$ attains its largest value for the highest temperature, $\theta = 8$, which contradicts the usual assumption that the nodal error decreases with increasing θ. Yet, in case of the exchange correlation energy, cf. Fig. 10, this trend seems to hold.

To explicitly demonstrate that the observed discrepancy between our results and the RPIMC data is not due to the systematic propagator error of PB-PIMC, in Fig. 12 we show all available data from CPIMC and PB-PIMC over the entire r_s range for two representative temperatures, $\theta = 1$ and $\theta = 4$. Evidently, the kinetic energy of our two methods is in excellent agreement (i.e., within the statistical uncertainty) even at small r_s, where the propagator error is expected to be most pronounced (cf. Fig. 2), whereas the RPIMC data clearly deviates. In panel (c), we show the relative differences in the potential energy between the PB-PIMC and CPIMC (dots) as well as between the PB-PIMC and RPIMC results (circles). Again, it can be seen that the PB-PIMC results agree with the exact CPIMC results, where they are available, while the RPIMC data are significantly too large for both $\theta = 1$ and $\theta = 4$.

We summarize that, while RPIMC exhibits significant deviations for both K and V separately, these almost exactly cancel and, therefore, the total energy (and E_{xc}) is in rather good agreement with our results. This trend is in agreement with previous observations for the spin-polarized case [27].
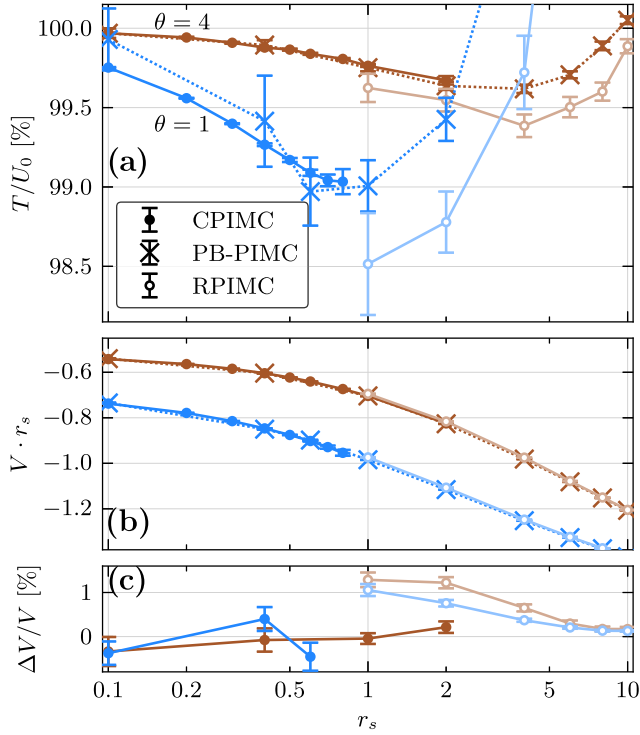
FIG. 12. Kinetic (a) and potential (b) energy of the unpolarized $N = 66$ particle UEG over the density parameter r_s for two different temperatures. As a supplement to Fig. 11, we show all available data points from CPIMC and PB-PIMC to illustrate their agreement where both approaches are available. Panel (c) shows the relative difference between the potential energy from PB-PIMC and CPIMC (filled dots) as well as between PB-PIMC and RPIMC (empty dots).

B. Pair distribution function

Up to this point, we have compared RPIMC data for various energies (E_{xc}, V, K) to our independent results. However, since only the total energy was in agreement while V and K both deviated, it remains an open question how other thermodynamic quantities are affected by the fixed node approximation. To address this issue, in Fig. 13 we show results for the pair distribution function (PDF) of the $N = 66$ unpolarized electrons at $r_s = 4$ and $\theta = 1$. This appears to be the most convenient parameter combination for a comparison since, on the one hand, there are significant differences for both K and V while, on the other hand, simulations with PB-PIMC are possible up to $P = 4$, which should allow for accurate results of both $g_{\uparrow\uparrow}$ and $g_{\uparrow\downarrow}$. In panel (a), the interspecies PDF $g_{\uparrow\downarrow}$ is plotted versus r and shown are PB-PIMC results for $P = 3$ (green crosses) and $P = 4$ (red squares) as well as RPIMC data (blue circles) from Ref. [21]. All three curves agree rather well and exhibit a distinct exchange correlation hole for $r \lesssim 1.5r_s$ and a featureless approach to unity at larger distances. The inset shows the short range part of the PDF, which is the only segment where deviations are visible. The PB-PIMC results for $P = 3$ and $P = 4$ are within each others' error bars and, for the smallest resolved r, slightly below the RPIMC data, although this trend hardly exceeds twice the error bars as well. The results for the intraspecies PDF $g_{\uparrow\uparrow}$ show a similar picture, although short range configurations of two
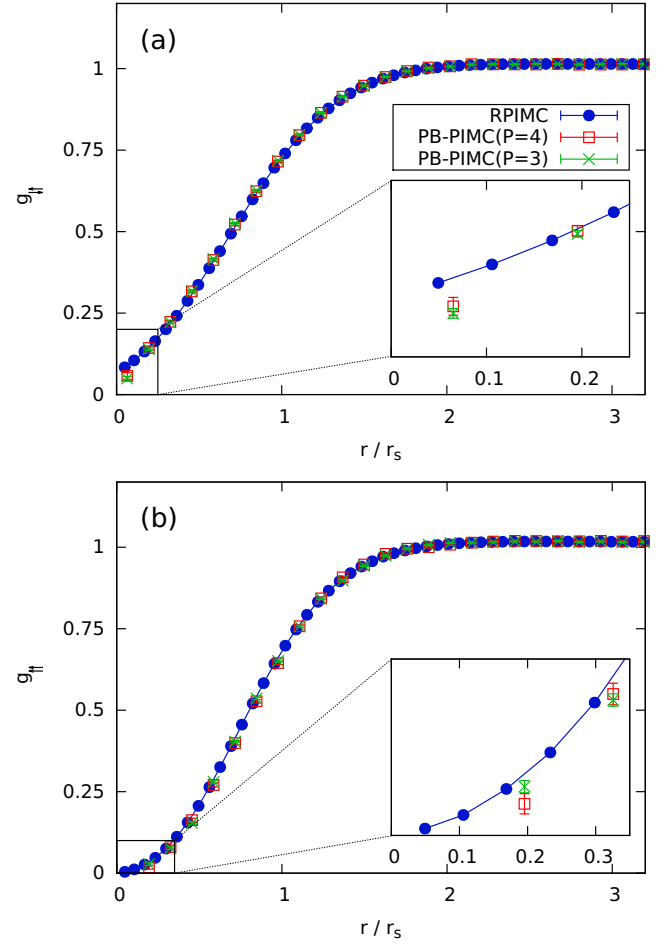
FIG. 13. Pair distribution function of $N = 66$ unpolarized electrons at $r_s = 4$ and $\theta = 1$—the PB-PIMC results have been obtained for $t_0 = 0.04$ and $a_1 = 0$, and the RPIMC data are taken from Ref. [21].

particles are even more suppressed due to the Pauli blocking. Again, there appears a slight difference between PB-PIMC and RPIMC, which, however, cannot clearly be resolved within the given statistical uncertainty. Therefore, we conclude that our independent simulation data are in good agreement with the fixed node approximation for both pair distribution functions despite the observed deviations in K and V for these particular system parameters.

V. DISCUSSION

In summary, we have successfully extended the combination of PB-PIMC and CPIMC, presented in paper I, to the unpolarized UEG and, thereby, presented different independent *ab initio* results at finite temperature.

For the unpolarized UEG, CPIMC suffers from a significantly more severe FSP due to the increased configuration weight of interspecies kinks. To overcome this problem, we have developed an additional enhancement of our extrapolation scheme. The introduction of a (very small) cutoff parameter V_c in the auxiliary kink potential prevents the number of kinks from diverging and, thereby, significantly extends the parameter range where simulations are feasible.

Furthermore, we note that in the warm dense matter regime with $N = 66$ the PB-PIMC approach, due to the FSP, is restricted to only two or three propagators. Hence, the asymptotic P^{-4}-convergence behavior of the utilized factorization scheme is not yet reached. Therefore, the presented PB-PIMC data are afflicted with an in principle uncontrolled systematic factorization error, which is particularly increased at high density ($r_s < 1$) compared to the spin-polarized case. However, the empirical optimization of the two free parameters (t_0 and a_1) still allows for accurate results, as we have demonstrated in detail in Figs. 1 and 2 for $N = 4$, where a maximum systematic factorization error (for $P = 2$) of $\Delta V/V \lesssim 3 \times 10^{-3}$ was observed. For larger systems, $N = 66$, CPIMC and PB-PIMC are in good agreement, where both are available (see Fig. 12). In particular, even at high density, where the factorization error of PB-PIMC with $P = 2$ is expected to be most pronounced, both agree within statistical uncertainty. This is a strong indication that the combination of both methods allows for accurate results over the entire density range, for $\theta \geqslant 1$ and $N = 66$ electrons.

Overall, the existing RPIMC data for the exchange correlation energy are in better agreement with our results than for the spin-polarized UEG, but there seems to be a similar unphysical systematic drop around $r_s = 1$ at low temperatures. Interestingly, the separate kinetic and potential contributions to the energy substantially deviate from our results by more than one percent. This is illustrated in Fig. 12, where, at $\theta = 4$ and intermediate r_s, CPIMC and PB-PIMC are within

error bars, whereas RPIMC significantly deviates from both. Furthermore, we have presented a comparison of the pair distribution functions $g_{\uparrow\uparrow}(r)$ and $g_{\uparrow\downarrow}(r)$, which are in good agreement with RPIMC.

It remains an important issue of future work to perform an extrapolation to the macroscopic limit, i.e., the development of finite-size corrections, e.g., [31–33]. To this end simulations with substantially larger particle numbers are required which should be possible with the presented enhancements. Furthermore, we expect that the presented combination of the complementary CPIMC and PB-PIMC approaches can be successfully applied to numerous other Fermi systems, such as two-component plasmas [52–54] and atoms embedded in jellium [55–57].

APPENDIX

As a supplement to Figs. 10 and 11, we have listed all combined simulation data from PB-PIMC and CPIMC in Table I.

TABLE I. Energies per particle for $N = 66$ unpolarized electrons: ideal energy, U_0, kinetic energy, T, potential energy, V, and exchange-correlation energy E_{xc}. While the unmarked results correspond to standard CPIMC simulations (without the auxiliary kink potential), the "a" marks CPIMC results that have been obtained by the extrapolation as explained in Sec. III B 3 and Ref. [22]. For the latter values, the error includes systematic effects. All other errors correspond to a 1σ standard deviation. A "b" marks results from PB-PIMC calculations. For CPIMC results, the utilized number of basis functions N_B is given in the last column and has been fixed for the same temperature. The ideal energies have been computed using the same number of basis functions as for the interacting system. Energies in units of Ryd.

θ	r_s	U_0	T	V	E_{xc}	N_B
0.50	0.1	374.8592(12)	373.463(6)	$-8.60129(19)$	$-9.997(6)$	11150
0.50	0.2	93.71481(30)	93.1294(25)	$-4.506(4)$	$-5.0911(25)$	11150
0.50	0.3	41.65102(13)	$41.3226(28)^a$	$-3.1130(10)^a$	$-3.4421(9)^a$	11150
0.50	0.4	23.42870(8)	$23.2220(29)^a$	$-2.409(4)^a$	$-2.618(6)^a$	11150
0.50	0.5	14.99437(5)	$14.871(18)^a$	$-1.992(20)^a$	$-2.126(16)^a$	11150
0.50	0.6	10.412756(34)	$10.327(15)^a$	$-1.702(33)^a$	$-1.791(19)^a$	11150
0.75	0.1	495.690(4)	494.119(16)	$-7.90080(19)$	$-9.472(17)$	11150
0.75	0.2	123.9225(10)	123.2322(29)	$-4.16057(12)$	$-4.8508(31)$	11150
0.75	0.3	55.0767(5)	$54.672(4)^a$	$-2.89413(31)^a$	$-3.2999(14)^a$	11150
0.75	0.4	30.98062(26)	$30.712(4)^a$	$-2.2506(18)^a$	$-2.5215(30)^a$	11150
0.75	0.5	19.82760(17)	$19.637(4)^a$	$-1.858(5)^a$	$-2.054(8)^a$	11150
0.75	0.6	13.76916(12)	$13.632(10)^a$	$-1.601(17)^a$	$-1.741(14)^a$	11150
0.75	0.7	10.11612(9)	$10.018(18)^a$	$-1.400(23)^a$	$-1.511(18)^a$	11150
0.75	3.0	0.550767(5)	$0.556(5)^b$	$-0.4098(8)^b$	$-0.405(5)^b$	
0.75	4.0	0.3098060(26)	$0.3173(18)^b$	$-0.3201(4)^b$	$-0.3127(18)^b$	
0.75	6.0	0.1376920(12)	$0.1469(6)^b$	$-0.22488(13)^b$	$-0.2157(5)^b$	
0.75	8.0	0.0774520(7)	$0.08610(19)^b$	$-0.17428(6)^b$	$-0.16563(19)^b$	
0.75	10.0	0.0495690(4)	$0.05687(9)^b$	$-0.142666(28)^b$	$-0.13536(9)^b$	
1.00	0.1	623.230(6)	621.686(15)	$-7.37511(9)$	$-8.918(17)$	11150
1.00	0.2	155.8074(15)	155.1203(34)	$-3.89359(12)$	$-4.581(4)$	11150
1.00	0.3	69.2477(7)	68.8312(18)	$-2.71561(11)$	$-3.1322(19)$	11150

TABLE I. (*Continued.*)

θ	r_s	U_0	T	V	E_{xc}	N_B
1.00	0.4	38.9518(4)	38.6661(33)[a]	−2.1165(8)[a]	−2.4025(25)[a]	11150
1.00	0.5	24.92918(24)	24.7222(32)[a]	−1.7508(17)[a]	−1.961(4)[a]	11150
1.00	0.6	17.31193(17)	17.1543(34)[a]	−1.503(4)[a]	−1.663(4)[a]	11150
1.00	0.7	12.71897(12)	12.597(5)[a]	−1.327(10)[a]	−1.450(7)[a]	11150
1.00	0.8	9.73796(9)	9.644(8)[a]	−1.192(16)[a]	−1.290(13)[a]	11150
1.00	1.0	6.23230(6)	6.170(10)[b]	−0.9844(10)[b]	−1.046(10)[b]	
1.00	2.0	1.558074(15)	1.5491(21)[b]	−0.55777(28)[b]	−0.5667(21)[b]	
1.00	4.0	0.389518(4)	0.39370(21)[b]	−0.31304(5)[b]	−0.30886(21)[b]	
1.00	6.0	0.1731190(17)	0.17863(15)[b]	−0.22107(4)[b]	−0.21556(15)[b]	
1.00	8.0	0.0973800(9)	0.10313(6)[b]	−0.171900(18)[b]	−0.16615(6)[b]	
1.00	10.0	0.0623230(6)	0.067639(31)[b]	−0.141041(11)[b]	−0.135725(31)[b]	
2.00	0.1	1155.227(11)	1154.031(32)	−6.22959(19)	−7.425(33)	18342
2.00	0.2	288.8066(28)	288.258(7)	−3.27971(9)	−3.828(7)	18342
2.00	0.3	128.3585(12)	128.0151(35)	−2.28648(6)	−2.630(4)	18342
2.00	0.4	72.2017(7)	71.9583(17)	−1.78368(6)	−2.0270(18)	18342
2.00	0.5	46.2091(4)	46.0256(11)	−1.47771(6)	−1.6612(11)	18342
2.00	0.6	32.08963(31)	31.9444(29)[a]	−1.27090(35)[a]	−1.419(4)[a]	18342
2.00	0.8	18.05042(17)	17.9532(27)[a]	−1.0069(11)[a]	−1.108(4)[a]	18342
2.00	1.0	11.55227(11)	11.483(4)[a]	−0.8440(32)[a]	−0.916(5)[a]	18342
2.00	2.0	2.888066(28)	2.8661(11)[b]	−0.48960(21)[b]	−0.5115(11)[b]	
2.00	4.0	0.722017(7)	0.71815(19)[b]	−0.28421(6)[b]	−0.28807(20)[b]	
2.00	6.0	0.3208960(31)	0.32120(7)[b]	−0.204649(24)[b]	−0.20434(8)[b]	
2.00	8.0	0.1805040(17)	0.18183(4)[b]	−0.161212(15)[b]	−0.15989(4)[b]	
2.00	10.0	0.1155230(11)	0.117282(28)[b]	−0.133507(13)[b]	−0.131748(32)[b]	
4.00	0.1	2245.508(30)	2244.80(9)	−5.42045(19)	−6.13(10)	88946
4.00	0.2	561.377(8)	561.050(26)	−2.81969(9)	−3.147(27)	88946
4.00	0.3	249.5008(34)	249.272(14)	−1.94887(8)	−2.177(15)	88946
4.00	0.4	140.3442(19)	140.173(8)	−1.51066(7)	−1.682(8)	88946
4.00	0.5	89.8203(12)	89.699(6)	−1.24591(7)	−1.367(6)	88946
4.00	0.6	62.3752(8)	62.275(4)	−1.06761(6)	−1.168(4)	88946
4.00	0.8	35.0861(5)	35.0182(19)	−0.84205(6)	−0.9099(19)	88946
4.00	1.0	22.45508(30)	22.4019(15)	−0.70405(7)	−0.7572(16)	88946
4.00	2.0	5.61377(8)	5.5953(15)[a]	−0.41230(33)[a]	−0.4317(4)[a]	88946
4.00	4.0	1.403442(19)	1.3981(4)[b]	−0.24535(17)[b]	−0.2507(4)[b]	
4.00	6.0	0.623752(8)	0.62192(14)[b]	−0.18022(7)[b]	−0.18205(16)[b]	
4.00	8.0	0.350861(5)	0.35047(9)[b]	−0.14402(4)[b]	−0.14441(11)[b]	
4.00	10.0	0.2245510(30)	0.22466(5)[b]	−0.120675(31)[b]	−0.12056(7)[b]	
8.00	0.1	4445.13(11)	4444.88(27)	−4.93048(19)	−5.18(29)	147050
8.00	0.2	1111.281(27)	1111.12(9)	−2.52994(12)	−2.69(10)	147050
8.00	0.3	493.903(12)	493.75(5)	−1.72864(9)	−1.88(5)	147050
8.00	0.4	277.820(7)	277.730(30)	−1.32690(8)	−1.417(31)	147050
8.00	0.5	177.805(4)	177.724(22)	−1.08505(7)	−1.166(22)	147050
8.00	0.6	123.4757(30)	123.431(15)	−0.92338(6)	−0.968(15)	147050
8.00	0.8	69.4551(17)	69.404(7)	−0.71997(5)	−0.771(8)	147050
8.00	1.0	44.4513(11)	44.415(6)	−0.59679(5)	−0.633(6)	147050
8.00	2.0	11.11281(27)	11.0997(16)	−0.34329(5)	−0.3564(16)	147050
8.00	3.0	4.93903(12)	4.9312(9)[a]	−0.2532(5)[a]	−0.2626(33)[a]	147050
8.00	4.0	2.77820(7)	2.7746(6)[b]	−0.20502(29)[b]	−0.2086(6)[b]	
8.00	6.0	1.234757(30)	1.23274(28)[b]	−0.15214(15)[b]	−0.1542(4)[b]	
8.00	8.0	0.694551(17)	0.69379(18)[b]	−0.12321(10)[b]	−0.12396(23)[b]	
8.00	10.0	0.444513(11)	0.44399(11)[b]	−0.10430(7)[b]	−0.10482(13)[b]	

---

[1] L. B. Fletcher *et al.*, Observations of Continuum Depression in Warm Dense Matter with X-ray Thomson Scattering, Phys. Rev. Lett. **112**, 145004 (2014).

[2] D. Kraus *et al.*, Probing the Complex Ion Structure in Liquid Carbon at 100 GPa, Phys. Rev. Lett. **111**, 255501 (2013).

[3] S. P. Regan *et al.*, Inelastic X-Ray Scattering from Shocked Liquid Deuterium, Phys. Rev. Lett. **109**, 265003 (2012).

[4] J. D. Lindl *et al.*, The physics basis for ignition using indirect-drive targets on the National Ignition Facility, Phys. Plasmas **11**, 339 (2004).

[5] S. X. Hu, B. Militzer, V. N. Goncharov, and S. Skupsky, First-principles equation-of-state table of deuterium for inertial confinement fusion applications, Phys. Rev. B **84**, 224109 (2011).

[6] O. A. Hurricane *et al.*, Fuel gain exceeding unity in an inertially confined fusion implosion, Nature (London) **506**, 343 (2014).

[7] R. Nora *et al.*, Gigabar Spherical Shock Generation on the OMEGA Laser, Phys. Rev. Lett. **114**, 045001 (2015).

[8] M. R. Gomez *et al.*, Experimental Demonstration of Fusion-Relevant Conditions in Magnetized Liner Inertial Fusion, Phys. Rev. Lett. **113**, 155003 (2014).

[9] P. F. Schmit *et al.*, Understanding Fuel Magnetization and Mix Using Secondary Nuclear Reactions in Magneto-Inertial Fusion, Phys. Rev. Lett. **113**, 155004 (2014).

[10] R. Ernstorfer *et al.*, The formation of warm dense matter: Experimental evidence for electronic bond hardening in gold, Science **323**, 1033 (2009).

[11] M. D. Knudson, M. P. Desjarlais, R. W. Lemke, T. R. Mattsson, M. French, N. Nettelmann, and R. Redmer, Probing the Interiors of the Ice Giants: Shock Compression of Water to 700 GPa and 3.8 **g**/cm^3, Phys. Rev. Lett. **108**, 091102 (2012).

[12] B. Militzer *et al.*, A massive core in jupiter predicted from first-principles simulations, Astrophys. J. **688**, L45 (2008).

[13] N. Nettelmann, A. Becker, B. Holst, and R. Redmer, Jupiter models with improved ab initio hydrogen equation of state (H-REOS.2), Astrophys. J. **750**, 52 (2012).

[14] E. Y. Loh, J. E. Gubernatis, R. T. Scalettar, S. R. White, D. J. Scalapino, and R. L. Sugar, Sign problem in the numerical simulation of many-electron systems, Phys. Rev. B **41**, 9301 (1990).

[15] M. Troyer and U. J. Wiese, Computational Complexity and Fundamental Limitations to Fermionic Quantum Monte Carlo Simulations, Phys. Rev. Lett. **94**, 170201 (2005).

[16] D. M. Ceperley, Fermion nodes, J. Stat. Phys. **63**, 1237 (1991).

[17] B. Militzer and E. L. Pollock, Variational density matrix method for warm, condensed matter: Application to dense hydrogen, Phys. Rev. E **61**, 3470 (2000).

[18] B. Militzer, Ph.D. dissertation, University of Illinois at Urbana-Champaign, 2000.

[19] V. S. Filinov, Cluster expansion for ideal Fermi systems in the 'fixed-node approximation', J. Phys. A: Math. Gen. **34**, 1665 (2001).

[20] V. S. Filinov, Analytical contradictions of the fixed-node density matrix, High Temp. **52**, 615 (2014).

[21] E. W. Brown, B. K. Clark, J. L. DuBois, and D. M. Ceperley, Path-Integral Monte Carlo Simulation of the Warm Dense Homogeneous Electron Gas, Phys. Rev. Lett. **110**, 146405 (2013).

[22] S. Groth, T. Schoof, T. Dornheim, and M. Bonitz, *Ab initio* quantum Monte Carlo simulations of the uniform electron gas without fixed nodes, Phys. Rev. B **93**, 085102 (2016).

[23] T. Schoof, M. Bonitz, A. V. Filinov, D. Hochstuhl, and J. W. Dufty, Configuration path integral Monte Carlo, Contrib. Plasma Phys. **51**, 687 (2011).

[24] T. Schoof, S. Groth and M. Bonitz, Towards *ab initio* thermodynamics of the electron gas at strong degeneracy, Contrib. Plasma Phys. **55**, 136 (2015).

[25] T. Schoof, S. Groth, J. Vorberger, and M. Bonitz, *Ab Initio* Thermodynamic Results for the Degenerate Electron Gas at Finite Temperature, Phys. Rev. Lett. **115**, 130402 (2015).

[26] T. Dornheim, S. Groth, A. Filinov, and M. Bonitz, Permutation blocking path integral Monte Carlo: A highly efficient approach to the simulation of strongly degenerate non-ideal fermions, New J. Phys. **17**, 073017 (2015).

[27] T. Dornheim, T. Schoof, S. Groth, A. Filinov, and M. Bonitz, Permutation blocking path integral Monte Carlo approach to the uniform electron gas at finite temperature, J. Chem. Phys. **143**, 204101 (2015).

[28] V. M. Zamalin, G. E. Norman, and V. S. Filinov, *The Monte-Carlo Method in Statistical Thermodynamics* (Nauka, Moscow, 1977).

[29] D. M. Ceperley, Path integrals in the theory of condensed helium, Rev. Mod. Phys. **67**, 279 (1995).

[30] D. M. Ceperley and B. J. Alder, Ground State of the Electron Gas by a Stochastic Method, Phys. Rev. Lett. **45**, 566 (1980).

[31] Louisa M. Fraser, W. M. C. Foulkes, G. Rajagopal, R. J. Needs, S. D. Kenny, and A. J. Williamson, Finite-size effects and Coulomb interactions in quantum Monte Carlo calculations for homogeneous systems with periodic boundary conditions, Phys. Rev. B **53**, 1814 (1996).

[32] N. D. Drummond, R. J. Needs, A. Sorouri, and W. M. C. Foulkes, Finite-size errors in continuum quantum Monte Carlo calculations, Phys. Rev. B **78**, 125106 (2008).

[33] C. Lin, F. H. Zong, and D. M. Ceperley, Twist-averaged boundary conditions in continuum quantum Monte Carlo algorithms, Phys. Rev. E **64**, 016702 (2001).

[34] N. S. Blunt, T. W. Rogers, J. S. Spencer and W. M. Foulkes, Density-matrix quantum Monte Carlo method, Phys. Rev. B **89**, 245124 (2014).

[35] F. D. Malone *et al.*, Interaction picture density matrix quantum Monte Carlo, J. Chem. Phys. **143**, 044116 (2015).

[36] M. Takahashi and M. Imada, Monte Carlo calculation of quantum systems, J. Phys. Soc. Jpn. **53**, 963 (1984).

[37] V. S. Filinov *et al.*, Thermodynamic properties and plasma phase transition in dense hydrogen, Contrib. Plasma Phys. **44**, 388 (2004).

[38] A. P. Lyubartsev, Simulation of excited states and the sign problem in the path integral Monte Carlo method, J. Phys. A: Math. Gen. **38**, 6659 (2005).

[39] M. Takahashi and M. Imada, Monte Carlo of quantum systems. II. Higher order correction, J. Phys. Soc. Jpn. **53**, 3765 (1984).

[40] S. A. Chin and C. R. Chen, Gradient symplectic algorithms for solving the Schrödinger equation with time-dependent potentials, J. Chem. Phys. **117**, 1409 (2002).

[41] K. Sakkos, J. Casulleras, and J. Boronat, High order Chin actions in path integral Monte Carlo, J. Chem. Phys. **130**, 204109 (2009).

[42] S. A. Chin, High-order path integral Monte Carlo methods for solving quantum dot problems, Phys. Rev. E **91**, 031301(R) (2015).

[43] N. Metropolis, A. W. Rosenbluth, M. N. Rosenbluth, A. H. Teller, and E. Teller, Equation of state calculations by fast computing machines, J. Chem. Phys. **21**, 1087 (1953).

[44] For completeness, we mention that, while the inclusion of the force terms in the employed fourth-order factorization significantly reduces the propagator error, it has no effect on the finite-size effects with which the well-defined thermodynamic expectation values for the periodic N-particle systems are afflicted.

[45] P. Gori-Giorgi, F. Sacchetti, and G. B. Bachelet, Analytic static structure factors and pair-correlation functions for the unpolarized homogeneous electron gas, Phys. Rev. B **61**, 7353 (2000).

[46] N. V. Prokof'ev, B. V. Svistunov, and I. S. Tupitsyn, Exact quantum Monte Carlo process for the statistics of discrete systems, Pis'ma Zh. Exp. Teor. Fiz. **64**, 853 (1996) [JETP Lett. **64**, 911 (1996)].

[47] N. V. Prokof'ev, B. V. Svistunov, and I. S. Tupitsyn, Exact, complete, and universal continuous-time worldline Monte Carlo approach to the statistics of discrete quantum systems, JETP **87**, 310 (1998).

[48] E. W. Brown, J. L. DuBois, M. Holzmann, and D. M. Ceperley, Exchange-correlation energy for the three-dimensional homogeneous electron gas at arbitrary temperature, Phys. Rev. B **88**, 081102(R) (2013).

[49] V. V. Karasiev, T. Sjostrom, J. Dufty, and S. B. Trickey, Accurate Homogeneous Electron Gas Exchange-correlation Free Energy for Local Spin-density Calculations, Phys. Rev. Lett. **112**, 076403 (2014).

[50] V. S. Filinov, V. E. Fortov, M. Bonitz, and Zh. Moldabekov, Fermionic path integral Monte Carlo results for the uniform electron gas at finite temperature, Phys. Rev. E **91**, 033108 (2015).

[51] We take the energy values from the supplement of Ref. [21] and subtract the finite size corrections. This allows for a meaningful comparison with the same model system of $N = 66$ unpolarized electrons.

[52] M. Bonitz, V. S. Filinov, V. E. Fortov, P. R. Levashov, and H. Fehske, Crystallization in Two-Component Coulomb Systems, Phys. Rev. Lett. **95**, 235006 (2005).

[53] M. A. Morales, C. Pierleoni, and D. Ceperley, Equation of state of metallic hydrogen from coupled electron-ion Monte Carlo simulations, Phys. Rev. E **81**, 021202 (2010).

[54] V. S. Filinov, M. Bonitz, H. Fehske, V. E. Fortov, and P. R. Levashov, Proton crystallization in a dense hydrogen plasma, Contrib. Plasma Phys. **52**, 224 (2012).

[55] M. J. Puska, R. M. Nieminen, and M. Manninen, Atoms embedded in an electron gas: Immersion energies, Phys. Rev. B **24**, 3037 (1981).

[56] V. U. Nazarov, C. S. Kim, and Y. Takada, Spin polarization of light atoms in jellium: Detailed electronic structures, Phys. Rev. B **72**, 233205 (2005).

[57] M. Bonitz, E. Pehlke, and T. Schoof, Attractive forces between ions in quantum plasmas: Failure of linearized quantum hydrodynamics, Phys. Rev. E **87**, 033105 (2013).

Chapter 5

Finite-Size Corrections, Static Structure Factors and Pair Correlation Functions

5.1 QMC Simulations in the Thermodynamic Limit

Hitherto, all of our QMC studies were devoted to the investigation of N electrons in a finite simulation cell subject to periodic boundary conditions[1]. However, to be of use for practical applications, for example, as input for a density functional theory calculation of a realistic warm dense matter system in the local density approximation, we had to extrapolate these data to the thermodynamic limit [190, 118].

Unfortunately, a direct extrapolation over the number of electrons is, in practice, not feasible, mainly due to two reasons: (i) the fermion sign problem leads to an exponential increase in computational cost with respect to system size and (ii) the exact functional behavior of the quantity of interest (e.g., the total or interaction energy) regarding N is not known, making an extrapolation highly unreliable. The usual strategy in this situation is the development of a so-called finite-size correction [188, 191–194], which, when added onto the data for a finite number of electrons N, approximately gives the thermodynamic limit without the need for an additional extrapolation. More specifically, Brown *et al.* [157] used the finite-temperature extension of the finite-size correction by Chiesa *et al.* [192] and presented separate results both for the kinetic and interaction contribution to the energy.

As it turned out, and is demonstrated in detail in the following paper[2], Ref. [164], these corrections are not appropriate over substantial parts of the warm dense matter regime. To

---

[1]The publication by Schoof *et al.* [59] constitutes an exception, as they performed an uncontrolled direct extrapolation to the thermodynamic limit for very high density.

[2]T. Dornheim, S. Groth, T. Sjostrom, F.D. Malone, W.M.C. Foulkes, and M. Bonitz, Phys. Rev. Lett. **117**, 156403 (2016). Copyright by the American Physical Society (2016).

overcome this issue, we investigated the main source of the system-size dependence in the interaction energy. In doing so, we found that the static structure factor (SSF) $S_N(k)$ converges remarkably well with N, and the finite-size error in $v = V/N$ is thus given by a discretization error in the integration of $S(k) \approx S_N(k)$. In particular, the main contribution is due to the small k-behavior in the SSF that cannot be accessed within our QMC simulations, which are restricted to $k \geq 2\pi/L$. To compensate for this missing contribution, we combined our QMC data with the SSF from the dielectric formalism, specifically using the Singwi–Tosi–Land–Sjölander (STLS) scheme [195], that was extended to finite temperature by Tanaka and Ichimaru [196], and is known to be exact in the limit $q \to 0$, see, e.g., Ref. [197].

This combination[3] allows for a vivid interpretation: our QMC simulations provide an exact treatment of the short-ranged exchange–correlation effects, but cannot access the long-range correlations due to the finite size of the simulation cell. In contrast, the STLS approximation captures the exact long-range behavior, but constitutes an uncontrolled approximation elsewhere. Together, this allows for the introduction of a dramatically improved finite-size correction procedure, which immediately reduces the system size dependence in our data by two orders of magnitude.

Finally, we carried out extensive new QMC simulations (using both PB-PIMC or CPIMC for strong and weak coupling, respectively) for the unpolarized electron gas at warm dense matter conditions over the entire relevant density range ($0.1 \leq r_\mathrm{s} \leq 10$) down to half the Fermi temperature, the accuracy attained being of an unprecedented order of 0.3%. As usual, we made all our results available, for example as a benchmark for the future development of other simulation methods. As an outlook, we used our new data for the interaction energy to compute the exchange–correlation free energy f_xc for fixed temperature[4], $\theta = $ const. A comparison of these results to the most recent parametrization of f_xc by Karasiev *et al.* [107] revealed systematic deviations of up to 9%, thereby highlighting the need of an improved exchange–correlation functional of the warm dense electron gas.

For completeness, I mention that the idea for the improved finite-size correction was worked out together with S. Groth in equal parts.

---

[3]Note that the STLS data throughout Ref. [164] was provided by T. Sjostrom, see also Ref. [128].

[4]I.e., $f_\mathrm{xc}^\theta(r_\mathrm{s})$, as opposed to a full parametrization with respect to temperature and density, $f_\mathrm{xc}(r_\mathrm{s}, \theta)$, which is the subject of Chpt. 6.

Ab Initio Quantum Monte Carlo Simulation of the Warm Dense Electron Gas in the Thermodynamic Limit

Tobias Dornheim,[1,*] Simon Groth,[1] Travis Sjostrom,[2] Fionn D. Malone,[3] W. M. C. Foulkes,[3] and Michael Bonitz[1]

[1]*Institut für Theoretische Physik und Astrophysik, Christian-Albrechts-Universität zu Kiel, D-24098 Kiel, Germany*
[2]*Theoretical Division, Los Alamos National Laboratory, Los Alamos, New Mexico 87545, USA*
[3]*Department of Physics, Imperial College London, Exhibition Road, London SW7 2AZ, United Kingdom*

We perform *ab initio* quantum Monte Carlo (QMC) simulations of the warm dense uniform electron gas in the thermodynamic limit. By combining QMC data with the linear response theory, we are able to remove finite-size errors from the potential energy over the substantial parts of the warm dense regime, overcoming the deficiencies of the existing finite-size corrections by Brown *et al.* [Phys. Rev. Lett. **110**, 146405 (2013)]. Extensive new QMC results for up to $N = 1000$ electrons enable us to compute the potential energy V and the exchange-correlation free energy F_{xc} of the macroscopic electron gas with an unprecedented accuracy of $|\Delta V|/|V|, |\Delta F_{xc}|/|F|_{xc} \sim 10^{-3}$. A comparison of our new data to the recent parametrization of F_{xc} by Karasiev *et al.* [Phys. Rev. Lett. **112**, 076403 (2014)] reveals significant deviations to the latter.

The uniform electron gas (UEG), consisting of electrons on a uniform neutralizing background, is one of the most important model systems in physics [1]. Besides being a simple model for metals, the UEG has been central to the development of the linear response theory and more sophisticated perturbative treatments of solids, the formulation of the concepts of quasiparticles and elementary excitations, and the remarkable successes of density functional theory (DFT)

The practical application of ground-state density functional theory in condensed matter physics, chemistry, and materials science rests on a reliable parametrization of the exchange-correlation energy of the UEG [2], which in turn is based on accurate quantum Monte Carlo (QMC) simulation data [3]. However, the charged quantum matter in astrophysical systems such as planet cores and white dwarf atmospheres [4,5] is at temperatures way above the ground state, as are inertial confinement fusion targets [6–8], laser-excited solids [9], and pressure-induced modifications of solids, such as insulator-metal transitions [10,11]. This unusual regime, in which strong ionic correlations coexist with electronic quantum effects and partial ionization, has been termed "warm dense matter" and is one of the most active frontiers in plasma physics and materials science.

The warm dense regime is characterized by the existence of two comparable length and energy scales: the mean interparticle distance $\bar{r}$ and the Bohr radius a_0; and the thermal energy $k_B T$ and the electronic Fermi energy E_F, respectively. The dimensionless parameters $r_s = \bar{r}/a_0$ and $\Theta = k_B T/E_F$ are of the order of unity. Because $\Theta \sim 1$, the use of the ground-state density functional theory is inappropriate and extensions to finite T are indispensable; these require accurate exchange-correlation functionals for finite

temperatures [12–16]. Because neither r_s nor Θ is small, there are no small parameters, and weak-coupling expansions beyond Hartree-Fock such as the Montroll-Ward (MW) and e^4 (e4) approximations [17,18] as well as the linear response theory within the random-phase approximation (RPA) break down [19,20], see Fig. 1. Finite-T Singwi-Tosi-Land-Sjölander (STLS) [21,22] local-field corrections allow for an extension to moderate coupling [22] but exhibit nonphysical behavior at short distances for moderate to low densities, so improved expressions are highly needed. Further, quantum-classical mapping [23,24] allows for semiquantitative descriptions of warm dense matter in limiting cases.

Therefore, an accurate description of warm dense matter, in general, and of the warm dense UEG, in particular, can be
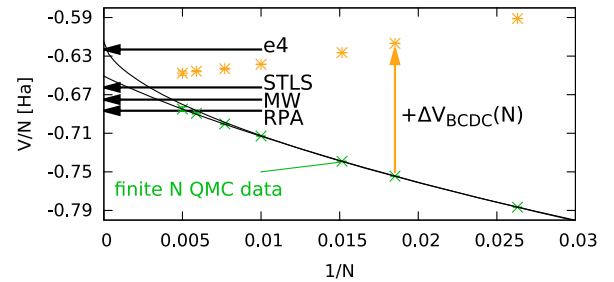

FIG. 1. Potential energy per particle of the unpolarized UEG at $\theta = 2$ and $r_s = 0.5$. The exact CPIMC results for different system sizes are indicated by green crosses; the yellow asterisks show these results after the ΔV_{BCDC} finite-size correction from Eq. (4) has been applied. The horizontal arrows refer to many-body theories (RPA, STLS [21], MW, and e4 [45]; see the text). The black lines are two different, equally plausible, extrapolations of the QMC data to infinite system size [44].

achieved only using computational approaches, primarily QMC methods which, however, are hampered by the fermion sign problem [25,26]. The pioneering QMC simulations of the warm dense UEG by Brown *et al.* [27] eliminated the sign problem by invoking the (uncontrolled) fixed-node approximation [28] but were nevertheless restricted to small systems of $N = 33$ (spin-polarized) and $N = 66$ (unpolarized) electrons and to moderate densities $r_s \geq 1$. Recently, we were able to show [29–31] that accurate simulations of these systems are possible over a broad parameter range without any nodal restriction. Our approach combines two independent methods, configuration path-integral Monte Carlo (CPIMC) calculations [32–34] and permutation blocking PIMC (PB-PIMC) calculations [35,36], which allow for accurate simulations at high ($r_s \lesssim 1$) and moderate densities ($r_s \gtrsim 1$ and $\theta \gtrsim 0.5$), respectively. An independently developed third approach, density matrix QMC [31,37,38], confirmed the excellent quality of these results. The only significant errors remaining are finite-size effects [34,39–43], which arise from the difference between the small systems simulated and the infinite [thermodynamic limit (TDL)] system of interest.

Direct extrapolation to the TDL [3,40,42] is extremely costly and also unreliable unless the form of the function to be extrapolated is known; the two black lines in Fig. 1 show two equally reasonable extrapolations [44] that reach different limits. Furthermore, the parameter-free finite-size correction (FSC) proposed in Ref. [27] [see Eq. (4) below] turns out to be inappropriate in parts of the warm dense regime. The problem is clear from inspection of the yellow asterisks in Fig. 1, which include this FSC but remain system-size dependent.

In this Letter, we close the gap between the finite-N QMC data and the TDL by deriving a highly accurate FSC for the interaction energy. This allows us to obtain precise (on the level of 0.1%) results for the exchange-correlation free energy, making possible the *ab initio* computation of arbitrary thermodynamic quantities for warm dense matter.

Theory.—Consider a finite unpolarized UEG of N electrons subject to periodic boundary conditions. The Hamiltonian is $\hat{H} = \hat{K} + \hat{V}_E$, where $\hat{K}$ is the kinetic energy of the N electrons in the cell and

$$\hat{V}_E = \frac{1}{2} \sum_{i \neq k}^{N} \phi_E(\mathbf{r}_i, \mathbf{r}_k) + \frac{1}{2} N \xi_M \quad (1)$$

is the Coulomb interaction energy per unit cell of an infinite periodic array of images of that cell. The Ewald pair potential $\phi_E(\mathbf{x}, \mathbf{y})$ and Madelung constant ξ_M are defined in Refs. [39,40]. We use Hartree atomic units throughout this work. The expected value of $\hat{V}_E/N$ carries a finite-size error [46] that is the difference between the potential energy v per electron in the infinite system and its value V_N/N in the finite system. This difference may be expressed in terms of the static structure factor (SF) as follows:

$$\frac{\Delta V_N[S(k), S_N(\mathbf{G})]}{N}$$
$$= \underbrace{\frac{1}{2} \int_{k < \infty} \frac{d\mathbf{k}}{(2\pi)^3} [S(k) - 1] \frac{4\pi}{k^2}}_{v}$$
$$- \underbrace{\left(\frac{1}{2L^3} \sum_{\mathbf{G} \neq \mathbf{0}} [S_N(\mathbf{G}) - 1] \frac{4\pi}{G^2} + \xi_M \right)}_{V_N/N}, \quad (2)$$

where L and $\mathbf{G}$ are, respectively, the length and reciprocal lattice vector of the simulation cell and $S(k)$ [$S_N(\mathbf{G})$] is the SF of the infinite [finite] system. A first source of FS error in Eq. (2) is the replacement of $S(k)$ in the first term by its finite-size analogue $S_N(\mathbf{G})$ in the second term. However, this effect is negligible, as we will demonstrate in Fig. 2.

Thus, the main source of error is the discretization of the integral in the first term to obtain the sum in the second. Chiesa *et al.* [41] suggested that the main contribution to Eq. (2) comes from the omission of the $\mathbf{G} = \mathbf{0}$ term from the summation [47]. As is well known, the RPA becomes exact in the limit of small k, and the expansion of $S(k)$ around $k = 0$ at finite T is given by [23]

$$S_0^{\mathrm{RPA}}(k) = \frac{k^2}{2\omega_p} \coth\left(\frac{\beta \omega_p}{2}\right), \quad (3)$$

where $\beta = 1/k_B T$ and $\omega_p = \sqrt{3/r_s^3}$ is the plasma frequency. The finite-T version [48] of the Chiesa FSC [27],
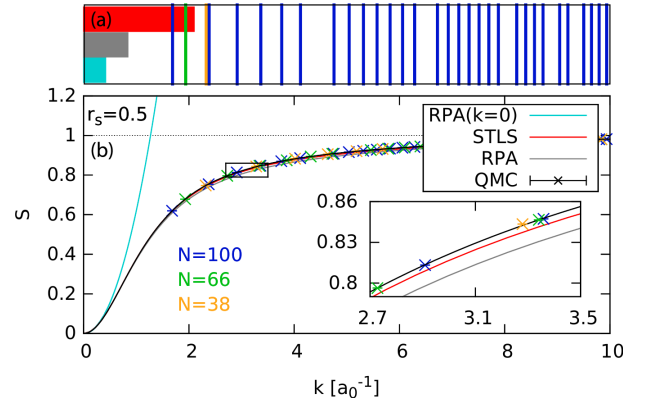

FIG. 2. Static structure factors for $\theta = 2$, $r_s = 0.5$, and three values of N. In (a), the discrete QMC k points are plotted as vertical lines for $N = 100$; the minimum k values for $N = 66$ and $N = 38$ are indicated by the green and yellow line, respectively. The colored horizontal bars indicate the k ranges where S^{STLS} (red), S^{RPA} RPA (gray), and S_0^{RPA} (light blue) are accurate. (b) shows that the QMC results for $S(k)$ converge rapidly with N (see the colored symbols in the inset). The black curve shows S_{comb} connecting $S^{\mathrm{STLS}}(k)$ at small k with the QMC data for $N = 100$ which yields accurate results for all k.

$$\Delta V_{\text{BCDC}}(N) = \lim_{k \to 0} \frac{S_0^{\text{RPA}}(k)4\pi}{2L^3 k^2} = \frac{\omega_p}{4N} \coth\left(\frac{\beta\omega_p}{2}\right), \quad (4)$$

would be sufficient if (i) $S_0^{\text{RPA}}(k)$ were accurate for the smallest nonzero k in the QMC simulation, $k_{\min} = 2\pi/L$, and (ii) all contributions to Eq. (2) not accounted for by the inclusion of the $\mathbf{G} = 0$ term were negligible. As we demonstrate below, for high temperatures and intermediate to high densities, both conditions are strongly violated. Thus, we require an improved model SF, $S_{\text{model}}(k)$, to compute the discretization error,

$$\Delta_N[S_{\text{model}}(k)] = \frac{\Delta V_N[S_{\text{model}}(k), S_{\text{model}}(k)]}{N}, \quad (5)$$

in Eq. (2). A natural strategy is to combine the QMC data for $k \geq k_{\min}$ with an approximation that is accurate for all k up to (at least) $k_{\min}$.

Results.—In Fig. 2, we analyze the static SF for $\theta = 2$ and a comparatively high-density case, $r_s = 0.5$, for three different particle numbers. The use of a finite simulation cell subject to periodic boundary conditions discretizes the momentum, so QMC data are available only at the discrete k points indicated by the vertical lines in the top panel. As shown in the inset, the QMC $S(k)$ is well converged with respect to the system size for surprisingly small N, providing justification to set $S_N(\mathbf{G}) \approx S(G)$. Therefore, the FS error of V_N/N reduces as N increases, primarily because the k grid becomes finer and $k_{\min}$ decreases. The figure also allows us to study the performance of the three analytical structure factors S^{RPA}, S^{STLS} [21,22], and S_0^{RPA}. We clearly observe that $S_0^{\text{RPA}}(k)$ is accurate only for $ka_0 \lesssim 0.3$, explaining why the BCDC FSC, Eq. (4), fails. In contrast, $S^{\text{RPA}}(k)$ and $S^{\text{STLS}}(k)$ match the QMC data much better. On the left-hand side of Fig. 2(a), we indicate the k ranges over which the three models are accurate, showing that only $S^{\text{STLS}}(k)$ connects smoothly to the QMC data. At larger k, S^{RPA} and S^{STLS} exhibit significant deviations from the QMC data, although STLS is more accurate. For completeness, we mention that, when the density is lowered, the k ranges of accurate behavior of S^{RPA}, S^{STLS}, and S_0^{RPA} continuously increase [49]. For example, at $r_s = 1$, both S^{RPA} and S^{STLS} smoothly connect to the QMC data, whereas for $r_s = 10$ this is observed even for $S_0^{\text{RPA}}(k)$, revealing that there the BCDC FSC is accurate.

Based on this behavior, an obvious way to construct a model SF that is accurate over the entire k range for all warm dense matter parameters is to combine the QMC data with the STLS data at small k. The result is denoted S_{comb} and computed via a spline function. The excellent behavior is illustrated by the black line in Fig. 2(b) and in the inset. This quasiexact SF is the proper input to compute the discretization error from Eq. (5).

The results of this procedure are shown in Fig. 3 for the most challenging high-density case, $r_s = 0.5$ and $\theta = 2$.
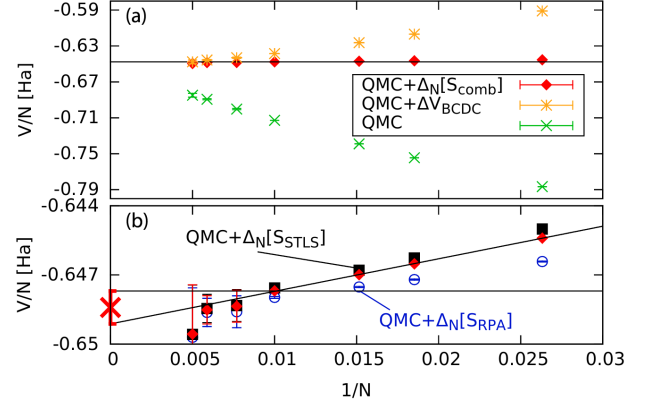

FIG. 3. (a) Finite-size corrected QMC data for the potential energy for $\theta = 2$ and $r_s = 0.5$. The yellow asterisks are obtained using Eq. (4); the red diamonds use the combined SF S_{comb} (cf. Fig. 2) to evaluate the discretization error, Eq. (5). (b) Magnified part of (a) including an extrapolation of the residual finite-size error to the TDL (the red cross). Results obtained using only the full RPA (blue) and STLS structure factors (black) in Eq. (5) are also shown.

Clearly, the raw QMC data (green crosses) suffer from severe finite-size errors of the order of 10% for system sizes from $N = 38$ to $N = 200$. These errors do not exhibit the $\Delta V \propto 1/N$ behavior predicted by Eq. (4), and the BCDC-corrected QMC data (yellow asterisks) do not fall on a horizontal line. In contrast, using $\Delta_N[S_{\text{comb}}]$ produces results that are very well converged for all system sizes considered, including even $N = 38$ (red diamonds). Figure 3(b) shows that the removal of the discretization error has reduced the FS bias by 2 orders of magnitude. The residual error $|\Delta V|/|V| \sim 10^{-3}$ is due to the small finite-size effects in the QMC data for $S_N(k)$ itself and exhibits a linear behavior in $1/N$. Thus, it is possible to determine the potential energy in the TDL (the red cross in the bottom panel) with a reliable error bar [50].

To further explore the properties of our discretization formula for the FS error, we recompute Δ_N using the purely theoretical STLS and RPA SFs as S_{model} in Eq. (5). The FS-corrected data are depicted by the black squares and blue circles, respectively, in Fig. 3(b). Surprisingly, we find very good agreement with the FSCs derived from the substantially more accurate S_{comb}. Hence, despite their significant deviations from the QMC data at intermediate k [cf. inset in Fig. 2(b)], $S^{\text{STLS}}(k)$ and $S^{\text{RPA}}(k)$ are sufficiently accurate to account for the discretization error of the potential energy [51]. Since S_{comb} is sensitive to statistical noise, computing the FSC solely from $S^{\text{STLS}}(k)$ or $S^{\text{RPA}}(k)$ is in fact the preferred approach. Of course, this does not eliminate the need for accurate finite-N QMC data, the quality of which sets the baseline for our thermodynamic result, $v = V_{\text{QMC},N}/N + \Delta_N[S_{\text{model}}]$. Using instead the STLS or RPA SF to estimate $V_{\text{QMC},N}$ as well as Δ_N poorly accounts for the short-range correlations and, even for $\theta = 2$ and

$r_s = 0.5$, leads to $\sim 10\%$ errors (cf. Fig. 1), which further increase with r_s.

By performing extensive QMC simulations and applying our FSC to results for various system sizes N to allow extrapolation of the residual FS error, we obtain the potential energy of the UEG in the TDL over a very broad density range, $0.1 \le r_s \le 10$. The results are displayed in Fig. 4 for five different temperatures and listed in a table in the Supplemental Material [49]. We also compare our results to the most accurate data previously available— the RPIMC results of Brown *et al.* (BCDC, circles), which were corrected using the BCDC FSC, Eq. (4) [27,49]. We underline that these results were limited to moderate densities $r_s \ge 1$ but even there substantially deviate from our data. The error increases rapidly with the density and temperature reaching 20% for $r_s = 1$ and $\theta = 8$ [49].

Finally, we obtain the exchange-correlation free energy from a fit to the potential energy, regarded as a function of r_s for fixed θ. Figure 4(b) shows that the functional form assumed [Eq. (S.2) in Ref. [49]] is indeed appropriate, as no systematic deviations between the QMC data and the fit (red crosses, $\theta = 8$) are observed. In Fig. 4(c), we compare our new data for F_{xc} to the recent parametrization by Karasiev *et al.* [52]. By design, both curves coincide in the limit $r_s \to 0$, approaching the exact asymptotic value known from the Hartree-Fock theory (for $r_s \ll 0.1$). While both results are in very good agreement for $\theta = 0.5$, we observe severe deviations of up to 9% at
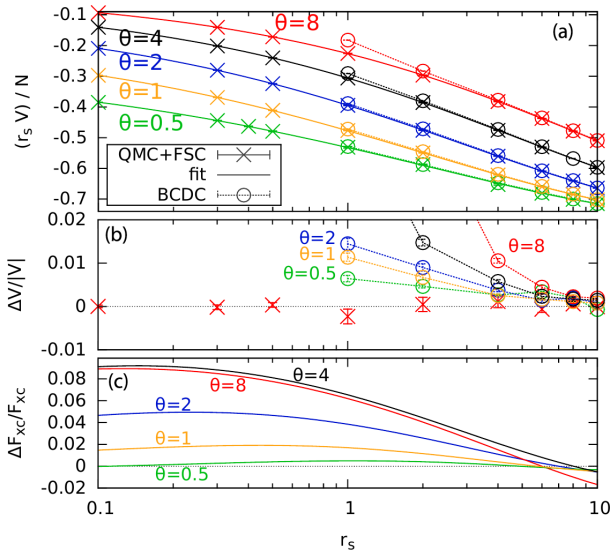

FIG. 4. Potential energy of the UEG in the TDL. (a) Our new FS-corrected QMC data, the fits to our data [see Eq. (S.2) of Ref. [49]], and the RPIMC results of Brown *et al.* [27], which include BCDC FSCs. (b) Relative deviations of our data (for $\Theta = 8$) and Brown's BCDC-corrected data from the corresponding fit. (c) Relative deviation of our exchange-correlation free energies from the fit of Ref. [52] for five temperatures. For details, see Ref. [49].

$\theta = 8$ [5% at $\theta = 2$]. Despite the systematic RPIMC bias and the lack of data for $r_s < 1$ prior to our work, the major cause of the disagreement is the inadequacy of the BCDC FSCs for a high temperature and small r_s. The absolute data for F_{xc} and the corresponding fit parameters are provided in Ref. [49].

Summary and discussion.—We have presented a simple but highly accurate procedure for removing finite-size errors from *ab initio* finite-N QMC data for the potential energy V of the UEG at a finite temperature. This is achieved by adding to the QMC results the discretization error $\Delta_N[S_{\mathrm{model}}(k)]$, Eq. (5), computed using simple approximate structure factors based on the RPA or STLS approximations. Our finite-size-corrected results include excellent descriptions of both the exchange and short-range correlation effects (from the QMC data) and the long-range correlations (via the RPA or STLS corrections). These results constitute the first unbiased *ab initio* thermodynamic data for the warm dense electron gas. For temperatures above half the Fermi temperature and a density range covering 6 orders of magnitude ($0.1 \le r_s \le 10$), we achieve an unprecedented accuracy not exceeding 0.3%; our results will therefore serve as valuable benchmarks for the development of accurate new theories and simulation schemes, including improved static local field corrections. The recent results of Brown *et al.* [27,49], which were obtained by applying the BCDC FSC from Eq. (4) to RPIMC data, exhibit deviations of up to 20%. The recent parametrization of F_{xc} by Karasiev *et al.* [52], which was mainly based on the data by Brown *et al.*, uses a good functional form but exhibits errors of up to 9% at high temperatures. Even though these inaccuracies constitute only a small fraction of the total free energy, which might not drastically influence subsequent density functional theory calculations of realistic multicomponent systems, it is indispensable to have a reliable and consistent fit of F_{xc} for all warm dense matter parameters to achieve predictive power and agreement with experiments. The construction of an improved complete parametrization of F_{xc} with respect to density, temperature, and spin polarization remains a challenging task for future work. In particular, the fermion sign problem presently limits our QMC simulations to $\theta \ge 0.5$ for $r_s \sim 1$ (although lower temperatures are feasible for both larger and smaller r_s with PB-PIMC and CPIMC, respectively). To overcome this bottleneck, it will be advantageous to incorporate the $T = 0$ limit of E_{xc} and, thus, to perform an interpolation across the remaining gap where no *ab initio* data are available [52]. In addition, our data will be an important input for time-dependent DFT and quantum hydrodynamics [53,54]. Finally, our FSC procedure is expected to be of value for other simulations of warm dense plasmas [55–57], as well as 2D systems, e.g., Refs. [58,59].

---

[*]dornheim@theo-physik.uni-kiel.de

[1] P.-F. Loos and P. M. W. Gill, The uniform electron gas, Comput. Mol. Sci. **6**, 410 (2016).

[2] J. P. Perdew and A. Zunger, Self-interaction correction to density-functional approximations for many-electron systems, Phys. Rev. B **23**, 5048 (1981).

[3] D. M. Ceperley and B. J. Alder, Ground State of the Electron Gas by a Stochastic Method, Phys. Rev. Lett. **45**, 566 (1980).

[4] M. D. Knudson, M. P. Desjarlais, R. W. Lemke, T. R. Mattsson, M. French, N. Nettelmann, and R. Redmer, Probing the Interiors of the Ice Giants: Shock Compression of Water to 700 GPa and 3.8 $\mathbf{g}/cm^3$, Phys. Rev. Lett. **108**, 091102 (2012).

[5] B. Militzer, W. B. Hubbard, J. Vorberger, I. Tamblyn, and S. A. Bonev, A massive core in Jupiter predicted from first-principles simulations, Astrophys. J. **688**, L45 (2008).

[6] R. Nora et al., Gigabar Spherical Shock Generation on the OMEGA Laser, Phys. Rev. Lett. **114**, 045001 (2015).

[7] P. F. Schmit et al., Understanding Fuel Magnetization and Mix Using Secondary Nuclear Reactions in Magneto-Inertial Fusion, Phys. Rev. Lett. **113**, 155004 (2014).

[8] O. A. Hurricane et al., Inertially confined fusion plasmas dominated by alpha-particle self-heating, Nat. Phys. **12**, 800 (2016).

[9] R. Ernstorfer, M. Harb, C. T. Hebeisen, G. Sciaini, T. Dartigalongue, and R. J. D. Miller, The formation of warm dense matter: Experimental evidence for electronic bond hardening in gold, Science **323**, 1033 (2009).

[10] G. Mazzola, S. Yunoki, and S. Sorella, Unexpectedly high pressure for molecular dissociation in liquid hydrogen by electronic simulation, Nat. Commun. **5**, 3487 (2014).

[11] M. D. Knudson, M. P. Desjarlais, A. Becker, R. W. Lemke, K. R. Cochrane, M. E. Savage, D. E. Bliss, T. R. Mattsson, and R. Redmer, Direct observation of an abrupt insulator-to-metal transition in dense liquid deuterium, Science **348**, 1455 (2015).

[12] T. Sjostrom and J. Daligault, Gradient corrections to the exchange-correlation free energy, Phys. Rev. B **90**, 155109 (2014).

[13] K. Burke, J. C. Smith, P. E. Grabowski, and A. Pribram-Jones, Exact conditions on the temperature dependence of density functionals, Phys. Rev. B **93**, 195132 (2016).

[14] M. W. C. Dharma-wardana, Current issues in finite-T density-functional theory and warm-correlated matter, Computation **4**, 16 (2016).

[15] V. V. Karasiev, L. Calderin, and S. B. Trickey, The importance of finite-temperature exchange-correlation for warm dense matter calculations, Phys. Rev. E **93**, 063207 (2016).

[16] A. Pribram-Jones, P. E. Grabowski, and K. Burke, Thermal Density Functional Theory: Time-Dependent Linear Response and Approximate Functionals from the Fluctuation-Dissipation Theorem, Phys. Rev. Lett. **116**, 233001 (2016).

[17] D. Kremp, M. Schlanges, and W. D. Kraeft, Quantum Statistics of Nonideal Plasmas (Springer, New York, 2005).

[18] J. Vorberger, M. Schlanges, and W.-D. Kraeft, Equation of state for weakly coupled quantum plasmas, Phys. Rev. E **69**, 046407 (2004).

[19] U. Gupta and A. K. Rajagopal, Exchange-correlation potential for inhomogeneous electron systems at finite temperatures, Phys. Rev. A **22**, 2792 (1980).

[20] F. Perrot and M. W. C. Dharma-wardana, Exchange and correlation potentials for electron-ion systems at finite temperatures, Phys. Rev. A **30**, 2619 (1984).

[21] S. Tanaka and S. Ichimaru, Thermodynamics and correlational properties of finite-temperature electron liquids in the Singwi-Tosi-Land-Sjölander approximation, J. Phys. Soc. Jpn. **55**, 2278 (1986).

[22] T. Sjostrom and J. Dufty, Uniform electron gas at finite temperatures, Phys. Rev. B **88**, 115123 (2013).

[23] S. Dutta and J. Dufty, Classical representation of a quantum system at equilibrium: Applications, Phys. Rev. E **87**, 032102 (2013).

[24] M. W. C. Dharma-wardana and F. Perrot, Simple Classical Mapping of the Spin-Polarized Quantum Electron Gas: Distribution Functions and Local-Field Corrections, Phys. Rev. Lett. **84**, 959 (2000).

[25] E. Y. Loh, J. E. Gubernatis, R. T. Scalettar, S. R. White, D. J. Scalapino, and R. L. Sugar, Sign problem in the numerical simulation of many-electron systems, Phys. Rev. B **41**, 9301 (1990).

[26] M. Troyer and U. J. Wiese, Computational Complexity and Fundamental Limitations to Fermionic Quantum Monte Carlo Simulations, Phys. Rev. Lett. **94**, 170201 (2005).

[27] E. W. Brown, B. K. Clark, J. L. DuBois, and D. M. Ceperley, Path-Integral Monte Carlo Simulation of the Warm Dense Homogeneous Electron Gas, Phys. Rev. Lett. **110**, 146405 (2013).

[28] D. M. Ceperley, Fermion nodes, J. Stat. Phys. **63**, 1237 (1991).

[29] S. Groth, T. Schoof, T. Dornheim, and M. Bonitz, Ab Initio quantum Monte Carlo simulations of the uniform electron gas without fixed nodes, Phys. Rev. B **93**, 085102 (2016).

[30] T. Dornheim, S. Groth, T. Schoof, C. Hann, and M. Bonitz, Ab initio quantum Monte Carlo simulations of the uniform

electron gas without fixed nodes: The unpolarized case, Phys. Rev. B **93**, 205134 (2016).

[31] F. D. Malone, N. S. Blunt, E. W. Brown, D. K. K. Lee, J. S. Spencer, W. M. C. Foulkes, and J. J. Shepherd, Accurate Exchange-Correlation Energies for the Warm Dense Electron Gas, Phys. Rev. Lett. **117**, 115701 (2016).

[32] T. Schoof, M. Bonitz, A. V. Filinov, D. Hochstuhl, and J. W. Dufty, Configuration path integral Monte Carlo, Contrib. Plasma Phys. **51**, 687 (2011).

[33] T. Schoof, S. Groth, and M. Bonitz, Towards *ab initio* thermodynamics of the electron gas at strong degeneracy, Contrib. Plasma Phys. **55**, 136 (2015).

[34] T. Schoof, S. Groth, J. Vorberger, and M. Bonitz, *Ab Initio* Thermodynamic Results for the Degenerate Electron Gas at Finite Temperature, Phys. Rev. Lett. **115**, 130402 (2015).

[35] T. Dornheim, S. Groth, A. Filinov, and M. Bonitz, Permutation blocking path integral Monte Carlo: A highly efficient approach to the simulation of strongly degenerate non-ideal fermions, New J. Phys. **17**, 073017 (2015).

[36] T. Dornheim, T. Schoof, S. Groth, A. Filinov, and M. Bonitz, Permutation blocking path integral Monte Carlo approach to the uniform electron gas at finite temperature, J. Chem. Phys. **143**, 204101 (2015).

[37] N. S. Blunt, T. W. Rogers, J. S. Spencer, and W. M. Foulkes, Density-matrix quantum Monte Carlo method, Phys. Rev. B **89**, 245124 (2014).

[38] F. D. Malone, N. S. Blunt, J. J. Shepherd, D. K. K. Lee, J. S. Spencer, and W. M. C. Foulkes, Interaction picture density matrix quantum Monte Carlo, J. Chem. Phys. **143**, 044116 (2015).

[39] L. M. Fraser, W. M. C. Foulkes, G. Rajagopal, R. J. Needs, S. D. Kenny, and A. J. Williamson, Finite-size effects and Coulomb interactions in quantum Monte Carlo calculations for homogeneous systems with periodic boundary conditions, Phys. Rev. B **53**, 1814 (1996).

[40] N. D. Drummond, R. J. Needs, A. Sorouri, and W. M. C. Foulkes, Finite-size errors in continuum quantum Monte Carlo calculations, Phys. Rev. B **78**, 125106 (2008).

[41] S. Chiesa, D. M. Ceperley, R. M. Martin, and M. Holzmann, Finite-Size Error in Many-Body Simulations with Long-Range Interactions, Phys. Rev. Lett. **97**, 076404 (2006).

[42] C. Lin, F. H. Zong, and D. M. Ceperley, Twist-averaged boundary conditions in continuum quantum Monte Carlo algorithms, Phys. Rev. E **64**, 016702 (2001).

[43] H. Kwee, S. Zhang, and H. Krakauer, Finite-Size Correction in Many-Body Electronic Structure Calculations, Phys. Rev. Lett. **100**, 126404 (2008).

[44] The two fits in Fig. 3 are $f(1/N) = a_f + b_f/N^{c_f}$ and $g(1/N) = a_g + b_g/N + b_c/N^{b_d}$.

[45] J. Vorberger (private communication).

[46] In the considered temperature range, shell-filling effects are negligible, and twist averaging [40,42] is not required.

[47] The Madelung constant is approximated by [40]

$$\xi_M \approx \frac{1}{L^3} \sum_{\mathbf{G} \neq \mathbf{0}} \frac{4\pi}{G^2} e^{-\epsilon G^2} - \frac{1}{(2\pi)^3} \int_{k < \infty} d\mathbf{k} \frac{4\pi}{k^2} e^{-\epsilon k^2}$$

for small ϵ and, therefore, cancels the minus unity contributions to both the sum and the integral in Eq. (2).

[48] For $\beta \to \infty$, $\coth(\frac{\beta \omega_p}{2}) \to 1$, and the ground-state result [40,41] is recovered.

[49] See Supplemental Material at http://link.aps.org/supplemental/10.1103/PhysRevLett.117.156403 containing technical details, additional numerical data and tables.

[50] We (i) perform a linear extrapolation and (ii) average over the last few data points where V/N are indistinguishable within the statistical error bars. Our final result for V/N is the mean of (i) and (ii), which constitute reasonable lower and upper bounds, respectively.

[51] The discretization FSC is insensitive to the choice of SF, because the discretization error is unaffected by constant shifts in the model SF (the three SFs in the inset in Fig. 2 are nearly parallel).

[52] V. V. Karasiev, T. Sjostrom, J. Dufty, and S. B. Trickey, Accurate Homogeneous Electron Gas Exchange-Correlation Free Energy for Local Spin-Density Calculations, Phys. Rev. Lett. **112**, 076403 (2014).

[53] N. Crouseilles, P.-A. Hervieux, and G. Manfredi, Quantum hydrodynamic model for the nonlinear electron dynamics in thin metal films, Phys. Rev. B **78**, 155412 (2008).

[54] D. Michta, F. Graziani, and M. Bonitz, Quantum hydrodynamics for plasmas—A Thomas-Fermi theory perspective, Contrib. Plasma Phys. **55**, 437 (2015).

[55] K. P. Driver and B. Militzer, All-Electron Path Integral Monte Carlo Simulations of Warm Dense Matter: Application to Water and Carbon Plasmas, Phys. Rev. Lett. **108**, 115502 (2012).

[56] K. P. Driver and B. Militzer, First-principles simulations and shock Hugoniot calculations of warm dense neon, Phys. Rev. B **91**, 045103 (2015).

[57] 3wB. Militzer and K. P. Driver, Development of Path Integral Monte Carlo Simulations with Localized Nodal Surfaces for Second-Row Elements, Phys. Rev. Lett. **115**, 176403 (2015).

[58] D. M. Ceperley, Ground state of the fermion one-component plasma: A Monte Carlo study in two and three dimensions, Phys. Rev. B **18**, 3126 (1978).

[59] M. Motta, D. E. Galli, S. Moroni, and E. Vitali, Imaginary time density-density correlations for two-dimensional electron gases at high density, J. Chem. Phys. **143**, 164108 (2015).

Supplementary Material: *Ab initio* Quantum Monte Carlo simulation of the warm dense electron gas in the thermodynamic limit

Tobias Dornheim[1], Simon Groth[1], Travis Sjostrom[2], Fionn D. Malone[3], W.M.C. Foulkes[3], and Michael Bonitz[1]

[1]Institut für Theoretische Physik und Astrophysik, Christian-Albrechts-Universität zu Kiel,
D-24098 Kiel, Germany
[2]Theoretical Division, Los Alamos National Laboratory, Los Alamos, New Mexico 87545, USA
[3]Department of Physics, Imperial College London, Exhibition Road, London SW7 2AZ, UK

A. Static structure factors

In Fig. S1, as a supplement to Fig. 2 of the main manuscript, we show the structure factors (SF) at $\theta = 2$ for intermediate ($r_s = 1$) and lower ($r_s = 10$) density. At both densities the STLS structure factor smoothly connects to the QMC data but exhibits significant deviations at larger k. The low k expansion of the RPA SF fails to connect to the QMC data at $r_s = 1$, indicating that the FSC by Brown *et al.* is inappropriate, while at $r_s = 10$ the RPA expansion smoothly connects to the QMC data so that the FSC by Brown *et al.* is applicable.

B. Practical details

For the evaluation of the discretization error (DE) according to Eq. (5) in the main manuscript,

$$\frac{\Delta V_N}{N}(G_{\max}) = 2\pi \left(\int_{k < G_{\max}} d\mathbf{k} \, \frac{S_{\text{model}}(k) - 1}{k^2 (2\pi)^3} \right. \quad \text{(S.1)}$$
$$\left. - \sum_{\mathbf{G} \neq \mathbf{0}}^{G_{\max}} \frac{S_{\text{model}}(\mathbf{G}) - 1}{G^2 V} - \xi_{\text{M}} \right) \quad ,$$

the maximum modulus of the discrete lattice vectors $G_{\max}$ has to be chosen large enough to ensure the convergence of the FSC, which is demonstrated in Fig. S2 for three different particle numbers at $\theta = 2$ and $r_s = 0.5$. Clearly, taking into account only the first k-vector is not sufficient. In fact, the convergence of the DE with respect to $G_{\max}$
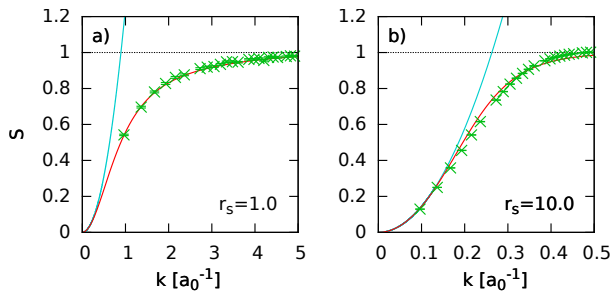

Figure S1: Static structure factors of $N = 66$ electrons at $\theta = 2$ for a) $r_s = 1.0$ and b) $r_s = 10.0$: QMC data (green crosses), STLS (red) and $k \to 0$ expansion of the the RPA SF (light blue).
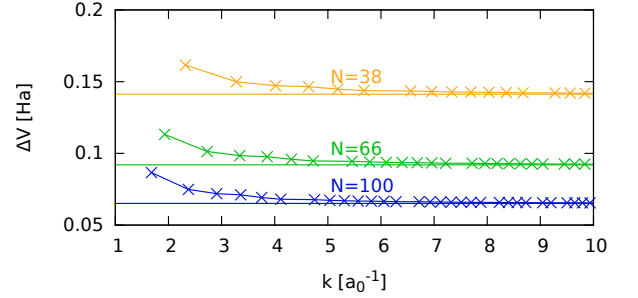

Figure S2: Convergence of the FSC with the maximum k-value for three particle numbers and $\theta = 2$ and $r_s = 0.5$, cf. Fig. 3 in the main manuscript.

is rather slow, and the number of k-vectors needed for convergence of the DE only weakly depends on N. The difference between the converged values is due to the different k-mesh for different N.

C. Finite-size corrections for selected parameters

To demonstrate the broad range of applicability of our finite size correction (FSC) procedure, we present some more examples for different parameter combinations. Figure S3 shows the convergence of the potential energy with system size for the most challenging (with respect to finite-size errors) case at $\theta = 8$ and $r_s = 0.1$. Evidently, the uncorrected QMC (CPIMC) data exhibit severe finite-size errors of $\Delta V / V \approx 200\%$ for $N = 34$. This is a direct consequence of the steep drop of the static structure factor $S(k)$ at small k, that is not properly accessed by the available k-values even in a QMC simulation of $N = 1000$ electrons. Further, the potential energy that is obtained by invoking the BCDC-FSCs even worsens the convergence, as $S_0^{\text{RPA}}(k)$ does not come anywhere near the QMC-data, even for $N = 1000$. In striking contrast, our FSCs (using either S^{STLS}, or a combination of STLS with the QMC data, S_{comb}) are converged to a remarkably high degree, even for relatively small systems (with $|\Delta V|/|V| \sim 10^{-3}$, for $N = 66$) and the additional extrapolation of the residual finite-size errors allows for an accurate result for V in the TDL even for such extreme parameters.

Figure S4 shows the convergence for $\theta = 2$ and $r_s = 1$. In this case, the uncorrected QMC (permutation blocking PIMC) data exhibit finite-size errors of $|\Delta V|/|V| \approx 10\%$
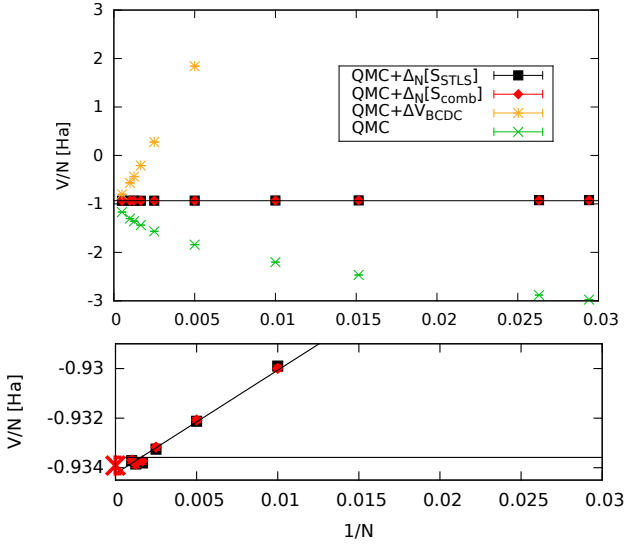
Figure S3: Finite-size correction of the QMC results for the potential energy with $\theta = 8$ and $r_s = 0.1$.
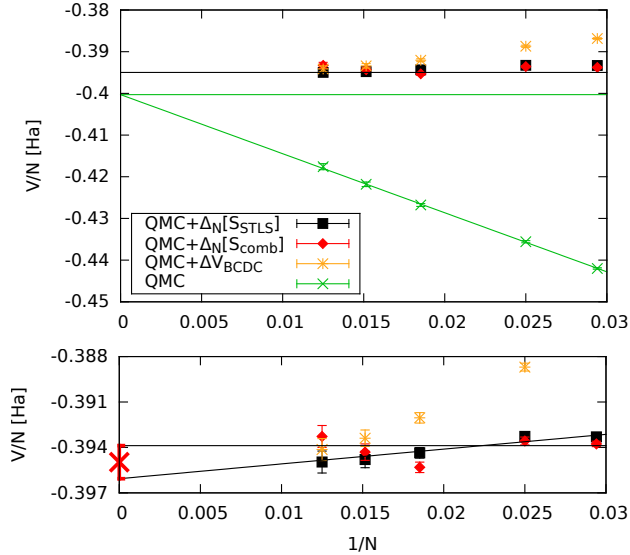

Figure S4: Same as Fig. S3, but for $\theta = 2$ and $r_s = 1$.

(for $N = 34$) and the convergence seems to follow $|\Delta V|/N \sim 1/N$, cf. the linear fit (the green line). Although, in principle, the $1/N$-behavior is predicted by the BCDC-FSCs, the slope is different and the corrected V/N-data do not agree with the linear extrapolation and are not converged. The data that have been obtained after adding our new FSCs are converged to a high degree, but do not agree with the linearly extrapolated value as well. This, again, clearly demonstrates the danger of a direct extrapolation of the QMC data without being certain about the exact functional form of the finite-size error.

D. Fit of the potential energy

Following Karasiev *et al.* [1], we use the following parametrization of the exchange-correlation free energy for fixed θ:

$$\frac{F_{xc}}{N}(r_s, \theta) = -\frac{1}{r_s}\left(\frac{a + b\sqrt{r_s} + cr_s}{1 + d\sqrt{r_s} + er_s}\right) \quad , \qquad \text{(S.2)}$$

which yields the potential energy via

$$V(r_s, \theta)r_s = 2r_s F_{xc}(r_s, \theta) + r_s^2 \frac{\partial F_{xc}(r_s, \theta)}{\partial r_s}\bigg|_\theta \quad , \qquad \text{(S.3)}$$

which allows us to fit the rhs. of Eq. (S.3) to our new corrected QMC data. The parameter a follows from the Hartree-Fock limit and the results of the fit procedure for the five isotherms shown in Fig. 4 in the main article are listed in table I.

E. STLS and RPA

The static structure factor (SF) is found by the fluctuation-dissipation theorem as a sum over the Matsubara frequencies for the polarizabilities of the interacting system as

$$S(\mathbf{k}) = \frac{-1}{\beta n}\sum_{l=-\infty}^{\infty}\frac{1}{v_k}\left(\frac{1}{\epsilon(\mathbf{k}, z_l)} - 1\right) , \qquad \text{(S.4)}$$

with the particle density n, the Matsubara frequencies $z_l = 2\pi i l/\beta\hbar$, and the Fourier transform of the Coulomb potential $v_k = 4\pi/k^2$. Following [2], the Singwi-Tosi-Land-Sjölander (STLS) SF is computed from the dielectric function

$$\epsilon(\mathbf{k}, \omega) = 1 - \frac{v_k \chi_0(\mathbf{k}, \omega)}{1 + G(\mathbf{k})v_k\chi_0(\mathbf{k}, \omega)} , \qquad \text{(S.5)}$$

with $\chi_0(\mathbf{q}, \omega)$ being the finite-temperature polarizability of the non-interacting UEG, G is the static local field correction

$$G(\mathbf{k}) = \frac{-1}{n}\int\frac{d\mathbf{k}'}{(2\pi)^3}\frac{\mathbf{k}\cdot\mathbf{k}'}{k'^2}[S(\mathbf{k} - \mathbf{k}') - 1], \qquad \text{(S.6)}$$

and Eq. (S.4), (S.5), and (S.6) are solved self-consistently. In the random phase approximation (RPA), $G(\mathbf{k}) \to 0$.

F. Finite-size corrections by Brown *et al.*

In Fig. 4 from the main manuscript, we have compared our new corrected data for the potential energy to RPIMC data (for $N = 66$) by Brown *et al.* that were corrected with the BCDC-FSC [Eq. (4) of the main article]. However, it should be noted that this corrected data differs from the data tabulated in the supplement of Ref. [3].
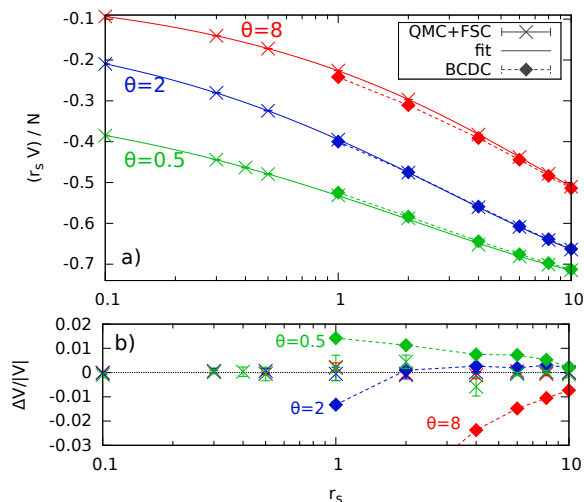
Figure S5: Potential energy of the warm dense electron gas in the TDL. Panel **a)** shows our new corrected data for three temperatures, the fits to our data (see Eq. (S.3)), and the data by Brown *et al.* (BCDC), taken directly from their supplement. Panel **b)** shows the corresponding relative deviations to the fits to our data.

For the latter, apparently, there was a problem caused by a mix of Hartree and Rydberg atomic units within their FSC. In Fig. S5, we compare our data to the BCDC results as they are given in their supplement. While the magnitude of the deviation is similar as in Fig. 4 from the main article, the sign changes with temperature. In particular, for $\theta = 8$ the BCDC values are lower by $\Delta V / V \approx 8\%$ than ours instead of being too high, and the two data sets significantly disagree even for $r_s = 10$.

G. Data

As a supplement to Fig. 4 from the main article, we have listed all data for the potential and exchange correlation free energy of the macroscopic UEG in Table II.

[1] V.V. Karasiev, T. Sjostrom, J. Dufty and S.B. Trickey, Accurate Homogeneous Electron Gas Exchange-Correlation Free Energy for Local Spin-Density Calculations, *Phys. Rev. Lett.* **112**, 076403 (2014)

[2] S. Tanaka and S. Ichimaru, Thermodynamics and Correlational Properties of Finite-Temperature Electron Liquids in the Singwi-Tosi-Land-Sjölander Approximation, *J. Phys. Soc. Jpn.* **55**, 2278-2289 (1986)

[3] E.W. Brown, B.K. Clark, J.L. DuBois and D.M. Ceperley, Path-Integral Monte Carlo Simulation of the Warm Dense Homogeneous Electron Gas, *Phys. Rev. Lett.* **110**, 146405 (2013)

Table I: Fit parameters from Eq. (S.3), see Fig. 4 in the main article.

θ	a	b	c	d	e
8.0	0.025 26	0.151 46	0.015 624	0.158 37	0.021 73
4.0	0.049 81	0.216 40	0.046 744	0.315 83	0.054 29
2.0	0.095 88	0.302 37	0.081 005	0.454 80	0.093 17
1.0	0.173 85	0.389 00	0.097 468	0.554 82	0.113 88
0.5	0.278 86	0.404 12	0.054 329	0.519 84	0.063 44

Table II: Energies per particle of the warm dense electron gas in the thermodynamic limit: Listed are the potential energy V/N (finite-size corrected QMC data where the residual error has been removed by an additional extrapolation, cf. Fig. 3 in the main article), the corresponding uncertainty $\delta V/N$ and the exchange correlation free energy F_{xc}/N that has been obtained by the fit, see Sec. D.

θ	r_s	V/N	$\delta V/N$	F_{xc}/N
8.0	10.0	$-0.051\,01$	0.000 02	$-0.038\,442$
8.0	8.0	$-0.059\,84$	0.000 04	$-0.044\,601$
8.0	6.0	$-0.072\,91$	0.000 05	$-0.053\,789$
8.0	4.0	-0.0956	0.0001	$-0.069\,583$
8.0	2.0	-0.1483	0.0002	$-0.106\,794$

Table II: *(continued)*.

θ	r_s	V/N	$\delta V/N$	F_{xc}/N
8.0	1.0	-0.2259	0.0004	$-0.162\,990$
8.0	0.5	-0.3442	0.000\,19	$-0.249\,668$
8.0	0.3	-0.4692	0.0003	$-0.344\,241$
8.0	0.1	-0.9341	0.0003	$-0.710\,052$
4.0	10.0	$-0.059\,74$	0.000\,01	$-0.047\,280$
4.0	6.0	$-0.088\,43$	0.000\,02	$-0.068\,305$
4.0	4.0	$-0.119\,06$	0.000\,04	$-0.090\,529$
4.0	2.0	-0.1929	0.0004	$-0.144\,405$
4.0	1.0	-0.3060	0.0003	$-0.228\,337$
4.0	0.5	-0.4811	0.0003	$-0.361\,760$
4.0	0.3	-0.6722	0.0003	$-0.511\,220$
4.0	0.1	-1.4091	0.0007	$-1.112\,758$
2.0	10.0	$-0.066\,409$	0.000\,003	$-0.055\,243$
2.0	8.0	$-0.080\,093$	0.000\,009	$-0.065\,910$
2.0	6.0	$-0.101\,461$	0.000\,014	$-0.082\,412$
2.0	4.0	$-0.140\,11$	0.000\,03	$-0.112\,123$
2.0	2.0	-0.2380	0.0004	$-0.187\,073$
2.0	1.0	-0.3950	0.0011	$-0.309\,220$
2.0	0.5	-0.6484	0.0007	$-0.511\,632$
2.0	0.3	-0.9350	0.0010	$-0.746\,033$
2.0	0.1	-2.0956	0.0013	$-1.732\,828$
1.0	10.0	$-0.070\,264$	0.000\,014	$-0.061\,098$
1.0	8.0	$-0.085\,593$	0.000\,009	$-0.073\,774$
1.0	6.0	$-0.109\,94$	0.000\,04	$-0.093\,763$
1.0	4.0	$-0.155\,37$	0.000\,10	$-0.130\,733$
1.0	2.0	-0.2749	0.0003	$-0.228\,179$
1.0	1.0	-0.4769	0.0005	$-0.395\,507$
1.0	0.5	-0.8225	0.0011	$-0.686\,721$
1.0	0.3	-1.2301	0.0010	$-1.037\,072$
1.0	0.1	-2.972	0.003	$-2.585\,960$
0.5	10.0	$-0.071\,47$	0.000\,10	$-0.064\,069$
0.5	8.0	$-0.087\,60$	0.000\,04	$-0.077\,981$
0.5	6.0	$-0.113\,52$	0.000\,08	$-0.100\,212$
0.5	4.0	-0.1631	0.0006	$-0.142\,231$
0.5	2.0	-0.2938	0.0008	$-0.257\,459$
0.5	1.0	-0.531	0.003	$-0.465\,543$
0.5	0.5	-0.959	0.003	$-0.845\,752$
0.5	0.4	-1.158	0.002	$-1.026\,811$
0.5	0.3	-1.4808	0.0011	$-1.320\,709$
0.5	0.1	-3.851	0.004	$-3.521\,367$

5.2   Spline Interpolations of Static Structure Factors

In the previous section, we explored the possible combination of the static structure factors from the dielectric formalism (in particular RPA and STLS) at small q (i.e., the long-range behavior that cannot be accessed via a simulation of a finite number of particles N) with our thermodynamic QMC data from either PB-PIMC or CPIMC elsewhere. In that context, the consideration of the SSF served as a means to an end, which was the derivation of an improved finite-size correction for the interaction energy. However, the availability of accurate data for $S(k)$ constitutes an important end in itself as it contains all information about two-particle correlations in the system. For this reason, we constructed cubic basis splines connecting the small-q behavior from STLS with a smooth interpolation of the QMC data for $q \geq 2\pi/L$. Extensive results of this procedure covering the entire relevant density range ($0.1 \leq r_\mathrm{s} \leq 20$) for the unpolarized UEG are shown in the following paper[5], Ref. [165]. All depicted results are freely available online. Possible applications of these data include the benchmarking of other techniques (see Chpt. 2), the approximate estimation of the static local-field correction [198], or the calculation of the dynamic structure factor using the method of frequency moments, see, e.g., Ref. [199]. Furthermore, it gives direct access to the pair correlation function, which is investigated in Sec. 5.2.1.

---

[5]T. Dornheim, S. Groth, and M. Bonitz, Contrib. Plasma Phys. (2017), **57**, p. 468-478. Copyright Wiley-VCH Verlag GmbH & Co. KGaA. Reproduced with permission.

Contributions to
Plasma Physics

Ab initio results for the static structure factor of the warm dense electron gas

Tobias Dornheim[*] | **Simon Groth** | **Michael Bonitz**

Institut für Theoretische Physik und Astrophysik, Christian-Albrechts-Universität zu Kiel, Kiel, Germany

* Correspondence
Tobias Dornheim, Institut für Theoretische Physik und Astrophysik, Christian-Albrechts-Universität zu Kiel, Kiel D-24098, Germany.
Email: dornheim@theo-physik.uni-kiel.de

The uniform electron gas at finite temperature is of high current interest for warm dense matter research. The complicated interplay of quantum degeneracy and Coulomb coupling effects is fully contained in the pair distribution function or, equivalently, the static structure factor. By combining exact quantum Monte Carlo results for large wave vectors with the long-range behaviour from the Singwi-Tosi-Land-Sjölander approximation, we are able to obtain highly accurate data for the static structure factor over the entire k-range. This allows us to gauge the accuracy of previous approximations and discuss their respective shortcomings. Further, our new data will serve as valuable input for the computation of other quantities.

KEYWORDS

electron gas, linear response theory, quantum Monte Carlo, static structure factor

1 | INTRODUCTION

Over recent years, there has emerged a growing interest in warm dense matter (WDM)—an exotic state where strong electronic excitations are realized at solid state densities.[1] In addition to astrophysical applications such as planet interiors[2,3] and white dwarf atmospheres, such extreme conditions are now routinely created in the lab, for example, in experiments with laser excited solids[4] or inertial confinement fusion.[5–7] Despite this remarkable experimental progress, a rigorous theoretical description remains notoriously difficult due to the simultaneous presence of three physical effects: (a) strong electronic excitations, (b) Coulomb coupling effects, and (c) fermionic exchange. This is typically expressed by two parameters being of the order of unity: the degeneracy temperature $\theta = k_B T/E_F$ (with $E_F = k_F^2/2$ and $k_F = (9\pi/4)^{1/3}/r_s$ being the Fermi energy and wave vector, respectively) and the Brueckner (coupling) parameter $r_s = \bar{r}/a_B$ with $\bar{r}$ and a_B being the mean interparticle distance and Bohr radius, respectively.

Of particular importance is the calculation of the thermodynamic properties of the uniform electron gas (UEG), which is comprised of Coulomb interacting electrons in a homogeneous neutralizing background. However, this has turned out to be surprisingly difficult. The extension of Quantum Monte Carlo (QMC) methods, which have been employed to obtain very accurate data in the ground state already three decades ago,[8,9] to finite temperature is severely limited by the fermion sign problem (FSP).[10,11] It was only recently that the combination of two novel methods (configuration path integral Monte Carlo [CPIMC][12,13]) and permutation blocking path integral Monte Carlo [PB-PIMC][14,15]) that are available at complementary parameter ranges allowed to conduct the first unbiased simulation of the UEG. At first, these efforts were limited to a finite number of electrons N in a finite simulation cell of volume V.[16,17] In practice, however, one is interested in the thermodynamic limit, which is given by the limit of an infinite number of particles at fixed density (or, equivalently, fixed r_s). This was realized by combining QMC data, which exactly incorporates all short-range exchange-correlation effects, but cannot capture the long-range effects due to the finite simulation cell, with the linear response theory, which is exact precisely in this limit.[18–21] The resulting accurate data for the UEG in the thermodynamic limit have subsequently been used to construct a complete parameterization of the exchange-correlation free energy with respect to temperature, density, and spin-polarization over the entire WDM regime.[22,23]

In this work, we further explore this strategy to investigate the static structure factor (SSF), $S(k)$, of the UEG at WDM conditions. In particular, we construct cubic basis splines to combine the SSF from the Singwi-Tosi-Land-Sjölander theory (STLS),[24–26] which is exact in the limit of small-wave vectors $(k \rightarrow 0)$,[27] with the exact QMC data elsewhere. These new extensive data for $S(k)$ are subsequently compared both to the random phase approximation (RPA)[28] and the full STLS results themselves over two orders of magnitude of the coupling parameter r_s and for three different temperatures. This allows us to gauge the performance of the dielectric approximations and to show when they break down.

2 | THEORY

2.1 | The uniform electron gas

The UEG is defined as an infinite system of Coulomb interacting electrons in a uniform positive background ensuring charge neutrality. Since QMC simulations are only possible in a finite simulation cell with box length L and volume $V = L^3$, we employ periodic boundary conditions and the standard Ewald summation to take into account the interactions of the electrons with the infinite array of periodic images. Since PB-PIMC and CPIMC are formulated in coordinate space and momentum space, respectively, both representations of the UEG Hamiltionian are given. We assume Hartree atomic units throughout this work.

2.2. | Coordinate representation of the Hamiltonian

Following Dornheim et al.[15] and Fraser et al.,[29] we express the Hamiltonian for $N = N_\uparrow + N_\downarrow$ unpolarized $(N_\uparrow = N_\downarrow)$ electrons in coordinate space as

$$\widehat{H} = -\frac{1}{2} \sum_{i=1}^{N} \nabla_i^2 + \frac{1}{2} \sum_{i=1}^{N} \sum_{j \neq i}^{N} \Psi(\mathbf{r}_i, \mathbf{r}_j) + \frac{N}{2} \xi_M \ , \tag{1}$$

with the Madelung constant ξ_M and the periodic Ewald pair interaction

$$\Psi(\mathbf{r}, \mathbf{s}) = \frac{1}{V} \sum_{\mathbf{G} \neq 0} \frac{e^{-\pi^2 \mathbf{G}^2/\kappa^2} e^{2\pi i \mathbf{G}(\mathbf{r}-\mathbf{s})}}{\pi \mathbf{G}^2} - \frac{\pi}{\kappa^2 V} + \sum_{\mathbf{R}} \frac{\text{erfc}(\kappa|\mathbf{r} - \mathbf{s} + \mathbf{R}|)}{|\mathbf{r} - \mathbf{s} + \mathbf{R}|}. \tag{2}$$

Here $\mathbf{R} = \mathbf{n}_1 L$ and $\mathbf{G} = \mathbf{n}_2/L$ denote the real and reciprocal space lattice vectors, respectively, with $\mathbf{n}_1$ and $\mathbf{n}_2$ three-component vectors of integers, and κ denotes the (freely adjustable) Ewald parameter.

2.3 | Hamiltonian in second quantization

In second quantization with respect to spin-orbitals of plane waves,

$$\langle \mathbf{r}\sigma \ |\mathbf{k}_i \sigma_i \rangle = \frac{1}{L^{3/2}} e^{i\mathbf{k}_i \cdot \mathbf{r}} \delta_{\sigma,\sigma_i} \ , \tag{3}$$

with $\mathbf{k}_i = \frac{2\pi}{L} \mathbf{m}_i$, $\mathbf{m}_i \in \mathbb{Z}^3$ and $\sigma_i \in \{\uparrow, \downarrow\}$, the Hamiltonian, Equation (1), is expressed as

$$\widehat{H} = \frac{1}{2} \sum_i \mathbf{k}_i^2 \hat{a}_i^\dagger \hat{a}_i + \sum_{\substack{i < j, \, k < l \\ i \neq k, \, j \neq l}} w_{ijkl}^- \hat{a}_i^\dagger \hat{a}_j^\dagger \hat{a}_l \hat{a}_k + \frac{N}{2} \xi M.$$

$$\tag{4}$$

Here, the antisymmetrized two-electron integrals are defined as $w_{ijkl}^- = w_{ijkl} - w_{ijlk}$, with

$$w_{ijkl} = \frac{4\pi e^2}{L^3 (\mathbf{k}_i - \mathbf{k}_k)^2} \delta_{\mathbf{k}_i + \mathbf{k}_j, \mathbf{k}_k + \mathbf{k}_l} \delta_{\sigma_i, \sigma_k} \delta_{\sigma_j, \sigma_l} \ , \tag{5}$$

and the Kronecker deltas ensure both momentum and spin conservation. The first (second) term in the Hamiltonian, Equation (4), describes the kinetic (interaction) energy. As usual, the operator $\hat{a}^\dagger_i$ $(\hat{a}_i)$ creates (annihilates) a particle in the (spin-) orbital $|\mathbf{k}_i \sigma_i\rangle$.

2.4 | QMC simulations

The task at hand to be solved using QMC methods is the calculation of canonic expectation values (temperature T, volume V, and particle number N are fixed), that follow from the canonical partition function

$$Z = \text{Tr}\hat{\rho}, \tag{6}$$

with $\widehat{\rho} = e^{-\beta\widehat{H}}$ being the canonic density operator and the inverse temperature $\beta = 1/k_B T$. In particular, the thermodynamic expectation value of an arbitrary observable $\widehat{A}$ can be written as

$$\langle \widehat{A} \rangle = \frac{1}{Z} \text{Tr} \widehat{\rho} \widehat{A}. \tag{7}$$

The underlying idea of both the CPIMC and the PB-PIMC method is to find a representation of the partition function Equation (6) of the form

$$Z = \sum \int_C W(\mathbf{C}), \tag{8}$$

That is, as a sum or integral over some, in general, high-dimensional variable $\mathbf{C}$, which is denoted as a configuration. The function $W(\mathbf{C})$ is the corresponding "configuration weight", which must be of a form that can be readily evaluated. The latter specification is not trivial as, for interacting electrons, the matrix elements of the density operator are not known when quantum effects are not negligible. Once a representation of the form of Equation (8) is found, the thermodynamic expectation value, Equation (7), becomes

$$\langle \widehat{A} \rangle = \frac{1}{Z} \sum \int_C W(\mathbf{C}) A(\mathbf{C}), \tag{9}$$

with $A(\mathbf{C})$ being the so-called Monte Carlo estimator. In practice, we use the Metropolis algorithm[30] to generate a set of N_{MC} random configurations $\{\mathbf{C}_1, \dots, \mathbf{C}_{N_{MC}}\}$ that are distributed according to the probability $P(\mathbf{C}) = W(\mathbf{C})/Z$, which is possible without explicit knowledge of the normalization Z. The Monte Carlo estimate for the thermodynamic expectation value from Equation (9) is then given by

$$\langle \widehat{A} \rangle \approx \langle \widehat{A} \rangle_{MC} = \frac{1}{N_{MC}} \sum_{i=1}^{N_{MC}} A(\mathbf{C}_i), \tag{10}$$

which in the limit of infinitely many random samples, $N_{MC} \to \infty$, becomes exact

$$\langle \widehat{A} \rangle = \lim_{N_{MC} \to \infty} \langle \widehat{A} \rangle_{MC}, \tag{11}$$

where the Monte Carlo error for any finite number of samples is given by

$$\Delta A = \left(\frac{\langle A^2 \rangle - \langle A \rangle^2}{N_{MC}} \right)^{1/2}. \tag{12}$$

Since the Monte Carlo estimates are exact within this statistical uncertainty, which is known accurately as well and can be made arbitrarily small by generating more random configurations, QMC simulations are often denoted as "quasi-exact".

Unfortunately, QMC simulations of electrons are not so straightforward as we shall briefly illustrate in the following. Due to the antisymmetry of the many-fermion wave function under exchange, the weight function W in Equation (8) can be both positive or negative. This, in turn, means that $P(\mathbf{C}) = W(\mathbf{C})/Z$ cannot be interpreted as a probability, which must be strictly positive. In order to still be able to use the Metropolis algorithm, we switch to a modified configuration space (indicated by the "prime" symbols) where the configurations are sampled according to the modulus weights.

$$Z' = \sum \int_C |W(\mathbf{C})|, \tag{13}$$

and the definition of the modified expectation value

$$\langle \widehat{A} \rangle = \frac{1}{Z'} \sum \int_C A(\mathbf{C}) |W(\mathbf{C})|. \tag{14}$$

The unbiased fermionic expectation value Equation (9) is then given by

$$\langle \widehat{A} \rangle = \frac{\langle \widehat{A}\widehat{S} \rangle'}{\langle \widehat{S} \rangle'}, \tag{15}$$

where $S(\mathbf{C}) = W(\mathbf{C})/|W(\mathbf{C})|$ is the so-called sign and, thus, $S = \langle \widehat{S} \rangle$ the "average sign" of the corresponding Monte Carlo simulation. It is important to note that the statistical uncertainty of the Monte Carlo estimation according to Equation (15) is (in leading order) inversely proportional to S,

$$\frac{\Delta A}{A} \sim \frac{1}{\langle \widehat{S} \rangle' \sqrt{N_{MC}}}, \tag{16}$$

while the average sign itself exponentially decreases both with inverse temperature and system size,

$$\langle \widehat{S} \rangle' = e^{-\beta N(f-f')}, \tag{17}$$

where f denotes the free energy per particle. Inserting Equation (17) into Equation (16) leads to

$$\frac{\Delta A}{A} \sim \frac{e^{\beta N(f-f')}}{\sqrt{N_{MC}}}.$$ (18)

Evidently, the statistical uncertainty exponentially increases both with system size and inverse temperature, which can only be compensated by increasing the number of Monte Carlo samples, thereby decreasing ΔA with the inverse square root of N_{MC}. This is the notorious fermion sign problem,[10,11,21] which has, for a long time, prevented ab initio PIMC (see Ceperley[31] for a review) simulations of electrons in the WDM regime.

The FSP has been shown to be *NP*-hard,[11] and a complete solution is not in sight. However, to nevertheless obtain accurate QMC results at WDM conditions, we have introduced two novel QMC methods that are efficient at complementary parameter regimes. The CPIMC method[12,13] is formulated in anti-symmetric Fock-space and can be interpreted as a Monte Carlo simulation of the exact, infinite perturbation expansion around the ideal (non-interacting) system. Therefore, it excels at strong degeneracy and high density, but becomes inefficient towards strong coupling. In contrast, the PB-PIMC approach[14,15] significantly extends standard PIMC towards lower temperature and higher density, while strong coupling does not pose an obstacle. Thus, the combination of both methods allows for accurate results over a broad parameter range.

A detailed comparison of the different ranges of applicability of fermionic QMC methods at WDM conditions can be found in Dornheim et al.[21]

2.5 | Dielectric approximations

The main advantage of QMC methods is the exact treatment of the short-range exchange-correlation effects, which are not described accurately by any approximation. On the other hand, the main disadvantage (despite the relatively large computational effort and non-universal range of applicability due to the sign problem) is that QMC simulations are limited to the finite simulation box. For this reason, QMC methods cannot be used to describe long-range correlations (corresponding to the limit of small wave vectors, $k \to 0$). On the other hand, it has long been known that the RPA becomes exact in the limit of small k for arbitrary coupling strength or temperature.[27]

Furthermore, the accuracy of RPA can be significantly increased by including a so-called (static) local field correction $G(\mathbf{q})$, which is defined by the equation[32]

$$\chi(\mathbf{q}, \omega) = \frac{\chi_0(\mathbf{q}, \omega)}{1 - \frac{4\pi}{q^2}[1 - G(\mathbf{q})]\chi_0(\mathbf{q}, \omega)},$$ (19)

with $\chi(\mathbf{q}, \omega)$ and $\chi_0(\mathbf{q}, \omega)$ denoting the density response function of the interacting and ideal system,[33] respectively. Furthermore, it is often convenient to compute the dielectric function

$$\varepsilon(\mathbf{k}, \omega) = 1 - \frac{\chi_0(\mathbf{k}, \omega)}{k^2/(4\pi) + G(\mathbf{k})\chi_0(\mathbf{k}, \omega)},$$ (20)

where the RPA limit is recovered by setting $G(\mathbf{q}) = 0$ in Equations (19) and (20). Unfortunately, the local field correction is not known in practice and one has to introduce an approximation. For the UEG, the most successful approach was introduced by Singwi et al.[24] and extended to finite temperature by Tanaka and Ichimaru.[25] The idea is to express $G(\mathbf{q})$ as a functional of the SSF.

$$G_{STLS}(\mathbf{k}) = -\frac{1}{n} \int \frac{d\mathbf{k}'}{(2\pi)^3} \frac{\mathbf{k} \cdot \mathbf{k}'}{k'^2}[S(\mathbf{k} - \mathbf{k}') - 1],$$ (21)

which, in turn, is used again to compute the SSF via the fluctuation dissipation theorem

$$S(\mathbf{k}) = -\frac{1}{\beta n} \sum_{l=-\infty}^{\infty} \frac{q^2}{4\pi} \left(\frac{1}{\varepsilon(\mathbf{k}, z_l)} - 1\right),$$ (22)

where the Matsubara frequencies are given by $z_l = 2\pi i l / \beta \hbar$. In practice, to obtain the SSF in STLS approximation we start with (1) computing $S(k)$ in RPA, (2) use it to compute $G_{STLS}(\mathbf{q})$ according to Equation (21), and (3) subsequently obtain a new SSF from Equation (22). Steps (2) and (3) are then repeated until the structure factor and local field correction are consistent, which is the case when convergence is achieved. For completeness, we mention that first QMC results for the (static) density response function $\chi(k)$ of the warm dense electron gas have been presented in Dornheim et al.[34] and Groth et al.[35]

FIGURE 1 Schematic illustration of static structure factors for the unpolarized electron gas at $\theta = 2$ and $r_s = 0.5$. In panel (a), the different ranges of validity are illustrated by the light blue (RPA expansion around $k = 0$, Equation (23)), grey (full RPA) and red (full STLS) results. The dark blue vertical lines depict the discrete k-grid for $N = 100$ electrons. In addition, the vertical green and yellow lines show the minimum k-values for $N = 66$ and $N = 38$, respectively. Panel (b) shows results for the static structure factor from Equation (23), full RPA, full STLS, and quantum Monte Carlo (crosses) with the same three particle numbers as above. The solid black line corresponds to a spline combining STLS for small k with QMC elsewhere. Reproduced from Dornheim et al.[20] with the permission of the authors
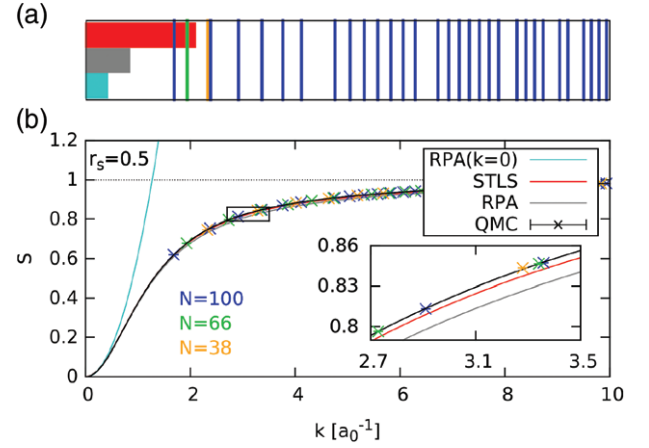
2.6 | Construction of SSFs

The construction of our new results for the SSF over the entire k-range is illustrated in Fig. 1 for the unpolarized UEG at $\theta = 2$ and $r_s = 0.5$. The blue vertical bars in panel (a) correspond to the discrete k-values (due to momentum quantization in a finite simulation cell) of a QMC simulation with $N = 100$ electrons. Evidently, QMC results are not available below $k_{min} = 2\pi/L$ and the k-grid becomes denser for increasing k. The vertical green and yellow line corresponds to the minimum k-value for $N = 66$ and $N = 38$, respectively. Furthermore, the horizontal bars illustrate the ranges of validity of an RPA expansion around $k = 0$ (light blue) given by Kugler[27]

$$S_0^{RPA}(k) = \frac{k^2}{2\omega_p} \coth\left(\frac{\beta\omega_p}{2}\right), \tag{23}$$

the full RPA results (grey) and the full STLS data (red). For the present example, only the STLS data exhibits an overlap with the QMC results.

In panel (b), we show results for $S(k)$ itself. The crosses correspond to the QMC results for the three different particle numbers shown in panel (a). The main difference between these data sets is the different k-grid, while the functional form of the SSF is remarkably well converged with system size, see the inset. The light blue curve depicts the parabolic RPA expansion from Equation (23), which is of interest for finite-size corrections of the interaction energy,[20,21,36] but does not provide a sufficient description of the long-range correlations beyond the QMC data. The grey and red curves correspond to the full RPA and STLS results (see Section 2.5), respectively, and are in perfect agreement with each other and Equation (23) for small k, as expected.[27] Further, the STLS curve exhibits an overlap with the QMC point at k_{min}, whereas the RPA data already exhibit a minor deviation. However, for larger k, both STLS and RPA exhibit systematic errors, although the inclusion of the local field correction leads to a significant increase in the accuracy, see the inset. Finally, the black line depicts a cubic basis spline (obtained using the GNU scientific library [GSL][37]) combining the red curve (for $k < k_{min}/2$) with the blue crosses (elsewhere). In this way, we have obtained an accurate, smooth description of the SSF (in the thermodynamic limit) over the entire k-range. All the new results presented in Section 3 are obtained analogously.

3 | RESULTS FOR THE SSF

Let us start our investigation with a discussion of the r_s-dependence of the SSF at $\theta = 1$, which is depicted in Fig. 2 (see also Table 1 in the appendix). Shown are results for the SSF from full RPA (dashed green) and STLS (solid red) calculations, QMC simulations (blue crosses) and the splines connecting STLS with QMC (dash-dotted blue). For high density ($r_s = 0.1$ and $r_s = 0.3$), the system is only weakly non-ideal and both RPA and STLS provide an accurate description over the entire k-range, as it is expected. With increasing r_s, coupling effects become more important and especially the RPA results become substantially less accurate. In particular, the green curves are always systematically too low at intermediate k, which is most pronounced at $r_s = 10$ and $r_s = 20$, where the bias is of the order of $\Delta S/S \sim 20\%$. This is due to a significant overestimation of short-range correlations, resulting in a (substantially) negative pair correlation function[38] at short distances. In stark contrast, the static local field correction due to Singwi et al.[24] significantly improves the accuracy even for large r_s. Still, with increasing coupling strength there occur systematic deviations to the ab initio QMC data. In particular, the STLS results for smaller k (but not for $k \to 0$, where it becomes exact) are too large, whereas they are too low in the region where $S(k)$ approaches unity. This is most evident at $r_s = 20$, where the STLS approximation does not capture the maximum around $k = 0.2$. Here, too, the PCF from STLS becomes negative for small r.[24] Another fortunate feature of the STLS scheme is an error cancellation in the interaction

FIGURE 2 Density dependence of the static structure factor at $\theta = 1$—Shown are results for the SSF from RPA (dashed green), STLS (solid red), a cublic basis spline connecting STLS and QMC (dashed-dotted blue), and the raw QMC data (blue crosses). The depicted density parameters are $r_s = 0.1, 0.5, 1, 2, 6,$ 10, and 20. All combined results for $S(k)$ are available in website[39], and selected data are given in Table 1

TABLE 1 Static structure factor $S(k)$ for the unpolarized electron gas at $\theta = 1$ (see Fig. 2)—all data have been obtained by combining STLS data for small k with QMC data elsewhere. Extensive data for $\theta = 1, 2, 4, 8$ and multiple r_s values are available in website[39]

$r_s = 20$		$r_s = 1$		$r_s = 0.1$	
k	$S(k)$	k	$S(k)$	k	$S(k)$
0.00837561	0.00186964	0.147084	0.014099	1.46222	0.11347
0.0168193	0.00755307	0.29553	0.0539904	2.94033	0.322402
0.025263	0.0170533	0.443975	0.113561	4.41844	0.484183
0.0337067	0.0303731	0.592421	0.18666	5.89656	0.593229
0.0421504	0.0475827	0.740867	0.267137	7.37467	0.662812
0.0505941	0.0689052	0.889313	0.348842	8.85278	0.70891
0.0590378	0.0945839	1.03776	0.425663	10.3309	0.741495
0.0674815	0.124863	1.1862	0.494009	11.809	0.766743
0.0759252	0.159989	1.33465	0.554356	13.2871	0.787148
0.0843689	0.200215	1.4831	0.60755	14.7652	0.804333
0.0928126	0.245794	1.63154	0.654436	16.2433	0.819583
0.101256	0.296967	1.77999	0.695858	17.7215	0.833513
0.1097	0.353825	1.92843	0.732662	19.1996	0.846342
0.118144	0.41634	2.07688	0.765664	20.6777	0.858384
0.126587	0.484484	2.22532	0.795312	22.1558	0.869857
0.135031	0.557997	2.37377	0.821801	23.6339	0.880723
0.143475	0.634963	2.52222	0.845323	25.112	0.891012
0.151919	0.712752	2.67066	0.86607	26.5901	0.900838
0.160362	0.78873	2.81911	0.884233	28.0682	0.910186
0.168806	0.860214	2.96755	0.900005	29.5464	0.918993
0.17725	0.924327	3.116	0.913588	31.0245	0.927267
0.185693	0.978152	3.26444	0.925229	32.5026	0.935014
0.194137	1.01878	3.41289	0.935189	33.9807	0.94223
0.202581	1.04501	3.56134	0.943728	35.4588	0.94892
0.211024	1.05927	3.70978	0.951108	36.9369	0.955095
0.219468	1.06441	3.85823	0.957587	38.415	0.960744
0.227912	1.0633	4.00667	0.963426	39.8931	0.965865
0.236356	1.05815	4.15512	0.968789	41.3713	0.970485
0.244799	1.05047	4.30356	0.973683	42.8494	0.974635
0.253243	1.04169	4.45201	0.978098	44.3275	0.978345
0.261687	1.03321	4.60046	0.982026	45.8056	0.981625
0.27013	1.02564	4.7489	0.985456	47.2837	0.984483
0.278574	1.01905	4.89735	0.98838	48.7618	0.986971
0.287018	1.01352	5.04579	0.990793	50.2399	0.989136
0.295461	1.00907	5.19424	0.99273	51.718	0.991
0.303905	1.00562	5.34268	0.994262	53.1962	0.992587
0.312349	1.00302	5.49113	0.995456	54.6743	0.993928
0.320793	1.00115	5.63958	0.996383	56.1524	0.995055
0.329236	0.999848	5.78802	0.99711	57.6305	0.995999
0.33768	0.999023	5.93647	0.997708	59.1086	0.99678

energy per particle v, which can be obtained from the SSF by the relation

$$v = \frac{1}{2} \int_{k<\infty} \frac{d\mathbf{k}}{(2\pi)^3} [S(k) - 1] \frac{4\pi}{k^2} = \frac{1}{\pi} \int_0^\infty dk \ [S(k) - 1] \ , \tag{24}$$

where for the second equality, we made use of the fact that the SSF only depends on the modulus of the wave vector $\mathbf{k}$ for homogeneous systems. Therefore, the too large and too small STLS results for $S(k)$ for small and large k cancel to some degree under the integral in Equation (24), leading to STLS interaction energies that are more accurate than the SSF, see for example, Dornheim et al.[21]

In Figs. 3 and 4, we show the same information as in Fig. 2, but for higher temperatures, $\theta = 2$ and $\theta = 8$. For $\theta = 2$, the behaviour of the SSF is quite similar to $\theta = 1$, although the maxima at $r_s = 20$ and even more so at $r_s = 10$ are substantially less
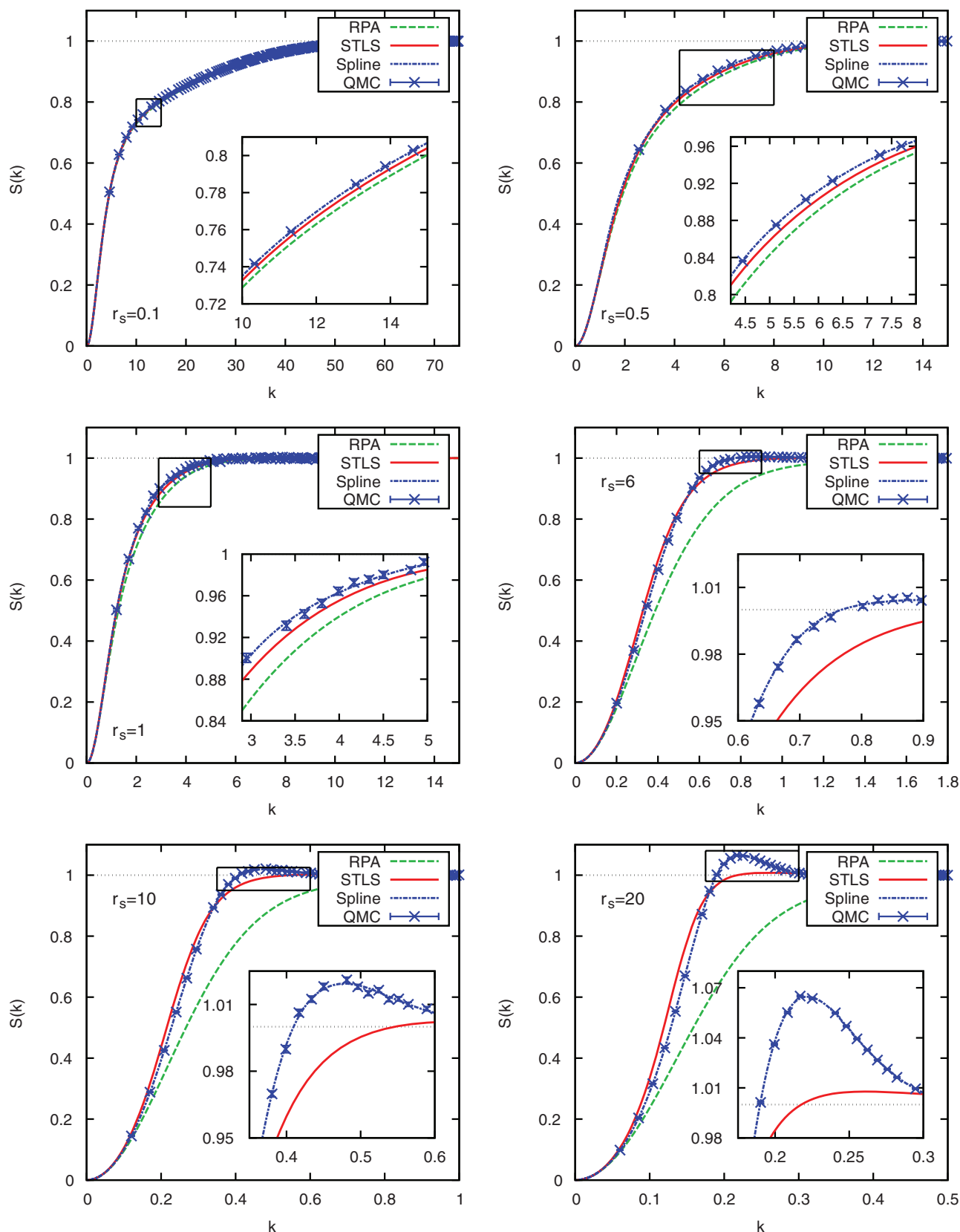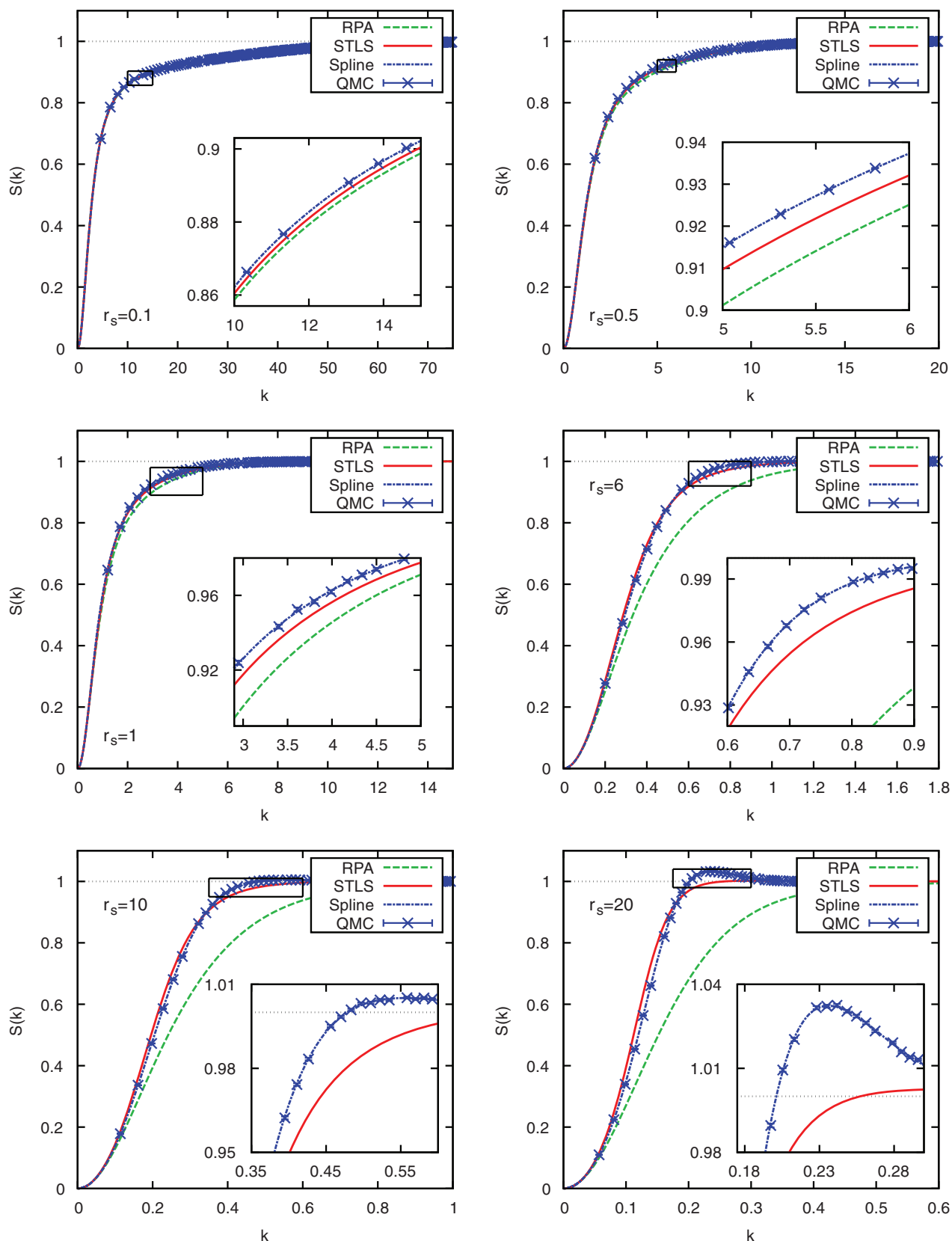
FIGURE 3 Density dependence of the static structure factor at $\theta = 2$—Shown are results for the SSF from RPA (dashed green), STLS (solid red), a cublic basis spline connecting STLS and QMC (dashed-dotted blue), and the raw QMC data (blue crosses). The depicted density parameters are $r_s = 0.1, 0.5, 1, 2, 6$, 10, and 20. All combined results for $S(k)$ are available in website[39]

FIGURE 4 Density dependence of the static structure factor at $\theta = 8$ – Shown are results for the SSF from RPA (dashed green), STLS (solid red), a cublic basis spline connecting STLS and QMC (dashed-dotted blue), and the raw QMC data (blue crosses). The depicted density parameters are $r_s = 0.1, 0.5, 1, 2, 6, 10$, and 20. All combined results for $S(k)$ are available in website[39]
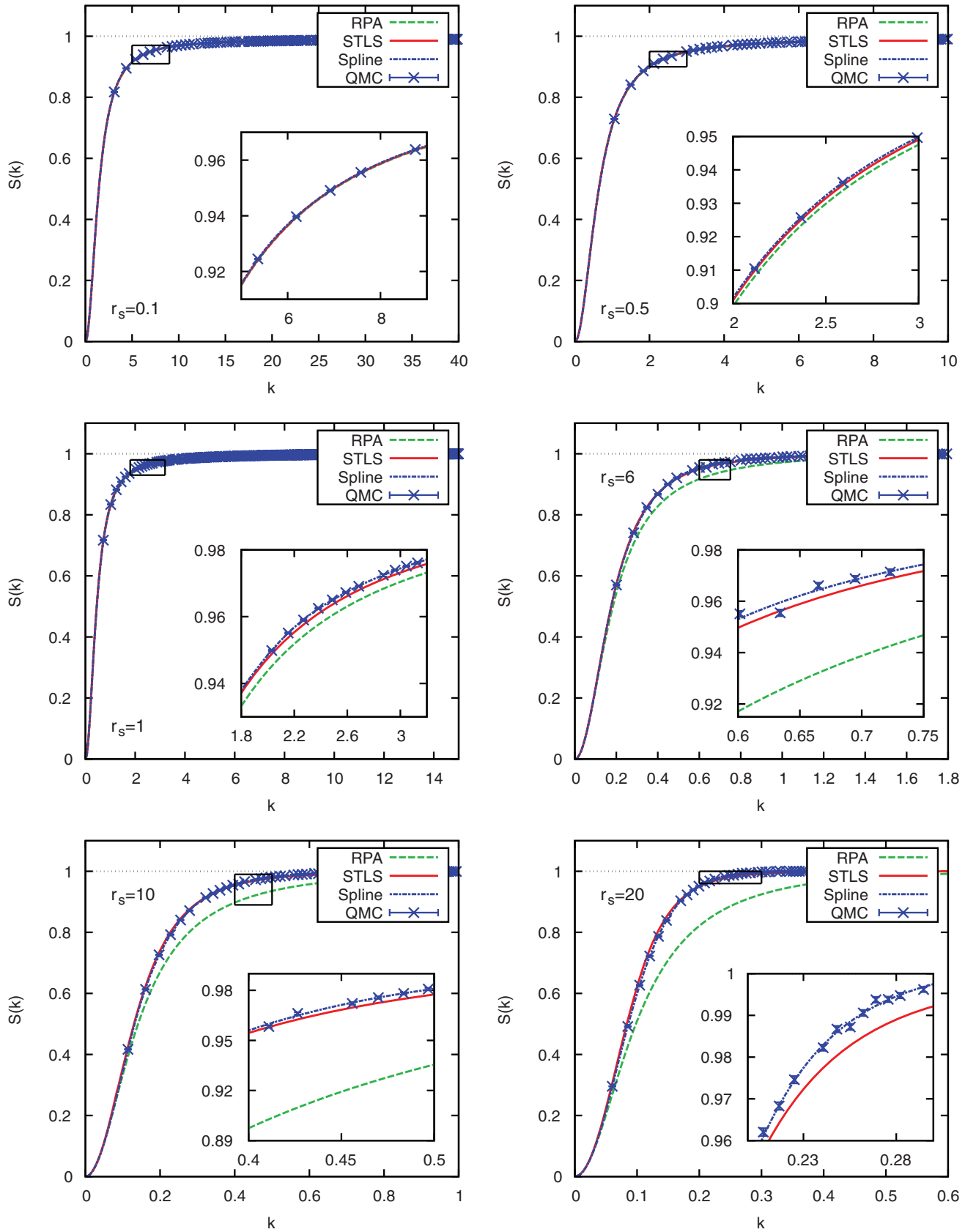
pronounced. At $\theta = 8$, which corresponds to a relatively high temperature where both quantum effects and Coulomb coupling are significantly less important, the situation is quite different. In particular, the correlation-induced maximum in $S(k)$ has vanished and the STLS approximation provides an accurate description over the entire k-range, even for large r_s. The largest deviations occur at $r_s = 20$, but even here $\Delta S/S$ does not exceed 1%. While the RPA, too, becomes more accurate, there remain significant systematic errors from intermediate to large r_s. Therefore, we conclude that, despite the high temperature, a mean field ansatz (RPA) for the density response function, Equation (19), is still not sufficient at the present parameters.

4 | SUMMARY AND CONCLUSION

In summary, we have combined the exact description of the short-range exchange-correlation effects from ab initio QMC simulations with results from the STLS approximation, which becomes exact in the long-range limit, $k \rightarrow 0$. In this way, we have been able to obtain accurate data for the SSF (in the thermodynamic limit) over the entire relevant k-range. This has allowed us to compare our new results both to the RPA and STLS over two orders of magnitude in the coupling parameter r_s and for three relevant temperatures θ. In agreement with findings in the ground state, we confirm that the RPA, due to the mean field ansatz for the density response function $\chi(\mathbf{q}, \omega)$, is only accurate for weak non-ideality, but rapidly breaks down with increasing r_s. Even at the largest investigated temperature $\theta = 8$, RPA exhibits substantial errors at intermediate r_s. In stark contrast, the inclusion of the static local field correction proposed by Singwi et al.[24] significantly increases the accuracy everywhere. Only at strong coupling, $r_s = 20$ and 10, the STLS fails to accurately describe the maxima around $k = 0.2$ and 0.5, respectively. Furthermore, we note that due to the too large SSF for small k and too small SSF for larger k, there occurs an error cancellation in the calculation of the interaction energy v, which means that STLS results for this quantity are more accurate than for $S(k)$.

We expect our new accurate SSFs (available at website[39]) of the warm dense electron gas to be of broad interest for various applications related to modern WDM research. In particular, they can be used to benchmark other dielectric approximations such as quantum STLS[40,41] or the recent local field correction based on the hypernetted-chain approximation by Tanaka.[42] Furthermore, accurate data for $S(k)$ can be used to approximate the local field correction itself[43] or as input for the calculation of dynamic quantities using the method of frequency moments.[44]

REFERENCES

[1] F. Graziani, M. P. Desjarlais, R. Redmer, S. B. Trickey, *Frontiers and Challenges in Warm Dense Matter*, Springer International Publishing Switzerland, Basel **2014**.

[2] M. D. Knudson, M. P. Desjarlais, R. W. Lemke, T. R. Mattsson, M. French, N. Nettelmann, R. Redmer, *Phys. Rev. Lett.* **2012**, *108*, 091102.

[3] B. Militzer, W. B. Hubbard, J. Vorberger, I. Tamblyn, S. A. Bonev, *Astrophys. J.* **2008**, *688*, L45.

[4] R. Ernstorfer, M. Harb, C. T. Hebeisen, G. Sciaini, T. Dartigalongue, R. J. Dwayne Miller, *Science* **2009**, *323*, 5917.

[5] R. Nora, W. Theobald, R. Betti, F. J. Marshall, D. T. Michel, W. Seka, B. Yaakobi, M. Lafon, C. Stoeckl, J. Delettrez, A. A. Solodov, A. Casner, C. Reverdin, X. Ribeyre, A. Vallet, J. Peebles, F. N. Beg, M. S. We, *Phys. Rev. Lett.* **2015**, *114*, 045001.

[6] P. F. Schmit, P. F. Knapp, S. B. Hansen, M. R. Gomez, K. D. Hahn, D. B. Sinars, K. J. Peterson, S. A. Slutz, A. B. Sefkow, T. J. Awe, E. Harding, C. A. Jennings, G. A. Chandler, G. W. Cooper, M. E. Cuneo, M. Geissel, A. J. Harvey-Thompson, M. C. Herrmann, M. H. Hess, O. Johns, D. C. Lamppa, M. R. Martin, R. D. McBride, J. L. Porter, G. K. Robertson, G. A. Rochau, D. C. Rovang, C. L. Ruiz, M. E. Savage, I. C. Smith, W. A. Stygar, R. A. Vesey, *Phys. Rev. Lett.* **2014**, *113*, 155004.

[7] O. A. Hurricane, D. A. Callahan, D. T. Casey, E. L. Dewald, T. R. Dittrich, T. Döppner, S. Haan, D. E. Hinkel, L. F. Berzak Hopkins, O. Jones, A. L. Kritcher, S. Le Pape, T. Ma, A. G. MacPhee, J. L. Milovich, J. Moody, A. Pak, H.-S. Park, P. K. Patel, J. E. Ralph, H. F. Robey, J. S. Ross, J. D. Salmonson, B. K. Spears, P. T. Springer, R. Tommasini, F. Albert, L. R. Benedetti, R. Bionta, E. Bond, D. K. Bradley, J. Caggiano, P. M. Celliers, C. Cerjan, J. A. Church, R. Dylla-Spears, D. Edgell, M. J. Edwards, D. Fittinghoff, M. A. Barrios Garcia, A. Hamza, R. Hatarik, H. Herrmann, M. Hohenberger, D. Hoover, J. L. Kline, G. Kyrala, B. Kozioziemski, G. Grim, J. E. Field, J. Frenje, N. Izumi, M. Gatu Johnson, S. F. Khan, J. Knauer, T. Kohut, O. Landen, F. Merrill, P. Michel, A. Moore, S. R. Nagel, A. Nikroo, T. Parham, R. R. Rygg, D. Sayre, M. Schneider, D. Shaughnessy, D. Strozzi, R. P. J. Town, D. Turnbull, P. Volegov, A. Wan, K. Widmann, C. Wilde, C. Yeamans, *Nat. Phys.* **2016**, *12*, 800.

[8] D. M. Ceperley, *Phys. Rev. B.* **1978**, *18*, 3126.

[9] D. M. Ceperley, B. J. Alder, *Phys. Rev. Lett.* **1980**, *45*, 566.

[10] E. Y. Loh, J. E. Gubernatis, R. T. Scalettar, S. R. White, D. J. Scalapino, R. L. Sugar, *Phys. Rev.* **1990**, *B41*, 9301.

[11] M. Troyer, U. J. Wiese, *Phys. Rev. Lett.* **2005**, *94*, 170201.

[12] T. Schoof, M. Bonitz, A. V. Filinov, D. Hochstuhl, J. W. Dufty, *Contrib. Plasma Phys.* **2011**, *51*, 687.

[13] T. Schoof, S. Groth, J. Vorberger, M. Bonitz, *Phys. Rev. Lett.* **2015**, *115*, 130402.

[14] T. Dornheim, S. Groth, A. Filinov, M. Bonitz, *New J. Phys.* **2015**, *17*, 073017.

[15] T. Dornheim, T. Schoof, S. Groth, A. Filinov, M. Bonitz, *J. Chem. Phys.* **2015**, *143*, 204101.

[16] S. Groth, T. Schoof, T. Dornheim, M. Bonitz, *Phys. Rev.* **2016**, *B93*, 085102.

[17] T. Dornheim, S. Groth, T. Schoof, C. Hann, M. Bonitz, *Phys. Rev.* **2016**, *B93*, 205134.

[18] N. D. Drummond, R. J. Needs, A. Sorouri, W. M. C. Foulkes, *Phys. Rev.* **2008**, *B78*, 125106.

[19] S. Chiesa, D. M. Ceperley, R. M. Martin, M. Holzmann, *Phys. Rev. Lett.* **2006**, *97*, 076404.

[20] T. Dornheim, S. Groth, T. Sjostrom, F. D. Malone, W. M. C. Foulkes, M. Bonitz, *Phys. Rev. Lett.* **2016**, *117*, 156403.

[21] T. Dornheim, S. Groth, F. D. Malone, T. Schoof, T. Sjostrom, W. M. C. Foulkes, M. Bonitz, *Phys. Plasma.* **2017**, *24*, 056303.

[22] S. Groth, T. Dornheim, T. Sjostrom, F. D. Malone, W. M. C. Foulkes, M. Bonitz, *Phys. Rev. Lett.* **2017**, *119*, 135001.

[23] S. Groth, T. Dornheim, M. Bonitz, *Contrib. Plasma Phys.* **2017**, *57*, 137.

[24] K. S. Singwi, M. P. Tosi, R. H. Land, A. Sjölander, *Phys. Rev.* **1968**, *176*, 589.

[25] S. Tanaka, S. Ichimaru, *J. Phys. Soc. Jpn.* **1986**, *55*, 2278.

[26] T. Sjostrom, J. Dufty, *Phys. Rev.* **2013**, *B88*, 115123.

[27] A. A. Kugler, *Phys. Rev.* **1970**, *A1*, 1688.

[28] D. Bohm, D. Pines, *Phys. Rev.* **1953**, *92*, 609.

[29] L. M. Fraser, W. M. C. Foulkes, G. Rajagopal, R. J. Needs, S. D. Kenny, and A. J. Williamson, *Phys. Rev.* **1996**, *B53*, 1814.

[30] N. Metropolis, A. W. Rosenbluth, M. N. Rosenbluth, A. H. Teller, E. Teller, *J. Chem. Phys.* **1953**, *21*, 1087.

[31] D. M. Ceperley, *Rev. Mod. Phys.* **1995**, *67*, 279.

[32] A. A. Kugler, *J. Stat. Phys.* **1975**, *12*, 35.

[33] G. Giuliani, G. Vignale, *Quantum Theory of the Electron Liquid*, Cambridge University Press, Cambridge **2008**.

[34] T. Dornheim, S. Groth, J. Vorberger, M. Bonitz, *Phys. Rev.* **2017**, *E96*, 023203.

[35] S. Groth, T. Dornheim, and M. Bonitz, *J. Chem. Phys.* **2017**, *147*, 164108.

[36] E. W. Brown, B. K. Clark, J. L. DuBois, D. M. Ceperley, *Phys. Rev. Lett.* **2013**, *110*, 146405.

[37] GNU Scientific Library. https://www.gnu.org/software/gsl/ (accessed July 2017)

[38] L. Hedin, *Phys. Rev.* **1965**, *139*, A796.

[39] GitHub. github.com/agbonitz/xc_functional

[40] H. Schweng, H. Böhm, *Phys. Rev.* **1993**, *B48*, 2037.

[41] P. Arora, K. Kumar, R. K. Moudgil, *Eur. Phys. J.* **2017**, *B90*, 76.

[42] S. Tanaka, *J. Chem. Phys.* **2016**, *145*, 214104.

[43] S. Hellal, J.-G. Gasser, A. Issolah, *Phys. Rev.* **2003**, *B68*, 094204.

[44] Y. V. Arkhipov, A. B. Ashikbayeva, A. Askaruly, A. E. Davletov, I. M. Tkachenko, *Phys. Rev.* **2014**, *E90*, 053102.
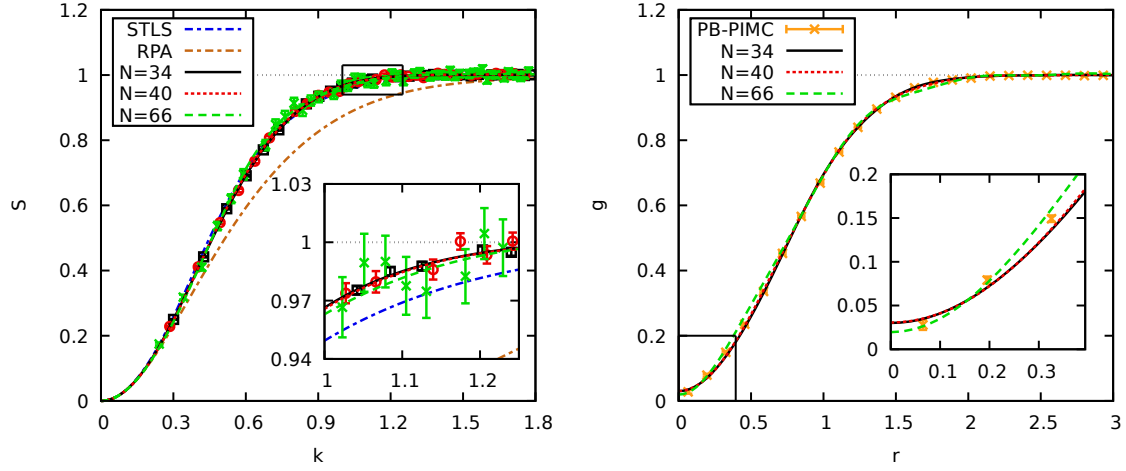
Fig. 5.1 Left: Static structure factor $S(k)$ for the unpolarized electron gas at $r_s = 4$ and $\theta = 1$. The dash-dotted blue and brown curves correspond to dielectric results via STLS and RPA, respectively. The symbols depict PB-PIMC data for three different particle numbers and the solid black, dotted red, and dashed green lines the respective cubic basis splines. Right: Corresponding pair correlation function $g(r)$ as computed from the splines via Eq. (5.2) [lines] and direct PB-PIMC estimation of $g(r)$ for $N = 66$ electrons taken from Dornheim *et al.* [163] [yellow crosses].

5.2.1 The Pair Correlation Function

The static structure factor $S(\mathbf{k})$ is directly connected to the pair distribution function by a Fourier transform,

$$g(\mathbf{r}) = 1 + \frac{1}{n} \int \frac{d\mathbf{k}}{(2\pi)^3} (S(\mathbf{k}) - 1) e^{i\mathbf{r}\cdot\mathbf{k}} \quad . \tag{5.1}$$

Note that, for a finite system, the integral in Eq. (5.1) is replaced by a sum over discrete reciprocal lattice vectors. For a uniform system with $g(\mathbf{r}) = g(r)$ and $S(\mathbf{k}) = S(k)$, we have

$$g(r) = 1 + \frac{1}{2n\pi^2 r} \int_0^\infty dk \, \sin(kr)[S(k) - 1] \quad , \tag{5.2}$$

i.e., a one-dimensional integral that can easily be evaluated numerically. This procedure is demonstrated in Fig. 5.1 for the unpolarized electron gas at $\theta = 1$ and $r_s = 4$. The left panel shows results for the static structure factor, where the blue and brown dash-dotted lines correspond to STLS and RPA data, respectively. The symbols depict PB-PIMC results for three different particle numbers. First and foremost, no system size dependence can be resolved in the SSF within the given statistical uncertainty, as already reported in Sec. 5.1. Secondly, we find that both RPA and STLS are in good agreement with the QMC data for

small q, but substantially deviate elsewhere, see also the inset depicting a magnified segment. Finally, the solid black, dotted red, and dashed green lines correspond to the cubic basis splines that were obtained by combining the STLS results for small q with QMC data for $N = 34$, $N = 40$, and $N = 66$ electrons, respectively. Evidently, the basis spline smoothly interpolates between the noisy QMC data and the red and black curves are in excellent agreement everywhere. Only the dashed green curve exhibits some minor deviations due to the significantly larger statistical uncertainty in the underlying QMC input data.

The right panel shows the corresponding results for the pair correlation function $g(r)$ computed from the cubic basis splines via Eq. (5.2). First of all, the pair correlation functions obtained from $N = 34$ and $N = 40$ coincide perfectly over the entire r-range, whereas the $N = 66$-curve somewhat deviates. Obviously, this is a direct consequence of the deviations observed in $S(k)$ in the left panel. The yellow symbols correspond to the direct PB-PIMC estimation[6] of $g(r)$ taken from Dornheim et al. [163] and is, overall, in good agreement with the spline-based results, as it is expected.

An interesting feature of the pair correlation function at the present conditions is the non-vanishing value for $r = 0$. This value, $g(0)$, is often denoted as the *on-top* pair correlation function and is of high importance for various theories, including the construction of gradient approximations for density functional theory calculations [117, 200] and the asymptotic large-k expansion of the momentum distribution [201, 202] that is closely connected to the nuclear fusion rate, e.g., in the solar interior [203]. The physical origin is a combination of the absence of Pauli blocking between spin-up and -down electrons (for a spin-polarized UEG, it always holds $g(0) = 0$) and the quantum mechanical delocalization alleviating the Coulomb repulsion.

Let us conclude this section with a systematic discussion of the coupling strength dependence of $g(r)$, as depicted in Fig. 5.2 for the unpolarized UEG at $\theta = 1$. The solid red curves were obtained using the splines from Dornheim et al. [165], and we find a decreasing value of $g(0)$ with increasing coupling strength, as it is expected. At $r_s = 0.1$, the system is only weakly nonideal and the on-top pair correlation function is close to the ideal value of $g_0(0) = 0.5$, whereas, at $r_s = 10$, it vanishes within the given degree of accuracy. Naturally, this is a direct consequence of the increased Coulomb repulsion, which even leads to a small but significant peak in $g(r)$ in the latter case. Finally, let us consider the dielectric approximations, which are depicted as dash-dotted blue and dotted brown lines for STLS and RPA, respectively. Somewhat surprisingly, even at $r_s = 0.1$ both curves exhibit deviations of several per cent regarding $g(0)$. Furthermore, it is well known that both the RPA and STLS

---

[6]Here *direct* means using a binned histogram estimator and not taking the route via the static structure factor.
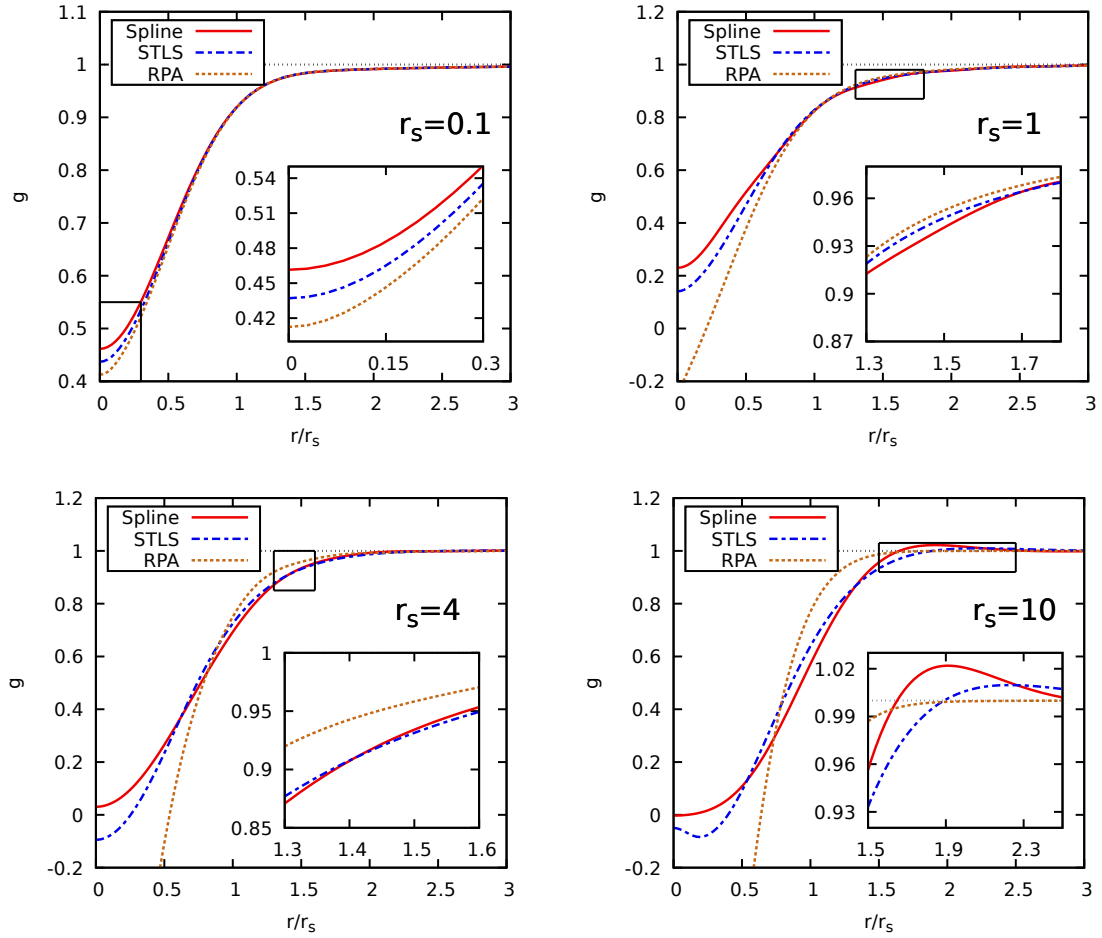
Fig. 5.2 Coupling strength dependence of the pair correlation function $g(r)$ of the unpolarized electron gas at $\theta = 1$. Shown are data computed from our spline fits to the static structure factor $S(k)$ (taken from Dornheim *et al.* [165]) according to Eq. (5.2) [solid red line], and dielectric results in the RPA (dotted brown) and STLS (dash-dotted blue) approximation.

pair correlation functions become negative with increasing r_s, which is usually interpreted as the overestimation of correlation effects [131]. For RPA, this is the case even for moderate coupling, $r_s = 1$, whereas the inclusion of the STLS local-field correction leads to a significant improvement. Nevertheless, for $r_s = 4$, the blue curve, too, exhibits a pronounced negative feature at small r. This is in stark contrast to the static structure factor, where STLS appears to be in much better agreement with our QMC based data, cf. the left panel of Fig. 5.1.

5.3   Overview, Intermediate Status, and Road Map

The publication of the first *ab initio* results for the warm dense electron gas in the thermodynamic limit, cf. Sec. 5.1, constituted a major leap on the road to our final goal: the construction of a reliable parametrization of the exchange–correlation free energy of the uniform electron gas with respect to temperature, density, and spin-polarization, $f_{xc}(r_s, \theta, \xi)$, covering the entire relevant warm dense matter range. As the supplement for an invited talk at the APS meeting of the division of plasma physics[7], we summarized the then state of the art of thermodynamic quantum Monte Carlo simulations of the UEG in the following paper, Ref. [42]. As such, it contains a concise overview of the relevant QMC methods, including the novel density matrix QMC (DMQMC) approach by Foulkes, Malone, and co-workers [171, 156, 204]. Of particular relevance is the given overview regarding the applicability of standard PIMC, PB-PIMC, CPIMC, and DMQMC (Fig. 2 of Ref. [42]) in the temperature–density plane and the emerging consensus with respect to the simulation of the UEG with a finite number of electrons (Fig. 3 of Ref. [42]), as the independent DMQMC data are in excellent agreement with our combination of CPIMC and PB-PIMC. Furthermore, the paper contains a broad discussion of finite-size effects, including various examples, and is concluded by a brief road map towards the desired complete description of the UEG at warm dense matter conditions.

---

[7]The talk was given by M. Bonitz on November 3rd, 2016 in San Jose, California.

Ab initio quantum Monte Carlo simulation of the warm dense electron gas

Tobias Dornheim,[1,a),b)] Simon Groth,[1,b)] Fionn D. Malone,[2] Tim Schoof,[1] Travis Sjostrom,[3] W. M. C. Foulkes,[2] and Michael Bonitz[1,c)]

[1]*Institut für Theoretische Physik und Astrophysik, Christian-Albrechts-Universität zu Kiel, D-24098 Kiel, Germany*
[2]*Department of Physics, Imperial College London, Exhibition Road, London SW7 2AZ, United Kingdom*
[3]*Theoretical Division, Los Alamos National Laboratory, Los Alamos, New Mexico 87545, USA*

Warm dense matter is one of the most active frontiers in plasma physics due to its relevance for dense astrophysical objects and for novel laboratory experiments in which matter is being strongly compressed, e.g., by high-power lasers. Its description is theoretically very challenging as it contains correlated quantum electrons at finite temperature—a system that cannot be accurately modeled by standard analytical or ground state approaches. Recently, several breakthroughs have been achieved in the field of fermionic quantum Monte Carlo simulations. First, it was shown that exact simulations of a finite model system (30…100 electrons) are possible, which avoid any simplifying approximations such as fixed nodes [Schoof *et al.*, Phys. Rev. Lett. **115**, 130402 (2015)]. Second, a novel way to accurately extrapolate these results to the thermodynamic limit was reported by Dornheim *et al.* [Phys. Rev. Lett. **117**, 156403 (2016)]. As a result, now thermodynamic results for the warm dense electron gas are available, which have an unprecedented accuracy on the order of 0.1%. Here, we present an overview on these results and discuss limitations and future directions. *Published by AIP Publishing.* [http://dx.doi.org/10.1063/1.4977920]

I. INTRODUCTION

The uniform electron gas (UEG) (i.e., electrons in a uniform positive background) is inarguably one of the most fundamental systems in condensed matter physics and quantum chemistry.[1] Most notably, the availability of accurate quantum Monte Carlo (QMC) data for its ground state properties[2,3] has been pivotal for the success of the Kohn-Sham density functional theory (DFT).[4,5]

Over the past few years, interest in the study of matter under extreme conditions has grown rapidly. Experiments with not only inertial confinement fusion targets[6–8] and laser-excited solids[9] but also astrophysical applications such as planet cores and white dwarf atmospheres[10,11] require a fundamental understanding of the warm dense matter (WDM) regime, a problem now at the forefront of plasma physics and materials science. In this peculiar state of matter, both the dimensionless Wigner-Seitz radius $r_s = \bar{r}/a_0$ (with the mean interparticle distance $\bar{r}$ and Bohr radius a_0) and the reduced temperature $\theta = k_B T/E_F$ (E_F being the Fermi energy) are of order unity, implying a complicated interplay of quantum degeneracy, coupling effects, and thermal excitations. Because of the importance of thermal excitation, the usual ground-state version of DFT does not provide an appropriate description of WDM. An explicitly thermodynamic generalization of DFT[12] has long been known in principle but requires an accurate parametrization of the exchange-correlation free energy (f_{xc}) of the UEG over the entire warm dense regime as an input.[13–17]

This seemingly manageable task turns out to be a major obstacle. The absence of a small parameter prevents a low-temperature or perturbation expansion, and consequently, Green function techniques in the Montroll-Ward and e^4 approximations[18,19] break down. Further, the linear response theory within the random phase approximation[20,21] (RPA) and also with the additional inclusion of static local field corrections as suggested by, e.g., Singwi, Tosi, Land, and Sjölander[22–24] (STLS) and Vashista and Singwi[24,25] (VS), is not reliable. Quantum classical mappings[26,27] are exact in some known limiting cases but constitute an uncontrolled approximation in the WDM regime.

The difficulty of constructing a quantitatively accurate theory of WDM leaves thermodynamic QMC simulations as the only available tool to accomplish the task at hand. However, the widely used path integral Monte Carlo[28] (PIMC) approach is severely hampered by the notorious fermion sign problem[29,30] (FSP), which limits simulations to high temperatures and low densities and precludes applications to the warm dense regime. In their pioneering work, Brown *et al.*[31] circumvented the FSP by using the fixed-node approximation[32] (an approach hereafter referred to as restricted PIMC, RPIMC), which allowed them to present the first comprehensive results for the UEG over a wide temperature range for $r_s \geq 1$.

Although these data have subsequently been used to construct the parametrization of f_{xc} required for thermodynamic DFT (see Refs. 24, 33, and 34), their quality has been called into question. First, RPIMC constitutes an uncontrolled approximation,[35–38] which means that the accuracy of the results for the finite model system studied by Brown *et al.*[31] was unclear. This unsatisfactory situation has sparked remarkable recent progress in the field of fermionic QMC.[39–50] In

particular, a combination of two complementary QMC approaches[51,52] has recently been used to simulate the warm dense UEG without nodal restrictions,[42] revealing that the nodal constraints in RPIMC cause errors exceeding 10%. Second, Brown *et al.*[31] extrapolated their QMC results for $N = 33$ spin-polarized ($N = 66$ unpolarized) electrons to the macroscopic limit by applying a finite-T generalization of the simple first-order finite-size correction (FSC) introduced by Chiesa *et al.*[53] for the ground state. As we have recently shown,[47] this is only appropriate for low temperature and strong coupling and, thus, introduces a second source of the systematic error.

In this paper, we give a concise overview of the current state of the art of quantum Monte Carlo simulations of the warm dense electron gas and present new results regarding the extrapolation to the thermodynamic limit (TDL). Further, we discuss the remaining open questions and challenges in the field.

After a brief introduction to the UEG model (II), we introduce various QMC techniques, starting with the standard path integral Monte Carlo approach (A) and a discussion of the origin of the FSP (B). The sign problem can be alleviated using the permutation blocking PIMC (PB-PIMC, C) method, the configuration PIMC algorithm (CPIMC, D), or the density matrix QMC (DMQMC, E) approach. In combination, these tools make it possible to obtain accurate results for a finite model system over almost the entire warm dense regime (IV). The second key issue is the extrapolation from the finite to the infinite system, i.e., the development of an appropriate finite-size correction,[47,53–57] which is discussed in detail in Sec. V. Finally, we compare our QMC results for the infinite UEG to other data (2) and finish with some concluding remarks and a summary of open questions.

II. THE UNIFORM ELECTRON GAS

A. Coordinate representation of the Hamiltonian

Following Refs. 44 and 54, we express the Hamiltonian (using Hartree atomic units) for $N = N_\uparrow + N_\downarrow$ unpolarized electrons in coordinate space as

$$\hat{H} = -\frac{1}{2} \sum_{i=1}^{N} \nabla_i^2 + \frac{1}{2} \sum_{i=1}^{N} \sum_{j \neq i}^{N} \Psi(\mathbf{r}_i, \mathbf{r}_j) + \frac{N}{2} \xi_M, \quad (1)$$

with the well-known Madelung constant ξ_M and the periodic Ewald pair interaction

$$\Psi(\mathbf{r}, \mathbf{s}) = \frac{1}{\Omega} \sum_{\mathbf{G} \neq 0} \frac{e^{-\pi^2 \mathbf{G}^2/\kappa^2} e^{2\pi i \mathbf{G}(\mathbf{r}-\mathbf{s})}}{\pi \mathbf{G}^2}$$
$$- \frac{\pi}{\kappa^2 \Omega} + \sum_{\mathbf{R}} \frac{\mathrm{erfc}(\kappa|\mathbf{r} - \mathbf{s} + \mathbf{R}|)}{|\mathbf{r} - \mathbf{s} + \mathbf{R}|}. \quad (2)$$

Here, $\mathbf{R} = \mathbf{n}_1 L$ and $\mathbf{G} = \mathbf{n}_2/L$ denote the real and reciprocal space lattice vectors, respectively, with $\mathbf{n}_1$ and $\mathbf{n}_2$ three-component vectors of integers, L the box length, $\Omega = L^3$ the box volume, and κ the usual Ewald parameter.

B. Hamiltonian in second quantization

In second quantized notation using a basis of spin-orbitals of plane waves, $\langle \mathbf{r}\sigma | \mathbf{k}_i \sigma_i \rangle = \frac{1}{L^{3/2}} e^{i\mathbf{k}_i \cdot \mathbf{r}} \delta_{\sigma,\sigma_i}$, with $\mathbf{k}_i = \frac{2\pi}{L} \mathbf{m}_i$, $\mathbf{m}_i \in \mathbb{Z}^3$ and $\sigma_i \in \{\uparrow, \downarrow\}$, the Hamiltonian, Eq. (1), becomes

$$\hat{H} = \frac{1}{2} \sum_i \mathbf{k}_i^2 \hat{a}_i^\dagger \hat{a}_i + \sum_{\substack{i < j, k < l \\ i \neq k, j \neq l}} w_{ijkl}^- \hat{a}_i^\dagger \hat{a}_j^\dagger \hat{a}_l \hat{a}_k + \frac{N}{2} \xi_M. \quad (3)$$

The antisymmetrized two-electron integrals take the form $w_{ijkl}^- = w_{ijkl} - w_{ijlk}$, where

$$w_{ijkl} = \frac{4\pi e^2}{L^3 (\mathbf{k}_i - \mathbf{k}_k)^2} \delta_{\mathbf{k}_i + \mathbf{k}_j, \mathbf{k}_k + \mathbf{k}_l} \delta_{\sigma_i, \sigma_k} \delta_{\sigma_j, \sigma_l}, \quad (4)$$

and the Kronecker deltas ensure both momentum and spin conservation. The first (second) term in the Hamiltonian, Eq. (3), describes the kinetic (interaction) energy. The operator $\hat{a}_i^\dagger$ ($\hat{a}_i$) creates (annihilates) a particle in the spin-orbital $|\mathbf{k}_i \sigma_i\rangle$.

III. QUANTUM MONTE CARLO

A. Path integral Monte Carlo

Let us consider N spinless distinguishable particles in the canonical ensemble, with the volume Ω, the inverse temperature $\beta = 1/k_B T$, and the density N/Ω being fixed. The partition function in coordinate representation is given by

$$Z = \int d\mathbf{R} \, \langle \mathbf{R} | e^{-\beta \hat{H}} | \mathbf{R} \rangle, \quad (5)$$

where $\mathbf{R} = \{\mathbf{r}_1, \ldots, \mathbf{r}_N\}$ contains all $3N$ particle coordinates, and the Hamiltonian $\hat{H} = \hat{K} + \hat{V}$ is given by the sum of a kinetic and a potential part, respectively. Since the low-temperature matrix elements of the density operator, $\hat{\rho} = e^{-\beta \hat{H}}$, are not readily known, we exploit the group property $e^{-\beta \hat{H}} = (e^{-\epsilon \hat{H}})^P$, with $\epsilon = \beta/P$ and positive integers P. Inserting $P - 1$ unities of the form $\hat{1} = \int d\mathbf{R}_\alpha |\mathbf{R}\rangle_\alpha \langle \mathbf{R}|_\alpha$ into Eq. (5) leads to

$$Z = \int d\mathbf{X} \left(\langle \mathbf{R}_0 | e^{-\epsilon \hat{H}} | \mathbf{R}_1 \rangle \langle \mathbf{R}_1 | \ldots | \mathbf{R}_{P-1} \rangle \langle \mathbf{R}_{P-1} | e^{-\epsilon \hat{H}} | \mathbf{R}_0 \rangle \right)$$
$$= \int d\mathbf{X} \, W(\mathbf{X}). \quad (6)$$

We stress that Eq. (6) is still exact and constitutes an integral over P sets of particle coordinates ($d\mathbf{X} = d\mathbf{R}_0 \ldots d\mathbf{R}_{P-1}$), the integrand being a product of P density matrices, each at P times the original temperature T. Despite the significantly increased dimensionality of the integral, this recasting is advantageous as the high temperature matrix elements can easily be approximated, most simply with the primitive approximation, $e^{-\epsilon \hat{H}} \approx e^{-\epsilon \hat{K}} e^{-\epsilon \hat{V}}$, which becomes exact for $P \to \infty$. In a nutshell, the basic idea of the path integral Monte Carlo method[28] is to map the quantum system onto a classical ensemble of ring polymers.[58] The resulting high

dimensional integral is evaluated using the Metropolis algorithm,[59] which allows one to sample the $3PN$-dimensional configurations $\mathbf{X}$ of the ring polymer according to the corresponding configuration weight $W(\mathbf{X})$.

B. The fermion sign problem

To simulate N spin-polarized fermions, the partition function from the previous Section III A has to be extended to include a sum over all $N!$ permutations of particles:

$$Z = \frac{1}{N!} \sum_{s \in S_N} \text{sgn}(s) \int d\mathbf{R} \, \langle \mathbf{R} | e^{-\beta \hat{H}} | \hat{\pi}_s \mathbf{R} \rangle, \tag{7}$$

where $\hat{\pi}_s$ denotes the exchange operator corresponding to the element s from the permutation group S_N. Evidently, Eq. (7) constitutes a sum over both positive and negative terms, so that the configuration weight function $W(\mathbf{X})$ can no longer be interpreted as a probability distribution. To allow fermionic expectation values to be computed using the Metropolis Monte Carlo method, we introduce the modified partition function

$$Z' = \int d\mathbf{X} \, |W(\mathbf{X})|, \tag{8}$$

and compute fermionic observables as

$$\langle O \rangle = \frac{\langle OS \rangle'}{\langle S \rangle'}, \tag{9}$$

with averages taken over the modified probability distribution $W'(\mathbf{X}) = |W(\mathbf{X})|$ and $S = W(\mathbf{X})/|W(\mathbf{X})|$ denoting the sign. The average sign, i.e., the denominator in Eq. (9), is a measure for the cancellation of positive and negative contributions and exponentially decreases with inverse temperature and system size, $\langle S \rangle' \propto e^{-\beta N(f-f')}$, with f and f' being the free energy per particle of the original and the modified system, respectively. The statistical error of the Monte Carlo average value ΔO is inversely proportional to $\langle S \rangle'$

$$\frac{\Delta O}{O} \propto \frac{1}{\langle S \rangle' \sqrt{N_{\text{MC}}}} \propto \frac{e^{\beta N(f-f')}}{\sqrt{N_{\text{MC}}}}. \tag{10}$$

The exponential increase in the statistical error with β and N evident in Eq. (10) can only be compensated by increasing the number of Monte Carlo samples, but the slow $1/\sqrt{N_{\text{MC}}}$ convergence soon makes this approach unfeasible. This is the notorious fermion sign problem,[29,30] which renders standard PIMC unfeasible even for the simulation of small systems at moderate temperature.

C. Permutation blocking path integral Monte Carlo

To alleviate the difficulties associated with the FSP, Dornheim *et al.*[43,44,48] recently introduced a novel simulation scheme that significantly extends fermionic PIMC simulations towards lower temperature and higher density. This so-called permutation blocking PIMC (PB-PIMC) approach combines (i) the use of antisymmetrized density matrix elements, i.e., determinants;[60–62] (ii) a fourth-order factorization scheme to

obtain accurate approximate density matrices for relatively low temperatures (large imaginary-time steps);[63–66] and (iii) an efficient Metropolis Monte Carlo sampling scheme based on the temporary construction of artificial trajectories.[43]

In particular, we use the factorization introduced in Refs. 64 and 65

$$e^{-\epsilon \hat{H}} \approx e^{-v_1 \epsilon \hat{W}_{a_1}} e^{-t_1 \epsilon \hat{K}} e^{-v_2 \epsilon \hat{W}_{1-2a_1}}$$
$$\times e^{-t_1 \epsilon \hat{K}} e^{-v_1 \epsilon \hat{W}_{a_1}} e^{-2t_0 \epsilon \hat{K}}, \tag{11}$$

where the $\hat{W}$ operators denote a modified potential term, which combines the usual potential energy $\hat{V}$ with double commutator terms of the form

$$\left[[\hat{V}, \hat{K}], \hat{V} \right] = \frac{\hbar^2}{m} \sum_{i=1}^{N} |\mathbf{F}_i|^2, \tag{12}$$

and, thus, requires the evaluation of all forces in the system. Furthermore, for each high-temperature factor, there appear three imaginary time steps. The final result for the partition function is given by

$$Z = \frac{1}{(N!)^{3P}} \int d\mathbf{X} \prod_{\alpha=0}^{P-1} \left(e^{-\epsilon \bar{V}_\alpha} e^{-\epsilon^3 u_0 \frac{\hbar^2}{m} \bar{F}_\alpha} \right.$$
$$\left. \times \det(\rho_\alpha) \det(\rho_{\alpha A}) \det(\rho_{\alpha B}) \right), \tag{13}$$

where the determinants incorporate the three diffusion matrices for each of the P factors[44]

$$\rho_\alpha(i,j) = \lambda_{t_1 \epsilon}^{-D} \sum_{\mathbf{n}} \exp \left(-\frac{\pi (\mathbf{r}_{\alpha,j} - \mathbf{r}_{\alpha A,i} + \mathbf{n}L)^2}{\lambda_{t_1 \epsilon}^2} \right). \tag{14}$$

The key problem of fermionic PIMC simulations is the sum over permutations, where each configuration can have a positive or a negative sign. By introducing determinants, we analytically combine both positive and negative contributions into a single configuration weight (hence the label "permutation blocking"). Therefore, parts of the cancellation are carried out beforehand, and the average sign of our simulations [Eq. (9)] is significantly increased. Since this effect diminishes with increasing P, we employ the fourth-order factorization, Eq. (11), to obtain sufficient (although limited,[44] $|\Delta V|/V \lesssim 0.1\%$) accuracy with only a small number of high-temperature factors. PB-PIMC is a substantial improvement over regular PIMC, but the determinants can still be negative, which means that the FSP is not removed by the PB-PIMC approach. To illustrate this point, in Fig. 1, we show simulation results for the average sign (here denoted as S) as a function of the density parameter r_s for a UEG simulation cell containing $N = 33$ spin-polarized electrons subject to periodic boundary conditions. The red, blue, and black curves correspond to PB-PIMC results for three isotherms and exhibit a qualitatively similar behavior. At high r_s, fermionic exchange is suppressed by the strong Coulomb repulsion, which means that almost all configuration weights are positive and S is large. With increasing density, the system becomes more ideal and the electron wave
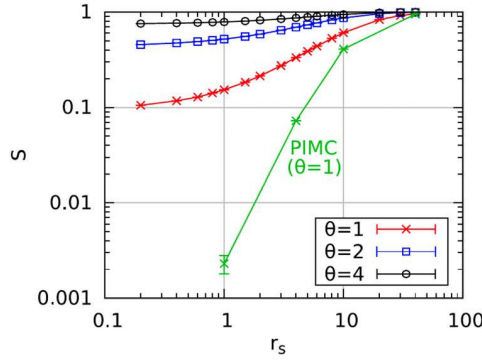
FIG. 1. Density dependence of the average sign of a PB-PIMC simulation of the uniform electron gas. Also shown are standard PIMC data taken from Ref. 31. Reproduced with permission from J. Chem. Phys. **143**, 204101 (2015). Copyright 2014 AIP Publishing LLC.[44]

functions overlap, an effect that manifests itself in an increased number of negative determinants. Nevertheless, the value of S remains significantly larger than zero, which means that, for the three depicted temperatures, PB-PIMC simulations are possible over the entire density range. In contrast, the green curve shows the density-dependent average sign for standard PIMC simulations[31] at $\theta = 1$ and exhibits a significantly steeper decrease with density, limiting simulations to $r_s \geq 4$.

D. Configuration path integral Monte Carlo

For CPIMC,[40,41] instead of performing the trace over the density operator in the coordinate representation [see Eq. (5)], we trace over Slater determinants of the form

$$|\{n\}\rangle = |n_1, n_2, \ldots\rangle, \tag{15}$$

where, in the case of the uniform electron gas, n_i denotes the fermionic occupation number ($n_i \in \{0, 1\}$) of the i-th plane wave spin-orbital $|\mathbf{k}_i \sigma_i\rangle$. To obtain an expression for the partition function suitable for Metropolis Monte Carlo, we split the Hamiltonian into diagonal and off-diagonal parts, $\hat{H} = \hat{D} + \hat{Y}$ (with respect to the chosen plane wave basis, see Sec. II), and explore a perturbation expansion of the density operator with respect to $\hat{Y}$

$$e^{-\beta\hat{H}} = e^{-\beta\hat{D}} \sum_{K=0}^{\infty} \int_0^\beta d\tau_1 \int_{\tau_1}^\beta d\tau_2 \ldots \int_{\tau_{K-1}}^\beta d\tau_K \\ \times (-1)^K \hat{Y}(\tau_K) \hat{Y}(\tau_{K-1}) \cdot \ldots \cdot \hat{Y}(\tau_1), \tag{16}$$

with $\hat{Y}(\tau) = e^{\tau\hat{D}} \hat{Y} e^{-\tau\hat{D}}$. In this representation, the partition function becomes

$$Z = \sum_{\substack{K=0 \\ (K \neq 1)}}^{\infty} \sum_{\{n\}} \sum_{s_1 \ldots s_{K-1}} \int_0^\beta d\tau_1 \int_{\tau_1}^\beta d\tau_2 \ldots \int_{\tau_{K-1}}^\beta d\tau_K \\ \times (-1)^K e^{-\sum_{i=0}^K D_{\{n^{(i)}\}}(\tau_{i+1}-\tau_i)} \prod_{i=1}^K Y_{\{n^{(i)}\},\{n^{(i-1)}\}}(s_i). \tag{17}$$

The matrix elements of the diagonal and off-diagonal operators are given by the Slater-Condon rules

$$D_{\{n^{(i)}\}} = \sum_l \mathbf{k}_l^2 n_l^{(i)} + \sum_{l<k} w_{lklk}^- n_l^{(i)} n_k^{(i)}, \tag{18}$$

$$Y_{\{n^{(i)}\},\{n^{(i-1)}\}}(s_i) = w_{s_i}^- (-1)^{\alpha_{s_i}}, \tag{19}$$

$$\alpha_{s_i} = \alpha_{pqrs}^{(i)} = \sum_{l=p}^{q-1} n_l^{(i-1)} + \sum_{l=r}^{s-1} n_l^{(i)}, \tag{20}$$

where the multi-index $s_i = (pqrs)$ defines the four orbitals in which $\{n^{(i)}\}$ and $\{n^{(i-1)}\}$ differ, and we note that $p < q$ and $r < s$. As in standard PIMC, each contribution to the partition function (17) can be interpreted as a β−periodic path in imaginary time, but the path is now in Fock space instead of coordinate space. Evidently, the weight corresponding to any given path (second line of Eq. (17)) can be positive or negative. Therefore, to apply the Metropolis algorithm, we have to proceed as explained in Sec. III B and use the modulus of the weight function as our probability density. In consequence, the CPIMC method is also afflicted with the FSP. However, as it turns out, the severity of the FSP as a function of the density parameter is complementary to that of standard PIMC, so that weakly interacting systems, which are the most challenging for PIMC, are easily tackled using CPIMC. For a detailed derivation of the CPIMC partition function and the Monte Carlo steps are required to sample it see, e.g., Refs. 40–42, and 51.

E. Density matrix quantum Monte Carlo

Instead of sampling contributions to the partition function, as in path integral methods, DMQMC samples the (unnormalized) thermal density matrix directly by expanding it in a discrete basis of outer products of Slater determinants

$$\hat{\rho} = \sum_{\{n\},\{n'\}} \rho_{\{n\},\{n'\}} |\{n\}\rangle\langle\{n'\}|, \tag{21}$$

where $\rho_{\{n\},\{n'\}} = \langle\{n\}|e^{-\beta\hat{H}}|\{n'\}\rangle$. The density-matrix coefficients $\rho_{\{n\},\{n'\}}$ appearing in Eq. (21) are found by simulating the evolution of the Bloch equation

$$\frac{d\hat{\rho}}{d\beta} = -\frac{1}{2}(\hat{\rho}\hat{H} + \hat{H}\hat{\rho}), \tag{22}$$

which may be finite-differenced as

$$\rho_{\{n\},\{n'\}}(\beta+\Delta\beta) = \rho_{\{n\},\{n'\}}(\beta) - \Delta\beta \sum_{\{n''\}} \left[\rho_{\{n\},\{n''\}}(\beta) H_{\{n''\},\{n'\}} + H_{\{n\},\{n''\}} \rho_{\{n''\},\{n'\}}(\beta)\right]. \tag{23}$$

The matrix elements of the Hamiltonian are as given as in Eqs. (18) and (19).

Following Booth and coworkers,[67] we note that Eq. (23) can be interpreted as a rate equation and can be solved by evolving a set of positive and negative walkers, which stochastically undergo birth and death processes that, on average, reproduce the full solution. The rules governing the

evolution of the walkers, as derived from Eq. (23), can be found elsewhere.[45,67] The form of $\hat{\rho}$ is known exactly at infinite temperature ($\beta = 0$, $\hat{\rho} = \hat{1}$), providing an initial condition for Eq. (22). For the electron gas, however, it turns out that simulating a differential equation that evolves a mean-field density matrix at inverse temperature β to the exact density matrix at inverse temperature β is much more efficient than solving Eq. (22), an insight that leads to the "interaction picture" version of DMQMC[39,46] used throughout this work.

The sign problem manifests itself in DMQMC as an exponential growth in the number of walkers required for the sampled density matrix to emerge from the statistical noise.[67–70] Working in a discrete Hilbert space helps to reduce the noise by ensuring a more efficient cancellation of positive and negative contributions, enabling larger systems and lower temperatures to be treated than would otherwise be possible. Nevertheless, at some point, the walker numbers required become overwhelming and approximations are needed. Recently, we have applied the initiator approximation[71–73] to DMQMC ($i - $DMQMC). In principle, at least, this allows a systematic approach to the exact result with an increasing walker number. More details on the use of the initiator approximation in DMQMC and its limitations can be found in Ref. 39.

F. Applicability of the QMC methods

To conclude the discussion of Quantum Monte Carlo, in Fig. 2, we give a schematic overview of the parameter combinations where the different methods can be used to obtain results in the thermodynamic limit (for a discussion of finite-size corrections, see Sec. V) with a relative accuracy of $\Delta V / V \sim 0.003$. Standard PIMC (black) is only useful for high temperatures and low densities where fermionic exchange does not play an important role and, therefore, does not give access to the WDM regime. PB-PIMC (green) significantly extends the possible parameter combinations to

lower temperature (down to $\theta = 0.5$ for $r_s \geq 1$) and is available over the entire density range for $\theta \gtrsim 2$. In contrast, both CPIMC (red) and DMQMC (blue) are feasible for all θ at small r_s and eventually break down with increasing r_s due to coupling effects. Despite their apparent similar range of applicability, it turns out that CPIMC is significantly more efficient at higher temperature, while DMQMC is superior at low θ.

IV. SIMULATION RESULTS FOR THE FINITE SYSTEM

The first step towards obtaining QMC results for the warm dense electron gas in the thermodynamic limit is to carry out accurate simulations of a finite model system. In Fig. 3, we compare results for the density dependence of the exchange correlation energy E_{xc} of the UEG for $N = 33$ spin-polarized electrons and two different temperatures. The first results, shown as blue squares, were obtained with RPIMC[31] for $r_s \geq 1$. Subsequently, Groth, Dornheim, and co-workers[44,51] showed that the combination of PB-PIMC (red crosses) and CPIMC (red circles) allows for an accurate description of this system for $\theta \geq 0.5$. In addition, it was revealed that RPIMC is afflicted with a systematic nodal error for densities greater than the relatively low value at which $r_s = 6$. Nevertheless, the FSP precludes the use of PB-PIMC at lower temperatures and, even at $\theta = 0.5$ and $r_s = 2$, the statistical uncertainty becomes large. The range of applicability of DMQMC is similar to that of CPIMC, and the DMQMC results (green diamonds) fully confirm the CPIMC results.[39,46] Further, the introduction of the initiator approximation (i-DMQMC) has made it possible to obtain results up to $r_s = 2$ for $\theta = 0.5$. Although i-DMQMC is, in principle, systematically improvable and controlled, the results suggest that the initiator approximation may introduce a small systematic shift at lower densities.

In summary, the recent progress in fermionic QMC methods has resulted in a consensus regarding the finite-N UEG for temperatures $\theta \geq 0.5$. However, there remains a gap at $r_s \approx 2 - 6$ and $\theta < 0.5$ where, at the moment, no reliable data are available.
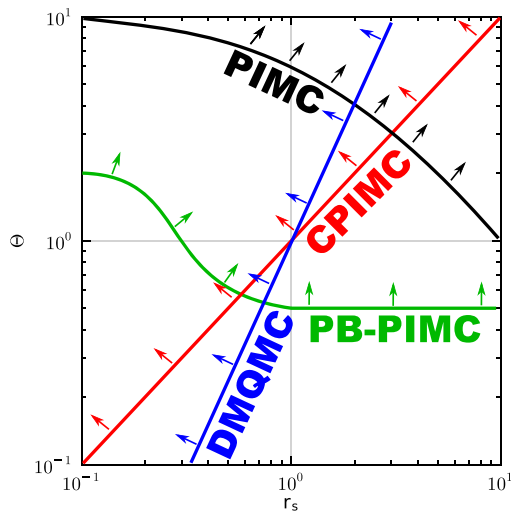

FIG. 2. Density-temperature-plane around the WDM regime. Shown are the parameter combinations where standard PIMC (black), PB-PIMC (green), CPIMC (red), and DMQMC (blue) can be used to obtain data in the thermodynamic limit with an accuracy of $\Delta V / V \sim 0.003$.
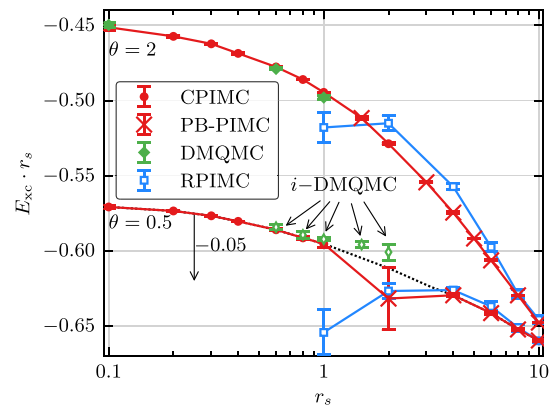

FIG. 3. Exchange-correlation energy of $N = 33$ spin-polarized electrons as a function of the density parameter r_s for two isotherms. Shown are results from CPIMC and PB-PIMC taken from Ref. 51, restricted PIMC from Ref. 31, and DMQMC from Ref. 39. For $\theta = 0.5$, all data have been shifted by 0.05 Hartree. In the case of DMQMC, the initiator approximation is used.

V. FINITE SIZE CORRECTIONS

In this section, we describe in detail the finite-size correction scheme introduced in Ref. 47 and subsequently present detailed results for two elucidating examples.

A. Theory

As introduced above (see Eq. (1) in Sec. II A), the potential energy of the finite simulation cell is defined as the interaction energy of the N electrons with each other, the infinite periodic array of images, and the uniform positive background. To estimate the finite-size effects, it is more convenient to express the potential energy in k-space. For the finite simulation cell of N electrons, the expression obtained is a sum over the discrete reciprocal lattice vectors $\mathbf{G}$

$$\frac{V_N}{N} = \frac{1}{2\Omega} \sum_{\mathbf{G} \neq 0} [S_N(\mathbf{G}) - 1] \frac{4\pi}{G^2} + \frac{\xi_M}{2} , \tag{24}$$

where $S(\mathbf{k})$ is the static structure factor. In the limit as the system size tends to infinity and $\xi_M \to 0$, this yields the integral

$$v = \frac{1}{2} \int_{k < \infty} \frac{d\mathbf{k}}{(2\pi)^3} [S(k) - 1] \frac{4\pi}{k^2} . \tag{25}$$

Combining Eqs. (24) and (25) yields the finite-size error for a given QMC simulation

$$\frac{\Delta V_N}{N} \left[S(k), S_N(k) \right] = v - \frac{V_N}{N}$$
$$= \underbrace{\frac{1}{2} \int_{k < \infty} \frac{d\mathbf{k}}{(2\pi)^3} (S(k) - 1) \frac{4\pi}{k^2}}_{v} \tag{26}$$
$$- \underbrace{\left(\frac{1}{2L^3} \sum_{\mathbf{G} \neq 0} (S_N(\mathbf{G}) - 1) \frac{4\pi}{G^2} + \frac{\xi_M}{2} \right)}_{V_N/N} . \tag{27}$$

The task at hand is to find an accurate estimate of the finite-size error from Eq. (26), which, when added to the QMC result for V_N/N, gives the potential energy in the thermodynamic limit. As a first step, we note that the Madelung constant may be approximated by[55]

$$\xi_M \approx \frac{1}{L^3} \sum_{\mathbf{G} \neq 0} \frac{4\pi}{G^2} e^{-\epsilon G^2} - \frac{1}{(2\pi)^3} \int_{k < \infty} d\mathbf{k} \frac{4\pi}{k^2} e^{-\epsilon k^2} , \tag{28}$$

an expression that becomes exact in the limit as $\epsilon \to 0$. The Madelung term thus cancels the minus unity contributions to both the sum and the integral in Eq. (27).

The remaining two possible sources of the finite-size error in Eq. (26) are (i) the substitution of the static structure factor of the infinite system $S(k)$ by its finite-size equivalent $S_N(k)$ and (ii) the approximation of the continuous integral by a discrete sum, resulting in a discretization error. As we will show in Sec. V B, $S_N(k)$ exhibits a remarkably fast convergence with system size, which leaves explanation (ii). In

particular, about a decade ago, Chiesa *et al.*[53] suggested that the main contribution to Eq. (26) stems from the $\mathbf{G} = 0$ term that is completely missing from the discrete sum. To remedy this shortcoming, they made use of the random phase approximation (RPA) for the structure factor, which becomes exact in the limit $k \to 0$. The leading term in the expansion of $S^{\mathrm{RPA}}(k)$ around $k = 0$ is[26]

$$S_0^{\mathrm{RPA}}(k) = \frac{k^2}{2\omega_p} \coth\left(\frac{\beta\omega_p}{2} \right), \tag{29}$$

with $\omega_p = \sqrt{3/r_s^3}$ being the plasma frequency. The finite-T generalization of the FSC introduced by Chiesa *et al.*, hereafter called the BCDC-FSC, is[31,47]

$$\Delta V_{\mathrm{BCDC}}(N) = \lim_{k \to 0} \frac{S_0^{\mathrm{RPA}}(k)4\pi}{2L^3 k^2}$$
$$= \frac{\omega_p}{4N} \coth\left(\frac{\beta\omega_p}{2} \right). \tag{30}$$

Eq. (30) would be sufficient if (i) $S_0^{\mathrm{RPA}}(k)$ were accurate for $k \lesssim 2\pi/L$ and (ii) all contributions to Eq. (26) beyond the $\mathbf{G} = 0$ term were negligible. As is shown in Sec. V B, both conditions are strongly violated in parts of the warm dense regime.

To overcome the deficiencies of Eq. (30), we need a continuous model function $S_{\mathrm{model}}(k)$ to accurately estimate the discretization error from Eq. (27)

$$\Delta V_N [S_{\mathrm{model}}(k)] = \frac{\Delta V_N}{N} \left[S_{\mathrm{model}}(k), S_{\mathrm{model}}(k) \right]. \tag{31}$$

A natural choice would be to combine the QMC results for $k \geq k_{\mathrm{min}}$, which include all short-ranged correlations and exchange effects, with the STLS structure factor for smaller k, which is exact as $k \to 0$ and incorporates the long-ranged behavior that cannot be reproduced using QMC due to the limited size of the simulation cell. However, as we showed in Ref. 47, a simpler approach using $S_{\mathrm{STLS}}(k)$ [or the full RPA structure factor $S_{\mathrm{RPA}}(k)$] for all k is sufficient to accurately estimate the discretization error.

B. Results

1. Particle number dependence

To illustrate the application of the different FSCs, Fig. 4 shows results for the unpolarized UEG at $\theta = 2$ and $r_s = 1$. The green crosses in panel (b) correspond to the raw, uncorrected QMC results that, clearly, are not converged with system size N. The raw data points appear to fall onto a straight line when plotted as a function of $1/N$. This agrees with the BCDC-FSC formula, Eq. (30), which also predicts a $1/N$ behavior, and suggests the use of a linear extrapolation (the green line). However, while the linear fit does indeed exhibit good agreement with the QMC results, the computed slope does not match Eq. (30). Further, the points that have been obtained by adding ΔV_{BCDC} to the QMC results, i.e., the yellow asterisks, do not fall onto a horizontal line and do not agree with the prediction of the linear extrapolation (see the horizontal green line). To resolve this peculiar situation, we
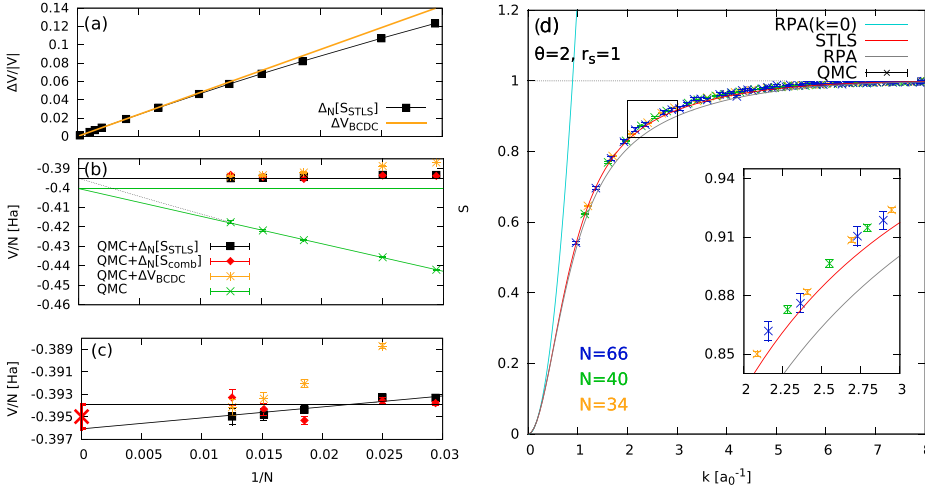
FIG. 4. Finite-size correction for the UEG at $\theta = 2$ and $r_s = 1$: (a) N dependence of the FSCs; (b) potential energy per particle, V/N; the dotted grey line corresponds to the TDL value where $\Delta_N[S_{STLS}]$ had been subtracted; (c) extrapolation of the residual finite-size error; and (d) corresponding static structure factors $S(k)$ from QMC (for $N = 34$, 40, and 66), STLS, RPA, and the RPA expansion around $k = 0$, Eq. (29). (b) and (c) Adapted with permission from Dornheim *et al.*, Phys. Rev. Lett. **117**, 156403 (2016). Copyright 2016 American Physical Society.

compute the improved finite-size correction [Eq. (31)] using both the static structure factor from STLS (S_{STLS}) and the combination of STLS with the QMC data (S_{comb}) as input. The resulting corrected potential energies are shown as black squares and red diamonds, respectively, and appear to exhibit almost no remaining dependence on system size. In panel (c), we show a segment of the corrected data, magnified in the vertical direction. Any residual finite-size errors [due to the QMC data for $S(k)$ not being converged with respect to N, see panel (d)] can hardly be resolved within the statistical uncertainty and are removed by an additional extrapolation. In particular, to compute the final result for V/N in the thermodynamic limit, we obtain a lower bound via a linear extrapolation of the corrected data (using S_{STLS}) and an upper bound by performing a horizontal fit to the last few points, all of which are converged to within the error bars. The dotted grey line in panel (b), which connects to the extrapolated result, shows clearly that the results of this procedure deviate from the results of a naive linear extrapolation.

Finally, in panel (d) of Fig. 4, we show results for the static structure factor $S(k)$ for the same system. As explained in Sec. V A, momentum quantization limits the QMC results to discrete k values above a minimum value $k_{min} = 2\pi/L$.

Nevertheless, the N dependence of the k grid is the only apparent change of the QMC results for $S(k)$ with system size, and no difference between the results for the three particle numbers studied can be resolved within the statistical uncertainty (see also the magnified segment in the inset). The STLS curve (red) is known to be exact in the limit $k \to 0$ and smoothly connects to the QMC data, although for larger k there appears an almost constant shift. The full RPA curve (grey) exhibits a similar behavior, albeit deviating more significantly at intermediate k. Finally, the RPA expansion around $k = 0$ [Eq. (29), light blue] only agrees with the STLS and full RPA curves at very small k and does not connect to the QMC data even for the largest system size simulated.

To further stress the importance of our improved finite-size correction scheme, Fig. 5 shows results again for $\theta = 2$ but at higher density, $r_s = 0.1$. In this regime, the CPIMC approach (and also DMQMC) is clearly superior to PB-PIMC and simulations of $N = 700$ unpolarized electrons in $N_b = 189\,234$ basis functions are feasible. Due to the high density, the finite-size errors are drastically increased compared to the previous case and exceed 50% for $N = 38$ particles [see panels (a) and (b)]. Further, we note that the BCDC-FSC is completely inappropriate for the N values considered, as the yellow asterisks are clearly not converged
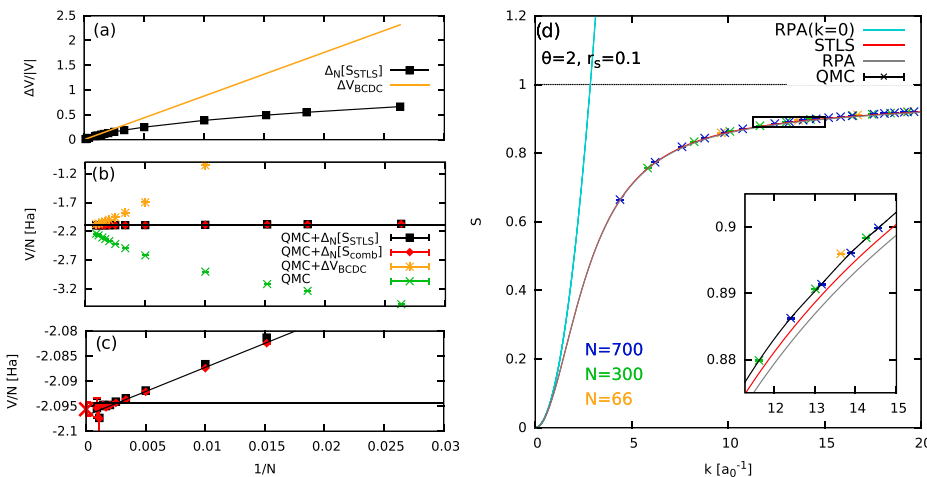

FIG. 5. Finite-size correction for the UEG at $\theta = 2$ and $r_s = 0.1$: (a) N dependence of the FSCs; (b) potential energy per particle, V/N; (c) extrapolation of the residual finite-size error; and (d) corresponding static structure factors $S(k)$ from QMC (for $N = 66$, 300, and 700), STLS, RPA, and the RPA expansion around $k = 0$, Eq. (29).

and differ even more strongly from the correct TDL than the raw uncorrected QMC data.

Our improved FSC, on the other hand, reduces the finite-size errors by two orders of magnitude (both with S_{STLS} and S_{comb}) and approaches Eq. (30) only in the limit of very large systems [$N \gtrsim 10^4$; see panel (a)]. The small residual error is again extrapolated, as shown in panel (c).

Finally, we show the corresponding static structure factors in panel (d). The RPA expansion is again insufficient to model the QMC data, while the full RPA and STLS curves smoothly connect to the latter.

2. Comparison to other methods

To conclude this section, we use our finite-size corrected QMC data for the unpolarized UEG to analyze the accuracy of various other methods that are commonly used. In Fig. 6(a), the potential energy per particle, V/N, is shown as a function of r_s for the isotherm with $\theta = 2$. Although all four depicted curves exhibit qualitatively similar behavior, there are significant deviations between them [see panel (b), where we show the relative deviations from a fit to the QMC data in the TDL]. Let us start with the QMC results: the black squares correspond to the uncorrected raw QMC data for $N = 66$ particles (see Ref. 52) and the red diamonds to the finite-size corrected data from Ref. 47. As expected, the finite-size effects drastically increase with density from $|\Delta V|/V \approx 1\%$, at $r_s = 10$, to $|\Delta V|/V \geq 50\%$, at $r_s = 0.1$. This again illustrates the paramount importance of accurate finite-size corrections for QMC simulations in the warm dense matter regime. The RPA calculation (green curve) is accurate at high density and weak coupling. However, with increasing r_s, the accuracy quickly deteriorates and, already at moderate coupling, $r_s = 1$, the systematic error is of the order of 10%. The yellow asterisks show the SLTS result,
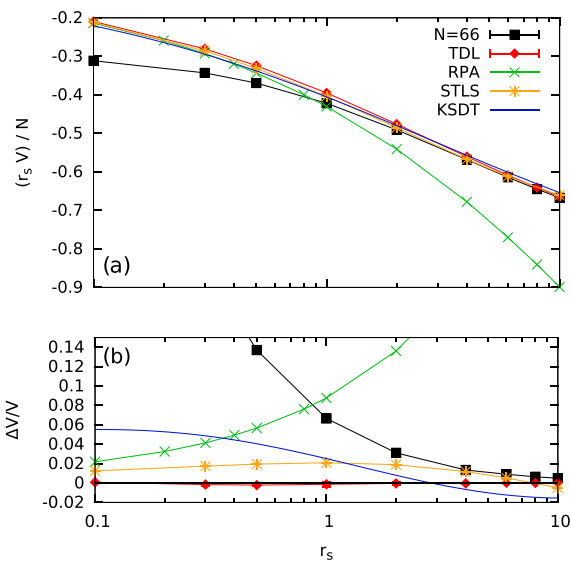
which agrees well with the simulations (the systematic error does not exceed 3%) over the entire r_s-range considered, i.e., up to $r_s = 10$. Finally, the blue curve has been obtained from the recent parametrization of f_{xc} by Karasiev *et al.*[34] (KSDT), for which RPIMC data have been used as an input. While there is a reasonable agreement with our new data for $r_s \gtrsim 1$ (with $|\Delta V|/V \sim 2\%$), there are significant deviations at smaller r_s, which only vanish for $r_s < 10^{-4}$.

VI. SUMMARY AND OPEN QUESTIONS

Let us summarize the status of *ab initio* thermodynamic data for the uniform electron gas at finite temperature. The present paper has given an overview of recent progress in *ab initio* finite temperature QMC simulations that avoid any additional simplifications such as fixed nodes. While these simulations do not "solve" the fermion sign problem, they provide a reasonable and efficient way on how to *avoid it*, in many practically relevant situations, by combining simulations that use different representations of the quantum many-body state: the coordinate representation (direct PIMC and PB-PIMC) and Fock states (CPIMC and DMQMC). With this, it is now possible to obtain highly accurate results for up to $N \sim 100$ particles in the entire density range and for temperatures $\theta \gtrsim 0.5$. As a second step, we demonstrated that these comparatively small simulation sizes are sufficient to predict results for the macroscopic uniform electron gas *not significantly losing accuracy*.[47] This unexpected result is a consequence of a new highly accurate finite-size correction that was derived by invoking STLS results for the static structure factor.

With this procedure, it is now possible to obtain thermodynamic data for the uniform electron gas with an accuracy on the order of 0.1%. Even though pure electron gas results cannot be directly compared to warm dense matter experiments, they are of high value to benchmark and improve additional theoretical approaches. Most importantly, this concerns finite-temperature versions of the density functional theory (such as orbital-free DFT), which is the standard tool to model realistic materials and which will benefit from our results for the exchange-correlation free energy. Furthermore, we have also presented a few comparisons with earlier models such as RPA, STLS, or the recent fit of Karasiev *et al.* (KSDT), the accuracy and errors of which can now be unambiguously quantified. We found that among the tested models, the STLS is the most accurate one. We wish to underline that even though exchange-correlation effects are often small compared to the kinetic energy, their accurate treatment is important to capture the properties of real materials, see e.g., Ref. 74.

In the following, we summarize the open questions and outline future research directions.

(1) Construction of an improved fit for the exchange-correlation free energy due to their key relevance as input for finite-temperature DFT. Such fits are straightforwardly generated from the current results but require a substantial extension of the simulations to arbitrary spin polarization. This work is currently in progress.

(2) The presently available accurate data are limited to temperatures above half the Fermi energy, as a consequence

FIG. 6. Potential energy per particle of the uniform electron gas at $\theta = 2$–simulations versus analytical models. Squares: QMC results for $N = 66$ particles,[52] (red) rhombs: finite-size corrected QMC data (TDL),[47] green (yellow) curves: RPA (STLS) data,[24] and blue: results of the parametrization of Ref. 34 (KSDT). Bottom: relative deviations of all curves from the fit to the thermodynamic QMC results.

of the fermion sign problem. A major challenge will be to advance to lower temperatures, $\Theta < 0.5$, and to reliably connect the results to the known ground state data. This requires substantial new developments in the area of the three quantum Monte Carlo methods presented in this paper (CPIMC, PB-PIMC and DMQMC) and new ideas on how to combine them. Another idea could be to derive simplified versions of these methods that treat the FSP more efficiently but still have acceptable accuracy.

(3) The present *ab initio* results allow for an entirely new view on previous theoretical models. For the first time, a clear judgment about the accuracy becomes possible, which more clearly maps out the sphere of applicability of the various approaches, e.g., Ref. 75. Moreover, the availability of our data will allow for improvements of many of these approaches via adjustment of the relevant parameters to the QMC data. This could yield, e.g., improved static structure factors, dielectric functions or local field correlations.

(4) Similarly, our data may also help to improve alternative quantum Monte Carlo concepts. In particular, this concerns the nodes for Restricted PIMC simulations, which can be tested against our data. This might help to extend the range of validity of those simulations to higher density and lower temperature. Since this latter method does not have a sign problem, it may allow to reach parameters that are not accessible otherwise.

(5) A major challenge of Metropolis-based QMC simulations that are highly efficient for thermodynamic and static properties is to extend them to dynamic quantities. This can, in principle, be done via analytical continuation from imaginary to real times (or frequencies). However, this is known to be an ill-posed problem. Recently, there has been significant progress by invoking stochastic reconstruction methods or genetic algorithms. For example, for Bose systems, accurate results for the spectral function and the dynamics structure factor could be obtained, e.g., Ref. 76 and references therein, which encourage also for applications to the uniform electron gas, in the near future.

(6) Finally, there are a large number of additional applications of the presented *ab initio* simulations. This includes the 2D warm dense UEG where thermodynamic results of similar accuracy should be straightforwardly accessible. Moreover, for the electron gas, at high density, $r_s \lesssim 0.1$, relativistic corrections should be taken into account. Among the presented simulations, CPIMC is perfectly suited to tackle this task and to provide *ab initio* data also for correlated matter at extreme densities.

ACKNOWLEDGMENTS

[1]P.-F. Loos and P. M. W. Gill, "The uniform electron gas," WIREs Comput. Mol. Sci. **6**, 410–429 (2016).

[2]J. P. Perdew and A. Zunger, "Self-interaction correction to density-functional approximations for many-electron systems," Phys. Rev. B **23**, 5048 (1981).

[3]D. M. Ceperley and B. J. Alder, "Ground state of the electron gas by a stochastic method," Phys. Rev. Lett. **45**, 566 (1980).

[4]W. Kohn and L. J. Sham, "Self-consistent equations including exchange and correlation effects," Phys. Rev. **140**, A1133 (1965).

[5]R. O. Jones, "Density functional theory: Its origins, rise to prominence, and future," Rev. Mod. Phys. **87**, 897–923 (2015).

[6]R. Nora, W. Theobald, R. Betti, F. J. Marshall, D. T. Michel, W. Seka, B. Yaakobi, M. Lafon, C. Stoeckl, J. Delettrez *et al.*, "Gigabar spherical shock generation on the OMEGA laser," Phys. Rev. Lett. **114**, 045001 (2015).

[7]P. F. Schmit, P. F. Knapp, S. B. Hansen, M. R. Gomez, K. D. Hahn, D. B. Sinars, K. J. Peterson, S. A. Slutz, A. B. Sefkow, T. J. Awe *et al.*, "Understanding fuel magnetization and mix using secondary nuclear reactions in magneto-inertial fusion," Phys. Rev. Lett. **113**, 155004 (2014).

[8]O. A. Hurricane, D. A. Callahan, D. T. Casey, E. L. Dewald, T. R. Dittrich, T. Döppner, S. Haan, D. E. Hinkel, L. F. Berzak Hopkins, O. Jones *et al.*, "Inertially confined fusion plasmas dominated by alpha-particle self-heating," Nat. Phys. **12**, 800–806 (2016).

[9]R. Ernstorfer, M. Harb, C. T. Hebeisen, G. Sciaini, T. Dartigalongue, and R. J. Dwayne Miller, "The formation of warm dense matter: experimental evidence for electronic bond hardening in gold," Science **323**, 1033 (2009).

[10]M. D. Knudson, M. P. Desjarlais, R. W. Lemke, T. R. Mattsson, M. French, N. Nettelmann, and R. Redmer, "Probing the interiors of the ice giants: Shock compression of water to 700 GPa and $3.8\,g/cm^3$," Phys. Rev. Lett. **108**, 091102 (2012).

[11]B. Militzer, W. B. Hubbard, J. Vorberger, I. Tamblyn, and S. A. Bonev, "A massive core in Jupiter predicted from first-principles simulations," Astrophys. J. **688**, L45 (2008).

[12]N. D. Mermin, "Thermal properties of the inhomogeneous electron gas," Phys. Rev. **137**, A1441 (1965).

[13]T. Sjostrom and J. Daligault, "Gradient corrections to the exchange-correlation free energy," Phys. Rev. B **90**, 155109 (2014).

[14]K. Burke, J. C. Smith, P. E. Grabowski, and A. Pribram-Jones, "Exact conditions on the temperature dependence of density functionals," Phys. Rev. B **93**, 195132 (2016).

[15]M. W. C. Dharma-wardana, "Current issues in finite-T Density-functional theory and warm-correlated matter," Computation **4**, 16 (2016).

[16]V. V. Karasiev, L. Calderin, and S. B. Trickey, "Importance of finite-temperature exchange-correlation for warm dense matter calculations," Phys. Rev. E **93**, 063207 (2016).

[17]A. Pribram-Jones, P. E. Grabowski, and K. Burke, "Thermal density functional theory: Time-dependent linear response and approximate functionals from the fluctuation-dissipation theorem," Phys. Rev. Lett. **116**, 233001 (2016).

[18]D. Kremp, M. Schlanges, and W. D. Kraeft, *Quantum Statistics of Nonideal Plasmas* (Springer, 2005).

[19]J. Vorberger, M. Schlanges, and W.-D. Kraeft, "Equation of state for weakly coupled quantum plasmas," Phys. Rev. E **69**, 046407 (2004).

[20]U. Gupta and A. K. Rajagopal, "Exchange-correlation potential for inhomogeneous electron systems at finite temperatures," Phys. Rev. A **22**, 2792 (1980).

[21]F. Perrot and M. W. C. Dharma-wardana, "Exchange and correlation potentials for electron-ion systems at finite temperatures," Phys. Rev. A **30**, 2619 (1984).

[22]K. S. Singwi, M. P. Tosi, R. H. Land, and A. Sjölander, "Electron correlations at metallic densities," Phys. Rev. **176**, 589–599 (1968).

[23]S. Tanaka and S. Ichimaru, "Thermodynamics and correlational properties of finite-temperature electron liquids in the Singwi-Tosi-Land-Sjölander approximation," J. Phys. Soc. Jpn. **55**, 2278–2289 (1986).

[24]T. Sjostrom and J. Dufty, "Uniform electron gas at finite temperatures," Phys. Rev. B **88**, 115123 (2013).

[25]P. Vashishta and K. S. Singwi, "Electron correlations at metallic densities. V," Phys. Rev. B **6**, 875 (1972).

[26]S. Dutta and J. Dufty, "Classical representation of a quantum system at equilibrium: Applications," Phys. Rev. B **87**, 032102 (2013).

[27]M. W. C. Dharma-wardana and F. Perrot, "Simple classical mapping of the spin-polarized quantum electron gas: Distribution functions and local-field corrections," Phys. Rev. Lett. **84**, 959–962 (2000).

[28]D. M. Ceperley, "Path integrals in the theory of condensed helium," Rev. Mod. Phys. **67**, 279–355 (1995).

[29]E. Y. Loh, J. E. Gubernatis, R. T. Scalettar, S. R. White, D. J. Scalapino, and R. L. Sugar, "Sign problem in the numerical simulation of many-electron systems," Phys. Rev. B **41**, 9301–9307 (1990).

[30]M. Troyer and U. J. Wiese, "Computational complexity and fundamental limitations to fermionic quantum Monte Carlo simulations," Phys. Rev. Lett. **94**, 170201 (2005).

[31]E. W. Brown, B. K. Clark, J. L. DuBois, and D. M. Ceperley, "Path-integral Monte Carlo simulation of the warm dense homogeneous electron gas," Phys. Rev. Lett. **110**, 146405 (2013).

[32]D. M. Ceperley, "Fermion nodes," J. Stat. Phys. **63**, 1237–1267 (1991).

[33]E. W. Brown, J. L. DuBois, M. Holzmann, and D. M. Ceperley, "Exchange-correlation energy for the three-dimensional homogeneous electron gas at arbitrary temperature," Phys. Rev. B **88**, 081102(R) (2013).

[34]V. V. Karasiev, T. Sjostrom, J. Dufty, and S. B. Trickey, "Accurate homogeneous electron gas exchange-correlation free energy for local spin-density calculations," Phys. Rev. Lett. **112**, 076403 (2014).

[35]B. Militzer and E. L. Pollock, "Variational density matrix method for warm, condensed matter: Application to dense hydrogen," Phys. Rev. E **61**, 3470–3482 (2000).

[36]B. Militzer, Ph.D. dissertation, University of Illinois at Urbana-Champaign, 2000.

[37]V. S. Filinov, "Cluster expansion for ideal Fermi systems in the 'fixed-node approximation'," J. Phys. A: Math. Gen. **34**, 1665–1677 (2001).

[38]V. S. Filinov, "Analytical contradictions of the fixed-node density matrix," High Temp. **52**, 615–620 (2014).

[39]F. D. Malone, N. S. Blunt, E. W. Brown, D. K. K. Lee, J. S. Spencer, W. M. C. Foulkes, and J. J. Shepherd, "Accurate exchange-correlation energies for the warm dense electron gas," Phys. Rev. Lett. **117**, 115701 (2016).

[40]T. Schoof, M. Bonitz, A. V. Filinov, D. Hochstuhl, and J. W. Dufty, "Configuration path integral Monte Carlo," Contrib. Plasma Phys. **51**, 687–697 (2011).

[41]T. Schoof, S. Groth, and M. Bonitz, "Towards ab initio thermodynamics of the electron gas at strong degeneracy," Contrib. Plasma Phys. **55**, 136–143 (2015).

[42]T. Schoof, S. Groth, J. Vorberger, and M. Bonitz, "*Ab Initio* thermodynamic results for the degenerate electron gas at finite temperature," Phys. Rev. Lett. **115**, 130402 (2015).

[43]T. Dornheim, S. Groth, A. Filinov, and M. Bonitz, "Permutation blocking path integral Monte Carlo: A highly efficient approach to the simulation of strongly degenerate non-ideal fermions," New J. Phys. **17**, 073017 (2015).

[44]T. Dornheim, T. Schoof, S. Groth, A. Filinov, and M. Bonitz, "Permutation blocking path integral Monte Carlo approach to the uniform electron gas at finite temperature," J. Chem. Phys. **143**, 204101 (2015).

[45]N. S. Blunt, T. W. Rogers, J. S. Spencer, and W. M. Foulkes, "Density-matrix quantum Monte Carlo method," Phys. Rev. B **89**, 245124 (2014).

[46]F. D. Malone, N. S. Blunt, J. J. Shepherd, D. K. K. Lee, J. S. Spencer, and W. M. C. Foulkes, "Interaction picture density matrix quantum Monte Carlo," J. Chem. Phys. **143**, 044116 (2015).

[47]T. Dornheim, S. Groth, T. Sjostrom, F. D. Malone, W. M. Foulkes, and M. Bonitz, "*Ab Initio* quantum Monte Carlo simulation of the warm dense electron gas in the thermodynamic limit," Phys. Rev. Lett. **117**, 156403 (2016).

[48]T. Dornheim, H. Thomsen, P. Ludwig, A. Filinov, and M. Bonitz, "Analyzing quantum correlations made simple," Contrib. Plasma Phys. **56**, 371 (2016).

[49]V. S. Filinov, V. E. Fortov, M. Bonitz, and Zh. Moldabekov, "Fermionic path integral Monte Carlo results for the uniform electron gas at finite temperature," Phys. Rev. E **91**, 033108 (2015).

[50]N. S. Blunt, A. Alavi, and G. H. Booth, "Krylov-projected quantum Monte Carlo method," Phys. Rev. Lett. **115**, 050603 (2015).

[51]S. Groth, T. Schoof, T. Dornheim, and M. Bonitz, "*Ab Initio* quantum Monte Carlo simulations of the uniform electron gas without fixed nodes," Phys. Rev. B **93**, 085102 (2016).

[52]T. Dornheim, S. Groth, T. Schoof, C. Hann, and M. Bonitz, "*Ab initio* quantum Monte Carlo simulations of the Uniform electron gas without fixed nodes: The unpolarized case," Phys. Rev. B **93**, 205134 (2016).

[53]S. Chiesa, D. M. Ceperley, R. M. Martin, and M. Holzmann, "Finite-size error in many-body simulations with long-range interactions," Phys. Rev. Lett. **97**, 076404 (2006).

[54]L. M. Fraser, W. M. C. Foulkes, G. Rajagopal, R. J. Needs, S. D. Kenny, and A. J. Williamson, "Finite-size effects and Coulomb interactions in quantum Monte Carlo calculations for homogeneous systems with periodic boundary conditions," Phys. Rev. B **53**, 1814 (1996).

[55]N. D. Drummond, R. J. Needs, A. Sorouri, and W. M. C. Foulkes, "Finite-size errors in continuum quantum Monte Carlo calculations," Phys. Rev. B **78**, 125106 (2008).

[56]C. Lin, F. H. Zong, and D. M. Ceperley, "Twist-averaged boundary conditions in continuum quantum Monte Carlo algorithms," Phys. Rev. E **64**, 016702 (2001).

[57]H. Kwee, S. Zhang, and H. Krakauer, "Finite-size correction in many-body electronic structure calculations," Phys. Rev. Lett. **100**, 126404 (2008).

[58]D. Chandler and P. G. Wolynes, "Exploiting the isomorphism between quantum theory and classical statistical mechanics of polyatomic fluids," J. Chem. Phys. **74**, 4078 (1981).

[59]N. Metropolis, A. W. Rosenbluth, M. N. Rosenbluth, A. H. Teller, and E. Teller, "Equation of state calculations by fast computing machines," J. Chem. Phys. **21**, 1087 (1953).

[60]M. Takahashi and M. Imada, "Monte Carlo calculation of quantum systems," J. Phys. Soc. Jpn. **53**, 963–974 (1984).

[61]V. S. Filinov, V. E. Fortov, W. Ebeling, P. Levashov, and M. Schlanges, "Thermodynamic properties and plasma phase transition in dense hydrogen," Contrib. Plasma Phys. **44**, 388–394 (2004).

[62]A. P. Lyubartsev, "Simulation of excited states and the sign problem in the path integral Monte Carlo method," J. Phys. A: Math. Gen. **38**, 6659–6674 (2005).

[63]M. Takahashi and M. Imada, "Monte Carlo of quantum systems. II. Higher order correction," J. Phys. Soc. Jpn. **53**, 3765–3769 (1984).

[64]S. A. Chin and C. R. Chen, "Gradient symplectic algorithms for solving the Schrödinger equation with time-dependent potentials," J. Chem. Phys. **117**, 1409 (2002).

[65]K. Sakkos, J. Casulleras, and J. Boronat, "High order Chin actions in path integral Monte Carlo," J. Chem. Phys. **130**, 204109 (2009).

[66]S. A. Chin, "High-order path integral Monte Carlo methods for solving quantum dot problems," Phys. Rev. E **91**, 031301(R) (2015).

[67]G. H. Booth, A. J. Thom, and A. Alavi, "Fermion Monte Carlo without fixed nodes: A game of life, death, and annihilation in Slater determinant space," J. Chem. Phys. **131**, 054106 (2009).

[68]J. S. Spencer, N. S. Blunt, and W. M. C. Foulkes, "The sign problem and population dynamics in the full configuration interaction quantum Monte Carlo method," J. Chem. Phys. **136**, 054110 (2012).

[69]M. H. Kolodrubetz, J. S. Spencer, B. K. Clark, and W. M. C. Foulkes, "The effect of quantization on the full configuration interaction quantum Monte Carlo sign problem," J. Chem. Phys. **138**, 024110 (2013).

[70]J. J. Shepherd, G. E. Scuseria, and J. S. Spencer, "Sign problem in full configuration interaction quantum Monte Carlo: Linear and sublinear representation regimes for the exact wave function," Phys. Rev. B **90**, 155130 (2014).

[71]D. Cleland, G. H. Booth, and A. Alavi, "Communications: Survival of the fittest: Accelerating convergence in full configuration-interaction quantum Monte Carlo," J. Chem. Phys. **132**, 041103 (2010).

[72]J. J. Shepherd, G. H. Booth, and A. Alavi, "Investigation of the full configuration interaction quantum Monte Carlo method using homogeneous electron gas models," J. Chem. Phys. **136**, 244101 (2012).

[73]J. J. Shepherd, G. H. Booth, A. Grüneis, and A. Alavi, "Full configuration interaction perspective on the homogeneous electron gas," Phys. Rev. B **85**, 081103 (2012).

[74]J. P. Perdew, "Climbing the ladder of density functional approximations," MRS Bull. **38**(9), 743–750 (2013).

[75]S. Groth, T. Dornheim, and M. Bonitz, "Free energy of the uniform electron gas: Analytical models vs. first principle simulations," Contrib. Plasma Phys. e-print arXiv:1611.05695.

[76]A. Filinov and M. Bonitz, "Collective and single-particle excitations in 2D dipolar Bose gases," Phys. Rev. A **86**, 043628 (2012).

Chapter 6

Parametrization of the Exchange–Correlation Free Energy

6.1 Overview of Existing Parametrizations

To finally realize the construction of a new *ab initio* QMC based exchange–correlation functional (cf. Sec. 6.2), it was indispensable to get an overview of the already existing zoo of parametrizations. These were obtained using different quantities as input (typically the exchange–correlation energy e_{xc} or the interaction energy v), which can be based on different kinds of approximations, and are valid over different parameter ranges. A further note of caution is in order regarding the different known limiting behaviors (i.e., Hartree–Fock [205] for $r_s \to 0$, Debye–Hückel [206] for $\theta \to \infty$, and the ground-state exchange–correlation energy [112, 113] for $\theta \to 0$), which are not fulfilled by all functionals.

Providing such an overview was one goal of the following paper[1], Ref. [129], in which we discuss the parametrizations of $f_{xc}(r_s, \theta)$ (limiting ourselves to the unpolarized case investigated in Sec. 5.1) by Ebeling and co-workers [119–121, 207, 208] (based on interpolations between various known limits), Ichimaru and co-workers [123, 209] (based on the STLS formalism [124, 196]), Perrot and Dharma-wardana [122] (based on the approximate mapping of the quantum system onto an effective classical one [210]), Sjostrom and Dufty [128] (based on the finite-temperature extension of the Vashista–Singwi local-field correction [211, 212]), and Karasiev and co-workers [107] (based on the RPIMC data by Brown *et al.* [157]).

A second goal was the comparison of f_{xc} to our new *ab initio* QMC data for the warm dense UEG in the thermodynamic limit [164], cf. Sec. 5.1, that was available for a few

---

constant temperatures down to $\theta = 0.5$. In a nutshell, we found that [129] *an accurate parametrization of the exchange–correlation free energy that is valid for all r_s-θ combinations* was not available, thereby further stressing the need for a new parametrization that is based on accurate QMC results.

ORIGINAL ARTICLE

Contributions to
Plasma Physics

Free energy of the uniform electron gas: Testing analytical models against first-principles results[†]

Simon Groth[*] | Tobias Dornheim | Michael Bonitz

Institut für Theoretische Physik und
Astrophysik,
Christian-Albrechts-Universität zu Kiel, Kiel,
Germany

*Correspondence
Simon Groth, Institut für Theoretische Physik und
Astrophysik, Christian-Albrechts-Universität zu
Kiel, D-24098 Kiel, Germany.
E-mail: groth@theo-physik.uni-kiel.de

The uniform electron gas is a key model system in the description of matter, including dense plasmas and solid-state systems. However, the simultaneous occurrence of quantum, correlation, and thermal effects makes the theoretical description challenging. For these reasons, over the last half century, many analytical approaches have been developed, the accuracy of which has remained unclear. We have recently obtained the first ab initio data for the exchange correlation free energy of the uniform electron gas, which now provides the opportunity to assess the quality of the mentioned approaches and parameterizations. Particular emphasis is placed on the warm, dense matter regime, where we find significant discrepancies between the different approaches.

KEYWORDS

free energy, quantum Monte Carlo, uniform electron gas, warm dense matter

1 | INTRODUCTION

Over the last decade, there has emerged growing interest in the so-called warm dense matter (WDM), which is of key importance for the description of, for example, astrophysical systems,[1,2] laser-excited solids,[3] and inertial confinement fusion targets.[4–6] The WDM regime is characterized by the simultaneous occurrence of strong (moderate) correlations of ions (electrons), thermal effects, as well as quantum effects of the electrons. In dimensionless units, typical parameters are the Brueckner parameter $r_s = \bar{r}/a_B$ and the reduced temperature $\theta = k_B T/E_F$, both being of the order of unity (more generally in the range 0.1–10). Here, $\bar{r}$ and a_B denote the mean interparticle distance and the Bohr radius, respectively. A third relevant parameter is the classical coupling parameter of the ionic component, $\Gamma_i = Z_i^2 e^2/\bar{r} k_B T$, which is often larger than unity indicating that the ionic component is far from an ideal gas. This makes the theoretical description of this peculiar state of matter particularly challenging, as there is no small parameter to perform an expansion around.

In the ground state, there exists a large toolkit of approaches that allow the accurate description of manifold physical systems, the most successful of which arguably being Kohn–Sham density functional theory (DFT) (e.g., [7,8]). The basic idea of DFT is to map the complicated and computationally demanding quantum many-body problem onto an effective single-particle problem. This would be exact if the correct exchange-correlation functional of the system of interest was available, which is, of course, not the case. In practice, therefore, one has to use an approximation. The foundation of the great success of DFT has been the local density approximation (LDA), that is, the use of the exchange-correlation energy E_{xc} of the uniform electron gas (UEG) with the same density as the more complicated system of interest. Accurate data for E_{xc} of the UEG was obtained by Ceperley and Alder[9] using a quantum Monte Carlo (QMC) method, from which Perdew and Zunger[10] constructed a simple parameterization with respect to density, $E_{xc}(r_s)$, which is still used to this day.

However, the accurate description of WDM requires the extension of DFT to finite temperature. This has been realized long ago by Mermin[11], who used a superposition of excited states weighted with their thermal occupation probability. A

[†]Dedicated to Werner Ebeling on the occasion of his 80th birthday.

strict approach to the thermodynamic properties of this system also requires an appropriate finite-temperature extension of the LDA, in particular, replacement of the ground-state energy functionals by free energies, that is $E \rightarrow f = E - TS$. This means, a finite-temperature version of the LDA requires accurate parameterizations of the *exchange correlation free energy* with respect to temperature and density,[12–17] that is, $f_{xc}(r_s, \theta)$, even though in some cases the entropic correction may be small. This seemingly benign task, however, turns out to be far from trivial because accurate data for the free energy are much more involved than the ground-state results. While for the ground state reliable QMC data have been known for a long time, until recently,[18–28] the notorious fermion sign problem[29,30] has prevented reliable QMC simulations in the warm, dense regime. Therefore, during the recent four decades, many theoretical approaches to $f_{xc}(r_s, \theta)$ have been developed that have lead to a variety of parameterizations (for an overview on early works, see e.g., Refs. [31,32]). Some of them have gained high popularity and been successfully applied in many fields, even though their accuracy has not been thoroughly tested. It is the purpose of this paper to present such a quantitative comparison of earlier models with new simulation results.

In Section 2, we introduce a selection of such functions. First, we analyze the purely analytical expression presented by Ebeling et al. (e.g., Ref. [33]). Next, we study functional fits to linear response data based on static local field correction schemes that were suggested by Singwi, Tosi, Land, and Sjölander (STLS)[34] (Section 2.2) and Vashishta and Singwi (VS)[35] (Section 2.3). As a fourth example, we consider the quantum-classical mapping developed by Dharma-wardana and Perrot (PDW)[36,37] (Section 2.4). Finally, we consider the recent parameterization by Karasiev, Sjostrom, Dufty, Trickey (KSDT)[38] (Section 2.5), which is based on the restricted path integral Monte Carlo (RPIMC) data by Brown et al. that became available recently.[39] However, those data have a limited accuracy because of (a) the use of the fixed-node approximation[40] and (b) an inappropriate finite-size correction (see Dornheim et al.[27]), giving rise to systematic errors in the free energy results, as we will show below. In Section 3, we compare all aforementioned parameterizations of f_{xc} to the new, accurate QMC data by Dornheim et al.[27], which are free from any systematic bias and, hence, allow us to gauge the accuracy of models. Particular emphasis is laid on the WDM regime.

2 | FREE-ENERGY PARAMETERIZATIONS

2.1 | Ebeling's Padé formulae

The idea to produce an analytical formula for the thermodynamic quantities that connects known analytical limits via a smooth Padé approximant is due to Ebeling, Kraeft, and Richert et al.[41–44] These approximations have been quite influential in the description of nonideal plasmas and electron–hole plasmas in the 1980s and 1990s, receiving, in part, a substantial number of citations. As they have been improved continuously in the following years, we, therefore, discuss only the more recent versions, compare [33,45] and references therein.

Ebeling et al. used Rydberg atomic units and introduced a reduced thermal density

$$\bar{n} = n\Lambda^3 = 6\sqrt{\pi} r_s^{-3} \tau^{-3/2} \tag{1}$$

with the usual thermal wavelength Λ, and $\tau = k_B T / \mathrm{Ry}$ being the temperature in energy units. The Padé approximation for f_{xc} then reads[33]

$$f_{xc}^{\mathrm{Ebeling,Ry}}(r_s, \tau) = -\frac{f_0(\tau)\bar{n}^{1/2} + f_3(\tau)\bar{n} + f_2\bar{n}^2 \epsilon^{\mathrm{Ry}}(r_s)}{1 + f_1(\tau)\bar{n}^{1/2} + f_2\bar{n}^2} \tag{2}$$

with the coefficients

$$f_0(\tau) = \frac{2}{3}\left(\frac{\tau}{\pi}\right)^{1/4}, \quad f_1(\tau) = \frac{1}{8f_0(\tau)}\sqrt{2}(1 + \log(2)), \quad f_2 = 3, \quad f_3(\tau) = \frac{1}{4}\left(\frac{\tau}{\pi}\right)^{1/2} \tag{3}$$

and the ground-state parameterization for the exchange correlation energy

$$\epsilon^{\mathrm{Ry}}(r_s) = \frac{0.9163}{r_s} + 0.1244 \log\left(1 + \frac{2.117 r_s^{-1/2}}{1 + 0.3008\sqrt{r_s}}\right). \tag{4}$$

To achieve better comparability with the other formulas discussed below, we re-express Equation 2 in Hartree atomic units as a function of r_s and the reduced temperature $\theta = k_B T / E_F$:

$$f_{xc}^{\mathrm{Ebeling,Ha}}(r_s, \theta) = -\frac{1}{2}\frac{A r_s^{-1/2}\theta^{-1/2} + B r_s^{-1}\theta^{-1} + C\theta^{-3}\epsilon^{\mathrm{Ry}}(r_s)}{1 + D\theta^{-1}r_s^{1/2} + C\theta^{-3}}, \quad \text{with} \tag{5}$$

$$A = \frac{2}{3\sqrt{\pi}} \left(\frac{8}{3}\right)^{1/2} \left(\frac{4}{9\pi}\right)^{-1/6}, \quad B = \frac{2}{3\pi} \left(\frac{4}{9\pi}\right)^{-1/3}, \quad C = \frac{64}{3\pi}, \tag{6}$$

$$D = \frac{(1 + \log(2))\sqrt{3}}{4} \left(\frac{4}{9\pi}\right)^{1/6}.$$

Evidently, Equation 5 incorporates the correct ground-state limit

$$\lim_{\theta \to 0} f_{xc}^{\text{Ebeling,Ha}}(r_s, \theta) = -\frac{1}{2} \epsilon^{\text{Ry}}(r_s), \tag{7}$$

where the pre-factor $1/2$ is due to the conversion between Rydberg and Hartree units. Similarly, in the high-temperature limit, the well-known Debye–Hückel result is recovered, for example Ref. [46]

$$\lim_{\theta \to \infty} f_{xc}^{\text{Ebeling,Ha}}(r_s, \theta) = -\frac{1}{2} A \, r_s^{-1/2} \theta^{-1/2} = -\frac{1}{\sqrt{3}} r_s^{-3/2} T^{-1/2}. \tag{8}$$

Results for the warm, dense UEG computed from these formulas are included in the following figures. For the Padé approximations to the UEG at strong coupling in the quasi-classical regime, see, for example, Ref. [47].

2.2 | Parameterization by Ichimaru et al.

In the mid-1980s, Tanaka, Ichimaru, and coworkers[48,49] extended the original STLS scheme[34] for the static local field corrections to finite temperature and numerically obtained the interaction energy V (per particle) of the UEG via integration of the static structure factor $S(k)$:

$$V = \frac{1}{2} \int_{k<\infty} \frac{d\mathbf{k}}{(2\pi)^3} [S(\mathbf{k}) - 1] \frac{4\pi}{\mathbf{k}^2} \tag{9}$$

for 70 parameter combinations with $\theta = 0.1, 1, 5$ and $r_s \sim 10^{-3}, \ldots, 74$. Subsequently, a parameterization for V was introduced as a function of r_s and θ[50,51]

$$V(r_s, \theta) = -\frac{1}{r_s} \frac{a_{\text{HF}}(\theta) + \sqrt{2}\lambda r_s^{1/2} \tanh(\theta^{-1/2}) B(\theta) + 2\lambda^2 r_s C(\theta) E(\theta) \tanh(\theta^{-1})}{1 + \sqrt{2}\lambda r_s^{1/2} D(\theta) \tanh(\theta^{-1/2}) + 2\lambda^2 r_s E(\theta)} \tag{10}$$

with the definitions

$$a_{\text{HF}}(\theta) = 0.610887 \tanh\left(\theta^{-1}\right) \frac{0.75 + 3.4363\theta^2 - 0.09227\theta^3 + 1.7035\theta^4}{1 + 8.31051\theta^2 + 5.1105\theta^4}, \tag{11}$$

$$B(\theta) = \frac{x_1 + x_2\theta^2 + x_3\theta^4}{1 + x_4\theta^2 + x_5\theta^4}, \quad C(\theta) = x_6 + x_7 \exp\left(-\theta^{-1}\right), \tag{12}$$

$$D(\theta) = \frac{x_8 + x_9\theta^2 + x_{10}\theta^4}{1 + x_{11}\theta^2 + x_{12}\theta^4}, \quad E(\theta) = \frac{x_{13} + x_{14}\theta^2 + x_{15}\theta^4}{1 + x_{16}\theta^2 + x_{17}\theta^4}. \tag{13}$$

In addition to the exact limits for $\theta \to 0$ and $\theta \to \infty$, the parameterization from Equation 10 also approaches the well-known Hartree–Fock limit for high density:

$$\lim_{r_s \to 0} V(r_s, \theta) = -\frac{a_{\text{HF}}(\theta)}{r_s}, \tag{14}$$

which has been parameterized by Perrot and Dharma-wardana,[52] see Equation 11. Naturally, the free parameters x_i, $i = 1, \ldots, 17$ have been determined by fitting Equation 10 to the STLS data for V, and the resulting values are listed in Table 1. From the interaction energy $V(r_s, \theta)$, the free exchange-correlation energy is obtained by integration:

$$f_{xc}(r_s, \theta) = \frac{1}{r_s^2} \int_0^{r_s} d\bar{r}_s \, \bar{r}_s V(\bar{r}_s, \theta). \tag{15}$$

TABLE 1 Fit parameters by Ichimaru[51] for the $f_{xc}(r_s, \theta)$ parameterization from Equation 16, fitted to STLS data[49]

x_1	x_2	x_3	x_4	x_5
3.4130800×10^{-1}	1.2070873×10	1.148889×10^0	1.0495346×10	1.326623×10^0
x_6	x_7	x_8	x_9	x_{10}
8.72496×10^{-1}	2.5248×10^{-2}	6.14925×10^{-1}	1.6996055×10	1.489056×10^0
x_{11}	x_{12}	x_{13}	x_{14}	x_{15}
1.010935×10	1.22184×10^0	5.39409×10^{-1}	2.522206×10^0	1.78484×10^{-1}
x_{16}	x_{17}			
2.555501×10^0	1.46319×10^{-1}			

Plugging in the expression for $V(r_s, \theta)$ from Equation 10 into 15 gives the final parameterization for $f_{xc}(r_s, \theta)$:

$$f_{xc}(r_s, \theta) = -\frac{1}{r_s} \frac{c(\theta)}{e(\theta)} \tag{16}$$

$$- \frac{\theta}{2e(\theta)r_s^2 \lambda^2} \left[\left(a_{\mathrm{HF}}(\theta) - \frac{c(\theta)}{e(\theta)} \right) - \frac{d(\theta)}{e(\theta)} \left(b(\theta) - \frac{c(\theta)d(\theta)}{e(\theta)} \right) \right]$$

$$\times \log \left| \frac{2e(\theta)\lambda^2 r_s}{\theta} + \sqrt{2}d(\theta)\lambda r_s^{1/2}\theta^{-1/2} + 1 \right|$$

$$- \frac{\sqrt{2}}{e(\theta)} \left(b(\theta) - \frac{c(\theta)d(\theta)}{e(\theta)} \right) \frac{\theta^{1/2}}{r_s^{1/2}\lambda}$$

$$+ \frac{\theta}{r_s^2 \lambda^2 e(\theta)\sqrt{4e(\theta) - d^2(\theta)}} \left[d(\theta) \left(a_{\mathrm{HF}}(\theta) - \frac{c(\theta)}{e(\theta)} \right) \right.$$

$$+ \left. \left(2 - \frac{d^2(\theta)}{e(\theta)} \right) \left(b(\theta) - \frac{c(\theta)d(\theta)}{e(\theta)} \right) \right]$$

$$\times \left[\mathrm{atan} \left(\frac{2^{3/2}e(\theta)\lambda r_s^{1/2}\theta^{-1/2} + d(\theta)}{\sqrt{4e(\theta) - d^2(\theta)}} \right) - \mathrm{atan} \left(\frac{d(\theta)}{\sqrt{4e(\theta) - d^2(\theta)}} \right) \right]$$

with the abbreviations

$$b(\theta) = \theta^{1/2} \tanh\left(\theta^{-1/2}\right) B(\theta), \quad c(\theta) = C(\theta)e(\theta),$$
$$d(\theta) = \theta^{1/2} \tanh\left(\theta^{-1/2}\right) D(\theta), \quad e(\theta) = \theta \tanh\left(\theta^{-1}\right) E(\theta). \tag{17}$$

2.3 | VS parameterization

Despite the overall good performance of STLS in the ground state,[53] it has long been known that this scheme does not fulfill the compressibility sum rule (CSR, see e.g., Ref. [54] for a detailed discussion). To overcome this obstacle, Vashishta and Singwi[35] introduced modified local field corrections (VS), where the CSR is automatically fulfilled. This idea had been extended in an approximate way to finite temperature by Stolzmann and Rösler,[55] and more recently Sjostrom and Dufty[54] obtained an exhaustive dataset of results that are exact within the VS framework.

As already explained in the previous section for the STLS data, they first calculated the static structure factor $S(k)$, computed the interaction energy V by integration (Equation 9), fitted the parameterization from Equation 10 to this data, and thereby obtained the desired parameterization of $f_{xc}(r_s, \theta)$ as given in Equation 16 (albeit with the new fit parameters listed in Table 2).

2.4 | PDW parameterization

Dharma-wardana and Perrot[36,37] introduced an independent, completely different idea. In particular, they employed a *classical mapping* such that the correlation energy of the electron gas at $T = 0$ (that has long been known from QMC calculations [9,10]) is exactly recovered by the simulation of a classical system at an effective "quantum temperature" T_q. However, due to the lack of accurate data at finite T, an exact mapping had not been possible, and the authors introduced a modified temperature T_c, where they assumed an interpolation between the exactly known ground state and classical (high T) regimes, $T_c = \sqrt{T^2 + T_q^2}$. Naturally, at WDM conditions this constitutes a largely uncontrolled approximation.

TABLE 2 Fit parameters by Sjostrom and Dufty[54] for the $f_{xc}(r_s, \theta)$ parameterization from Equation 16, fitted to VS data

x_1	x_2	x_3	x_4	x_5
1.8871493×10^{-1}	1.0684788×10	1.1088191×10^2	1.8015380×10	1.2803540×10^2
x_6	x_7	x_8	x_9	x_{10}
8.3331352×10^{-1}	$-1.1179213 \times 10^{-1}$	6.1492503×10^{-1}	1.6428929×10	2.5963096×10
x_{11}	x_{12}	x_{13}	x_{14}	x_{15}
1.0905162×10	2.9942171×10	5.3940898×10^{-1}	5.8869626×10^4	3.1165052×10^3
x_{16}	x_{17}			
3.8887108×10^4	2.1774472×10^3			

TABLE 3 Fit parameters by Perrot and Dharma-wardana[37] for the $f_{xc}(r_s, \theta)$ parameterization from Equation 18

k	$a_{1,k}$	$b_{1,k}$	$c_{1,k}$	$a_{2,k}$	$b_{2,k}$	$c_{2,k}$	v_k	r_k
1	5.6304	−2.2308	1.7624	2.6083	1.2782	0.16625	1.5	4.4467
2	5.2901	−2.0512	1.6185	−15.076	24.929	2.0261	3	4.5581
3	3.6854	−1.5385	1.2629	2.4071	0.78293	0.095869	3	4.3909

To obtain the desired parameterization for f_{xc}, extensive simulations of the UEG in the range $r_s = 1$–10 and $\theta = 0$–10 were performed. These were used as input for a fit (see Table 3 for the corresponding fit parameters) with the functional form

$$f_{xc}(r_s, \theta) = \frac{\epsilon(r_s) - P_1(r_s, \theta)}{P_2(r_s, \theta)}, \tag{18}$$

$$P_1(r_s, \theta) = \left(A_2(r_s)u_1(r_s) + A_3(r_s)u_2(r_s)\right)\theta^2 Q^2(r_s) + A_2(r_s)u_2(r_s)\theta^{5/2}Q^{5/2}(r_s),$$

$$P_2(r_s, \theta) = 1 + A_1(r_s)\theta^2 Q^2(r_s) + A_3(r_s)\theta^{5/2}Q^{5/2}(r_s) + A_2(r_s)\theta^3 Q^3(r_s),$$

$$Q(r_s) = \left(2r_s^2\lambda^2\right)^{-1}, \quad n(r_s) = \frac{3}{4\pi r_s^3}, \quad u_1(r_s) = \frac{\pi n(r_s)}{2}, \quad u_2(r_s) = \frac{2\sqrt{\pi n(r_s)}}{3},$$

$$A_k(r_s) = \exp\left(\frac{y_k(r_s) + \beta_k(r_s)z_k(r_s)}{1 + \beta_k(r_s)}\right), \quad \beta_k(r_s) = \exp\left(5(r_s - r_k)\right),$$

$$y_k(r_s) = v_k \log(r_s) + \frac{a_{1,k} + b_{1,k}r_s + c_{1,k}r_s^2}{1 + r_s^2/5}, \quad z_k(r_s) = r_s\frac{a_{2,k} + b_{2,k}r_s}{1 + c_{2,k}r_s^2},$$

which becomes exact for $\theta \to 0$ and $\theta \to \infty$, but is limited to the accuracy of the classical mapping data in between. Further, it does not include the exact Hartree–Fock limit for $r_s \to 0$, so that it cannot reasonably be used for $r_s < 1$. For completeness, we mention that a functional form similar to Equation 18 was recently used by Brown et al. [56] for a fit to their RPIMC data[39].

Similar ideas of quantum-classical mappings were recently investigated by Dufty and Dutta (see e.g., Ref. [57,58]).

2.5 | Parameterization by Karasiev et al.

Karasiev et al.[38] (KSDT) utilized as the functional form for f_{xc} an expression similar to Equation 10, which Ichimaru and coworkers[50,51] suggested for the interaction energy:

$$f_{xc}(r_s, \theta) = -\frac{1}{r_s}\frac{a_{HF}(\theta) + b(\theta)r_s^{1/2} + c(\theta)r_s}{1 + d(\theta)r_s^{1/2} + e(\theta)r_s}, \tag{19}$$

$$b(\theta) = \tanh\left(\theta^{-1/2}\right)\frac{b_1 + b_2\theta^2 + b_3\theta^4}{1 + b_4\theta^2 + \sqrt{1.5\lambda^{-1}b_3}\theta^4}, \quad c(\theta) = \left[c_1 + c_2\exp\left(-\frac{c_3}{\theta}\right)\right]e(\theta),$$

$$d(\theta) = \tanh\left(\theta^{-1/2}\right)\frac{d_1 + d_2\theta^2 + d_3\theta^4}{1 + d_4\theta^2 + d_5\theta^4}, \quad e(\theta) = \tanh\left(\theta^{-1}\right)\frac{e_1 + e_2\theta^2 + e_3\theta^4}{1 + e_4\theta^2 + e_5\theta^4}.$$

Further, instead of fitting to the interaction energy V, they used the relation

$$E_{xc}(r_s, \theta) = f_{xc}(r_s, \theta) - \theta\frac{\partial f_{xc}(r_s, \theta)}{\partial \theta}\bigg|_{r_s} \tag{20}$$

TABLE 4 Fit parameters by Karasiev et al. [38] for the $f_{xc}(r_s, \theta)$ parameterization from Equation 19

b_1	b_2	b_3	b_4	c_1	c_2	c_3
0.283997	48.932154	0.370919	61.095357	0.870089	0.193077	2.414644
d_1	d_2	d_3	d_4	d_5	e_1	e_2
0.579824	94.537454	97.839603	59.939999	24.388037	0.212036	16.731249
e_3	e_4	e_5				
28.485792	34.028876	17.235515				

and fitted the rhs of Equation 20 to the recently published RPIMC data for the exchange correlation energy E_{xc} by Brown et al. [39] that are available for the parameters $r_s = 1$–40 and $\theta = 0.0625$–8 (see Table 4 for the corresponding fit parameters).

3 | RESULTS

In this section we analyze the behavior of the analytical approximations for the exchange-correlation free energies that were summarized above by comparison with our recent simulation results that cover the entire relevant density range for temperatures $\theta \geq 0.5$. These data have an unprecedented accuracy on the order of 0.1% (for details, see Refs. [27,28]).

3.1 | Temperature dependence

In Figure 1, we show the temperature dependence of the exchange-correlation free energy as a function of the reduced temperature θ for two densities that are relevant for contemporary WDM research, namely $r_s = 1$ (left) and $r_s = 6$ (right). For both cases, all depicted parameterizations reproduce the correct classical limit for large θ [cf. Equation 8] and four of them (Ebeling, KSDT, STLS, and PDW) are in excellent agreement for the ground state as well. For completeness, we note that the small differences between KSDT and Ebeling and PDW are due to different ground-state QMC input data. In particular, Karasiev et al. used more recent QMC results by Spink et al.,[59] although in the context of WDM research the deviations to older parameterizations are negligible. The VS parameterization, on the other hand, does not incorporate any ground-state limit and, consequently, the behavior of $f_{xc}^{VS}(r_s, \theta)$ becomes unreasonable below $\theta = 0.0625$. Similarly, the lowest temperature (despite the ground-state limit) included in the fit for $f_{xc}^{PDW}(r_s, \theta)$ is $\theta = 0.25$ and the rather unsmooth connection between this point and $\theta = 0$ does not appear to be trustworthy as well.

Let us now check the accuracy of the different models at intermediate WDM temperatures. As a reference, we use the recent accurate QMC results for the macroscopic UEG by Dornheim et al.,[27] that is, the red squares. For $r_s = 1$, the semi-analytic expression by Ebeling (blue) exhibits the largest deviations exceeding $\Delta f_{xc}/f_{xc} = 25\%$ for $\theta \sim 1$. For lower density, $r_s = 6$, the Ebeling parameterization is significantly more accurate, although here, too, appear deviations of $\Delta f_{xc}/f_{xc} \sim 10\%$ to the exact data at intermediate temperature. Therefore, this parameterization produces reliable data in the two limiting cases of zero and high temperature, but is less accurate in between.

Next we consider the STLS curve (black). It is in very good agreement with the QMC data, and the error does not exceed $\Delta f_{xc}/f_{xc} = 4\%$ over the entire θ range for both depicted r_s values. The largest deviations appear for intermediate temperatures as well.

Third, we consider the VS model (yellow line). For $r_s = 1$, the VS parameterization by Sjostrom and Dufty[54] exhibits the same trends as the STLS curve, albeit with larger deviations, $\Delta f_{xc}/f_{xc} > 5\%$. Further, for $r_s = 6$, f_{xc}^{VS} exhibits much larger deviations to the exact result and the error reaches $\Delta f_{xc}/f_{xc} \approx 8\%$. Evidently, the constraint to automatically fulfill the CSR does not improve the accuracy of other quantities, in particular the interaction energy V (which was used as an input for the parameterization (see Section 2.3) or the static structure factor $S(k)$ itself.

Fourth, the parameterization based on the classical mapping (PDW, light blue) exhibits somewhat opposite trends as compared to Ebeling, STLS, and VS and predicts too large an exchange-correlation free energy for all θ. The magnitude of the deviations is comparable to VS and does not exceed $\Delta f_{xc}/f_{xc} = 5\%$.

Finally, we consider the recent parameterization by Karasiev et al. (KSDT, green),[38] which is based on RPIMC results[39]. For $r_s = 6$, there is excellent agreement with the new reference QMC data with a maximum deviation of $\Delta f_{xc}/f_{xc} \sim 1\%$ for $\theta = 4$. This is, in principle, expected since the main sources of error for their input data, that is, the nodal error and the insufficient finite-size correction, are less important for larger r_s. However, for $r_s = 1$ there appear significantly larger deviations exceeding $\Delta f_{xc}/f_{xc} = 5\%$ at high temperature. In fact, for $r_s = 1$ and the largest considered temperature, $\theta = 8$, the KSDT parameterization exhibits the largest deviations of all depicted parameterizations.
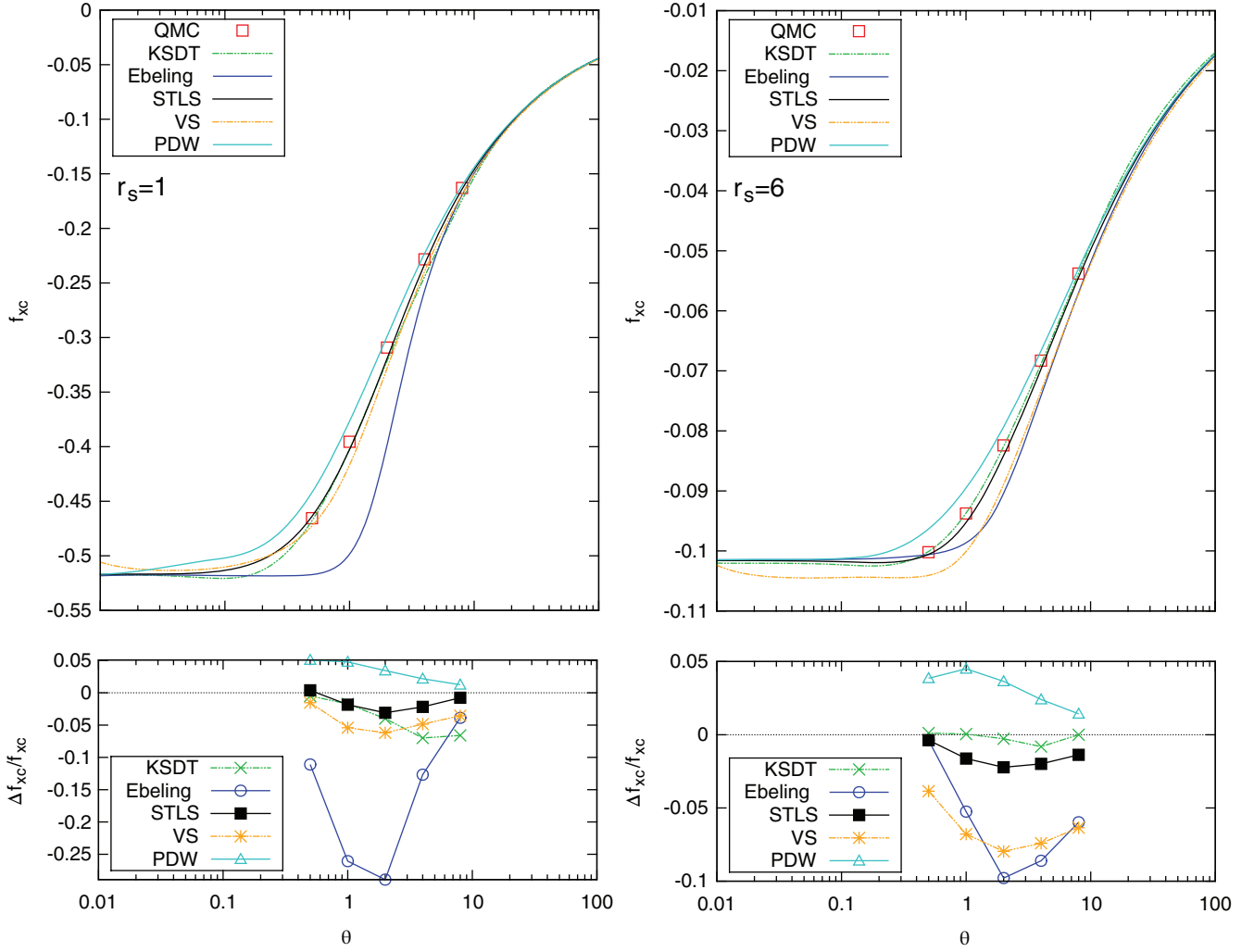
FIGURE 1 Temperature dependence of f_{xc} at fixed density $r_s = 1$ (left) and $r_s = 6$ (right). Top: Quantum Monte Carlo (QMC) data (symbols) taken from Dornheim et al.,[27] a parameterization of RPIMC data by Karasiev, Sjostrom, Dufty, Trickey (KSDT),[38] a semi-analytic Padé approximation by Ebeling,[33] a parameterization fitted to Singwi, Tosi, Land, and Sjölander (STLS) and Vashishta and Singwi (VS) data by Ichimaru[51] and Sjostrom and Dufty,[54] respectively, and a fit to classical mapping data by Perrot and Dharma-wardana (PDW).[37] Bottom: Relative deviation to the QMC data.

3.2 | Density dependence

As a complement to Section 3.1, in Figure 2 we investigate in more detail the density dependence of the different parameterizations for two relevant temperatures, $\theta = 0.5$ (left) and $\theta = 4$ (right).

Most notably, the Ebeling and PDW parameterizations do not include the correct high-density ($r_s \to 0$) limit, that is Equation 11, and therefore are not reliable for $r_s < 1$. For $\theta = 0.5$, f_{xc}^{Ebeling} is in qualitative agreement with the correct results, but the deviations rapidly increase with density and exceed $\Delta f_{xc}/f_{xc} = 10\%$, for $r_s = 1$. At higher temperature, $\theta = 4$, the situation is worse, and the Ebeling parameterization shows systematic deviations over the entire density range. The STLS fit displays a similarly impressive agreement with the exact data as for the θ dependence (cf. Figure 1), and the deviations do not exceed $\Delta f_{xc}/f_{xc} \sim 3\%$ for both depicted θ values. On the other hand, the VS results are again significantly less accurate than STLS although the deviation remains below $\Delta f_{xc}/f_{xc} = 8\%$ for both temperatures. Further, we notice that the largest deviations occur for $r_s \geq 2$, that is, toward stronger coupling, which is expected since here the pair distribution function exhibits unphysical negative values at short distance (see e.g., Ref. [54]). Again, the incorporation of the CSR has not improved the quality of the interaction energy or the structure factor compared to STLS. The classical mapping data (PDW) does exhibit deviations not exceeding $\Delta f_{xc}/f_{xc} = 5\%$ for $r_s \geq 1$, that is, in the range where numerical data have been incorporated into the fit. Overall, the quality of this parameterization is comparable to the VS curve although the relative deviation appears to be almost constant with respect to the density. This is not surprising, as the approximation has not been conducted with respect to coupling (the effective classical system is solved with the hypernetted chain method, which is expected to be accurate in this regime) but, instead, in the interpolation of the effective temperature T_c. Further, we notice a peculiar nonsmooth and almost oscillatory behavior of f_{xc}^{PDW} around $r_s = 5$, which is more pronounced for $\theta = 0.5$ and the origin of which remains unclear. Finally, we again consider
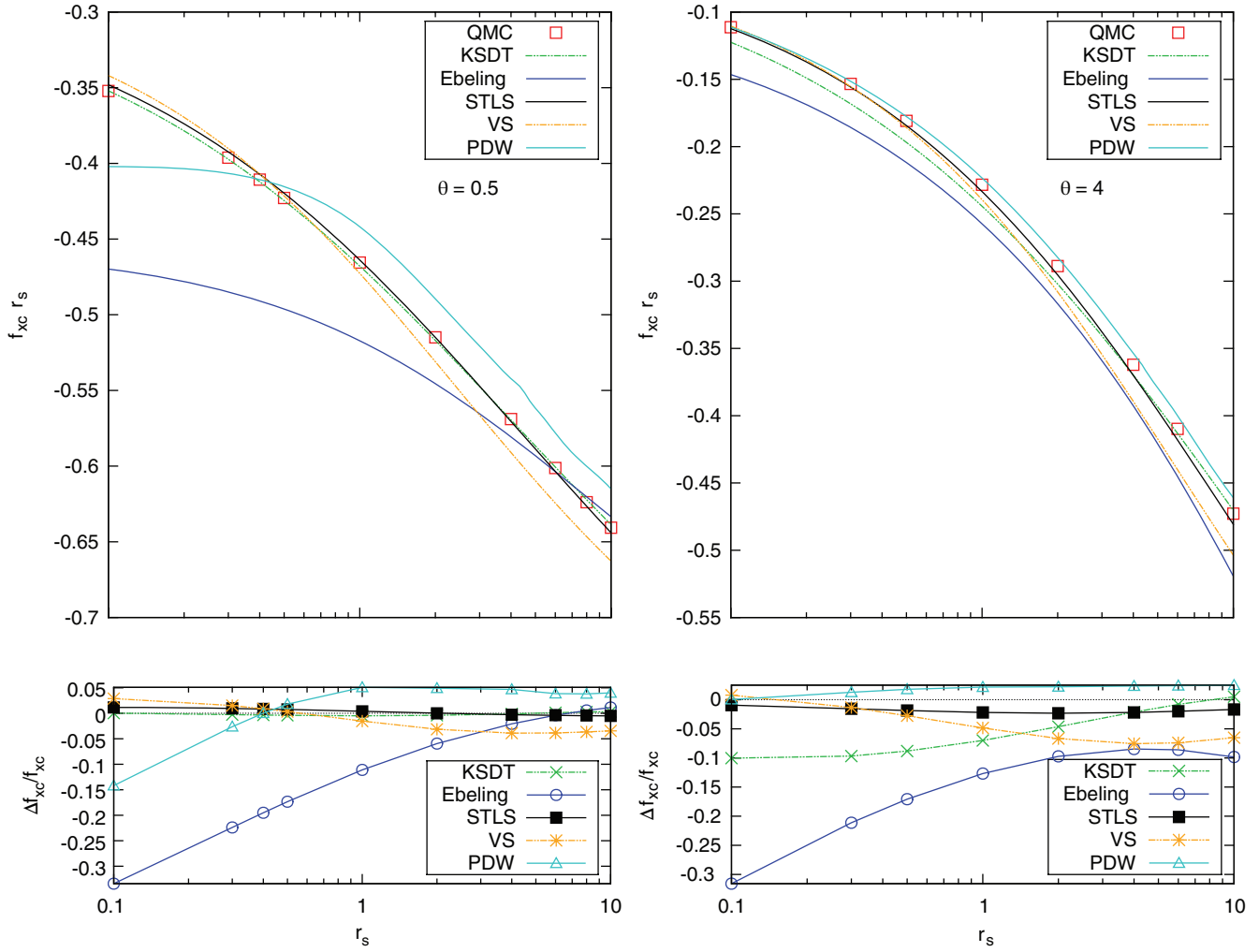
FIGURE 2 Density dependence of f_{xc} at fixed temperature $\theta = 0.5$ (left) and $\theta = 4$ (right). Top: Quantum Monte Carlo (QMC) data taken from Dornheim et al.,[27] a parameterization of RPIMC data by Karasiev, Sjostrom, Dufty, Trickey (KSDT),[38] a semi-analytic Padé approximation by Ebeling,[33] a parameterization fitted to Singwi, Tosi, Land, and Sjölander (STLS) and Vashishta and Singwi (VS) data by Ichimaru[51] and Sjostrom and Dufty,[54] respectively, and a fit to classical mapping data by Perrot and Dharma-wardana (PDW).[37] Bottom: Relative deviation to the QMC data.

the KSDT fit based on the RPIMC data by Brown et al. [39] (a similar analysis for more temperatures can be found by Dornheim et al.[27]). For $\theta = 0.5$, this parameterization is in excellent agreement with the reference QMC data and the deviations are in the sub-percent regime over the entire depicted r_s range. However, for larger temperatures there appear significant errors that, at $\theta = 4$, reach a maximum of $\Delta f_{xc}/f_{xc} \sim 10\%$ for $r_s = 0.1$, that is, at parameters where STLS, VS, and PDW are in very good agreement with the reference QMC data. Interestingly, these deviations vanish only for $r_s \leq 10^{-4}$. Naturally, the inaccuracies of the KSDT fit are a direct consequence of the systematic errors of the input data and the lack of accurate simulation data for $r_s < 1$, prior to Dornheim et al.[27]

4 | DISCUSSION

In summary, we have compared five different parameterizations of the exchange-correlation free energy of the unpolarized UEG to the recent QMC data by Dornheim et al.[27] and, thereby, have been able to gauge their accuracy with respect to θ and r_s over large parts of the WDM regime. We underline that all these parameterizations are highly valuable, the main merit being their easy and flexible use and rapid evaluation. At the same time, an unbiased evaluation of their accuracy had not been done and appears highly important, as this allows constraining the field of applicability of these models and indicating directions for future improvements.

Summarizing our findings, we have observed that the semi-analytic parameterization by Ebeling[33] is mostly reliable in the high and zero temperature limits but exhibits substantial deviations in between. The STLS fit given by Ichimaru and coworkers[50,51], on the other hand, exhibits a surprisingly high accuracy for all investigated r_s–θ combinations with a typical

relative systematic error of $\sim 2\%$. The more recent VS results,[54] which automatically fulfill the CSR, display a qualitatively similar behavior but are significantly less accurate everywhere. The classical mapping suggested by Perrot and Dharma-wardana[37] constitutes an approximation rather with respect to temperature than to the coupling strength and, consequently, exhibits different trends. In particular, we have found that the relative systematic error is nearly independent of r_s, but decreases with increasing θ and eventually vanishes for $\theta \to \infty$. Overall, the accuracy of the PDW parameterization is comparable to VS and, hence, inferior to STLS. Finally, the more recent fit by Karasiev et al. [38] to RPIMC data[39] is accurate for large r_s and low temperature, where the input data is not too biased by the inappropriate treatment of finite size errors in the underlying RPIMC results. For higher temperatures (where the exchange-correlation free energy constitutes only a small fraction of the total free energy), there occur relative deviations of up to $\sim 10\%$.

Thus we conclude that an accurate parameterization of the exchange-correlation free energy that is valid for all r_s–θ combinations is presently not available. However, the recent QMC data by Dornheim et al.[27] most certainly constitute a promising basis for the construction of such a functional. In the mean time, of all the considered parameterizations, KSDT appears to be the most accurate at low θ and large r_s while the STLS fit exhibits smaller deviations elsewhere. Further, thermal DFT calculations in the local spin-density approximation require a parameterization of f_{xc} also as a function of the spin polarization $\xi = (N_\uparrow - N_\downarrow)/(N_\uparrow + N_\downarrow)$, that is, $f_{xc}(r_s, \theta, \xi)$ for all WDM parameters. Obviously, this will require an extension of the QMC simulations beyond the unpolarized case, $\xi \in (0, 1]$; in addition, reliable data for $\theta < 0.5$ are indispensable. This work is presently under way. We also note that the quality of the currently available KSDT fit for $f_{xc}(r_s, \theta, \xi)$ remains to be tested for $\xi > 0$. The accuracy of this parameterization is limited by (a) the quality of the RPIMC data (for the spin-polarized UEG ($\xi = 1$), they are afflicted with a substantially larger nodal error than for the unpolarized case that we considered in the present paper, see Ref. [22]), and (b) by the quality of the PDW results[37] that have been included as the only input to the KSDT fit for $0 < \xi < 1$ at finite θ. Therefore, we conclude that the construction of a new accurate function $f_{xc}(r_s, \theta, \xi)$ is still of high importance for thermal DFT and semi-analytical models, for comparisons with experiments, but also for explicitly time-dependent approaches such as time-dependent DFT and quantum hydrodynamics.[60,61]

Acknowledgements

REFERENCES

[1] M. D. Knudson, M. P. Desjarlais, R. W. Lemke, T. R. Mattsson, M. French, N. Nettelmann, R. Redmer, *Phys. Rev. Lett.* **2012**, *108*, 091102.

[2] B. Militzer, W. B. Hubbard, J. Vorberger, I. Tamblyn, S. A. Bonev, *Astrophys. J.* **2008**, *688*, L45.

[3] R. Ernstorfer, M. Harb, C. T. Hebeisen, G. Sciaini, T. Dartigalongue, R. J. Dwayne Miller, *Science* **2009**, *323*, 5917.

[4] R. Nora, W. Theobald, R. Betti, F. J. Marshall, D. T. Michel, W. Seka, B. Yaakobi, M. Lafon, C. Stoeckl, J. Delettrez, A. A. Solodov, A. Casner, C. Reverdin, X. Ribeyre, A. Vallet, J. Peebles, F. N. Beg, M. S. Wei, *Phys. Rev. Lett.* **2015**, *114*, 045001.

[5] P. F. Schmit, P. F. Knapp, S. B. Hansen, M. R. Gomez, K. D. Hahn, D. B. Sinars, K. J. Peterson, S. A. Slutz, A. B. Sefkow, T. J. Awe, E. Harding, C. A. Jennings, G. A. Chandler, G. W. Cooper, M. E. Cuneo, M. Geissel, A. J. Harvey-Thompson, M. C. Herrmann, M. H. Hess, O. Johns, D. C. Lamppa, M. R. Martin, R. D. McBride, J. L. Porter, G. K. Robertson, G. A. Rochau, D. C. Rovang, C. L. Ruiz, M. E. Savage, I. C. Smith, W. A. Stygar, R. A. Vesey, *Phys. Rev. Lett.* **2014**, *113*, 155004.

[6] O. A. Hurricane, D. A. Callahan, D. T. Casey, E. L. Dewald, T. R. Dittrich, T. Döppner, S. Haan, D. E. Hinkel, L. F. Berzak Hopkins, O. Jones, A. L. Kritcher, S. Le Pape, T. Ma, A. G. MacPhee, J. L. Milovich, J. Moody, A. Pak, H.-S. Park, P. K. Patel, J. E. Ralph, H. F. Robey, J. S. Ross, J. D. Salmonson, B. K. Spears, P. T. Springer, R. Tommasini, F. Albert, L. R. Benedetti, R. Bionta, E. Bond, D. K. Bradley, J. Caggiano, P. M. Celliers, C. Cerjan, J. A. Church, R. Dylla-Spears, D. Edgell, M. J. Edwards, D. Fittinghoff, M. A. Barrios Garcia, A. Hamza, R. Hatarik, H. Herrmann, M. Hohenberger, D. Hoover, J. L. Kline, G. Kyrala, B. Kozioziemski, G. Grim, J. E. Field, J. Frenje, N. Izumi, M. Gatu Johnson, S. F. Khan, J. Knauer, T. Kohut, O. Landen, F. Merrill, P. Michel, A. Moore, S. R. Nagel, A. Nikroo, T. Parham, R. R. Rygg, D. Sayre, M. Schneider, D. Shaughnessy, D. Strozzi, R. P. J. Town, D. Turnbull, P. Volegov, A. Wan, K. Widmann, C. Wilde, C. Yeamans, *Nat. Phys.* **2016**, *3720*.

[7] W. Kohn, L. J. Sham, *Phys. Rev.* **1965**, *140*, A1144.

[8] R. O. Jones, *Rev. Mod. Phys.* **2015**, *87*, 897.

[9] D. M. Ceperley, B. J. Alder, *Phys. Rev. Lett.* **1980**, *45*, 566.

[10] J. P. Perdew, A. Zunger, *Phys. Rev. B* **1981**, *23*, 5048.

[11] N. D. Mermin, *Phys. Rev.* **1965**, *137*, A1441.

[12] V. V. Karasiev, L. Calderin, S. B. Trickey, *Phys. Rev. E* **2016**, *93*, 063207.

[13] M. W. C. Dharma-wardana, *Computation* **2016**, *4*, 16.

[14] M. W. C. Dharmawardana, *Contrib. Plasma Phys.* **2015**, *55*, 85.

[15] T. Sjostrom, J. Daligault, *Phys. Rev. B* **2014**, *90*, 155109.

[16] K. Burke, J. C. Smith, P. E. Grabowski, A. Pribram-Jones, *Phys. Rev. B* **2016**, *93*, 195132.

[17] A. Pribram-Jones, P. E. Grabowski, K. Burke, *Phys. Rev. Lett.* **2016**, *116*, 233001.

[18] T. Schoof, S. Groth, M. Bonitz, *Contrib. Plasma Phys.* **2015**, *55*, 136.

[19] T. Schoof, S. Groth, J. Vorberger, M. Bonitz, *Phys. Rev. Lett.* **2015**, *115*, 130402.

[20] T. Dornheim, S. Groth, A. Filinov, M. Bonitz, *New J. Phys.* **2015**, *17*, 073017.

[21] T. Dornheim, T. Schoof, S. Groth, A. Filinov, M. Bonitz, *J. Chem. Phys.* **2015**, *143*, 204101.

[22] S. Groth, T.Schoof, T. Dornheim, M. Bonitz, *Phys. Rev. B* **2016**, *93*, 085102.

[23] T. Dornheim, S. Groth, T. Schoof, C. Hann, M. Bonitz, *Phys. Rev. B* **2016**, *93*, 205134.

[24] T. Dornheim, H. Thomsen, P. Ludwig, A. Filinov, M. Bonitz, *Contrib. Plasma Phys.* **2016**, *56*, 371.

[25] F. D. Malone, N. S. Blunt, J. J. Shepherd, D. K. Lee, J. S. Spencer, W. M. Foulkes, *J. Chem. Phys.* **2015**, *143*, 044116.

[26] F. D. Malone, N. S. Blunt, E. W. Brown, D. K. K.Lee, J. S. Spencer, W. M. C. Foulkes, J. J. Shepherd, *Phys. Rev. Lett.* **2016**, *117*, 115701.

[27] T. Dornheim, S. Groth, T. Sjostrom, F. D. Malone, W. M. C. Foulkes, M. Bonitz, *Phys. Rev. Lett.* **2016**, *117*, 156403.

[28] T. Dornheim, S. Groth, F. D. Malone, T. Schoof, T. Sjostrom, W. M. C. Foulkes, M. Bonitz, *Phys. Plasmas.* arXiv:1611.02658.

[29] E. Y. Loh, J. E. Gubernatis, R. T. Scalettar, S. R. White, D. J. Scalapino, R. L. Sugar, *Phys. Rev. B* **1990**, *41*, 9301.

[30] M. Troyer, U. J. Wiese, *Phys. Rev. Lett.* **2005**, *94*, 170201.

[31] W.-D. Kraeft, D.Kremp, W. Ebeling, G. Röpke, *Quantum Statistics of Charged Particle Systems*, Akademie-Verlag, Berlin **1986**.

[32] H. D. Whitley, A. Alastuey, J. A. Gaffney, R. Cauble, W.-D. Kraeft, M. Bonitz, *Contrib. Plasma Phys.* **2015**, *55*, 102.

[33] W. Ebeling, *Contrib. Plasma Phys.* **1989**, *29*, 165.

[34] K. S. Singwi, M. P.Tosi, R. H. Land, A. Sjölander, *Phys. Rev.* **1968**, *176*, 589.

[35] P. Vashishta, K. S. Singwi, *Phys. Rev. B* **1972**, *6*, 875.

[36] M. W. C. Dharma-wardana, F. Perrot, *Phys. Rev. Lett.* **2000**, *84*, 959.

[37] F. Perrot, M. W. C. Dharma-wardana, *Phys. Rev. B* **2000**, *62*, 16536.

[38] V. V. Karasiev, T. Sjostrom, J. Dufty, S. B. Trickey, *Phys. Rev. Lett.* **2014**, *112*, 076403.

[39] E. W. Brown, B. K. Clark, J. L. DuBois, D. M. Ceperley, *Phys. Rev. Lett.* **2013**, *110*, 146405.

[40] D. M. Ceperley, *J. Stat. Phys.* **1991**, *63*, 1237.

[41] W. Ebeling, W. Richert, W.-D. Kraeft, *Phys. Stat. Sol. (b)* **1981**, *104*, 193.

[42] W. Ebeling, W. Richert, *Ann. Phys. (Leipzig)* **1982**, *39*, 362.

[43] W. Ebeling, W. Richert, *Phys. Stat. Sol. (b)* **1985**, *128*, 467.

[44] W. Ebeling, W. Richert, *Phys. Lett. A* **1985**, *108*, 80.

[45] W. Ebeling, *Contrib. Plasma Phys.* **1990**, *30*, 553.

[46] H. E. DeWitt, *J. Math. Phys.* **1966**, *7*, 616.

[47] W. Stolzmann, W. Ebeling, *Phys. Lett. A* **1998**, *248*, 242.

[48] S. Tanaka, S. Mitake, S. Ichimaru, *Phys. Rev. A* **1985**, *32*, 1896.

[49] S. Tanaka, S. Ichimaru, *J. Phys. Soc. Jpn.* **1986**, *55*, 2278.

[50] S. Ichimaru, H.Iyetomi, S. Tanaka, *Phys. Rep.* **1987**, *149*, 91.

[51] S. Ichimaru, *Rev. Mod. Phys.* **1993**, *65*, 255.

[52] F. Perrot, M. W. C. Dharma-wardana, *Phys. Rev. A* **1984**, *30*, 2619.

[53] H. Schweng, H. Böhm, *Phys. Rev. B* **1993**, *48*, 2037.

[54] T. Sjostrom, J. Dufty, *Phys. Rev. B* **2013**, *88*, 115123.

[55] W. Stolzmann, M. Rösler, *Contrib. Plasma Phys.* **2001**, *41*, 203.

[56] E. W. Brown, J. L. DuBois, M. Holzmann, D. M. Ceperley, *Phys. Rev. B.* **2013**, *88*, 081102(R).

[57] J. Dufty, S. Dutta, *Phys. Rev. E* **2013**, *87*, 032101.

[58] S. Dutta, J. Dufty, *Eurphys. Lett.* **2013**, *102*, 67005.

[59] G. G. Spink, R. J. Needs, N. D. Drummond, *Phys. Rev. B* **2013**, *88*, 085121.

[60] N. Crouseilles, P.-A. Hervieux, G. Manfredi, *Phys. Rev. B* **2008**, *78*, 155412.

[61] D. Michta, F. Graziani, M. Bonitz, *Contrib. Plasma Phys.* **2015**, *55*, 437.

6.2 *Ab initio* **Thermodynamic Description of the Warm Dense Electron Gas**

Obviously, the ultimate goal regarding the investigation of the warm dense uniform electron gas is the construction of a complete parametrization of the exchange–correlation free energy with respect to temperature, density, and spin-polarization, $f_{xc}(r_s, \theta, \xi)$. As mentioned before, such an exchange–correlation functional is of paramount importance for various applications, including finite-temperature DFT calculations [104, 115, 116], quantum hydrodynamics [141, 142], and astrophysical models [143–145]. For this reason, many publications had been devoted to this topic, although still no consensus had emerged, see Sec. 6.1. This is in stark contrast to the ground state, where the QMC results by Ceperley and Alder from 1980 [111] already provided sufficient accuracy to facilitate the success of DFT.

Up to this point, using our new PB-PIMC and CPIMC methods and the improved finite-size correction scheme, we had obtained an exhaustive and highly accurate data set for the interaction energy v of the unpolarized electron gas over the entire relevant r_s-range down to half the Fermi temperature ($\theta = 0.5$). While the interaction energy is fully sufficient to parametrize f_{xc} (see Eq. (2) in the following paper, Ref. [166]) there remained two major obstacles that had to be solved: (i) the absence of accurate QMC data[2] for $0 < \theta < 0.5$ and (ii) the need for QMC data for different spin-polarizations, i.e., $\xi > 0$. While the second point can be viewed as a matter of diligent work[3], the lower boundary of our QMC methods regarding θ due to the fermion sign problem constituted a serious problem.

The solution to both issues, resulting in our new complete *ab initio* exchange–correlation functional of the warm dense UEG, is presented in the following paper[4], Ref. [166]. Having been inspired by the overall good accuracy of the STLS formalism regarding the interaction energy (for a detailed discussion of this feature, see the review in Chpt. 2), we bridged the gap between $\theta = 0$ and our QMC data by adding onto the exact ground-state QMC data [174] a small temperature correction computed within STLS (see Eq. (1) in the following paper, Ref. [166]). In addition, we implemented the STLS formalism for arbitrary spin-polarization (which was necessary for the finite-size correction) and carried out extensive new QMC simulations for $\xi = 0, 1/3, 0.6$. Of course, all data were carefully extrapolated to the thermodynamic limit.

---

[2]Note that, for $\theta = 0$, there exist accurate ground-state QMC data, the most recent set having been obtained by Spink *et al.* [174].

[3]Note that T. Sjostrom only provided STLS data for $\xi = 0$ and $\xi = 1$, but not for intermediate polarizations. For this reason, the STLS formalism was implemented for arbitrary spin-polarization together with S. Groth, in equal parts.

[4]S. Groth, T. Dornheim, T. Sjostrom, F.D. Malone, W.M.C. Foulkes, and M. Bonitz, Phys. Rev. Lett. **119**, 135001 (2017). Copyright by the American Physical Society (2017).

Together with the unpolarized data from Sec. 5.1, this made it possible to construct a complete parametrization of f_{xc} in the following way: we first parametrized $f_{xc}^{\xi}(r_s, \theta)$ for the para- and ferromagnetic cases over the entire r_s-θ-plane and subsequently obtained a spin-interpolation function that allows for an evaluation at continuous spin-polarizations, $f_{xc}(r_s, \theta, \xi)$ with $0 \leq \xi \leq 1$, as required, e.g., for DFT calculations in the local spin density approximation.

We note that this was the first time that said spin-interpolation has been obtained on the basis of QMC data (in this case for $\xi = 1/3$ and $\xi = 0.6$) and that our new parametrization has an unprecedented accuracy of 0.3%. Furthermore, we presented exhaustive comparisons to previous results and provided a cross-check with independent new QMC data for the exchange–correlation energy e_{xc}. In particular, this demonstrates the consistency of our functional with respect to exact thermodynamic relations, which are known to be violated by the RPIMC data and the parametrizations that are based on it [107, 213]. Needless to say, our new results (both the new QMC data and the parametrization of f_{xc} itself) are freely available online.

For completeness, I note that the STLS-temperature correction and the specifics regarding the construction of the exchange–correlation functional, $f_{xc}(r_s, \theta, \xi)$, as well as the implementation of the STLS algorithm for arbitrary spin-polarizations were worked out together with Simon Groth, in equal parts.

Ab initio Exchange-Correlation Free Energy of the Uniform Electron Gas at Warm Dense Matter Conditions

Simon Groth,[1,*] Tobias Dornheim,[1] Travis Sjostrom,[2] Fionn D. Malone,[3,4] W. M. C. Foulkes,[3] and Michael Bonitz[1]

[1]*Institut für Theoretische Physik und Astrophysik, Christian-Albrechts-Universität zu Kiel, D-24098 Kiel, Germany*
[2]*Theoretical Division, Los Alamos National Laboratory, Los Alamos, New Mexico 87545, USA*
[3]*Department of Physics, Imperial College London, Exhibition Road, London SW7 2AZ, United Kingdom*
[4]*Physics Division, Lawrence Livermore National Laboratory, 7000 East Avenue, Livermore, California 94550, USA*

In a recent Letter [T. Dornheim *et al.*, Phys. Rev. Lett. **117**, 156403 (2016)], we presented the first quantum Monte Carlo (QMC) results for the warm dense electron gas in the thermodynamic limit. However, a complete parametrization of the exchange-correlation free energy with respect to density, temperature, and spin polarization remained out of reach due to the absence of (i) accurate QMC results below $\theta = k_B T / E_F = 0.5$ and (ii) QMC results for spin polarizations different from the paramagnetic case. Here we overcome both remaining limitations. By closing the gap to the ground state and by performing extensive QMC simulations for different spin polarizations, we are able to obtain the first completely *ab initio* exchange-correlation free energy functional; the accuracy achieved is an unprecedented ∼0.3%. This also allows us to quantify the accuracy and systematic errors of various previous approximate functionals.

The past decade has witnessed a rapid growth of interest in matter under extreme excitation or compression, as in laser-excited solids [1] and inertial confinement fusion targets [2–5]. Astrophysical examples such as white dwarf atmospheres and planet interiors [6,7] provide further motivation. More down-to-earth examples appear in radiation damage cascades in the walls of fission or fusion reactors [8]. Plasmonic catalysts use hot electrons created by the decay of plasmons in otherwise cold metallic nanoparticles to accelerate chemical reactions [9,10]. Systems such as these, with thermal energies $k_B T$ comparable to the Fermi energy E_F and densities comparable to or greater than those of ordinary solids, are said to be in the "warm dense matter" (WDM) regime [11]. Because the degeneracy parameter $\Theta = k_B T / E_F$ is of the order of unity, neither the Pauli exclusion principle nor electronic excitations can be ignored and there are no small parameters in which to expand. This makes WDM challenging to understand theoretically.

The density functional theory (DFT) is by far the most important computational approach used to study molecules and solids at low temperatures [12–14] but relies for its success on the availability of good approximations to the unknown exchange-correlation (XC) energy functional. The development in the early 1980s of accurate parametrizations [15,16] of the ground-state local density approximation to this functional played a decisive role in the ensuing rise of the DFT.

The DFT was generalized to finite temperatures [17] soon after its invention, but applications to warm dense systems are a recent development. In part, this is because the finite-temperature equivalent of the local density approximation is not known accurately. This Letter presents the first accurate and fully *ab initio* calculation and parametrization of the XC free energy per electron, f_{xc}, as a functional of the temperature, density, and spin polarization, covering the entire range of conditions of interest in applications. The result is the natural generalization of Perdew and Zunger's famous zero-temperature functional [16]. It is key input not only to the thermal DFT [17–19] but also for quantum hydrodynamics [20,21] and the construction of equations of state for astrophysical objects [22–24].

The local density approximation is based on properties of the uniform electron gas (UEG), one of the seminal model systems in physics [25]. Studies of the UEG led to key insights such as the Fermi liquid theory [26,27], the quasiparticle picture of collective excitations [28,29], and the theory of superconductivity [30]. Accurate parametrizations of its ground-state properties [15,16,31–34] based on quantum Monte Carlo (QMC) simulations [35–39] have sparked many applications [40–42] in addition to facilitating the remarkable successes of the DFT [12–14].

QMC methods for the warm dense electron gas are much less developed, so the first parametrizations of f_{xc} were based instead on uncontrolled approximations such as interpolations between known limits [43], semiempirical quantum-classical mappings [41,44], and dielectric (linear response) methods [45–49]. To overcome the severe limitations imposed by the fermion sign problem [50,51], the pioneering QMC simulations of the UEG by Brown *et al.* [52] used the approximate restricted path integral Monte Carlo (RPIMC) approach, in which the nodal structure of the density matrix is assumed. These data were used as input for several parametrizations of f_{xc} [46,53,54],
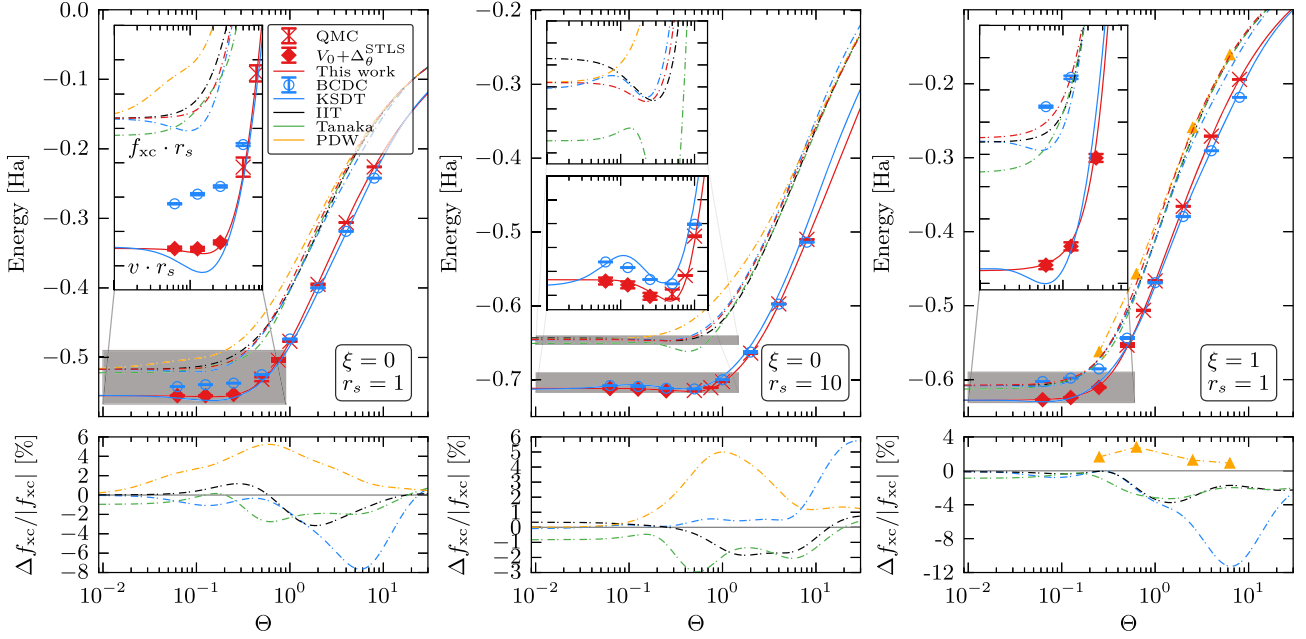
FIG. 1.   Temperature dependence of the XC free energy and potential energy—the top row shows f_{xc} (dashed lines) from this work (red), KSDT (blue [53]), IIT (black [48,49]), Tanaka (green [47]), and Perrot–Dharma-wardana (yellow dashed line and triangles, PDW [44]), as well as the corresponding interaction energy v (solid lines) from this work, KSDT, and the restricted PIMC results by Brown *et al.* (blue dots [52]). The red rhombs correspond to ground-state QMC results plus a temperature correction function obtained from the STLS theory. The inset corresponds to an enlargement of the gray box. The bottom row displays the relative deviations of the different models of f_{xc} with respect to our new parametrization.

the most sophisticated being that of Karasiev, Sjostrom, Dufty, and Trickey (KSDT) [53], but were later shown to be inaccurate [55]. The errors were ~10% near $r_s = 1$, where $r_s \equiv \bar{r}/a_B$, $\bar{r}$ is the radius of a sphere containing one electron on average, and a_B is the Bohr radius. Unsurprisingly, the aforementioned models for f_{xc} disagree substantially (cf. Fig. 1) in the WDM regime [56].

This unsatisfactory situation has sparked much recent work on finite-temperature fermionic QMC algorithms [55,57–65]. By developing three complementary new methods—configuration PIMC [55], permutation blocking PIMC [62,63], and density matrix QMC [64,65]—we are now able to overcome the sign problem in a broad parameter range without relying on a fixed-node approximation [66,67]. In a recent Letter [61], we presented an improved procedure to extrapolate the QMC results to the thermodynamic limit and thereby obtained data for the unpolarized UEG with an unprecedented accuracy of the order of 0.1%. At that time, however, the construction of a complete parametrization of f_{xc} with respect to r_s, θ, and $\xi = (N^\uparrow - N^\downarrow)/(N^\uparrow + N^\downarrow)$, where $N^\uparrow$ ($N^\downarrow$) is the number of spin-up (spin-down) electrons, was not possible. The fermion sign problem prevented us from performing QMC simulations for $0 < \theta < 0.5$. Further, we had no results for spin polarizations other than $\xi = 0$. The polarization dependence of f_{xc} is used, for example, in DFT calculations in the local spin-density approximation, which require the evaluation of f_{xc} at arbitrary ξ.

Here we solve these problems and present a new functional. Inspired by Tanaka and Ichimaru [48,49] and the impressive accuracy of the Singwi-Tosi-Land-Sjölander (STLS) formalism [45,46] in the warm dense regime [56], we bridge the gap between $\theta = 0$ and $\theta = 0.25$ by adding the (small) temperature dependence of the STLS interaction energy,

$$\Delta_\theta^{\mathrm{STLS}}(r_s, \theta, \xi) := v^{\mathrm{STLS}}(r_s, \theta, \xi) - v^{\mathrm{STLS}}(r_s, 0, \xi), \quad (1)$$

to the ground-state QMC interaction energy, which is known very accurately [39]. Second, we carry out extensive QMC simulations of the warm dense UEG for $\xi = 1/3, 0.6$, and 1 (179 data points in the ranges $0.1 \leq r_s \leq 20$ and $0.5 \leq \theta \leq 8$; see Table III in the Supplemental Material [68]). In combination with the results from Ref. [61], this allows us to construct the first complete *ab initio* parametrization of the XC free energy, $f_{xc}(r_s, \theta, \xi)$, and to attain an unprecedented accuracy of ~0.3%. The high quality of our new results is verified by various cross-checks and compared to the widely used parametrizations by KSDT [53], Perrot and Dharma-wardana [44], Ichimaru, Iyetomi, and Tanaka (IIT [48,49]), and the recent improved dielectric approach by Tanaka [47].

Parametrization of f_{xc} for $\xi = 0$ and $\xi = 1$.—Following Refs. [48,49], we obtain f_{xc}^ξ from our QMC data for the electron-electron interaction energy $v^\xi(r_s, \theta)$ via the coupling-constant integration formula

$$f_{xc}^{\xi}(r_s, \theta) = \frac{1}{r_s^2} \int_0^{r_s} d\bar{r}_s \bar{r}_s v^{\xi}(\bar{r}_s, \theta) \qquad (2)$$

$$\Rightarrow v^{\xi}(r_s, \theta) = 2 f_{xc}^{\xi}(r_s, \theta) + r_s \frac{\partial f_{xc}^{\xi}(r_s, \theta)}{\partial r_s} \bigg|_{\theta}. \qquad (3)$$

We employ Padé representations of f_{xc}^1 and f_{xc}^0 (see Supplemental Material [68], which includes Refs. [69,70]) and fit the right-hand side of Eq. (3) to our combined data for $v^{1,0}$. To ensure the correct ground-state behavior, we note that $\lim_{\theta \to 0} f_{xc}^{\xi}(r_s, \theta) = e_{xc}^{\xi}(r_s, 0)$ and fit the zero-temperature limit of our Padé formula to the recent ground-state QMC results of Spink, Needs, and Drummond [39]. In addition, the classical Debye-Hückel limit for large θ and the Hartree-Fock limit $f_{xc}^{HF}(r_s, \theta) = a(\theta)/r_s \equiv a^{HF}(\theta)/r_s$ [71] for $r_s \to 0$ are exactly incorporated.

The new results for $f_{xc}^{\xi}(r_s, \theta)$ are depicted in Fig. 1 (red dashed line) and compared to various approximations. While all curves exhibit a qualitatively similar behavior with respect to the temperature, there are deviations of 5%–12% for intermediate θ (bottom row). The IIT parametrization exhibits the smallest errors when $\xi = 0$, whereas, for $\xi = 1$, the Perrot–Dharma-wardana points are superior, although the IIT curve is of a similar quality. The recent parametrization by Tanaka (green) does not constitute an improvement compared to IIT. Finally, the KSDT curves are relatively accurate at low θ but systematically deviate for $\theta \gtrsim 0.5$, especially at a high density ($r_s \lesssim 4$ [68]). The deviation of $\Delta f / f \sim 10\%$ at its maximum can be traced to an inappropriate finite-size correction of the QMC data by Brown *et al.* [52]; see Ref. [61]. The deviations are even more severe for $\xi = 1$, in agreement with previous findings about the systematic bias in the RPIMC input data [66,67] and with recent investigations [47,49] of f_{xc} itself. Also notice the pronounced bump of f_{xc}^0 occurring for large r_s and a low temperature (see the inset in the middle panel), which induces an unphysical negative total entropy [72] in the KSDT fit.

Consider now our results for the interaction energy, shown as red rhombs and crosses in Fig. 1. We observe a smooth connection between our QMC data for $\theta \geq 0.5$ (crosses) and the temperature-corrected ground-state data (rhombs) in all three parts of the figure. The connection is equally smooth at all other densities investigated. The solid red line depicts the fit to v^{ξ} [Eq. (3)]. The Padé ansatz proves an excellent fitting function, able to reproduce the input data (v^{ξ}) for $\xi = 0$ ($\xi = 1$) with a mean and maximum deviation of 0.12% and 0.68% (0.17% and 0.63%), respectively [73].

To further illustrate the high quality of our XC functional and to verify the accuracy of the applied temperature correction at low θ, we carried out extensive new QMC simulations for the XC internal energy per particle, e_{xc}, for $r_s = 1$ and $\xi = 1$, over the entire range of temperatures down to $\theta = 0.0625$ (see Ref. [68] for details). The
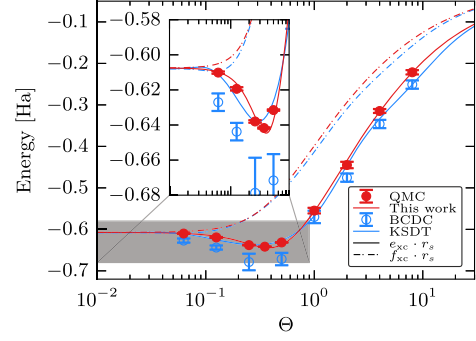

FIG. 2. Cross-check of our parametrization ($\xi = 1$, $r_s = 1$). The XC energy per electron (red line), as calculated from our Padé function for f_{xc} (dashed line), is compared to new, independent finite-size-corrected QMC data (red dots) [68]. While our functional has been constructed solely using the interaction energy v [cf. Eq. (3)], the KSDT curve [53] (solid blue) was fitted to the restricted PIMC data [52] for e_{xc} (blue circles, BCDC).

finite-size-corrected data are compared to e_{xc} reconstructed from our parametrization of $f_{xc}^{\xi}(r_s, \theta)$ via [53]

$$e_{xc}^{\xi}(r_s, \theta) = f_{xc}^{\xi}(r_s, \theta) - \theta \frac{\partial f_{xc}^{\xi}(r_s, \theta)}{\partial \theta} \bigg|_{r_s}. \qquad (4)$$

This allows us to gauge not only the accuracy of f_{xc} itself but also its temperature derivative, which is directly linked to the XC entropy. The results are presented in Fig. 2 and demonstrate excellent agreement between our parametrization (red solid line) and the independent new QMC data (red dots) over the entire range of θ. Since the new data for e_{xc} were not used for our fit, this constitutes a strong confirmation of the accuracy of the low-temperature results obtained by using the STLS theory to correct the $T = 0$ XC energy and demonstrates the consistency of our parametrization. Other functionals are much less consistent (see blue symbols and line) [73,74].

Spin interpolation.—To obtain an accurate parametrization of f_{xc} at arbitrary spin polarization $0 \leq \xi \leq 1$, we employ the ansatz [44]

$$f_{xc}(r_s, \theta, \xi) = f_{xc}^0(r_s, \theta^0) + [f_{xc}^1(r_s, \theta^0 \cdot 2^{-2/3}) - f_{xc}^0(r_s, \theta^0)] \Phi(r_s, \theta^0, \xi), \qquad (5)$$

with $\theta^0 = \theta(1 + \xi)^{2/3}$. The form and fitting procedure used for the interpolation function $\Phi(r_s, \theta^0, \xi)$ are described in the Supplemental Material [68]. Interestingly, we find that a single fitting parameter is sufficient to capture the full temperature dependence of Φ for all values of ξ, with a mean and maximum deviation from the QMC data at intermediate ξ of 0.15% and 0.8%, respectively.

Note that this is the first time that $\Phi(r_s, \theta, \xi)$ has been obtained accurately from *ab initio* data. A comparison of the
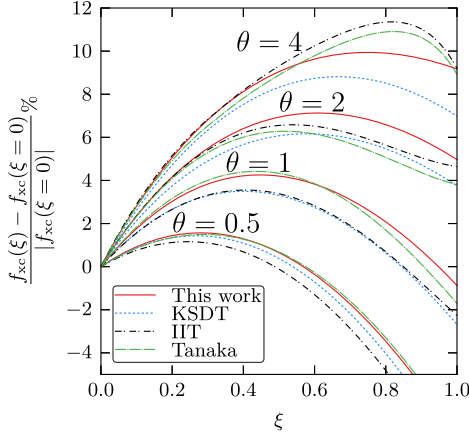
FIG. 3.   Dependence of the XC free energy on spin polarization at $r_s = 1$. The *ab initio* functional derived here (red curve) is compared to the parametrizations of KSDT (blue curve) [53], IIT (black curve) [48,49], and Tanaka (green curve) [47].

ξ dependence of f_{xc} with various earlier parametrizations is depicted in Fig. 3. The IIT and Tanaka curves, which utilize a different functional form for the spin interpolation [75], exhibit the largest deviations at intermediate temperatures. Our spin-interpolation function has the same form [68] as that employed in the KSDT parametrization. However, due to the absence of restricted PIMC data for intermediate ξ, KSDT used the classical mapping of Ref. [44] to determine the coefficients of Φ. Overall, the KSDT fit is closest to our parametrization at low θ, while for $\theta > 1$ the IIT curve is more accurate. Nevertheless, we conclude that no previous model satisfactorily captures the ξ dependence uncovered by our data.

Summary and discussion.—In summary, we have presented the first accurate and fully *ab initio* XC free energy functional for the UEG at WDM conditions, achieving an unprecedented precision of $\Delta f_{xc}/f_{xc} \sim 0.3\%$. To cover the entire parameter range relevant to experiments, we carried out extensive QMC simulations for multiple spin polarizations at $0.1 \leq r_s \leq 20$ and $0.5 \leq \theta \leq 8$. In addition, we obtained accurate data for $0.0625 \leq \theta \leq 0.25$ by combining ground-state QMC results with a small STLS-based temperature correction. All of our results are tabulated in the Supplemental Material [68] and provide benchmarks for the development of new theories and simulation schemes as well as for the improvement of existing models.

The first step in our construction of the complete XC functional, $f_{xc}(r_s, \theta, \xi)$, was to parametrize the completely polarized and unpolarized cases. This was achieved by fitting the right-hand side of Eq. (3) to our new data for the interaction energy, v^ξ, for $\xi = 0$ and $\xi = 1$. The resulting parametrization reproduces the input data with a mean deviation of 0.17%, better by at least an order of magnitude than the KSDT fit. As an additional test of our parametrization, we performed independent QMC calculations of e_{xc} (the XC energy per electron) for a wide range of values of θ

down to $\theta = 0.0625$ and compared the results with values of e_{xc} calculated using our functional for f_{xc}. The striking agreement obtained constitutes strong evidence for the accuracy of the STLS-based corrections used at a low temperature and for the consistency of our work, in general.

Equipped with our new XC functional, we have also investigated the systematic errors of previous parametrizations. Overall, the functional by Ichimaru, Iyetomi, and Tanaka [48,49] deviates the least from our results, although at $\xi = 1$ the classical mapping results by Perrot and Dharma-wardana [44] are similarly accurate. The KSDT parametrization exhibits large deviations exceeding 10% at a high temperature and density. At low temperatures, however, it performs surprisingly well, in part because it does not reproduce the systematic biases in the restricted PIMC data on which it was based.

The construction of the first *ab initio* spin-interpolation function $\Phi(r_s, \theta, \xi)$ at WDM conditions constitutes the capstone of this work. Surprisingly, we find that a one-parameter fit is sufficient to capture the whole temperature dependence of the spin-interpolation function. Furthermore, we show that no previously suggested spin interpolation gives the correct ξ dependence throughout the WDM regime.

We are confident that our extensive QMC data set and accurate parametrization of the thermodynamic functions of the warm dense electron gas will be useful in many applications. Given recent developments in the thermal Kohn-Sham DFT [76,77], time-dependent Kohn-Sham DFT [78], and orbital-free DFT [79,80], our parametrization of f_{xc} is directly applicable for calculations in the local spin-density approximation. Furthermore, our functional can be used as a basis for gradient expansions [81,82] or as a benchmark for nonlocal functionals based on the fluctuation-dissipation theorem [83]. In addition, it can be straightforwardly incorporated into widely used approximations in quantum hydrodynamics [20,21] or for the equations of state of astrophysical objects [22–24]. Finally, our XC functional should help resolve several exciting and controversial issues in warm dense matter physics, such as the existence and locations of the phase transitions in warm dense hydrogen [84–86] or details of hydrogen-helium demixing [87].

Computational implementations of our XC functional (in FORTRAN, C++, and PYTHON) are available online [88].

—————

*groth@theo-physik.uni-kiel.de

[1] R. Ernstorfer, M. Harb, C. T. Hebeisen, G. Sciaini, T. Dartigalongue, and R. J. D. Miller, The formation of warm dense matter: Experimental evidence for electronic bond hardening in gold, Science **323**, 1033 (2009).

[2] R. Nora *et al.*, Gigabar Spherical Shock Generation on the OMEGA Laser, Phys. Rev. Lett. **114**, 045001 (2015).

[3] P. F. Schmit *et al.*, Understanding Fuel Magnetization and Mix Using Secondary Nuclear Reactions in Magneto-Inertial Fusion, Phys. Rev. Lett. **113**, 155004 (2014).

[4] O. A. Hurricane *et al.*, Inertially confined fusion plasmas dominated by alpha-particle self-heating, Nat. Phys. **12**, 800 (2016).

[5] A. L. Kritcher, T. Döppner, C. Fortmann, T. Ma, O. L. Landen, R. Wallace, and S. H. Glenzer, In-Flight Measurements of Capsule Shell Adiabats in Laser-Driven Implosions, Phys. Rev. Lett. **107**, 015002 (2011).

[6] M. D. Knudson, M. P. Desjarlais, R. W. Lemke, T. R. Mattsson, M. French, N. Nettelmann, and R. Redmer, Probing the Interiors of the Ice Giants: Shock Compression of Water to 700 GPa and 3.8 g/cm^3, Phys. Rev. Lett. **108**, 091102 (2012).

[7] B. Militzer, W. B. Hubbard, J. Vorberger, I. Tamblyn, and S. A. Bonev, A massive core in Jupiter predicted from first-principles simulations, Astrophys. J. **688**, L45 (2008).

[8] E. Zarkadoula, S. L. Daraszewicz, D. M. Duffy, M. A. Seaton, I. T. Todorov, K. Nordlund, M. T. Dove, and K. Trachenko, Electronic effects in high-energy radiation damage in iron, J. Phys. Condens. Matter **26**, 085401 (2014).

[9] S. Mukherjee, F. Libisch, N. Large, O. Neumann, L. V. Brown, J. Cheng, J. Britt Lassiter, E. A. Carter, P. Nordlander, and N. J. Halas, Hot electrons do the impossible: Plasmon-induced dissociation of H_2 on Au, Nano Lett. **13**, 240 (2013).

[10] M. L. Brongersma, N. J. Halas, and P. Nordlander, Plasmon-induced hot carrier science and technology, Nat. Nanotechnol. **10**, 25 (2015).

[11] F. Graziani, M. P. Desjarlais, R. Redmer, and S. B. Trickey, *Frontiers and Challenges in Warm Dense Matter* (Springer, New York, 2014).

[12] W. Kohn and L. J. Sham, Self-consistent equations including exchange and correlation effects, Phys. Rev. **140**, A1133 (1965).

[13] R. O. Jones, Density functional theory: Its origins, rise to prominence, and future, Rev. Mod. Phys. **87**, 897 (2015).

[14] K. Burke, Perspective on density functional theory, J. Chem. Phys. **136**, 150901 (2012).

[15] S. H. Vosko, L. Wilk, and M. Nusair, Accurate spin-dependent electron liquid correlation energies for local spin density calculations: A critical analysis, Can. J. Phys. **58**, 1200 (1980).

[16] J. P. Perdew and A. Zunger, Self-interaction correction to density-functional approximations for many-electron systems, Phys. Rev. B **23**, 5048 (1981).

[17] N. D. Mermin, Thermal properties of the inhomogeneous electron gas, Phys. Rev. **137**, A1441 (1965).

[18] B. Holst, M. French, and R. Redmer, Electronic transport coefficients from *ab initio* simulations and application to dense liquid hydrogen, Phys. Rev. B **83**, 235120 (2011).

[19] J. C. Smith, F. Sagredo, and K. Burke, Warming up density functional theory, arXiv:1701.00873.

[20] N. Crouseilles, P.-A. Hervieux, and G. Manfredi, Quantum hydrodynamic model for the nonlinear electron dynamics in thin metal films, Phys. Rev. B **78**, 155412 (2008).

[21] D. Michta, F. Graziani, and M. Bonitz, Quantum hydro-dynamics for plasmas—A Thomas-Fermi theory perspective, Contrib. Plasma Phys. **55**, 437 (2015).

[22] A. Y. Potekhin and G. Chabrier, Equation of state for magnetized Coulomb plasmas, Astron. Astrophys. **550**, A43 (2013).

[23] D. Saumon, G. Chabrier, and H. M. van Horn, An equation of state for low-mass stars and giant planets, Astrophys. J. Suppl. Ser. **99**, 713 (1995).

[24] A. Becker, W. Lorenzen, J. J. Fortney, N. Nettelmann, M. Schöttler, and R. Redmer, *Ab initio* equations of state for hydrogen (H-REOS.3) and helium (He-REOS.3) and their implications for the interior of brown dwarfs, Astrophys. J. Suppl. Ser. **215**, 21 (2014).

[25] P.-F. Loos and P. M. W. Gill, The uniform electron gas, Comput. Mol. Sci. **6**, 410 (2016).

[26] G. Giuliani and G. Vignale, *Quantum Theory of the Electron Liquid* (Cambridge University Press, Cambridge, England, 2008).

[27] G. Baym and C. Pethick, *Landau Fermi-Liquid Theory: Concepts and Applications* (Wiley, New York, 1991).

[28] D. Pines and D. Bohm, A collective description of electron interactions: II. collective vs individual particle aspects of the interactions, Phys. Rev. **85**, 338 (1952).

[29] D. Bohm and D. Pines, A collective description of electron interactions: III. Coulomb interactions in a degenerate electron gas, Phys. Rev. **92**, 609 (1953).

[30] J. Bardeen, L. N. Cooper, and J. R. Schrieffer, Theory of superconductivity, Phys. Rev. **108**, 1175 (1957).

[31] J. P. Perdew and Y. Wang, Pair-distribution function and its coupling-constant average for the spin-polarized electron gas, Phys. Rev. B **46**, 12947 (1992).

[32] M. Corradini, R. Del Sole, G. Onida, and M. Palummo, Analytical expressions for the local-field factor $G(q)$ and the exchange-correlation kernel $K_{xc}(r)$ of the homogeneous electron gas, Phys. Rev. B **57**, 14569 (1998).

[33] P. Gori-Giorgi, F. Sacchetti, and G. B. Bachelet, Analytic static structure factors and pair-correlation functions for the unpolarized homogeneous electron gas, Phys. Rev. B **61**, 7353 (2000).

[34] P. Gori-Giorgi and J. P. Perdew, Pair distribution function of the spin-polarized electron gas: A first-principles analytic model for all uniform densities, Phys. Rev. B **66**, 165118 (2002).

[35] D. M. Ceperley, Ground state of the fermion one-component plasma: A Monte Carlo study in two and three dimensions, Phys. Rev. B **18**, 3126 (1978).

[36] D. M. Ceperley and B. J. Alder, Ground State of the Electron Gas by a Stochastic Method, Phys. Rev. Lett. **45**, 566 (1980).

[37] G. Ortiz and P. Ballone, Correlation energy, structure factor, radial distribution function, and momentum distribution of the spin-polarized uniform electron gas, Phys. Rev. B **50**, 1391 (1994).

[38] G. Ortiz, M. Harris, and P. Ballone, Zero Temperature Phases of the Electron Gas, Phys. Rev. Lett. **82**, 5317 (1999).

[39] G. G. Spink, R. J. Needs, and N. D. Drummond, Quantum Monte Carlo study of the three-dimensional spin-polarized homogeneous electron gas, Phys. Rev. B **88**, 085121 (2013).

[40] B. Farid, V. Heine, G. E. Engel, and I. J. Robertson, Extremal properties of the Harris-Foulkes functional and an improved screening calculation for the electron gas, Phys. Rev. B **48**, 11602 (1993).

[41] M. W. C. Dharma-wardana and F. Perrot, Simple Classical Mapping of the Spin-Polarized Quantum Electron Gas: Distribution Functions and Local-Field Corrections, Phys. Rev. Lett. **84**, 959 (2000).

[42] Y. Takada, Emergence of an excitonic collective mode in the dilute electron gas, Phys. Rev. B **94**, 245106 (2016).

[43] W.-D. Kraeft, D. Kremp, W. Ebeling, and G. Röpke, *Quantum Statistics of Charged Particle Systems* (Akademie-Verlag, Berlin, 1986).

[44] F. Perrot and M. W. C. Dharma-wardana, Spin-polarized electron liquid at arbitrary temperatures: Exchange-correlation energies, electron-distribution functions, and the static response functions, Phys. Rev. B **62**, 16536 (2000).

[45] S. Tanaka and S. Ichimaru, Thermodynamics and correlational properties of finite-temperature electron liquids in the Singwi-Tosi-Land-Sjölander approximation, J. Phys. Soc. Jpn. **55**, 2278 (1986).

[46] T. Sjostrom and J. Dufty, Uniform electron gas at finite temperatures, Phys. Rev. B **88**, 115123 (2013).

[47] S. Tanaka, Correlational and thermodynamic properties of finite-temperature electron liquids in the hypernetted-chain approximation, J. Chem. Phys. **145**, 214104 (2016).

[48] S. Ichimaru, H. Iyetomi, and S. Tanaka, Statistical physics of dense plasmas: Thermodynamics, transport coefficients and dynamic correlations, Phys. Rep. **149**, 91 (1987).

[49] S. Tanaka, Improved equation of state for finite-temperature spin-polarized electron liquids on the basis of Singwi-Tosi-Land-Sjolander approximation, Contrib. Plasma Phys. **57**, 126 (2017).

[50] E. Y. Loh, J. E. Gubernatis, R. T. Scalettar, S. R. White, D. J. Scalapino, and R. L. Sugar, Sign problem in the numerical simulation of many-electron systems, Phys. Rev. B **41**, 9301 (1990).

[51] M. Troyer and U. J. Wiese, Computational Complexity and Fundamental Limitations to Fermionic Quantum Monte Carlo Simulations, Phys. Rev. Lett. **94**, 170201 (2005).

[52] E. W. Brown, B. K. Clark, J. L. DuBois, and D. M. Ceperley, Path-Integral Monte Carlo Simulation of the Warm Dense Homogeneous Electron Gas, Phys. Rev. Lett. **110**, 146405 (2013).

[53] V. V. Karasiev, T. Sjostrom, J. Dufty, and S. B. Trickey, Accurate Homogeneous Electron Gas Exchange-Correlation Free Energy for Local Spin-Density Calculations, Phys. Rev. Lett. **112**, 076403 (2014).

[54] E. W. Brown, J. L. DuBois, M. Holzmann, and D. M. Ceperley, Exchange-correlation energy for the three-dimensional homogeneous electron gas at arbitrary temperature, Phys. Rev. B **88**, 081102(R) (2013).

[55] T. Schoof, S. Groth, J. Vorberger, and M. Bonitz, *Ab Initio* Thermodynamic Results for the Degenerate Electron Gas at Finite Temperature, Phys. Rev. Lett. **115**, 130402 (2015).

[56] S. Groth, T. Dornheim, and M. Bonitz, Free energy of the uniform electron gas: Testing analytical models against first principle results, Contrib. Plasma Phys. **57**, 137 (2017).

[57] V. Filinov, V. Fortov, M. Bonitz, and Zh. Moldabekov, Fermionic path integral Monte Carlo results for the uniform electron gas at finite temperature, Phys. Rev. E **91**, 033108 (2015).

[58] J. L. DuBois, E. W. Brown, and B. J. Alder, Overcoming the fermion sign problem in homogeneous systems, arXiv:1409.3262.

[59] T. Schoof, M. Bonitz, A. V. Filinov, D. Hochstuhl, and J. W. Dufty, Configuration path integral Monte Carlo, Contrib. Plasma Phys. **51**, 687 (2011).

[60] T. Dornheim, S. Groth, F. D. Malone, T. Schoof, T. Sjostrom, W. M. C. Foulkes, and M. Bonitz, *Ab initio* quantum Monte Carlo simulation of the warm dense electron gas, Phys. Plasmas **24**, 056303 (2017).

[61] T. Dornheim, S. Groth, T. Sjostrom, F. D. Malone, W. M. C. Foulkes, and M. Bonitz, *Ab Initio* Quantum Monte Carlo Simulation of the Warm Dense Electron Gas in the Thermodynamic Limit, Phys. Rev. Lett. **117**, 156403 (2016).

[62] T. Dornheim, S. Groth, A. Filinov, and M. Bonitz, Permutation blocking path integral Monte Carlo: A highly efficient approach to the simulation of strongly degenerate non-ideal fermions, New J. Phys. **17**, 073017 (2015).

[63] T. Dornheim, T. Schoof, S. Groth, A. Filinov, and M. Bonitz, Permutation blocking path integral Monte Carlo approach to the uniform electron gas at finite temperature, J. Chem. Phys. **143**, 204101 (2015).

[64] F. D. Malone, N. S. Blunt, J. J. Shepherd, D. K. K. Lee, J. S. Spencer, and W. M. C. Foulkes, Interaction picture density matrix quantum Monte Carlo, J. Chem. Phys. **143**, 044116 (2015).

[65] F. D. Malone, N. S. Blunt, E. W. Brown, D. K. K. Lee, J. S. Spencer, W. M. C. Foulkes, and J. J. Shepherd, Accurate Exchange-Correlation Energies for the Warm Dense Electron Gas, Phys. Rev. Lett. **117**, 115701 (2016).

[66] S. Groth, T. Schoof, T. Dornheim, and M. Bonitz, *Ab initio* quantum Monte Carlo simulations of the uniform electron gas without fixed nodes, Phys. Rev. B **93**, 085102 (2016).

[67] T. Dornheim, S. Groth, T. Schoof, C. Hann, and M. Bonitz, *Ab initio* quantum Monte Carlo simulations of the uniform electron gas without fixed nodes: The unpolarized case, Phys. Rev. B **93**, 205134 (2016).

[68] See Supplemental Material at http://link.aps.org/supplemental/10.1103/PhysRevLett.119.135001 for additional information and data tables.

[69] N. D. Drummond, R. J. Needs, A. Sorouri, and W. M. C. Foulkes, Finite-size errors in continuum quantum Monte Carlo calculations, Phys. Rev. B **78**, 125106 (2008).

[70] C. Lin, F. H. Zong, and D. M. Ceperley, Twist-averaged boundary conditions in continuum quantum Monte Carlo algorithms, Phys. Rev. E **64**, 016702 (2001).

[71] F. Perrot and M. W. C. Dharma-wardana, Exchange and correlation potentials for electron-ion systems at finite temperatures, Phys. Rev. A **30**, 2619 (1984).

[72] K. Burke, J. C. Smith, P. E. Grabowski, and A. Pribram-Jones, Exact conditions on the temperature dependence of density functionals, Phys. Rev. B **93**, 195132 (2016).

[73] In contrast, the KSDT interaction energy (solid blue line) exhibits severe deviations to the corresponding data by Brown *et al.* [52] (blue dots). This indicates that using the systematically biased restricted PIMC data as input for a parametrization of f_{xc} does not allow one to consistently recover other quantities (see also the discussion of Fig. 2).

[74] Note that the KSDT parametrization is the result of a direct fit to the restricted PIMC data for e_{xc} but reproduces these data only for $\theta \geq 1$ and strongly deviates below (the KSDT fit exhibits a mean and maximum deviation to the underlying restricted PIMC data of 1.2% and 7.8% for $\xi = 1$).

[75] S. Tanaka and S. Ichimaru, Spin-dependent correlations and thermodynamic functions for electron liquids at arbitrary degeneracy and spin polarization, Phys. Rev. B **39**, 1036 (1989).

[76] S. Zhang, H. Wang, W. Kang, P. Zhang, and X. T. He, Extended application of Kohn-Sham first-principles molecular dynamics method with plane wave approximation at high energy—From cold materials to hot dense plasmas, Phys. Plasmas **23**, 042707 (2016).

[77] C. Gao, S. Zhang, W. Kang, C. Wang, P. Zhang, and X. T. He, Validity boundary of orbital-free molecular dynamics method corresponding to thermal ionization of shell structure, Phys. Rev. B **94**, 205115 (2016).

[78] A. D. Baczewski, L. Shulenburger, M. P. Desjarlais, S. B. Hansen, and R. J. Magyar, X-Ray Thomson Scattering in Warm Dense Matter without the Chihara Decomposition, Phys. Rev. Lett. **116**, 115004 (2016).

[79] T. Sjostrom and J. Daligault, Fast and Accurate Quantum Molecular Dynamics of Dense Plasmas Across Temperature Regimes, Phys. Rev. Lett. **113**, 155006 (2014).

[80] V. V. Karasiev, T. Sjostrom, and S. B. Trickey, Finite-temperature orbital-free DFT molecular dynamics: Coupling Profess and Quantum Espresso, Comput. Phys. Commun. **185**, 3240 (2014).

[81] T. Sjostrom and J. Daligault, Gradient corrections to the exchange-correlation free energy, Phys. Rev. B **90**, 155109 (2014).

[82] V. V. Karasiev, J. W. Dufty, and S. B. Trickey, Nonempirical semi-local free-energy density functional for warm dense matter, arXiv:1612.06266.

[83] A. Pribram-Jones, P. E. Grabowski, and K. Burke, Thermal Density Functional Theory: Time-Dependent Linear Response and Approximate Functionals from the Fluctuation-Dissipation Theorem, Phys. Rev. Lett. **116**, 233001 (2016).

[84] G. Norman and A. Starostin, Insufficiency of classical description of a nondegenerate dense plasma, High Temp. **6**, 394399 (1968).

[85] V. E. Fortov, R. I. Ilkaev, V. A. Arinin, V. V. Burtzev, V. A. Golubev, I. L. Iosilevskiy, V. V. Khrustalev, A. L. Mikhailov, M. A. Mochalov, V. Ya. Ternovoi, and M. V. Zhernokletov, Phase Transition in a Strongly Nonideal Deuterium Plasma Generated by Quasi-Isentropical Compression at Megabar Pressures, Phys. Rev. Lett. **99**, 185001 (2007).

[86] C. Pierleoni, M. A. Morales, G. Rillo, M. Holzmann, and D. M. Ceperley, Liquid-liquid phase transition in hydrogen by coupled electron-ion Monte Carlo simulations, Proc. Natl. Acad. Sci. U.S.A. **113**, 4953 (2016).

[87] M. A. Morales, E. Schwegler, D. M. Ceperley, C. Pierleoni, S. Hamel, and K. Caspersen, Phase separation in hydrogen-helium mixtures at Mbar pressures, Proc. Natl. Acad. Sci. U.S.A. **106**, 1324 (2009).

[88] https://github.com/agbonitz/xc_functional.

Supplementary Material: *Ab initio* Exchange-Correlation Free Energy of the Uniform Electron Gas at Warm Dense Matter conditions

Simon Groth[1], Tobias Dornheim[1], Travis Sjostrom[2], Fionn D. Malone[3], W.M.C. Foulkes[3], and Michael Bonitz[1]

[1]Institut für Theoretische Physik und Astrophysik, Christian-Albrechts-Universität zu Kiel,
D-24098 Kiel, Germany
[2]Theoretical Division, Los Alamos National Laboratory, Los Alamos, New Mexico 87545, USA
[3]Department of Physics, Imperial College London, Exhibition Road, London SW7 2AZ, UK

A. Parametrization of the exchange correlation free energy

To represent the XC free energy for the spin-polarized and unpolarized case, $f_{\rm xc}^1(r_s,\theta)$ and $f_{\rm xc}^0(r_s,\theta)$, we use Padé formulae as introduced in Ref. [1]

$$f_{\rm xc}^\xi(r_s,\theta) = -\frac{1}{r_s}\frac{\omega_\xi a(\theta) + b^\xi(\theta)\sqrt{r_s} + c^\xi(\theta)r_s}{1 + d^\xi(\theta)\sqrt{r_s} + e^\xi(\theta)r_s} , \quad (\text{S.1})$$

where $\theta = k_B T/E_F$, $r_s = \bar{r}/a_{\rm B}$, $\xi = (N^\uparrow - N^\downarrow)/(N^\uparrow + N^\downarrow)$, $\omega_0 = 1$ and $\omega_1 = 2^{1/3}$, and $a(\theta)$ denotes the Hartree-Fock limit as parametrized in Ref. [2]

$$a(\theta) = 0.610887 \tanh\left(\theta^{-1}\right) \times$$
$$\frac{0.75 + 3.04363\theta^2 - 0.09227\theta^3 + 1.7035\theta^4}{1 + 8.31051\theta^2 + 5.1105\theta^4} .$$

The coefficients b,c,d,e are again Padé formulae with respect to temperature

$$b^\xi(\theta) = \tanh\left(\frac{1}{\sqrt{\theta}}\right)\frac{b_1^\xi + b_2^\xi\theta^2 + b_3^\xi\theta^4}{1 + b_4^\xi\theta^2 + b_5^\xi\theta^4}$$
$$c^\xi(\theta) = \left[c_1^\xi + c_2^\xi \cdot \exp\left(-\theta^{-1}\right)\right]e^\xi(\theta)$$
$$d^\xi(\theta) = \tanh\left(\frac{1}{\sqrt{\theta}}\right)\frac{d_1^\xi + d_2^\xi\theta^2 + d_3^\xi\theta^4}{1 + d_4^\xi\theta^2 + d_5^\xi\theta^4}$$
$$e^\xi(\theta) = \tanh\left(\frac{1}{\theta}\right)\frac{e_1^\xi + e_2^\xi\theta^2 + e_3^\xi\theta^4}{1 + e_4^\xi\theta^2 + e_5^\xi\theta^4} .$$

For completeness, we note that in Ref. [1], the parametrization from Eq. (S.1) was used for the interaction energy v instead of f_{xc}.

To parameterize $f_{\rm xc}$ as a function of the spin polarization $0 \leq \xi \leq 1$, we employ the ansatz [3]

$$f_{\rm xc}(r_s,\theta,\xi) = f_{\rm xc}^0(r_s,\theta^0) + \left[f_{\rm xc}^1(r_s,\theta^0 \cdot 2^{-2/3})\right.$$
$$\left. - f_{\rm xc}^0(r_s,\theta^0)\right]\Phi(r_s,\theta^0,\xi) , \quad (\text{S.2})$$

with $\theta^0 = \theta(1+\xi)^{2/3}$ and the interpolation function

$$\Phi(r_s,\theta,\xi) = \frac{(1+\xi)^{\alpha(r_s,\theta)} + (1-\xi)^{\alpha(r_s,\theta)} - 2}{2^{\alpha(r_s,\theta)} - 2}, \quad (\text{S.3})$$
$$\alpha(r_s,\theta) = 2 - h(r_s)e^{-\theta\lambda(r_s,\theta)},$$
$$h(r_s) = \frac{2/3 + h_1 r_s}{1 + h_2 r_s}, \quad \lambda(r_s,\theta) = \lambda_1 + \lambda_2\theta r_s^{1/2} .$$

First, h_1 and h_2 are obtained by fitting $f_{\rm xc}(r_s,0,\xi)$ to the ground state data of Ref. [4] for $\xi = 0.34$ and $\xi = 0.66$. Subsequently, we use our extensive new QMC data set for $v^\xi(r_s,\theta)$ [107 data points for $\xi = 1/3$ and $\xi = 0.6$, see Tab. III] to determine λ_1 and λ_2. Interestingly, we find that the spin interpolation depends only very weakly on θ, i.e., λ_2 vanishes within the accuracy of the fit and, thus, we set $\lambda_2 = 0$.

All coefficients are listed in Tabs. I and II.

Table I: Parameters entering $f_{\rm xc}^\xi$ [cf. Eq. (S.1)], for $\xi = 0$ and $\xi = 1$.

	$\xi = 0$	$\xi = 1$
b_1	0.3436902	0.84987704
b_2	7.82159531356	3.04033012073
b_3	0.300483986662	0.0775730131248
b_4	15.8443467125	7.57703592489
b_5	$b_3(3/2)^{1/2}\omega_0\left(\frac{4}{9\pi}\right)^{-1/3}$	$b_3(3/2)^{1/2}\omega_1\left(\frac{4}{9\pi}\right)^{-1/3}$
c_1	0.8759442	0.91126873
c_2	-0.230130843551	-0.0307957123308
d_1	0.72700876	1.48658718
d_2	2.38264734144	4.92684905511
d_3	0.30221237251	0.0849387225179
d_4	4.39347718395	8.3269821188
d_5	0.729951339845	0.218864952126
e_1	0.25388214	0.27454097
e_2	0.815795138599	0.400994856555
e_3	0.0646844410481	2.88773194962
e_4	15.0984620477	6.33499237092
e_5	0.230761357474	24.823008753

Table II: Parameters entering the spin-interpolation function $\Phi(r_s,\theta,\xi)$ [cf. Eq. (S.3)].

h_1	-3.18747258
h_2	-7.74662802
λ_1	-1.85909536
λ_2	0

B. STLS

The static structure factor (SF) is found by the fluctuation-dissipation theorem as a sum over the Matsubara frequencies for the polarizabilities of the interacting

system as

$$S(\mathbf{k}) = \frac{-1}{\beta n} \sum_{l=-\infty}^{\infty} \frac{1}{v_k} \left(\frac{1}{\epsilon(\mathbf{k}, z_l)} - 1 \right) , \qquad \text{(S.4)}$$

with the particle density n, the Matsubara frequencies $z_l = 2\pi i l/\beta\hbar$, and the Fourier transform of the Coulomb potential $v_k = 4\pi/k^2$. Following [7], the Singwi-Tosi-Land-Sjölander (STLS) SF is computed from the dielectric function

$$\epsilon(\mathbf{k}, \omega) = 1 - \frac{v_k \chi_0(\mathbf{k}, \omega)}{1 + G(\mathbf{k})v_k\chi_0(\mathbf{k}, \omega)} , \qquad \text{(S.5)}$$

with $\chi_0(\mathbf{q}, \omega)$ being the finite-temperature polarizability of the non-interacting UEG and G the static local field correction in STLS approximation

$$G(\mathbf{k}) = \frac{-1}{n} \int \frac{d\mathbf{k}'}{(2\pi)^3} \frac{\mathbf{k} \cdot \mathbf{k}'}{k'^2}[S(\mathbf{k} - \mathbf{k}') - 1] . \qquad \text{(S.6)}$$

The STLS SF is then obtained via a self-consistent solution of Eq. (S.4), (S.5), and (S.6), which straight-forwardly allows to compute the corresponding interaction energy

$$v^{\text{STLS}} = \frac{1}{\pi} \int_0^{\infty} dk[S(k) - 1] . \qquad \text{(S.7)}$$

C.   Finite-size correction of QMC data

Since QMC simulations are only feasible for a finite particle number N, it is necessary to extrapolate the results to the thermodynamic limit (TDL), $N \to \infty$. This is shown for the interaction energy in Fig. S1, where we plot v versus N^{-1} for the partially spin-polarized electron gas with $r_s = 1$, $\theta = 4$ and $\xi = 0.6$. The green crosses correspond to the original QMC data which, evidently, are strongly dependent on N. Therefore, we require a finite-size correction (FSC) ΔV_N that, in principle, should allow for the exact TDL using only a single QMC simulation:

$$v = \frac{V_N^{\text{QMC}}}{N} + \frac{\Delta V_N}{N} . \qquad \text{(S.8)}$$

The first estimate for ΔV_N at finite T was proposed by Brown *et al.* [5] (BCDC). However, the results of adding the BCDC correction to the QMC data (the yellow asterisks in Fig. S1) are still not converged with N and, therefore, an improved approach is needed. In a recent Letter [6], we have shown that the main contribution to ΔV_N is a discretization error in the integration of the static structure factor $S(k)$ that can be accurately estimated by invoking the Singwi-Tosi-Land-Sjölander formalism [7] (hereafter denoted FS-STLS). The thus corrected data are depicted as the black squares. Evidently, simply adding the new FSC onto the bare QMC interaction energies immediately improves the accuracy by two orders of magnitude. The small residual error is due to an intrinsic N-dependence in the QMC results for $S(k)$ itself and can be removed by an additional extrapolation, the results of which is given by the red rhomb (for additional details see Refs. [6, 8]).
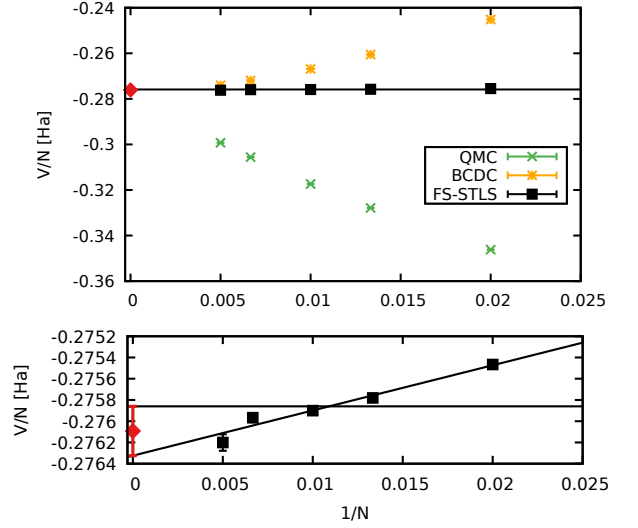
Figure S1:   **Top:** Finite-size correction of the interaction energy for $\theta = 4$, $r_s = 1$, and $\xi = 0.6$. The green crosses correspond to the raw QMC data, the yellow asterisks are obtained by adding the FSC by Brown *et al.* [5] (BCDC), and the black squares by adding the recent FSC by Dornheim *et al.* [6] (FS-STLS). The red rhomb depicts the final result for the interaction energy obtained by an additional extrapolation of all residual errors. **Bottom:** Magnified part of the top panel.

D.   QMC results for the XC energy

To calculate the finite-size correction for e_{xc} used in Fig. 2 of the main text, we first use the exact relationship between the exchange-correlation free energy and the potential energy:

$$f_{\text{xc}} = \frac{1}{r_s^2} \int_0^{r_s} d\bar{r}_s \bar{r}_s v(\bar{r}_s, \theta). \qquad \text{(S.9)}$$

This allows us to write the finite size correction for f_{xc} as

$$\Delta f_{\text{xc}}(r_s, \theta) = \frac{1}{r_s^2} \int_0^{r_s} d\bar{r}_s \bar{r}_s \Delta v(\bar{r}_s, \theta), \qquad \text{(S.10)}$$

and, inserting this correction into Eq. (6) of the main text, we find

$$\Delta e_{\text{xc}}(r_s, \theta) = \Delta f_{\text{xc}}(r_s, \theta) - \theta \left(\frac{\partial \Delta f_{\text{xc}}(r_s, \theta)}{\partial \theta} \right)_{r_s} . \quad \text{(S.11)}$$

Thus, we first evaluate Δf_{xc}, before inserting this correction into Eq. (S.11), where the derivative term is evaluated numerically. More details of this procedure will be presented in a separate publication. For completeness, we mention that for $0.0625 \leq \theta \leq 0.5$ we have performed an additional twist-averaging of the QMC data as described in Refs. [9, 10].

E.   Data tables

All interaction energies given in Table III have been obtained by performing QMC simulations for different N, adding the FS-STLS correction, and removing any residual errors by an additional extrapolation. Furthermore, Fig. S2 shows our entire data set and the resulting fit as well as a comparison to the KSDT parametrization [11] for both the potential energy v and the XC free energy $f_{\rm xc}$.

Table III: Finite-size corrected potential energy from finite temperature QMC simulations.

ξ	θ	r_s	$v \cdot r_s$	$\delta v \cdot r_s$
0	8.00	20.0	−0.604 414	0.000 094
0	4.00	20.0	−0.677 788	0.000 041
0	2.00	20.0	−0.726 928	0.000 022
0	1.00	20.0	−0.752 044	0.000 020
0	0.75	20.0	−0.752 948	0.000 050
0	0.75	10.0	−0.710 858	0.000 052
0	0.75	4.0	−0.637 257	0.000 267
0	0.75	2.0	−0.570 146	0.000 821
0	0.75	1.0	−0.503 977	0.002 348
0	0.75	0.5	−0.443 621	0.000 918
0	0.75	0.3	−0.403 418	0.000 537
0	0.75	0.1	−0.335 412	0.000 230
0	0.50	20.0	−0.756 936	0.000 184
1/3	8.00	20.0	−0.580 376	0.000 120
1/3	8.00	10.0	−0.484 172	0.000 294
1/3	8.00	6.0	−0.411 857	0.000 449
1/3	8.00	4.0	−0.357 279	0.000 398
1/3	8.00	2.0	−0.274 122	0.000 604
1/3	8.00	1.0	−0.209 039	0.000 126
1/3	8.00	0.5	−0.158 207	0.000 089
1/3	8.00	0.3	−0.129 225	0.000 092
1/3	8.00	0.1	−0.085 583	0.000 081
1/3	4.00	20.0	−0.659 796	0.000 055
1/3	4.00	10.0	−0.575 249	0.000 103
1/3	4.00	6.0	−0.506 857	0.000 226
1/3	4.00	4.0	−0.451 411	0.000 177
1/3	4.00	2.0	−0.362 040	0.000 303
1/3	4.00	1.0	−0.285 290	0.000 262
1/3	4.00	0.5	−0.222 982	0.000 083
1/3	4.00	0.3	−0.186 455	0.000 060
1/3	4.00	0.1	−0.129 779	0.000 045
1/3	2.00	20.0	−0.716 060	0.000 022
1/3	2.00	10.0	−0.648 594	0.000 050
1/3	2.00	6.0	−0.589 913	0.000 100
1/3	2.00	4.0	−0.540 310	0.000 082
1/3	2.00	2.0	−0.453 908	0.000 271
1/3	2.00	1.0	−0.373 593	0.000 539
1/3	2.00	0.5	−0.305 016	0.000 481
1/3	2.00	0.3	−0.262 926	0.000 177
1/3	2.00	0.1	−0.195 205	0.000 098
1/3	1.00	20.0	−0.746 370	0.000 016
1/3	1.00	10.0	−0.695 351	0.000 060
1/3	1.00	6.0	−0.649 843	0.000 125
1/3	1.00	4.0	−0.609 682	0.000 275
1/3	1.00	2.0	−0.533 920	0.000 330
1/3	1.00	1.0	−0.461 622	0.000 655
1/3	1.00	0.5	−0.395 233	0.000 664
1/3	1.00	0.3	−0.353 105	0.000 245
1/3	1.00	0.1	−0.282 035	0.000 135
1/3	0.75	20.0	−0.752 258	0.000 024
1/3	0.75	10.0	−0.706 095	0.000 112
1/3	0.75	6.0	−0.665 854	0.000 305
1/3	0.75	4.0	−0.629 244	0.000 194
1/3	0.75	2.0	−0.561 332	0.000 627
1/3	0.75	1.0	−0.491 727	0.001 049
1/3	0.75	0.5	−0.430 284	0.000 834
1/3	0.75	0.3	−0.389 745	0.000 636
1/3	0.75	0.1	−0.321 438	0.000 135
1/3	0.50	20.0	−0.756 208	0.000 265
1/3	0.50	10.0	−0.717 354	0.001 175
1/3	0.50	6.0	−0.675 084	0.001 677
1/3	0.50	4.0	−0.647 064	0.000 515
1/3	0.50	2.0	−0.586 194	0.002 044
1/3	0.50	1.0	−0.525 908	0.002 428
1/3	0.50	0.5	−0.472 038	0.001 061
1/3	0.50	0.3	−0.436 211	0.000 508
1/3	0.50	0.1	−0.374 860	0.000 130
0.6	8.00	20.0	−0.564 678	0.000 130
0.6	8.00	10.0	−0.467 239	0.000 265
0.6	8.00	6.0	−0.396 677	0.000 580
0.6	8.00	4.0	−0.342 476	0.000 305
0.6	8.00	2.0	−0.262 646	0.000 269
0.6	8.00	1.0	−0.200 652	0.000 122
0.6	8.00	0.5	−0.152 350	0.000 110
0.6	8.00	0.3	−0.124 913	0.000 116
0.6	8.00	0.1	−0.084 291	0.000 419
0.6	4.00	20.0	−0.647 332	0.000 054
0.6	4.00	10.0	−0.560 424	0.000 094
0.6	4.00	6.0	−0.491 593	0.000 175
0.6	4.00	4.0	−0.437 054	0.000 291
0.6	4.00	2.0	−0.349 670	0.000 316
0.6	4.00	1.0	−0.276 092	0.000 232
0.6	4.00	0.5	−0.216 875	0.000 074
0.6	4.00	0.3	−0.182 187	0.000 253
0.6	4.00	0.1	−0.128 691	0.000 238
0.6	2.00	20.0	−0.708 140	0.000 025
0.6	2.00	10.0	−0.638 071	0.000 060
0.6	2.00	6.0	−0.578 400	0.000 092
0.6	2.00	4.0	−0.528 572	0.000 173
0.6	2.00	2.0	−0.443 764	0.000 460
0.6	2.00	1.0	−0.365 352	0.000 547
0.6	2.00	0.5	−0.300 452	0.000 180
0.6	2.00	0.3	−0.260 321	0.000 110
0.6	2.00	0.1	−0.196 527	0.000 285
0.6	1.00	20.0	−0.742 986	0.000 015
0.6	1.00	10.0	−0.690 110	0.000 058
0.6	1.00	6.0	−0.643 421	0.000 551
0.6	1.00	4.0	−0.602 959	0.000 130
0.6	1.00	2.0	−0.529 821	0.000 309
0.6	1.00	1.0	−0.458 146	0.000 503
0.6	1.00	0.5	−0.395 825	0.001 016
0.6	1.00	0.3	−0.354 692	0.000 300
0.6	1.00	0.1	−0.287 919	0.000 131
0.6	0.75	20.0	−0.750 356	0.000 017
0.6	0.75	10.0	−0.703 143	0.000 485
0.6	0.75	6.0	−0.661 680	0.000 177
0.6	0.75	4.0	−0.624 412	0.000 407
0.6	0.75	2.0	−0.559 316	0.000 421
0.6	0.75	1.0	−0.491 014	0.002 800
0.6	0.75	0.5	−0.433 163	0.000 603
0.6	0.75	0.3	−0.394 409	0.000 533
0.6	0.75	0.1	−0.329 384	0.000 093
0.6	0.50	20.0	−0.755 894	0.000 093
0.6	0.50	10.0	−0.714 236	0.001 111
0.6	0.50	6.0	−0.678 234	0.000 645
0.6	0.50	2.0	−0.589 876	0.000 620

ξ	θ	r_s	$v \cdot r_s$	$\delta v \cdot r_s$
0.6	0.50	1.0	$-0.531\,667$	$0.000\,524$
0.6	0.50	0.5	$-0.480\,832$	$0.001\,670$
0.6	0.50	0.3	$-0.445\,028$	$0.000\,740$
0.6	0.50	0.1	$-0.386\,802$	$0.000\,116$
1	8.00	0.1	$-0.086\,133$	$0.000\,027$
1	8.00	0.3	$-0.124\,165$	$0.000\,047$
1	8.00	0.5	$-0.149\,504$	$0.000\,047$
1	8.00	1.0	$-0.194\,203$	$0.000\,066$
1	8.00	2.0	$-0.252\,452$	$0.000\,303$
1	8.00	4.0	$-0.327\,037$	$0.000\,261$
1	8.00	6.0	$-0.378\,252$	$0.000\,426$
1	8.00	8.0	$-0.417\,303$	$0.000\,404$
1	8.00	10.0	$-0.448\,115$	$0.000\,486$
1	8.00	20.0	$-0.544\,914$	$0.000\,177$
1	4.00	0.1	$-0.135\,554$	$0.000\,036$
1	4.00	0.3	$-0.184\,652$	$0.000\,070$
1	4.00	0.5	$-0.216\,525$	$0.000\,082$
1	4.00	1.0	$-0.270\,858$	$0.000\,615$
1	4.00	2.0	$-0.339\,262$	$0.000\,172$
1	4.00	4.0	$-0.421\,696$	$0.000\,232$
1	4.00	6.0	$-0.474\,381$	$0.000\,083$
1	4.00	8.0	$-0.512\,738$	$0.000\,137$
1	4.00	10.0	$-0.542\,639$	$0.000\,076$
1	4.00	20.0	$-0.631\,370$	$0.000\,078$
1	2.00	0.1	$-0.211\,965$	$0.000\,104$
1	2.00	0.3	$-0.269\,952$	$0.000\,134$
1	2.00	0.5	$-0.306\,107$	$0.000\,140$
1	2.00	1.0	$-0.365\,728$	$0.000\,374$
1	2.00	2.0	$-0.436\,766$	$0.000\,385$
1	2.00	4.0	$-0.516\,652$	$0.000\,170$
1	2.00	6.0	$-0.564\,960$	$0.000\,167$
1	2.00	8.0	$-0.599\,070$	$0.000\,084$
1	2.00	10.0	$-0.624\,687$	$0.000\,078$
1	2.00	20.0	$-0.697\,464$	$0.000\,038$
1	1.00	0.1	$-0.318\,360$	$0.000\,133$
1	1.00	0.3	$-0.376\,986$	$0.000\,132$
1	1.00	0.5	$-0.412\,091$	$0.000\,138$
1	1.00	1.0	$-0.466\,598$	$0.000\,999$
1	1.00	2.0	$-0.529\,651$	$0.000\,478$
1	1.00	4.0	$-0.597\,449$	$0.000\,123$
1	1.00	6.0	$-0.636\,542$	$0.000\,086$
1	1.00	8.0	$-0.663\,264$	$0.000\,075$
1	1.00	10.0	$-0.683\,287$	$0.000\,074$
1	1.00	20.0	$-0.738\,042$	$0.000\,021$
1	0.75	0.1	$-0.368\,039$	$0.000\,107$
1	0.75	0.3	$-0.423\,521$	$0.000\,149$
1	0.75	0.5	$-0.456\,112$	$0.000\,261$
1	0.75	1.0	$-0.506\,379$	$0.000\,646$
1	0.75	2.0	$-0.564\,127$	$0.000\,187$
1	0.75	4.0	$-0.624\,104$	$0.000\,543$
1	0.75	6.0	$-0.658\,458$	$0.000\,136$
1	0.75	10.0	$-0.699\,291$	$0.000\,053$
1	0.75	20.0	$-0.747\,552$	$0.000\,012$
1	0.50	0.1	$-0.436\,852$	$0.000\,150$
1	0.50	0.3	$-0.484\,687$	$0.000\,114$
1	0.50	0.5	$-0.512\,677$	$0.000\,305$
1	0.50	1.0	$-0.553\,536$	$0.001\,915$
1	0.50	2.0	$-0.600\,776$	$0.002\,929$
1	0.50	4.0	$-0.651\,476$	$0.000\,679$

ξ	θ	r_s	$v \cdot r_s$	$\delta v \cdot r_s$
1	0.50	6.0	$-0.680\,010$	$0.001\,349$
1	0.50	8.0	$-0.699\,106$	$0.000\,564$
1	0.50	10.0	$-0.713\,698$	$0.000\,201$
1	0.50	20.0	$-0.755\,328$	$0.000\,037$

[1] S. Ichimaru, H. Iyetomi, and S. Tanaka, Statistical physics of dense plasmas: Thermodynamics, transport coefficients and dynamic correlations, *Physics Reports* **149**, 91 (1987)

[2] F. Perrot and M.W.C. Dharma-wardana, Exchange and correlation potentials for electron-ion systems at finite temperatures, *Phys. Rev. A* **30**, 2619 (1984)

[3] F. Perrot and M.W.C. Dharma-wardana, Spin-polarized electron liquid at arbitrary temperatures: Exchange-correlation energies, electron-distribution functions, and the static response functions, *Phys. Rev. B* **62**, 16536 (2000)

[4] G.G. Spink, R.J. Needs, and N.D. Drummond, Quantum Monte Carlo Study of the Three-Dimensional Spin-Polarized Homogeneous Electron Gas, *Phys. Rev. B* **88**, 085121 (2013)

[5] E.W. Brown, B.K. Clark, J.L. DuBois and D.M. Ceperley, Path-Integral Monte Carlo Simulation of the Warm Dense Homogeneous Electron Gas, *Phys. Rev. Lett.* **110**, 146405 (2013)

[6] T. Dornheim, S. Groth, T. Sjostrom, F.D. Malone, W.M.C. Foulkes, and M. Bonitz, *Ab Initio* Quantum Monte Carlo Simulation of the Warm Dense Electron Gas in the Thermodynamic Limit, *Phys. Rev. Lett.* **117**, 156403 (2016)

[7] S. Tanaka and S. Ichimaru, Thermodynamics and Correlational Properties of Finite-Temperature Electron Liquids in the Singwi-Tosi-Land-Sjölander Approximation, *J. Phys. Soc. Jpn.* **55**, 2278-2289 (1986)

[8] T. Dornheim, S. Groth, F.D. Malone, T. Schoof, T. Sjostrom, W.M.C. Foulkes, and M. Bonitz, *Ab Initio* Quantum Monte Carlo Simulation of the Warm Dense Electron Gas, *Physics of Plasmas* **24**, 056303 (2017)

[9] N.D. Drummond, R.J. Needs, A. Sorouri and W.M.C. Foulkes, Finite-size errors in continuum quantum Monte Carlo calculations, *Phys. Rev. B* **78**, 125106 (2008)

[10] C. Lin, F.H. Zong and D.M. Ceperley, Twist-averaged boundary conditions in continuum quantum Monte Carlo algorithms, *Phys. Rev. E* **64**, 016702 (2001)

[11] V.V. Karasiev, T. Sjostrom, J. Dufty and S.B. Trickey, Accurate Homogeneous Electron Gas Exchange-Correlation Free Energy for Local Spin-Density Calculations, *Phys. Rev. Lett.* **112**, 076403 (2014)
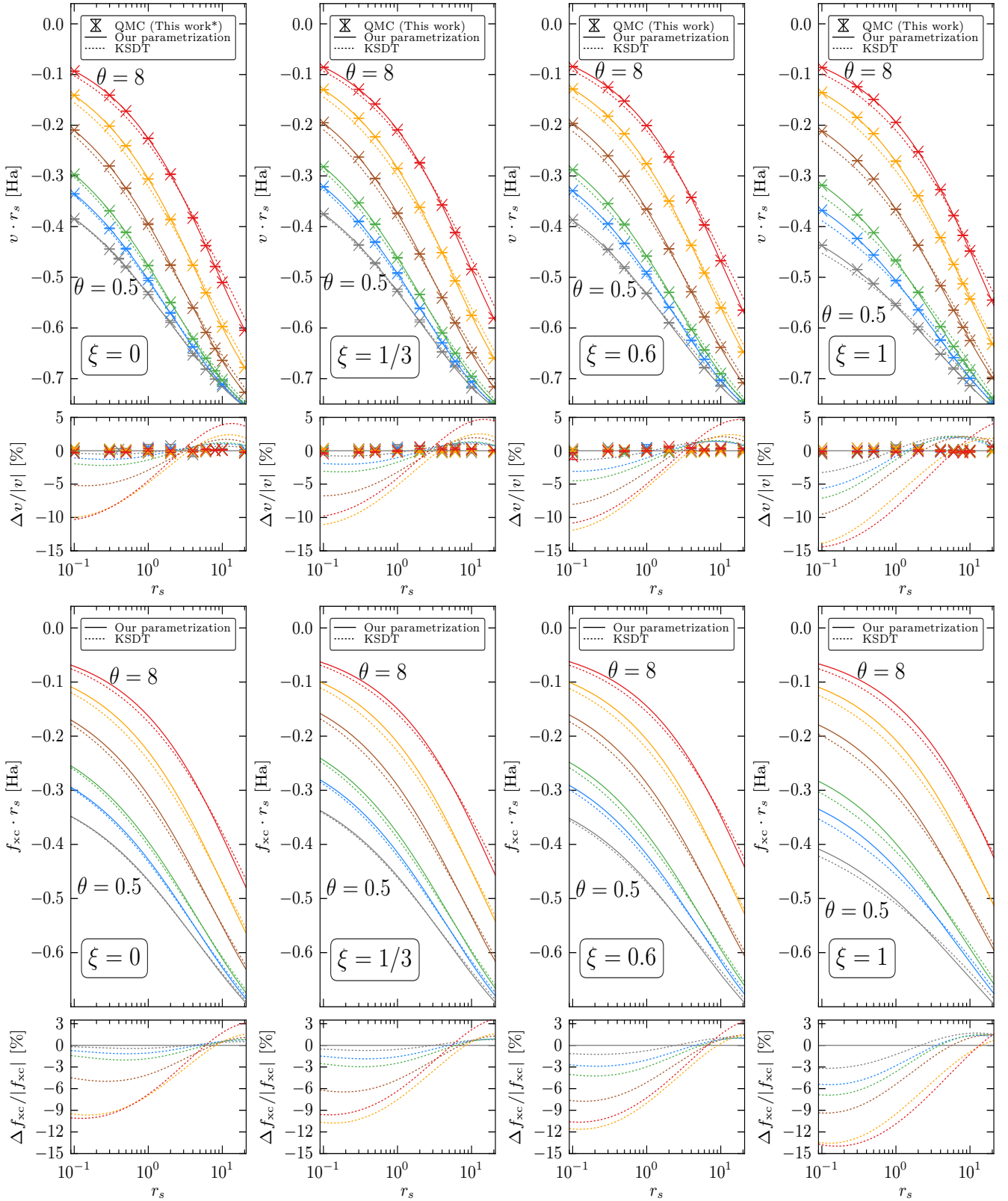
Figure S2: **Top row:** Upper panel: Density dependence of the potential energy for different temperatures (top to bottom: $\theta = 8, 4, 2, 1, 0.75, 0.5$). Crosses: new QMC data of this work for $\xi = 1/3, 0.6$, and 1. For $\xi = 0$, the data from Ref. [6] are plotted (indicated by the $*$ in the legend) in addition to the new data points for $\theta = 0.75$ and also for $r_s = 20$. Solid line: Our parametrization ($r_s - \theta - \xi$-fit to the QMC data). Dashed line: KSDT parametrization [11]. Lower panel: Deviation of the QMC data (crosses) and the KSDT parametrization (dashed line) from our parametrization. **Bottom row:** Upper panel: Density dependence of the exchange-correlation free energy for different temperatures (top to bottom: $\theta = 8, 4, 2, 1, 0.75, 0.5$). Solid line: Our parametrization. Dashed line: KSDT prametrization. Lower panel: Deviation of KSDT from our parametrization.

Chapter 7

The Inhomogeneous Electron Gas

Another interesting topic regarding the uniform electron gas is its response to an external perturbation, which, within linear response theory [131], is described by the density–density response function $\chi(\mathbf{q}, \omega)$, with $\mathbf{q}$ and ω denoting the wave vector and frequency of the perturbation, respectively. The response function is the central quantity of the dielectric formalism, for example in the random-phase approximation (RPA), which, however, does not incorporate correlations regarding the description of the density response beyond the mean field level. Correlation effects are usually incorporated via the so-called local-field correction [214] (LFC) $G(\mathbf{q}, \omega)$. While formally exact, the latter is, in practice, not known and one has to rely on approximations (such as STLS).

Hitherto, we treated the dielectric methods merely as a means to end, i.e., to exploit the fluctuation–dissipation theorem and use the linear response function to compute static properties of the UEG like the static structure factor (for the finite-size correction, see Sec. 5.1) or a temperature correction to the interaction energy (see Sec. 6.2). However, it is important to note that accurate knowledge of $\chi(\mathbf{q}, \omega)$ (and therefore of $G(\mathbf{q}, \omega)$) constitutes an important end in itself. For example, the local-field correction can directly be used as input for density functional theory calculations within the adiabatic-connection fluctuation–dissipation formulation [215–217]. In contrast to the simple local density approximation or the ubiquitous generalized gradient approximations [114, 200], this approach is based on the construction of a truly nonlocal exchange–correlation functional. Despite the increased computational cost, this idea constitutes a promising route towards an improved predictive capability of DFT, in particular at warm dense matter conditions [79]. A concise overview of further applications of the local-field correction can be found in the following two papers, Refs. [167] and [168], as well as in the review [161], Chpt. 2.

In principle, the density response function for a specific combination of $\mathbf{q}$ and ω can be directly obtained from the simulation of an electron gas that is subject to an external harmonic

perturbation with the corresponding frequency and wave vector. More specifically, for weak perturbations, linear response theory is accurate and the modified density is proportional to the perturbation amplitude with $\chi(\mathbf{q}, \omega)$ being the slope. Unfortunately, time-dependent QMC simulations[1] are prohibited by an additional dynamical sign problem, see, e.g., Refs. [218–220]. For this reason, here we limit ourselves to the static limit of χ and G (i.e., $\omega \to 0$ [131]).

In the ground state, extensive results for the static density response were computed by Ceperley and co-workers [221, 222] and Alder and co-workers [223, 224], and later used as input for a parametrization by Corradini *et al.* [225]. The following two papers, Refs. [167] and [168], constitute proofs of principle regarding the extension of this idea to finite temperature both in the PB-PIMC and CPIMC formalism. In particular, in the following paper[2], Ref. [167], I extended the PB-PIMC formalism to the simulation of an inhomogeneous electron gas and considered the possibility to compute $\chi(\mathbf{q})$ for several wave vectors within a single simulation.

The extension of these simulations to obtain exhaustive data for the static density response function and a subsequent construction of a parametrization of the local-field correction at warm dense matter conditions remains an important task for the future.

For completeness, I mention that I was not involved in the extension of the CPIMC method to the inhomogeneous case as described in Ref. [168], but worked on the computation of the finite-size correction for $\chi(\mathbf{q}, 0)$ that is described therein together with S. Groth in equal parts. In additions, I provided the PB-PIMC benchmark data.

---

[1]Note that, in principle, the dynamic structure factor $S(\mathbf{q}, \omega)$ and, thus, the dynamic density response function $\chi(\mathbf{q}, \omega)$ can be reconstructed from thermodynamic QMC data for an imaginary-time correlation function, see Sec. 9.2.3.

[2]T. Dornheim, S. Groth, J. Vorberger, and M. Bonitz, Phys. Rev. E **96**, 023203 (2017). Copyright by the American Physical Society (2017).

Permutation-blocking path-integral Monte Carlo approach to the static density response of the warm dense electron gas

Tobias Dornheim,[1,*] Simon Groth,[1] Jan Vorberger,[2] and Michael Bonitz[1]

[1]*Institut für Theoretische Physik und Astrophysik, Christian-Albrechts-Universität zu Kiel, D-24098 Kiel, Germany*
[2]*Helmholtz-Zentrum Dresden-Rossendorf, D-01328 Dresden, Germany*

The static density response of the uniform electron gas is of fundamental importance for numerous applications. Here we employ the recently developed *ab initio* permutation blocking path integral Monte Carlo (PB-PIMC) technique [T. Dornheim *et al.*, New J. Phys. **17**, 073017 (2015)] to carry out extensive simulations of the harmonically perturbed electron gas at warm dense matter conditions. In particular, we investigate in detail the validity of linear response theory and demonstrate that PB-PIMC allows us to obtain highly accurate results for the static density response function and, thus, the static local field correction. A comparison with dielectric approximations to our new *ab initio* data reveals the need for an exact treatment of correlations. Finally, we consider a superposition of multiple perturbations and discuss the implications for the calculation of the static response function.

I. INTRODUCTION

The uniform electron gas (UEG), which is composed of Coulomb interacting electrons in a homogeneous neutralizing background, is one of the most seminal model system in quantum many-body physics and chemistry [1]. In addition to the UEG's importance for, e.g., the formulation of Fermi liquid theory [2,3] and the quasiparticle picture of collective excitations [4,5], accurate parametrizations of its ground-state properties [6–10] based on *ab initio* quantum Monte Carlo calculations [11–15] have been pivotal for the arguably unrivaled success of density-functional-theory simulations of real materials [16–18].

The density response of the UEG to a small external perturbation as described by the density response function is of high importance for many applications [2]. The well-known random-phase approximation (RPA) [5] provides a qualitative description for weak coupling strength (high density),

$$\chi_{\mathrm{RPA}}(\mathbf{q},\omega) = \frac{\chi_0(\mathbf{q},\omega)}{1 - \frac{4\pi}{q^2}\chi_0(\mathbf{q},\omega)}, \qquad (1)$$

where $\chi_0(\mathbf{q},\omega)$ denotes the density response function of the ideal (i.e., noninteracting) system. However, since Eq. (1) does not incorporate correlations beyond the mean-field level, RPA breaks down even for moderate coupling. This shortcoming is usually corrected in the form of a local field correction (LFC) $G(\mathbf{q},\omega)$ [19], modifying Eq. (1) to

$$\chi_{\mathrm{LFC}}(\mathbf{q},\omega) = \frac{\chi_0(\mathbf{q},\omega)}{1 - \frac{4\pi}{q^2}[1 - G(\mathbf{q},\omega)]\chi_0(\mathbf{q},\omega)}. \qquad (2)$$

Hence, by definition, the exact LFC contains all exchange-correlation effects beyond RPA. Common approximations for G include the approaches by Singwi-Tosi-Land-Sjölander (STLS) [20] and Vashishta and Singwi (VS) [21]. It is important to note that the accurate determination of $G(\mathbf{q},\omega)$ is an important end in itself as it can be straightforwardly

utilized as input for other calculations. For example, it is directly related to the XC kernel

$$K_{\mathrm{xc}}(\mathbf{q},\omega) = -\frac{4\pi}{q^2}G(\mathbf{q},\omega) \qquad (3)$$

of density functional theory in the adiabatic-connection fluctuation-dissipation formulation [22–24]. This allows for the construction of a true nonlocal XC functional, which is a promising approach to go beyond the ubiquitous gradient approximations [18,25] and thereby increase the predictive capabilities of DFT. Further applications of the LFCs for current warm dense matter (WDM, see below) research include the calculation of the dynamic structure factor [26–29] as it can be obtained with x-ray Thomson scattering from a variety of systems, energy transfer rates [30,31], the electrical and optical conductivity [32,33], and equation of state models of ionized plasmas [34–36]. Finally, we mention the construction of effective potentials both for WDM [37,38] and beyond [39,40].

In the ground state, Moroni *et al.* [41] obtained accurate QMC results for the static response function [i.e., $\omega \to 0$, see Eq. (27)]—and thereby the static LFC—by simulating an electron gas with a weak external harmonic perturbation [42–45]. This has allowed for a systematic assessment of the accuracy of previous approximations. Further, the *ab initio* data for the LFC have subsequently been parametrized by Corradini *et al.* [46], and the zero temperature limit of the static density response is well understood.

However, recently there has emerged a growing interest in matter under extreme conditions, i.e., at high density and temperature, which occurs in astrophysical objects such as brown dwarfs and planet interiors [47,48]. Furthermore, similar conditions are now routinely realized in experiments with laser excited solids [49] or inertial confinement fusion targets [50–53]. This "warm dense matter" (WDM) regime is characterized by two parameters being of the order of unity [54]: (i) the Wigner-Seitz radius $r_s = \bar{r}/a_B$ and (ii) the reduced temperature $\theta = k_B T/E_F$, where $\bar{r}$, a_B and E_F denote the mean interparticle distance, Bohr radius, and Fermi energy [55], respectively. Naturally, accurate data for the static LFC

_____
*dornheim@theo-physik.uni-kiel.de

at such extreme conditions are highly desirable. In fact, in lieu of thermodynamic data often ground-state results are used at WDM conditions, which might not be appropriate [54].

Yet, a theoretical description of warm dense electrons is notoriously hard since it must account for the nontrivial interplay of (a) the strong quantum Coulomb collisions, (b) excitation effects due to the high temperature, and (c) quantum degeneracy effects (e.g. fermionic exchange). In particular, conditions (a) and (b) rule out perturbation expansions and ground-state methods, respectively, leaving thermodynamic quantum Monte Carlo methods as the most promising option. Unfortunately, QMC simulations of degenerate electrons suffer from the fermion sign problem (FSP) [56,57] so that the widespread path integral Monte Carlo (PIMC) approach [58] is limited to small system sizes and high temperatures, preventing simulations under WDM conditions [59]. Despite its remarkable success in the ground state, at finite temperature, the fixed node approximation [60,61] (which avoids the FSP) can lead to systematic errors exceeding 10% [62]. This unsatisfactory situation has sparked remarkable progress in the field of fermionic QMC simulations. In particular, the joint usage of two novel complementary approaches (in combination with an improved finite-size correction [63]) has recently allowed us to obtain the first complete *ab initio* description of the warm dense electron gas [63,64]: (i) At high density and weak to moderate coupling, the configuration PIMC (CPIMC) approach [65–67], which is formulated in Fock space and can be understood as a Monte Carlo calculation of the (exact) perturbation expansion around the ideal system, is capable to deliver exact results over a broad temperature range. (ii) The permutation blocking PIMC (PB-PIMC) approach [68–70] extends standard PIMC towards higher density and lower temperature and allows for accurate results in large parts of the WDM regime. In this work, we use the latter method to carry out simulations of the harmonically perturbed electron gas under warm dense matter conditions.

A brief introduction of the UEG model (Sec. II A) is followed by a comprehensive introduction to fermionic QMC simulations at finite temperature. In particular, we explain how the antisymmetry of the density operator leads to the fermion sign problem in standard PIMC (Sec. II B 1) and how this is addressed by the idea of permutation blocking (Sec. II B 2). Further, we give a concise overview of linear response theory and how the static density response can be obtained by simulating the harmonically perturbed system (Sec. II C). In Sec. III, we show extensive PB-PIMC results to investigate the dependence on the perturbation strength (Sec. III A), the convergence with the number of imaginary time propagators (Sec. III B), and the wave-vector dependence (Sec. III C), which also allows to address possible finite-size effects. Finally, in Sec. III E we consider the response to a superposition of multiple perturbations with different wave vectors and the resulting implications for the calculation of χ.

II. THEORY

A. Uniform electron gas

The uniform electron gas is a model system of N electrons in a positive homogeneous background that ensures charge

neutrality. Throughout this work, we assume an unpolarized (paramagnetic) system, i.e., $N^\uparrow = N^\downarrow = N/2$ [with $\uparrow$ ($\downarrow$) denoting the number of spin-up (-down) electrons] and, thus,

$$\xi = \frac{N^\uparrow - N^\downarrow}{N} = 0. \tag{4}$$

To alleviate the differences between a finite model system and the thermodynamic limit (finite-size effects), we employ Ewald summation for the repulsive pair interaction. Therefore, the Hamiltonian (in Hartree atomic units) is given by

$$\hat{H} = -\frac{1}{2} \sum_{i=1}^N \nabla_i^2 + \frac{1}{2} \sum_{i=1}^N \sum_{j \neq i}^N \Psi_E(\mathbf{r}_i, \mathbf{r}_j) + \frac{N}{2} \xi_M, \tag{5}$$

where $\Psi_E(\mathbf{r}, \mathbf{s})$ and ξ_M denote the Ewald pair potential and the well-known Madelung constant, see, e.g., Ref. [71].

B. Quantum Monte Carlo

1. Path-integral Monte Carlo

Throughout the entire work, we consider the canonical ensemble where the volume $V = L^3$ (with L being the box length), particle number N, and inverse temperature $\beta = 1/k_B T$ are fixed. To derive the path integral Monte Carlo formalism [58], we consider the partition function

$$Z = \text{Tr}\hat{\rho}, \tag{6}$$

which is defined as the trace over the canonical density operator $\hat{\rho}$

$$\hat{\rho} = e^{-\beta \hat{H}}. \tag{7}$$

Let us temporarily restrict ourselves to distinguishable particles and rewrite Eq. (6) in coordinate representation:

$$Z = \int d\mathbf{R} \, \langle \mathbf{R} | e^{-\beta \hat{H}} | \mathbf{R} \rangle, \tag{8}$$

where $\mathbf{R} = \{\mathbf{r}_1, \ldots, \mathbf{r}_N\}$ contains the all $3N$ particle coordinates. Since the matrix elements of $\hat{\rho}$ are not readily known, we use the group property

$$e^{-\beta \hat{H}} = \prod_{\alpha=0}^{P-1} e^{-\epsilon \hat{H}}, \tag{9}$$

with $\epsilon = \beta/P$ and α labeling the P identical factors. Furthermore, we insert $P - 1$ unity operators of the form $\hat{1} = \int d\mathbf{R}_\alpha |\mathbf{R}_\alpha\rangle \langle \mathbf{R}_\alpha|$ into Eq. (8) and obtain

$$Z = \int d\mathbf{X} \, \langle \mathbf{R}_0 | e^{-\epsilon \hat{H}} | \mathbf{R}_1 \rangle \langle \mathbf{R}_1 | \ldots$$
$$| \mathbf{R}_{P-1} \rangle \langle \mathbf{R}_{P-1} | e^{-\epsilon \hat{H}} | \mathbf{R}_0 \rangle, \tag{10}$$

and the integration is carried out over P sets of particle coordinates, $d\mathbf{X} = d\mathbf{R}_0 \ldots d\mathbf{R}_{P-1}$. We stress that Eq. (10) is still exact. The main benefit of this recasting is that the new expression involves P density matrix elements, but at a P times higher temperature. Each of these high temperature factors can now be substituted using some suitable high-T approximation, e.g., the simple primitive factorization

$$e^{-\epsilon \hat{H}} \approx e^{-\epsilon \hat{V}} e^{-\epsilon \hat{K}}, \tag{11}$$

with $\hat{V}$ and $\hat{K}$ being the operators for the potential and kinetic contribution to the Hamiltonian, respectively, and which becomes exact in the limit $P \to \infty$ [72]. The resulting high-dimensional integral is then evaluated using the Metropolis algorithm [73] (we employ a simulation scheme based on the worm algorithm [74,75]).

However, to simulate fermions we must extend the partition function from Eq. (8) by the sum over all particle permutations, which, for an unpolarized system, gives

$$Z = \frac{1}{N^{\uparrow}!N^{\downarrow}!} \sum_{\sigma^{\uparrow} \in S_{N^{\uparrow}}} \sum_{\sigma^{\downarrow} \in S_{N^{\downarrow}}} \mathrm{sgn}(\sigma^{\uparrow})\mathrm{sgn}(\sigma^{\downarrow})$$

$$\times \int d\mathbf{R} \; \langle \mathbf{R} | \, e^{-\beta\hat{H}} \, | \hat{\pi}_{\sigma^{\uparrow}}\hat{\pi}_{\sigma^{\downarrow}}\mathbf{R} \rangle \,, \tag{12}$$

with $\sigma^{\uparrow,\downarrow}$ denoting particular elements from the permutation groups $S_N^{\uparrow,\downarrow}$ and $\hat{\pi}_{\sigma^{\uparrow\downarrow}}$ being the corresponding permutation operators. In practice, this leads to the occurrence of so-called exchange cycles within the PIMC simulations, which are paths incorporating more than a single particle, see Fig. 1. The problem is that the sign of each configuration depends on the parity of the permutations involved which can be both positive and negative. Let $\{\mathbf{X}\}$ denote the set of all possible paths in the QMC simulation. The partition function, Eq. (12), is then given by

$$Z = \int_{\{\mathbf{X}\}} d\mathbf{X} \; W(\mathbf{X}), \tag{13}$$

where the so-called configuration weight $W(\mathbf{X})$ can be negative. However, since a probability must be strictly positive, we sample the paths according to the absolute values $|W(\mathbf{X})|$, where the normalization of this modified configuration space is given by

$$Z' = \int_{\{\mathbf{X}\}} d\mathbf{X} \; |W(\mathbf{X})|. \tag{14}$$

The correct fermionic expectation value of an arbitrary observable $\hat{A}$ is then computed as

$$\langle A \rangle = \frac{\langle \hat{A} \, \hat{S} \rangle'}{\langle \hat{S} \rangle'}, \tag{15}$$

where $\langle \dots \rangle'$ denotes the expectation value corresponding to Z', and $S(\mathbf{X}) = W(\mathbf{X})/|W(\mathbf{X})|$ is the sign of the configuration $\mathbf{X}$. In particular, the denomininator in Eq. (15) is the so-called average sign,

$$\langle \hat{S} \rangle' = \frac{1}{Z'} \int_{\{\mathbf{X}\}} d\mathbf{X} \; |W(\mathbf{X})|S(\mathbf{X}). \tag{16}$$

Note that the abbreviation $S = \langle \hat{S} \rangle'$ is used henceforth throughout this work.

At low temperature and high density, permutation cycles with both positive and negative signs appear with a similar frequency and, thus, both the enumerator and the denominator in Eq. (15) vanish simultaneously. In this case, the signal-to-noise ratio of the fermionic expactation value vanishes, leading to an exponentially increasing statistical uncertainty [59]. This is the notorious fermion sign problem [56,57], which limits standard PIMC to weak degeneracy where fermionic exchange
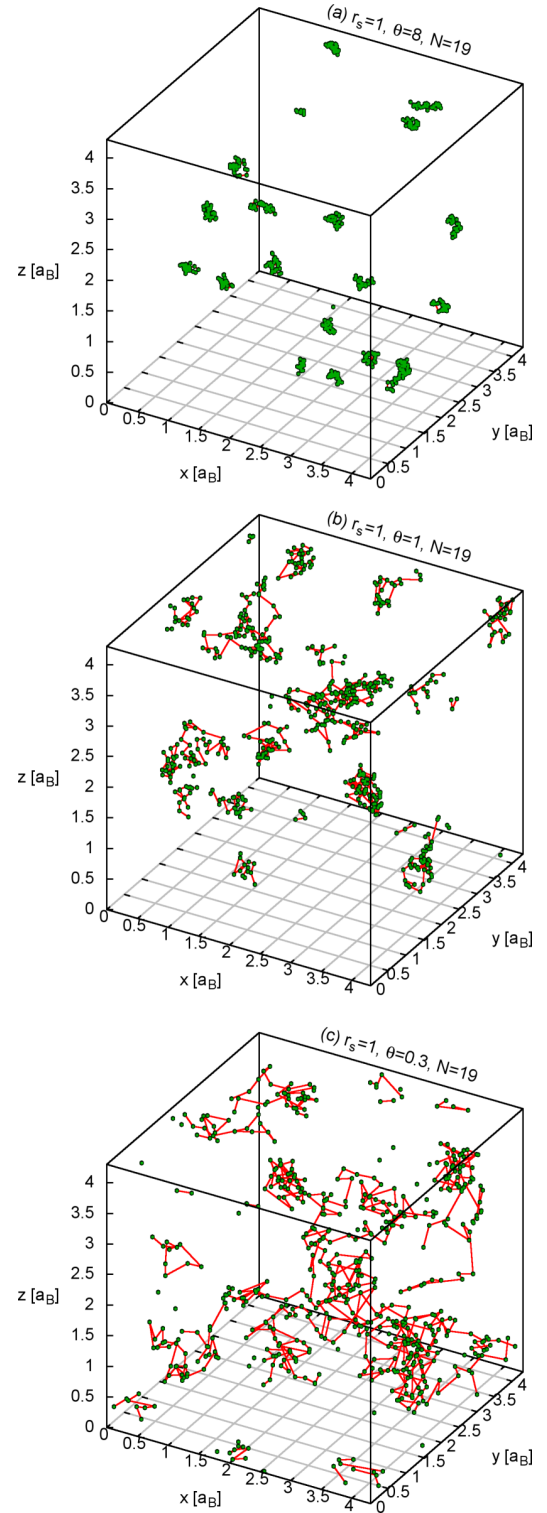

FIG. 1. Screen shots of standard path integral Monte Carlo simulations of the warm dense UEG for $N = 19$ spin-polarized electrons, $r_s = 1$, and $P = 32$, with $\theta = 8$ (a), $\theta = 1$ (b), and $\theta = 0.3$ (c).

plays only a minor role and, therefore, precludes its application to warm dense matter [59]. This is illustrated in Fig. 1, where we show random configurations from standard PIMC simulations of the UEG with $N = 19$ spin-polarized electrons

at a density parameter $r_s = 1$ and three different temperatures. Each particle is represented by $P = 32$ so-called beads, which are connected by the (red) kinetic density matrix elements and thus form the eponymous paths. At high temperature, $\theta = 8$ [Fig. 1(a)], each particle is represented by a distinct, separate path and exchange cycles occur only infrequently. Therefore, the FSP is not severe and PIMC simulations are feasible. At moderate, WDM temperatures [$\theta = 1$, Fig. 1(b)], fermionic exchange is influencing the system significantly, and multiple exchange cycles are visible in the screenshot. Since each pair exchange causes a sign change in the Monte Carlo simulation, a standard PIMC simulation is no longer feasible. Finally, at low temperature [$\theta = 0.3$, Fig. 1(c)] nearly all particles are involved in exchange cycles, and the system is dominated by the antisymmetric nature of the electrons (i.e., Pauli blocking).

2. Permutation blocking

The fermion sign problem is NP-hard [57] and a general solution is, at the time of this writing, not in sight. Therefore, there does not exist a single QMC method that is applicable for all parameters. Nonetheless, it is possible to go beyond standard PIMC by employing the recently introduced permutation blocking PIMC approach [68,69]. The first key ingredient is the usage of antisymmetric imaginary time propagators, i.e., determinants, which allows for a combination of positive and negative terms into a single configuration weight [76–78]. However, while this "permutation blocking" can indeed lead to a significant reduction of the fermion sign problem, with an increasing number of propagators P this advantage quickly vanishes. For this reason, as the second key ingredient, we utilize a higher-order factorization of the density matrix [79,80]

$$e^{-\epsilon \hat{H}} \approx e^{-v_1 \epsilon \hat{W}_{a_1}} e^{-t_1 \epsilon \hat{K}} e^{-v_2 \epsilon \hat{W}_{1-2a_1}}$$
$$\times e^{-t_1 \epsilon \hat{K}} e^{-v_1 \epsilon \hat{W}_{a_1}} e^{-2t_0 \epsilon \hat{K}}, \qquad (17)$$

which allows for sufficient accuracy even for a small number of imaginary time slices, for the definitions of the coefficients v_1, t_1, v_2, a_1, and t_0, see Refs. [68,69]. The $\hat{W}$ operators correspond to modified potential terms combining the standard potential contribution $\hat{V}$ with double commutator terms of the form [80]

$$[[\hat{V}, \hat{K}], \hat{V}] = \frac{\hbar^2}{m} \sum_{i=1}^{N} |\mathbf{F}_i|^2,$$
$$\mathbf{F}_i = -\boldsymbol{\nabla}_i V(\mathbf{R}), \qquad (18)$$

where $\mathbf{F}_i$ denotes the total force on a particle "i". Finally, this allows one to obtain the PB-PIMC partition function [70]

$$Z = \frac{1}{(N_\uparrow! N_\downarrow!)^{3P}} \int d\mathbf{X}$$
$$\times \prod_{\alpha=0}^{P-1} \left(e^{-\epsilon \tilde{V}_\alpha} e^{-\epsilon^3 u_0 \frac{\hbar^2}{m} \tilde{F}_\alpha} D_{\alpha,\uparrow} D_{\alpha,\downarrow} \right), \qquad (19)$$

with $\tilde{V}_\alpha$ and $\tilde{F}_\alpha$ containing all contributions of the potential energy and the forces, respectively, and the exchange-diffusion functions

$$D_{\alpha,\uparrow} = \det(\rho_{\alpha,\uparrow}) \det(\rho_{\alpha A,\uparrow}) \det(\rho_{\alpha B,\uparrow}),$$
$$D_{\alpha,\downarrow} = \det(\rho_{\alpha,\downarrow}) \det(\rho_{\alpha A,\downarrow}) \det(\rho_{\alpha B,\downarrow}). \qquad (20)$$
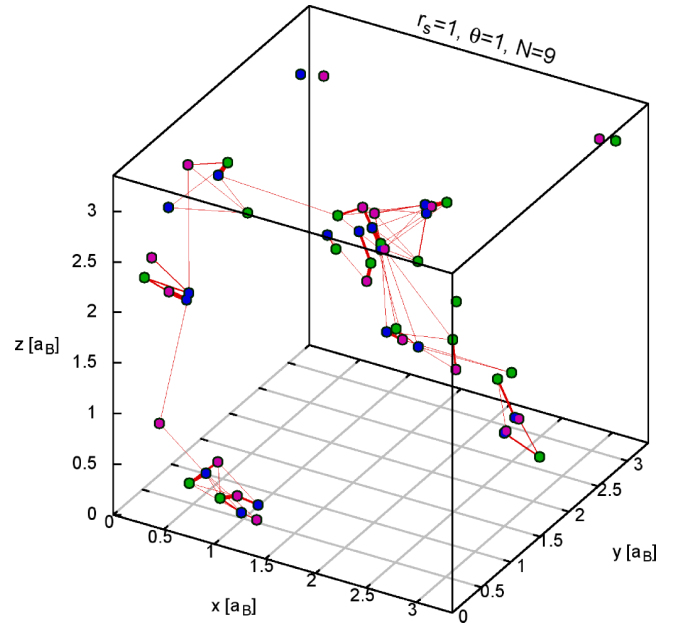

FIG. 2. Screen shot of a permutation blocking path integral Monte Carlo simulation of the UEG with $N = 9$ spin-polarized electrons with $r_s = 1$, $\theta = 1$, and $P = 2$ imaginary time propagators. The green, blue, and purple points correspond to the three different kinds of time slices, see Refs. [68–70].

Here $\rho_{\alpha,\uparrow}$ denotes the diffusion matrix of a single time slice

$$\rho_{\alpha,\uparrow}(i,j) = \lambda_{t_1 \epsilon}^{-3} \sum_{\mathbf{n}} e^{-\frac{\pi}{\lambda_{t_1 \epsilon}^2} (\mathbf{r}_{\alpha,\uparrow,j} - \mathbf{r}_{\alpha A,\uparrow,i} + \mathbf{n}L)^2}, \qquad (21)$$

with $\lambda_{t_1 \epsilon} = \sqrt{2\pi \epsilon t_1 \hbar^2 / m}$ being the corresponding thermal wavelength. Observe that Eq. (17) implies that there are three imaginary time slices for each propagator $\alpha = 0, \ldots, P - 1$, with $\mathbf{R}_\alpha$, $\mathbf{R}_{\alpha A}$, and $\mathbf{R}_{\alpha B}$ denoting the corresponding sets of particle coordinates.

In a nutshell, in the PB-PIMC approach, we do not have to explicitly sample each positive or negative permutation cycle. Instead, we combine configuration weights with different signs in the determinants, which results in an analytical cancellation of terms and, thus, a significantly alleviated sign problem. This is illustrated in Fig. 2, where we show a random configuration from a PB-PIMC simulation of the warm dense UEG with $N = 9$ spin-polarized electrons, $r_s = 1$ and $\theta = 1$ for $P = 2$. The green, blue, and purple beads correspond to the three different kinds of imaginary time slices due to the higher-order factorization of the density operator, cf. Eq. (17). In contrast to the standard PIMC configurations from Fig. 1, every bead can be involved in multiple connections here. In fact, each bead is connected to all N beads on the next and previous slices although the weight of the connection exponentially decreases with spatial difference, which is expressed by the different line widths of the (red) connections. Evidently, many beads of the depicted screen shot exhibit multiple visible connections, which means that a significant amount of analytical cancellation is accomplished within the determinants and, unlike standard PIMC, simulations are still feasible [59].

This permutation blocking is most effective when $\lambda_{t_1\epsilon}$ is comparable (or larger) than the mean interparticle distance. However, for $P \to \infty$ the beneficial effect vanishes and the original sign problem from standard PIMC is recovered. This plainly illustrates the paramount importance of a sophisticated higher-order factorization scheme such as Eq. (17).

C. Linear response theory

In linear response theory (LRT), we consider the effect of a small external perturbation on the density of the system of interest

$$\hat{H} = \hat{H}_0 + \hat{H}_{\text{ext}}(t). \tag{22}$$

Note that, in general, $\hat{H}_{\text{ext}}(t)$ is time dependent. Throughout this work, the unperturbed Hamiltonian $\hat{H}_0$ corresponds to the UEG as introduced in Eq. (5) and the perturbation is given by a sinusoidal external charge density of wave vector $\mathbf{q}$,

$$\hat{H}_{\text{ext}}(t) = 2A \sum_{i=1}^{N} \cos(\mathbf{r}_i \cdot \mathbf{q} - \Omega\, t), \tag{23}$$

which corresponds to the potential

$$\phi_{\text{ext}}(\mathbf{r},t) = 2A \cos(\mathbf{r} \cdot \mathbf{q} - \Omega\, t). \tag{24}$$

The standard definition of the density response function is given by

$$\tilde{\chi}(\mathbf{q},\tau) = \frac{-i}{\hbar} \langle [\rho(\mathbf{q},\tau),\rho(-\mathbf{q},0)] \rangle_0 \, \Theta(\tau), \tag{25}$$

where the expectation value is with respect to the unperturbed system. Note that Eq. (25) only depends on the time difference $\tau = t - t'$ and, due to the homogeneity of the unperturbed system, χ only depends on the modulus of the wave vector. The corresponding Fourier transform is given by

$$\chi(\omega,\mathbf{q}) = \lim_{\eta \to 0} \int_{-\infty}^{\infty} d\tau \; e^{(i\omega - \eta)\tau} \, \tilde{\chi}(\mathbf{q},\tau). \tag{26}$$

Throughout this work, we restrict ourselves to the static limit [81] that is defined as

$$\lim_{\omega \to 0} \chi(\omega,\mathbf{q}) = \chi(\mathbf{q}), \tag{27}$$

i.e., the response of the electron gas to a time-independent external perturbation

$$\phi_{\text{ext}}(\mathbf{r}) = 2A \cos(\mathbf{r} \cdot \mathbf{q}), \tag{28}$$

and, henceforth, the ω dependence is simply dropped. More precisely, the physical interpretation of $\chi(\mathbf{q})$ is the description of the density response [i.e., the induced charge density $\rho_{\text{ind}}(\mathbf{q})$] due to the external charge density $\rho_{\text{ext}}(\mathbf{q})$

$$\rho_{\text{ind}}(\mathbf{q}) = \rho_{\text{ext}}(\mathbf{q}) \frac{4\pi}{q^2} \chi(\mathbf{q}). \tag{29}$$

The external density follows from the Poisson equation as

$$\rho_{\text{ext}}(\mathbf{r}) = -\frac{1}{4\pi} \nabla^2 \phi_{\text{ext}}(\mathbf{r})$$

$$= \frac{q^2}{4\pi} \phi_{\text{ext}}(\mathbf{r}) = \frac{q^2}{4\pi} 2A \cos(\mathbf{r} \cdot \mathbf{q}) \tag{30}$$

$$\Rightarrow \rho_{\text{ext}}(\mathbf{q}) = \frac{q^2}{2\pi} \frac{A}{(2\pi)^3} \int d\mathbf{r} \; e^{-i\mathbf{k}\cdot\mathbf{r}} \left(\frac{e^{i\mathbf{q}\cdot\mathbf{r}} + e^{-i\mathbf{q}\cdot\mathbf{r}}}{2} \right)$$

$$= \frac{q^2 A}{4\pi} (\delta_{\mathbf{k},\mathbf{q}} + \delta_{\mathbf{k},-\mathbf{q}}), \tag{31}$$

and the induced density is the difference between the perturbed and unperturbed systems:

$$\rho_{\text{ind}}(\mathbf{q}) = \langle \hat{\rho}_{\mathbf{q}} \rangle_A - \langle \hat{\rho}_{\mathbf{q}} \rangle_0 = \frac{1}{V} \left\langle \sum_{j=1}^{N} e^{-i\mathbf{q}\cdot\mathbf{r}_j} \right\rangle_A, \tag{32}$$

where we made use of the fact that $\langle \hat{\rho}_{\mathbf{q}} \rangle_0 = 0$. Thus, it holds

$$\chi(\mathbf{q}) = \frac{1}{A} \langle \hat{\rho}_{\mathbf{q}} \rangle_A. \tag{33}$$

In order to obtain the desired static density response function, we carry out multiple QMC simulations for each wave vector $\mathbf{q} = 2\pi L^{-1}(a,b,c)^T$ (with $a,b,c \in \mathbb{Z}$) for different values of A and compute the expectation value from Eq. (32). For sufficiently small A, $\langle \hat{\rho}_{\mathbf{q}} \rangle_A$ is linear with respect to A with $\chi(\mathbf{q})$ being the slope.

Another way to obtain the response function from the QMC simulation of the perturbed system is via the perturbed density profile in coordinate space:

$$\langle n(\mathbf{r}) \rangle_A = n_0 + 2A \cos(\mathbf{q} \cdot \mathbf{r}) \chi(\mathbf{q}). \tag{34}$$

In practice, we compute the left-hand side of Eq. (34) using QMC and perform a fit of the right-hand side with $\chi(\mathbf{q})$ being the only free parameter. Naturally, in the linear response regime both ways to obtain $\chi(\mathbf{q})$ are equal.

For completeness, we mention that the dynamic response can be obtained in a similar fashion by considering explicitly time-dependent perturbations, e.g., using nonequilibrium Green function techniques [82,83] for quantum systems or molecular dynamics [84,85] in the classical case.

A second strategy to compute the density response from thermodynamic QMC simulations in LRT is by considering imaginary-time correlation functions (ITCF) of the unperturbed system. In particular, the static response function can be obtained from the fluctuation dissipation theorem [43],

$$\chi(\mathbf{q}) = -\frac{1}{V} \int_0^\beta d\tau \; \langle \rho(\mathbf{q},\tau)\rho(-\mathbf{q},0) \rangle_0, \tag{35}$$

as an integral over the imaginary time τ. If one is solely interested in the linear response of the system, then invoking Eq. (35) constitutes the superior strategy since all $\mathbf{q}$ vectors can be computed from a single simulation. However, this requires a QMC estimation of the ITCF on a sufficient τ grid, which is straightforward in standard PIMC where $P > 100$ is not an obstacle. For PB-PIMC, simulations are only possible for a small number of imaginary-time propagators (typically $P \lesssim 4$), see Sec. II B 2, which precludes the evaluation of Eq. (35). Nevertheless, we stress that it is only the permutation blocking idea that allows us to carry out simulations at warm dense matter conditions in the first place, since standard PIMC simulations are not feasible due to the FSP. In addition, the application of an external perturbation allows us to go beyond LRT and to consider arbitrarily strong perturbation strengths.

III. RESULTS

A. Dependence on perturbation strength

Let us start our investigation of the harmonically perturbed electron gas by considering the dependence on the perturbation amplitude A. In Fig. 3, we show PB-PIMC results for the
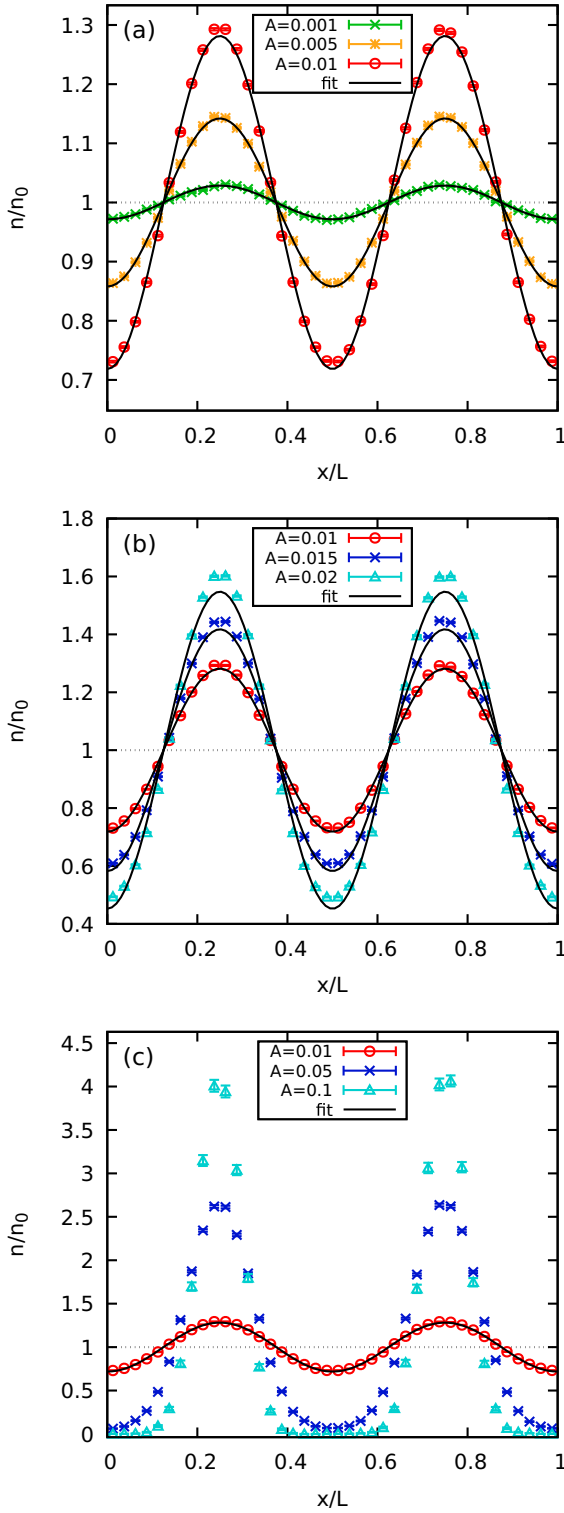
FIG. 3. Density profiles along the x direction for $N = 54$, $r_s = 10$, and $\theta = 1$. Shown are PB-PIMC results for $P = 4$ with $\mathbf{q} = 2\pi L^{-1}(2,0,0)^T$ and weak (a), medium (b), and strong (c) perturbations. The black lines correspond to fits according to Eq. (34).

to Eq. (34). Evidently, for $A = 0.001$ and $A = 0.005$, those curves are in perfect agreement with the QMC results, which indicates that here the linear response theory is accurate. In contrast, for $A = 0.01$ significant (although small, $\Delta A/A \sim 1\%$) deviations appear, which are most pronounced around the minima and maxima. In Fig. 3(a), we systematically increase A up to a factor two. Clearly, with increasing perturbation amplitude, the deviations between the exact QMC results and the cosine fit predicted by LRT become more severe, as is expected. Finally, in Fig. 3(c) we show the density profiles for even larger perturbations. Eventually, the external potential becomes the dominating feature, resulting in a strongly inhomogeneous electron gas. For the largest depicted perturbation, $A = 0.1$, there appear two distinct shells with a vanishing density in between.

To systematically investigate the effect of the perturbation amplitude on our QMC estimation of the static response function $\chi(\mathbf{q})$, we show results in Fig. 4 for the induced density $\rho_{\text{ind}}(\mathbf{q})$ for the same system and two different wave vectors, $\mathbf{q} = 2\pi L^{-1}(q_x,0,0)^T$ with $q_x = 2$ [Fig. 4(a)] and $q_x = 1$ [Fig. 4(b)]. The black squares correspond to the direct QMC results, cf. Eq. (32), and the green crosses have been obtained by performing a cosine fit to the density profiles according to Eq. (34). The red lines depict a linear fit to the black squares for $A < 0.01$. First and foremost, we observe a perfect agreement between the direct QMC results and the cosine fits for small A as predicted by the linear response theory. Even for $A = 0.01$, where the cosine fit exhibits significant deviations to the density profile from QMC, we find perfect agreement between the black and green points and also to the fit. With increasing A, however, the assumptions of linear response theory are no longer valid. Interestingly, the ρ values obtained from the cosine fit exhibit significantly larger deviations to the linear response prediction (red line) than the direct QMC results. For example, at $A = 0.05$ the deviation of the green points is twice as large as for the black squares.

In Fig. 4(b), the same information is shown for a smaller wave vector, $q_x = 1$. First, we observe a significantly smaller density response (cf. Fig. 8). This, in turn, means that linear response theory is accurate up to much larger A values as the system only weakly reacts to such an external perturbation.

To further illustrate this point, in Fig. 5(a) we show the corresponding average signs from the QMC simulations for both wave vectors investigated in Fig. 4. For small perturbations, S is equal for both $\mathbf{q}$ and approaches the result for the unperturbed system. With increasing A, the system becomes more inhomogeneous, i.e., there appear regions of increased (and also decreased) density, see Fig. 5(b), where we show the corresponding density profiles for strong perturbations, $A = 0.1$. This, in turn, leads to increased fermionic exchange, resulting in a significantly decreased average sign in our PB-PIMC simulations. Since the density response is more pronounced for $q_x = 2$, here S exhibits a faster decrease in dependence of A. We conclude that PB-PIMC (and also standard PIMC) simulations of the inhomogeneous electron gas are significantly more computationally demanding than simulations of the UEG at equal conditions. Nevertheless, this is of no consequence for the determination of the static response function as this is only possible for A values that are sufficiently small for the linear response theory to deliver an

density profile along the x direction for $N = 54$ unpolarized electrons at $r_s = 10$ and $\theta = 1$ for the perturbation wave vector $\mathbf{q} = 2\pi L^{-1}(2,0,0)^T$. In Fig. 3(a), the depicted A values are relatively small. The black lines correspond to fits according
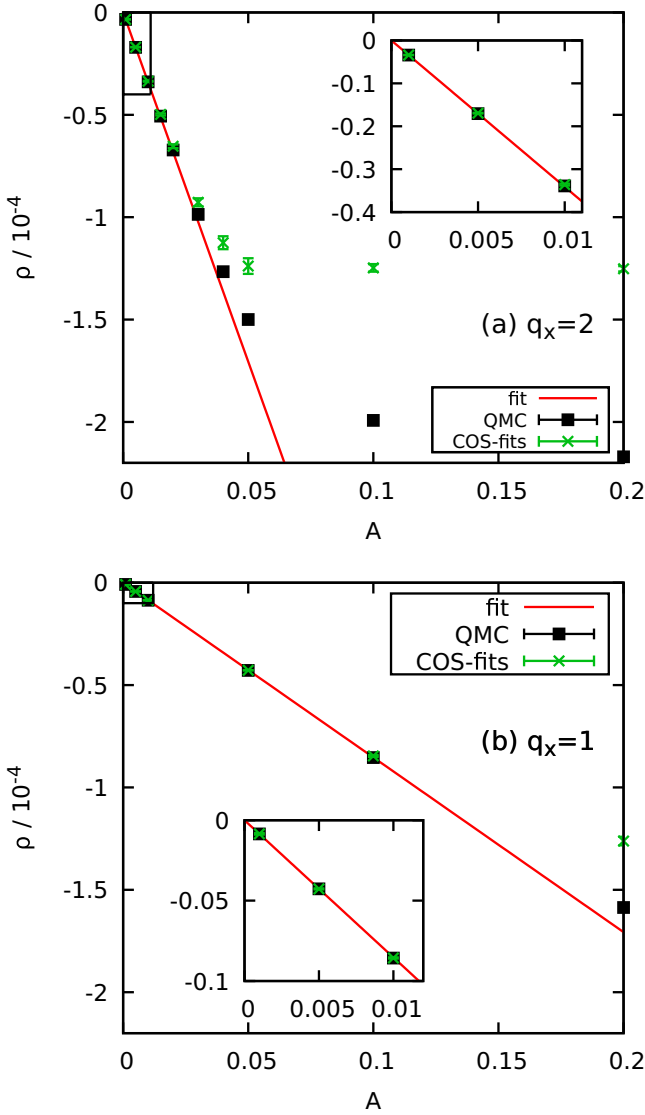
FIG. 4. Induced density modulation for $N = 54$, $r_s = 10$, and $\theta = 1$. Shown are PB-PIMC results for $P = 4$ with $\mathbf{q} = 2\pi L^{-1}(q_x, 0, 0)^T$ [$q_x = 2$ (a) and $q_x = 1$ (b)] directly computed from QMC, cf. Eq. (32), and from fits according to Eq. (34).
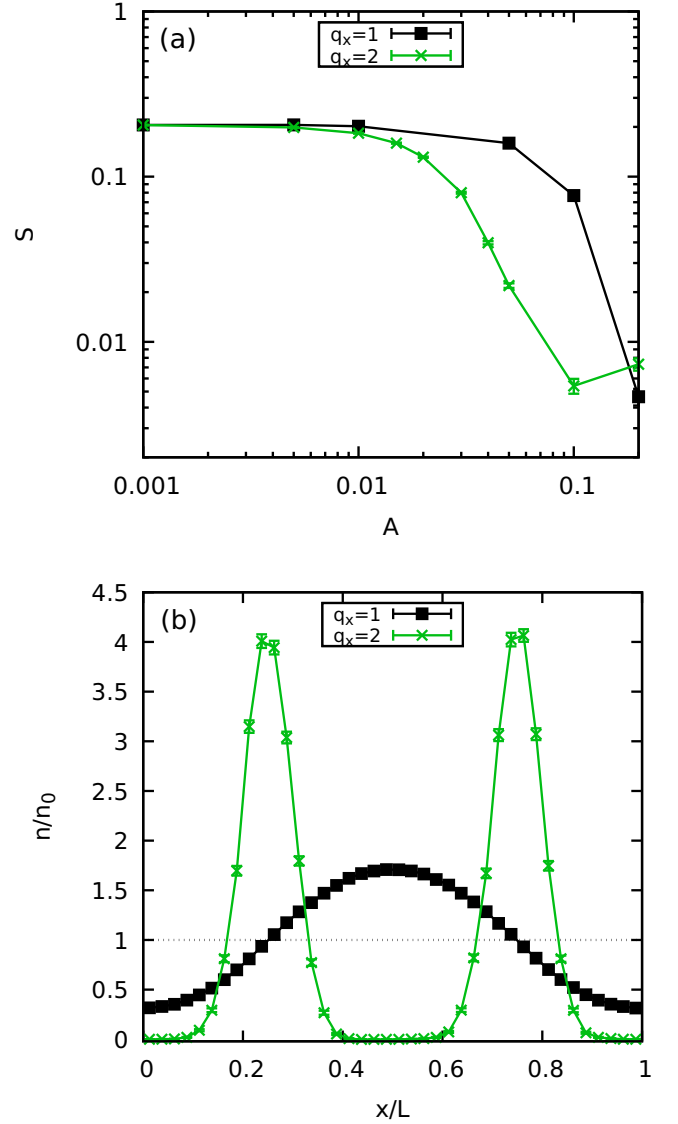

FIG. 5. Average sign for $N = 54$, $r_s = 10$, and $\theta = 1$ (a). Shown are PB-PIMC results for $P = 4$ with $\mathbf{q} = 2\pi L^{-1}(q_x, 0, 0)^T$. Corresponding density profiles along the x direction for $A = 0.1$ (b).

accurate description, i.e., systems that are close to the uniform case.

B. Convergence with propagators

As discussed in Sec. II B 2, PB-PIMC crucially relies on the higher-order factorization of the density operator, Eq. (17), to allow for sufficient accuracy with only few imaginary time propagators. In the following section, this situation is investigated in detail.

In Fig. 6(a), we plot direct QMC results for the induced density for the unpolarized UEG with $r_s = 10$, $\theta = 1$, and $N = 34$ electrons versus the inverse number of propagators P^{-1}. The perturbation is given by the wave vector $\mathbf{q} = 2\pi L^{-1}(1, 0, 0)^T$ and amplitude $A = 0.01$, which is well within the linear response regime. Evidently, only the result for ρ with $P = 2$ propagators significantly deviates from the rest and,

for the $P = 4$ propagators used above, the PB-PIMC results are converged within the statistical uncertainty. Figure 6(b) shows the corresponding density profiles along the x direction. Here, even the results for only $P = 2$ propagators exhibits no significant deviations to the other curves.

As a second example, in Fig. 7 we consider the same system as in Fig. 6 but with $N = 54$ electrons and a larger wave vector for the perturbation, $\mathbf{q} = 2\pi L^{-1}(5, 0, 0)^T$. In Fig. 7(a), we again show direct QMC results for ρ in dependence of the inverse number of propagators. However, in contrast to the data depicted in Fig. 6, here we see significant differences for different P. The black line corresponds to a parabolic fit of the form

$$\rho(P^{-1}) = a + \frac{b}{P^2}, \tag{36}$$

which reproduces all QMC results within error bars. Nevertheless, we stress that the functional form in Eq. (36)
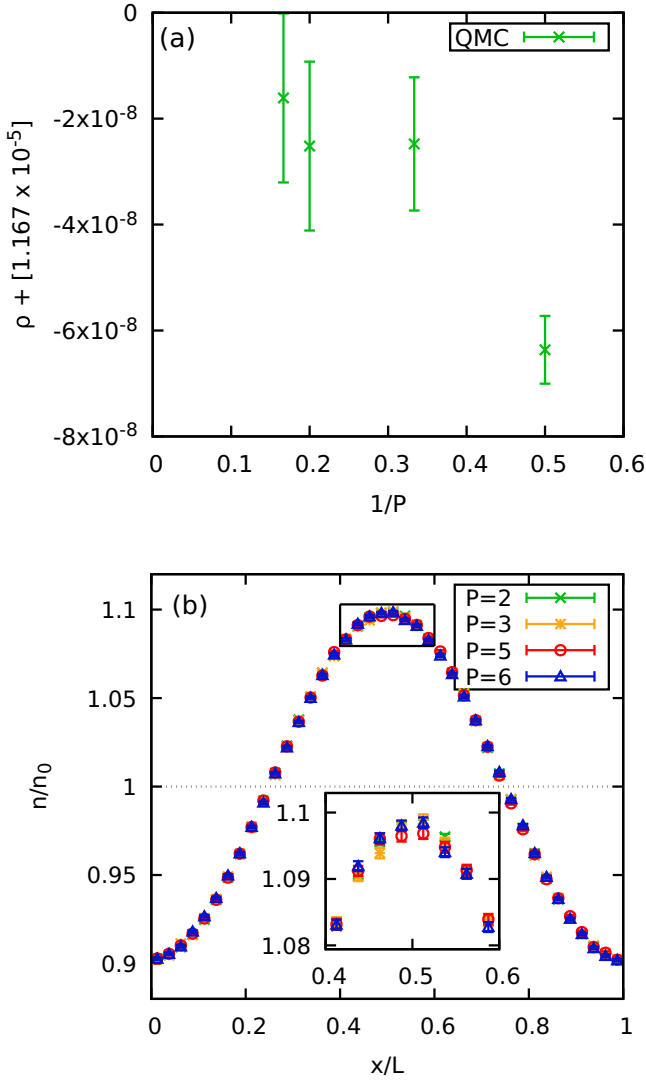
FIG. 6. Convergence with number of propagators P for $N = 34$, $r_s = 10$, and $\theta = 1$ with a perturbation of wave vector $\mathbf{q} = 2\pi L^{-1}(1,0,0)^T$ and amplitude $A = 0.01$. Shown are QMC results for the density matrix (a) and the density profile along the x direction (b).

FIG. 7. Convergence with number of propagators P for $N = 54$, $r_s = 10$, and $\theta = 1$ with the perturbation of wave vector $\mathbf{q} = 2\pi L^{-1}(5,0,0)^T$ and amplitude $A = 0.01$. Shown are QMC results for the density matrix (a) and the potential energy, i.e., the sum of Ewald interaction and external field (b).

has been empirically chosen and does merely serve as a guide to the eye since, for large P, the propagator error is expected to exhibit a fourth-order decay, see Ref. [80] for a comprehensive discussion. Evidently, for $P = 4$ there occurs a systematic bias of $\Delta\rho/\rho \approx 2\%$ at such a large wave vector. This is reflected in the increasing error bars towards large $\mathbf{q}$ in the wave-vector dependence plot, i.e., Fig. 8, and can be understood as follows: The propagator error is a direct consequence of the noncommuting of the kinetic ($\hat{K}$) and potential ($\hat{V}$) contributions of the Hamiltonian. The larger the wave vector $\mathbf{q}$, the faster the spatial variations of the external potential and, because $\hat{K} \propto \nabla^2$, the larger the error terms, which involve nested commutators of $\hat{K}$ and $\hat{V}$.

Figure 7(b) shows the corresponding results for the total potential energy, i.e., the sum of the Ewald interaction and the external perturbation. Evidently, no deviations can be resolved within the given statistical uncertainty, even for
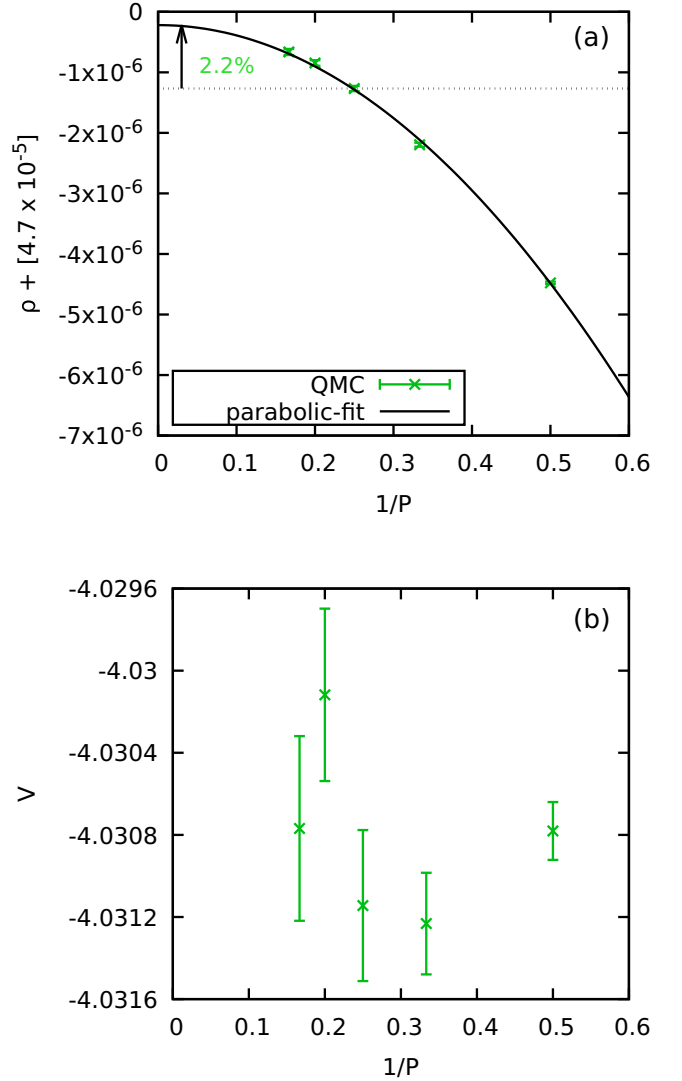
$P = 2$ propagators. This is similar to previous findings for the unperturbed UEG [69,70] and reflects the circumstance that for V the particle interaction dominates. In stark contrast, the induced density ρ is particularly sensitive to the small external perturbation which, as explained above, requires a larger number of propagators to be sufficiently incorporated.

C. Wave-vector dependence of $\chi(q)$ and finite-size effects

Due to the momentum quantization in a finite simulation box, QMC calculations are only possible at an N-dependent discrete $\mathbf{q}$ grid. Therefore, the investigation of finite-size effects in the static response function requires us to obtain results over a broad wave-vector range, as shown in Fig. 8. The gray and red curves correspond to the predictions due to the RPA, cf. Eq. (1), and with a LFC from the (finite-T) STLS formalism [86,87], respectively. For small $\mathbf{q}$, both
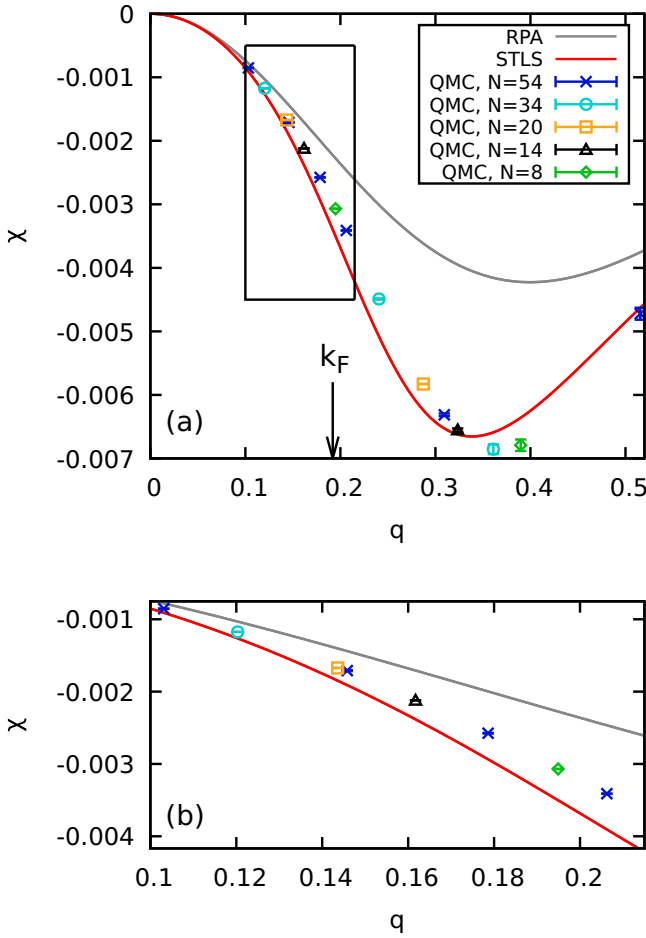
FIG. 8. Wave-vector dependence of the static response function for the unpolarized UEG at $r_s = 10$ and $\theta = 1$. Shown are QMC results according to Eq. (33) for different particle numbers (symbols) and the predictions from RPA (gray) and STLS (red). The black arrow indicates the Fermi wave vector, $k_F = (9\pi/4)^{1/3}/r_s$. Panel (b) shows a magnified segment.

approximations exhibit the same exact parabolic behavior [88]. With increasing $\mathbf{q}$, however, there appear significant systematic deviations with a maximum of $\Delta\chi/\chi \sim 50\%$ around $q \approx 0.35$ [i.e., around twice the Fermi vector $k_F = (9\pi/4)^{1/3}/r_s$]. The symbols correspond to our QMC results obtained according to Eq. (33) and the colors distinguish different particle numbers, in particular $N = 54$ (blue crosses), $N = 34$ (light blue circles), $N = 20$ (yellow squares), $N = 14$ (black triangles), and $N = 8$ (green diamonds). First and foremost, we note that the main effect of different system size is the $\mathbf{q}$ grid, while the functional form itself is remarkably well converged, even for as few as $N = 8$ particles, cf. Fig. 8(b) showing a magnified segment. This is similar to the analogous behavior of the static structure factor $S(\mathbf{q})$ of the warm dense UEG found in Refs. [59,63]. Evidently, momentum shell effects as observed at $T = 0$ in Refs. [41,44] do not appear above $\theta = 0.5$. Second, we find that the static local field correction due to the STLS closure relation leads to a significant improvement compared to RPA due to the improved treatment of correlations.

We thus conclude that our QMC approach allows us, for the first time, to unambiguously assess the accuracy of the
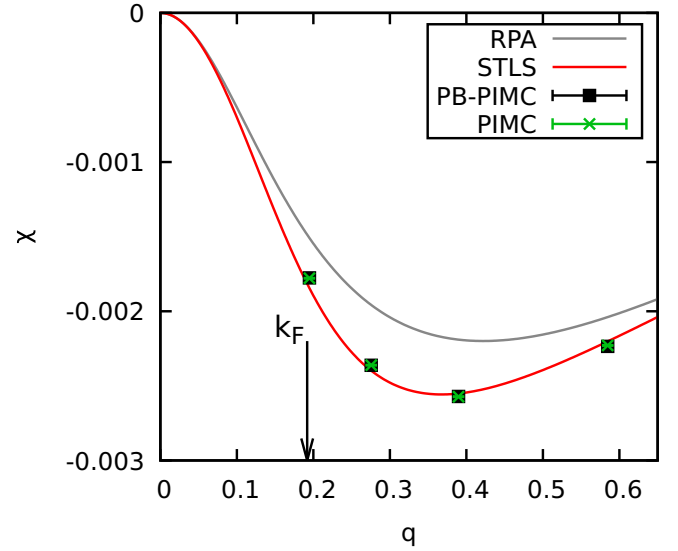

FIG. 9. Wave-vector dependence of the static response function for the unpolarized UEG at $r_s = 10$ and $\theta = 4$. Shown are QMC results according to Eq. (33) for $N = 8$ electrons obtained from PB-PIMC with $P = 4$ (black squares) and standard PIMC with $P = 100$ (green crosses). As a reference, we also show the predictions from RPA (gray) and STLS (red).

multitude of existing and widely used dielectric approximations and, in addition, to provide highly accurate data, which can subsequently be used as input for other theories. However, a comprehensive study over a broad parameter range is beyond the scope of this work and will be provided in a future publication.

D. Comparison of PB-PIMC to standard PIMC

As an additional benchmark for the static response obtained with PB-PIMC, in Fig. 9 we show $\chi(\mathbf{q})$ for the unpolarized UEG with $N = 8$, $r_s = 10$, and $\theta = 4$. Since for such a temperature fermionic exchange plays only a minor role, in addition to PB-PIMC (green crosses) also standard PIMC (black squares) calculations are feasible. Evidently, both independent data sets are in excellent agreement over the entire $\mathbf{q}$ range, as expected. In addition, we again show results from RPA (gray) and STLS (red) and find qualitatively similar behavior to Fig. 8. However, due to the 4 times higher temperature correlations play a less important role, which means that (i) RPA and STLS exhibit less deviations towards each other and (ii) the density response from STLS is in much better agreement with the QMC data. For completeness, we note that a more meaningful assessment of the systemic error due to the STLS approximation requires to eliminate the possibility of finite-size effects in the QMC data (as done in Fig. 8 at lower temperature, $\theta = 1$) and, thus, to consider larger particle numbers N.

E. Multiple q vectors from a single simulation

When we have to perform at least a single (or even a few for different A) QMC simulation for each $\mathbf{q}$ value, the investigation of the wave-vector dependence as depicted in Fig. 8 is computationally quite involved. However, by
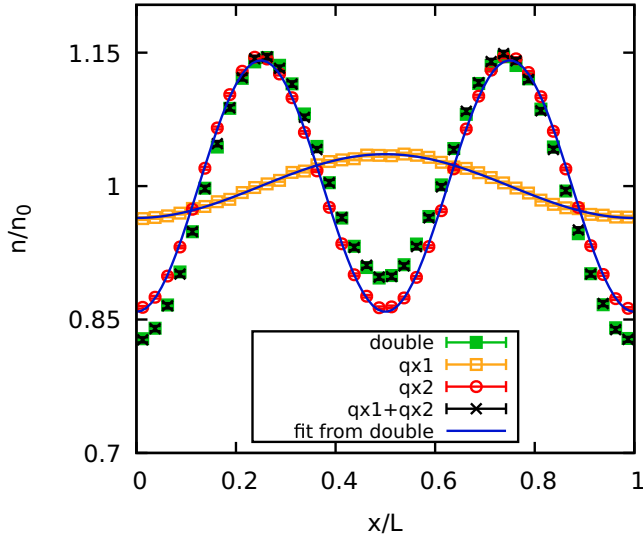
FIG. 10. Density profile along x direction for $N = 54$, $r_s = 10$, and $\theta = 1$ with a perturbation amplitude of $A = 0.005$. The green squares correspond to a QMC simulation with a superposition of two $\mathbf{q}$ vectors ($q_x = 1$ and $q_x = 2$), see Eq. (37), whereas the yellow and red points have been obtained using two separate QMC simulations each with a single perturbation. The black crosses correspond to a superposition of the latter two. The blue lines have been reconstructed from a fit to the green squares according to Eq. (38), i.e., by obtaining both $\chi(\mathbf{q}_1)$ and $\chi(\mathbf{q}_2)$ from the density response of the system with two simultaneous perturbations.

definition in linear response theory the response of a system to multiple perturbations is described by a superposition of the responses to each perturbation. Therefore, it should be possible to obtain the response function for multiple $\mathbf{q}$ values from a single QMC simulation where we apply a superposition of N_A harmonic perturbations,

$$\hat{H}_{\text{ext}} = 2 \sum_{k=1}^{N_A} \left[A_k \sum_{i=1}^{N} \cos(\mathbf{r}_i \cdot \mathbf{q}_k) \right]. \tag{37}$$

The induced density is then calculated for each wave vector $\mathbf{q}_k$ according to Eq. (32). Furthermore, the density profile in coordinate space is given by

$$\langle n(\mathbf{r}) \rangle_A = n_0 + 2 \sum_{k=1}^{N_A} [A_k \cos(\mathbf{r} \cdot \mathbf{q}_k) \chi(\mathbf{q}_k)], \tag{38}$$

which means that we have to perform a fit where the free parameters are given by the N_A values of $\chi(\mathbf{q}_k)$.

In Fig. 10, we show QMC results for the density profile in the x direction for $N = 54$, $r_s = 10$, and $\theta = 1$. The green squares have been obtained from a simulation with a superposition of $N_A = 2$ perturbations with $\mathbf{q}_1 = 2\pi L^{-1}(1,0,0)^T$ and $\mathbf{q}_2 = 2\pi L^{-1}(2,0,0)^T$ and $A_1 = A_2 = 0.005$, i.e., an amplitude that is expected to be well within the linear response regime. As a comparison, the yellow and red points correspond to the QMC results with a single perturbation with $q_x = 1$ (yellow) and $q_x = 2$ (red). Further, the black crosses have been obtained as a superposition of the latter and are in perfect agreement with the green squares. This is a strong indication that the
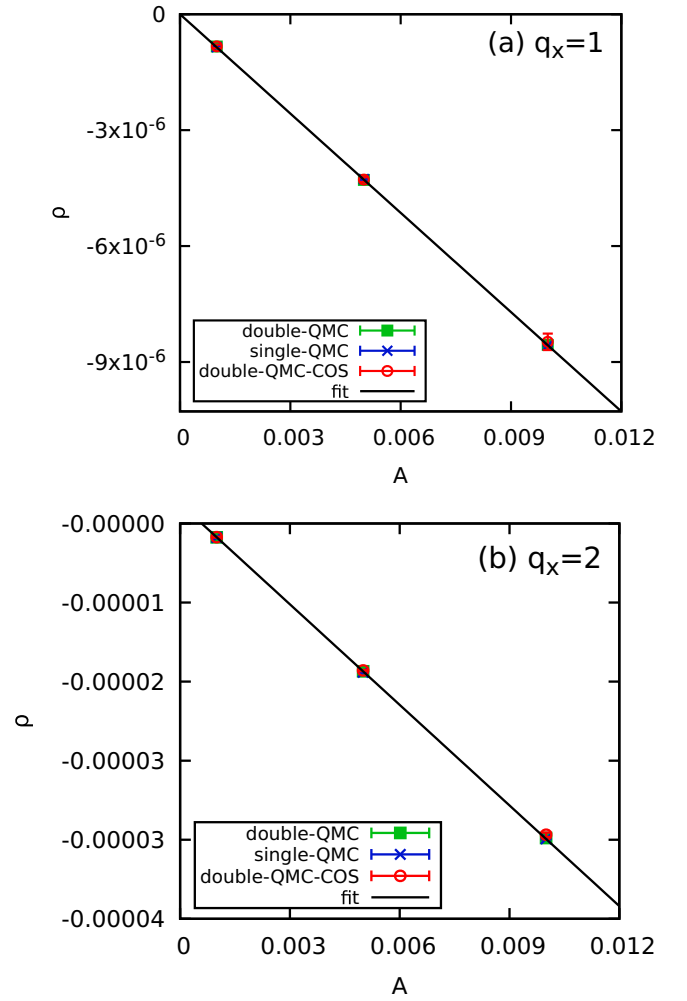

FIG. 11. Induced density for $N = 54$, $r_s = 10$, and $\theta = 1$ for a perturbation of wave vector $\mathbf{q} = 2\pi L^{-1}(q_x,0,0)^T$. The blue crosses have been obtained from a QMC simulation with a single perturbation, whereas the green squares and red circles correspond to the direct and cosine-fit results from the simulation with a double perturbation. Finally, the black lines has been obtained by a linear fit to the green squares.

linear response is still valid for multiple perturbations under the present conditions. In addition, we have fitted the right-hand side of Eq. (38) to the green squares and in this way obtained $\chi(\mathbf{q}_k)$ for both $\mathbf{q}_k$ values. This, in turn, allows us to reconstruct the density response of the system to a perturbation with only a single $\mathbf{q}_k$ value, i.e., the blue curves. Again, we find excellent agreement to the corresponding QMC simulations.

To further pursue this point, in Fig. 11 we show the induced density matrix for different amplitudes A. The green squares and red circles have been obtained from a simulation with two $\mathbf{q}_k$ vectors and correspond to the direct QMC estimate and the cosine fit according to Eq. (38), respectively. The blue crosses have been obtained from the QMC simulation with only a single harmonic perturbation and the red line depicts a linear fit. Evidently, all points are in excellent agreement for all A values both for $q_x = 1$ (panel a) and $q_x = 2$ [Fig. 11(b)]. Therefore, we conclude that it is indeed possible to obtain
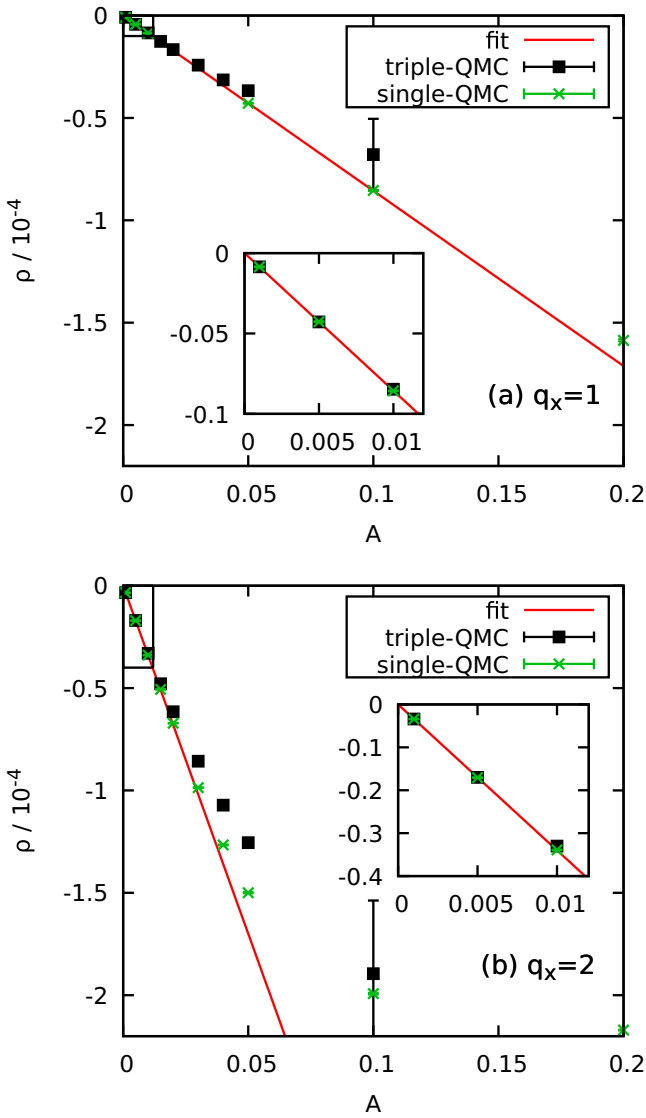
FIG. 12. Perturbation strength dependence for a combination of three wave vectors $\mathbf{q}_i = 2\pi L^{-1}(q_{x,i},0,0)$ with $q_{x,1} = 1$, $q_{x,2} = 2$, and $q_{x,3} = 3$. The black squares correspond to direct QMC results according to Eq. (32), the green crosses to direct QMC results from a simulation with a single perturbation, and the red line to a fit in the linear response regime.

multiple values of the static density response function $\chi(\mathbf{q})$ simultaneously.

Finally, to investigate the perturbation strength dependence for a QMC simulation with a superposition of multiple $\mathbf{q}$ vectors in more detail, we consider a combination of $N_A = 3$ perturbations with $\mathbf{q}_1 = 2\pi L^{-1}(1,0,0)^T$, $\mathbf{q}_2 = 2\pi L^{-1}(0,2,0)^T$, and $\mathbf{q}_3 = 2\pi L^{-1}(0,0,3)^T$ and equal amplitude, $A_1 = A_2 = A_3$, over a broad A range. The results are shown in Fig. 12 where direct QMC results for the induced density matrix are shown both from the simulation with the superposition (black squares) and, as a reference, from a simulation with only a single perturbation (green crosses). As usual, the red line corresponds to a linear fit within the linear response regime. For both $q_x = 1$ [Fig. 12(a)] and $q_x = 2$ [Fig. 12(b)] we observe that the linear response is accurate up to larger A.

This is expected, since the more perturbations we apply at the same time, the more inhomogeneous the system becomes and, thus, the stronger the total perturbation will be. Further, we note that this effect is more pronounced for $q_x = 2$. This is again a consequence of the larger $\chi(\mathbf{q})$ value which implies that the density response is even larger in this case.

In a nutshell, we find that, while it is possible to obtain multiple $\mathbf{q}$ values of the response function within a single QMC simulation, this comes at the cost that the linear response is valid only up to smaller perturbation amplitudes A. However, the smaller A, the larger the relative statistical uncertainty of the induced density, which means that there is a trade-off between more Monte Carlo steps for a simulation with multiple $\mathbf{q}$ vectors or multiple QMC simulations with only a single perturbation and fewer MC steps. In practice, applying a superposition of $N_A \approx 3$ perturbations is reasonable.

IV. SUMMARY AND DISCUSSION

In summary, we have carried out extensive permutation blocking PIMC simulations of a harmonically perturbed electron gas to investigate the static density response at warm dense matter conditions. To investigate the dependence of the response on the perturbation strength, we varied the amplitude A over three orders of magnitude. For small A, linear response theory is accurate and both ways to obtain the response function $\chi(\mathbf{q})$ [i.e., Eqs. (33) and (34)] give equal results. With increasing A, the system becomes strongly inhomogeneous, which leads to a significantly increased sign problem due to the regions with increased density. The second important issue investigated in this work is the convergence of the PB-PIMC results for $\chi(\mathbf{q})$ with the number of propagators P. For small to medium $\mathbf{q}$, we find that $P = 4$ propagators are sufficient at WDM conditions, which agrees with previous findings for the uniform system [69,70]. However, for large $\mathbf{q}$, the external potential exhibits fast spatial variations, which lead to increased commutator errors and thus require a larger number of propagators to achieve the same level of accuracy. For the largest considered wave vector, $\mathbf{q} = 2\pi L^{-1}(5,0,0)^T$, at $\theta = 1$, $r_s = 10$, and $N = 54$, we find a propagator error of $\Delta\chi/\chi \sim 2\%$. The main effect of system size on the QMC results for the static response function is given by the different $\mathbf{q}$ grid (which is a consequence of momentum quantization in a finite box), whereas the functional form of $\chi(\mathbf{q})$ is remarkably well converged even for small particle numbers. This is in stark contrast to previous findings at zero temperature [41,44] and can be ascribed to the absence of momentum shell effects at WDM conditions.

Our first brief comparison of the wave-vector dependence of $\chi(\mathbf{q})$ computed from QMC to the approximate results from RPA and STLS for $r_s = 10$ and $\theta = 1$ reveals the stark breakdown of the former when coupling effects are non-negligible. The LFC from the STLS closure relation, on the other hand, constitutes a significant improvement, although there remain significant deviations at intermediate $\mathbf{q}$ values. Finally, we have investigated the possibility to obtain the static response function at multiple wave vectors from a single QMC simulation. As predicted by the linear response theory, we found that the density response of the electron gas to a superposition of N_A external harmonic

perturbations is given by a linear combination of the responses to each of the perturbations. Unfortunately, however, this means that the linear response is valid only up to smaller perturbation amplitudes A as the system becomes increasingly inhomogeneous for multiple N_A. Thus, there is a trade-off between N_A and A, and applying a superposition of $N_A = 3$ perturbations is a reasonable strategy.

As mentioned in the Introduction, accurate QMC results for the static density response function—and, thus, for the static local field correction—are of high importance for contemporary warm dense matter research. Based on the findings of this work, the construction of a comprehensive set of QMC results for $\chi(\mathbf{q})$ over the entire relevant r_s range and temperatures $\theta \geqslant 0.5$ appears to be within reach. First and foremost, this will allow one to systematically benchmark previous approximate results for the warm dense UEG, such as STLS [86,87] (and "dynamic STLS" [89,90]), VS [87,91], or the recent improved LFC by Tanaka [92] that is based on the hypernetted chain equation, as well as semiempirical quantum classical mappings [93,94]. Furthermore, the construction of an accurate parametrization of $G(\mathbf{q}; r_s, \theta)$ with respect to r_s and θ at WDM conditions [95–97] is highly desirable due to its utility for, e.g., new DFT exchange-correlations functionals [22–24], the description of Thomson scattering experiments [26,27], and the construction of pseudopotentials [37–39]. Finally, accurate QMC results for the (weakly and strongly) inhomogeneous electron gas can be used as a highly needed benchmark for different exchange-correlation functionals that are used at WDM conditions [25,64,98–102].

[1] P.-F. Loos and P. M. W. Gill, The uniform electron gas, Comput. Mol. Sci. **6**, 410 (2016).

[2] G. Giuliani and G. Vignale, *Quantum Theory of the Electron Liquid* (Cambridge University Press, Cambridge, 2008).

[3] G. Baym and C. Pethick, *Landau Fermi-Liquid Theory: Concepts and Applications* (John Wiley & Sons, New York, 1991).

[4] D. Pines and D. Bohm, A collective description of electron interactions. II. Collective vs individual particle aspects of the interactions, Phys. Rev. **85**, 338 (1952).

[5] D. Bohm and D. Pines, A collective description of electron interactions. III. Coulomb interactions in a degenerate electron gas, Phys. Rev. **92**, 609 (1953).

[6] S. H. Vosko, L. Wilk, and M. Nusair, Accurate spin-dependent electron liquid correlation energies for local spin density calculations: A critical analysis, Can. J. Phys. **58**, 1200 (1980).

[7] J. P. Perdew and A. Zunger, Self-interaction correction to density-functional approximations for many-electron systems, Phys. Rev. B **23**, 5048 (1981).

[8] J. P. Perdew and Y. Wang, Pair-distribution function and its coupling-constant average for the spin-polarized electron gas, Phys. Rev. B **46**, 12947 (1992).

[9] P. Gori-Giorgi, F. Sacchetti, and G. B. Bachelet, Analytic static structure factors and pair-correlation functions for the unpolarized homogeneous electron gas, Phys. Rev. B **61**, 7353 (2000).

[10] P. Gori-Giorgi and J. P. Perdew, Pair distribution function of the spin-polarized electron gas: A first-principles analytic model for all uniform densities, Phys. Rev. B **66**, 165118 (2002).

[11] D. M. Ceperley, Ground state of the fermion one-component plasma: A Monte Carlo study in two and three dimensions, Phys. Rev. B. **18**, 3126 (1978).

[12] D. M. Ceperley and B. J. Alder, Ground State of the Electron Gas by a Stochastic Method, Phys. Rev. Lett. **45**, 566 (1980).

[13] G. Ortiz and P. Ballone, Correlation energy, structure factor, radial distribution function, and momentum distribution of the spin-polarized uniform electron gas, Phys. Rev. B **50**, 1391 (1994).

[14] G. Ortiz, M. Harris, and P. Ballone, Zero Temperature Phases of the Electron Gas, Phys. Rev. Lett. **82**, 5317 (1999).

[15] G. G. Spink, R. J. Needs, and N. D. Drummond, Quantum Monte Carlo study of the three-dimensional spin-polarized homogeneous electron gas, Phys. Rev. B **88**, 085121 (2013).

[16] W. Kohn and L. J. Sham, Self-consistent equations including exchange and correlation effects, Phys. Rev. **140**, A1133 (1965).

[17] R. O. Jones, Density functional theory: Its origins, rise to prominence, and future, Rev. Mod. Phys. **87**, 897 (2015).

[18] K. Burke, Perspective on density functional theory, J. Chem. Phys. **136**, 150901 (2015).

[19] A. A. Kugler, Theory of the local field correction in an electron gas, J. Stat. Phys. **12**, 35 (1975).

[20] K. S. Singwi, M. P. Tosi, R. H. Land, and A. Sjölander, Electron correlations at metallic densities, Phys. Rev. **176**, 589 (1968).

[21] P. Vashishta and K. S. Singwi, Electron correlations at metallic densities. V, Phys. Rev. B **6**, 875 (1972).

[22] D. Lu, Evaluation of model exchange-correlation kernels in the adiabatic connection fluctuation-dissipation theorem for inhomogeneous systems, J. Chem. Phys. **140**, 18A520 (2014).

[23] C. E. Patrick and K. S. Thygesen, Adiabatic-connection fluctuation-dissipation DFT for the structural properties of solids—The renormalized ALDA and electron gas kernels, J. Chem. Phys. **143**, 102802 (2015).

[24] A. Pribram-Jones, P. E. Grabowski, and K. Burke, Thermal Density Functional Theory: Time-Dependent Linear Response and Approximate Functionals from the Fluctuation-Dissipation Theorem, Phys. Rev. Lett. **116**, 233001 (2016).

[25] J. P. Perdew, K. Burke, and M. Ernzerhof, Generalized Gradient Approximation Made Simple, Phys. Rev. Lett. **77**, 3865 (1996).

[26] P. Neumayer, C. Fortmann, T. Döppner, P. Davis, R. W. Falcone, A. L. Kritcher, O. L. Landen *et al.*, Plasmons in

Strongly Coupled Shock-Compressed Matter, Phys. Rev. Lett. **105**, 075003 (2010).

[27] C. Fortmann, A. Wierling, and G. Röpke, Influence of local-field corrections on Thomson scattering in collision-dominated two-component plasmas, Phys. Rev. E **81**, 026405 (2010).

[28] K.-U. Plagemann, P. Sperling, R. Thiele, M. P. Desjarlais, C. Fortmann, T. Döppner, H. J. Lee, S. H. Glenzer, and R. Redmer, Dynamic structure factor in warm dense beryllium, New J. Phys. **14**, 055020 (2012).

[29] S. H. Glenzer and R. Redmer, X-ray Thomson scattering in high energy density plasmas, Rev. Mod. Phys. **81**, 1625 (2009).

[30] J. Vorberger, D. O. Gericke, Th. Bornath, and M. Schlanges, Energy relaxation in dense, strongly coupled two-temperature plasmas, Phys. Rev. E **81**, 046404 (2010).

[31] L. X. Benedict, M. P. Surh, L. G. Stanton, C. R. Scullard, A. A. Correa, J. I. Castor, F. R. Graziani *et al.*, Molecular dynamics studies of electron-ion temperature equilibration in hydrogen plasmas within the coupled-mode regime, Phys. Rev. E **95**, 043202 (2017).

[32] H. Reinholz, G. Röpke, S. Rosmej, and R. Redmer, Conductivity of warm dense matter including electron-electron collisions, Phys. Rev. E **91**, 043105 (2015).

[33] M. Veysman, G. Röpke, M. Winkel, and H. Reinholz, Optical Cconductivity of warm dense matter within a wide frequency range using quantum statistical and kinetic approaches, Phys. Rev. E **94**, 013203 (2016).

[34] G. Chabrier and A. Y. Potekhin, Equation of state of fully ionized electron-ion plasmas, Phys. Rev. E **58**, 4941 (1998).

[35] D. Kremp, M. Schlanges, and W.-D. Kraeft, *Quantum Statistics of Nonideal Plasmas* (Springer, Berlin, 2005).

[36] J. Vorberger, D. O. Gericke, and W.-D. Kraeft, The equation of state for hydrogen at high densities, High Energy Density Phys. **9**, 448 (2013).

[37] C. E. Starrett and D. Saumon, A simple method for eetermining the ionic structure of warm dense matter, High Energy Density Phys. **10**, 35 (2014).

[38] A. N. Souza, D. J. Perkins, C. E. Starrett, D. Saumon, and S. B. Hansen, Predictions of x-ray scattering spectra for warm dense matter, Phys. Rev. E **89**, 023108 (2014).

[39] G. Senatore, S. Moroni, and D. M. Ceperley, Local field factor and effective potentials in liquid metals, J. Non-Cryst. Solids **205–207**, 851 (1996).

[40] S. Gravel and N. W. Ashcroft, Nonlinear response theories and effective pair potentials, Phys. Rev. B **76**, 144103 (2007).

[41] S. Moroni, D. M. Ceperley, and G. Senatore, Static Response and Local Field Factor of the Electron Gas, Phys. Rev. Lett. **75**, 689 (1995).

[42] S. Moroni, D. M. Ceperley, and G. Senatore, Static Response from Quantum Monte Carlo Calculations, Phys. Rev. Lett. **69**, 1837 (1992).

[43] G. Sugiyama, C. Bowen, and B. J. Alder, Static dielectric response of charged bosons, Phys. Rev. B **46**, 13042 (1992).

[44] C. Bowen, G. Sugiyama, and B. J. Alder, Static dielectric response of the electron gas, Phys. Rev. B **50**, 14838 (1994).

[45] G. Senatore, S. Moroni, and D. M. Ceperley, Static response of homogeneous quantum fluids by diffusion Monte Carlo, in *Quantum Monte Carlo Methods in Physics and Chemistry*, M. P. Nightingale and C. J. Umrigar (eds.) (Springer, Berlin, 1998).

[46] M. Corradini, R. Del Sole, G. Onida, and M. Palummo, Analytical expressions for the local-field factor $G(q)$ and the exchange-correlation kernel $K_{xc}(r)$ of the homogeneous electron gas, Phys. Rev. B **57**, 14569 (1998).

[47] M. D. Knudson, M. P. Desjarlais, R. W. Lemke, T. R. Mattsson, M. French, N. Nettelmann, and R. Redmer, Probing the Interiors of the Ice Giants: Shock Compression of Water to 700 GPa and $3.8 \, g/cm^3$, Phys. Rev. Lett. **108**, 091102 (2012).

[48] B. Militzer *et al.*, A massive core in Jupiter predicted from first-principles simulations, Astrophys. J. **688**, L45 (2008).

[49] R. Ernstorfer *et al.*, The formation of warm dense matter: Experimental evidence for electronic bond hardening in gold, Science **323**, 1033 (2009).

[50] R. Nora, W. Theobald, R. Betti, F. J. Marshall, D. T. Michel, W. Seka, B. Yaakobi, M. Lafon, C. Stoeckl, J. Delettrez, A. A. Solodov, A. Casner, C. Reverdin, X. Ribeyre, A. Vallet, J. Peebles, F. N. Beg, and M. S. Wei, Gigabar Spherical Shock Generation on the OMEGA Laser, Phys. Rev. Lett. **114**, 045001 (2015).

[51] P. F. Schmit, P. F. Knapp, S. B. Hansen, M. R. Gomez, K. D. Hahn, D. B. Sinars, K. J. Peterson, S. A. Slutz, A. B. Sefkow, T. J. Awe, E. Harding, C. A. Jennings, G. A. Chandler, G. W. Cooper, M. E. Cuneo, M. Geissel, A. J. Harvey-Thompson, M. C. Herrmann, M. H. Hess, O. Johns, D. C. Lamppa, M. R. Martin, R. D. McBride, J. L. Porter, G. K. Robertson, G. A. Rochau, D. C. Rovang, C. L. Ruiz, M. E. Savage, I. C. Smith, W. A. Stygar, and R. A. Vesey, Understanding Fuel Magnetization and Mix Using Secondary Nuclear Reactions in Magneto-Inertial Fusion, Phys. Rev. Lett. **113**, 155004 (2014).

[52] O. A. Hurricane *et al.*, Inertially confined fusion plasmas dominated by alpha-particle self-heating, Nat. Phys. **12**, 800 (2016).

[53] A. L. Kritcher, T. Döppner, C. Fortmann, T. Ma, O. L. Landen, R. Wallace, and S. H. Glenzer, In-Flight Measurements of Capsule Shell Adiabats in Laser-Driven Implosions, Phys. Rev. Lett. **107**, 015002 (2011).

[54] F. Graziani, M. P. Desjarlais, R. Redmer, and S. B. Trickey, *Frontiers and Challenges in Warm Dense Matter* (Springer International, Switzerland, 2014).

[55] In Hartree atomic units, it holds $E_F = k_F^2/2$, with $k_F = (9\pi/4)^{1/3}/r_s$ being the Fermi wave vector.

[56] E. Y. Loh, J. E. Gubernatis, R. T. Scalettar, S. R. White, D. J. Scalapino, and R. L. Sugar, Sign problem in the numerical simulation of many-electron systems, Phys. Rev. B **41**, 9301 (1990).

[57] M. Troyer and U. J. Wiese, Computational Complexity and Fundamental Limitations to Fermionic Quantum Monte Carlo Simulations, Phys. Rev. Lett. **94**, 170201 (2005).

[58] D. M. Ceperley, Path integrals in the theory of condensed helium, Rev. Mod. Phys. **67**, 279 (1995).

[59] T. Dornheim, S. Groth, F. D. Malone, T. Schoof, T. Sjostrom, W. M. C. Foulkes, and M. Bonitz, *Ab Initio* auantum Monte Carlo simulation of the warm dense electron gas, Phys. Plasmas **24**, 056303 (2017).

[60] D. M. Ceperley, Fermion nodes, J. Stat. Phys. **63**, 1237 (1991).

[61] E. W. Brown, B. K. Clark, J. L. DuBois and D. M. Ceperley, Path-Integral Monte Carlo Simulation of the Warm Dense

Homogeneous Electron Gas, Phys. Rev. Lett. **110**, 146405 (2013).

[62] T. Schoof, S. Groth, J. Vorberger, and M. Bonitz, *Ab Initio* Thermodynamic Results for the Degenerate Electron Gas at Finite Temperature, Phys. Rev. Lett. **115**, 130402 (2015).

[63] T. Dornheim, S. Groth, T. Sjostrom, F. D. Malone, W. M. C. Foulkes, and M. Bonitz, *Ab Initio* Quantum Monte Carlo Simulation of the Warm Dense Electron Gas in the Thermodynamic Limit, Phys. Rev. Lett. **117**, 156403 (2016).

[64] S. Groth, T. Dornheim, T. Sjostrom, F. D. Malone, W. M. C. Foulkes, and M. Bonitz, *Ab initio* exchange-correlation free energy of the uniform electron gas at warm dense matter conditions, arXiv:1703.08074.

[65] T. Schoof, M. Bonitz, A. V. Filinov, D. Hochstuhl, and J.W. Dufty, Configuration path integral Monte Carlo, Contrib. Plasma Phys. **51**, 687 (2011).

[66] T. Schoof, S. Groth, and M. Bonitz, Towards *ab initio* thermodynamics of the electron gas at strong degeneracy, Contrib. Plasma Phys. **55**, 136 (2015).

[67] S. Groth, T. Schoof, T. Dornheim, and M. Bonitz, *Ab initio* quantum Monte Carlo simulations of the uniform electron gas without fixed nodes, Phys. Rev. B **93**, 085102 (2016).

[68] T. Dornheim, S. Groth, A. Filinov, and M. Bonitz, Permutation blocking path integral Monte Carlo: A highly efficient approach to the simulation of strongly degenerate non-ideal fermions, New J. Phys. **17**, 073017 (2015).

[69] T. Dornheim, T. Schoof, S. Groth, A. Filinov, and M. Bonitz, Permutation blocking path integral Monte Carlo approach to the uniform electron gas at finite temperature, J. Chem. Phys. **143**, 204101 (2015).

[70] T. Dornheim, S. Groth, T. Schoof, C. Hann, and M. Bonitz, *Ab initio* quantum Monte Carlo simulations of the uniform electron gas without fixed nodes: The unpolarized case, Phys. Rev. B **93**, 205134 (2016).

[71] L. M. Fraser, W. M. C. Foulkes, G. Rajagopal, R. J. Needs, S. D. Kenny, and A. J. Williamson, Finite-size effects and Coulomb interactions in quantum Monte Carlo calculations for homogeneous systems with periodic boundary conditions, Phys. Rev. B **53**, 1814 (1996).

[72] H. De Raedt and B. De Raedt, Applications of the generalized Trotter formula, Phys. Rev. A **28**, 3575 (1983).

[73] N. Metropolis, A. W. Rosenbluth, M. N. Rosenbluth, A. H. Teller, and E. Teller, Equation of state calculations by fast computing machines, J. Chem. Phys. **21**, 1087 (1953).

[74] M. Boninsegni, N. Prokof'ev, and B. Svistunov, Worm Algorithm for Continuous-Space Path Integral Monte Carlo Simulations, Phys. Rev. Lett. **96**, 070601 (2006).

[75] M. Boninsegni, N. V. Prokov'ev, and B. V. Svistunov, Worm algorithm and diagrammatic Monte Carlo: A new approach to continuous-space path integral Monte Carlo simulations, Phys. Rev. E **74**, 036701 (2006).

[76] M. Takahashi and M. Imada, Monte Carlo calculation of quantum systems, J. Phys. Soc. Jpn. **53**, 963 (1984).

[77] V. S. Filinov *et al.*, Thermodynamic properties and plasma phase transition in dense hydrogen, Contrib. Plasma Phys. **44**, 388 (2004).

[78] A. P. Lyubartsev, Simulation of excited states and the sign problem in the path integral Monte Carlo method, J. Phys. A: Math. Gen. **38**, 6659 (2005).

[79] S. A. Chin and C. R. Chen, Gradient symplectic algorithms for solving the Schrödinger equation with time-dependent potentials, J. Chem. Phys. **117**, 1409 (2002).

[80] K. Sakkos, J. Casulleras, and J. Boronat, High order Chin actions in path integral Monte Carlo, J. Chem. Phys. **130**, 204109 (2009).

[81] For completeness, we mention that the density response to a static perturbation is fully described by a static local field correction. This is in contrast to other static properties like the static structure factor or the interaction energy, for which the frequency integration over a dynamic local field correction is required.

[82] N.-H. Kwong and M. Bonitz, Real-Time Kadanoff-Baym Approach to Plasma Oscillations in a Correlated Electron Gas, Phys. Rev. Lett. **84**, 1768 (2000).

[83] K. Balzer and M. Bonitz, Nonequilibrium Green's functions approach to inhomogeneous systems, *Lecture Notes in Physics*, Vol. 867 (Springer, Heidelberg, 2013).

[84] J. Vorberger, Z. Donko, I. M. Tkachenko, and D. O. Gericke, Dynamic Ion Structure Factor of Warm Dense Matter, Phys. Rev. Lett. **109**, 225001 (2012).

[85] T. Ott, M. Bonitz, P. Hartmann, and Z. Donkó, Spontaneous generation of temperature anisotropy in a strongly coupled magnetized plasma, Phys. Rev. E **95**, 013209 (2017).

[86] S. Tanaka and S. Ichimaru, Thermodynamics and correlational properties of finite-temperature electron liquids in the Singwi-Tosi-Land-Sjölander approximation, J. Phys. Soc. Jpn. **55**, 2278 (1986).

[87] T. Sjostrom and J. Dufty, Uniform electron gas at finite temperatures, Phys. Rev. B **88**, 115123 (2013).

[88] A. A. Kugler, Bounds for some equilibrium properties of an electron gas, Phys. Rev. A **1**, 1688 (1970).

[89] H. Schweng and H. Böhm, Finite-temperature electron correlations in the framework of a dynamic local-field correction, Phys. Rev. B **48**, 2037 (1993).

[90] P. Arora, K. Kumar, and R. K. Moudgil, Spin-resolved correlations in the warm-dense homogeneous electron gas, Eur. Phys. J. B **90**, 76 (2017).

[91] W. Stolzmann and M. Rösler, Static local-field corrected dielectric and thermodynamic functions, Contrib. Plasma Phys. **41**, 203 (2001).

[92] S. Tanaka, Correlational and thermodynamic properties of finite-temperature electron liquids in the hypernetted-chain approximation, J. Chem. Phys. **145**, 214104 (2016).

[93] M. W. C. Dharma-wardana and F. Perrot, Simple Dlassical Mapping of the Spin-Polarized Quantum Electron Gas: Distribution Functions and Local-Field Corrections, Phys. Rev. Lett. **84**, 959 (2000).

[94] F. Perrot and M. W. C. Dharma-wardana, Spin-polarized electron liquid at arbitrary temperatures: Exchange-correlation energies, electron-distribution functions, and the static response functions, Phys. Rev. B **62**, 16536 (2000).

[95] K. Utsumi and S. Ichimaru, Dielectric formulation of strongly coupled electron liquids at metallic eensities. VI. Analytic expression for the local-field correction, Phys. Rev. A **26**, 603 (1982).

[96] B. Farid, V. Heine, G. E. Engel, and I. J. Robertson, Extremal properties of the Harris-Foulkes functional and an improved screening calculation for the electron gas, Phys. Rev. B **48**, 11602 (1993).

[97] G. Gregori, A. Ravasio, A. Höll, S. H. Glenzer, and S. J. Rose, Derivation of the static structure factor in strongly coupled non-equilibrium plasmas for x-ray scattering studies, High Energy Density Phys. **3**, 99 (2007).

[98] S. Groth, T. Dornheim, and M. Bonitz, Free energy of the uniform electron gas: Testing analytical models against first principle results, Contrib. Plasma Phys. **57**, 137 (2017).

[99] T. Sjostrom and J. Daligault, Gradient corrections to the exchange-correlation free energy, Phys. Rev. B **90**, 155109 (2014).

[100] V. V. Karasiev, J. W. Dufty, and S. B. Trickey, Climbing Jacob's ladder in the warm dense environment: Generalized gradient approximation exchange-correlation free-energy functional, arXiv:1612.06266.

[101] J. Heyd, G. E. Scuseria, and M. Ernzerhof, Hybrid functionals based on a screened Coulomb potential, J. Chem. Phys. **118**, 8207 (2003).

[102] V. V. Karasiev, L. Calderin, and S. B. Trickey, The importance of finite-temperature exchange-correlation for warm dense matter calculations, Phys. Rev. E **93**, 063207 (2016).

Configuration path integral Monte Carlo approach to the static density response of the warm dense electron gas

Simon Groth,[a)] Tobias Dornheim, and Michael Bonitz
Institut für Theoretische Physik und Astrophysik, Christian-Albrechts-Universität zu Kiel,
D-24098 Kiel, Germany

Precise knowledge of the static density response function (SDRF) of the uniform electron gas serves as key input for numerous applications, most importantly for density functional theory beyond generalized gradient approximations. Here we extend the configuration path integral Monte Carlo (CPIMC) formalism that was previously applied to the spatially uniform electron gas to the case of an inhomogeneous electron gas by adding a spatially periodic external potential. This procedure has recently been successfully used in permutation blocking path integral Monte Carlo simulations (PB-PIMC) of the warm dense electron gas [T. Dornheim *et al.*, Phys. Rev. E **96**, 023203 (2017)], but this method is restricted to low and moderate densities. Implementing this procedure into CPIMC allows us to obtain highly accurate finite temperature results for the SDRF of the electron gas at *high to moderate densities* closing the gap left open by the PB-PIMC data. In this paper, we demonstrate how the CPIMC formalism can be efficiently extended to the spatially inhomogeneous electron gas and present the first data points. Finally, we discuss finite size errors involved in the quantum Monte Carlo results for the SDRF in detail and present a solution how to remove them that is based on a generalization of ground state techniques. *Published by AIP Publishing.* https://doi.org/10.1063/1.4999907

I. INTRODUCTION

The uniform electron gas (UEG) is one of the most important model systems of quantum physics and chemistry.[1,2] It is composed of electrons embedded in a uniform positive background—to ensure charge neutrality. Thus, the UEG is well suited for thorough studies of physical effects induced by the long range Coulomb interaction of electrons in infinite quantum systems, such as collective excitations[3,4] or the emergence of superconductivity.[5] The equilibrium state of the UEG is commonly determined by three parameters: (1) the density (Brueckner) parameter $r_s = [3/(4\pi n)]^{1/3}/a_B$, with a_B being the Bohr radius and n, the total density of spin-up and spin-down electrons, $n = n^\uparrow + n^\downarrow$; (2) the degeneracy parameter $\theta = k_B T/E_F$, with the Fermi energy[6] E_F; and (3) the spin-polarization, $\xi = (n^\uparrow - n^\downarrow)/n$, where, in this work, we focus on the most relevant case $\xi = 0$, i.e., the unpolarized (paramagnetic) electron gas. Of particular current importance is the so-called "warm dense matter" regime[7] where the thermal energy is of the order of the Fermi energy ($\theta \sim 1$) while the densities are of the order of those found in solids ($r_s \sim 1$) or higher. Prominent examples for such extreme conditions are astrophysical applications,[9,10] dense quantum plasmas,[11–13] inertial confinement fusion experiments,[14–17] or laser or ion beam excited solids.[18,19]

The static density response function (SDRF), $\chi(\mathbf{q})$, governs the density response to an external harmonic excitation of low amplitude A and wave vector $\mathbf{q}$, $\phi_\mathbf{q}(\mathbf{r}) = 2A\cos(\mathbf{r}\cdot\mathbf{q})$,

$$\langle \hat{n}(\mathbf{r})\rangle_A - \langle \hat{n}(\mathbf{r})\rangle_0 = \chi(\mathbf{q})\,\phi_\mathbf{q}(\mathbf{r})\,.$$

The SDRF (or longitudinal polarization function[11]) is closely related to the static limit of the dielectric function and contains a wealth of information on the correlations and collective properties. Therefore, the SDRF is a key property of any correlated many-body system, for details, see Sec. II A.

In particular, the SDRF of the UEG at warm dense matter conditions constitutes a key ingredient for finite temperature density functional theory[7,8] (FTDFT) simulations within the adiabatic-connection fluctuation-dissipation formulation,[20–22] the currently most promising way to improve DFT beyond the wide-spread generalized gradient approximation[23,24] and thereby enhance its predictive capabilities. In addition, the SDRF of the UEG can be used to directly compute the dynamic structure factor within the Born-Mermin-approach,[25–28] which is nowadays routinely measured for systems at warm dense matter conditions via X-ray Thomson scattering experiments. Moreover, knowledge of the exact SDRF of the UEG is highly useful for the computation of energy transfer rates,[29,30] electrical conductivity,[31] as well as for the construction of effective potentials.[32–35]

In the ground state, *ab initio* results for the SDRF,[36–40] including a subsequent parametrization over a wide range of densities,[41] have been obtained long ago via diffusion Monte Carlo simulations of the UEG subject to a weak periodic perturbation. However, even though the UEG effectively represents a one-component system, its simulation at warm dense matter conditions is highly challenging due to the fermion sign problem[42,44] (FSP), which is particularly severe at finite temperature (cf. Sec. II B for a detailed discussion of the FSP).

---
a)Electronic mail: groth@theo-physik.uni-kiel.de

Within the last years, significant progress in this field could be achieved[45–49] via the introduction of two novel quantum Monte Carlo (QMC) methods, which excel at complementary parameter regimes: permutation blocking path integral Monte Carlo (PB-PIMC)[50–52] is most efficient at low densities and strong coupling, whereas the configuration path integral Monte Carlo (CPIMC) approach[53–56] has no FSP at high densities, i.e., at weak coupling. Only recently, the PB-PIMC approach has been used to compute the first *ab initio* results for the SDRF of the strongly coupled UEG at finite temperature.[57] However, these results are limited to density parameters of the order of $r_s = 1$ and larger and cannot access the important regime of higher densities.

Therefore, in this work, we turn to the complementary CPIMC approach[53] to compute the SDRF of the high density warm electron gas. This means, we extend the CPIMC formalism from the homogeneous to the inhomogeneous electron gas such that it allows for the exact inclusion of a (in principle arbitrarily strong) periodic external potential. This allows us to obtain the first *ab initio* data for the SDRF in the high-density regime ($r_s = 0.5$; 1, $0.0625 \leq \Theta \leq 1$) and opens the way for systematic studies in the near future.

Moreover, since the simulations are restricted to finite systems with a few tens of electrons in a finite simulation volume V, we provide a detailed discussion of and a highly efficient solution to the problem of finite size errors involved in the SDRF. This is crucial because one is actually interested in the thermodynamic limit (TDL) properties, $N \to \infty$ at $N/V = $ const. Finally, we compare our exact result for the SDRF in the TDL with dielectric approaches such as the random phase approximation and the self-consistent scheme proposed by Singwi, Tosi, Land, and Sjölander (STLS).[58,59]

This paper is structured as follows: in Sec. II A, we briefly discuss the model Hamiltonian of the inhomogeneous electron gas and the basic linear response equations that are utilized for the computation of the SDRF. Thereafter, Sec. II B continues with a detailed introduction to the general quantum Monte Carlo approach including the origin and consequences of the FSP, followed by the generalization of the CPIMC formalism to the inhomogeneous electron gas in Secs. II C and II D. We proceed with a discussion of the CPIMC results for the SDRF of the ideal and non-ideal electron gas in Secs. III A and III B. In Sec. III C, finite size errors are investigated in detail, and an effective solution is presented to obtain the exact SDRF in the TDL from CPIMC simulations.

II. THEORETICAL BASIS OF THE CPIMC APPROACH TO THE INHOMOGENEOUS ELECTRON GAS

A. Linear response theory of the uniform electron gas

The model system of the unperturbed UEG consists of N electrons in a finite volume $V = L^3$ subject to periodic boundary conditions, where a positive homogeneous background is assumed to ensure charge neutrality. The Hamiltonian of this system in Hartree atomic units reads

$$\hat{H}_0 = -\frac{1}{2}\sum_{i=1}^{N} \nabla_i^2 + \frac{1}{2}\sum_{i=1}^{N}\sum_{j\neq i}^{N} \Psi_E(\mathbf{r}_i, \mathbf{r}_j) + \frac{N}{2}\xi_M, \quad (1)$$

with $\Psi_E(\mathbf{r}, \mathbf{s})$ being the Ewald pair potential and ξ_M the Madelung constant, see, e.g., Ref. 60. For the purpose of computing the SDRF of the UEG, we apply a weak periodic external potential of the form[36–40]

$$\hat{H}_{ext}(A) = \sum_{i=1}^{N} 2A \cos(\hat{\mathbf{r}}_i \cdot \mathbf{q}), \quad (2)$$

with $\mathbf{q} = \frac{2\pi}{L}\mathbf{m}, \mathbf{m} \in \mathbb{Z}^3$ so that the (total) perturbed Hamiltonian is given by

$$\hat{H}_A = \hat{H}_0 + \hat{H}_{ext}(A). \quad (3)$$

In the linear response regime, i.e., for sufficiently small amplitudes A, the induced density modulation is entirely determined by the SDRF[2] χ,

$$\langle \hat{n}(\mathbf{r})\rangle_A - \langle \hat{n}(\mathbf{r})\rangle_0 = \chi(\mathbf{q})\, 2A \cos(\mathbf{r} \cdot \mathbf{q}), \quad (4)$$

where $\langle \hat{n}(\mathbf{r})\rangle_0 = n_0 = \frac{N}{V}$ is the electron density of the unperturbed UEG. Hence, one may obtain $\chi(\mathbf{q})$ by computing the expectation value of the density operator $\hat{n}(\mathbf{r}) = \sum_{i=1}^{N}\delta(\mathbf{r} - \hat{\mathbf{r}}_i)$ in the perturbed system and then fit the RHS of Eq. (4) to the LHS (see, e.g., Ref. 57). However, it turns out to be more convenient to compute χ directly from the Fourier transform of the density operator $\hat{\rho}_\mathbf{q} = \frac{1}{V}\sum_{i=1}^{N} e^{-i\mathbf{q}\mathbf{r}_i}$ via the well-known relation[2,39]

$$\chi(\mathbf{q}) = \frac{1}{A}\langle \hat{\rho}_\mathbf{q}\rangle_A. \quad (5)$$

In practice, we carry out several simulations for different amplitudes A of the external field and then perform a linear fit to $\langle \hat{\rho}_\mathbf{q}\rangle_A$ in dependence of A where the resulting slope is χ.

B. Path integral Monte Carlo and the fermion sign problem

Throughout this work, we are interested in the computation of thermodynamic expectation values in the canonical ensemble, i.e., at fixed electron number N, volume V, and temperature T. For this task, path integral Monte Carlo (PIMC) methods have proven to be a very powerful tool. The general idea of all existing PIMC approaches is to find a suitable expansion of the partition function of the form

$$Z = \text{Tr} e^{-\beta \hat{H}} = \sum_C W(C), \quad (6)$$

where $\beta = 1/k_B T$ and C denotes some high-dimensional multi-variable with an associated weight $W(C) \in \mathbb{R}$ that is readily evaluated. In the context of QMC, we commonly refer to C as being a configuration. Given some concrete expansion of Z, thermodynamic expectation values of an arbitrary observable $\hat{O}$ are written as

$$\langle \hat{O}\rangle = \frac{1}{Z}\sum_C O(C) W(C), \quad (7)$$

with $O(C)$ being the so-called estimator. If the weight function is strictly positive for all configurations, $W(C) > 0 \,\forall\, C$, such expressions can be efficiently computed via the Metropolis algorithm.[61] The strength of this algorithm is that it allows us to randomly sample configurations $\{C_0, C_1, \ldots, C_{N_C}\}$ with the correct probability $P(C) = \frac{1}{Z}W(C)$ without knowing the

normalization constant Z. Starting from some initial configuration C_0 this is achieved by proposing a transition from C_i to some randomly chosen C' and accepting this change, i.e., setting $C_{i+1} = C'$, with the probability

$$A(C \rightarrow C') = \min \left\{ 1, \frac{W(C')}{W(C)} \right\}. \qquad (8)$$

Having properly sampled the configurations in the described way, an asymptotically exact estimator of the expectation value Eq. (7) is immediately given by the average

$$\langle \hat{O} \rangle = \lim_{N_C \rightarrow \infty} \frac{1}{N_C} \sum_{i=1}^{N_C} O(C_i). \qquad (9)$$

In practice, we are of course restricted to a finite number of sampled configurations C_i so that the results are generally afflicted with a statistical uncertainty that can, in principle, be made arbitrarily small by increasing the computation time [see Eq. (14)]. Therefore, one may refer to Monte Carlo methods as being "quasi-exact."

However, to this day, there exists no exact expansion of the form Eq. (6) for generic fermionic quantum systems with a strictly positive weight function, and hence, it cannot be interpreted as a probability. To nevertheless utilize the Metropolis algorithm, one can circumvent this issue by defining a modified (artificial) partition function

$$Z' = \sum_C |W(C)| \qquad (10)$$

and rewrite the expectation values as

$$\langle O \rangle = \frac{\langle Os \rangle'}{\langle s \rangle'}, \qquad (11)$$

where $s = \text{sign}(W)$ so that

$$\langle s \rangle' = \frac{1}{Z'} \sum_C \text{sign}(W)|W(C)| = \frac{Z}{Z'} \qquad (12)$$

is simply the average sign of all sampled configurations in the modified configuration space. It is easy to see that the relative statistical uncertainty of expectation values computed in this way is inversely proportional to the average sign. Further, with $Z = e^{-\beta N f}$, where f is the free energy per particle, it is

$$\langle s \rangle' = e^{-\beta N(f - f')}. \qquad (13)$$

Consequently, the relative statistical error of observables grows exponentially with the particle number N and the inverse temperature β, while it can only be reduced with the square root of the number of generated samples N_C (see, e.g., Ref. 43),

$$\frac{\Delta O}{\langle O \rangle} \sim \frac{1}{\sqrt{N_C}} e^{\beta N(f - f')}. \qquad (14)$$

This is the manifestation of the well-known fermion sign problem, which causes the simulation of fermions to be a highly demanding task even in thermodynamic equilibrium. Moreover, the sign problem may even be NP-hard.[44] However, this has only been shown for a small subclass of Hamiltonians not subject to this paper.

In the standard PIMC approach,[62] the utilized expansion of the partition function is obtained by evaluating the trace in Eq. (6) in coordinate representation, leading to configurations

C that can be interpreted as paths or trajectories of all N particles in imaginary time. In this formulation, the required antisymmetrization of the density operator to correctly account for the Fermi statistics is the source of the sign changes in the weight function, and hence, of the FSP itself. Fortunately, the permutation blocking PIMC (PB-PIMC) method,[50–52] developed by one of us, significantly reduces the FSP through a sophisticated rewriting of the partition function whereby paths with a different sign are combined into a single configuration. However, due to the formulation in coordinate representation, the PB-PIMC approach excels at strong coupling but still suffers from an increasing FSP towards lower temperature, preventing simulations of the UEG below half the Fermi temperature.

An alternative strategy, which is pursued in this paper, is given by the configuration path integral Monte Carlo (CPIMC) approach.[53–56] In contrast to standard PIMC, this method is formulated in Fock-space, which leads to a FSP that is complementary to that of PB-PIMC: there is no sign problem at all for the ideal fermi gas but the FSP increases with coupling. For this reason, CPIMC has been highly valuable regarding the simulation of the (unperturbed) UEG at densities $r_s \lesssim 1$, practically across the entire relevant temperature range.[55] In Sec. II C, the CPIMC formalism will be generalized to the perturbed (inhomogeneous) electron gas described by the Hamiltonian Eq. (3).

C. CPIMC approach to the inhomogeneous electron gas

For the CPIMC formulation of the electron gas, we switch to second quantization with respect to plane wave spin orbitals $\langle \mathbf{r}\sigma \, |\mathbf{k}_i \sigma_i \rangle = \frac{1}{L^{3/2}} e^{i\mathbf{k}_i \cdot \mathbf{r}} \delta_{\sigma,\sigma_i}$ with $\mathbf{k} = \frac{2\pi}{L}\mathbf{m}$, $\mathbf{m} \in \mathbb{Z}^3$, and $\sigma_i \in \{\uparrow, \downarrow\}$. The N-particle states are then given by Slater determinants in Fock space

$$|\{n\}\rangle = |n_1, n_2, \ldots\rangle, \qquad (15)$$

with the fermionic occupation number $n_i \in \{0, 1\}$ of the ith plane wave spin-orbital naturally satisfying $\sum_i n_i = N$. In this representation, the Hamiltonian is expressed in terms of the creation ($\hat{a}_i^\dagger$) and annihilation ($\hat{a}_i$) operators, which, when acting on the states [Eq. (15)], create or annihilate a particle in the spin-orbital i. These operators satisfy the usual fermionic anti-commutation relations, thereby automatically incorporating the correct Fermi statistics. The UEG Hamiltonian Eq. (1) takes the explicit form[2]

$$\hat{H}_0 = \frac{1}{2} \sum_i \mathbf{k}_i^2 \hat{a}_i^\dagger \hat{a}_i + \sum_{\substack{i<j, k<l \\ i \neq k, j \neq l}} w_{ijkl}^- \hat{a}_i^\dagger \hat{a}_j^\dagger \hat{a}_l \hat{a}_k + N\frac{\xi_M}{2}, \qquad (16)$$

with the antisymmetrized two-electron integrals $w_{ijkl}^- = w_{ijkl} - w_{ijlk}$, where

$$w_{ijkl} = \frac{4\pi e^2}{L^3 (\mathbf{k}_i - \mathbf{k}_k)^2} \delta_{\mathbf{k}_i + \mathbf{k}_j, \mathbf{k}_k + \mathbf{k}_l} \delta_{\sigma_i, \sigma_k} \delta_{\sigma_j, \sigma_l}. \qquad (17)$$

Likewise, for the external potential Eq. (2), we have

$$\hat{H}_{\text{ext}} = \sum_{i \neq j} a_{ij} \hat{a}_i^\dagger \hat{a}_i, \qquad (18)$$

with the corresponding one-electron integrals

$$a_{ij} = A\delta_{\sigma_i \sigma_j} (\delta_{\mathbf{k}_j - \mathbf{k}_i, \mathbf{q}} + \delta_{\mathbf{k}_j - \mathbf{k}_i, -\mathbf{q}}). \qquad (19)$$

The main idea of CPIMC is to split the total Hamiltonian into an off-diagonal ($\hat{Y}$) and diagonal part ($\hat{D}$) with respect to the Fock states, Eq. (15), so that $\hat{H}_A = \hat{H}_0 + \hat{H}_{\text{ext}} = \hat{D} + \hat{Y}$. The matrix elements of these operators are readily computed according to the well-known Slater-Condon rules[53]

$$D_{\{n\}} = \frac{1}{2} \sum_l \mathbf{k}_l^2 n_l + \frac{1}{2} \sum_{l<k} w^-_{lklk} n_l n_k, \tag{20}$$

$$Y_{\{n\},\{\bar{n}\}} = \begin{cases} a_{ij}(-1)^{\alpha_{\{n\},pq}}, & \{n\} = \{\bar{n}\}^p_q \\ w^-_{pqrs}(-1)^{\alpha_{\{n\},pq}+\alpha_{\{\bar{n}\},rs}}, & \{n\} = \{\bar{n}\}^{p<q}_{r<s} \end{cases}$$

with the fermionic phase factor

$$\alpha_{\{n\},pq} = \sum_{l=\min(p,q)+1}^{\max(p,q)-1} n_l. \tag{21}$$

The notation $\{n\}^p_q$ describes an excitation from an occupied orbital q to a free orbital p in the state $|\{n\}\rangle$. Hence, we observe that there are only two possibilities for non-vanishing off-diagonal elements: the states $|\{n\}\rangle$ and $|\{\bar{n}\}\rangle$ can differ in either exactly two (pq) or four orbitals ($pqrs$). This is a direct consequence of the fact that the Hamiltonian only contains strings of two or four creation and annihilation operators. For completeness, we mention that for the general case of an arbitrary system Hamiltonian, there is an additional contribution to the off-diagonal elements where $\{n\} = \{\bar{n}\}^p_q$,

$$Y_{\{n\},\{\bar{n}\}} = \sum_{\substack{i=0 \\ i \neq p,q}} w^-_{ipiq} n_i (-1)^{\alpha_{\{n\},pq}}. \tag{22}$$

For the electron gas, this contribution vanishes since here the two-particle integrals with only two equal indices are always zero due to the Kronecker delta in Eq. (17), which ensures that the total momentum of the two particles before and after the excitation is conserved.

After having split the Hamiltonian into its diagonal and off-diagonal part, we switch to the interaction picture in imaginary time with respect to $\hat{D}$ and make use of the identity,

$$e^{-\beta\hat{H}} = e^{-\beta\hat{D}} \hat{T}_\tau e^{-\int_0^\beta \hat{Y}(\tau)d\tau},$$
$$\hat{Y}(\tau) = e^{\tau\hat{D}} \hat{Y} e^{-\tau\hat{D}}, \tag{23}$$

with $\hat{T}_\tau$ being the time-ordering operator. Plugging this identity into Eq. (6) and computing the trace using the Slater determinants, Eq. (15), finally yields[53]

$$Z = \sum_{\substack{K=0, \\ K \neq 1}}^{\infty} \sum_{\{n\}} \sum_{s_1 \dots s_{K-1}} \int_0^\beta d\tau_1 \int_{\tau_1}^\beta d\tau_2 \dots \int_{\tau_{K-1}}^\beta d\tau_K$$
$$\times (-1)^K e^{-\sum_{i=0}^K D_{\{n^{(i)}\}}(\tau_{i+1}-\tau_i)} \times \prod_{i=1}^K Y_{\{n^{(i)}\},\{n^{(i-1)}\}}(s_i). \tag{24}$$

Here, we have introduced the multi-index s_i which defines the two or four orbitals in which the states $|\{n^{(i)}\}\rangle$ and $|\{n^{(i-1)}\}\rangle$ differ, i.e., $s_i = (pq)$ or $s_i = (pqrs)$. Further, all non-vanishing contributions in Eq. (24) obey the condition $\{n\} = \{n^{(0)}\} = \{n^{(K)}\}$. This way we have transformed the partition function, Eq. (6), into an exact infinite perturbation expansion with respect to the off-diagonal part of the Hamiltonian.

Comparing Eq. (24) with Eq. (6), we straightforwardly identify the multi-variable C of each configuration contributing to the partition function,

$$C = (K, \{n\}, s_1, \dots, s_{K-1}, \tau_1, \dots, \tau_K) \tag{25}$$

with the corresponding weight function

$$W(C) = (-1)^K e^{-\sum_{i=0}^K D_{\{n^{(i)}\}}(\tau_{i+1}-\tau_i)} \prod_{i=1}^K Y_{\{n^{(i)}\},\{n^{(i-1)}\}}(s_i). \tag{26}$$

Each configuration C can be visualized as a β−periodic "path in imaginary time." But in contrast to standard PIMC which is formulated in coordinate space, here the path proceeds in Fock space and can be understood as follows: starting from an initial set of occupation numbers $\{n\}$ at $\tau_0 = 0$, one subsequently applies one- or two-particle excitations at times τ_i, where the involved orbitals are defined by the multi-index s_i. An example of a typical path for a system of $N = 3$ particles is shown in Fig. 1.

According to the number of involved orbitals, we refer to one- and two-particle excitations as "kinks" of type 2 and 4, respectively. Hence, in CPIMC, one randomly samples all possible closed paths with their associated weight, i.e., the modulus of Eq. (26), and computes observables via Eq. (11). This is achieved by a highly complex set of Monte Carlo steps in which one proposes to add, remove, and change a single kink or pairs of kinks and accept or reject those changes with the Metropolis acceptance probability Eq. (8). Starting from an initial path without kinks, one can propose three changes: (1) one can simply excite a whole occupied orbital (from $\tau = 0$ to $\tau = \beta$), which is illustrated in Fig. 2. (2) One can propose to add a pair of type 2 kinks or (3) a pair of type 4 kinks via a one- or two-particle excitation (see Fig. 3). Adding a single kink is not possible since this would violate the condition of β-periodicity, $\{n^{(0)}\} = \{n^{(K)}\}$.

Once one has successfully added a pair of kinks, one can also add a single kink by changing another. A careful analysis reveals that there are in total 14 elementary diagrams for adding
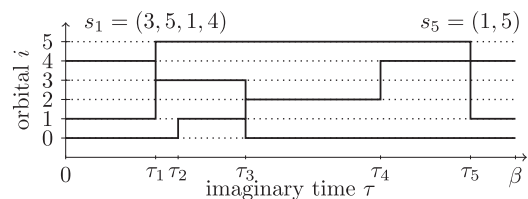

FIG. 1. Typical "path" in a CPIMC simulation of $N = 3$ particles: the starting Slater determinant at time $\tau_0 = 0$ with the set of occupation numbers $\{n\} = \{110010\dots\}$ undergoes five different one- or two-particle excitations of type s_i at times τ_i, $i = 1\dots5$.
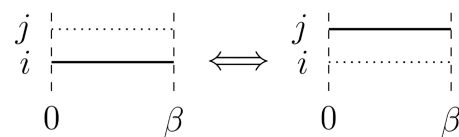

FIG. 2. Diagram for exciting a whole occupied orbital i (from $\tau = 0$ to $\tau = \beta$) to an unoccupied orbital j.
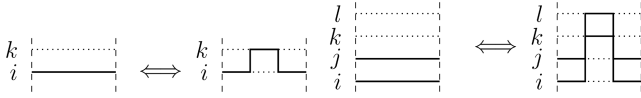
FIG. 3. Diagrams for adding a pair of type 2 (top) or type 4 kinks (bottom) via a one- or two-particle excitation, respectively.

a single kink via a one- or two-particle excitation, which are all depicted in Fig. 13 in the Appendix. Naturally, to maximize the efficiency of the CPIMC simulation, one only proposes to add such kinks that are associated with a non-vanishing off-diagonal matrix element, Eq. (20), i.e., which have a non-vanishing one- or two-electron integral. For example, when randomly choosing the two orbitals q and p for a one-particle excitation, one ensures that $|\mathbf{k}_p - \mathbf{k}_q| = |\mathbf{q}|$ with $\mathbf{q}$ being the wave vector of the periodic external potential, Eq. (18). Likewise, whenever proposing to add a type 4 kink one makes sure that momentum conservation is fulfilled.

Finally, we point out that the major difference between the previous CPIMC formulation for the (unperturbed) UEG[54] and the present extension to the inhomogeneous electron gas lies in the occurrence of type 2 kinks (one-particle excitations), which are solely induced by the one-particle matrix elements a_{ij} of the external potential in Eq. (20). In the case of the UEG, $a_{ij} = 0$, and hence, there are only momentum conserving type 4 kinks. This causes a large simplification of the algorithm since the 14 elementary diagrams of adding a single kink (see Fig. 13) reduce to only three, i.e., those containing solely type 4 kinks.

D. CPIMC estimator for the static response function

To compute the SDRF with CPIMC via Eq. (5), we need to derive an estimator for the Fourier transform of the density operator, $\hat{\rho}_\mathbf{q}$, in correspondence to the CPIMC expansion of the partition function Eq. (24), i.e., we have to write its expectation value in the form of Eq. (7). Taking into account that $\langle \hat{\rho}_{-\mathbf{q}} \rangle = \langle \hat{\rho}_\mathbf{q} \rangle$, its second quantization representation is given by

$$\langle \hat{\rho}_\mathbf{q} \rangle = \frac{1}{2V} \sum_{i \neq j} \delta_{\sigma_i \sigma_j} (\delta_{\mathbf{k}_j - \mathbf{k}_i, \mathbf{q}} + \delta_{\mathbf{k}_j - \mathbf{k}_i, -\mathbf{q}}) \langle \hat{a}_i^\dagger \hat{a}_j \rangle, \quad (27)$$

and we immediately see that it can be computed directly from the off-diagonal elements of the one-particle density matrix $\langle \hat{a}_p^\dagger \hat{a}_q \rangle$. An estimator for these elements is readily obtained by using the relation

$$\langle \hat{a}_p^\dagger \hat{a}_q \rangle = \frac{1}{Z} \text{Tr} \left\{ \hat{a}_p^\dagger \hat{a}_q e^{-\beta \hat{H}} \right\} = -\frac{1}{\beta} \frac{1}{Z} \frac{\partial Z}{\partial a_{pq}}, \quad (28)$$

and carrying out the derivative with the CPIMC expansion of the partition function, Eq. (24). This yields

$$\langle \hat{a}_p^\dagger \hat{a}_q \rangle = \frac{1}{Z} \sum_C \left(-\frac{1}{\beta} \sum_{i=1}^K \frac{1}{a_{pq}} \delta_{s_i,(pq)} \right) W(C), \quad (29)$$

where the abbreviation

$$\sum_C := \sum_{\substack{K=0, \\ K \neq 1}}^\infty \sum_{\{n\}} \sum_{s_1 \dots s_{K-1}} \int_0^\beta d\tau_1 \int_{\tau_1}^\beta d\tau_2 \dots \int_{\tau_{K-1}}^\beta d\tau_K \quad (30)$$

has been used. By inserting Eqs. (29) and (19) into (27), the estimator reduces to

$$\langle \hat{\rho}_\mathbf{q} \rangle = \frac{1}{Z} \sum_C \left(-\frac{1}{2V\beta} \sum_{i=1}^K \frac{1}{A} \delta_{s_i, s\,\text{T2}} \right) W(C), \quad (31)$$

where $\delta_{s_i, s\,\text{T2}}$ ensures that only those kinks contribute which are of type 2. Simply speaking, we just have to average over the number of type 2 kinks in all sampled paths and divide by $-2V\beta A$.

III. CPIMC SIMULATION RESULTS

A. Ideal electron gas

Besides being highly valuable for the finite size correction of the SDRF discussed in Sec. III C, the ideal Fermi system constitutes the natural first test case for CPIMC due to its formulation as an exact perturbation expansion in second quantization. It is realized by setting all two-particle matrix elements Eq. (17) to zero. In the case of the (unperturbed) UEG there are, consequently, no kinks at all so that the weight function [Eq. (26)] is always positive, meaning that the average sign is always one. However, in simulations of the perturbed ideal electron gas, the sampled paths contain type 2 kinks induced by the external field, where each of them may cause up to two sign changes in the weight function Eq. (26) through: (1) the factor $(-1)^K$ and (2) the phase factor Eq. (21) occurring in its matrix element Eq. (20). Yet, the average sign still remains unity. This is because in the absence of type 4 kinks, type 2 kinks can only be added and removed in symmetric pairs as shown in Fig. 3—this is a simple consequence of the fact that all type 2 kinks $s = (pq)$ must fulfill $|\mathbf{k}_p - \mathbf{k}_q| = |\mathbf{q}|$. The induced sign changes of such pairs exactly compensate each other so that the strict positive definiteness of the weight function remains preserved, and hence, the FSP remains absent, in striking contrast to standard PIMC in coordinate space.

As a first demonstration, we perform CPIMC simulations of the unpolarized ideal electron gas at $r_s = 1$ with $N = 4$ particles for different amplitudes A of the external field with a wave vector $\mathbf{q} = \frac{2\pi}{L}(1, 0, 0)^\text{T}$. Figure 4 shows the results for the induced density $\langle \hat{\rho}_\mathbf{q} \rangle$ (top) and the average number of type 2 kinks (bottom) in dependence of the amplitude for two different temperatures $\theta = 0.0625$ (left) and $\theta = 1$ (right). As a cross-check, the dotted black line has been computed from the unperturbed ideal UEG according to Eq. (40) as discussed in Sec. III C. In the linear response regime, both results must coincide, which is observed for $A \lesssim 0.2$ at $\theta = 0.0625$, while at $\theta = 1$ the linear response regime remains valid for much larger amplitudes, i.e., up to $A \sim 0.5$. This behaviour is also reflected in the average number of type 2 kinks for the same amplitude which is reduced by about two orders of magnitude at $\theta = 1$ compared to $\theta = 0.0625$. Interestingly, in both cases, the linear regime is reached where $\langle K_{\text{T2}} \rangle \lesssim 1$. In addition, since the next order beyond the linear regime is given by the cubic response function[37] $\chi^{(3)}$, we also perform a cubic fit (blue line) of the form

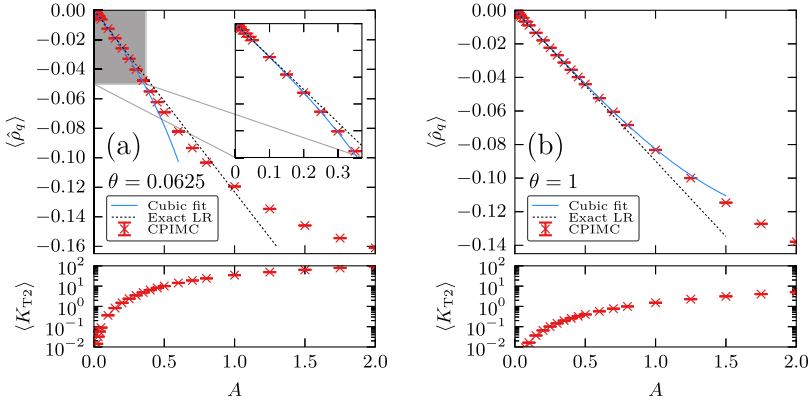$$\langle \hat{\rho}_q \rangle = \chi(q) A + \chi^{(3)}(q) A^3 \quad (32)$$

FIG. 4. Top panels: Dependence of the induced density $\langle \hat{\rho}_q \rangle$ for $\mathbf{q} = \frac{2\pi}{L}(1,0,0)^T$ on the amplitude of the external field. Shown are CPIMC results (red crosses) for the ideal electron gas with $N = 4$ electrons at $r_s = 1$ for two different temperatures: (a) $\theta = 0.0625$ and (b) $\theta = 1$ (right). The blue curve represents a fit of Eq. (32) to the CPIMC data. The black dotted line corresponds to the exact LR behavior computed from Eq. (40). Bottom panels: Dependence of the average number of type 2 kinks on the amplitude of the external field.

to the CPIMC data up to $A = 0.25$, for $\theta = 0.0625$ and $A = 0.5$, for $\theta = 1$, respectively. Clearly, also the cubic regime remains valid for much larger amplitudes at higher temperatures.

B. Interacting electron gas

Next, we perform the same CPIMC simulations for the interacting system (identical system parameters) as for the ideal case discussed in Sec. III A. The results are shown in Fig. 5 where a linear fit (dotted black) and a cubic fit (solid blue) to the CPIMC data are depicted. For these parameters, we observe that the range of amplitudes for which the linear and cubic response regimes are valid is similar to that found for the ideal system. This is because the response of $N = 4$ particles at $r_s = 1$ is comparable to that of the ideal system (grey line). In addition, in the bottom panels, the average number of type 4 kinks (green curve) is depicted, which are induced solely by the Coulomb interaction and which cause the average sign (orange curve) to deviate from one. In the linear regime, the dependence of the number of type 4 kinks on the amplitude is negligible.

However, for larger values of A not only the average number of type 2 kinks becomes very large but also the number of type 4 kinks increases significantly. The main reason for this behavior is the substantial increase of the configuration space with increasing amplitude. In particular, at $\theta = 0.0625$ (left graphic) the average sign drops below 10^{-3} at $A > 1$ and,

according to Eq. (14), the statistical error of the corresponding CPIMC results is clearly enhanced. As a further cross-check of the correctness of the presented algorithm, at $\theta = 1$ we also compare with the PB-PIMC method (green diamonds), which are in perfect agreement with CPIMC, as expected.

In Fig. 6, a similar investigation is carried out for a larger system containing $N = 14$ electrons at $r_s = 0.5$ and $\theta = 0.5$. For these system parameters, the average sign (orange curve in the bottom panel) does not drop below 0.1, even up to values of the amplitude $A \sim 1.5$. Thus, very precise CPIMC results for the induced density can be obtained. In comparison to the smaller system of $N = 4$ electrons in Fig. 5, the linear response regime is valid up to about twice as large amplitudes so that the SDRF χ, given by the slope of the linear fit (dotted black line), can be obtained with a relative accuracy of up to 0.02%. Further, we observe that the average number of type 2 kinks $\langle K_{T2} \rangle$ (red curve in the bottom panel) is significantly larger than one for amplitudes $A > 1.5$, and still, the deviation from the LR behaviour is only minor. Recalling that, for the smaller $N = 4$ system in Fig. 5, the LR regime is valid for $\langle K_{T2} \rangle \lesssim 1$, we conclude that the average number of type 2 kinks alone is not a reliable indicator for the validity of the linear response regime.

When further increasing the system size to $N = 20$, while keeping the density and degeneracy parameters unchanged at $r_s = 0.5$ and $\theta = 0.5$, the CPIMC simulations become significantly more demanding. This is demonstrated in Fig. 7,
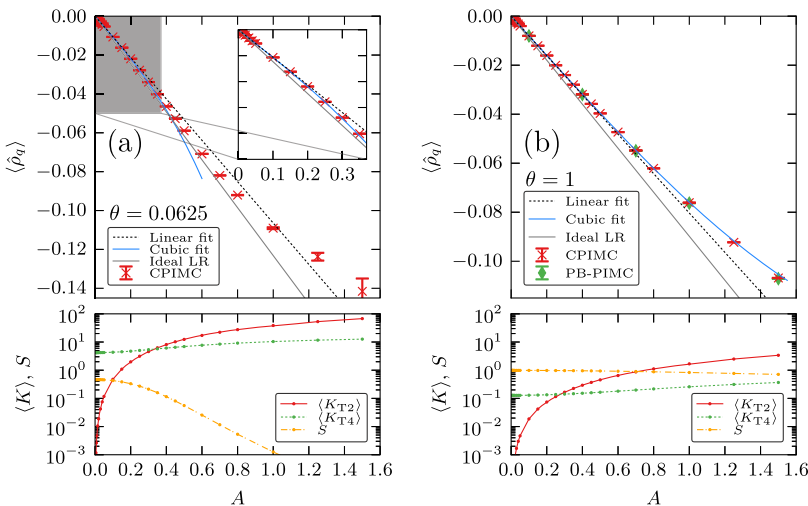

FIG. 5. Top panels: Dependence of the induced density $\langle \hat{\rho}_q \rangle$ for $\mathbf{q} = \frac{2\pi}{L}(1,0,0)^T$ on the amplitude of the external field. Shown are CPIMC results (red crosses) for the interacting electron gas with $N = 4$ electrons at $r_s = 1$ for two different temperatures: (a) $\theta = 0.0625$ and (b) $\theta = 1$. The blue (black dotted) curve represents a cubic (linear) fit [cf. Eq. (32)] to the CPIMC data. The grey solid line shows the ideal LR behavior computed from Eq. (40). For comparison, at $\theta = 1$, we also plot the PB-PIMC results (green diamonds). Bottom panels: Dependence of the average number of type 2 kinks (red), type 4 kinks (green), and the average sign (orange) on the amplitude of the external field.

FIG. 6. Top panel: Dependence of the induced density $\langle \hat{\rho}_\mathbf{q} \rangle$ for $\mathbf{q} = \frac{2\pi}{L}(1, 0, 0)^\mathrm{T}$ on the amplitude of the external field. Shown are CPIMC results (red crosses) for $N = 14$ electrons at $r_s = 0.5$ and $\theta = 0.5$. The dotted black line corresponds to a linear fit. For comparison, we also plot the ideal LR behaviour (grey solid line). Bottom panel: Dependence of the average number of type 2 kinks (red), type 4 kinks (green), and the average sign (orange) on the amplitude of the external field.
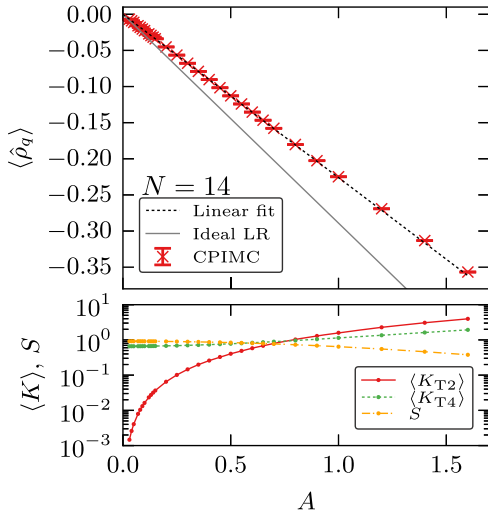

FIG. 7. Top panel: Dependence of the induced density $\langle \hat{\rho}_\mathbf{q} \rangle$ for $\mathbf{q} = \frac{2\pi}{L}(1, 0, 0)^\mathrm{T}$ on the amplitude of the external field. Shown are CPIMC results for $N = 20$ electrons at $r_s = 0.5$ and $\theta = 0.5$, where the maximum total number of kinks in the sampled paths has been restricted to $K_\mathrm{max} = 40$ (blue), $K_\mathrm{max} = 60$ (red), and $K_\mathrm{max} = \infty$, i.e., no restriction (green). The solid blue line corresponds to a linear fit to the data for $K_\mathrm{max} = 40$. The black dotted line shows the ideal LR behaviour. Bottom panel: Dependence of the average number of type 2 kinks (solid lines), type 4 kinks (dotted lines), and the average sign (dashed-dotted lines) on the amplitude of the external field. The colors correspond to the restrictions on the maximum number of kinks as labeled in the top panel.

where we artificially restricted the simulation to those configurations containing a maximum of 40 (blue), 60 (red), or arbitrarily many (green) kinks. More precisely, once a path with $K = K_\mathrm{max}$ kinks is realized, we do not propose to add any further kinks. First, for the result obtained without any restrictions (green), we see that these data are afflicted with a clearly visible statistical noise, which is due to an average sign (bottom panel, dashed-dotted) that is smaller than 0.1 even in the homogeneous case ($A = 0$). Naturally, the resulting value for the SDRF from a linear fit to these data (not depicted) would only be of very poor quality. However, by restricting the total maximum number of kinks (blue and red curves), the average number of kinks (bottom panel, solid and dotted lines) is reduced by an order of magnitude, whereby the average sign is increased by an order of magnitude (dashed-dotted lines).

Normally, one would expect this procedure to bias the result for the density response since by imposing these restrictions, one only samples paths from a small region of the total configuration space. Instead, one observes that, within statistical error bars, all three simulations are in perfect agreement, both for large and small amplitudes A (see inset in the upper panel). This very favourable behaviour is explained by a complete cancellation of all contributions from paths with a number of kinks larger than the maximum. In other words, due to the sign changes in the weight function Eq. (26), the expansion of the physical partition function Eq. (24) converges for much smaller values of K than the simulated primed partition function Eq. (10).

A similar observation has already been reported for the total energy of the homogeneous (unperturbed) electron gas in Ref. 56. There, a systematic extrapolation over the maximum number of kinks (to the exact result) was conveniently realized by the use of an auxiliary kink potential,
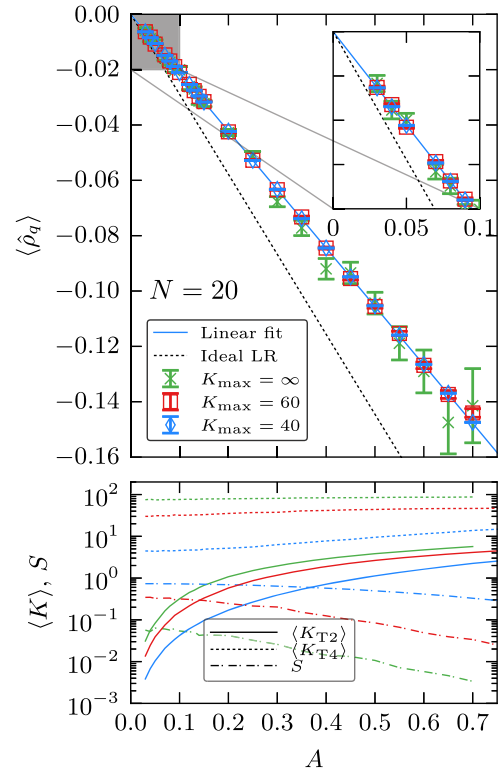
$$V_\kappa(K) = \frac{1}{e^{-(\kappa - K + 0.5)} + 1} \tag{33}$$

that depends on the number of kinks K of a configuration and the maximum number κ. The procedure works as follows: the weight function $W(C)$, Eq. (26), is replaced by

$$W_\kappa(C) = W(C) \cdot V_\kappa(K), \tag{34}$$

and one performs simulations for fixed values of κ. Since it is $\lim_{\kappa \to \infty} V_\kappa(K) = 1$, the exact partition function (and hence the exact result) is recovered by an extrapolation to $\kappa \to \infty$. This is demonstrated in Fig. 8, where we have increased the system size to $N = 38$ electrons (again at $\theta = 0.5$ and $r_s = 0.5$). First, we focus on the blue data points, which have been obtained from a complete CPIMC simulation with a fixed value of the parameter κ in the artificially modified weight function $W_\kappa(C)$. Here, the kink potential acts as a smooth but exponentially increasing penalty for all paths that contain a total number of kinks larger than κ. As expected, the results for the SDRF [Fig. 8(a)] converge for sufficiently large κ, in this case at about $\kappa \gtrsim 10$. And since the average number of kinks [panels (b) and (d)] and, consequently, the average sign [panel (c)] are clearly not converged for $\kappa \sim 10$, we can indeed conclude that all contributions from paths containing more than some critical number of kinks seem to completely cancel.
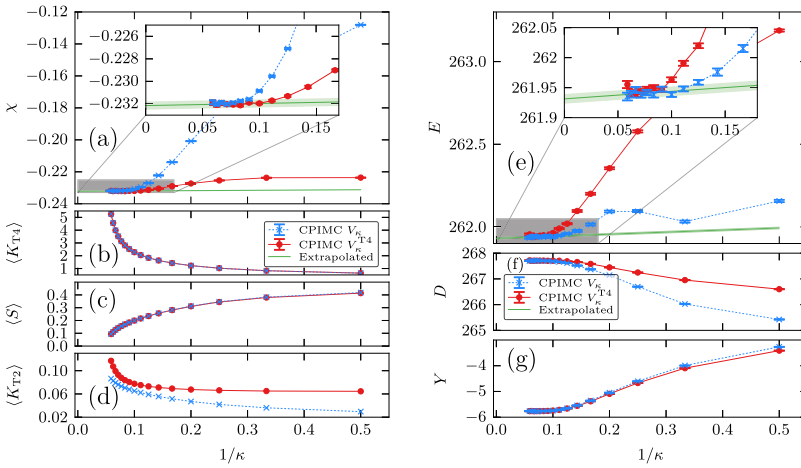
FIG. 8. Kink potential extrapolation of (a) the SDRF and (e) the total energy to the exact limit, $\kappa \to \infty$. Shown are the results from CPIMC simulations of the inhomogeneous electron gas containing $N = 38$ electrons at $\theta = 0.5$ and $r_s = 0.5$. The amplitude of the external field has been set to $A = 0.2$ with a wave-vector $\mathbf{q} = \frac{2\pi}{L}(1, 1, 1)^T$. Each data point has been obtained from a complete simulation with a fixed value for the parameter κ in the kink potential Eq. (33). Red points: the kink potential is applied solely to the type 4 kinks (no restriction on the number of type 2 kinks) in the sampled paths. Blue crosses: the kink potential has been applied to the total number of type 2 and 4 kinks. Green line: linear fit to the last red data points. In addition, for both potentials, the dependence on the parameter κ is plotted for the average number of type 4 kinks (b), average sign (c), type 2 kinks (d), diagonal (f), and off-diagonal contribution to the energy (g).

We again stress that the difference between CPIMC simulations of the homogeneous and perturbed electron gas lies in the existence of type 2 kinks in the latter. In particular, the SDRF is solely computed from the type 2 kinks [cf. its estimator, Eq. (31)]. In the LR regime, the average number of type 2 kinks, $\langle K_{T2} \rangle$, is significantly smaller than $\langle K_{T4} \rangle$ meaning that its practical influence on the sign is negligible. Therefore, it is reasonable to apply the kink potential only to the type 4 kinks and impose no restriction on the number of type 2 kinks. Recalling that the type 4 kinks are solely due to the Coulomb correlations, this procedure is equivalent to extrapolating the true static response with respect to the correlations in the system—this procedure converges to the exact result with increasing κ. The result is shown by the red dots in Fig. 8. Evidently, the convergence with κ is greatly accelerated. Even at $\kappa = 2$, the result for the response function has only a small bias of a few percent. In contrast, when also restricting the type 2 kinks (blue crosses), the result is off by roughly a factor 2.

We now analyze the total energy of the inhomogeneous electron gas. Here the convergence behaviour with respect to the kink parameter κ is different [see Fig. 8(e)]. Here, imposing no restrictions on the type 2 kinks (red points) seemingly slows down the convergence with κ. This is due to a coincidental error cancellation of the diagonal [panel (f)] and off-diagonal contributions [panel (g)] to the total energy, $E = D + Y$. Both contributions, at fixed κ, are closer to the exact result when leaving the number of type 2 kinks unrestricted. Moreover, even in the case where one is particularly interested in the total energy, the potential V_κ^{T4} (red dots) should still be used since only this potential ensures a monotonic convergence of the energy with κ. Naturally, a monotonic convergence is preferred when performing a reliable extrapolation to $\kappa \to \infty$.

From the investigations in this section we conclude that the general concept of an auxiliary kink potential to enhance the performance of CPIMC simulations that has been previously introduced for the unperturbed UEG[55,56] can be used in a similar way for the inhomogeneous electron gas. At fixed temperature and density, this allows us to obtain the SDRF for twice as large systems. This is an impressive efficiency gain when considering that the FSP increases exponentially with the system size, cf. Eq. (14). For the presented example with

$\theta = 0.5$ and $r_s = 0.5$, CPIMC simulations without the kink potential are feasible for up to $N \sim 20$ electrons whereas, with the kink potential, simulations of $N = 38$ particles pose no problem. On the other hand, for fixed temperature and electron number, the use of the kink potential roughly doubles the accessible r_s-range, which corresponds to a factor 8 in the density. Most importantly, it turns out that, in the LR regime, the number of type 2 kinks is small compared to the number of type 4 kinks so that their practical influence on the average sign is negligible. For this reason, the accessible parameter range regarding the particle number, temperature, and density for which the SDRF can be computed by means of CPIMC simulations of the inhomogeneous electron gas is almost identical to the range of applicability of CPIMC to the unperturbed spatially homogeneous electron gas.

C. Finite size correction of the static density response function

1. Theory

In this section, the issue of finite size errors in the computation of the SDRF χ and ways to correct them are discussed in detail. These errors are a direct consequence of the fact that Monte Carlo simulations can only be performed for a finite particle number N in a finite simulation box with volume V. This often causes the resulting functional form of $\chi_N(\mathbf{q})$ to differ significantly from its thermodynamic limit

$$\chi(\mathbf{q}) = \lim_{\substack{N \to \infty \\ N/V = \text{const.}}} \chi_N(\mathbf{q}) . \tag{35}$$

In particular, when simulating fermionic systems with Monte Carlo methods, one is usually limited to rather small systems, due to the FSP, so that finite size errors are not negligible. In addition, $\mathbf{q}$-dependent quantities can only be computed for $\mathbf{q}$-vectors that satisfy the natural condition of momentum quantization in the simulation box, $\mathbf{q} = \frac{2\pi}{L}\mathbf{m}$ with $\mathbf{m} \in \mathbb{Z}^3$. Thus, standard techniques to reduce finite size errors, e.g., those for the total energy,[45] which are all based on an extrapolation of the finite–N results to $N \to \infty$ (at constant density) cannot be used for the correction of χ.

In the ground state, the most sophisticated approach to tackle finite size errors is based on the assumption that the so-called static local field correction (LFC) $G(\mathbf{q})$ is only weakly

dependent on the system size.[37] The LFC is commonly defined by the equation[63,64]

$$\chi(\mathbf{q}) = \frac{\chi^0(\mathbf{q})}{1 - v_q[1 - G(\mathbf{q})]\chi^0(\mathbf{q})}, \tag{36}$$

where χ^0 denotes the ideal response function and $v_q = 4\pi/q^2$. The random phase approximation (RPA) χ^{RPA} is obtained by setting $G = 0$ in Eq. (36). Hence, the LFC contains all information beyond the RPA and should thus be dominated by short-range correlations, which are expected to be captured sufficiently well in a finite simulation cell. Naturally, instead of computing the LFC from the ideal response function in the TDL, $\chi^0(\mathbf{q})^2$, i.e., via

$$G_N(\mathbf{q}) = \frac{1}{v_q}\left(\frac{1}{\chi_N(\mathbf{q})} - \frac{1}{\chi^0(\mathbf{q})}\right) + 1, \tag{37}$$

it is important to obtain it consistently from the corresponding finite-N ideal response function $\chi_N^0(\mathbf{q})$,

$$G_N^{\mathrm{FSC}}(\mathbf{q}) = \frac{1}{v_q}\left(\frac{1}{\chi_N(\mathbf{q})} - \frac{1}{\chi_N^0(\mathbf{q})}\right) + 1. \tag{38}$$

Assuming that the finite size errors in this consistent LFC are negligible, i.e., $G_N^{\mathrm{FSC}}(\mathbf{q}) \approx G(\mathbf{q})$, the finite size corrected response function is given by

$$\chi^{\mathrm{FSC}}(\mathbf{q}) = \frac{\chi^0(\mathbf{q})}{1 + \left[\frac{1}{\chi_N(\mathbf{q})} - \frac{1}{\chi_N^0(\mathbf{q})}\right]\chi^0(\mathbf{q})}. \tag{39}$$

Therefore, in addition to the response function of the interacting finite-N system, $\chi_N(\mathbf{q})$, we also need precise data for the corresponding ideal response function $\chi_N^0(\mathbf{q})$. In principle, these can be obtained from a complete CPIMC simulation of the ideal perturbed electron gas for each $\mathbf{q}$-vector and particle number N, as was demonstrated in Sec. III A. A more convenient way to achieve this is given by making use of the spectral representation of the ideal response function, which, in the case of the UEG, takes the form[2]

$$\chi_N^0(\mathbf{q}) = \frac{1}{V}\sum_{\mathbf{p},\sigma}\frac{n_\sigma(\mathbf{p}+\mathbf{q}) - n_\sigma(\mathbf{p})}{\epsilon_{\mathbf{p}+\mathbf{q}} - \epsilon_{\mathbf{p}}}, \tag{40}$$

where $\epsilon_{\mathbf{p}} = p^2/2$, and $n_\sigma(\mathbf{p}) = \langle \hat{n}_{\mathbf{p},\sigma}\rangle$ is the momentum distribution of the unperturbed ideal UEG, which converges to the Fermi distribution, in the TDL, and constitutes a natural observable that is straightforwardly computed observable within the CPIMC formalism. Thus, Eq. (40) in principle enables us to gain access to all $\mathbf{q}$-vectors of the ideal response function from a single CPIMC simulation of the unperturbed UEG.

However, the concrete evaluation of Eq. (40) has to be done carefully because there are terms in which both the numerator and denominator vanish, i.e., where $|\mathbf{p}+\mathbf{q}| = |\mathbf{p}|$. In the ground state, it is correct to simply set those terms to zero[2] and to rewrite

$$\chi_{*,N}^0(\mathbf{q}) = \frac{1}{V}\sum_{\substack{\mathbf{p},\sigma \\ |\mathbf{p}+\mathbf{q}|\neq|\mathbf{p}|}}\frac{n_\sigma(\mathbf{p}+\mathbf{q}) - n_\sigma(\mathbf{p})}{\epsilon_{\mathbf{p}+\mathbf{q}} - \epsilon_{\mathbf{p}}}. \tag{41}$$

However, at finite temperature[65] this leads to completely wrong results, which is illustrated in Fig. 9, where the ideal
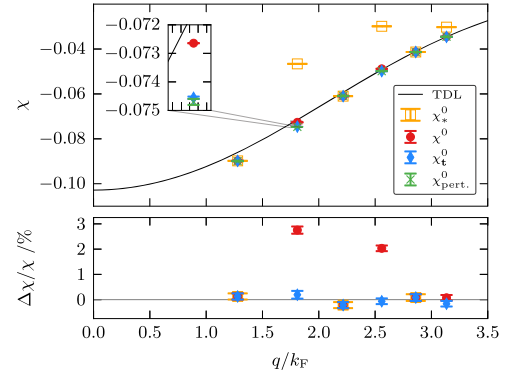

FIG. 9. Comparison of different ways to compute the ideal response function for the UEG with $N = 4$ electrons at $\theta = 1$ and $r_s = 1$. The orange squares correspond to the evaluation of Eq. (41). The blue diamonds show the result from Eq. (44) for a small twist-angle $\mathbf{t} = 0.01 \cdot (1/e, 1/\pi, 1/\sqrt{(2)})^T$. The red dots correspond to Eq. (46). For comparison, the result obtained from CPIMC simulations of the perturbed ideal electron gas, as discussed in Sec. III A, is depicted by the green crosses. The bottom panel shows the relative deviation to these exact data. The black solid line corresponds to the ideal response function in the TDL.

response function of $N = 4$ electrons at $\theta = 1$ and $r_s = 1$ is shown. The green crosses correspond to the exact result obtained from simulations of the perturbed ideal electron gas as discussed in Sec. III A. The orange squares, which correspond to the evaluation of Eq. (41), exhibit a large bias for every second $\mathbf{q}$-vector, while every other is in perfect agreement with the result from the unperturbed system (see deviation in the bottom panel of Fig. 9). This is due to the fact that the condition $|\mathbf{p} + \mathbf{q}| = |\mathbf{p}|$ can only be fulfilled if $\tilde{q}^2 = q^2 L^2/(2\pi)^2$ is an even number (in what follows the tilde denotes dimensionless q-vectors with the components $\tilde{q}_i \in \mathbb{Z}$). The proof is obvious when rewriting said condition as

$$\tilde{p}^2 = \tilde{p}^2 + \tilde{q}^2 + 2\tilde{\mathbf{p}}\tilde{\mathbf{q}} \tag{42}$$

$$\Leftrightarrow \tilde{q}^2 = -2\tilde{\mathbf{p}}\tilde{\mathbf{q}}\,. \tag{43}$$

Since the factor 2 ensures that the RHS is always an even number, the equality can only be fulfilled if $\tilde{q}^2$ is also even. Thus, there are no critical (diverging) terms in the evaluation of Eq. (40) for odd $\tilde{q}^2$.

To determine the proper contribution of the critical terms for even $\tilde{q}^2$, we may write Eq. (40) for the UEG Hamiltonian, Eq. (1), subject to generalized periodic boundary conditions. Following Refs. 66 and 67, this is realized by shifting the entire $\mathbf{q}$-grid of our simulation box by a so-called twist-angle $\mathbf{t} \in \mathbb{R}^3$ so that the modified momentum quantization reads $\mathbf{q} = \frac{2\pi}{L}\mathbf{m} + \mathbf{t}$, with $\mathbf{m} \in \mathbb{Z}^3$. For the ideal response function, we then have

$$\chi_{\mathbf{t},N}^0(\mathbf{q}) = \frac{1}{V}\sum_{\mathbf{p},\sigma}\frac{n_\sigma(\mathbf{p}+\mathbf{t}+\mathbf{q}) - n_\sigma(\mathbf{p}+\mathbf{t})}{\epsilon_{\mathbf{p}+\mathbf{t}+\mathbf{q}} - \epsilon_{\mathbf{p}+\mathbf{t}}}, \tag{44}$$

where, in this notation, the sum still runs over all $\mathbf{p}$-vectors with $\mathbf{p} = \frac{2\pi}{L}\mathbf{m}$, where $\mathbf{m} \in \mathbb{Z}^3$. Obviously, the condition for a vanishing denominator now reads

$$|\mathbf{p} + \mathbf{t} + \mathbf{q}| = |\mathbf{p} + \mathbf{t}|, \tag{45}$$

which cannot be fulfilled if the components of the twist-angle t_i are irrational and linearly independent, e.g., for the choice $\mathbf{t} = (1/e, 1/\pi, 1/\sqrt{2})^T$. In addition, for a sufficiently small

modulus of the twist-angle, we can expect the induced bias to be negligible. The blue diamonds in Fig. 9 clearly show that this is indeed the case since they perfectly agree with the exact result (see the bottom panel).

Finally, we determine the contribution of the critical terms in Eq. (40) by performing the limit $|\mathbf{t} \rightarrow \mathbf{0}|$ of those terms in Eq. (44) with the aid of L'Hospitals's rule yielding

$$\chi_N^0(\mathbf{q}) = \chi_{*,N}^0(\mathbf{q}) - \frac{\beta}{V} \sum_{\substack{\mathbf{p},\sigma \\ |\mathbf{p}+\mathbf{q}|=|\mathbf{p}|}} \left[n_\sigma(\mathbf{p}) - n_\sigma^2(\mathbf{p}) \right]. \quad (46)$$

The corresponding result is depicted by the red dots in Fig. 9. Evidently, compared to simply omitting the contribution of the critical terms (orange squares) the improvement is substantial. Yet, the relative deviation to the exact result is still of the order of a few percent (bottom panel).

The residual bias is explained as follows: mathematically it is only valid to use L'Hospital's rule if the functional form of the momentum distribution does not change with the twist-angle. This condition only holds in good approximation for large particle numbers but is increasingly violated for smaller system sizes. Since a systematic error of a few percent in the ideal response function is not sufficient for a reliable finite size correction, we conclude that Eq. (46) cannot be used to achieve this. Nevertheless, we can instead use Eq. (44), which has been demonstrated to be asymptotically correct for small twist-angles, to efficiently compute the finite-N ideal response function of the UEG with high accuracy. For completeness, we mention that L'Hospital terms vanish in the ground state, and the functional form of the momentum distribution is independent of the twist-angle here since it is always given by a step function at the Fermi vector k_F. Hence, Eq. (41) is indeed correct in the ground state.

2. CPIMC results

At high densities, we expect the finite size errors involved in the response function of the interacting system to be comparable to those of the ideal system. Therefore, Fig. 10 shows the dependence of the ideal response function on the particle number at three different temperatures. At $\theta = 0.0625$ [panel (a)], which is close to the ground state, the finite size errors are extremely large even for $N = 54$ electrons (blue) and are most pronounced for small $\mathbf{q}$-vectors, which correspond to large distances in real space that are not sufficiently described in small simulation cells. It is only at a few hundred electrons
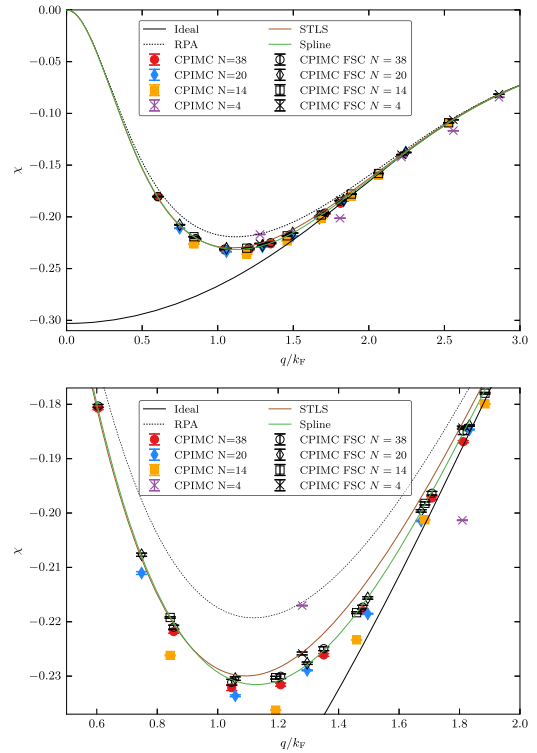

FIG. 11. Finite size correction of the density response function of the UEG at $\theta = 0.5$ and $r_s = 0.5$. Top panel: Shown are the uncorrected CPIMC results for different electron numbers in the simulation box: 4 (purple crosses), 14 (orange squares), 20 (blue diamonds), and 38 (red dots). The black symbols correspond to the finite size corrected results computed via Eq. (39), and the green curve shows a smooth spline fit through these data with $N > 4$. For comparison, the ideal (solid black), RPA (dotted black), and STLS (brown) results are plotted. Bottom panel: Zoom into the minimum regime of the response function.

(red) where the convergence of the functional form eventually becomes visible. With increasing temperature, these finite size errors are significantly reduced; yet the relative bias of, e.g., $N = 14$ electrons at $\theta = 0.5$ [green dots in panel (c)] is still substantial. This reduction of finite size errors is due to the fact that shell effects, which also cause quantities like the total energy to converge non-monotonically towards the TDL, vanish with increasing temperature.

Finally, in Fig. 11 the wave-vector dependence of the interacting response function of the UEG is depicted for $\theta = 0.5$ and $r_s = 0.5$. The colored symbols show the uncorrected CPIMC results for N = 4, 14, 20, and 38 electrons, which have been

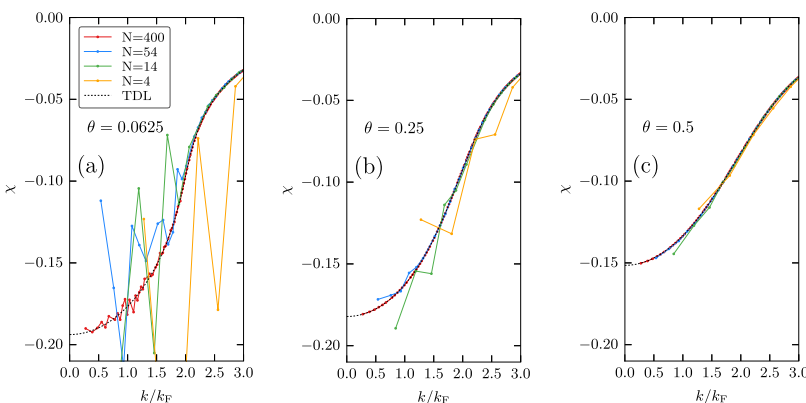FIG. 10. Dependence of the ideal response function on the particle number at $r_s = 1$ and three different temperatures: $\theta = 0.0625$ (a), $\theta = 0.25$ (b), and $\theta = 0.5$ (c). The results for finite particle numbers have been computed via Eq. (44) from the CPIMC result of the corresponding finite $- N$ momentum distribution. For comparison, black dotted curves show the TDL result of the ideal response function.

obtained as discussed in Sec. III B. For $N = 38$, the extrapolation technique with the kink potential has been used. First, we clearly see that the uncorrected results do not lie on a smooth curve. In particular for $N = 4$ and $N = 14$ electrons, the finite size errors are of the order of a few percent when zooming into the minimum region of the response function (bottom panel). Before applying the presented finite size correction to χ, we check if the underlying assumption regarding the weak finite size dependence of the LFC is actually valid. For this purpose, in Fig. 12 we plot the LFC of the UEG for the same parameters. Evidently, using the ideal response function in the TDL to compute the LFC according to Eq. (37) leads to substantial finite size errors in its functional form. However, when consistently using our computed CPIMC result for the finite – N ideal response function [cf. Eq. (38)], the functional form of the LFC is indeed indistinguishable for all three particle numbers so that a smooth spline can be fitted through these data (green line). For comparison, we also plot the LFC obtained from the Singwi-Tosi-Land-Sjölander (STLS) scheme, which is of good quality for $q/k_F \lesssim 1$ but deviates by up to a factor of two from the exact CPIMC result, for larger q-vectors.

Now we use the consistent LFC to correct the SDRF according to Eq. (39). The result is shown by the black symbols in Fig. 11. Clearly, for $N > 4$ all results lie on a smooth curve, which is demonstrated by a smooth spline fit through these data (green curve). Even though for $N = 4$ (black crosses), the correction is not quite sufficient to describe the TDL behavior, the reduction of the bias is still impressive (cf. purple crosses). In addition, we plot the response function in RPA (dotted black) and STLS (solid brown) approximation. While the RPA exhibits systematic errors of a few percent, the STLS approximation is accurate up to about one percent. In particular, STLS exhibits no resolvable bias for $q/k_F \lesssim 1$, which is in agreement with its accuracy regarding the LFC (cf. Fig. 12) in this regime. However, even though at $q/k_F \gtrsim 2$ the systematic error of the STLS result for the LFC is nearly a factor two, the influence of the LFC on the total response function is suppressed by the factor $v_q = 4\pi/q^2$ in Eq. (36) so that for $q \to \infty$ the response function becomes equal to the ideal case.
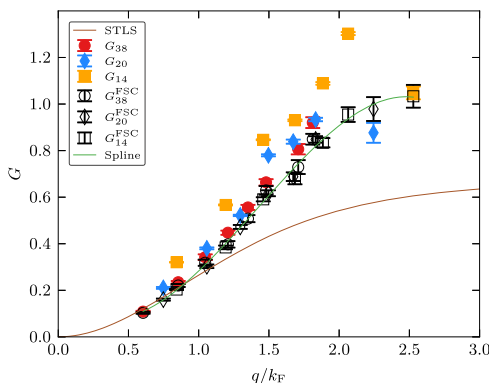

FIG. 12. Local field correction of the UEG at $\theta = 0.5$ and $r_s = 0.5$ for different particle numbers indicated in the legend (subscripts). Colored filled symbols: LFC computed from the ideal response function in the TDL, Eq. (37). Black symbols: LFC obtained from the finite – N ideal response function according to Eq. (38). Green curve: spline fit to the finite size corrected LFC. Brown curve: STLS local field correction.

We conclude that the ground state finite size correction of the LFC and the SDRF can be generalized to finite temperatures, as presented in this section. The benefit of this correction is dramatic: it allows one to obtain accurate results for the thermodynamic limit from CPIMC simulations for systems as small as $N = 14$ electrons. The price one has to pay is to compute highly accurate results of the finite–N ideal response function. This can be efficiently achieved via CPIMC simulations of the unperturbed UEG by using its spectral representation. However, in contrast to the ground state, the correct evaluation of the spectral representation is only possible when switching to a system subject to generalized boundary conditions, which has been verified by cross-checks to the exact result obtained from simulations of the perturbed electron gas. Finally, we mention that the presented finite size correction is not only highly valuable for CPIMC but can be used for finite–N data obtained with any other finite temperature method.

IV. SUMMARY AND DISCUSSION

In summary, we have successfully generalized the CPIMC formalism from the homogeneous electron gas to the general inhomogeneous case. We have shown that the applied external periodic potential results in the occurrence of type 2 kinks that correspond to one-particle excitations in the simulated imaginary time paths. This leads to numerous additional diagrams, which have to be taken into account, so that the complexity of the algorithm is significantly increased. Next, we have demonstrated that the technique of an artificial kink-potential, which had been introduced in Refs. 55 and 56 to mitigate the FSP regarding the computation of the energy of the UEG, is similarly effective for the computation of the SDRF. This concept may even be improved when being applied solely to the type 4 kinks while imposing no restrictions on the type 2 kinks. Interestingly, we observed that the induced type 2 kinks only influence the fermion sign problem of CPIMC for large amplitudes of the external potential. For amplitudes that are sufficiently small for the linear response theory to be valid their influence is negligible. Therefore, the presented CPIMC algorithm can be used to compute the SDRF for the same parameters (density, temperature, and electron number) that are accessible for the simulation of the UEG without the external potential.

A further achievement of this work consists in the extension of ground state finite size corrections for the SDRF to finite temperature. We have demonstrated that the SDRF obtained from quantum Monte Carlo simulations of finite systems, i.e., a finite number of electrons in a finite simulation box, may differ substantially from the TDL result. For the investigated example of intermediate temperature ($\theta = 0.5$) and rather high density ($r_s = 0.5$), the finite size errors are of the order of several percent. Similarly to previous findings in the ground state, the finite size effects are almost exclusively ascribed to the ideal part of the SDRF, whereas the LFC is remarkably well converged with system size even for small N, i.e., $G_N^{\text{FSC}}(q) \approx G(q)$.

To compute G_N^{FSC} from the QMC data for the SDRF, we found that it is crucial to use the ideal SDRF for the same finite

number of electrons (instead of using the macroscopic result), which turns out to be surprisingly difficult. While the finite – N ideal SDRF is linked to the momentum distribution function via its spectral representation, at finite temperature, the corresponding expression can only be evaluated when introducing generalized boundary conditions by means of a finite but small twist-angle. Thereby, unbiased results for the finite – N ideal SDRF for all wave-vectors can be obtained from a single CPIMC simulation of the unperturbed UEG. This has been confirmed by cross-checks with the exact results from simulations of the perturbed UEG. In this way, the SDRF can be computed in the TDL with an accuracy of $\sim 0.1\%$. Finally, our *ab initio* results for the SDRF allow us to benchmark standard approximations. In particular, the RPA SDRF reveals

systematic errors of a few percent, while the STLS approximation[58,59] exhibits deviations of up to one percent, even at $r_s = 0.5$.

We expect the presented results to be of high importance for future warm dense matter research, in particular in the context of advanced truly non-local exchange-correlation functionals for DFT or as valuable input for the computation of the dynamic structure factor, e.g., within the extended Born-Mermin approach.[26] Furthermore, a more detailed investigation of the LFC will certainly help in determining the large k-vector behavior of the LFC, which, in particular at finite temperature, is an open question. In addition, a possible maximum in the LFC is known to indicate the possibility for charge-density waves.[2]
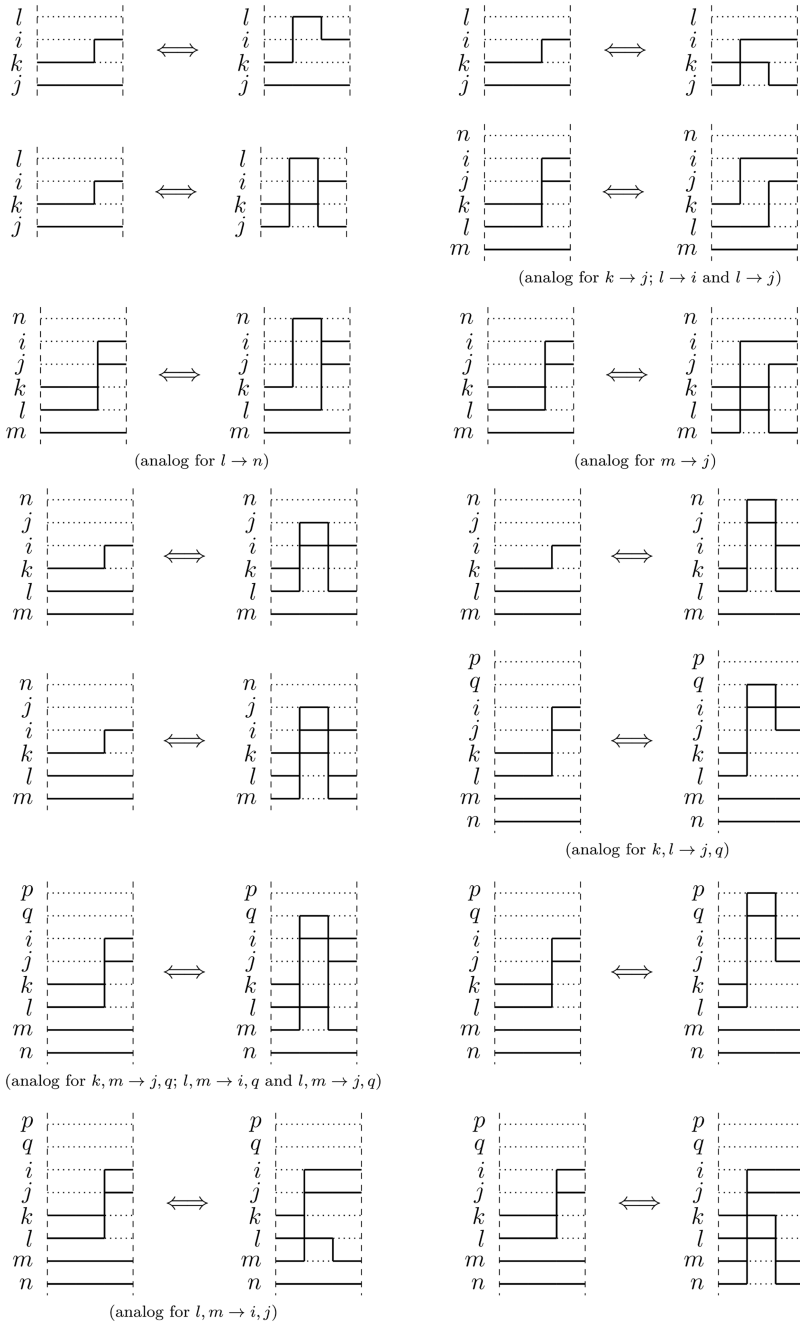

FIG. 13. All 14 elementary diagrams for adding a type 2 or 4 kink via a one- or two-particle excitation, respectively, and thereby changing another kink left of the added one.

APPENDIX: ALGORTHM DETAILS

In this appendix, we present additional information on the CPIMC procedure for the harmonically modulated electron gas. Figure 13 shows all possible 14 elementary diagrams for adding a type 2 or 4 kink via a one- or two-particle excitation, and thereby changing another kink left of the added one.

[1] P.-F. Loos and P. M. W. Gill, "The uniform electron gas," Comput. Mol. Sci. **6**, 410–429 (2016).

[2] G. Giuliani and G. Vignale, *Quantum Theory of the Electron Liquid* (Cambridge University Press, 2008).

[3] D. Pines and D. Bohm, "A collective description of electron interactions: II. Collective vs individual particle aspects of the interactions," Phys. Rev. **85**, 338 (1952).

[4] D. Bohm and D. Pines, "A collective description of electron interactions: III. Coulomb interactions in a degenerate electron gas," Phys. Rev. **92**, 609 (1953).

[5] J. Bardeen, L. N. Cooper, and J. R. Schrieffer, "Theory of superconductivity," Phys. Rev. **108**, 1175 (1957).

[6] In Hartree atomic units, it holds $E_F = k_F^2/2$, with $k_F = (9\pi/4)^{1/3}/r_s$ being the Fermi wave vector.

[7] F. Graziani, M. P. Desjarlais, R. Redmer, and S. B. Trickey, *Frontiers and Challenges in Warm Dense Matter* (Springer International Publishing, Switzerland, 2014).

[8] N. D. Mermin, "Thermal properties of the inhomogeneous electron gas," Phys. Rev. **137**, A1441 (1965).

[9] M. D. Knudson *et al.*, "Probing the interiors of the ice giants: Shock compression of water to 700 GPa and 3.8 g/cm³," Phys. Rev. Lett. **108**, 091102 (2012).

[10] B. Militzer *et al.*, "A massive core in Jupiter predicted from first-principles simulations," Astrophys. J. **688**, L45 (2008).

[11] M. Bonitz, *Quantum Kinetic Theory*, 2nd ed. (Springer, 2016).

[12] M. Bonitz, E. Pehlke, and T. Schoof, "Attractive forces between ions in quantum plasmas: Failure of linearized quantum hydrodynamics," Phys. Rev. E **87**, 033105 (2013).

[13] D. Michta, F. Graziani, and M. Bonitz, "Quantum hydrodynamics for plasmas—A Thomas-Fermi theory perspective," Contrib. Plasma Phys. **55**, 437–443 (2015).

[14] R. Nora *et al.*, "Gigabar spherical shock generation on the OMEGA laser," Phys. Rev. Lett. **114**, 045001 (2015).

[15] P. F. Schmit *et al.*, "Understanding fuel magnetization and mix using secondary nuclear reactions in magneto-inertial fusion," Phys. Rev. Lett. **113**, 155004 (2014).

[16] O. A. Hurricane *et al.*, "Inertially confined fusion plasmas dominated by alpha-particle self-heating," Nat. Phys. **12**, 800 (2016).

[17] A. L. Kritcher, T. Döppner, C. Fortmann, T. Ma, O. L. Landen, R. Wallace, and S. H. Glenzer, "In-flight measurements of capsule shell adiabats in laser-driven implosions," Phys. Rev. Lett. **107**, 015002 (2011).

[18] K. Balzer, N. Schlünzen, and M. Bonitz, "Stopping dynamics of ions passing through correlated honeycomb clusters," Phys. Rev. B **94**, 245118 (2016).

[19] R. Ernstorfer *et al.*, "The formation of warm dense matter: Experimental evidence for electronic bond hardening in gold," Science **323**(5917), 1033 (2009).

[20] D. Lu, "Evaluation of model exchange-correlation kernels in the adiabatic connection fluctuation-dissipation theorem for inhomogeneous systems," J. Chem. Phys. **140**, 18A520 (2014).

[21] C. E. Patrick and K. S. Thygesen, "Adiabatic-connection fluctuation-dissipation DFT for the structural properties of solids—The renormalized ALDA and electron gas kernels," J. Chem. Phys. **143**, 102802 (2015).

[22] A. Pribram-Jones, P. E. Grabowski, and K. Burke, "Thermal density functional theory: Time-dependent linear response and approximate functionals from the fluctuation-dissipation theorem," Phys. Rev. Lett. **116**, 233001 (2016).

[23] K. Burke, "Perspective on density functional theory," J. Chem. Phys. **136**, 150901 (2012).

[24] J. P. Perdew, K. Burke, and M. Ernzerhof, "Generalized gradient approximation made simple," Phys. Rev. Lett. **77**, 3865 (1996).

[25] P. Neumayer, C. Fortmann, T. Döppner, P. Davis, R. W. Falcone, A. L. Kritcher, O. L. Landen *et al.*, "Plasmons in strongly coupled shock-compressed matter," Phys. Rev. Lett. **105**, 075003 (2010).

[26] C. Fortmann, A. Wierling, and G. Röpke, "Influence of local-field corrections on Thomson scattering in collision-dominated two-component plasmas," Phys. Rev. E **81**, 026405 (2010).

[27] K.-U. Plagemann, P. Sperling, R. Thiele, M. P. Desjarlais, C. Fortmann, T. Döppner, H. J. Lee, S. H. Glenzer, and R. Redmer, "Dynamic structure factor in warm dense beryllium," New J. Phys. **14**, 055020 (2012).

[28] S. H. Glenzer and R. Redmer, "X-ray Thomson scattering in high energy density plasmas," Rev. Mod. Phys. **81**, 1625–1663 (2009).

[29] J. Vorberger, D. O. Gericke, Th. Bornath, and M. Schlanges, "Energy relaxation in dense, strongly coupled two-temperature plasmas," Phys. Rev. E **81**, 046404 (2010).

[30] L. X. Benedict, M. P. Surh, L. G. Stanton, C. R. Scullard, A. A. Correa, J. I. Castor, F. R. Graziani *et al.*, "Molecular dynamics studies of electron-ion temperature equilibration in hydrogen plasmas within the coupled-mode regime," Phys. Rev. E **95**, 043202 (2017).

[31] H. Reinholz, G. Röpke, S. Rosmej, and R. Redmer, "Conductivity of warm dense matter including electron-electron collisions," Phys. Rev. E **91**, 043105 (2015).

[32] C. E. Starrett and D. Saumon, "A simple method for determining the ionic structure of warm dense matter," High Energy Density Phys. **10**, 35 (2014).

[33] A. N. Souza, D. J. Perkins, C. E. Starrett, D. Saumon, and S. B. Hansen, "Predictions of X-ray scattering spectra for warm dense matter," Phys. Rev. E **89**, 023108 (2014).

[34] G. Senatore, S. Moroni, and D. M. Ceperley, "Local field factor and effective potentials in liquid metals," J. Non-Cryst. Solids **205**, 851 (1996).

[35] Z. Moldabekov, T. Schoof, P. Ludwig, M. Bonitz, and T. Ramazanov, "Statically screened ion potential and Bohm potential in a quantum plasma," Phys. Plasmas **22**, 102104 (2015).

[36] S. Moroni, D. M. Ceperley, and G. Senatore, "Static response from quantum Monte Carlo calculations," Phys. Rev. Lett. **69**, 1837 (1992).

[37] S. Moroni, D. M. Ceperley, and G. Senatore, "Static response and local field factor of the electron gas," Phys. Rev. Lett. **75**, 689 (1995).

[38] G. Sugiyama, C. Bowen, and B. J. Alder, "Static dielectric response of charged bosons," Phys. Rev. B **46**, 13042 (1992).

[39] C. Bowen, G. Sugiyama, and B. J. Alder, "Static dielectric response of the electron gas," Phys. Rev. B **50**, 14838 (1994).

[40] G. Senatore, S. Moroni, and D. M. Ceperley, "Static response of homogeneous quantum fluids by diffusion Monte Carlo," in *Quantum Monte Carlo Methods in Physics and Chemistry*, edited by M. P. Nightingale and C. J. Umrigar (Springer, 1998).

[41] M. Corradini, R. Del Sole, G. Onida, and M. Palummo, "Analytical expressions for the local-field factor $G(q)$ and the exchange-correlation kernel $K_{xc}(r)$ of the homogeneous electron gas," Phys. Rev. B **57**, 14569 (1998).

[42] E. Y. Loh, J. E. Gubernatis, R. T. Scalettar, S. R. White, D. J. Scalapino, and R. L. Sugar, "Sign problem in the numerical simulation of many-electron systems," Phys. Rev. B **41**, 9301–9307 (1990).

[43] D. M. Ceperley, "Path integral Monte Carlo methods for fermions," in *Monte Carlo and Molecular Dynamics of Condensed Matter Systems*, edited by E. K. Binder, G. Ciccotti, and E. Compositori (Bologna, Italy, 1996).

[44] M. Troyer and U. J. Wiese, "Computational complexity and fundamental limitations to fermionic quantum Monte Carlo simulations," Phys. Rev. Lett. **94**, 170201 (2005).

[45] T. Dornheim, S. Groth, T. Sjostrom, F. D. Malone, W. M. C. Foulkes, and M. Bonitz, "*Ab initio* quantum Monte Carlo simulation of the warm dense electron gas in the thermodynamic limit," Phys. Rev. Lett. **117**, 156403 (2016).

[46] S. Groth, T. Dornheim, and M. Bonitz, "Free energy of the uniform electron gas: Testing analytical models against first principle results," Contrib. Plasma Phys. **57**, 137 (2017).

[47] T. Dornheim, S. Groth, F. D. Malone, T. Schoof, T. Sjostrom, W. M. C. Foulkes, and M. Bonitz, "*Ab initio* quantum Monte Carlo simulation of the warm dense electron gas," Phys. Plasmas **24**, 056303 (2017).

[48] S. Groth, T. Dornheim, T. Sjostrom, F. D. Malone, W. M. C. Foulkes, and M. Bonitz, "*Ab initio* exchange-correlation free energy of the uniform electron gas at warm dense matter conditions," Phys. Rev. Lett. **119**, 135001 (2017).

[49] T. Dornheim, S. Groth, and M. Bonitz, "*Ab initio* results for the static structure factor of the warm dense electron gas," Contrib. Plasma Phys. (2017); e-print arXiv: 1709.02199 (unpublished).

[50] T. Dornheim, S. Groth, A. Filinov, and M. Bonitz, "Permutation blocking path integral Monte Carlo: A highly efficient approach to the simulation of strongly degenerate non-ideal fermions," New J. Phys. **17**, 073017 (2015).

[51] T. Dornheim, T. Schoof, S. Groth, A. Filinov, and M. Bonitz, "Permutation blocking path integral Monte Carlo approach to the uniform electron gas at finite temperature," J. Chem. Phys. **143**, 204101 (2015).

[52] T. Dornheim, S. Groth, T. Schoof, C. Hann, and M. Bonitz, "*Ab initio* quantum Monte Carlo simulations of the uniform electron gas without fixed nodes: The unpolarized case," Phys. Rev. B **93**, 205134 (2016).

[53] T. Schoof, M. Bonitz, A. V. Filinov, D. Hochstuhl, and J. W. Dufty, "Configuration path integral Monte Carlo," Contrib. Plasma Phys. **51**, 687–697 (2011).

[54] T. Schoof, S. Groth, and M. Bonitz, "Towards *ab initio* thermodynamics of the electron gas at strong degeneracy," Contrib. Plasma Phys. **55**, 136 (2015).

[55] T. Schoof, S. Groth, J. Vorberger, and M. Bonitz, "*Ab initio* thermodynamic results for the degenerate electron gas at finite temperature," Phys. Rev. Lett. **115**, 130402 (2015).

[56] S. Groth, T. Schoof, T. Dornheim, and M. Bonitz, "*Ab initio* quantum Monte Carlo simulations of the uniform electron gas without fixed nodes," Phys. Rev. B **93**, 085102 (2016).

[57] T. Dornheim, S. Groth, J. Vorberger, and M. Bonitz, "Permutation blocking path integral Monte Carlo approach to the static density response of the warm dense electron gas," Phys. Rev. E **96**, 023203 (2017).

[58] K. S. Singwi, M. P. Tosi, R. H. Land, and A. Sjölander, "Electron correlations at metallic densities," Phys. Rev. **176**, 589 (1968).

[59] S. Tanaka and S. Ichimaru, "Thermodynamics and correlational properties of finite-temperature electron liquids in the Singwi-Tosi-Land-Sjölander approximation," J. Phys. Soc. Jpn. **55**, 2278–2289 (1986).

[60] L. M. Fraser *et al.*, "Finite-size effects and Coulomb interactions in quantum Monte Carlo calculations for homogeneous systems with periodic boundary conditions," Phys. Rev. B **53**, 1814 (1996).

[61] N. Metropolis, A. W. Rosenbluth, M. N. Rosenbluth, A. H. Teller, and E. Teller, "Equation of state calculations by fast computing machines," J. Chem. Phys. **21**, 1087 (1953).

[62] D. M. Ceperley, "Path integrals in the theory of condensed helium," Rev. Mod. Phys. **67**, 279–355 (1995).

[63] A. A. Kugler, "Theory of the local field correction in an electron gas," J. Stat. Phys. **12**, 35 (1975).

[64] A. A. Kugler, "Bounds for some equilibrium properties of an electron gas," Phys. Rev. A **1**, 1688 (1970).

[65] Note that the commonly used expansions around $\mathbf{q} = 0$ cannot be used since the denominator can vanish for arbitrarily large $\mathbf{q}$.

[66] N. D. Drummond, R. J. Needs, A. Sorouri, and W. M. C. Foulkes, "Finite-size errors in continuum quantum Monte Carlo calculations," Phys. Rev. B **78**, 125106 (2008).

[67] C. Lin, F. H. Zong, and D. M. Ceperley, "Twist-averaged boundary conditions in continuum quantum Monte Carlo algorithms," Phys. Rev. E **64**, 016702 (2001).

Chapter 8

Other Works

In this section, I briefly mention two other publications to which I contributed during this thesis, but which do not fit into the previous sections. However, due to my small contribution (see Sec. 1.3.1), they are not included as full-text documents in this work.

In Ref. [169], results for the static density response function (from RPA, STLS and the ground-state QMC based parametrization by Corradini *et al.* [225]) were used to compute the ion–ion potential in a correlated dense quantum plasma. Such a screened effective potential can then be plugged into a molecular dynamics or classical Monte Carlo simulation, or into the hypernetted chain scheme [226, 227]. This work constitutes a proof of principle study and outlines the possibility to use our finite-temperature QMC results for the static local-field correction (cf. Chpt. 7) in order to derive further improved pair-potentials.

Further, Ref. [98] constitutes a brief review of some aspects of the recent research initiative *SFB-TR24*, of which I was a part. In particular, it contrasts the properties and key parameters of classical and quantum plasmas, and, in addition, contains PB-PIMC results for the center-two particle correlation function (see Sec. 3.2) and for the pair distribution function of the unpolarized electron gas (see Sec. 5.2.1).

Chapter 9

Summary and Outlook

9.1 Summary and Discussion

9.1.1 Development of PB-PIMC

The accurate description of correlated degenerate fermions at finite temperature is one of the most fundamental and important topics in statistical physics and quantum chemistry. The main challenge in this context is the notorious fermion sign problem, which causes an exponential increase in computation time with respect to system size and inverse temperature, and, usually, prevents QMC simulations for the most interesting parameters such as the warm dense matter regime.

The main goal of this thesis has been the development of a new, improved path integral Monte Carlo method that is capable to provide accurate results at moderate to high quantum degeneracy where standard PIMC is no longer feasible. The result of these efforts is the new permutation blocking path integral Monte Carlo approach, which is based on the combination of three different ingredients:

1. The introduction of antisymmetric imaginary-time propagators, i.e., determinants. This allows one to combine a large number of positive and negative terms into a single configuration weight, hence the term *blocking*. Thereby, a substantial part of the cancellation is carried out beforehand, which, in turn leads to a significant reduction of the fermion sign problem within Metropolis Monte Carlo simulations.

2. The usage of a fourth-order factorization of the density matrix. The beneficial cancellation only occurs when the mean inter-particle distance is comparable to the thermal wavelength of a single imaginary time slice, and, thus, vanishes with an increasing number of propagators. Yet, these are particularly necessary at low temperature, which

is precisely where the sign problem is most severe. This dilemma is solved via the introduction of fourth-order propagators, which allow for sufficient accuracy with only few imaginary time slices, thereby maximizing the benefits due to the determinants (ingredient 1) for a degree of quantum degeneracy that is beyond the capabilities of standard PIMC.

3. The development of a new Metropolis Monte Carlo update scheme. This has been necessary to ensure an efficient sampling of all configurations in the modified configuration space. Strictly speaking, there are no fixed paths in a permutation blocking path integral Monte Carlo simulation as all possible connections between beads on adjacent imaginary time slices are evaluated simultaneously within the determinants. Nevertheless, there can occur situations where only one or two such connections carry a non-negligible weight, and changing these links is analogous to the generation or modification of exchange-cycles within the standard PIMC algorithm. For this reason, I have developed an update scheme that is based on the worm algorithm paradigm from standard PIMC [36, 35], which has proven to be highly efficient especially regarding the sampling of exchange effects. To work around the absence of real paths within the PB-PIMC configuration space, I temporarily construct artificial trajectories, which can then be updated in the spirit of the worm algorithm in standard PIMC.

As a first test system for the new PB-PIMC method, I have considered electrons in a 2*D* harmonic confinement for which highly accurate data were available both at strong coupling (using the standard PIMC implementation that I wrote during my Master thesis [43]) and weak coupling (using the CPIMC method). Although this system had initially been thought of as little more than a test bed for method development and benchmarks, PB-PIMC has proven to be capable to provide accurate results over the entire transition from the strong coupling regime, where fermionic exchange is negligible, to the ideal limit—an interesting feature in its own right.

Furthermore, due to its formulation in coordinate space, PB-PIMC is perfectly suited for the investigation of spatial correlation functions, one of which—the so-called center-two particle correlation function—I have implemented and applied to the investigation of exchange and correlation effects of charged particles in traps (Sec. 3.2).

9.1.2   Towards a Complete Description of the Uniform Electron Gas

Due to its high current relevance for warm dense matter research, shortly after having published the original PB-PIMC method, I extended it to the simulation of the uniform electron gas (as described in Sec. 3.3). In a nutshell, I found (i) that accurate PB-PIMC

simulations are feasible over a broad range of parameters, thereby being significantly superior to standard PIMC, (ii) that the RPIMC results by Brown *et al.* [157] are surprisingly inaccurate even at moderate temperature and coupling, and (iii) that PB-PIMC is complementary to the CPIMC method. The last point means that a combination of the two allows for accurate QMC simulations of the UEG over significant parts of the warm dense matter regime—a theme that has permeated the remainder of this thesis.

Shortly thereafter, said combination was explored in detail (Chpt. 4) both for the spin-polarized (ferromagnetic) and unpolarized (paramagnetic) case. For the latter, I, with the help of the Daad–Rise student Connor Hann, extended the implementation of PB-PIMC to the simulation of multiple particle species, which, in this case, are given by spin-up and -down electrons. Overall, we were able to obtain extensive, accurate QMC data covering the entire relevant density range down to half the Fermi temperature. All these results were made freely available (e.g., for the further development of other methods), and a detailed comparison to the RPIMC data by Brown *et al.* [157] allowed us to quantify the nodal error for different quantities over a broad range of parameters.

A significant milestone on our quest for a complete *ab initio* thermodynamic description of the UEG was the development of a new finite-size correction that makes it possible to extrapolate the QMC results for N electrons in a finite simulation cell to the thermodynamic limit (Sec. 5.1). The problem that one encounters here is the fact that QMC methods, while properly taking into account all short-range exchange–correlation effects, cannot access long-range effects due to the finite simulation box. It was demonstrated that previous attempts to overcome this issue are not appropriate over substantial parts of the warm dense matter regime. To solve this problem, in Ref. [164] we proposed to combine our QMC data with those of dielectric approximations (such as the STLS scheme), which are known to provide the exact long-range behavior. In this way, we were able to devise a dramatically improved finite-size correction that works for all density–temperature combinations. Subsequently, we obtained an exhaustive data set for the interaction energy of the paramagnetic electron gas in the thermodynamic limit with an unprecedented accuracy of 0.3%, covering the entire r_s-range down to half the Fermi temperature. In addition, from these data we computed the exchange–correlation free energy, $f_{xc}^{\theta}(r_s)$, at fixed temperature, and compared it to previous parametrizations (see also Sec. 6.1). The large deviations to our *ab initio* results clearly demonstrated that an improved description of the warm dense UEG was highly needed.

As a side product of the combination of QMC data with the STLS formalism for the extrapolation to the thermodynamic limit, we produced accurate data for the static structure factor $S(k)$, see Sec. 5.2. The SSF contains the complete information about two-particle correlations and can be used as input for the computation of other quantities, see, e.g.,

Refs. [199, 198]. Moreover, it is connected to the pair correlation function via Fourier transform, which was explored in some detail in Sec. 5.2.1.

At this point, the realization of the final goal—the construction of a parametrization of the exchange–correlation free energy with respect to temperature, density, and spin-polarization, $f_{xc}(r_s, \theta, \xi)$—required us to solve two remaining problems: (i) the QMC simulation of arbitrary spin-polarizations in the thermodynamic limit and (ii) the lack of QMC data for $0 < \theta < 0.5$.

9.1.3   Complete Description of the Warm Dense Uniform Electron Gas

The construction of the first *ab initio* parametrization of the thermodynamic properties of the warm dense electron gas presented in Sec. 6.2 constitutes the capstone of this thesis. In particular, the two remaining problems mentioned at the bottom of the previous section were overcome in the following way: (i) we carried out extensive new QMC simulations for different spin-polarizations $0 < \xi \leq 1$ (using CPIMC at strong degeneracy and PB-PIMC at moderate to strong coupling) and carefully extrapolated these data to the thermodynamic limit.[1] Further, to accurately bridge the gap to the zero temperature limit, we added onto the available ground-state QMC data [174] a small temperature correction computed in the STLS formalism for temperatures $0 < \theta \leq 0.25$. In combination with our thermodynamic QMC data for $\theta \geq 0.5$, we thereby produced a vast set of accurate results for the interaction energy spanning the entire warm dense matter regime.

In particular, these data are fully sufficient to compute f_{xc} via the well-known coupling constant integration, which we exploited to construct our parametrization in the following way: we obtained parametrizations for the ferro- and paramagnetic cases, $f_{xc}^1(r_s, \theta)$ and $f_{xc}^0(r_s, \theta)$, over the entire r_s–θ-plane, and subsequently used our QMC data for intermediate polarizations to construct a spin-interpolation function. Together, all these ingredients were combined into the final result: the parametrization of the exchange–correlation energy with respect to all three relevant parameters, i.e., $f_{xc}(r_s, \theta, \xi)$.

This complete thermodynamic description of the UEG put us into the unprecedented position to gauge the accuracy of previous results, regarding many different quantities like f_{xc} itself, different energies, or the static structure factor $S(k)$. Very detailed comparisons to the dielectric approximations (RPA, STLS, Vashista–Singwi, *quantum STLS*[2], and the recent scheme by Tanaka [125]), RPIMC data [157], finite-temperature Green functions [59,

---

[1]For this purpose, we implemented the STLS formalism for arbitrary spin-polarization.

[2]I.e., the STLS closure relation for the local-field correction, but with the latter depending on frequency, see Refs. [158, 228, 229].

155, 159], and various exchange–correlation functions [107, 121–123, 125, 126, 207] can be found in our recent review [161], see Chpt. 2.

9.1.4   The Inhomogeneous Electron Gas

The final topic that I explored during this thesis is the computation of the static density–density response function from QMC simulations, see Chpt. 7. For this purpose, I extended the PB-PIMC method to the simulation of the inhomogeneous electron gas by applying a (static) harmonic perturbation of wave vector $\mathbf{q}$. Of course, QMC simulations allow for an accurate description of this system for arbitrarily strong perturbations. The point is that, for small perturbation amplitudes, linear response theory is valid. Therefore, in this regime, the modified density grows linearly with the perturbation, where the slope is given by the desired static density response function $\chi(\mathbf{q})$. Nevertheless, it should be noted that this procedure is quite involved, since it is required to carry out multiple simulations for different perturbation amplitudes to obtain $\chi(\mathbf{q})$ for a single wave vector $\mathbf{q}$. A more efficient, alternative strategy is presented in the outlook of Ref. [167].

The first results at moderate coupling and temperature revealed significant systematic errors both of the RPA and STLS schemes, thereby highlighting the impact of correlations on the static density response of the UEG. Overall, Chpt. 7 can be understood as a proof of concept regarding an interesting topic for future research, see also Sec 9.2.3.

9.2   Outlook

9.2.1   Further Applications of PB-PIMC

Throughout the bulk of this thesis, I applied the permutation blocking PIMC method to the simulation of the uniform electron gas in $3D$. However, it should be noted that the *ab initio* simulation of correlated fermions at finite temperature is of high importance within many fields of many-body physics and quantum chemistry. In the following, I will give a brief overview of interesting future applications of PB-PIMC:

- The $2D$ electron gas has been extensively investigated in the ground state [151, 230–232], but, at finite temperature, results remain sparse. In addition, I note that the reduced dimensionality will lead to a less severe manifestation of the fermion sign problem, making the application of PB-PIMC (possibly again in combination with CPIMC) very promising.

- Electrons in quantum dots, which are often modeled by a harmonic confinement [175, 233–236, 72], exhibit various interesting phenomena such as Wigner crystallization [183, 185] and Fermi-liquid like behavior [237]. Of particular use can be the application of many-particle correlation functions and the following computation of reduced entropies to spatially resolve crossovers and correlation effects [181, 179, 38]. An additional topic of interest might be the comparison between $2D$ and $3D$ systems, see, e.g., Ref. [28].

- Possibly the most challenging, yet highly intriguing, future application of the PB-PIMC method is the *ab initio* simulation of electron–ion plasmas at warm dense matter conditions, such as hydrogen, deuterium, or helium. A first step towards this goal would be the implementation of a *quantum pair potential* [238–240] that removes the Coulomb divergence between electrons and ions, or of the incorporation of the exact solution to the two-particle problem, often denoted as pair approximation [241, 242]. The latter could potentially be combined with a fourth-order factorization of the density matrix [243], thereby enhancing the effect of the permutation blocking. If successful, the new PB-PIMC data can be used to benchmark previous results such as the RPIMC data by Militzer *et al.* [53, 55, 58, 54], the direct PIMC data by Filinov *et al.* [64–66, 68] or thermal Kohn–Sham [244, 245] and orbital-free DFT results [246–250, 244].

- Spatially separated electron–hole bilayers [251] constitute a more exotic, yet nevertheless potentially useful application for PB-PIMC. Particularly interesting phenomena include the transition from Coulomb to dipolar interaction [252] and the superfluid crossover [253].

- Finally, I mention the possibility to simulate ultracold Fermi gases [254, 255] (such as ^{6}Li [256] or ^{3}He [49]), which constitute a topic of high current interest, among other things due to the exciting possibility of a BCS-BEC crossover [257, 258].

9.2.2   Utility of the Electron Gas Results

We expect our complete thermodynamic description of the warm dense electron gas to be of high importance for various future applications.

Firstly, the jellium model has always been an important test bed for the development of theories and algorithms, see, e.g., Refs. [147–152, 139]. Therefore, we expect our new accurate data—both in the thermodynamic limit and for a finite number of electrons—to be highly useful for the future development of simulation methods, and it was already used in Refs. [125, 126, 204, 158].

More importantly, our parametrization of the exchange–correlation free energy can easily
be incorporated into density functional theory simulations at finite temperature [104, 115,
116, 101], either directly within the local density approximation, or as the basis for more
sophisticated generalized gradient expansions [114, 200]. Another use of our parametrization
in the context of thermal DFT would be the benchmarking of a novel kind of functional based
on the adiabatic-connection fluctuation–dissipation formulation [217].

Further direct applications include its incorporation into quantum hydrodynamic simula-
tions [141, 142], various astrophysical models, see, e.g., Refs. [259, 260, 80, 144, 145], and
the further development of Fermi-liquid theory [146].

Another important point is our data set of accurate static structure factors [165], that is
currently being used as input for the calculation of the dynamic structure factor of the UEG
via the method of frequency moments, see, e.g., Ref. [199].

Our proof of principle investigation of the inhomogeneous electron gas has laid the
foundations for the future QMC investigation (using, in principle, standard PIMC, PB-PIMC,
or CPIMC, see also Sec. 9.2.3) of the static density response of the UEG, which could finally
result in the construction of a parametrization of the static local-field correction, as it already
exists for the ground state [225, 261].

9.2.3 Reconstruction of Dynamic Quantities from Imaginary-Time Cor-relation Functions

Throughout this thesis, I performed QMC simulations to compute static properties like the
interaction energy v or static structure factor $S(q)$. Arguably, accurate results for dynamic
quantities such as the single particle spectrum $A(\mathbf{q}, \omega)$ or the dynamic structure factor $S(\mathbf{q}, \omega)$
are of even higher importance, but, unfortunately, cannot be directly obtained by means of
QMC simulations due to an additional dynamical sign problem [218–220]. However, there is
a way to circumvent this obstacle, as it shall be briefly outlined in the following.

A particularly interesting quantity in this context is the imaginary-time density–density
correlation function, which is defined as

$$G_n(\mathbf{q}, \tau) = \frac{1}{N} \langle \rho(\mathbf{q}, \tau) \rho(-\mathbf{q}, 0) \rangle \quad , \tag{9.1}$$

with $\rho(\mathbf{q}, \tau)$ corresponding to the Fourier transform of the density operator evaluated at a
specific imaginary time τ. Obviously, such a quantity is straightforwardly evaluated in a
path integral Monte Carlo simulation [262]. For example, in the left panel of Fig. 9.1 I show
PIMC results for Eq. (9.1) for the unpolarized electron gas with $N = 34$, $r_s = 10$, and $\theta = 1$.
Firstly, I note that the number of imaginary time slices P determines the number of data
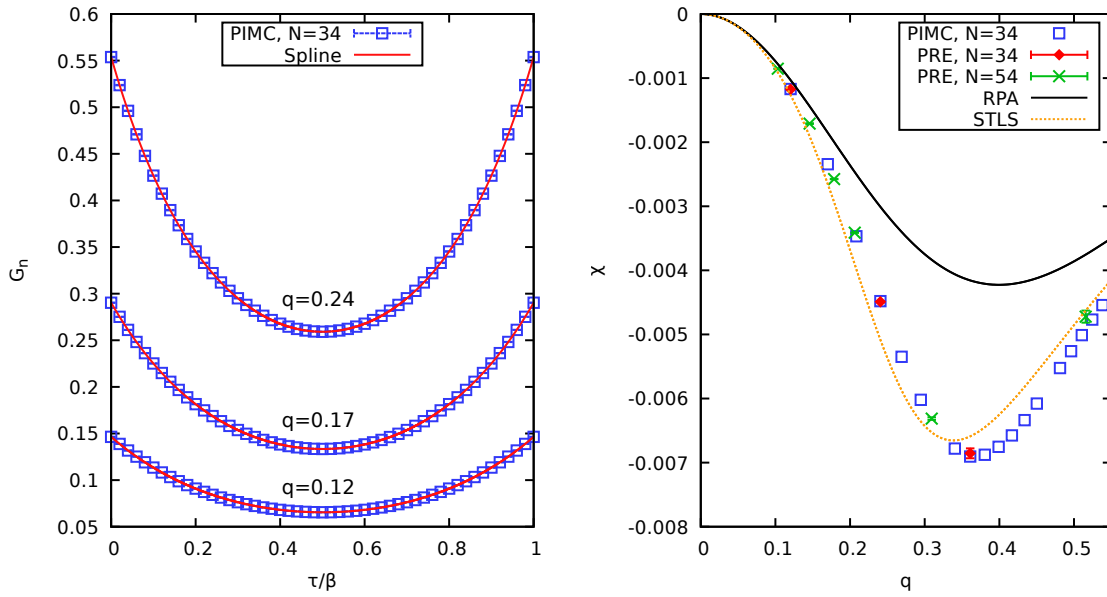
Fig. 9.1 Standard PIMC investigation of the density–density correlation function of the uniform electron gas at $\theta = 1$ and $r_s = 10$ for $N = 34$ unpolarized electrons with $P = 50$ time slices. Left: PIMC results for $G_n(q, \tau)$ (blue squares) for three q-values and corresponding spline fits (red lines). Right: Static density response function computed via integration of $G_n(q, \tau)$ (Eq. (9.2), blue squares), PB-PIMC estimations from the simulation of the harmonically perturbed electron gas for $N = 34$ (red diamonds) and $N = 54$ (green crosses) taken from Dornheim *et al.* [167], and dielectric results from RPA (solid black) and STLS (dotted yellow).

points for each wave vector (in this case, we have $P = 50$). Secondly, $G_n(\mathbf{q}, \tau)$ is symmetric with respect to $\tau = \beta/2$, so that only half of the points contain real information.

One of the useful features of the density correlation function is its direct connection to the static density response function (see Chpt. 7),

$$\chi(\mathbf{q}) = -\frac{N}{V} \int_0^\beta \mathrm{d}\tau \, G_n(\mathbf{q}, \tau) \quad . \tag{9.2}$$

To evaluate Eq. (9.2), I interpolate the discrete G_n data with a spline (the red curves in the left panel of Fig. 9.1), which can then be integrated numerically. The results of this procedure (for each q-value) are depicted in the right panel of Fig. 9.1 and correspond to the blue squares. For completeness, I again show the corresponding static density response functions from RPA and STLS and the PB-PIMC results from the simulation of the harmonically perturbed system (see Chpt. 7, and Ref. [167]) for two different particle numbers. Evidently, the new results are in excellent agreement with the previous PB-PIMC data, as it is expected. The main advantage of the present strategy is that the entire wave vector dependence of χ can be obtained within a single simulation of the unperturbed system, whereas the procedure from Chpt. 7 requires multiple simulations of the perturbed system for each q-value. Unfortunately, this only works when standard PIMC simulations are not prevented by the fermion sign problem, which means that significant parts of the warm dense matter regime cannot be accessed, leaving the PB-PIMC simulation of the harmonically perturbed system as the only viable option in that case[3].

The most important application of $G_n(\mathbf{q}, \tau)$ is its connection to the dynamic structure factor $S(\mathbf{q}, \omega)$,

$$G_n(\mathbf{q}, \tau) = \int_{-\infty}^\infty \mathrm{d}\omega \, e^{-\tau\omega} S(\mathbf{q}, \omega) \tag{9.3}$$

$$= \int_0^\infty \mathrm{d}\omega \, (e^{-\tau\omega} + e^{-(\beta-\tau)\omega}) S(\mathbf{q}, \omega) \quad , \tag{9.4}$$

where the second equality follows from the well-known symmetry relation $S(\mathbf{q}, -\omega) = S(\mathbf{q}, \omega)e^{-\beta\omega}$. Obviously, the task at hand is to solve Eq. (9.3) for $S(\mathbf{q}, \omega)$, i.e., to perform an inverse Laplace transform [263]. This can be interpreted as follows: the standard PIMC simulations allow for the computation of a limited amount of information about the dynamic structure factor, i.e., the $P/2 + 1$ independent values of the imaginary-time density correlation function G_n for different τ values. In practice, this makes possible a *reconstruction* of $S(\mathbf{q}, \omega)$ by finding a model structure factor that, when plugged into Eq. (9.3), correctly reproduces

---

[3]Note that a PB-PIMC evaluation of Eq. (9.2) is not possible due to the small number of imaginary time slices.

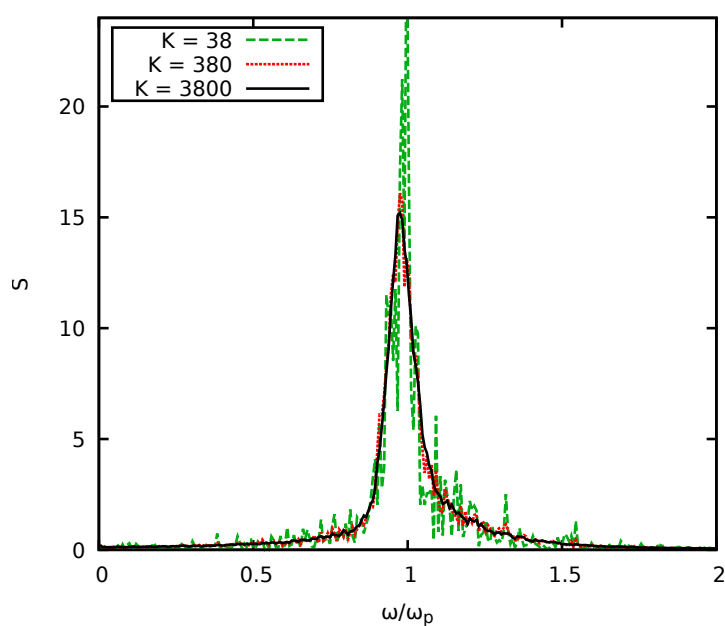Fig. 9.2 GIFT reconstruction of the dynamic structure factor for the unpolarized electron gas at $r_s = 10$ and $\theta = 1$ for $N = 34$ electrons and $\mathbf{q} = 2\pi/L(1,0,0)^T$. Shown are averages over $K = 38$ (dashed green), $K = 380$ (dotted red), and $K = 3800$ (solid black) independently reconstructed structure factors. The frequency is given in units of the plasma frequency $\omega_p = \sqrt{3/r_s^3}$.

all known $G_n(\tau)$ values within the given Monte Carlo error bars. This is a notoriously difficult problem, in particular, since said statistical uncertainty implies that the solution is, in general, not unique [263], and unphysically sharp peaks in $S(\mathbf{q}, \omega)$ may arise. The most common approach to prevent this issue is the maximum entropy method [264, 265], which is based on Bayes theorem and requires some prior knowledge about the spectrum of interest. For example, one might demand the absence of very sharp peaks and thereby receive a smooth result for S, although this can potentially lead to the suppression of unexpected, interesting features. A different strategy is the computation of a large number, K, of random functions $S_i(\mathbf{q}, \omega)$, where the final result is then given as the average. Examples for this paradigm include the stochastic optimization method by Mishchenko *et al.* [32, 266, 267] or the genetic inversion by falsification of theories (GIFT) proposed by Vitali *et al.* [268]. In the present work, I use a GIFT implementation that I wrote during my Master thesis [43] to reconstruct the dynamic structure factor of the uniform electron gas for the same parameters as in Fig. 9.1.

In Fig. 9.2, I show GIFT results for the smallest wave vector that is available in the PIMC simulation, $q \approx 0.12$. As each individual solution, S_i, can be almost arbitrarily noisy, the average over $K = 38$ spectra (dashed green) is still heavily fluctuating, although we can clearly resolve a pronounced peak around the plasma frequency ω_p. For $K = 380$ (dotted red), we already have a sufficiently smooth curve, which is further improved for $K = 3800$ (solid black).

Of particular importance is the dispersion relation, i.e., the behavior of the dynamic structure factor both with respect to frequency and wave vector. This information is shown for the present example in Fig. 9.3. First, let us consider the dotted red curves corresponding to ideal fermions at the same parameters. In this case, the dynamic structure factor follows the ideal dispersion relation $\omega = q^2/2$, and is broadened towards large q. Second, the dashed blue curves have been computed within the random-phase approximation (RPA, see Ref. [131] for all necessary details) and exhibit a substantially modified behavior. For small to intermediate q-values, S_{RPA} is significantly sharper than the ideal curve and roughly follows a parabolic dispersion relation that is shifted by the plasma frequency, cf. the solid blue curve. Finally, the solid black curves correspond to the new *ab initio* results for the dynamic structure factor that were obtained via the reconstruction from the PIMC data for $G_n(\mathbf{q}, \tau)$. Overall, the agreement to the random-phase approximation is only qualitative both with respect to the peak position and the particular width and shape, as it is expected at $r_s = 10$, see Sec. 5.2 for a comparison of the corresponding static structure factors. Nevertheless, to allow for quantitative judgments, one should carefully investigate possible finite-size effects (which are absent in the static structure factor $S(k)$, but could potentially lead to a broadening of the
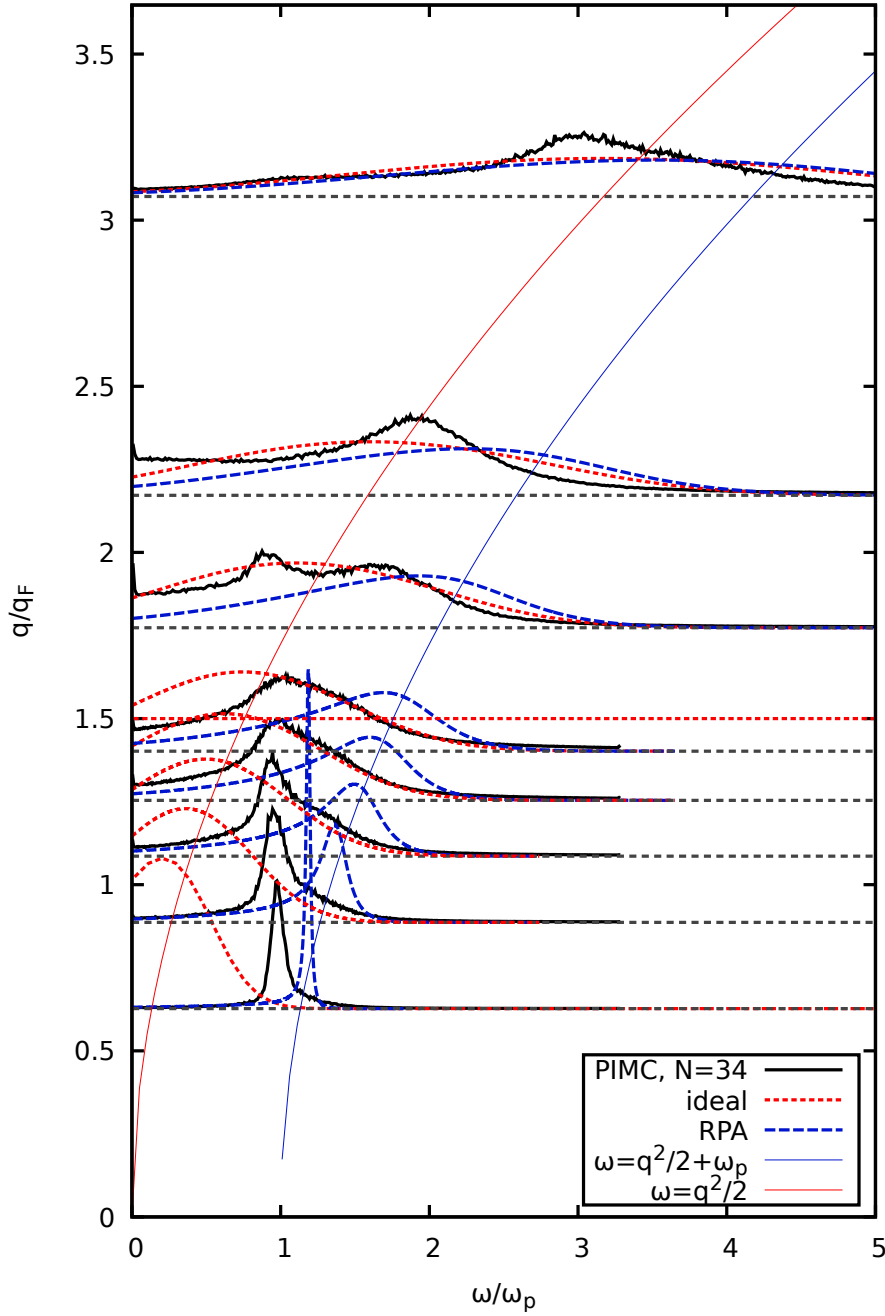
Fig. 9.3 *Ab initio* data for the dynamic structure factor of the unpolarized UEG at $r_s = 10$ and $\theta = 1$. Shown are the results from a reconstruction using PIMC data for $G_n(q, \tau)$ (solid black), the corresponding results for the ideal system (dotted red) and the random-phase approximation (dashed blue). The solid red and blue curves correspond to the ideal and shifted ideal dispersion relations, respectively. The wave vector is given in units of the Fermi vector $q_F = (3\pi^2 n)^{1/3}$.

peaks) and check if the known frequency moments (sum-rules [269]) are fulfilled (see, e.g., the Appendix of Ref. [33] for a detailed discussion).

In a nutshell, the reconstruction of the dynamic structure factor $S(\mathbf{q}, \omega)$ that has been presented in this outlook provides the unique possibility to study the collective dynamics of moderately to strongly correlated electrons (or weakly coupled electrons at moderate to large temperature) from first principles. This is particularly interesting with respect to the recent prediction of previously unexpected collective modes at sparse density, see Refs. [270, 271]. Although a direct investigation at warm dense matter conditions will probably remain unfeasible due to the fermion sign problem, the combination of standard PIMC and GIFT can provide potentially valuable benchmark data at high density and moderate temperature, which can then be used to gauge the accuracy of other approximate schemes such as the method of frequency moments [199], nonequilibrium Green functions [160, 155, 272–274], or the interpolation of the dynamic local-field correction between known limits [275].

Appendix A

List of Acronyms

- **BCS :** Bardeen–Cooper–Schrieffer
- **BEC :** Bose–Einstein-Condensation
- **CPIMC :** configuration path integral Monte Carlo
- **DFT :** density functional theory
- **DMQMC :** density matrix quantum Monte Carlo
- **FSP :** fermion sign problem
- **GIFT :** genetic inversion by falsification of theories
- **LDA :** local density approximation
- **LFC :** local field correction
- **MD :** molecular dynamics
- **PB-PIMC :** permutation blocking path integral Monte Carlo
- **PIMC :** path integral Monte Carlo
- **QMC :** quantum Monte Carlo
- **RPA :** random phase approximation
- **RPIMC :** restricted path integral Monte Carlo
- **SSF :** static structure factor
- **STLS :** Singwi–Tosi–Land–Sjölander
- **UEG :** uniform electron gas
- **WDM :** warm dense matter
- **XC :** exchange–correlation

Appendix B

Complete List of Contributions to International Conferences

2014

- **Berlin, Germany, DPG spring meeting (Poster):**
  Quantum breathing frequency of trapped dipolar gases
  – Tobias Dornheim, Alexey Filinov, and Michael Bonitz

- **Berlin, Germany, DPG spring meeting (Poster):**
  Quantum breathing frequency of nanoplasmas
  – Tobias Dornheim, Alexey Filinov, Jan-Willem Abraham, and Michael Bonitz
  → This contribution has been awarded the prize for *Best Theory Poster*.

2015

- **Berlin, Germany, DPG spring meeting (Poster):**
  QMC Results for the Breathing Mode of Trapped Bosons
  – Tobias Dornheim, Alexey Filinov, Jan-Willem Abraham, and Michael Bonitz

- **Lausanne, Switzerland, CECAM workshop: Stochastic Wavefunction Methods in Quantum Chemistry, Electronic Structure Theory and Condensed Matter Physics (Poster):**
  Permutation blocking path integral Monte Carlo simulations of strongly degenerate non-ideal fermions
  – Tobias Dornheim, Simon Groth, Alexey Filinov, and Michael Bonitz

- **Bad Honnef, Germany, WEH seminar: Isolated Quantum Many-Body Systems out of Equilibrium (Poster):**
  Ab Initio Thermodynamic Results for the Uniform Electron Gas at Finite Temperature
  – Tobias Dornheim, Tim Schoof, Simon Groth, and Michael Bonitz

- **Almaty, Kazakhstan, 15th International Conference on the physics of Non-Ideal Plasmas (contributed talk):**
  Permutation blocking path integral Monte Carlo simulations of strongly degenerate nonideal fermions
  – Tobias Dornheim, Tim Schoof, Simon Groth, Alexey Filinov, and Michael Bonitz

2016

- **Hannover, Germany, DPG spring meeting (contributed talk):**
  Ab Initio Thermodynamic Results for the Uniform Electron Gas at Finite Temperature
  – Tobias Dornheim, Simon Groth, Tim Schoof, and Michael Bonitz

- **Hannover, Germany, DPG spring meeting (Poster):**
  Thermodynamic Fermionic Monte Carlo Simulations of Continuous Systems without Fixed Nodes
  – Tobias Dornheim, Tim Schoof, Simon Groth, and Michael Bonitz
  → This contribution has been awarded the prize for *Best Theory Poster*.

- **Hamburg, Germany, Quo vadis - complex plasmas (Poster):**
  Resolving phase transitions in finite dust clusters and quantum dots
  – Tobias Dornheim, Hauke Thomsen, Patrick Ludwig, and Michael Bonitz

2017

- **Hirschegg, Austria, 37th International Workshop on High Energy Density Physics with Intense Ion and Laser Beams (contributed talk):**
  Ab Initio Quantum Monte Carlo Simulation of the Warm Dense Electron Gas
  – Tobias Dornheim, Simon Groth, Travis Sjostrom, Fionn D. Malone, W.M.C. Foulkes, and Michael Bonitz

- **Bremen, Germany, DPG spring meeting (Poster):**
  Ab Initio Quantum Monte Carlo Simulation of the Warm Dense Electron Gas
  – Tobias Dornheim, Simon Groth, Travis Sjostrom, and Michael Bonitz

- **Vancouver, Canada, The 9th International Workshop on Warm Dense Matter (Poster):**
  Ab initio Quantum Monte Carlo simulation of the warm dense electron gas
  – Tobias Dornheim, Simon Groth, Travis Sjostrom, Fionn D. Malone, W.M.C. Foulkes, and Michael Bonitz

- **Belfast, United Kingdom, EPS meeting: 44th Conference on Plasma Physics (contributed talk):**
  Ab initio Thermodynamic Description of the Uniform Electron Gas at Warm Dense Matter Conditions
  – Tobias Dornheim, Simon Groth, Travis Sjostrom, Fionn D. Malone, W.M.C. Foulkes, and Michael Bonitz

- **Kiel, Germany, Strongly Coupled Coulomb Systems 2017 (invited talk):**
  Ab initio Quantum Monte Carlo results for the Warm Dense Electron Gas
  – Tobias Dornheim, Simon Groth, Travis Sjostrom, Fionn D. Malone, W.M.C. Foulkes, and Michael Bonitz

Appendix C

Complete List of Publications

1. T. Dornheim, A.V. Filinov, and M. Bonitz, Superfluidity of strongly correlated bosons in two-and three-dimensional traps, *Phys. Rev. B* **91**, 054503 (2015)

2. T. Dornheim, S. Groth, A. Filinov and M. Bonitz, Permutation blocking path integral Monte Carlo: a highly efficient approach to the simulation of strongly degeneratenon-ideal fermions, *New J. Phys.* **17**, 073017 (2015)

3. T. Dornheim, T. Schoof, S. Groth, A. Filinov, and M. Bonitz, Permutation Blocking Path Integral Monte Carlo Approach to the Uniform Electron Gas at Finite Temperature, *J. Chem. Phys.* **143**, 204101 (2015)

4. T. Dornheim, H. Thomsen, P. Ludwig, A. Filinov, and M. Bonitz, Analyzing quantum correlations made simple, *Contrib. Plasma Phys.* **56**, 371 (2016)

5. S. Groth, T. Schoof, T. Dornheim, and M. Bonitz, Ab Initio Quantum Monte Carlo Simulations of the Uniform Electron Gas without Fixed Nodes, *Phys. Rev. B* **93**, 085102 (2016)

6. T. Dornheim, S. Groth, T. Schoof, C. Hann, and M. Bonitz, Ab initio quantum Monte Carlo simulations of the Uniform electron gas without fixed nodes: The unpolarized case, *Phys. Rev. B* **93**, 205134 (2016)

7. B. Dupé, C.N. Kruse, T. Dornheim, and S. Heinze, How to reveal metastable skyrmionic spin structures by spin-polarized scanning tunneling microscopy, *New J. Phys.* **18**, 055015 (2016)

8. T. Dornheim, S. Groth, T. Sjostrom, F.D. Malone, W.M.C. Foulkes, and M. Bonitz, Ab Initio Quantum Monte Carlo Simulation of the Warm Dense Electron Gas in the Thermodynamic Limit, *Phys. Rev. Lett.* **117**, 156403 (2016)

9. S. Groth, T. Dornheim, and M. Bonitz, Free Energy of the Uniform Electron Gas: Testing Analytical Models against First Principle Results, *Contrib. Plasma Phys.* **57**, 137 (2017)

10. T. Dornheim, S. Groth, F.D. Malone, T. Schoof, T. Sjostrom, W.M.C. Foulkes, and M. Bonitz, Ab Initio Quantum Monte Carlo Simulation of the Warm Dense Electron Gas, *Phys. Plasmas* **24**, 056303 (2017)

11. S. Groth, T. Dornheim, T. Sjostrom, F.D. Malone, W.M.C. Foulkes, and M. Bonitz, Ab initio Exchange-Correlation Free Energy of the Uniform Electron Gas at Warm Dense Matter Conditions, *Phys. Rev. Lett.* **119**, 135001 (2017)

12. T. Dornheim, S. Groth, J. Vorberger, and M. Bonitz, Permutation Blocking Path Integral Monte Carlo approach to the Static Density Response of the Warm Dense Electron Gas, *Phys. Rev. E* **96**, 023203 (2017)

13. S. Groth, T. Dornheim, and M. Bonitz, Configuration Path Integral Monte Carlo Approach to the Static Density Response of the Warm Dense Electron Gas, *J. Chem. Phys.* **147**, 164108 (2017)

14. T. Dornheim, S. Groth, and M. Bonitz, Ab Initio results for the Static Structure Factor of the Warm Dense Electron Gas, *Contrib. Plasma Phys.* **57**, 468 (2017)
    → The paper has been selected as *Editor's Choice*.

15. Zh.A. Moldabekov, S. Groth, T. Dornheim, M. Bonitz, and T.S. Ramazanov, Ion Potential in Non-ideal Dense Quantum Plasmas, *Contrib. Plasma Phys.* **57**, 532 (2017)

16. T. Ott, H. Thomsen, J.W. Abraham, T. Dornheim, and M. Bonitz, Recent progress in the theory and simulation of strongly correlated plasmas: phase transitions, transport, quantum, and magnetic field effects, accepted for publication in *Eur. Phys. J. D* (2018)

17. T. Dornheim, S. Groth, and M. Bonitz, The Uniform Electron Gas at Warm Dense Matter Conditions, *arXiv:1801.05783*, submitted as an invited article to *Phys. Reports.* (2018)

References

[1] H. Quadbeck-Seeger. *Aphorismen und Zitate über Natur und Wissenschaft*. Wiley-VCH, 2013.

[2] R. P. Feynman. Simulating physics with computers. *International Journal of Theoretical Physics*, **21**(6):467–488, Jun 1982.

[3] D. P. DiVincenzo. Quantum computation. *Science*, **270**(5234):255–261, 1995.

[4] A. Barenco, C. H. Bennett, R. Cleve, D. P. DiVincenzo, N. Margolus, P. Shor, T. Sleator, J. A. Smolin, and H. Weinfurter. Elementary gates for quantum computation. *Physical Review A*, **52**:3457–3467, Nov 1995.

[5] R. Feynman, A. Hibbs, and D. Styer. *Quantum Mechanics and Path Integrals*. Dover Books on Physics. Dover Publications, 2010.

[6] D. Chandler and P. Wolynes. Exploiting the isomorphism between quantum theory and classical statistical mechanics of polyatomic fluids. *The Journal of Chemical Physics*, **74**:4078, 1981.

[7] K. Temme, T. J. Osborne, K. G. Vollbrecht, D. Poulin, and F. Verstraete. Quantum Metropolis sampling. *Nature*, **471**(7336):87, Mar. 2011.

[8] M.-H. Yung and A. Aspuru-Guzik. A quantum–quantum Metropolis algorithm. *Proceedings of the National Academy of Sciences*, **109**(3):754–759, Jan. 2012.

[9] G. Ortiz, J. E. Gubernatis, E. Knill, and R. Laflamme. Quantum algorithms for fermionic simulations. *Physical Review A*, **64**(2):022319, July 2001.

[10] S. Akama. *Elements of Quantum Computing: History, Theories and Engineering Applications*. Springer International Publishing, 2014.

[11] M. Saffman. Quantum computing with atomic qubits and rydberg interactions: progress and challenges. *Journal of Physics B: Atomic, Molecular and Optical Physics*, **49**(20):202001, 2016.

[12] H. Kleinert. *Path Integrals in Quantum Mechanics, Statistics, Polymer Physics, and Financial Markets*. EBL-Schweitzer. World Scientific, 2009.

[13] A. Filinov and M. Bonitz. Classical and Quantum Monte Carlo. In M. Bonitz and D. Semkat, editors, *Introduction to Computational Methods in Many Body Physics*, chapter 5, page 237. Rinton Press, Paramus, New Jersey (United States of America), 2006.

[14] J. Liu. *Monte Carlo Strategies in Scientific Computing*. Springer Series in Statistics. Springer New York, 2013.

[15] N. Metropolis and S. Ulam. The Monte Carlo Method. *Journal of the American Statistical Association*, **44**(247):335–341, 1949.

[16] N. Metropolis, A. W. Rosenbluth, M. N. Rosenbluth, A. H. Teller, and E. Teller. Equation of State Calculations by Fast Computing Machines. *The Journal of Chemical Physics*, **21**(6):1087–1092, June 1953.

[17] W. K. Hastings. Monte Carlo sampling methods using Markov chains and their applications. *Biometrika*, **57**(1):97–109, 1970.

[18] S. Chib and E. Greenberg. Understanding the Metropolis-Hastings Algorithm. *The American Statistician*, **49**(4):327–335, 1995.

[19] M. F. Herman, E. J. Bruskin, and B. J. Berne. On path integral Monte Carlo simulations. *The Journal of Chemical Physics*, **76**(10):5150–5155, May 1982.

[20] E. Pollock and D. Ceperley. Simulation of quantum many-body systems by path-integral methods. *Physical Review B*, **30**(5):2555–2568, Sept. 1984.

[21] D. M. Ceperley. Path integrals in the theory of condensed helium. *Reviews of Modern Physics*, **67**(2):279–355, Apr. 1995.

[22] L. D. Fosdick and H. F. Jordan. Path-Integral Calculation of the Two-Particle Slater Sum for He^4. *Physical Review*, **143**:58–66, Mar 1966.

[23] H. F. Jordan and L. D. Fosdick. Three-Particle Effects in the Pair Distribution Function for He^4 Gas. *Physical Review*, **171**:128–149, Jul 1968.

[24] E. L. Pollock and D. M. Ceperley. Path-integral computation of superfluid densities. *Physical Review B*, **36**(16):8343–8352, Dec. 1987.

[25] P. Sindzingre, M. L. Klein, and D. M. Ceperley. Path-integral Monte Carlo study of low-temperature ^{4}He clusters. *Physical Review Letters*, **63**(15):1601–1604, Oct. 1989.

[26] Y. Kwon, F. Paesani, and K. Whaley. Local superfluidity in inhomogeneous quantum fluids. *Physical Review B*, **74**(17), Nov. 2006.

[27] A. Filinov, N. V. Prokof'ev, and M. Bonitz. Berezinskii-Kosterlitz-Thouless Transition in Two-Dimensional Dipole Systems. *Physical Review Letters*, **105**:070401, Aug 2010.

[28] T. Dornheim, A. Filinov, and M. Bonitz. Superfluidity of strongly correlated bosons in two- and three-dimensional traps. *Physical Review B*, **91**(5):054503, Feb. 2015.

[29] S. Pilati, S. Giorgini, M. Modugno, and N. Prokof'ev. Dilute Bose gas with correlated disorder: a path integral Monte Carlo study. *New Journal of Physics*, **12**(7):073003, 2010.

[30] H. Saito. Path-Integral Monte Carlo Study on a Droplet of a Dipolar Bose–Einstein Condensate Stabilized by Quantum Fluctuation. *Journal of the Physical Society of Japan*, **85**(5):053001, Apr. 2016.

[31] M. Boninsegni and D. M. Ceperley. Density fluctuations in liquid ^{4}He. Path integrals and maximum entropy. *Journal of Low Temperature Physics*, **104**(5-6):339–357, Sept. 1996.

[32] A. Filinov and M. Bonitz. Collective and single-particle excitations in two-dimensional dipolar Bose gases. *Physical Review A*, **86**(4), Oct. 2012.

[33] A. Filinov. Correlation effects and collective excitations in bosonic bilayers: Role of quantum statistics, superfluidity, and the dimerization transition. *Physical Review A*, **94**(1):013603, July 2016.

[34] G. Ferré and J. Boronat. Dynamic structure factor of liquid ^{4}He across the normal-superfluid transition. *Physical Review B*, **93**(10):104510, Mar. 2016.

[35] M. Boninsegni, N. Prokof'ev, and B. Svistunov. Worm Algorithm for Continuous-Space Path Integral Monte~Carlo Simulations. *Physical Review Letters*, **96**(7):070601, Feb. 2006.

[36] M. Boninsegni, N. V. Prokof'ev, and B. V. Svistunov. Worm algorithm and diagrammatic Monte Carlo: A new approach to continuous-space path integral Monte Carlo simulations. *Physical Review E*, **74**(3):036701, Sept. 2006.

[37] B. Clark, M. Casula, and D. Ceperley. Hexatic and Mesoscopic Phases in a 2d Quantum Coulomb System. *Physical Review Letters*, **103**(5), July 2009.

[38] T. Dornheim, H. Thomsen, P. Ludwig, A. Filinov, and M. Bonitz. Analyzing Quantum Correlations Made Simple. *Contributions to Plasma Physics*, **56**(5):371–379, June 2016.

[39] E. Loh, J. Gubernatis, R. Scalettar, S. White, D. Scalapino, and R. Sugar. Sign problem in the numerical simulation of many-electron systems. *Physical Review B*, **41**(13):9301–9307, May 1990.

[40] M. Troyer and U.-J. Wiese. Computational Complexity and Fundamental Limitations to Fermionic Quantum Monte Carlo Simulations. *Physical Review Letters*, **94**(17), May 2005.

[41] M. Takahashi and M. Imada. Monte Carlo Calculation of Quantum Systems. *Journal of the Physical Society of Japan*, **53**(3):963–974, Mar. 1984.

[42] T. Dornheim, S. Groth, F. D. Malone, T. Schoof, T. Sjostrom, W. M. C. Foulkes, and M. Bonitz. Ab initio quantum Monte Carlo simulation of the warm dense electron gas. *Physics of Plasmas*, **24**(5):056303, Mar. 2017.

[43] T. Dornheim. Path Integral Monte Carlo Simulations of Correlated Bosons and Fermions in Traps. Master's thesis, Christian-Albrechts Universität zu Kiel, 2014.

[44] J. B. Anderson. A random-walk simulation of the Schrödinger equation: H+3. *The Journal of Chemical Physics*, **63**(4):1499–1503, 1975.

[45] J. B. Anderson. Quantum chemistry by random walk. H 2P, H+3 D3h 1A1, H2 3Σ+u, H4 1Σ+g, Be 1S. *The Journal of Chemical Physics*, **65**(10):4121–4127, 1976.

[46] W. M. C. Foulkes, L. Mitas, R. J. Needs, and G. Rajagopal. Quantum Monte Carlo simulations of solids. *Reviews of Modern Physics*, **73**(1):33–83, Jan. 2001.

[47] J. Anderson. *Quantum Monte Carlo: Origins, Development, Applications*. Oxford University Press, 2007.

[48] D. M. Ceperley. Fermion nodes. *Journal of Statistical Physics*, **63**(5-6):1237–1267, June 1991.

[49] D. M. Ceperley. Path-integral calculations of normal liquid ^{3}He. *Physical Review Letters*, **69**(2):331–334, July 1992.

[50] V. Filinov. Cluster expansion for ideal Fermi systems in the 'fixed-node approximation'. *Journal of Physics A: Mathematical and General*, **34**(8):1665, Mar. 2001.

[51] V. S. Filinov. Analytical contradictions of the fixed-node density matrix. *High Temperature*, **52**(5):615–620, Oct. 2014.

[52] E. Brown. *Path integral Monte Carlo and the electron gas*. PhD thesis, University of Illinois at Urbana-Champaign, 2014.

[53] K. P. Driver and B. Militzer. All-Electron Path Integral Monte Carlo Simulations of Warm Dense Matter: Application to Water and Carbon Plasmas. *Physical Review Letters*, **108**(11):115502, Mar. 2012.

[54] B. Militzer and K. P. Driver. Development of Path Integral Monte Carlo Simulations with Localized Nodal Surfaces for Second-Row Elements. *Physical Review Letters*, **115**(17):176403, Oct. 2015.

[55] K. P. Driver and B. Militzer. First-principles equation of state calculations of warm dense nitrogen. *Physical Review B*, **93**(6):064101, Feb. 2016.

[56] S. Zhang, K. P. Driver, F. Soubiran, and B. Militzer. First-principles equation of state and shock compression predictions of warm dense hydrocarbons. *Physical Review E*, **96**(1):013204, July 2017.

[57] K. P. Driver, F. Soubiran, S. Zhang, and B. Militzer. Comparison of path integral Monte Carlo simulations of helium, carbon, nitrogen, oxygen, water, neon, and silicon plasmas. *High Energy Density Physics*, **23**:81–89, June 2017.

[58] K. P. Driver and B. Militzer. First-principles simulations of warm dense lithium fluoride. *Physical Review E*, **95**(4):043205, Apr. 2017.

[59] T. Schoof, S. Groth, J. Vorberger, and M. Bonitz. *Ab Initio* Thermodynamic Results for the Degenerate Electron Gas at Finite Temperature. *Physical Review Letters*, **115**(13):130402, Sept. 2015.

[60] V. Zamalin, G. E. Norman, and V. S. Filinov. *The Monte Carlo Method in Statistical Thermodynamics*. Nauka, Moscow, 1977.

[61] A. P. Lyubartsev. Simulation of excited states and the sign problem in the path integral Monte Carlo method. *Journal of Physics A: Mathematical and General*, **38**(30):6659, July 2005.

[62] S. A. Chin. High-order path-integral Monte Carlo methods for solving quantum dot problems. *Physical Review E*, **91**(3):031301, Mar. 2015.

[63] V. S. Filinov. Construction of a Monte-Carlo method for calculating Feynman integrals. *USSR Computational Mathematics and Mathematical Physics*, **26**(1):21–29, Jan. 1986.

[64] V. S. Filinov, M. Bonitz, W. Ebeling, and V. E. Fortov. Thermodynamics of hot dense H-plasmas: path integral Monte Carlo simulations and analytical approximations. *Plasma Physics and Controlled Fusion*, **43**(6):743, 2001.

[65] V. S. Filinov, V. E. Fortov, M. Bonitz, and P. R. Levashov. Phase transition in strongly degenerate hydrogen plasma. *Journal of Experimental and Theoretical Physics Letters*, **74**(7):384–387, Oct. 2001.

[66] V. S. Filinov, M. Bonitz, V. E. Fortov, W. Ebeling, P. Levashov, and M. Schlanges. Thermodynamic Properties and Plasma Phase Transition in dense Hydrogen. *Contributions to Plasma Physics*, **44**(5-6):388–394, Sept. 2004.

[67] V. S. Filinov, H. Fehske, M. Bonitz, V. E. Fortov, and P. Levashov. Correlation effects in partially ionized mass asymmetric electron-hole plasmas. *Physical Review E*, **75**(3):036401, Mar. 2007.

[68] V. S. Filinov, M. Bonitz, H. Fehske, V. E. Fortov, and P. R. Levashov. Proton Crystallization in a Dense Hydrogen Plasma. *Contributions to Plasma Physics*, **52**(3):224–228, Apr. 2012.

[69] V. S. Filinov, V. E. Fortov, M. Bonitz, and Z. Moldabekov. Fermionic path-integral Monte Carlo results for the uniform electron gas at finite temperature. *Physical Review E*, **91**(3):033108, Mar. 2015.

[70] V. Filinov, M. Bonitz, Y. Ivanov, E.-M. Ilgenfritz, and V. Fortov. Thermodynamics of the Quark-Gluon Plasma at Finite Chemical Potential: Color Path Integral Monte Carlo Results. *Contributions to Plasma Physics*, **55**(2-3):203–208, Feb. 2015.

[71] V. S. Filinov, V. E. Fortov, M. Bonitz, and Z. Moldabekov. Total and correlation energy of the uniform polarized electron gas at finite temperature: Direct path integral simulations. *Journal of Physics: Conference Series*, **653**(1):012113, 2015.

[72] T. Dornheim, S. Groth, A. Filinov, and M. Bonitz. Permutation blocking path integral Monte Carlo: a highly efficient approach to the simulation of strongly degenerate non-ideal fermions. *New Journal of Physics*, **17**(7):073017, July 2015.

[73] T. Schoof, M. Bonitz, A. Filinov, D. Hochstuhl, and J. Dufty. Configuration Path Integral Monte Carlo. *Contributions to Plasma Physics*, **51**(8):687–697, Sept. 2011.

[74] T. Schoof, S. Groth, and M. Bonitz. Towards ab Initio Thermodynamics of the Electron Gas at Strong Degeneracy. *Contributions to Plasma Physics*, **55**(2-3):136–143, Feb. 2015.

[75] T. Schoof. *Configuration Path Integral Monte Carlo: Ab initio simulations of fermions in the warm dense matter regime*. PhD thesis, Christian-Albrechts Universität zu Kiel, 2016.

[76] S. Groth. Strongly Degenerate Nonideal Fermi Systems: Configuration Path Integral Monte Carlo Simulation. Master's thesis, Christian-Albrechts Universität zu Kiel, 2014.

[77] T. Dornheim, T. Schoof, S. Groth, A. Filinov, and M. Bonitz. Permutation blocking path integral Monte Carlo approach to the uniform electron gas at finite temperature. *The Journal of Chemical Physics*, **143**(20):204101, Nov. 2015.

[78] V. E. Fortov. Extreme states of matter on Earth and in space. *Physics-Uspekhi*, **52**(6):615, 2009.

[79] F. Graziani, M. Desjarlais, R. Redmer, and S. Trickey. *Frontiers and Challenges in Warm Dense Matter*. Lecture Notes in Computational Science and Engineering. Springer International Publishing, 2014.

[80] D. Saumon, W. B. Hubbard, G. Chabrier, and H. M. van Horn. The role of the molecular-metallic transition of hydrogen in the evolution of Jupiter, Saturn, and brown dwarfs. *Astrophysical Journal*, **391**:827–831, June 1992.

[81] W. B. Hubbard, T. Guillot, J. I. Lunine, A. Burrows, D. Saumon, M. S. Marley, and R. S. Freedman. Liquid metallic hydrogen and the structure of brown dwarfs and giant planets. *Physics of Plasmas*, **4**(5):2011–2015, May 1997.

[82] G. W. Collins, L. B. D. Silva, P. Celliers, D. M. Gold, M. E. Foord, R. J. Wallace, A. Ng, S. V. Weber, K. S. Budil, and R. Cauble. Measurements of the Equation of State of Deuterium at the Fluid Insulator-Metal Transition. *Science*, **281**(5380):1178–1181, Aug. 1998.

[83] S. H. Glenzer, L. B. Fletcher, E. Galtier, B. Nagler, R. Alonso-Mori, B. Barbrel, S. B. Brown, D. A. Chapman, Z. Chen, C. B. Curry, F. Fiuza, E. Gamboa, M. Gauthier, D. O. Gericke, A. Gleason, S. Goede, E. Granados, P. Heimann, J. Kim, D. Kraus, M. J. MacDonald, A. J. Mackinnon, R. Mishra, A. Ravasio, C. Roedel, P. Sperling, W. Schumaker, Y. Y. Tsui, J. Vorberger, U Zastrau, A. Fry, W. E. White, J. B. Hasting, and H. J. Lee. Matter under extreme conditions experiments at the Linac Coherent Light Source. *Journal of Physics B: Atomic, Molecular and Optical Physics*, **49**(9):092001, 2016.

[84] G. Chabrier, P. Brassard, G. Fontaine, and D. Saumon. Cooling Sequences and Color-Magnitude Diagrams for Cool White Dwarfs with Hydrogen Atmospheres. *The Astrophysical Journal*, **543**(1):216, Nov. 2000.

[85] N. Nettelmann, K. Wang, J. J. Fortney, S. Hamel, S. Yellamilli, M. Bethkenhagen, and R. Redmer. Uranus evolution models with simple thermal boundary layers. *Icarus*, **275**(Supplement C):107–116, Sept. 2016.

[86] M. D. Knudson, M. P. Desjarlais, R. W. Lemke, T. R. Mattsson, M. French, N. Nettelmann, and R. Redmer. Probing the Interiors of the Ice Giants: Shock Compression of Water to 700 GPa and 3.8 g/cm^3. *Physical Review Letters*, **108**(9):091102, Feb. 2012.

[87] F. Soubiran, B. Militzer, K. P. Driver, and S. Zhang. Properties of hydrogen, helium, and silicon dioxide mixtures in giant planet interiors. *Physics of Plasmas*, **24**(4):041401, Mar. 2017.

[88] B. Militzer, W. B. Hubbard, J. Vorberger, I. Tamblyn, and S. A. Bonev. A Massive Core in Jupiter Predicted from First-Principles Simulations. *The Astrophysical Journal Letters*, **688**(1):L45, Nov. 2008.

[89] P. F. Schmit, P. F. Knapp, S. B. Hansen, M. R. Gomez, K. D. Hahn, D. B. Sinars, K. J. Peterson, S. A. Slutz, A. B. Sefkow, T. J. Awe, E. Harding, C. A. Jennings, G. A. Chandler, G. W. Cooper, M. E. Cuneo, M. Geissel, A. J. Harvey-Thompson, M. C. Herrmann, M. H. Hess, O. Johns, D. C. Lamppa, M. R. Martin, R. D. McBride, J. L. Porter, G. K. Robertson, G. A. Rochau, D. C. Rovang, C. L. Ruiz, M. E. Savage, I. C. Smith, W. A. Stygar, and R. A. Vesey. Understanding Fuel Magnetization and Mix Using Secondary Nuclear Reactions in Magneto-Inertial Fusion. *Physical Review Letters*, **113**(15):155004, Oct. 2014.

[90] R. Nora, W. Theobald, R. Betti, F. J. Marshall, D. T. Michel, W. Seka, B. Yaakobi, M. Lafon, C. Stoeckl, J. Delettrez, A. A. Solodov, A. Casner, C. Reverdin, X. Ribeyre, A. Vallet, J. Peebles, F. N. Beg, and M. S. Wei. Gigabar Spherical Shock Generation on the OMEGA Laser. *Physical Review Letters*, **114**(4):045001, Jan. 2015.

[91] S. X. Hu, B. Militzer, V. N. Goncharov, and S. Skupsky. First-principles equation-of-state table of deuterium for inertial confinement fusion applications. *Physical Review B*, **84**(22):224109, Dec. 2011.

[92] E. I. Moses, R. N. Boyd, B. A. Remington, C. J. Keane, and R. Al-Ayat. The National Ignition Facility: Ushering in a new age for high energy density science. *Physics of Plasmas*, **16**(4):041006, Apr. 2009.

[93] Y. Ding, A. Brachmann, F.-J. Decker, D. Dowell, P. Emma, J. Frisch, S. Gilevich, G. Hays, P. Hering, Z. Huang, R. Iverson, H. Loos, A. Miahnahri, H.-D. Nuhn, D. Ratner, J. Turner, J. Welch, W. White, and J. Wu. Measurements and Simulations of Ultralow Emittance and Ultrashort Electron Beams in the Linac Coherent Light Source. *Physical Review Letters*, **102**(25):254801, June 2009.

[94] L. B. Fletcher, H. J. Lee, T. Döppner, E. Galtier, B. Nagler, P. Heimann, C. Fortmann, S. LePape, T. Ma, M. Millot, A. Pak, D. Turnbull, D. A. Chapman, D. O. Gericke, J. Vorberger, T. White, G. Gregori, M. Wei, B. Barbrel, R. W. Falcone, C.-C. Kao, H. Nuhn, J. Welch, U. Zastrau, P. Neumayer, J. B. Hastings, and S. H. Glenzer. Ultrabright X-ray laser scattering for dynamic warm dense matter physics. *Nature Photonics*, **9**(4):274–279, Apr. 2015.

[95] P. Sperling, E. J. Gamboa, H. J. Lee, H. K. Chung, E. Galtier, Y. Omarbakiyeva, H. Reinholz, G. Röpke, U. Zastrau, J. Hastings, L. B. Fletcher, and S. H. Glenzer. Free-Electron X-Ray Laser Measurements of Collisional-Damped Plasmons in Isochorically Heated Warm Dense Matter. *Physical Review Letters*, **115**(11):115001, Sept. 2015.

[96] U. Zastrau, P. Sperling, M. Harmand, A. Becker, T. Bornath, R. Bredow, S. Dziarzhyt-ski, T. Fennel, L. B. Fletcher, E. Förster, S. Göde, G. Gregori, V. Hilbert, D. Hochhaus, B. Holst, T. Laarmann, H. J. Lee, T. Ma, J. P. Mithen, R. Mitzner, C. D. Murphy, M. Nakatsutsumi, P. Neumayer, A. Przystawik, S. Roling, M. Schulz, B. Siemer, S. Skruszewicz, J. Tiggesbäumker, S. Toleikis, T. Tschentscher, T. White, M. Wöst-mann, H. Zacharias, T. Döppner, S. H. Glenzer, and R. Redmer. Resolving Ultrafast Heating of Dense Cryogenic Hydrogen. *Physical Review Letters*, **112**(10):105002, Mar. 2014.

[97] T. Tschentscher, C. Bressler, J. Grünert, A. Madsen, A. P. Mancuso, M. Meyer, A. Scherz, H. Sinn, and U. Zastrau. Photon Beam Transport and Scientific Instruments at the European XFEL. *Applied Sciences*, **7**(6):592, June 2017.

[98] T. Ott, H. Thomsen, J. Abraham, T. Dornheim, and M. Bonitz. Recent progress in the theory and simulation of strongly correlated plasmas: phase transitions, transport, quantum, and magnetic field effects. *European Physics Journal D (in print)*, 2018.

[99] P. Balbuena and J. Seminario. *Molecular Dynamics: From Classical to Quantum Methods*. Theoretical and Computational Chemistry. Elsevier Science, 1999.

[100] M. P. Desjarlais. Density-functional calculations of the liquid deuterium Hugoniot, reshock, and reverberation timing. *Physical Review B*, **68**(6):064204, Aug. 2003.

[101] B. Holst, R. Redmer, and M. P. Desjarlais. Thermophysical properties of warm dense hydrogen using quantum molecular dynamics simulations. *Physical Review B*, **77**(18):184201, May 2008.

[102] B. Holst, M. French, and R. Redmer. Electronic transport coefficients from ab initio simulations and application to dense liquid hydrogen. *Physical Review B*, **83**(23):235120, June 2011.

[103] B. B. L. Witte, L. B. Fletcher, E. Galtier, E. Gamboa, H. J. Lee, U. Zastrau, R. Redmer, S. H. Glenzer, and P. Sperling. Warm Dense Matter Demonstrating Non-Drude Conductivity from Observations of Nonlinear Plasmon Damping. *Physical Review Letters*, **118**(22):225001, May 2017.

[104] N. D. Mermin. Thermal Properties of the Inhomogeneous Electron Gas. *Physical Review*, **137**(5A):A1441–A1443, Mar. 1965.

[105] U. Gupta and A. K. Rajagopal. Density functional formalism at finite temperatures with some applications. *Physics Reports*, **87**(6):259–311, July 1982.

[106] A. Pribram-Jones, S. Pittalis, E. K. U. Gross, and K. Burke. *Thermal Density Functional Theory in Context*, pages 25–60. Springer International Publishing, Cham, 2014.

[107] V. V. Karasiev, T. Sjostrom, J. Dufty, and S. B. Trickey. Accurate Homogeneous Electron Gas Exchange-Correlation Free Energy for Local Spin-Density Calculations. *Physical Review Letters*, **112**(7):076403, Feb. 2014.

[108] R. O. Jones. Density functional theory: Its origins, rise to prominence, and future. *Reviews of Modern Physics*, **87**(3):897–923, Aug. 2015.

[109] K. Burke. Perspective on density functional theory. *The Journal of Chemical Physics*, **136**(15):150901, Apr. 2012.

[110] R. O. Jones and O. Gunnarsson. The density functional formalism, its applications and prospects. *Reviews of Modern Physics*, **61**(3):689–746, July 1989.

[111] D. M. Ceperley and B. J. Alder. Ground State of the Electron Gas by a Stochastic Method. *Physical Review Letters*, **45**(7):566, 1980.

[112] S. H. Vosko, L. Wilk, and M. Nusair. Accurate spin-dependent electron liquid correlation energies for local spin density calculations: a critical analysis. *Canadian Journal of Physics*, **58**(8):1200–1211, Aug. 1980.

[113] J. P. Perdew and A. Zunger. Self-interaction correction to density-functional approximations for many-electron systems. *Physical Review B*, **23**(10):5048–5079, May 1981.

[114] J. P. Perdew, K. Burke, and M. Ernzerhof. Generalized Gradient Approximation Made Simple. *Physical Review Letters*, **77**(18):3865–3868, Oct. 1996.

[115] V. V. Karasiev, L. Calderín, and S. B. Trickey. Importance of finite-temperature exchange correlation for warm dense matter calculations. *Physical Review E*, **93**(6):063207, June 2016.

[116] M. W. C. Dharma-wardana. Current Issues in Finite-T Density-Functional Theory and Warm-Correlated Matter. *Computation*, **4**(2):16, Mar. 2016.

[117] T. Sjostrom and J. Daligault. Gradient corrections to the exchange-correlation free energy. *Physical Review B*, **90**(15):155109, Oct. 2014.

[118] J. W. Dufty. Density Functional Theory for the Electron Gas and for Jellium. *arXiv:1705.07495 [cond-mat.stat-mech]*, May 2017.

[119] W. Ebeling and W. Richert. Thermodynamic Functions of Nonideal Hydrogen Plasmas. *Annalen der Physik*, **494**(5):362–370, Jan. 1982.

[120] W. Ebeling. Free Energy and Ionization in Dense Plasmas of the Light Elements. *Contributions to Plasma Physics*, **30**(5):553–561, Jan. 1990.

[121] W. Ebeling and H. Lehmann. Nonideal Ionization in Plasmas with Higher Charges. *Contributions to Plasma Physics*, **29**(4-5):365–371, Jan. 1989.

[122] F. Perrot and M. W. C. Dharma-wardana. Spin-polarized electron liquid at arbitrary temperatures: Exchange-correlation energies, electron-distribution functions, and the static response functions. *Physical Review B*, **62**(24):16536–16548, Dec. 2000.

[123] S. Ichimaru, H. Iyetomi, and S. Tanaka. Statistical physics of dense plasmas: Thermodynamics, transport coefficients and dynamic correlations. *Physics Reports*, **149**(2):91–205, May 1987.

[124] S. Tanaka, S. Mitake, and S. Ichimaru. Parametrized equation of state for electron liquids in the Singwi-Tosi-Land-Sjölander approximation. *Phys.ical Review A*, **32**(3):1896–1899, Sept. 1985.

[125] S. Tanaka. Correlational and thermodynamic properties of finite-temperature electron liquids in the hypernetted-chain approximation. *The Journal of Chemical Physics*, **145**(21):214104, Dec. 2016.

[126] S. Tanaka. Improved equation of state for finite-temperature spin-polarized electron liquids on the basis of Singwi–Tosi–Land–Sjölander approximation. *Contributions to Plasma Physics*, **57**:126–136, Mar. 2017.

[127] E. W. Brown, J. L. DuBois, M. Holzmann, and D. M. Ceperley. Exchange-correlation energy for the three-dimensional homogeneous electron gas at arbitrary temperature. *Physical Review B*, **88**(8):081102, Aug. 2013.

[128] T. Sjostrom and J. Dufty. Uniform electron gas at finite temperatures. *Physical Review B*, **88**(11):115123, Sept. 2013.

[129] S. Groth, T. Dornheim, and M. Bonitz. Free energy of the uniform electron gas: Testing analytical models against first-principles results. *Contributions to Plasma Physics*, **57**(3):137–146, Mar. 2017.

[130] G. Baym and C. Pethick. *Landau Fermi-Liquid Theory: Concepts and Applications*. Wiley, 2008.

[131] G. Giuliani and G. Vignale. *Quantum Theory of the Electron Liquid*. Masters Series in Physics and Astronomy. Cambridge University Press, 2005.

[132] D. Pines and D. Bohm. A Collective Description of Electron Interactions: II. Collective vs Individual Particle Aspects of the Interactions. *Physical Review*, **85**(2):338–353, Jan. 1952.

[133] D. Bohm and D. Pines. A Collective Description of Electron Interactions: III. Coulomb Interactions in a Degenerate Electron Gas. *Physical Review*, **92**(3):609–625, Nov. 1953.

[134] J. Bardeen, L. N. Cooper, and J. R. Schrieffer. Theory of Superconductivity. *Physical Review*, **108**(5):1175–1204, Dec. 1957.

[135] G. Mahan. *Many-Particle Physics*. Physics of Solids and Liquids. Springer US, 1990.

[136] S. Huotari, J. A. Soininen, T. Pylkkänen, K. Hämäläinen, A. Issolah, A. Titov, J. McMinis, J. Kim, K. Esler, D. M. Ceperley, M. Holzmann, and V. Olevano. Momentum Distribution and Renormalization Factor in Sodium and the Electron Gas. *Physical Review Letters*, **105**(8):086403, Aug. 2010.

[137] E. Wigner. On the Interaction of Electrons in Metals. *Physical Review*, **46**(11):1002–1011, Dec. 1934.

[138] N. D. Drummond, Z. Radnai, J. R. Trail, M. D. Towler, and R. J. Needs. Diffusion quantum Monte Carlo study of three-dimensional Wigner crystals. *Physical Review B*, **69**(8):085116, Feb. 2004.

[139] P.-F. Loos and P. M. W. Gill. The uniform electron gas. *Wiley Interdisciplinary Reviews: Computational Molecular Science*, **6**(4):410–429, July 2016.

[140] F. H. Zong, C. Lin, and D. M. Ceperley. Spin polarization of the low-density three-dimensional electron gas. *Physical Review E*, **66**(3):036703, Sept. 2002.

[141] D. Michta, F. Graziani, and M. Bonitz. Quantum Hydrodynamics for Plasmas – a Thomas-Fermi Theory Perspective. *Contributions to Plasma Physics*, **55**(6):437–443, June 2015.

[142] A. Diaw and M. S. Murillo. A viscous quantum hydrodynamics model based on dynamic density functional theory. *Scientific Reports*, **7**(1):15352, Nov. 2017.

[143] G. Chabrier. Quantum effects in dense Coulumbic matter - Application to the cooling of white dwarfs. *The Astrophysical Journal*, **414**:695, Sept. 1993.

[144] A. Y. Potekhin and G. Chabrier. Thermodynamic Functions of Dense Plasmas: Analytic Approximations for Astrophysical Applications. *Contributions to Plasma Physics*, **50**(1):82–87, Jan. 2010.

[145] A. Y. Potekhin and G. Chabrier. Equation of state for magnetized Coulomb plasmas. *Astronomy & Astrophysics*, **550**:A43, Feb. 2013.

[146] F. G. Eich, M. Holzmann, and G. Vignale. Effective mass of quasiparticles from thermodynamics. *Physical Review B*, **96**(3):035132, July 2017.

[147] J. J. Shepherd, G. Booth, A. Grüneis, and A. Alavi. Full configuration interaction perspective on the homogeneous electron gas. *Physical Review B*, **85**(8):081103, Feb. 2012.

[148] J. J. Shepherd, A. Grüneis, G. H. Booth, G. Kresse, and A. Alavi. Convergence of many-body wave-function expansions using a plane-wave basis: From homogeneous electron gas to solid state systems. *Physical Review B*, **86**(3):035111, July 2012.

[149] J. J. Shepherd, G. H. Booth, and A. Alavi. Investigation of the full configuration interaction quantum Monte Carlo method using homogeneous electron gas models. *The Journal of Chemical Physics*, **136**(24):244101, June 2012.

[150] P. López Ríos, A. Ma, N. D. Drummond, M. D. Towler, and R. J. Needs. Inhomogeneous backflow transformations in quantum Monte Carlo calculations. *Physical Review E*, **74**(6):066701, Dec. 2006.

[151] D. Ceperley. Ground state of the fermion one-component plasma: A Monte Carlo study in two and three dimensions. *Physical Review B*, **18**(7):3126–3138, Oct. 1978.

[152] S. Ichimaru. Strongly coupled plasmas: high-density classical plasmas and degenerate electron liquids. *Reviews of Modern Physics*, **54**(4):1017–1059, Oct. 1982.

[153] E. W. Montroll and J. C. Ward. Quantum Statistics of Interacting Particles; General Theory and Some Remarks on Properties of an Electron Gas. *Physics of Fluids (1958-1988)*, **1**(1):55–72, Jan. 1958.

[154] A. L. Kutepov and G. Kotliar. One-electron spectra and susceptibilities of the three-dimensional electron gas from self-consistent solutions of Hedin's equations. *Physical Review B*, **96**(3):035108, July 2017.

[155] J. J. Kas and J. J. Rehr. Finite Temperature Green's Function Approach for Excited State and Thermodynamic Properties of Cool to Warm Dense Matter. *Physical Review Letters*, **119**(17):176403, Oct. 2017.

[156] F. D. Malone, N. S. Blunt, J. J. Shepherd, D. K. K. Lee, J. S. Spencer, and W. M. C. Foulkes. Interaction picture density matrix quantum Monte Carlo. *The Journal of Chemical Physics*, **143**(4):044116, July 2015.

[157] E. W. Brown, B. K. Clark, J. L. DuBois, and D. M. Ceperley. Path-Integral Monte Carlo Simulation of the Warm Dense Homogeneous Electron Gas. *Physical Review Letters*, **110**(14):146405, Apr. 2013.

[158] P. Arora, K. Kumar, and R. K. Moudgil. Spin-resolved correlations in the warm-dense homogeneous electron gas. *European Physics Journal B*, **90**(4):76, Apr. 2017.

[159] D. Kremp, T. Bornath, M. Schlanges, and W. Kraeft. *Quantum Statistics of Nonideal Plasmas*. Springer Series on Atomic, Optical, and Plasma Physics. Springer Berlin Heidelberg, 2006.

[160] J. Vorberger, M. Schlanges, and W. D. Kraeft. Equation of state for weakly coupled quantum plasmas. *Physical Review E*, **69**(4):046407, Apr. 2004.

[161] T. Dornheim, S. Groth, and M. Bonitz. The Uniform Electron Gas at Warm Dense Matter conditions. *arXiv:1801.05783 (submitted for publication to Physics Reports)*, 2018.

[162] S. Groth, T. Schoof, T. Dornheim, and M. Bonitz. Ab initio quantum Monte Carlo simulations of the uniform electron gas without fixed nodes. *Physical Review B*, **93**(8):085102, Feb. 2016.

[163] T. Dornheim, S. Groth, T. Schoof, C. Hann, and M. Bonitz. Ab initio quantum Monte Carlo simulations of the uniform electron gas without fixed nodes: The unpolarized case. *Physical Review B*, **93**(20):205134, May 2016.

[164] T. Dornheim, S. Groth, T. Sjostrom, F. D. Malone, W. M. C. Foulkes, and M. Bonitz. Ab Initio Quantum Monte Carlo Simulation of the Warm Dense Electron Gas in the Thermodynamic Limit. *Physical Review Letters*, **117**(15):156403, Oct. 2016.

[165] T. Dornheim, S. Groth, and M. Bonitz. Ab initio results for the static structure factor of the warm dense electron gas. *Contributions to Plasma Physics*, **57**(10):468–478, 2017.

[166] S. Groth, T. Dornheim, T. Sjostrom, F. D. Malone, W. M. C. Foulkes, and M. Bonitz. Ab initio Exchange-Correlation Free Energy of the Uniform Electron Gas at Warm Dense Matter Conditions. *Physical Review Letters*, **119**(13):135001, Sept. 2017.

[167] T. Dornheim, S. Groth, J. Vorberger, and M. Bonitz. Permutation-blocking path-integral Monte Carlo approach to the static density response of the warm dense electron gas. *Physical Review E*, **96**(2):023203, Aug. 2017.

[168] S. Groth, T. Dornheim, and M. Bonitz. Configuration path integral Monte Carlo approach to the static density response of the warm dense electron gas. *The Journal of Chemical Physics*, **147**(16):164108, Oct. 2017.

[169] Z. Moldabekov, S. Groth, T. Dornheim, M. Bonitz, and T. Ramazanov. Ion potential in non-ideal dense quantum plasmas. *Contributions to Plasma Physics*, **57**(10):532–538, 2017.

[170] J. L. DuBois, E. W. Brown, and B. J. Alder. Overcoming the fermion sign problem in homogeneous systems. *arXiv:1409.3262 [cond-mat]*, Sept. 2014.

[171] N. S. Blunt, T. W. Rogers, J. S. Spencer, and W. M. C. Foulkes. Density-matrix quantum Monte Carlo method. *Physical Review B*, **89**(24):245124, June 2014.

[172] N. S. Blunt, A. Alavi, and G. H. Booth. Krylov-Projected Quantum Monte Carlo Method. *Physical Review Letters*, **115**(5):050603, July 2015.

[173] S. Groth. *The Uniform Electron Gas at Wam Dense Matter Conditions: A Configuration Path Integral Monte Carlo Perspective (submitted)*. PhD thesis, Christian-Albrechts Universität zu Kiel, 2018.

[174] G. G. Spink, R. J. Needs, and N. D. Drummond. Quantum Monte Carlo study of the three-dimensional spin-polarized homogeneous electron gas. *Physical Review B*, **88**(8):085121, Aug. 2013.

[175] R. Egger and C. H. Mak. Multilevel blocking monte carlo simulations for quantum dots. *International Journal of Modern Physics B*, **15**(10n11):1416–1425, May 2001.

[176] M. Takahashi and M. Imada. Monte Carlo Calculation of Quantum Systems. II. Higher Order Correction. *Journal of the Physical Society of Japan*, **53**(11):3765–3769, Nov. 1984.

[177] S. A. Chin and C. R. Chen. Gradient symplectic algorithms for solving the Schrödinger equation with time-dependent potentials. *The Journal of Chemical Physics*, **117**(4):1409–1415, July 2002.

[178] K. Sakkos, J. Casulleras, and J. Boronat. High order Chin actions in path integral Monte Carlo. *The Journal of Chemical Physics*, **130**(20):204109, May 2009.

[179] H. Thomsen and M. Bonitz. Resolving structural transitions in spherical dust clusters. *Physical Review E*, **91**(4):043104, Apr. 2015.

[180] P. Ludwig. *Structure formation in strongly correlated few-particle systems in traps*. PhD thesis, Universität Rostock, 2008.

[181] H. Thomsen. *Melting Processes and Laser Manipulation of Strongly Coupled Yukawa Systems*. PhD thesis, Christian-Albrechts Universität zu Kiel, 2015.

[182] J. Böning, A. Filinov, P. Ludwig, H. Baumgartner, M. Bonitz, and Y. E. Lozovik. Melting of Trapped Few-Particle Systems. *Physical Review Letters*, **100**(11):113401, Mar. 2008.

[183] A. Filinov, M. Bonitz, and Y. Lozovik. Wigner Crystallization in Mesoscopic 2d Electron Systems. *Physical Review Letters*, **86**(17):3851–3854, Apr. 2001.

[184] A. Ghosal, A. D. Güçlü, C. J. Umrigar, D. Ullmo, and H. U. Baranger. Correlation-induced inhomogeneity in circular quantum dots. *Nature Physics*, **2**(5):336–340, May 2006.

[185] A. Ghosal, A. D. Güçlü, C. J. Umrigar, D. Ullmo, and H. U. Baranger. Incipient Wigner localization in circular quantum dots. *Physical Review B*, **76**(8):085341, Aug. 2007.

[186] V. Ballenegger. Communication: On the origin of the surface term in the Ewald formula. *The Journal of Chemical Physics*, **140**(16):161102, Apr. 2014.

[187] A. Y. Toukmaji and J. A. Board. Ewald summation techniques in perspective: a survey. *Computer Physics Communications*, **95**(2):73–92, June 1996.

[188] L. M. Fraser, W. M. C. Foulkes, G. Rajagopal, R. J. Needs, S. D. Kenny, and A. J. Williamson. Finite-size effects and Coulomb interactions in quantum Monte Carlo calculations for homogeneous systems with periodic boundary conditions. *Physical Review B*, **53**(4):1814–1832, Jan. 1996.

[189] S. W. d. Leeuw, J. W. Perram, and E. R. Smith. Simulation of electrostatic systems in periodic boundary conditions. I. Lattice sums and dielectric constants. *Proceeding of the Royal Society of London*, **373**(1752):27–56, Oct. 1980.

[190] E. H. Lieb and H. Narnhofer. The thermodynamic limit for jellium. *Journal of Statistical Physics*, **12**(4):291–310, Apr. 1975.

[191] C. Lin, F. H. Zong, and D. M. Ceperley. Twist-averaged boundary conditions in continuum quantum Monte Carlo algorithms. *Physical Review E*, **64**(1):016702, June 2001.

[192] S. Chiesa, D. M. Ceperley, R. M. Martin, and M. Holzmann. Finite-Size Error in Many-Body Simulations with Long-Range Interactions. *Physical Review Letters*, **97**(7):076404, Aug. 2006.

[193] N. D. Drummond, R. J. Needs, A. Sorouri, and W. M. C. Foulkes. Finite-size errors in continuum quantum Monte Carlo calculations. *Physical Review B*, **78**(12):125106, Sept. 2008.

[194] M. Holzmann, R. C. Clay, M. A. Morales, N. M. Tubman, D. M. Ceperley, and C. Pierleoni. Theory of finite size effects for electronic quantum Monte Carlo calculations of liquids and solids. *Physical Review B*, **94**(3):035126, July 2016.

[195] K. S. Singwi, M. P. Tosi, R. H. Land, and A. Sjölander. Electron Correlations at Metallic Densities. *Physical Review*, **176**(2):589–599, Dec. 1968.

[196] S. Tanaka and S. Ichimaru. Thermodynamics and Correlational Properties of Finite-Temperature Electron Liquids in the Singwi-Tosi-Land-Sjölander Approximation. *Journal of the Physical Society of Japan*, **55**(7):2278–2289, July 1986.

[197] A. A. Kugler. Bounds for Some Equilibrium Properties of an Electron Gas. *Physical Review A*, **1**(6):1688–1696, June 1970.

[198] S. Hellal, J.-G. Gasser, and A. Issolah. Static local-field correction from Monte Carlo studies of the homogeneous electron gas. *Physical Review B*, **68**(9):094204, Sept. 2003.

[199] Y. V. Arkhipov, A. B. Ashikbayeva, A. Askaruly, A. E. Davletov, and I. M. Tkachenko. Dielectric function of dense plasmas, their stopping power, and sum rules. *Physical Review E*, **90**(5):053102, Nov. 2014.

[200] V. V. Karasiev, J. W. Dufty, and S. B. Trickey. Nonempirical semi-local free-energy density functional for matter under extreme conditions. *arXiv:1612.06266 [cond-mat]*, Nov. 2017.

[201] H. Yasuhara and Y. Kawazoe. A note on the momentum distribution function for an electron gas. *Physica A: Statistical Mechanics and its Applications*, **85**(2):416–424, Jan. 1976.

[202] Y. Takada and H. Yasuhara. Momentum distribution function of the electron gas at metallic densities. *Physical Review B*, **44**(15):7879–7887, Oct. 1991.

[203] A. N. Starostin, A. B. Mironov, N. L. Aleksandrov, N. J. Fisch, and R. M. Kulsrud. Quantum corrections to the distribution function of particles over momentum in dense media. *Physica A: Statistical Mechanics and its Applications*, **305**(1–2):287–296, Mar. 2002.

[204] F. D. Malone, N. S. Blunt, E. W. Brown, D. K. K. Lee, J. S. Spencer, W. M. C. Foulkes, and J. J. Shepherd. Accurate Exchange-Correlation Energies for the Warm Dense Electron Gas. *Physical Review Letters*, **117**(11):115701, Sept. 2016.

[205] F. Perrot and M. W. C. Dharma-wardana. Exchange and correlation potentials for electron-ion systems at finite temperatures. *Physical Review A*, **30**(5):2619–2626, Nov. 1984.

[206] H. E. DeWitt. Statistical Mechanics of High-Temperature Quantum Plasmas Beyond the Ring Approximation. *Journal of Mathematical Physics*, **7**(4):616–626, Apr. 1966.

[207] W. Richert and W. Ebeling. Thermodynamic Functions of the Electron Fluid for a Wide Density—Temperature Range. *physica status solidi (b)*, **121**(2):633–639, Feb. 1984.

[208] W. Ebeling and W. Richert. Plasma phase transition in hydrogen. *Physics Letters A*, **108**(2):80–82, Mar. 1985.

[209] S. Ichimaru. Nuclear fusion in dense plasmas. *Reviews of Modern Physics*, **65**(2):255–299, Apr. 1993.

[210] M. W. C. Dharma-wardana and F. Perrot. Simple Classical Mapping of the Spin-Polarized Quantum Electron Gas: Distribution Functions and Local-Field Corrections. *Physical Review Letters*, **84**(5):959–962, Jan. 2000.

[211] P. Vashishta and K. S. Singwi. Electron Correlations at Metallic Densities. V. *Physical Review B*, **6**(3):875–887, Aug. 1972.

[212] W. Stolzmann and M. Rösler. Static Local-Field Corrected Dielectric and Thermodynamic Functions. *Contributions to Plasma Physics*, **41**(2-3):203–206, Mar. 2001.

[213] K. Burke, J. C. Smith, P. E. Grabowski, and A. Pribram-Jones. Exact conditions on the temperature dependence of density functionals. *Physical Review B*, **93**(19):195132, May 2016.

[214] A. A. Kugler. Theory of the local field correction in an electron gas. *Journal of Statistical Physics*, **12**(1):35–87, Jan. 1975.

[215] D. Lu. Evaluation of model exchange-correlation kernels in the adiabatic connection fluctuation-dissipation theorem for inhomogeneous systems. *The Journal of Chemical Physics*, **140**(18):18A520, May 2014.

[216] C. E. Patrick and K. S. Thygesen. Adiabatic-connection fluctuation-dissipation DFT for the structural properties of solids—The renormalized ALDA and electron gas kernels. *The Journal of Chemical Physics*, **143**(10):102802, Sept. 2015.

[217] A. Pribram-Jones, P. E. Grabowski, and K. Burke. Thermal Density Functional Theory: Time-Dependent Linear Response and Approximate Functionals from the Fluctuation-Dissipation Theorem. *Physical Review Letters*, **116**(23):233001, June 2016.

[218] L. Mühlbacher and E. Rabani. Real-Time Path Integral Approach to Nonequilibrium Many-Body Quantum Systems. *Physical Review Letters*, **100**(17):176403, May 2008.

[219] M. Schiró and M. Fabrizio. Real-time diagrammatic Monte Carlo for nonequilibrium quantum transport. *Physical Review B*, **79**(15):153302, Apr. 2009.

[220] M. Schiró. Real-time dynamics in quantum impurity models with diagrammatic Monte Carlo. *Physical Review B*, **81**(8):085126, Feb. 2010.

[221] S. Moroni, D. M. Ceperley, and G. Senatore. Static response from quantum Monte Carlo calculations. *Physical Review Letters*, **69**(13):1837–1840, Sept. 1992.

[222] S. Moroni, D. M. Ceperley, and G. Senatore. Static Response and Local Field Factor of the Electron Gas. *Physical Review Letters*, **75**(4):689–692, July 1995.

[223] G. Sugiyama, C. Bowen, and B. J. Alder. Static dielectric response of charged bosons. *Physical Review B*, **46**(20):13042–13050, Nov. 1992.

[224] C. Bowen, G. Sugiyama, and B. J. Alder. Static dielectric response of the electron gas. *Physical Review B*, **50**(20):14838–14848, Nov. 1994.

[225] M. Corradini, R. Del Sole, G. Onida, and M. Palummo. Analytical expressions for the local-field factor $G(q)$ and the exchange-correlation kernel $K_{xc}(r)$ of the homogeneous electron gas. *Physical Review B*, **57**(23):14569–14571, June 1998.

[226] K.-C. Ng. Hypernetted chain solutions for the classical one-component plasma up to gamma=7000. *The Journal of Chemical Physics*, **61**(7):2680–2689, Oct. 1974.

[227] Y. Liu and J. Wu. A bridge-functional-based classical mapping method for predicting the correlation functions of uniform electron gases at finite temperature. *The Journal of Chemical Physics*, **140**(8):084103, Feb. 2014.

[228] H. K. Schweng and H. M. Böhm. Finite-temperature electron correlations in the framework of a dynamic local-field correction. *Physical Review B*, **48**(4):2037–2045, July 1993.

[229] A. Holas and S. Rahman. Dynamic local-field factor of an electron liquid in the quantum versions of the Singwi-Tosi-Land-Sjölander and Vashishta-Singwi theories. *Physical Review B*, **35**(6):2720–2731, Feb. 1987.

[230] M. Motta, D. E. Galli, S. Moroni, and E. Vitali. Imaginary time correlations and the phaseless auxiliary field quantum Monte Carlo. *The Journal of Chemical Physics*, **140**(2):024107, Jan. 2014.

[231] M. Motta, D. E. Galli, S. Moroni, and E. Vitali. Imaginary time density-density correlations for two-dimensional electron gases at high density. *The Journal of Chemical Physics*, **143**(16):164108, Oct. 2015.

[232] B. Tanatar and D. M. Ceperley. Ground state of the two-dimensional electron gas. *Physical Review B*, **39**:5005–5016, Mar 1989.

[233] C. H. Mak, R. Egger, and H. Weber-Gottschick. Multilevel Blocking Approach to the Fermion Sign Problem in Path-Integral Monte Carlo Simulations. *Physical Review Letters*, **81**(21):4533–4536, Nov. 1998.

[234] S. M. Reimann and M. Manninen. Electronic structure of quantum dots. *Reviews of Modern Physics*, **74**(4):1283–1342, Nov. 2002.

[235] J. Harting, O. Mülken, and P. Borrmann. Interplay between shell effects and electron correlations in quantum dots. *Physical Review B*, **62**(15):10207–10211, Oct. 2000.

[236] S. Weiss and R. Egger. Path-integral monte carlo simulations for interacting few-electron quantum dots with spin-orbit coupling. *Physical Review B*, **72**:245301, Dec 2005.

[237] R. Egger, W. Häusler, C. H. Mak, and H. Grabert. Crossover from fermi liquid to wigner molecule behavior in quantum dots. *Physical Review Letters*, **82**:3320–3323, Apr 1999.

[238] G. Kelbg. Theorie des Quanten-Plasmas. *Annalen der Physik*, **467**(3-4):219–224, 1963.

[239] A. V. Filinov, V. O. Golubnychiy, M. Bonitz, W. Ebeling, and J. W. Dufty. Temperature-dependent quantum pair potentials and their application to dense partially ionized hydrogen plasmas. *Physical Review E*, **70**:046411, Oct 2004.

[240] W. Ebeling, A. Filinov, M. Bonitz, V. Filinov, and T. Pohl. The method of effective potentials in the quantum-statistical theory of plasmas. *Journal of Physics A: Mathematical and General*, **39**(17):4309, 2006.

[241] R. G. Storer. Path-Integral Calculation of the Quantum-Statistical Density Matrix for Attractive Coulomb Forces. *Journal of Mathematical Physics*, **9**(6):964–970, June 1968.

[242] E. L. Pollock. Properties and computation of the Coulomb pair density matrix. *Computer Physics Communications*, **52**(1):49–60, Dec. 1988.

[243] R. E. Zillich. Combination of the pair density approximation and the Takahashi–Imada approximation for path integral Monte Carlo simulations. *Journal of Computational Physics*, **301**:111–118, Nov. 2015.

[244] C. Gao, S. Zhang, W. Kang, C. Wang, P. Zhang, and X. T. He. Validity boundary of orbital-free molecular dynamics method corresponding to thermal ionization of shell structure. *Physical Review B*, **94**(20):205115, Nov. 2016.

[245] S. Zhang, H. Wang, W. Kang, P. Zhang, and X. T. He. Extended application of Kohn-Sham first-principles molecular dynamics method with plane wave approximation at high energy—From cold materials to hot dense plasmas. *Physics of Plasmas*, **23**(4):042707, Apr. 2016.

[246] F. Lambert, J. Clérouin, and S. Mazevet. Structural and dynamical properties of hot dense matter by a Thomas-Fermi-Dirac molecular dynamics. *EPL (Europhysics Letters)*, **75**(5):681, Aug. 2006.

[247] F. Lambert, J. Clérouin, S. Mazevet, and D. Gilles. Properties of Hot Dense Plasmas by Orbital-Free Molecular Dynamics. *Contributions to Plasma Physics*, **47**(4-5):272–280, July 2007.

[248] V. V. Karasiev, T. Sjostrom, and S. B. Trickey. Generalized-gradient-approximation noninteracting free-energy functionals for orbital-free density functional calculations. *Physical Review B*, **86**(11):115101, Sept. 2012.

[249] T. Sjostrom and J. Daligault. Fast and Accurate Quantum Molecular Dynamics of Dense Plasmas Across Temperature Regimes. *Physical Review Letters*, **113**(15):155006, Oct. 2014.

[250] V. V. Karasiev, T. Sjostrom, and S. B. Trickey. Finite-temperature orbital-free DFT molecular dynamics: Coupling Profess and Quantum Espresso. *Computer Physics Communications*, **185**(12):3240–3249, Dec. 2014.

[251] J. Schleede, A. Filinov, M. Bonitz, and H. Fehske. Phase Diagram of Bilayer Electron-Hole Plasmas. *Contributions to Plasma Physics*, **52**(10):819–826, Nov. 2012.

[252] P. Ludwig, K. Balzer, A. Filinov, H. Stolz, and M. Bonitz. On the Coulomb–dipole transition in mesoscopic classical and quantum electron–hole bilayers. *New Journal of Physics*, **10**(8):083031, Aug. 2008.

[253] A. Filinov, P. Ludwig, M. Bonitz, and Y. E. Lozovik. Effective interaction potential and superfluid–solid transition of spatially indirect excitons. *Journal of Physics A: Mathematical and Theoretical*, **42**(21):214016, May 2009.

[254] S. Giorgini, L. P. Pitaevskii, and S. Stringari. Theory of ultracold atomic fermi gases. *Reviews of Modern Physics*, **80**:1215–1274, Oct 2008.

[255] I. Bloch, J. Dalibard, and W. Zwerger. Many-body physics with ultracold gases. *Reviews of Modern Physics*, **80**:885–964, Jul 2008.

[256] A. G. Truscott, K. E. Strecker, W. I. McAlexander, G. B. Partridge, and R. G. Hulet. Observation of fermi pressure in a gas of trapped atoms. *Science*, **291**(5513):2570–2572, 2001.

[257] A. Perali, P. Pieri, L. Pisani, and G. C. Strinati. BCS-BEC Crossover at Finite Temperature for Superfluid Trapped Fermi Atoms. *Physical Review Letters*, **92**:220404, Jun 2004.

[258] Y. Ohashi and A. Griffin. BCS-BEC Crossover in a Gas of Fermi Atoms with a Feshbach Resonance. *Physical Review Letters*, **89**:130402, Sep 2002.

[259] G. Chabrier and A. Y. Potekhin. Equation of state of fully ionized electron-ion plasmas. *Physical Review E*, **58**(4):4941–4949, Oct. 1998.

[260] D. Saumon and G. Chabrier. Fluid hydrogen at high density: Pressure dissociation. *Physical Review A*, **44**(8):5122–5141, Oct. 1991.

[261] B. Farid, V. Heine, G. E. Engel, and I. J. Robertson. Extremal properties of the Harris-Foulkes functional and an improved screening calculation for the electron gas. *Physical Review B*, **48**(16):11602–11621, Oct. 1993.

[262] B. J. Berne. Path integral Monte Carlo methods: Static- and time-correlation functions. *Journal of Statistical Physics*, **43**(5-6):911–929, June 1986.

[263] M. Jarrell and J. E. Gubernatis. Bayesian inference and the analytic continuation of imaginary-time quantum Monte Carlo data. *Physics Reports*, **269**(3):133–195, May 1996.

[264] R. N. Silver, D. S. Sivia, and J. E. Gubernatis. Maximum-entropy method for analytic continuation of quantum Monte Carlo data. *Physical Review B*, **41**(4):2380–2389, Feb. 1990.

[265] R. Levy, J. P. F. LeBlanc, and E. Gull. Implementation of the maximum entropy method for analytic continuation. *Computer Physics Communications*, **215**(Supplement C):149–155, June 2017.

[266] A. S. Mishchenko, N. V. Prokof'ev, A. Sakamoto, and B. V. Svistunov. Diagrammatic quantum Monte Carlo study of the Fröhlich polaron. *Physical Review B*, **62**(10):6317–6336, Sept. 2000.

[267] J. Schött, E. G. C. P. van Loon, I. L. M. Locht, M. I. Katsnelson, and I. Di Marco. Comparison between methods of analytical continuation for bosonic functions. *Physical Review B*, **94**(24):245140, Dec. 2016.

[268] E. Vitali, M. Rossi, L. Reatto, and D. E. Galli. Ab initio low-energy dynamics of superfluid and solid ^{4}He. *Physical Review B*, **82**(17), Nov. 2010.

[269] P. A. Martin. Sum rules in charged fluids. *Reviews of Modern Physics*, **60**(4):1075–1127, Oct. 1988.

[270] Y. Takada. Emergence of an excitonic collective mode in the dilute electron gas. *Physical Review B*, **94**(24):245106, Dec. 2016.

[271] G. J. Kalman, K. I. Golden, and L. G. Silvestri. Correlation induced second plasmon in an electron liquid. *arXiv:1609.09029 [cond-mat, physics:physics]*, Sept. 2016.

[272] N.-H. Kwong and M. Bonitz. Real-Time Kadanoff-Baym Approach to Plasma Oscillations in a Correlated Electron Gas. *Physical Review Letters*, **84**(8):1768–1771, Feb. 2000.

[273] M. Bonitz. *Quantum Kinetic Theory*. Springer International Publishing, 2015.

[274] G. Stefanucci and R. van Leeuwen. *Nonequilibrium Many-Body Theory of Quantum Systems: A Modern Introduction*. Cambridge University Press, 2013.

[275] G. Gregori, A. Ravasio, A. Höll, S. H. Glenzer, and S. J. Rose. Derivation of the static structure factor in strongly coupled non-equilibrium plasmas for X-ray scattering studies. *High Energy Density Physics*, **3**(1–2):99–108, May 2007.

Acknowledgements

First and foremost, I would like to thank Prof. Dr. Michael Bonitz for giving me the opportunity to pursue my PhD in his group, and for suggesting this interesting topic. It was him, who sparked my interest in theoretical physics in the first place in a Bachelor's course on quantum theory, and who (thankfully) nudged me into the direction of quantum Monte Carlo simulations during my Master's degree.

Second, I am highly indebted to Priv.-Doz. Dr. Alexei Filinov, who introduced me to the world of quantum Monte Carlo simulations. His in-depth knowledge of this topic can hardly be overstated and I will always consider my apprenticeship and subsequent collaboration with him a true privilege.

Moreover, I am sincerely grateful to my friend, colleague, and office room mate Simon Groth for his close collaboration, both during our Master's and PhD theses. In addition to his large contribution to the present thesis, he truly improved my method of operating, both at work and beyond, and I gladly acknowledge his influence on my perception of the world.

In addition, I want to thank all members of our group, and, in particular, Niclas Schlünzen, Tim Schoof, and Patrick Ludwig for many interesting and stimulating discussions and their companionship during innumerable trips and conferences. Further, I am grateful to Patrick, Niclas, and Simon for thoroughly proofreading this thesis. Needless to say, that all remaining errors are entirely my own fault.

Finally, I would like to sincerely thank my parents Susanne and Andreas Dornheim, for their perennial support throughout my life and, in particular, during my time as a Bachelor, Master, and PhD student.

Selbstständigkeitserklärung

Ich erkläre, dass die vorliegende Dissertation nach Inhalt und Form meine eigene Arbeit darstellt und unter Einhaltung der Regeln guter wissenschaftlicher Praxis der Deutschen Forschungsgemeinschaft entstanden ist. Ausgewählte Ergebnisse wurden in den in Abschnitt 1.3.1 angegebenen Fachartikeln publiziert, was an entsprechender Stelle in dieser Arbeit gekennzeichnet wurde. Weiterhin bestätige ich, dass diese Arbeit weder ganz noch in Teilen in einem anderen Prüfungsverfahren zur Begutachtung vorgelegen hat.

———————————————

Tobias Dornheim

Kiel, den 22. Januar 2018